

4

GL-TR-90-0033(II)
ENVIRONMENTAL RESEARCH PAPERS, NO. 1053

AD-A220 382

**Atmospheric Density and Aerodynamic Drag
Models for Air Force Operations**

**Proceedings of Workshop Held at AFGL
20-22 October 1987**

EDITOR:

FRANK A. MARCOS



13 February 1990

DTIC
APR 12 1990
Co E



Approved for public release; distribution unlimited.



IONOSPHERIC PHYSICS DIVISION
GEOPHYSICS LABORATORY
PROJECT 4643
HANSCOM AFB, MA 01731-5000

BEST

AVAILABLE

COPY

REPORT DOCUMENTATION PAGE			Form Approved OMB No. 0704-0188	
<small>Public reporting burden for this collection of information is estimated to average 1 hour per response, including the time for reviewing instructions, searching existing data sources, gathering and maintaining the data needed, and completing and reviewing the collection of information. Send comments regarding this burden estimate or any other aspect of this collection of information, including suggestions for reducing this burden, to Washington Headquarters Services, Directorate for Information Operations and Reports, 1215 Jefferson Davis Highway, Suite 1204, Arlington, VA 22202-4302, and to the Office of Management and Budget, Paperwork Reduction Project (0704-0188), Washington, DC 20503.</small>				
1. AGENCY USE ONLY (leave blank)	2. REPORT DATE 13 February 1990	3. REPORT TYPE AND DATES COVERED Scientific Interim		
4. TITLE AND SUBTITLE Atmospheric Density and Aerodynamic models for Air Force Operations		5. FUNDING NUMBERS		
6. AUTHOR(S) Frank A. Marcos (ED)		PE 62101F PR4643 TA14 WU01		
7. PERFORMING ORGANIZATION NAME(S) AND ADDRESS(ES) Geophysics Laboratory (LIS) Hanscom AFB, MA 01731-5000		8. PERFORMING ORGANIZATION REPORT NUMBER GL-TR-90-0033(II) ERP, No. 1053		
9. SPONSORING/MONITORING AGENCY NAME(S) AND ADDRESS(ES) Same as Above		10. SPONSORING/MONITORING AGENCY REPORT NUMBER		
11. SUPPLEMENTARY NOTES Volume I consists of pages 1 - 1 through 4 - 196. Volume II consists of pages 5 - 1 through 9 - 10.				
12a. DISTRIBUTION/AVAILABILITY STATEMENT Approved for public release; Distribution unlimited		12b. DISTRIBUTION CODE		
13. ABSTRACT (If maximum 200 words) This report contains papers presented at a Workshop on Atmospheric Density and Aerodynamic Drag Models for Air Force Operations held at the Air Force Geophysics Laboratory from 20-22 Oct 87. The major objective was to assess the capability for significant improvement in models of absolute density, winds, temperature and composition. Emphasis was focused on the altitude region 80-250 Km. Papers were presented in the following areas: Air Force requirements, physics of density and drag variability, empirical models, thermospheric general circulation models, new density and drag measurement techniques (direct and remote sensing), aerodynamic drag coefficients, and solar and magnetospheric inputs. A set of recommendations for improved modeling capabilities was developed by the participants.				
14. SUBJECT TERMS Upper Atmosphere Density; Models of Upper Atmosphere; Neutral Density; Density Specification; Density Forecasting; Satellite Drag		15. NUMBER OF PAGES 424		
		16. PRICE CODE		
17. SECURITY CLASSIFICATION OF REPORT UNCLASSIFIED	18. SECURITY CLASSIFICATION OF THIS PAGE UNCLASSIFIED	19. SECURITY CLASSIFICATION OF ABSTRACT UNCLASSIFIED	20. LIMITATION OF ABSTRACT SAR	

PREFACE

The meeting concept was strongly supported by Col John R. Kidd, AFGL Commander and Robert A. Skrivanek, Director, Ionospheric Physics Division. Vital help in planning and conducting the meeting came from the following members of the Ionospheric Physics Division: David Anderson, Dorothy Gillette, John Rasmussen, Dwight Sipler, Phan Dao, Lt. Ross McNutt, Wayne Klemetti, John Borghetti, and Nadine Mayo; from Charles Howard, Aerospace Instrumentation Division and Robert Stuart of Systems Integration Engineering, and from the Workshop chairmen: Capt Tom Schott, Timothy L. Killeen, Raymond G. Roble, Paul Hays, Jeffrey M. Forbes, Robert Blanchard, Herbert C. Carlson and Nelson Maynard.

Accession For	
REF ID: A6441	<input checked="" type="checkbox"/>
REF ID: A6441	<input checked="" type="checkbox"/>
REF ID: A6441	<input type="checkbox"/>
REF ID: A6441	<input type="checkbox"/>
By _____	
Date _____	
Approved by _____	
Initials _____	
Dist _____	
A-1	



CONTENTS

1. Overview

1.1 Introduction

1.2 Meeting Agenda

2. Air Force Requirements

2.1 Air Weather Service's Neutral Atmospheric Model

2.2 Point Density Specification

2.3 X-30 National Aero-space Plane (NASP) Environmental Support

2.4 Atmospheric Density Models in Operational Systems

3. Physics of Density and Drag Variability

3.1 Mesosphere-Thermosphere Coupling

3.2 Atmospheric Gravity Waves

3.3 Tidal Effects on Thermospheric Circulation, Densities and Temperatures

3.4 Thermosphere Dynamics and Its Influence on Atmospheric Density: The Dynamics Explorer Experience

3.5 Thermosphere Dynamics: Recent Contributions from Dynamics Explorer-2

4. New Density and Drag Measurements

- 4.1 AFGL Lidar Facility**
- 4.2 Lidar and Rocket Measurements of Atmospheric Structure Properties**
- 4.3 Gravity Wave Density Variations Inferred from Ground-Based Radar Measurements of Winds in the Lower Thermosphere**
- 4.4 Incoherent Scatter Density**
- 4.5 Incoherent Scatter Measurements of High-Latitude Lower Thermospheric Density and Dynamics**
- 4.6 Remote Measurement of Upper Atmospheric Density**
- 4.7 Determination of Atomic Oxygen Density and Temperature of the Thermosphere By Remote Sensing**
- 4.8 Atmospheric Density Measurements with the Remote Atmospheric and Ionospheric Detection System (RAIDS)**
- 4.9 The Atmospheric Density Specification Satellite (ADS)**
- 4.10 Accelerometer Measurements of Density and Winds for ADS**
- 4.11 ADS Mass Spectrometer Absolute Density**
- 4.12 In Situ Measurements of the Neutral Wind and Their Application to the ADS Mission**
- 4.13 Fabry-Perot Interferometer for ADS**
- 4.14 Shuttle Reentry Density Measurements (Between 60 and 160 km)**

5. Empirical Models

- 5.1 MSIS-86 Empirical Model Status and Future Directions**
- 5.2 Atmospheric Structure Between 80 and 120 Km**
- 5.3 GRAM Model and Various NASA Density Measurement Projects**
- 5.4 Accuracy of Satellite Drag Models**

6. Thermospheric General Circulation Models

- 6.1 Modeling the Global Structure of the Thermosphere: Circulation, Temperature and Density**
- 6.2 Numerical Computation of Thermospheric Density, Using Coupled Ionospheric/Thermospheric Codes and Parameterised Solar and Geomagnetic Inputs**
- 6.3 Developing an Operational Version of Thermosphere General Circulation Models**
- 6.4 Future Thermospheric General Circulation Model (TGCM) Needs**
- 6.5 Thermosphere-Ionosphere-Magnetosphere Coupling**
- 6.6 Ionospheric Coupling With Thermosphere General Circulation Models**
- 6.7 Global Thermospheric Specifications and Forecasting**

7. Drag Coefficients

- 7.1 High Altitude Drag Coefficients**
- 7.2 Direct Simulation Monte Carlo (DSMC) Drag Predictions**
- 7.3 Satellite Drag and Lift Deduced From Measured Gas-Surface Interaction at 5 ev**

7.4 Variability in the Satellite Drag Coefficient, CD

7.5 Satellite Drag Coefficient Variability

7.6 Drag Coefficients-Remarks

8. Solar and Magnetospheric Inputs

8.1 Solar X-Ray, EUV and UV Flux

8.2 Solar Flares and the Solar EUV Flux

8.3 Ground-Based Solar Coronal Observations as a Possible Input to Atmospheric Models

8.4 Taking the First Steps in Real-Time EUV Monitoring for Drag: the Series of USAF-NOAA Solar X-Ray Imagers (SXIs) on GOES

8.5 Solar Activity Measurements Experiment (SAMEX) on the High Resolution Solar Observatory (HRSO)

8.6 SIMPL

8.7 Absolute Extreme Ultraviolet Solar Spectral Irradiance Monitor (AESSIM)

8.8 The Geomagnetic Activity Outlook for 1987-1997 (Cycle 22)

8.9 Magnetospheric Convection and DMSP

8.10 Particles and Joule Energy Input

8.11 Solar and Magnetospheric Inputs/ Summary

9. Summary and Conclusions

Attendance List

5. *EMPIRICAL MODELS*

MSIS-86 Empirical Model Status and Future Directions
by A. E. Hedin (NASA/GSFC) for AFGL workshop Oct. 20-22, 1987

1. Introduction

Empirical models of the upper atmosphere can be divided into several historically related series (Fig. 1). The US Standard Atmospheres trace back to early efforts to establish atmospheric standards by the International Civil Aviation Organization (ICAO) and the Air Research and Development Command (ARDC) of the U. S. Air Force, starting before the era of satellite measurements. These models provide altitude profiles of temperature and density for one or a small number of places and geophysical conditions taken to be typical or average for the atmosphere. They are neither intended nor suitable for detailed comparison with satellite or rocket data taken globally and under a wide variety of conditions.

The Committee on Space Research (COSPAR) has issued a series of COSPAR International Reference Atmospheres (CIRA) which essentially adopted previously published models.

With the detection of atmospheric drag effects in early artificial satellites, data became available which led to the well known series of Jacchia models. The J65 model was the earliest comprehensive global model based on satellite drag (orbital decay) and had a lower boundary at 120 km. This model was the first to include the principal types of thermospheric density variations and, unlike the standard atmospheres, provides an approximation to the true spatial and temporal variations of the thermosphere. While drag based models use temperature and composition as intermediate parameters for the calculation of total density, these intermediate parameters may be in error since drag data provide no direct information on composition and temperature. The J77 model introduced separate pseudo-temperatures for each constituent, but this significant artificial complication was only partially successful in reproducing composition variations.

The OGO-6 satellite mass spectrometer launched in 1969 provided the first extensive measurements of the densities of molecular nitrogen, atomic oxygen, and helium in the thermosphere. Their sum provides an independent determination of total density. The observed variations in composition were quite different from the Jacchia model predictions and led to a new approach to represent the observed variability. The ground based incoherent scatter measurements of temperature were subsequently combined with the in situ composition measurements in the MSIS (Mass Spectrometer and Incoherent Scatter) models to produce composition and temperature as well as total density predictions of equivalent accuracy for various geographical, temporal, and solar conditions. The latest model, MSIS-86, was chosen for CIRA 1986, but publication of CIRA 1986 has been delayed.

The database for MSIS-86 (Fig. 2) consists of composition, temperature, and density data from scientific satellites with in situ thermospheric measurements as well as rockets (for the lower thermosphere) and ground based incoherent scatter stations. The predicted thermospheric variability between 100 and 300 km will be illustrated for the principal variations. Solar EUV, as represented by the average F10.7 cm flux, has the largest single influence on the thermosphere (Fig. 3 shows log base e variations for total density) with a factor of 5 from solar minimum to maximum at 300 km. Variations correlated with short term F10.7 variations (daily minus mean) are about one third as large. Magnetic activity variations can be almost as large as EUV variations (Fig 4 for $A_p=100$). Differences between pole and equator are relatively small in total density. Under quiet magnetic conditions (Fig. 5) latitude variations in the upper thermosphere are very small (5%). Global annual and semiannual variations are about plus or minus 20% (Fig. 6)

but do not vary strongly with altitude. Daily variations are of the same order of magnitude (Fig. 7) but change amplitude and period with altitude such that semidiurnal variations are more important in the lower thermosphere (a fact not included in Jacchia's models) and the diurnal amplitude grows with altitude. Pure seasonal variations (Fig. 8) are somewhat smaller than daily variations in the upper thermosphere. The magnetic pole rotating around the geographical pole produces UT variations (Fig. 9) on the order of 5% in total density and longitudinal variations are the same order or smaller. In all cases except the EUV and global annual/semiannual variations, the temperature and composition variations are much larger than the total density variations with out of phase behavior (not realized before mass spectrometer measurements) of various constituents resulting in smaller net effects.

II. Present accuracy

Comparisons of measured total densities with various models (Fig. 10 showing standard deviations and Fig. 11 showing absolute differences, both in terms of log to base e) indicates a general accuracy of 15% in the 200 to 400 km range with somewhat better accuracy down to 150 km and 25 to 30% at higher altitudes. With some exceptions, inter-model differences are small and not of great significance.

The data set labeled Jacchia drag, for instance, consists of densities determined from orbital decay by the Smithsonian group and were used in generating the Jacchia models but not the MSIS models. The comparison results point to both consistency (within 15%) between two quite different techniques (mass spectrometer and drag) and between two different time periods, since the drag data generally come from a much older time period than the mass spectrometer measurements. While total density predictions have improved relatively little, if at all, the predictions of composition and temperature have improved dramatically.

Turning to the AE-C OSS mass spectrometer measurements, these were a major factor in generating MSIS-77 and the fit here is quite good (10%) but gets worse for the later models where later data became more important. However, the fit for the Jacchia drag data got better between MSIS-77 and MSIS-86 illustrating that the more diverse database for MSIS-86 did help provide a better fit for the rather diverse Jacchia data set. Thus more data certainly does help to provide better overall predictions in a statistical sense, but may not help for a particular narrow data set unless new insights are gained.

One possibility to go beyond the current accuracy limit is to discover new systematic variations. Comparisons of the Jacchia drag data with MSIS-86 and J70 (Fig. 12 and 13), for example, show systematic variations F10.7 (difference between daily and mean) which suggest the opportunity for improvement. However, note that even if these plots were flat the standard deviation (as shown by the error bars for the binned data) would still be quite large. There is unlikely to be any single simple undiscovered systematic variation that is going to make a dramatic difference in our predictive capability, but a number of small improvements may make a significant cumulative effect.

Comparisons of the Jacchia drag data with MSIS-86 over the course of years (Fig. 14, 15, and 16) show evidence that the global annual/semiannual variation is not the same from year to year (note 1967 and 1968). This is a well known phenomena and is not understood. The dominant source for the semiannual variation is not known. Gaining a better understanding of the sources may lead to better predictive capabilities. Until that day it is clear that the best model we can make now from a given data set may not predict next years density correctly if the semiannual variation changes.

The AE-C OSS (mass spectrometer) and MESA (accelerometer) data both have small

systematic differences with the MSIS-86 model as a function of latitude (Fig. 17 and 18) which are not identical. The instrument ratios (Fig. 19) vary with latitude on the order of 10 to 15%. No model can be better than 15% unless we understand the source of these technique differences. AE-D data (Fig. 20) show similar effects.

It is possible that the instrumental differences noted above are caused by wind, although this is by no means certain. In any case, it is clear that large winds blow in the polar region (Fig. 21 illustrates winds for a quiet equinox day from an empirical model being developed. The plot grid is too coarse to show the largest polar winds.) and a 200 m/sec wind has a 5% effect on drag and a 2.5% effect on a mass spectrometer density measurement. Winds around 400 m/sec are not atypical in the quiet polar thermosphere and much larger during storms. Little has been done to this point to correct density measurements or to correct drag force calculations given a model. Note that to some degree an empirical density model will average out wind errors if the measurements are made under sufficiently diverse conditions, but standard deviations may be correspondingly high.

III. Directions for improvement

The causes for the current accuracy limit in density predictions seem to be diverse, ranging from uncertainty in absolute measurements and differences between techniques, to complex systematic variations yet to be discovered, to natural variability in the thermosphere and its variations (e.g. semiannual) which we may or may not be able to easily predict, and to short time scale aperiodic forcing (e.g. magnetic storms) which may be better predicted by theoretical models if the true spatial and temporal variability of the energy input can be measured and specified. Wave activity will provide an ultimate floor on point predictions on the order of 5% in the upper thermosphere, depending on latitude, and to an unknown degree in the lower thermosphere. Significant improvement will only come from a multifaceted attack (Fig. 22) which must involve further analysis of old measurements as well as new measurement programs since without measurements to the required accuracy and a complete specification of wave activity, there is no appropriate standard for model improvements.

Historical Development of Empirical Thermosphere Models

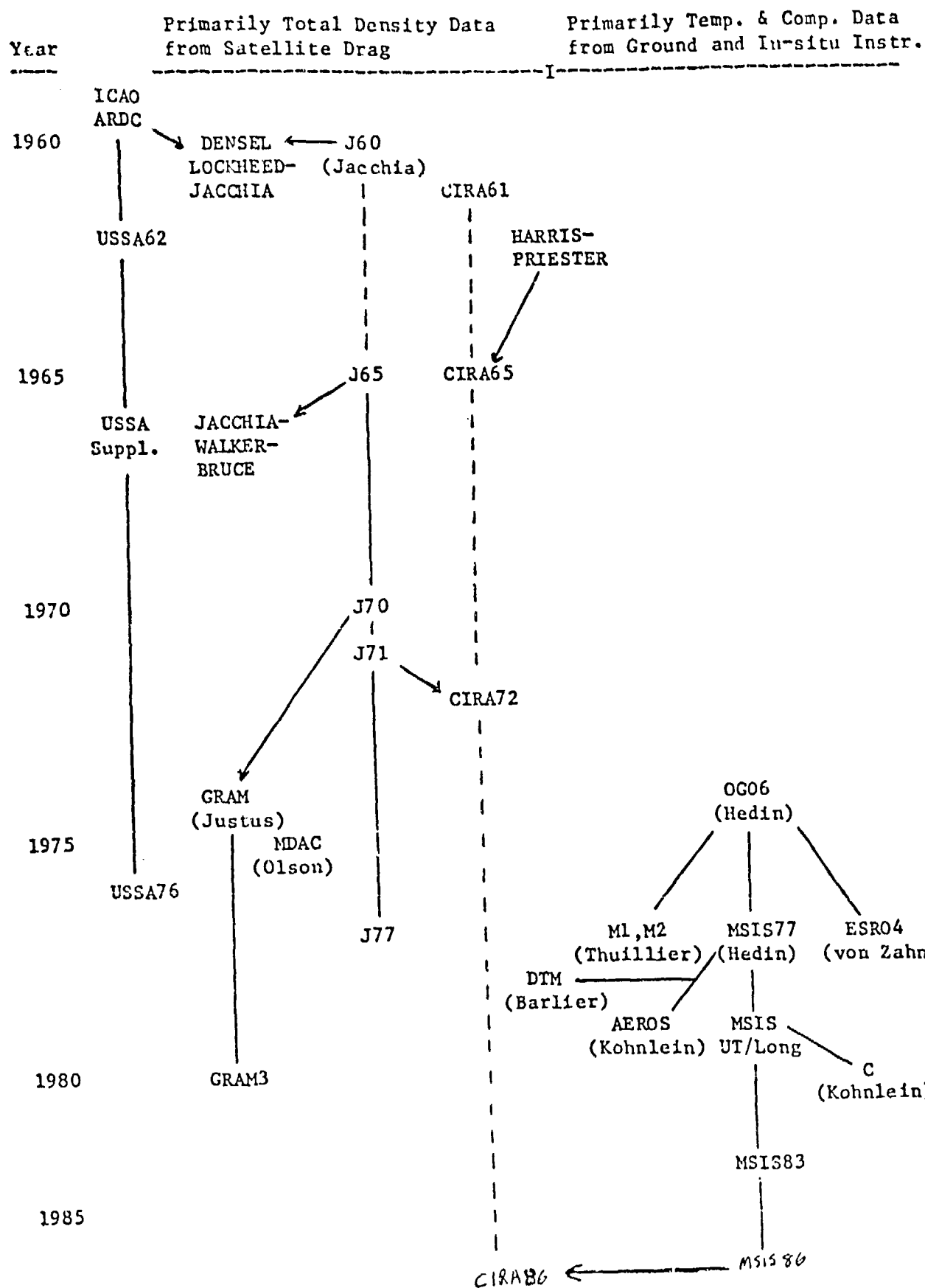


Fig. 1

Table 1. Data Sources for CIRA 1986

Data Set	Measurement	Nominal Altitudes	References
OGJ-6 (MS)	N ₂ , O, He	400-700 km	[29][5]
San Marco-3 (MS)	N ₂ , O, He, Ar	160-250 km	[30][31]
Aeros-A NATE (MS)	N ₂ , O, He, Ar	200-500 km	[32][33]
AE-C NATE (MS)	N ₂ , O, He, Ar	250-400 km	[34]
AE-C NATE (MS)	Tp	135-300 km	[34]
AE-C GSS (MS)	N ₂ , O, He, Ar, O ₂ , N	140-500 km	[35][36][37][38]
AE-C BIMS (IMS)	H	200-500 km	[39][40]
AE-C MIMS (IMS)	H	160-300 km	[17]
AE-C EUVS (absorp)	O ₂	100-150 km	[41][42]
AE-D OSS (MS)	N ₂ , O, He, Ar, O ₂ , N	140-450 km	[35][36][37][43]
AE-D NATE (MS)	Tp	140-400 km	[34]
AE-E NACE (MS)	N ₂ , O, He, Ar	140-450 km	[44]
AE-E NATE (MS)	Tp	140-400 km	[34]
AE-E OSS (MS)	O ₂ , N	140-400 km	[35][36][37][45]
AE-E BIMS (IMS)	H	200-500 km	[39][40]
AE-E EUVS (absorp)	O ₂	100-150 km	[41][42]
ESRO-4 (MS)	N ₂ , O, He, Ar	200-350 km	[46][47][48][39]
DE-B NACS (MS)	N ₂ , O, He, Ar, N	200-900 km	[50][28][65]
DE-B WATS (MS)	Tp	200-500 km	[64]
Rockets (MS)	N ₂ , Ar, O ₂ , Tp	100-300 km	[51][52][53][54]
Rockets (absorp)	O ₂	120-150 km	[51][55]
Rockets (gauge)	Rho, Tp	85-130 km	[55][56]
Rockets (falling sphere)	Rho, Tp	85-120 km	[55][56]
Rockets (grenade)	Rho, Tp	85-110 km	[55][56]
Millstone Hill (IS)	Tp	100-130 km	[22][25]
Millstone Hill (IS)	Tp	Exospheric	[57][27]
St. Santin (IS)	Tp	Exospheric	[58]
Arecibo (IS)	Tp	Exospheric	[59]
Arecibo (IS)	Tp, N ₂	100-135 km	[60]
Jicamarca (IS)	Tp	Exospheric	[61]
Malvern (IS)	Tp	240-400 km	[62][63]

Tp: neutral temperature either measured directly or indirectly from ion temperature; Rho: total mass density; MS: neutral mass spectrometer; IMS: ion mass spectrometer; IS: incoherent scatter.

Fig. 2

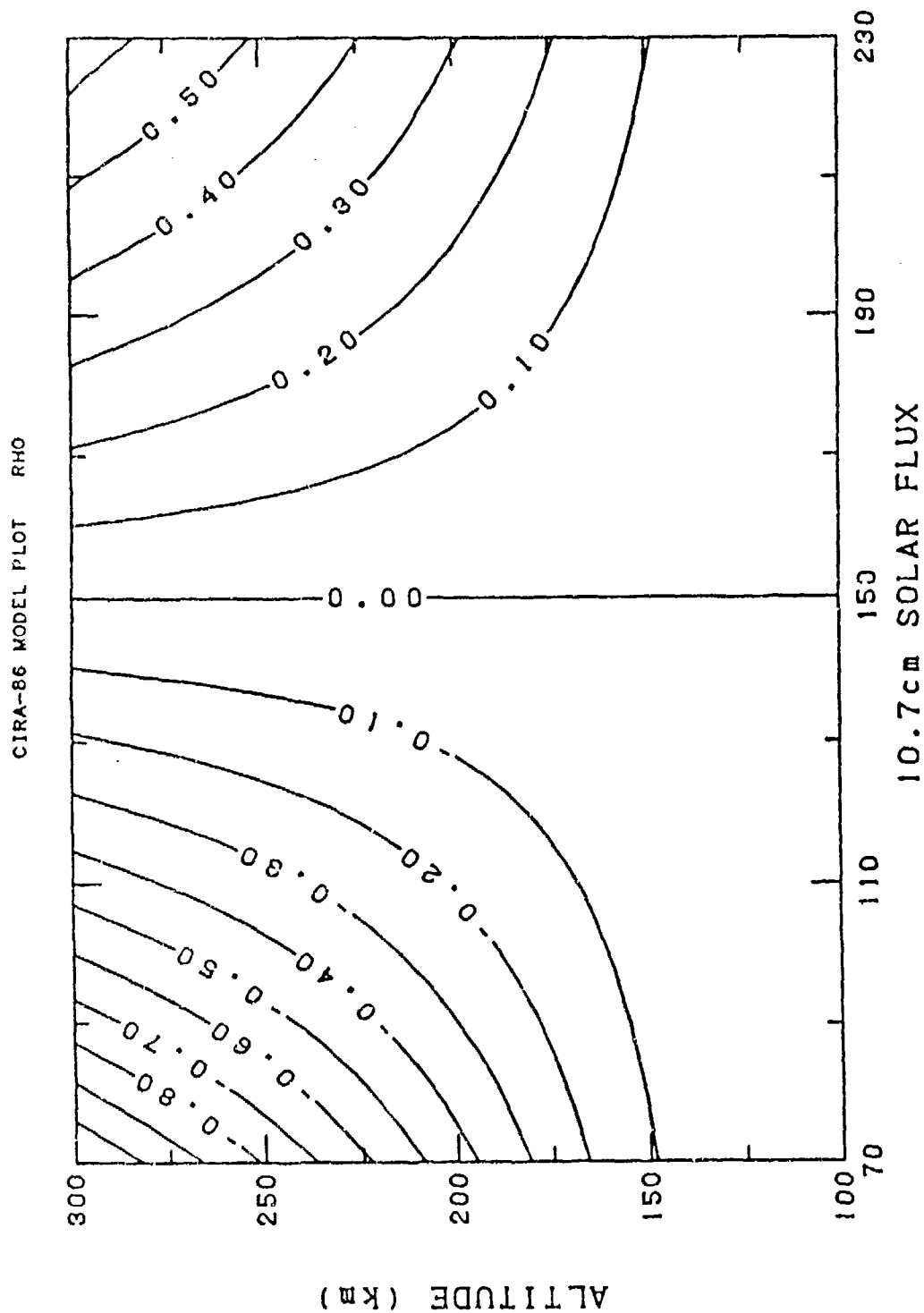


Fig. 3

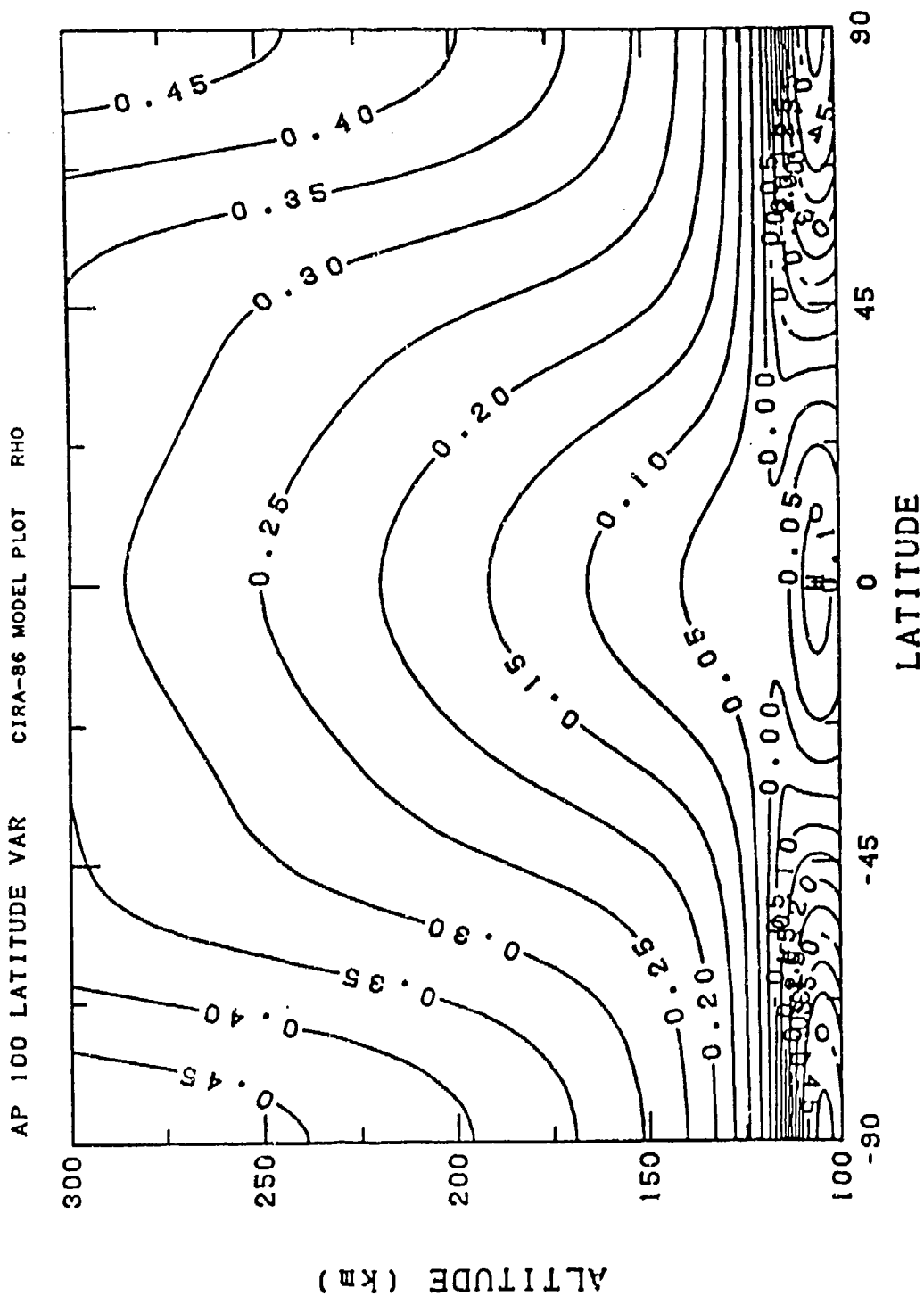


Fig. 4

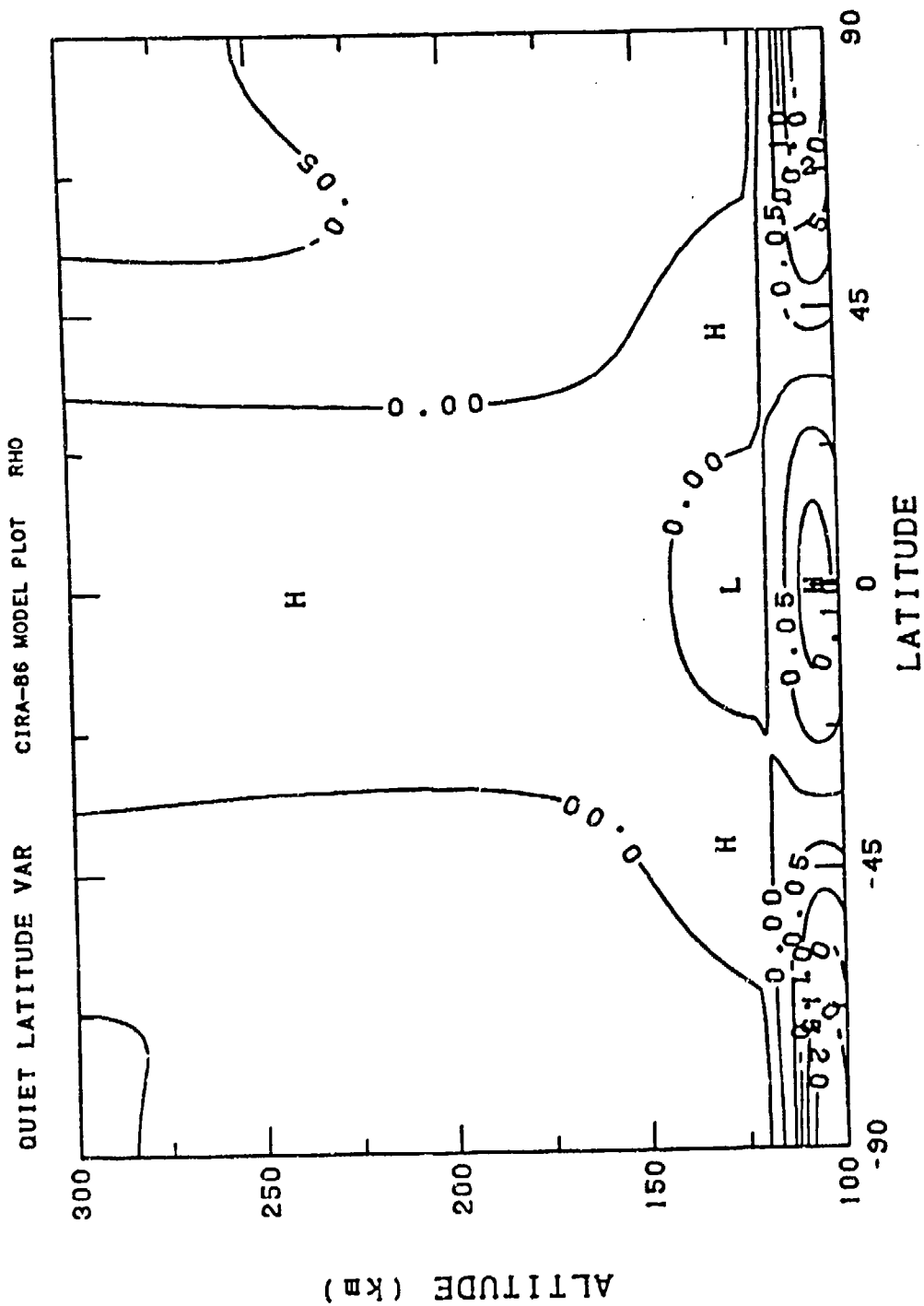


Fig. 5

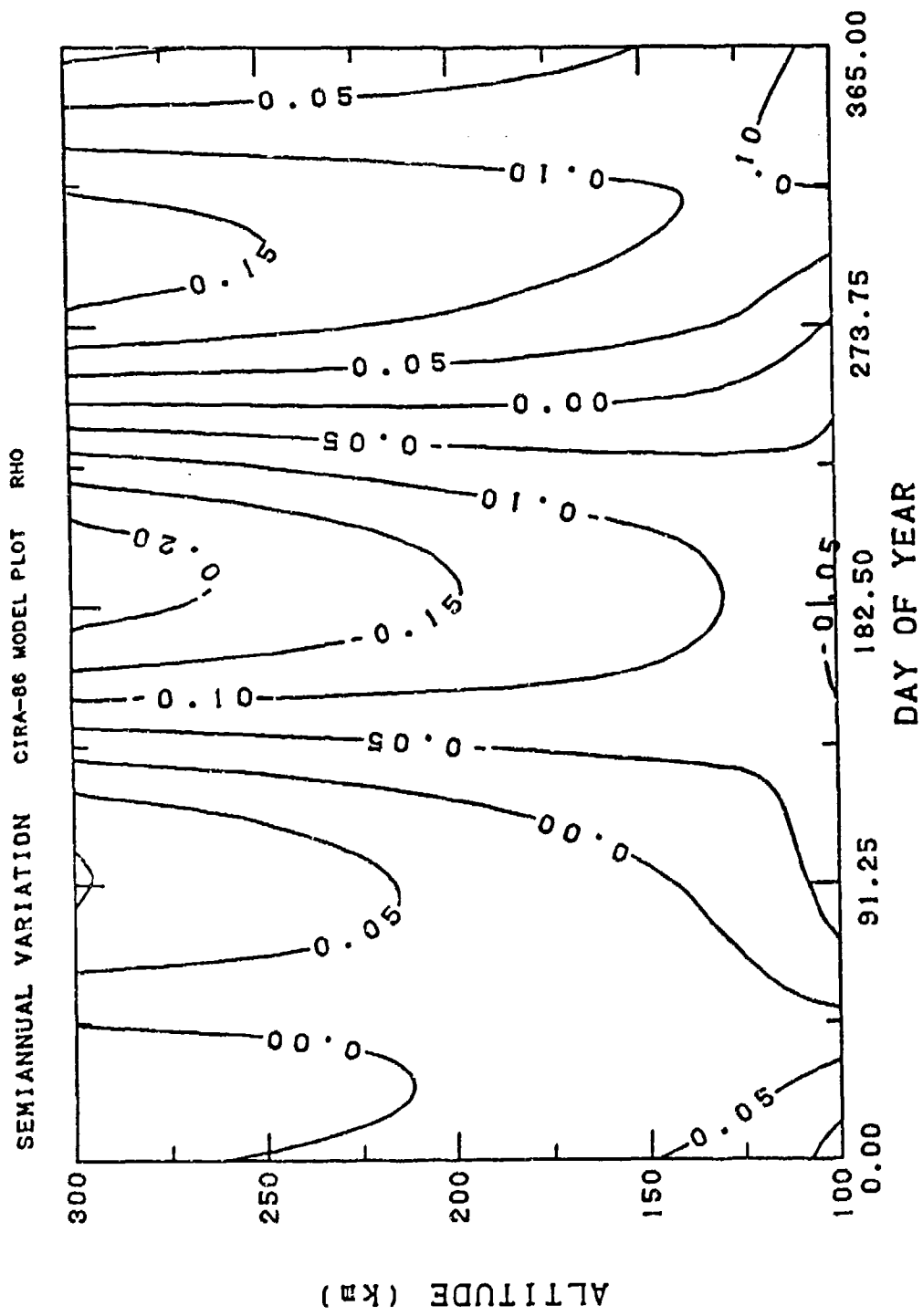


Fig. 6

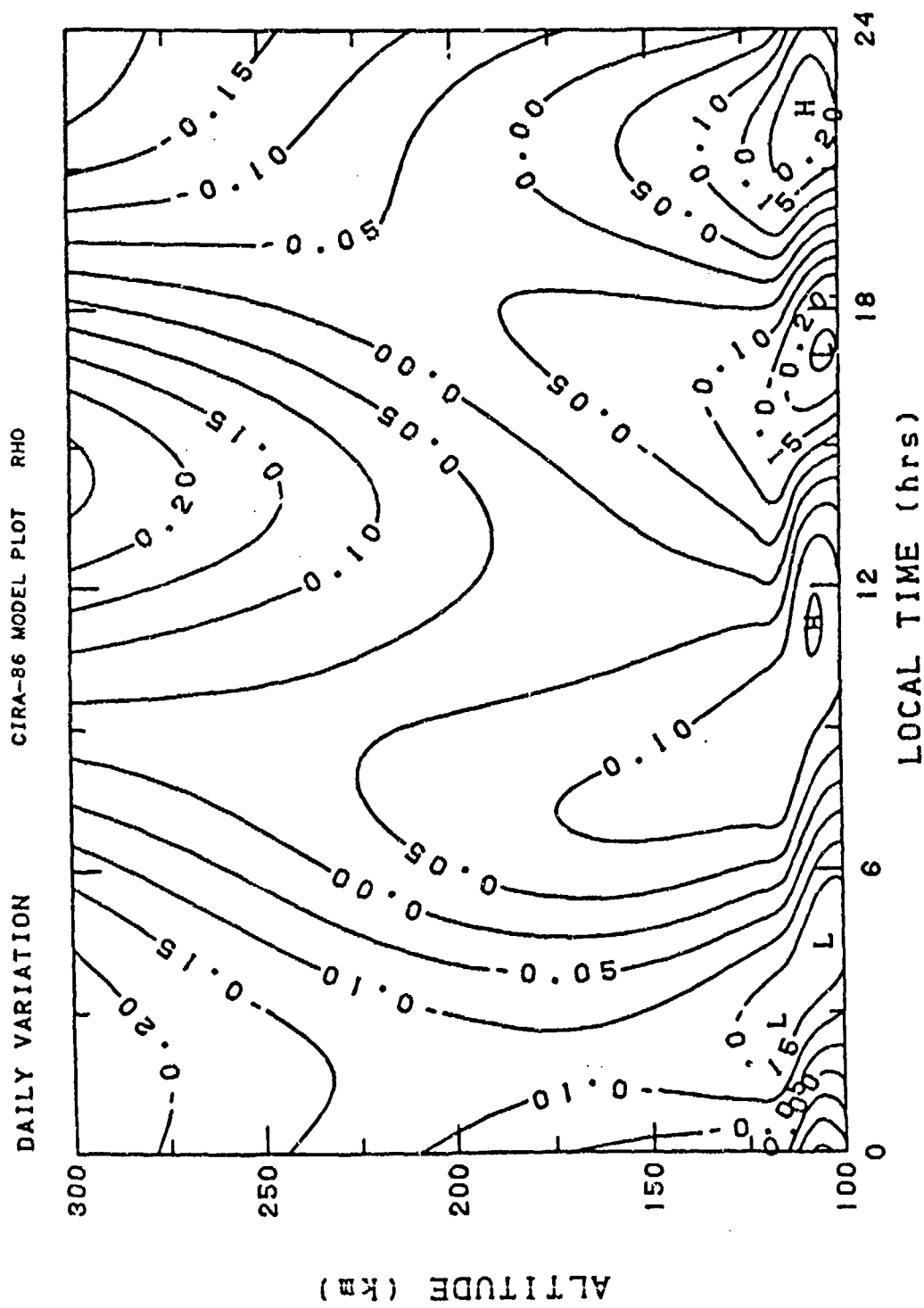


Fig. 7

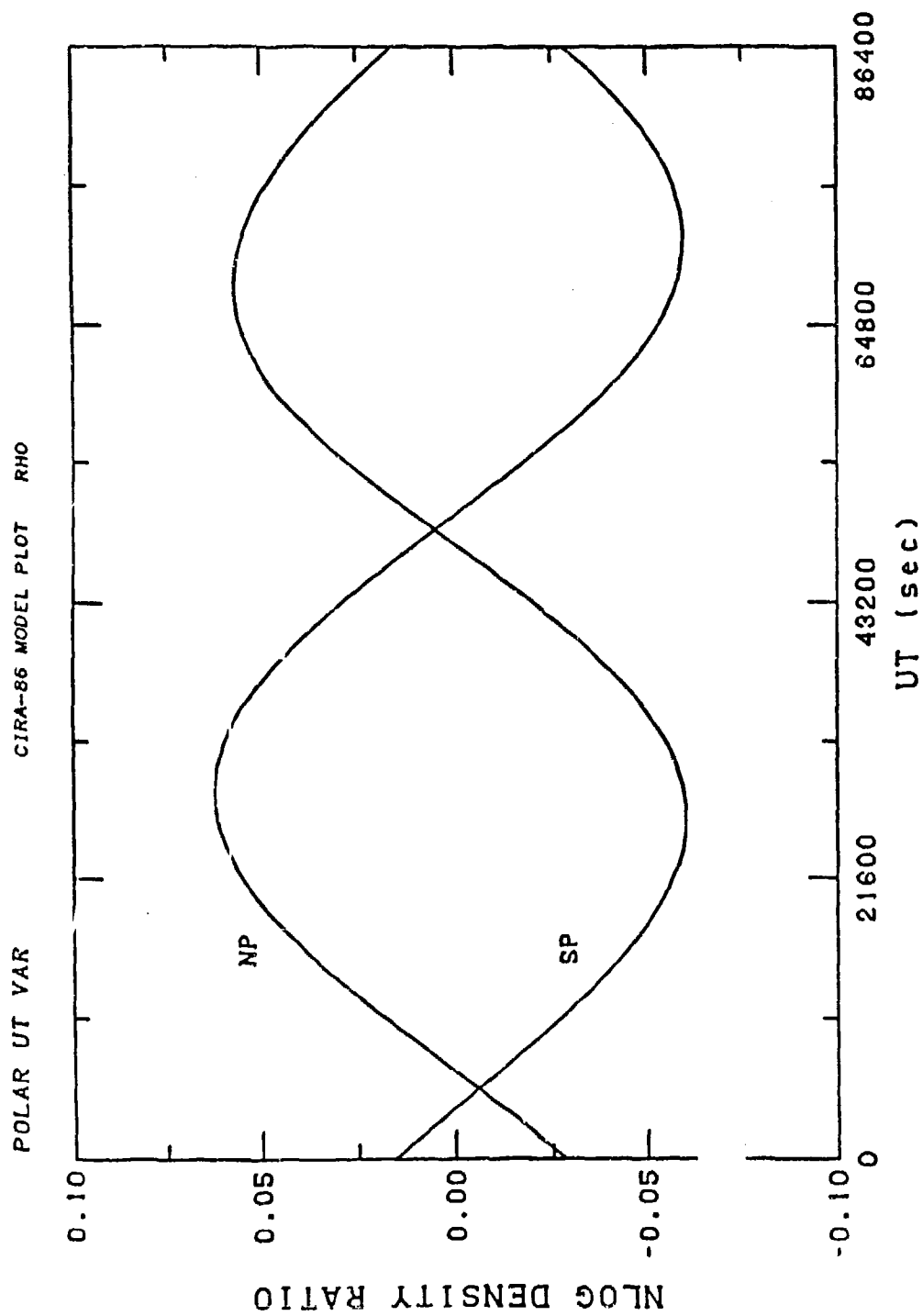


Fig. 9

Overall Standard Deviation (magnetically quiet)

(preliminary)

	Alt	Pts	MSIS-86	MSIS-83	MSIS-77	J77	J70
Jacchia	200-400	3197	.15 (1)	.16 (2)	.18 (3)	.15 (1)	.16 (2)
drag	400-800	6516	.26 (2)	.26 (2)	.29 (3)	.25 (1)	.26 (2)
	800-1200	3386	.27 (3)	.26 (2)	.30 (4)	.29 (3)	.22 (1)
Barlier	120-200	1050	.22 (1)	.23 (2)	.22 (1)	.22 (1)	.23 (2)
drag	200-400	4761	.20 (1)	.20 (1)	.21 (2)	.21 (2)	.21 (2)
	400-800	1447	.31 (1)	.31 (1)	.33 (3)	.32 (2)	.31 (1)
AE-C MESA	120-200	5746(.25)	.16 (2)	.16 (2)	.15 (1)	.18 (3)	.18 (3)
accel	200-250	6101(.55)	.21 (1)	.21 (1)	.21 (1)	.21 (1)	.21 (1)
AE-C OSS	120-200	6447(.65)	.12 (2)	.12 (2)	.10 (1)	.13 (3)	.13 (3)
ms	200-390	6279(.2)	.14 (1)	.14 (1)	.14 (1)	.15 (2)	.16 (3)
AE-D MESA	120-200	11024(.7)	.15 (2)	.15 (2)	.14 (1)	.15 (2)	.14 (1)
accel	200-250	4399	.18 (1)	.19 (2)	.18 (1)	.18 (1)	.18 (1)
AE-D OSS	120-200	11787	.11 (1)	.11 (1)	.11 (1)	.13 (2)	.11 (1)
ms	200-390	10923(.75)	.17 (1)	.18 (2)	.18 (2)	.17 (1)	.17 (1)
			1-9	1-5	1-8	1-6	1-7
			2-4	2-9	2-2	2-5	2-4
			3-1	3-0	3-3	3-3	3-3
			4-0	4-0	4-1	4-0	4-0

Fig. 10

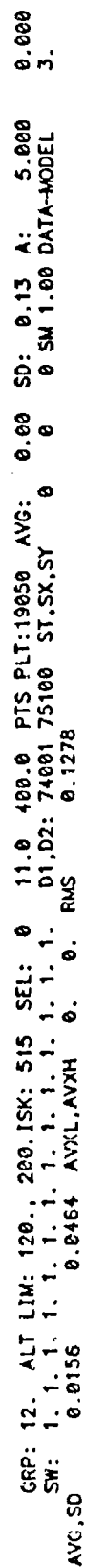
Overall mean (magnetically quiet)

(preliminary)

	Alt	Pts	MSIS-86	MSIS-83	MSIS-77	J77	J70
Jacchia	200-400	3197	-.05 (3)	-.05 (3)	-.21 (4)	-.03 (1)	-.04 (2)
drag	400-800	6516	-.05 (1)	-.06 (2)	-.23 (3)	-.05 (1)	-.06 (2)
	800-1200	3386	.04 (2)	.04 (2)	-.04 (2)	-.03 (1)	-.05 (3)
Barlier	120-200	1050	.02 (1)	-.03 (2)	-.02 (1)	-.04 (3)	-.07 (4)
drag	200-400	4761	.04 (3)	.02 (1)	-.06 (4)	-.04 (3)	.03 (2)
	400-800	1447	.10 (2)	.10 (2)	-.04 (1)	.10 (2)	.15 (3)
AE-C MESA	120-200	5746(.25)	.11 (3)	.11 (3)	.05 (2)	.05 (2)	.00 (1)
accel	200-250	6101(.55)	.02 (1)	.04 (3)	-.08 (4)	.03 (2)	-.03 (2)
AE-C OSS	120-200	6447(.65)	-.01 (1)	-.01 (1)	-.05 (3)	-.02 (2)	-.07 (4)
ms	200-390	6279(.2)	.02 (2)	.06 (3)	-.08 (4)	.09 (5)	.01 (1)
AE-D MESA	120-200	11024(.7)	-.03 (3)	.00 (1)	.00 (1)	.02 (2)	-.02 (2)
accel	200-250	4399	-.08 (3)	-.04 (2)	-.11 (4)	.01 (1)	-.04 (2)
AE-D OSS	120-200	11787	-.01 (1)	.01 (1)	.01 (1)	.04 (2)	.01 (1)
ms	200-390	10923(.75)	-.06 (3)	-.02 (1)	-.20 (4)	.03 (2)	-.03 (2)
			1-5	1-5	1-4	1-4	1-3
			2-3	2-5	2-2	2-7	2-7
			3-6	3-4	3-2	3-2	3-2
			4-0	4-0	4-6	4-0	4-2
						5-1	

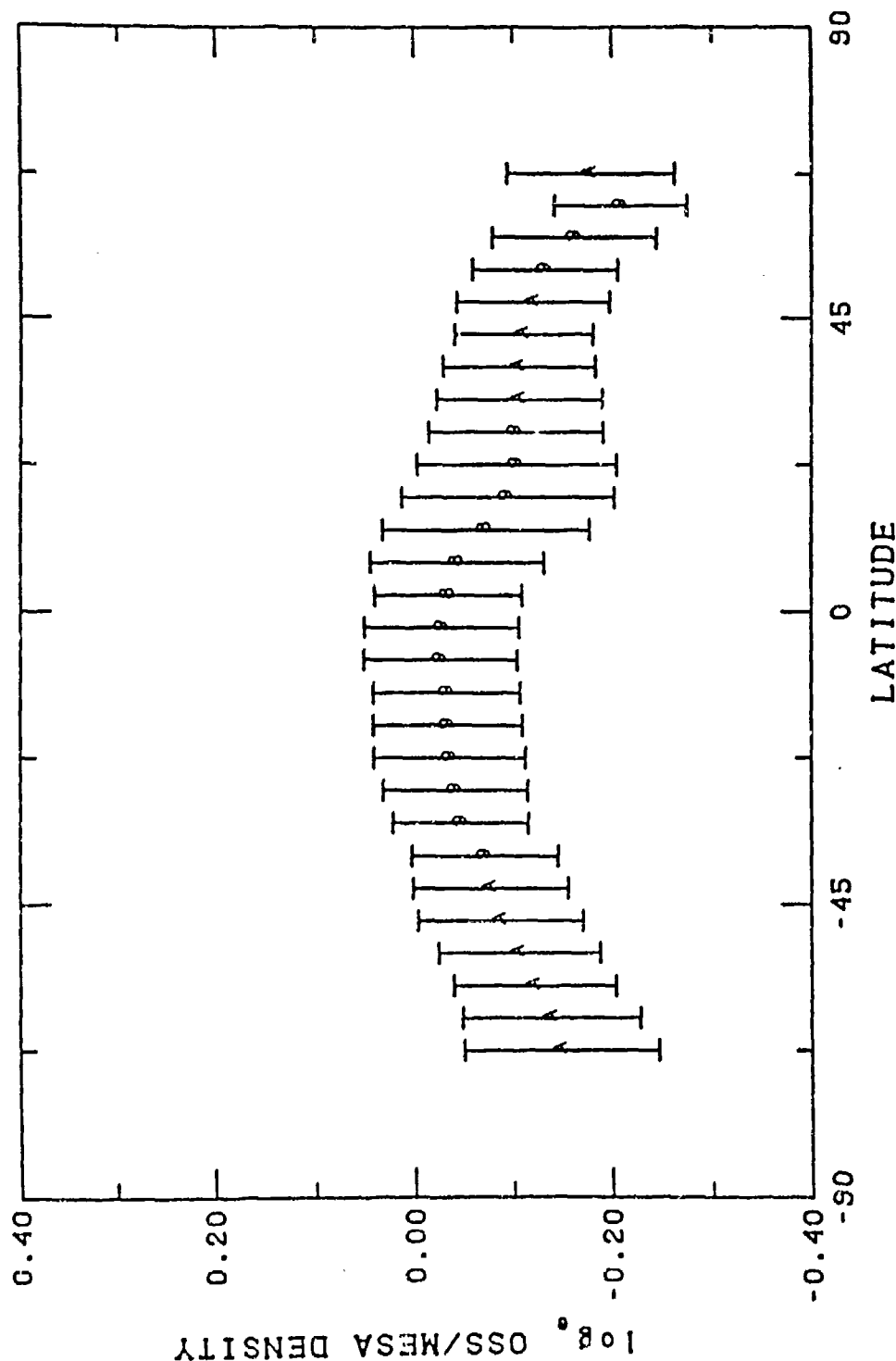
Fig. 11

0.65 PLOTTED: 8/24/87
JHEDIN. TAPE J05SC48



5 - 22

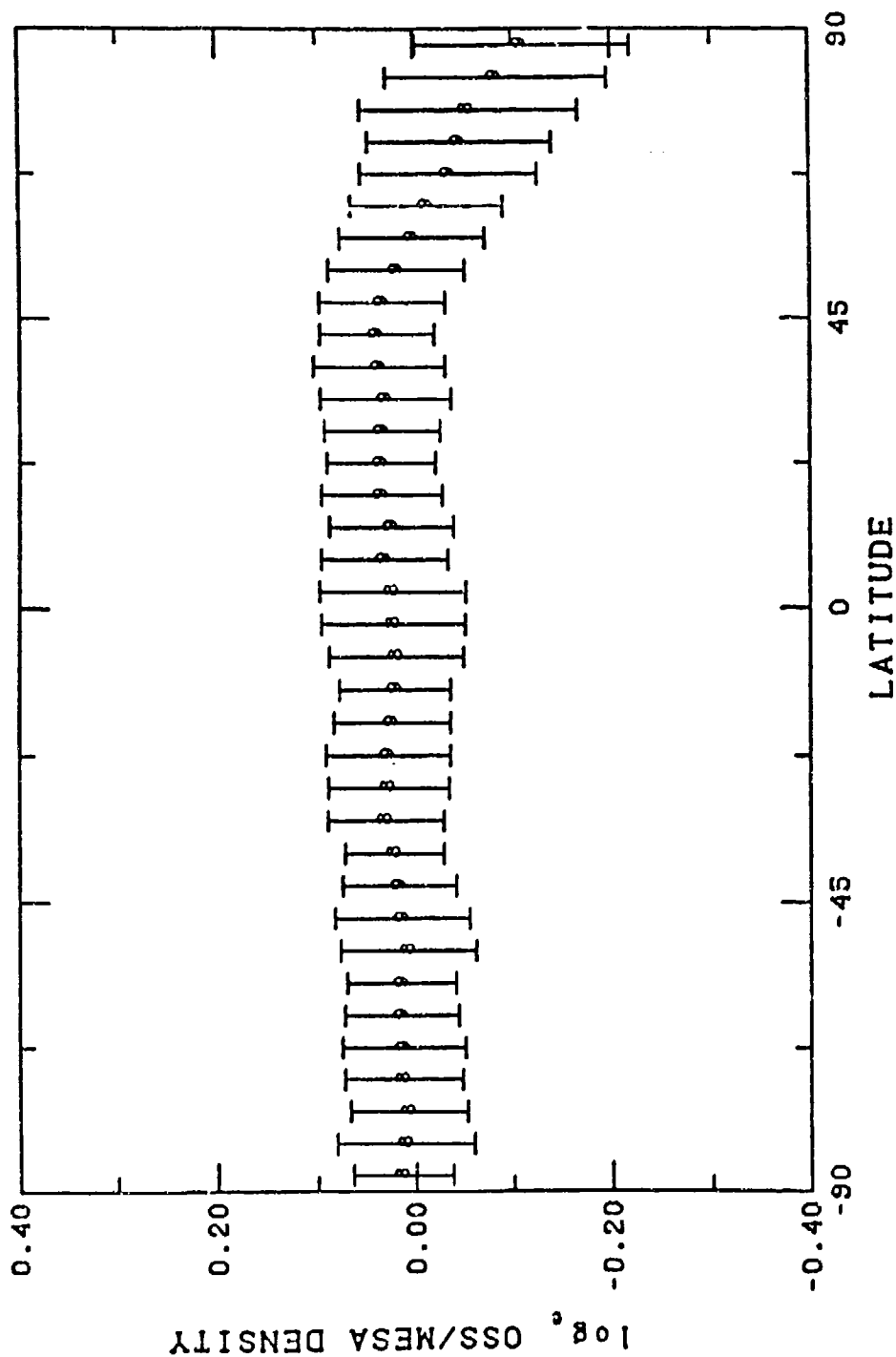
PARAMETERS DETERMINED :
11-FEB-86 18:23:31



GRP: 12. ALT LIM: 120., 200.ISK: 0 SEL: 23 -0.4 0.4 PTS PLT:18805 AVG: -0.10 SD: 0.09 A: 5.000 0.000
SW: 1. 1. 1. 1. 1. 1. 1. 1. 1. D1,D2: 74001 75100 ST,SX,SY 660 0 0 SM 1.00 3.
AVG.SD -0.0920 0.0484 AVXL,AVXH 0. RMS 0.1370

Fig. 19

PARAMETERS
11-18-88
DETERMINED ::



GRP: 16. ALT LIM: 120.. 200.ISK: 0 SEL: 23 -0.4 0.4 PTS PLT:14551 AVG: 0.01 SD: 0.08 A: 5.000 0.000
SW: 1. 1. 1. 1. 1. 1. 1. 1. 1. 1. D1.D2: 75291 76029 ST.SX.SY 3299 0 0 SM 1.00 3.
AVG.SD 0.0084 0.0334 AVXL.AYXH 0. 0. RUS 0.0786

Fig. 20

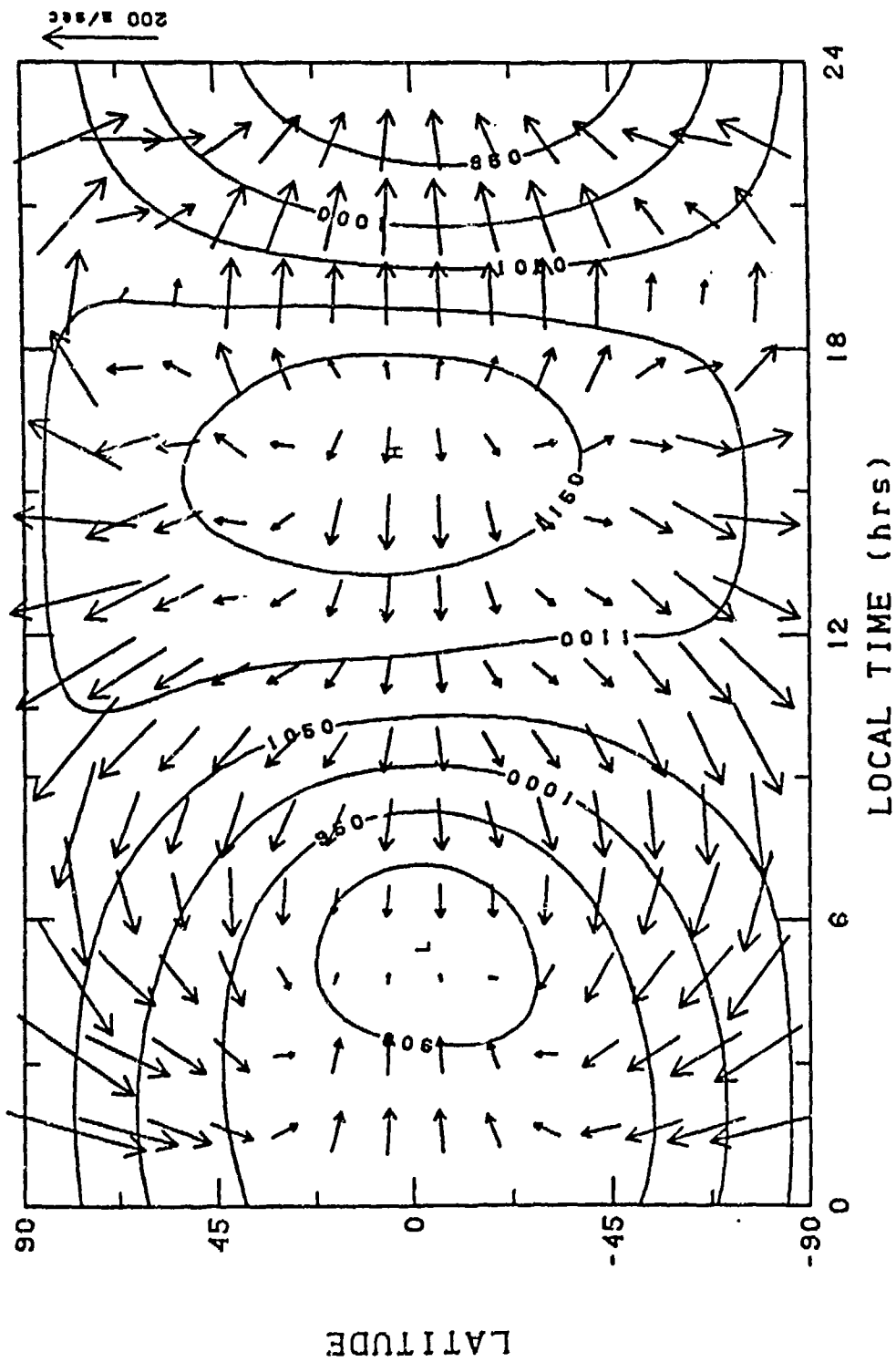


Fig. 21

Directions for improvement

density measurements must:

- be designed to surpass required accuracy
- be corrected for wind
- be cross-checked by different techniques
- be appropriately distributed
- be timely
- have basic assumptions checked (drag coef, recombination)

existing data should be analyzed for better understanding of:

- mag storm effects
- semiannual variations
- EUV (F10.7) variations
- differences between solar cycles
- differences between techniques

theory (GCM):

- can provide guidance for organizing measurements
- can fill in where measurements missing (lower thermosphere)
- cannot currently replace empirical models since they do not include all important variations, but hybrids may be valuable for highly dynamic effects

To provide energy input for theoretical models and correlation parameters for empirical models we must continue or improve measurements such as:

- solar radio flux
- solar EUV flux
- Interplanetary Magnetic Field
- magnetic indices
- auroral morphology
- particle precipitation

Fig. 22

5.2 ATMOSPHERIC STRUCTURE BETWEEN 80 and 120 Km

J.M. Forbes* and G.V. Groves**

*Department of Electrical, Computer, and Systems Engineering, Boston University,
Boston, MA 02215, U.S.A.. **Department of Physics and Astronomy, University
College London, London WC1E 6BT, England

ABSTRACT

Recent progress in modelling the temperature, density, and pressure specifications between 80 and 100 km is reported. The data base consists primarily of rocket and incoherent scatter measurements of temperature. An analytic polynomial scheme is described whereby smooth transitions with tabulations below 80 km and the MSIS-83 model above 120 km are obtained. Evaluations of the quality of fit to the data and possible directions for future work are also presented.

INTRODUCTION:

Specific recommendations for the new CIRA made in 1964 were that /1/:

- (i) Tabulations between 80 and 120 km should represent zonally- averaged values, and
- (ii) The temperature, density and pressure specifications between 80 and 100 km should provide a smooth transition with zonally-averaged satellite data below and MSIS-83 /2/ above.

This paper reviews work in progress to meet these recommendations.

METHOD OF TEMPERATURE MODELLING

Monthly temperature cross-sections in height and latitude have been determined that meet the following conditions (Fig. 1):

- (1) A smooth transition at 130 km to the temperature profile of MSIS-83 for mid-month dates and mean solar activity of $F10.7 = 120$ units, $A_p = 10$, longitudinal and diurnal (also semi-diurnal and terdiurnal) dependences being neglected.
- (2) A smooth transition at 70 km to the zonal mean temperatures of the monthly mean models to 80 km previously prepared /3/. The models to 80 km are taken to represent mesospheric structure for mean solar conditions ($F10.7 = 120$ units) as their database extends over years for which solar activity averages to about this level.
- (3) A constrained least-squares fit to observed temperature differences (from an initial temperature model), the imposed constraint being that the ratio (partial pressure of N_2 at 130 km)/(partial pressure of N_2 at 70 km) that is calculated for a fitted temperature profile should equal the same ratio as calculated from the pressure values provided by the upper and lower matching models.

The analytical procedure is to express the reciprocal of temperature T (or more precisely g/T , g being the gravity acceleration) as a polynomial in height, then by integration the $\ln(N_2 - \text{pressure ratio})$ may also be expressed as a polynomial in height and the coefficients chosen to satisfy (3) above. Temperature data (70 to 130 km) that have been utilized for (3) above are:

- (a) The temperature data previously utilized in the construction of CIRA 1972 /4/, and

(b) Subsequent data, reviewed in /1/, which have been obtained either by rocket techniques or incoherent scatter (I.S.) measurements, the latter being the main source of data above 100 km.

The incoherent scatter data utilized were from:

- (a) The Millstone Hill model (/5/, Table 1) for $F_{10.7} = 120$ units, $A = 10$.
- (b) The St. Santin model (/6/, Table 1) which is applicable for $K_p=2$, i.e. $A_p=7$, and which was evaluated for $F_{10.7}=120$ units.
- (c) An Arecibo model based on observations for 1970-1975, i.e. from solar maximum to solar minimum, which could be taken to represent mean solar conditions.

Individual temperature profiles that were utilized were from rocket launchings extending over a wide range of years and solar conditions. These values were processed without making any correction to mean solar conditions to individual profiles on the assumption that this dependence would average out in the overall analysis.

The monthly tabulations of observed temperature differences have been prepared from the above sources of data at each 5 km height interval from 70 to 130 km and each 10° latitude interval from pole to pole. In the absence of data, values are used from the MSIS-83 model which extends down to 85 km. Very little southern hemisphere data are available but if an observed temperature difference were available at a N. latitude for the same season it would be taken to apply at the same S. latitude in the absence of any data there.

As a consequence of the polynomial fitting procedure, each monthly temperature cross-section has an analytical representation and mean zonal temperature may be readily calculated for any height and latitude, and also for any date by interpolating between consecutive months.

COMPARISONS BETWEEN MODELS AND DATA

At Low Latitudes

Above 100 km the main sources of data are (1) the incoherent scatter measurements over Arecibo, Puerto Rico (18°N , 67°W) and (2) the Kwajalein (9°N , 168°E) Reference Atmospheres, 1979 /7/ which are based on rocket data. The open and filled-in circles in Fig. 1 show April data from these sources when corrected to 10°N latitude. The point of interest is that the profile satisfactorily fits the data while simultaneously satisfying the N_2 -pressure constraint. The same can also be said of the data below 100 km, most of which are single temperature profiles. Differences between temperature data and the calculated profiles have been averaged over 11 months at 5 km height intervals as shown in Fig. 1. (Symbols may be plotted just above or below the height to which they refer for reasons of clarity). On averaging these means with weights according to the number of observations on which they are based the line profile shown in Fig. 1 is obtained for their weighted average, which does not generally differ significantly from zero. This leads to the conclusion that the introduction of the N_2 -pressure constraint has not biased the fit to the temperature data, or in other words that the upper and lower models can be matched in a way that is consistent with the temperature data in the intermediate height region.

A comparison is also made in Fig. 1 between the fitted profile and MSIS-83. At 115-120 km, the profile gives lower temperatures than MSIS-83 in all months, the difference being greatest in April and reaching 40 K as shown in Fig. 1. A comparison between MSIS-83 and observed values is shown in Fig. 2 and MSIS-83 exceeds observed values in most months, whereas the new profile for 9°N lies much closer than MSIS-83 to the Kwajalein data for all months and the new 18°N profile lies closer to the Arecibo data than MSIS-83 on average. There are however considerations that tell against the ready acceptance of the new profiles, whereas MSIS-83 temperatures 'follow the sun', being 1 or 2K higher at 18°N than at 9°N in summer with small equinox maxima, the new profiles show a consistent equatorwards temperature decrease throughout the year that averages 15K between 18°N and 9°N and has an annual variation with maxima and minima at consecutive equinoxes. Without any clear understanding of the physical origin of such variations at low latitudes, the possibility must remain open that the differences between the Kwajalein and Arecibo data have a dependence other than the latitudinal one which this analysis is set up to model. Consideration is currently being given to the best way to utilize the data from these two low latitude sites.

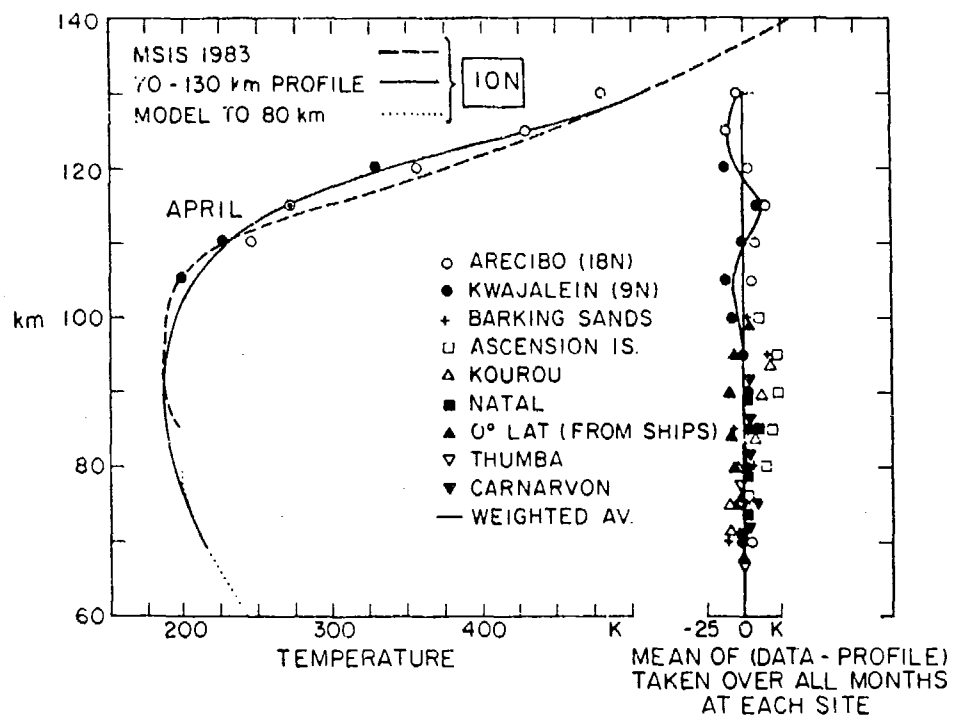


Fig. 1. A 70-130 km temperature profile determined for April at 10°N latitude. Annual mean deviation of observations from calculated profiles for individual low latitude stations.

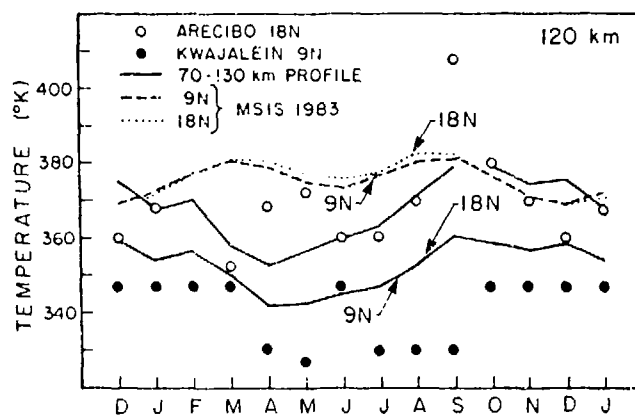


Fig. 2. Monthly mean temperatures observed at Arecibo (18°N) and Kwajalein (9°N) at 120 km compared with (i) MSIS-83 (dashed and dotted lines) and (ii) calculated values (continuous lines).

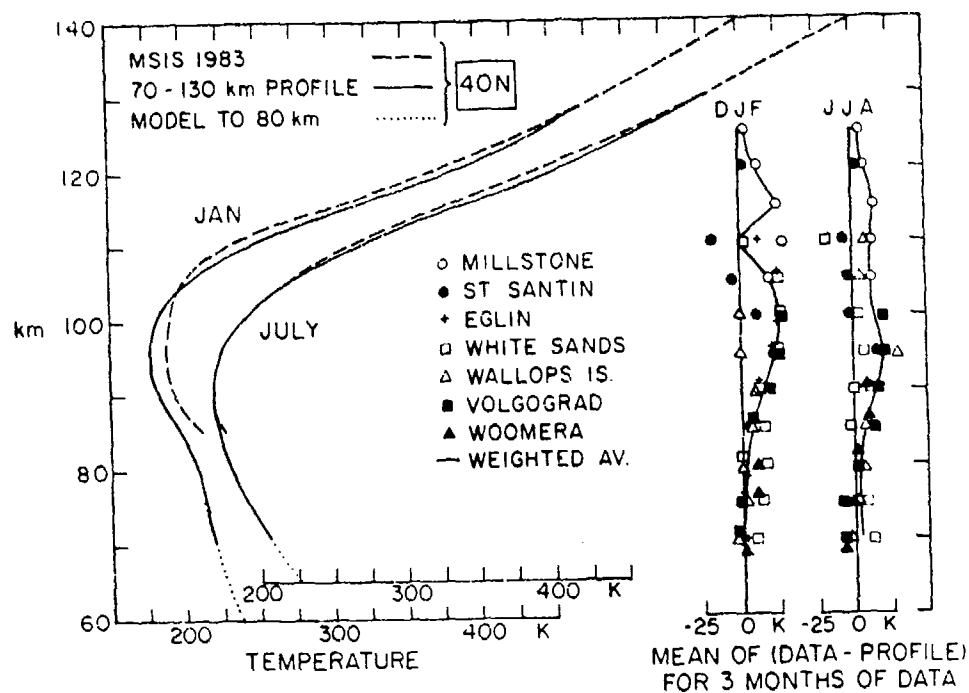


Fig. 3. January and July 70-130 km temperature profiles at 40°N latitude. Mean deviation of observations from calculated profiles for winter months (DJF) and summer months (JJA) at individual middle latitude sites.

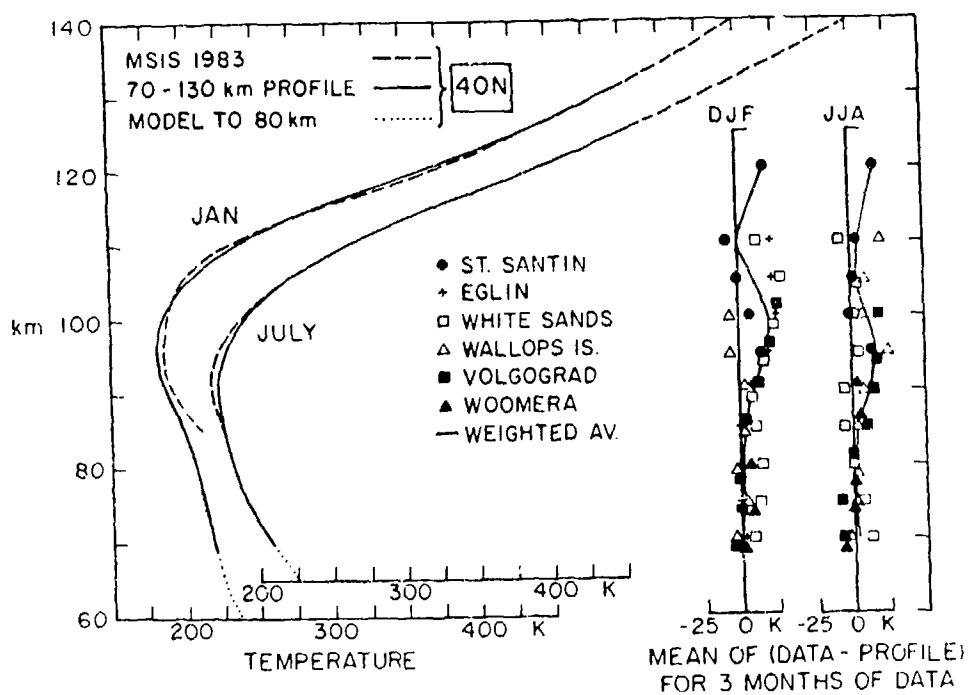


Fig. 4. The same as Fig. 3 without the inclusion of Millstone Hill data

At Middle Latitudes

Fig. 3 is for 40°N and shows both January and July profiles and mean deviations of the data from the model for each site averaged over winter months (DJF) and summer months (JJA). The main result to be noted is that for both seasons (and also for other times of the year), observed values are consistently higher than those of the profiles calculated. This bias arises from the imposed N₂-pressure constraint, the fall off in pressure between the 70 km value of the lower model and the 130 km value of MSIS-83 being greater than that implied by the temperature observations at the intermediate heights. It should however also be noted that MSIS-83 values between 105 and 125 km are even lower than the new profiles and are therefore still lower than the observed values.

Consideration is being given to possible revisions in the modelling technique that might lead to a reduction in the bias that is apparent at all heights in the mean deviations (Fig. 3).

One possible revision would be to exclude the Millstone Hill I.S. data as these values are noticeably high. Fig. 4 shows the results obtained when Fig. 3 is reworked without the Millstone Hill values; and it is seen that although the biases are reduced they are still significant, particularly from 55 to 105 km, and the matter warrants further consideration.

At High Latitudes

Fig. 5 shows the January and July profiles determined for 70°N and also the mean deviations of the data from the new profiles for each of the three high latitude sites averaged over winter months (DJF) and summer months (JJA). In this case the mean deviations do not show any consistent bias, but no definite conclusion is possible with the limited data samples available.

It is of interest to note that a July mesopause is obtained at 88 km with a temperature of 155K (Fig. 5), which agrees with the discussion of McKay /8/ who states: 'Moderately low mesopause temperatures (150-160K) are a consistent feature at 60N during summer. These temperatures are the result of adiabatic cooling associated with rising motions in the general circulation. There is an additional cooling effect which can occasionally lower the mesopause temperature to 130-240K. This effect persists over timescales of weeks and during this time NLC will be seen'. It therefore follows that if observations are biased to the time of NLC, the lower values of close to 142K which are shown by CIRA 1972 /4/ and Air Force Reference Atmospheres /9/ are more representative of these times of additional cooling, whereas the present profiles which match upper and lower models represent mesopause conditions without the additional cooling.

TEMPERATURE VARIABILITY

In addition to the mean deviations of observed temperatures from the calculated profiles that have been shown in Figs. 1, 3, 4 and 5, the RMS deviations from these means have been calculated with averaging over all months and these are shown in Fig. 6 for low, middle and high latitude grouping of sites. Fig. 6 shows that at all latitudes the RMS deviations increase with height except possibly at 100-105 km at middle and high latitudes where values may decrease slightly before increasing again more rapidly up to 130 km. At low latitudes data are lacking above 95 km but there is an indication that a more rapid increase begins at 85 km. A likely origin of these variations is the upward propagation of tides and gravity waves. Theoretical tidal amplitudes (/10/, Fig. 14 and /11/, Fig. 11) indicate that the increase above 85 km at low latitudes might be associated with the diurnal tide, that above 105 km at middle latitudes with the semi-diurnal tide plus a possible smaller contribution from the diurnal tide and that above 105 km at high latitudes with the semi-diurnal tide alone. At lower heights, the variations are likely to arise from a spectrum of gravity waves and the slow rate of increase of amplitude with height would be indicative of wave breaking with the possible extinction of most of the energy of these waves at 100-105 km. In this 'gravity wave' region RMS values increase noticeably from low to high latitudes. At 80 km, for example, RMS values are 8, 12 and 16 K for the low, middle and high latitude data.

DENSITIES AND PRESSURES

At the present stage of this work, profiles have been constructed for temperatures and partial N₂ pressures. The calculation of the latter is based on the equation of state and the barometric law and account is taken of the transition from a mixing region at 70 km to diffusive conditions at 130 km using the relations from MSIS-83. The effect of this transition in the case of N₂ is particularly small as its molecular weight of 28 lies very close to that of air in the mixing region (28.96).

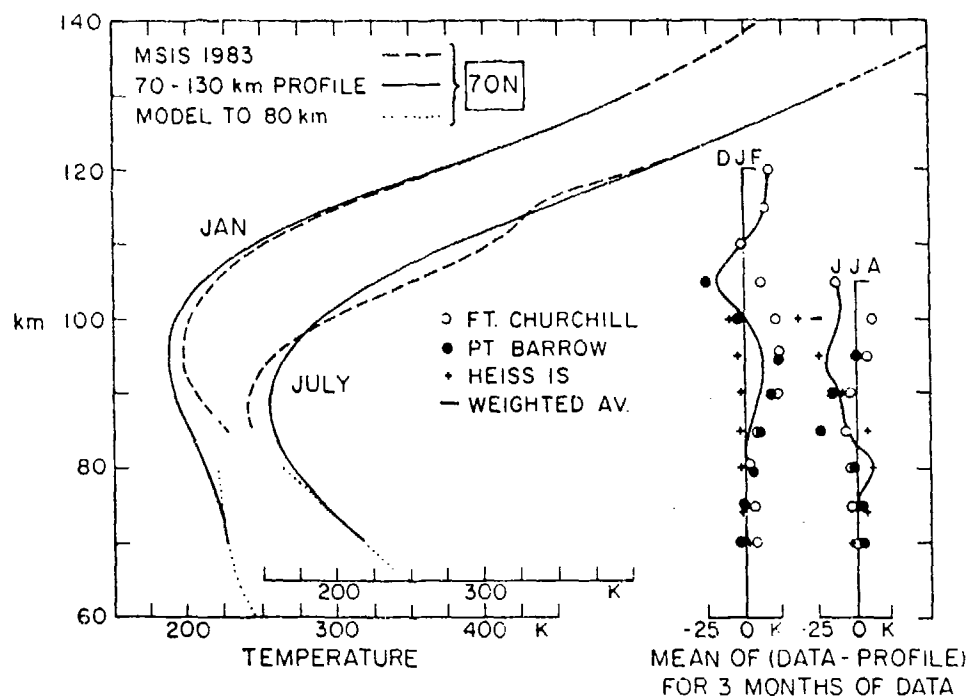


Fig. 5. January and July 70-130 km temperature profiles at 70°N latitude. Mean deviation of observations from calculated profiles for winter months (DJF) and summer months (JJA) at individual high latitude sites.

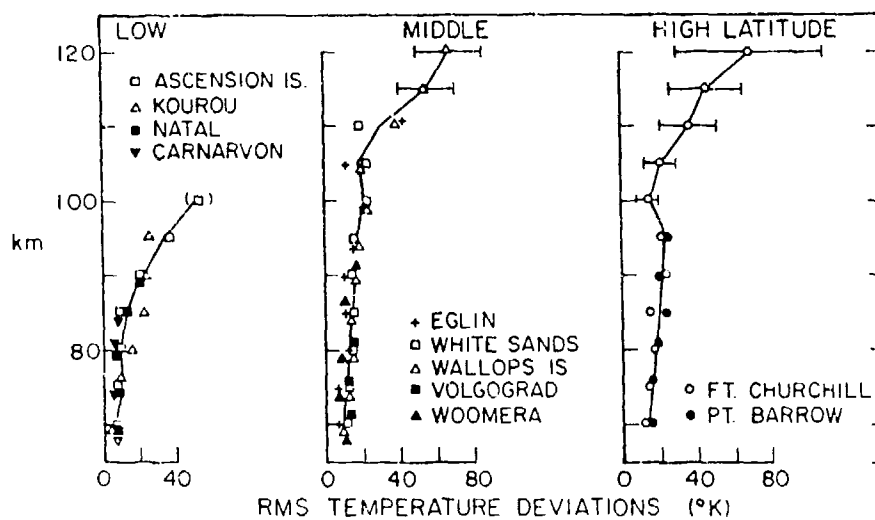


Fig. 6. Annual RMS deviation of observed temperature differences (from calculated profiles) with respect to their mean deviation for each site.

Attention has yet to be given to the vertical distribution of other gas constituents and to the possibility of making these continuous with the upper and lower models at 130 and 70 km respectively. The final step to the modelling of total densities and pressures would then be a relatively simple one.

It may be recorded that mean pressure distributions have now been extended upwards to the 0.005 mb (83 km) and 0.001 mb (91 km) levels by Koshelkov /12/ and are in the height range of interest.

DISCUSSION

A theoretical and numerical analysis is being developed for modelling atmospheric structure between 70 and 130 km for mean solar conditions. Monthly profiles have been analytically generated for all latitudes and heights from 70 to 130 km in temperature and partial N_2 pressure which have a smooth transition to MSIS-83 at 130 km and an 18-80 km model at 70 km. Attention will be given to the modelling of other gas constituents and to the possibility of combining the three models for the height regions 18-70, 70-130 and above 130 km to provide an analytical model for all heights above 18 km. Treatment of the 70-130 km region is however limited by available data and there are important variations that have yet to be considered. These are with (i) solar activity, (ii) longitude, (iii) time of day and (iv) seasonal asymmetry between N. and S. hemispheres. Although the present analysis extends over both hemispheres, the small seasonal asymmetry generated via the upper and lower matching models at 70 and 130 km lacks direct observational support on account of the lack of S. hemisphere data.

Acknowledgements. GVG gratefully acknowledges support to University College London for this work from the Air Force Office of Scientific Research under Grant No. AFOSR - 84-0045.

REFERENCES

1. J.M. Forbes, Temperature Structure of the 80 km to 120 km Region, presented at the XXV COSPAR Meeting, Graz, Austria, June 1984.
2. A. Hedin, A Revised Thermospheric Model based on Mass Spectrometer and incoherent Scatter Data: MSIS-83, *J. Geophys. Res.* **88**, 10170 (1983).
3. G.V. Groves, A Global Reference Atmosphere From 18 to 80 km, *Air Force Surveys in Geophysics*, No. 448, AFGL-TR-85-0129, Air Force Geophysics Laboratory, Hanscom AFB, MA 01731, (1986), AD A162499.
4. COSPAR Working Group 4, *COSPAR International Reference Atmosphere, CIRA 1972*, Akademie Verlag, Berlin (1972).
5. R.H. Wand, Lower Thermospheric Structure From Millstone Hill Incoherent Scatter Radar Measurements 2. Semidiurnal Temperature Component, *J. Geophys. Res.* **88**, 7211 (1983).
6. D. Alcayde, Temperature, molecular nitrogen concentration and turbulence in the lower thermosphere inferred from incoherent scatter data, *Ann. Geophys.* **35**, 41 (1979).
7. A.E. Cole, A.J. Kantor, and C. Philbrick, *Kwajalein Reference Atmospheres, 1979. Environmental Research Papers*, No. 677, AFGL-79-0241, Air Force Geophysics Laboratory, Hanscom AFB, MA 01731, AD A081780.
8. C.P. McKay, Noctilucent cloud formation and the effects of water vapor variability on temperatures in the middle atmosphere, *Planet. Space Sci.* **33**, 761 (1985).
9. A.E. Cole and A.J. Kantor, Air Force Reference Atmospheres, *Air Force Survey in Geophysics*, No. 382, AFGL-TR-78-0051, Air Force Geophysics Laboratory, Hanscom AFB, MA 01731, (1978), AD A058505.
10. J.M. Forbes, Atmospheric Tides 1. Model Description and Results for the Solar Diurnal Component, *J. Geophys. Res.* **87**, 5222 (1982).
11. J.M. Forbes, Atmospheric Tides 2. The Solar and Lunar Semidiurnal Components, *J. Geophys. Res.* **87**, 5241 (1982).
12. Y.P. Koshelkov and E.N. Kovshova, *Antarctica*, **24**, 29 (1985).

5.3 GRAM Model and Various NASA Density Measurement Projects
- Dale Johnson/George Fichtl/NASA-MSFC

GLOBAL REFERENCE ATMOSPHERE MODEL DEVELOPMENT

With the advent of the Space Shuttle and future vehicles such as National Aerospace Plane, Shuttle II, etc., it was perceived back in the early 1970's that site-based standard or reference atmospheres would not fulfill all the demanding engineering studies needed to simulate design work on such vehicles. The Global Reference Atmosphere Model (GRAM) is a 3-dimensional, world-wide, monthly atmospheric model. It consists of parameters of pressure, temperature, density, and winds from surface to 2000 km altitude. Monthly mean values of the parameters are obtainable along with their daily variability about the monthly mean. Vertical profiles as well as trajectory outputs are obtainable. The initial GRAM model was issued by MSFC's Atmospheric Effects Branch in 1974. Subsequent modifications were made to GRAM with the latest being made May 1986, giving the model the identity of GRAM-86. Current efforts to improve the model in middle atmospheric regions include use of world-wide satellite radiance measurements to infer mean density structure of both hemispheres on a monthly basis. MST Radar measurements of mesospheric density perturbations taken (from gravity waves) over a semitropical site in Taiwan are currently being analyzed with regard to gravity wave induced mesospheric density perturbation statistics for inclusion in GRAM. One type of measurement technique being used on Taiwan, not mentioned at this workshop, is the HF Ionospheric Doppler Sounder system which is being used in conjunction with the Taiwan MST VHF radar for gravity wave/density perturbation studies extending from 60 km upwards to orbital altitudes. Other modeling efforts, like those from AFGL (Groves 1985) and the Middle Atmosphere Project (MAP Handbook #16, 1985), will also be used. A thermospheric study above 90 km altitude is also being conducted in the area of modeling gravity wave density perturbations throughout these high altitudes. The COSPAR-CIRA 86 thermospheric atmosphere is also being considered for future inclusion in GRAM, as is an improved MSFC/J70 orbital model with a geomagnetic storm and gravity wave feature incorporated within it. It is the goal of NASA to compile a realistic atmospheric model that includes large and small-scale effects which can be easily accessible via computer for engineering design studies of space vehicles.

HF RADAR NETWORK FOR DENSITY PERTURBATION MEASUREMENTS

With the inclusion of two additional partial reflection (PR) HF radar sites, there will shortly be in existence 8 to 9 PR radars located around the Pacific area. Spacial coverage from 65°N to 70°S latitude will offer a unique network in which upper mesospheric and lower thermospheric gravity wave activity can be

measured, monitored and analyzed within this Pacific network during daytime and nighttime hours. Climatologies and correlations of gravity wave activity (with mean winds, tides, and density/wind perturbations) can then be established by altitude, area and season. Density perturbations will be inferred from the measured gravity wave parameters. These statistical results can then be modeled in the GRAM program for use in various NASA and DOD engineering design studies. Programs such as Shuttle, NASP, Shuttle II, AFE, AOTV, etc. will benefit. NASA is supporting Dr. David Fritts of the University of Alaska in the set up of a PR radar site at Poker Flat, Alaska and at Hawaii. It is hoped that other agencies and projects will join in support of this endeavor. With NASA involvement in the Taiwan MST radar, this site could also be used as part of this measurement network. A three-year program is envisioned to set up and coordinate all sites, acquire and reduce data, analyze data and perform statistical modeling. It is anticipated that a few partial reflection radar measurement data workshops will be set up for the involved network scientists to report their findings and coordinate efforts aimed at better understanding of global gravity wave activity and its climatology.

APPLICATION OF AIRGLOW MEASUREMENTS TO DETERMINE ATMOSPHERIC DENSITY VARIABILITY AT ORBITAL ALTITUDES

The objective of this study is to develop a theoretical/computer model which will enable correct interpretation of airglow data to infer density variability at orbital altitudes. Utilization of the model in combination with the extensive airglow data base to be developed in the CEDAR Experiment (Coupling, Energetics, and Dynamics of Atmospheric Regions) and other sources will be useful in deriving a statistical picture of density variations. The approach to follow will be to develop a theoretical/computational model of wave-driven fluctuations in the thermospheric airglow which incorporates (a) the full Eulerian dynamics of linearized internal gravity waves including diffusive dissipation, thermal conduction, viscosity, and ion drag; and (b) chemical reactions. Acquisition of airglow data and the application of the above model to determine the statistics of the important gravity wave (density fluctuation) parameters will be done. Justification for this effort involves the fact that current theory does not allow for an accurate estimate of the relationship between thermospheric airglow data, which is readily available, and density fluctuations driven by internal gravity waves at orbital altitudes. Recently, important improvements have been made in the corresponding theory for lower (mesospheric) altitudes by MSFC contractor. This effort would extend this approach to orbital altitudes. Funding is needed to support this effort.

NASP NATURAL ENVIRONMENT GROUP

Dr. George Fichtl of NASA/MSFC (ED41) has recently been asked to chair the National Aerospace Plane's natural environment advisory group. Since this group will deal with the problem involving the density environment within the stratosphere, mesosphere and thermospheric regions, this group's functions and activities are mentioned at this workshop. The charter for the National Aerospace Plane (NASP) Committee on Natural Environment is provided in the following:

Charter For The National Aerospace Plane (NASP) Committee on Natural Environment

The NASP will operate in a broad range of natural environments, including continuum and free molecular flows, encompassing ground based preflight operations, launch from the ground or deployment from an aircraft, ascent to the middle atmosphere (30 to 100 km), suborbital missions in the middle atmosphere, orbital missions above 100 km, entry, return flight, and landing. The NASP Natural Environment Committee will be responsible for providing guidance and expert advice to the NASP program on the natural environment for the above stated range of operating flight regimes relative to (1) design and operation of the NASP, and (2) impact of NASP on the natural environment. The committee includes a broad representation to encompass natural environment technical and scientific specialities relevant to NASP, major Middle atmosphere research programs, and sufficient engineering representation to assure all natural environment/engineering considerations are accommodated. Natural environment specialities include atmospheric dynamics (theory, measurements, data bases, models), chemistry, particulates, aerosols and cloud processes and radiation. The functions of the committee consist of the following:

- o Serves as the technical and scientific authority on natural environment for the NASP program.
- o Reviews NASP program and design requirements to identify natural environment needs.
- o Assesses the state of knowledge, available data bases and anticipated future developments on the natural environment for the full range of NASP operating environments.
- o Identifies natural environment deficiencies relative to NASP design and operation, and environmental impact.
- o Develops recommendations to eliminate these deficiencies with the goals of (1) reducing design/operation risk, (2) developing the most accurate assessment of environmental impact, and

(3) developing a NASP design which minimizes adverse impact on the natural environment. This also includes development of resource requirements and schedules.

- o Coordinates definition, development, and maintenance of a consistent set of NASP natural environment design criteria and environmental impact assessments.

- o Reviews proposals to the NASP program on natural environment efforts.

- o Advocates needed natural environment research, technology development, and implementation activities.

- o Maintains liaison with appropriate NASP program, government agency, industry, university, and professional society groups to assure a coordinated NASP natural environment activity.

GRA MODEL ATMOSPHERE

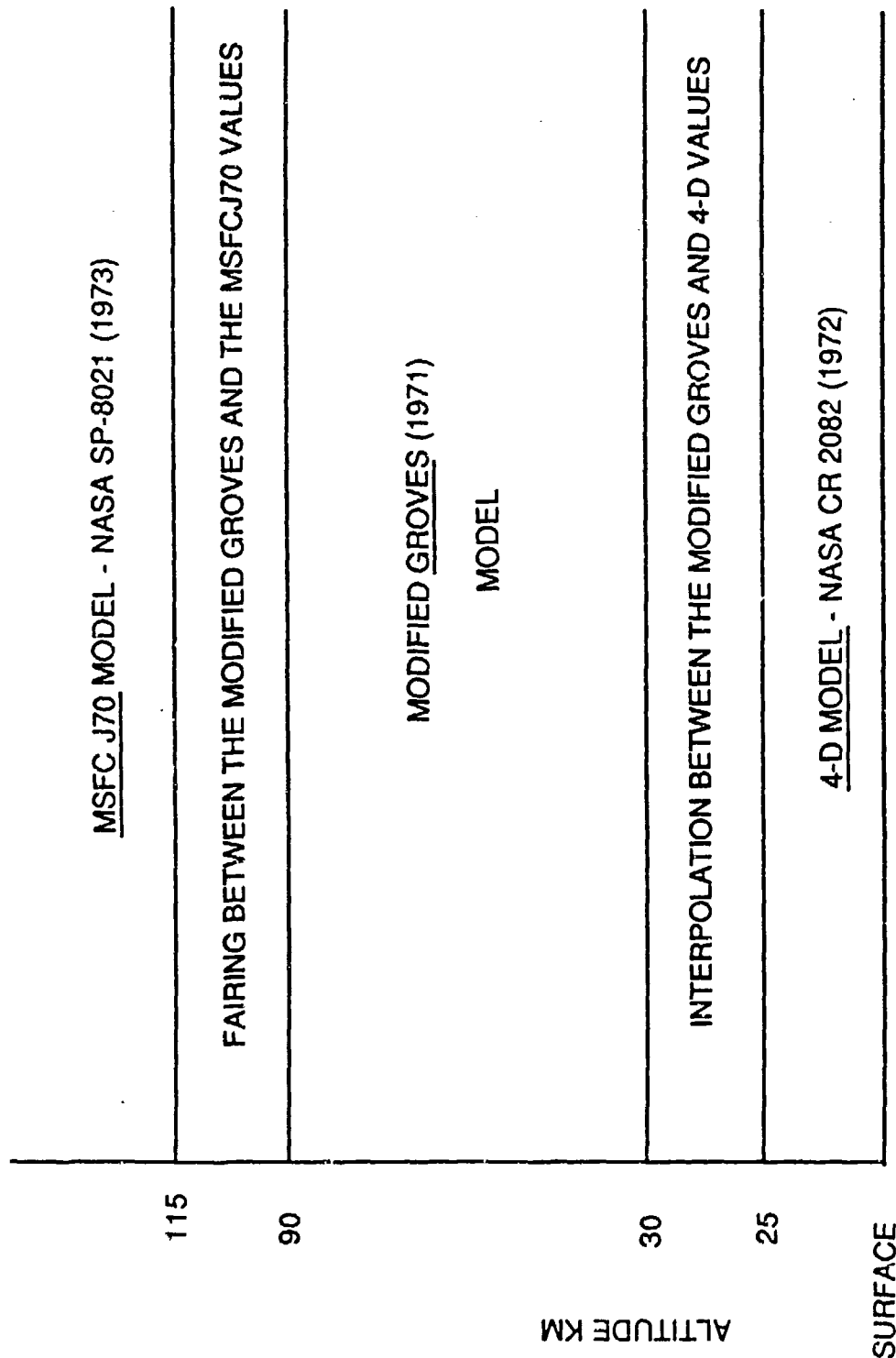
- GLOBAL REFERENCE ATMOSPHERE (GRA) MODEL: (1972-1980)
- FOR WORLD-WIDE LAT./LONG LOCATIONS.
 - BY MONTH
 - VERTICAL PROFILE VS. ALTITUDE (0-2500 KM)
 - TRAJECTORY OPTION
- CONSISTS OF:
 - WIND & THERMO. PARAMETERS (T,P,D, & CONSTITUENTS*)
 - MONTHLY MEAN & SD
 - DIFFERENT REALIZATIONS (SIMULATION OPTION)
 - 4-D,** GROVES, AND NASA-MSFC J70** MODELS

*MSFC J70 THERMOSPHERIC MODEL (NASA SP-8021) CONTAINS CONSTITUENT PARAMETERS:
(O, O₂, N, Ar, He, H)

**SEPARATE MODELS AVAILABLE

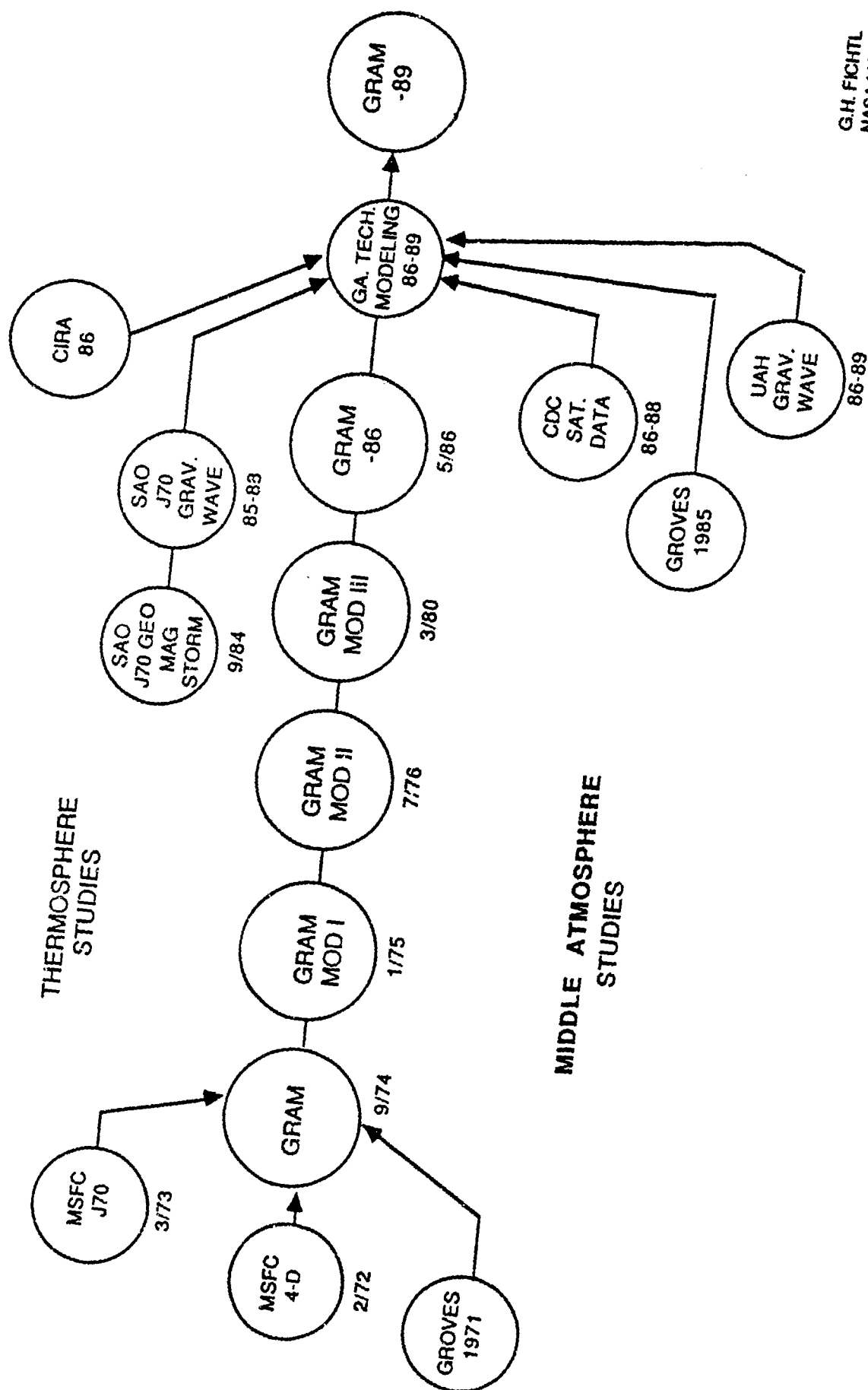
G.H. FICHTL
NASA-MSFC
ED41
205-544-1626
FTS-F24-1626
5-620-7-8

SCHEMATIC SUMMARY OF THE ATMOSPHERIC REGIONS IN THE GRA MODEL



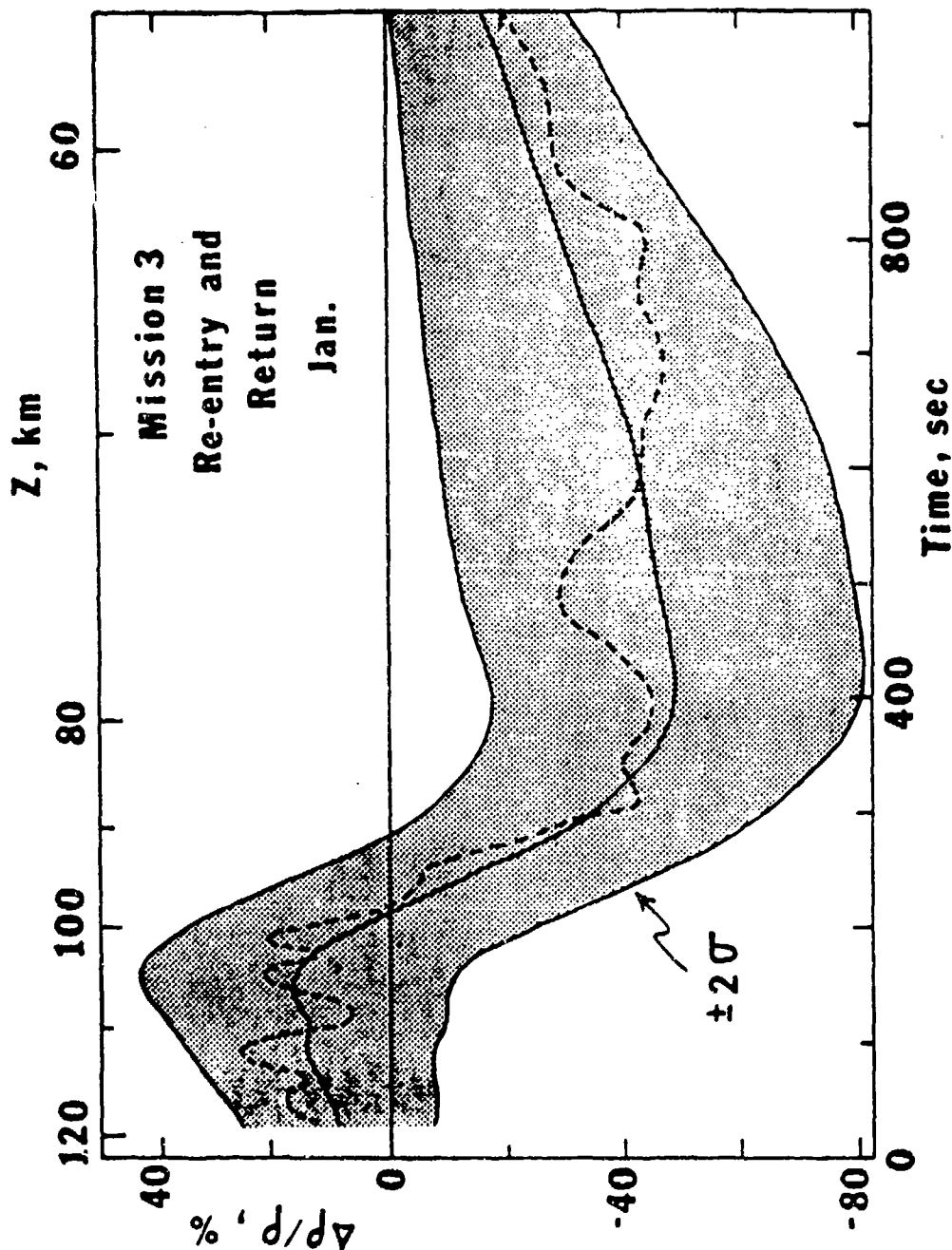
G.H. FICHTL
NASA-MSFC
ED41
205-544-1626
FTS-F24-1626
5-621-7-8

GRAM MODEL DEVELOPMENT HISTORY

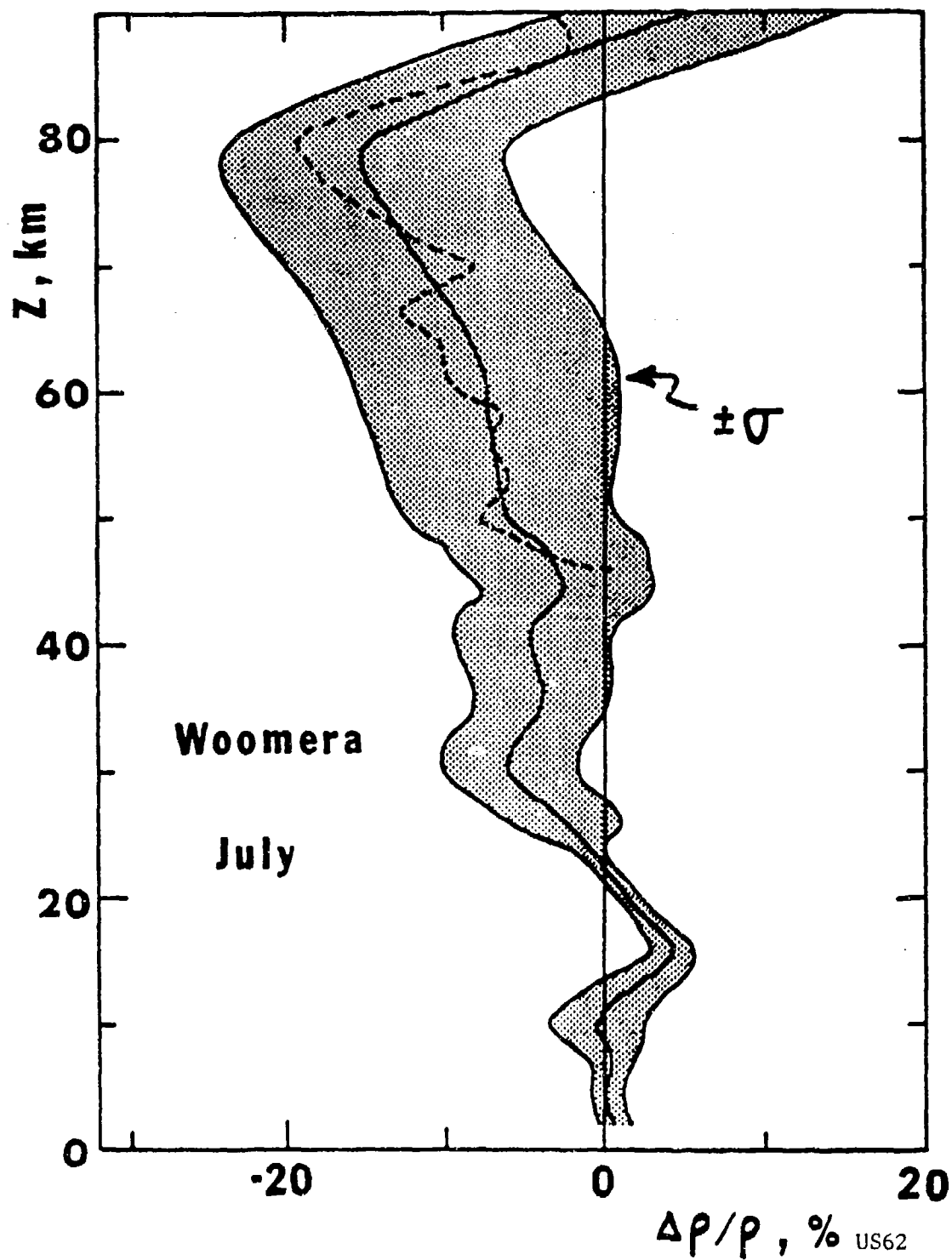


G.H. FICHTL
NASA-MSFC
ED41
205-544-1626
FTS-824-1626

5-625-7-8



Gram Density along a January mission 3 (Vandenberg polar orbit) re-entry and return trajectory. Density deviations are with respect to the 1962 U.S. Standard Atmosphere



EXAMPLE OF DENSITY PERTURBATIONS AS
FUNCTION OF ALTITUDE FROM GRAM

G.H. FICHTL
NASA-MSFC
ED41
205-544-1626
FTS-F24-1626

ORGANIZATION: NASA - MSFC / ED44		MARSHALL SPACE FLIGHT CENTER		NAME: DALE JOINSON
CHART NO.:		GRAM STATUS NASA / MSFC , ED41		DATE: OCTOBER 1987

<ul style="list-style-type: none"> 0 CONTRACTED EFFORTS : <ul style="list-style-type: none"> 0 UAH - DR. RU HUNG : " TURBULENCE AND GRAVITY WAVES IN THE TROPICAL UPPER ATMOSPHERE " 0 CDC - DR. ART BELMONT : " ATMOSPHERIC DATA SETS " ; FROM SATELLITE RADIANCE DATA 0 SAO - MR. JACK SLOWEY : " MODELING LIMITATIONS AND FINE STRUCTURE IN THE NEUTRAL UPPER ATMOSPHERE " 0 GA. TECH. - DR. C. G. JUSTUS : " IMPROVEMENTS IN THE GRAM AND COMPARISONS WITH A GLOBAL 3-D NUMERICAL MODEL " 0 J70/MSIS-86 COMPARISON FOR TETHER SATELLITE APPLICATIONS BETWEEN 130 & 230 KM ALT. - PAPER AT JANUARY 1988 AIAA RENO MEETING 0 UPDATES IN MSFC/J70 THERMOSPHERIC MODEL 0 GRAM TECH. MEMO. REPORT DUE OUT IN EARLY 1988 <ul style="list-style-type: none"> 0 TO INCLUDE THE 1-KM VERTICAL STEP DENSITY PERTURBATION CORRECTION 0 PARTIAL REFLECTION RADAR NETWORK 0 NASP : DR. GEORGE FICHTL - CHAIRMAN OF NASP NATURAL ENVIRONMENT GROUP 0 DENSITY PERTURBATIONS FROM THERMOSPHERIC EMISSION DATA - THEORY NEEDED : DR. MICHAEL HICKEY
--

ORGANIZATION NASA - MSFC / ED44 CHART NO.:	MARSHALL SPACE FLIGHT CENTER GRAM STATUS UNIVERSITY OF ALABAMA IN HUNTSVILLE DR. RU J. HUNG	NAME: DALE JOINSON DATE: OCTOBER 1987
--	--	--

CURRENT UAH GRANT STATUS (NAG8-063) - "TURBULENCE AND GRAVITY WAVES IN THE TROPICAL UPPER ATMOSPHERE":

FIRST YEAR :

- VHF RADAR MEASUREMENTS OF STORMS
 - THREE TYPHOONS: WAYNE (1986), VELLA (1986), AND SALOME (1987)
 - TROPICAL STORMS/CONVECTIVE WEATHER - PROJECT TAMEX
 - CLEAR WEATHER
- RAW DATA PROCESSING AT UAH
 - TAKES 3 HOURS TO REDUCE 1 HOUR OF DATA
 - FOUR COMPUTER SYSTEMS USED: VAX, PC, HP & EADS
 - SOME DATA NOT USED (LOW S/N RATIO)
- PRELIMINARY DENSITY PERTURBATION RESULTS :

Convective Activity	Hrs of Data
• NON-STORM	> 25
• CONVECTIVE STORMS	} > 100
• TROPICAL STORMS	
• TYPHOONS	> 15

SECOND YEAR :

- INCORPORATE HF DOPPLER IONOSPHERIC SOUNDER DATA WITH VHF RADAR DATA
- START DAILY MEASUREMENT PROGRAM TO ESTABLISH DENSITY PERTURBATION CLIMATOLOGY FOR AREA

THIRD YEAR :

- CONTINUE MEASUREMENTS
- ADAPT RESULTS FOR USE IN MODELS (GRAM)

ORGANIZATION: NASA - MSFC / FID44		MARSHALL SPACE FLIGHT CENTER GRAM STATUS CONTROL DATA CORPORATION DR. ART BELMONT		NAME: DALE JOINSON
CHART NO.:		DATE: OCTOBER 1987		

CDC DNR CONTRACT N00014-86-G-0076, " ATMOSPHERIC DATA SETS "

☐ DATA STATUS :
 ☐ SCR DATA
 ☐ N. HEMISPHERE T & G.P. HT. FIELDS - COMPLETED
 ☐ S. HEMISPHERE T FIELDS - COMPLETED
 ☐ BOUNDARY VALUES NEEDED FOR S. HTS, GEOPOT. HT. DATA
 ☐ ELEMENTARY STATISTICS GENERATED

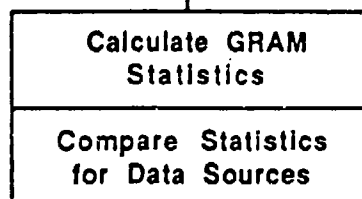
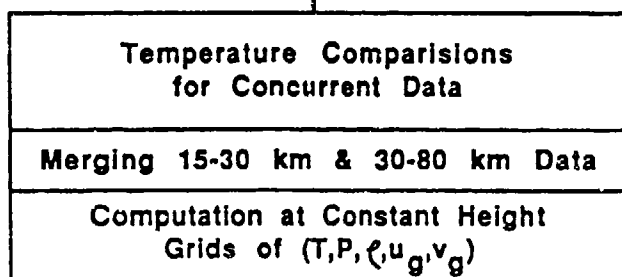
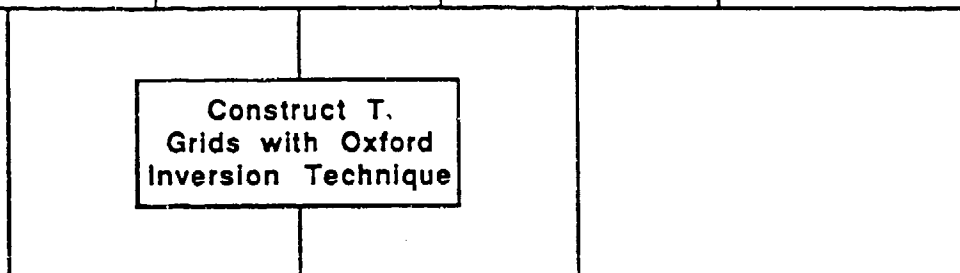
☐ SAMS DATA
 ☐ N. & S. HEMISPHERE DATA COMPLETED IN CONSTANT
 PRESSURE SETS

☐ PMR DATA
 ☐ MOST ANALYSIS COMPLETED
 ☐ RE-CONSTRUCTION OF OXFORD MONTHLY RADIANCE DATA
 INTO DAILY FORMAT
 ☐ DATA BEING EXAMINED & COMPARISONS WITH ALTERNATE
 DATA (ROCKETSONDE, SCR, ETC.)

☐ TIME SCHEDULE :
 ☐ ALL PMR RETRIEVALS COMPLETED BY NOV. 1987
 ☐ SCR S. HEMISPHERE BOUNDARY ANALYSES BY JAN. 1988
 ☐ ALL SATELLITE DATA IN GRAM FORMAT BY MAY 1988

CDC Middle Atmosphere Data & Analysis for GRAM

Daily Temperature and Radiance Data, 30-80 km			Temperature & Geopotential (15-30 km)
Nimbus 4,5 SCR T.	Nimbus 6 PMR Rad.	Nimbus 7 SAMS T.	NMC Grids Berlin Grids Australian 100mb SCR Rad.
1970-78 80°N-80°S 30-50 km	1975-1978 80°N-80°S 30-80 km	1979-1983 65°N-50°S 30-80 km	



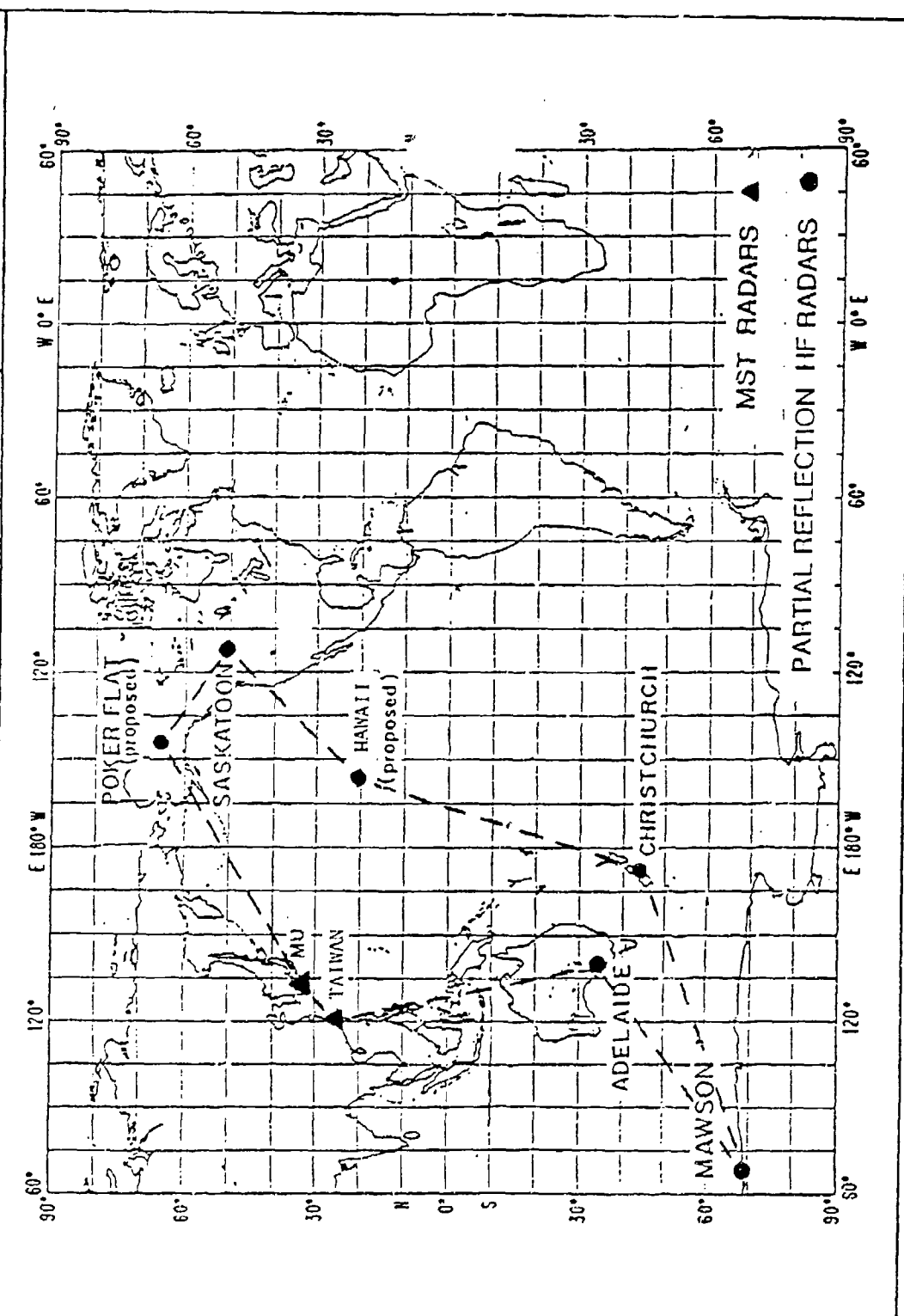
ORGANIZATION: NASA - MSFC / ED44 CHART NO.:	MARSHALL SPACE FLIGHT CENTER GRAH STATUS SMITHSONIAN ASTROPHYSICAL OBSERVATORY MR. JACK W. SLOVEY	NAME: DALE JOHNSON DATE: OCTOBER 1987
---	--	--

SAD CONTRACT NAS2-36405, "MODELING LIMITATIONS AND FINE STRUCTURE
IN THE NEUTRAL UPPER ATMOSPHERE".

- ☐ OBJECTIVE :
 - ☐ STATISTICAL DESCRIPTION OF THE EFFECTS OF MODELING ERRORS AND WAVES/TURBULENCE AND MASS MOTIONS ON THERMOSPHERIC DENSITY.
- ☐ DATA BASE :
 - ☐ DENSITIES FROM SPO SATELLITE DRAG, AND MASS SPECTROMETER OBSERVATIONS (ESRO-4, AE-D).
- ☐ PARAMETERIZATION :
 - ☐ HEIGHT AND LATITUDE, SOLAR AND GEOMAGNETIC ACTIVITY, AND TIME RESOLUTION MODELING.
- ☐ COMPLETION :
 - ☐ FEBRUARY 1988
 - ☐ PAPER PRESENTED AT JAN. 1988 AIAA RENO MEETING.

ORGANIZATION NASA - DSFC / EDMA CHART NO.	MARSHALL SPACE FLIGHT CENTER GRANT STATUS GEORGIA TECH RESEARCH CORPORATION DR. G. G. JUSTUS	NAME DALE JOHNSON DATE OCTOBER 1987
<p> GEORGIA TECH GRANT NAG9-078, "IMPROVEMENTS IN THE GLOBAL REFERENCE ATMOSPHERIC MODEL AND COMPARISONS WITH A GLOBAL 3-D NUMERICAL MODEL " </p> <ul style="list-style-type: none"> 0 1-KM STEP PROBLEM SOLVED : 0 USING A MODIFIED EXPONENTIAL CORRELATION FUNCTION 0 SHUTTLE INU ACCELERATION DATA (FINDLAY) USED TO VERIFY UEN FUNCTION 0 MINOR CODE CHANGES IN GFAM - EXPECTED DECEMBER 1987 0 TO BE DOCUMENTED IN GA. TECH. SEMI-ANNUAL PROGRESS REPORT <ul style="list-style-type: none"> 0 ALL MAP HANDBOOK VOL. 16 DATA PROCESSED : <ul style="list-style-type: none"> 0 FUTURE PLANS : TO PROCESS DATA SUMMARIES FROM: <ul style="list-style-type: none"> 0 CDC - BELMONT (GLOBAL SATELLITE DATA) 0 AFGL - REVISED GROVES MODEL? 0 AFGL - PHILBRICK LIDAR DATA, ETC. 0 OPEN LITERATURE SUMMARIES OF RADAR DATA (S ROCKET DATA) (MST, PARTIAL REFLECT., INCOF. SCAT., NETEOR, LIDARS, ETC.) 		

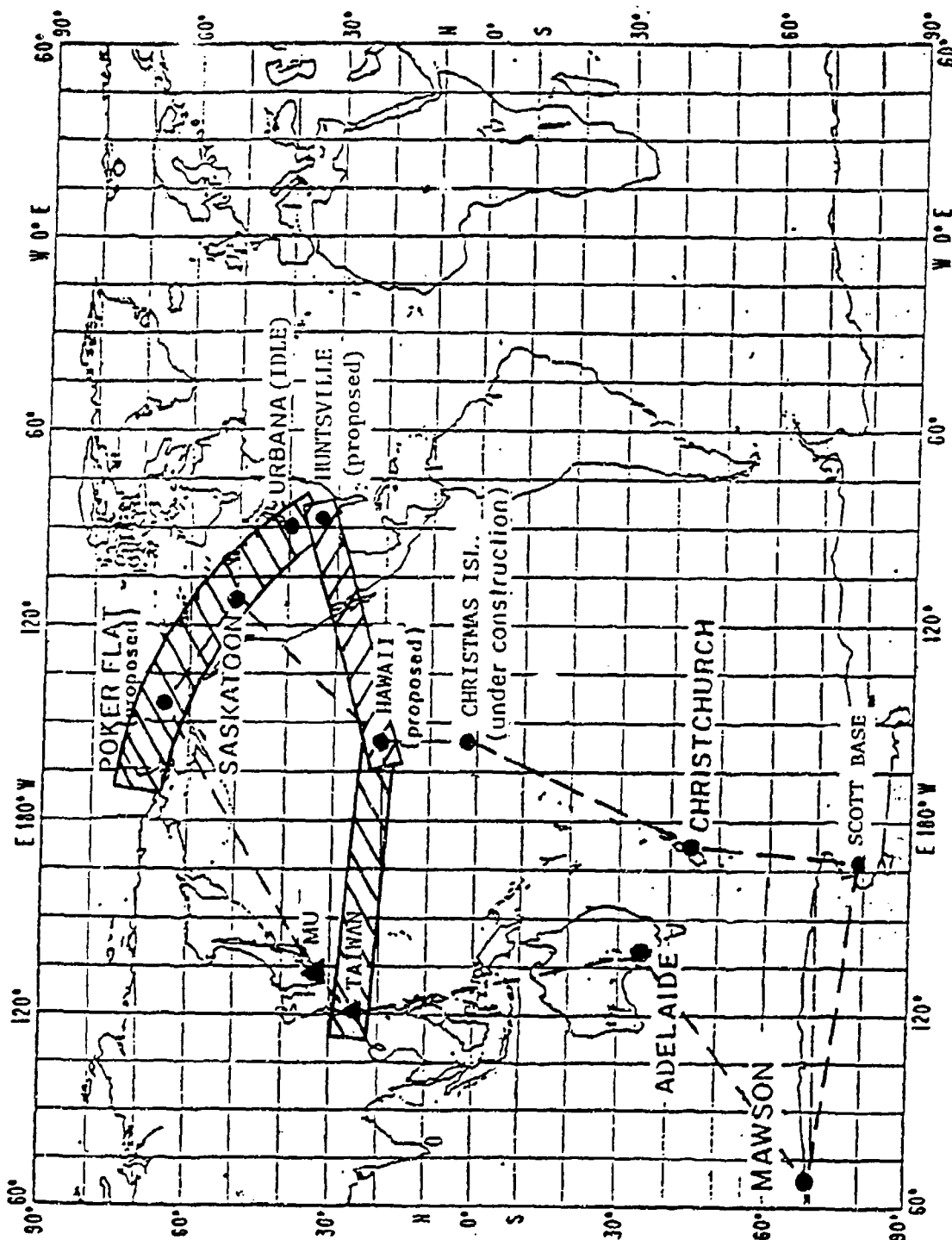
ORGANIZATION: NASA/MSFC CHART NO.	MARSHALL SPACE FLIGHT CENTER PROPOSED NASA MIDDLE ATMOSPHERE DENSITY PERTURBATION PROGRAM USING A GLOBAL NET- WORK OF PARTIAL REFLECTION HF RADARS		NAME: D. JOHNSON, ED44
			DATE: SEPTEMBER 29, 1987



NASA MIDDLE ATMOSPHERE DENSITY PERTURBATION PROGRAM

PARTIAL REFLECTION HF RADARS ●

MST RADARS ▲



D. Johnson NASA-MSFC/ED44
 June 1987
 Revised Oct. 1987

ACCURACY OF SATELLITE DRAG MODELS

Frank A. Marcos

Accelerometers flown on low-altitude satellites have provided our most extensive density data base in the 150-250 km region. These data have been obtained over a wide region of solar and geomagnetic conditions. A comprehensive comparison of our measurements, obtained 1974-1982, with several empirical models, has resulted in assessment of the current status and improvement prospects of our capability to specify and forecast density (drag). The model accuracies are compared by their mean values and standard deviations relative to the accelerometer data. Results indicate a lack of significant model accuracy improvements during the past two decades. Mean values are estimated to be given typically within $\pm 10\%$ and standard deviations are approximately $\pm 15\%$. Improved representation of atmospheric variability requires a program including coordinated measurements of atmospheric structure and dynamics, development of more accurate indicators of solar and geomagnetic activity and theoretical investigations using self-consistent numerical models.

INTRODUCTION

Empirical atmospheric density models based on large data sets have been developed to describe variations of the upper atmosphere. In atmospheric research these models serve as a reference and permit analysis of discrepancies with respect to new measurements. For practical applications models are also required for problems concerned with the effects of aerodynamic drag on satellites. Satellite lifetime, design, control, tracking, on-board fuel requirements and reentry are all affected by atmospheric drag and its variability. Two versions of models are currently used. Those of Jacchia [1-4] are based mainly on total density data derived from satellite orbital decay observations. Models based on in situ composition data and temperatures inferred from ground-based incoherent scatter radar have been formulated by Hedin et al [5-6] and Hedin [7-8]. A common feature of all the models is the use of relatively simplified physical concepts. Variations are described as a function of altitude, solar and geomagnetic activity, latitude, longitude [4, 6-8], local time and day of year.

Several limitations of present models with regard to solar and geomagnetic variations are recognized. Heating due to solar EUV radiation activity is taken into account by relations involving ground-based measurements of the 10.7 cm solar flux, $F_{10.7}$, and some mean value, \bar{F} , measured over several solar rotations. This index does not necessarily represent the complex mechanisms of interactions between the solar extreme ultraviolet (EUV) flux and the thermosphere. Since it has been found to generally reflect variations in the thermospheric energy input, it is routinely used as a readily available, but imperfect, indicator of solar activity. Studies to determine the relationship between $F_{10.7}$ and satellite measurements of EUV [9] reveal correlations that are non-linear and both wavelength and solar cycle dependent. Similarly, the planetary 3-hr Kp or daily Ap index used as a geomagnetic activity indicator does not necessarily represent the physical mechanisms responsible for density variations. The indices are derived from ground-based magnetic field fluctuations. They are used as indicators of heating at high latitudes caused by the interaction of solar plasma with the upper atmosphere. However, it is the only routinely available index for geomagnetic activity. Based on a network of midlatitude stations, it is particularly limited when describing data at high latitudes. The need for improved geomagnetic indicators is particularly borne out by the data presented in this study.

Lack of comprehensive experimental data over the range of variables described in models also contributes to their limitations: (a) The dominance of the semidiurnal tide below 200 km has recently been revealed by low altitude satellite measurements. [10-11] This feature is incorporated in the MSIS models but not in those of Jacchia. However, the considerable phase and amplitude structure of the semidiurnal tide as a function of altitude and latitude is beyond the scope of these models. (b) Density variations with annual and sub-annual periodicities are characterized as a "semiannual variation" with maxima near equinox and minima near solstice. The cause of this variation has not been unambiguously resolved. Measured data show irregular variations from year to year in maxima and minima. (c) Satellite composition measurements have provided evidence of longitudinal variations. Density maxima for heavy constituents occur at the longitude of the north and south magnetic poles while the behavior of the lighter constituents is negatively correlated. This behavior is related to ionospheric plasma density and motion influenced by earth's magnetic field. The MSIS models rely on geographic coordinates and relatively few terms to describe the broad features of this variation. (d) Large scale gravity wave structures also occur. These have periods different from those of tidal waves and are not directly related to the earth-moon-sun geometry. They may be generated either locally in the thermosphere or at lower altitudes. Gravity waves with the largest amplitudes (~ 70% peak-to-peak) observed at high altitudes detected by accelerometers on the OV1-15 satellite, [12] were related to high-latitude heating as indicated by the auroral electrojet index. [13] Wave struc-

tures are not incorporated into present models. (e) Latitude dependences, associated with all of the atmospheric variations, are not well understood. A particular problem for the geomagnetic activity effect is that the time delay between storm onset and density variation is latitude-dependent.

In the lower thermosphere, below about 250 km, model deficiencies are particularly acute since they are based primarily on data at higher altitudes. Physical and mathematical difficulties limit extrapolation of these data to lower altitudes: the assumption of diffusive equilibrium is not always valid, and the lower thermosphere boundary conditions are poorly known and variable. AFGL is accumulating an extensive atmospheric density data base, from satellite accelerometer measurements, for the 150-240 km region [14]. The present study uses these data to determine the validity of empirical models and establishes phenomena not contained in them. Definitive low-altitude satellite measurement programs, to guide development of computationally efficient dynamic models utilizing realistic indicators of atmospheric energy sources, are recommended. The effects of high latitude processes on lower thermosphere dynamics are emphasized.

DATA DESCRIPTION

Extensive measurements of the lower thermosphere neutral density have been derived using the satellite accelerometer experiment. Instrument operating principles have been described by Marcos and Swift [15]. Density is derived from direct measurements of aerodynamic drag together with knowledge of the satellite's mass, area, velocity and drag coefficient. Figure 1 shows the flight history of the accelerometer from 1974 to the present. All spacecraft had near-polar orbits except for AE-C (68°) and AE-E (19°). This extensive lower thermosphere data set has been obtained over a wide range of latitudes and solar and geomagnetic conditions. Data from the first seven flights have been used in the present analysis of empirical models. The satellites used and the dates of data acquisition are given in Table 1. The altitude range of the data is generally 150-240 km for AE-C, -D, and -E and S3-1 and 170-240 km for S3-4 and SETA-1 and -2.

Data reduction techniques implemented for the SETA flight data are described in Reference 15. Because of the high length-to-diameter ratio of the host vehicle, the equations used for determination of atmospheric density (ρ) and cross-track winds [16] are:

$$a_D = \frac{A_{ref}}{2M} C_i \rho V^2 \quad (2)$$

where $i = x, y, z$

M = satellite mass

A_{ref} = satellite frontal area

$$\vec{V} = -\vec{V}_G + \vec{V}_A + \vec{V}_W$$

with \vec{V}_G , \vec{V}_A and \vec{V}_W representing respectively inertial satellite velocity, the atmospheric rotation velocity (assumed equal to earth's rotation velocity) and the neutral wind velocity.

C_i = drag coefficients; $C_i = C_i (V_x, V_y, V_z)$.

The equation for the component, in a particular direction, of the total force on an element of area is given by:

$$dC = \frac{1}{A_{ref}} \cdot \{ (\xi k + \gamma \lambda + \eta t) [\gamma \cdot (1 + \operatorname{erf} \gamma S) + \frac{1}{S/\pi} e^{-\gamma^2 S^2}] + \frac{\lambda}{2S^2} (1 + \operatorname{erf} \gamma S) + \frac{\lambda}{2} \sqrt{\frac{T_r}{T_i}} \left[\frac{\gamma \sqrt{\pi}}{S} (1 + \operatorname{erf} \gamma S) + \frac{1}{S^2} e^{-\gamma^2 S^2} \right] \} dA,$$

where

$$dC = \frac{2 dF}{A_{ref} \rho V^2}$$

F = aerodynamic force

ξ, γ, η = direction cosines between mass velocity vector and axes of element of area, respectively

k, λ, t = direction cosines between the axes of element of area, and the direction in which force is desired (accelerometer axis)

$\operatorname{erf} \gamma S$ = error function of γS

S = molecular speed ratio = (mass velocity of gas)/(most probable random speed of molecules)

T_i = temperature of incident molecules

T_r = temperature of reflected molecules (assumed = 300°K)

This equation is integrated over the entire satellite surface area to obtain the drag coefficient for a particular axis. Values appropriate to this satellite were used with the MSIS model and the above equation to derive drag coefficients. For AE-C, -D and -E and S3-1, which had length-to-diameter ratios near unity, a constant value of $C_D=2.2$ was used.

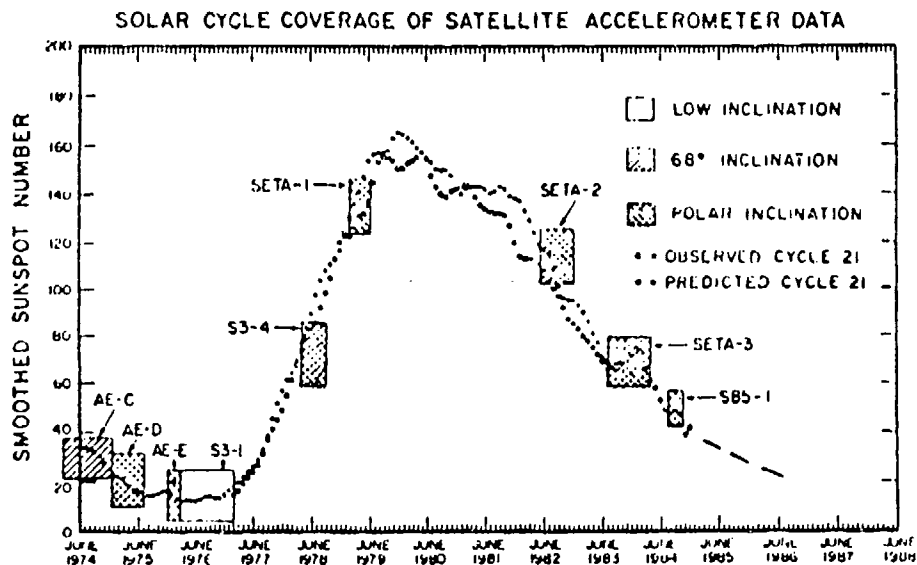


Fig. 1. Satellite accelerometer flight history and solar activity vs. time.

TABLE 1. SATELLITE ACCELEROMETER DATA SOURCES

Satellite	Data Acquisition Period
AE-C	Jan - Dec 74
S3-1	Oct 74 - May 75
AE-D	Oct 75 - Jan 76
AE-E	Nov 75 - Nov 76
S3-4	May - Aug 78
SETA-1	Mar - Apr 79
SETA-2	May - Nov 82

MODEL EVALUATIONS USING ACCELEROMETER DATA

The models considered were those of Jacchia, designated J65 [1], J70, [2] J71, [3] J73 (unpublished, see Ref 17) and J77, [4] Jacchia-Walker-Bruce, [17] Densel, [17] Lockheed-NASA, [18] U.S. Standard Atmosphere, 1962, [19] U.S. Standard Atmosphere Supplements, 1966 [20] and the Mass Spectrometer Incoherent Scatter models designated MSIS77, [5] MSIS79 [6], MSIS83 [7] and MSIS86 [8]. Two versions of the 1983 MSIS model were tested: MSIS83A used a daily averaged Ap index for the geomagnetic activity effect and MSIS83B used a weighted average of the 3-hr index over a 59 hour interval. The latter version of MSIS86 was used in this study.

Comparisons of model predictions with measurements not used in the model construction are valuable for testing the model reliability. While some AE mass spectrometer data were used in developing the MSIS models the density data were not. Also the S3-1 and -4 and the SETA-1 and -2 data were not used in construction of any of the models. The quantity statistically analyzed is the ratio (R) between measured density and model density. Results are given for mean ratios (\bar{R}) and standard deviations (σ_R) in Table 2. Models are listed in chronological order. This Table indicates the lack of significant improvement in model accuracies during the past two decades.

The results of Table 2 indicate some of the difficulties in improving the accuracy of empirical models. The MSIS79 model added longitude variations, based on direct satellite composition measurements, to the MSIS77 model. This was done without changing the zonally averaged values. Incorporation of an observed phenomenon resulted in a less accurate model (by 0.1 to 0.5% in σ) for every data set. The MSIS83 models are based on a data set much more extensive than that used for MSIS77. While a small accuracy improvement results in MSIS83B from a weighted average vs a daily average for MSIS83A, neither model is generally more accurate than MSIS77. As part of a revised and updated J71 model, a more complex geomagnetic variation was incorporated into the J77 model. For all data sets, the standard deviations of J77 are 0.4 to 2.8% higher than those of J71. Revisions made to the J71 coefficients and formulas to produce the J73 model resulted in the most accurate of the Jacchia models; yet, this model was never published. MSIS86 is very similar to MSIS83 but with additional terms to represent seasonal differences in polar composition variations. The modifications are based mainly on Dynamics Explorer satellite composition data obtained above 300 km. The model provides typically a 1% reduction in standard deviations over MSIS83 in the 150-240 km region. However, the MSIS86 errors remain comparable to those in J71 and J73.

TABLE 2. ACCELEROMETER, TOTAL MASS DENSITY RATIOS TO MODELS
(ALTITUDE 150-240 KM)

	AE-C		AE-D		AE-E		S3-1	
	\bar{R}	σ_R	\bar{R}	σ_R	\bar{R}	σ_R	\bar{R}	σ_R
MSIS86B	1.10	14.5	0.95	15.1	1.02	13.0	1.03	14.4
MSIS83B	1.11	15.0	0.98	15.6	1.02	13.0	1.07	14.6
MSIS83A	1.12	15.2	0.99	16.2	1.03	13.6	1.08	14.8
MSIS79	1.05	14.2	0.98	16.5	1.01	13.6	1.00	14.7
MSIS77	1.05	14.0	0.98	16.3	1.01	13.5	1.00	14.2
J77	1.05	15.9	1.01	15.3	1.02	15.3	1.04	14.3
J73	1.07	14.0	1.02	14.7	1.07	13.7	1.06	13.5
J71	1.10	14.7	1.05	14.8	1.08	15.0	1.08	13.7
J70	1.05	17.1	0.98	15.4	1.00	15.8	1.04	14.6
J64	0.94	17.0	0.89	17.4	0.92	15.5	0.92	17.8
L-N	0.94	17.7	0.86	16.5	0.86	15.8	0.94	14.9
JWB	0.99	19.5	0.99	18.8	1.01	19.4	0.99	19.6
US66	0.95	16.5	0.89	15.6	0.92	15.5	0.95	14.4
US62	0.84	30.0	0.70	32.4	0.72	30.3	0.73	32.7
DENS	1.45	21.3	1.00	21.0	0.94	23.0	1.31	19.5

Number of Points	56908	28273	33835	25825
------------------	-------	-------	-------	-------

	S3-4		SETA-1		SETA-2	
	\bar{R}	σ_R	\bar{R}	σ_R	\bar{R}	σ_R
MSIS86B	1.04	11.1	1.01	9.8	0.94	11.0
MSIS83B	0.98	11.8	0.92	9.7	0.87	11.6
MSIS83A	0.99	12.1	0.93	10.1	0.88	11.8
MSIS79	0.98	11.5	0.96	11.7	0.92	11.7
MSIS77	0.98	11.2	0.96	11.5	0.92	11.2
J77	0.94	13.7	0.88	12.6	0.89	13.9
J73	0.95	11.6	0.92	9.8	0.92	10.2
J71	0.99	12.1	0.94	9.9	0.95	10.1
J70	0.97	12.0	0.99	9.3	0.93	10.4
J64	0.90	11.6	0.99	11.1	0.88	11.3
L-N	0.93	14.6	0.99	9.9	0.91	11.4
JWB	0.86	11.0	0.90	10.4	0.82	10.9
US66	0.90	11.5	0.99	11.0	0.88	11.2
US62	0.93	17.6	1.13	12.0	0.96	15.0
DENS	0.79	19.9	0.87	14.9	0.99	15.2

Number of Points	38215	56530	277442
------------------	-------	-------	--------

More detailed analyses of the statistical properties of the SETA accelerometer data have been made by partitioning data (to 240 km) into 5° geographic latitude bins and day/night local time bins as well as four K_p four bins. Local time bins of 08-16 hr and 16-24 hr were used to separate SETA dayside and nightside northern hemisphere data occurring at the same latitude.

Mean values relative to the J71 MSIS83B and MSIS86 models for SETA-1 data (Mar-Apr 79) are shown in Figs. 2-4 respectively as a function of geographic latitude. Part a of each Figure consists of daytime measurements (~ 1000 hours local time) and part b consists of nighttime measurements (~ 2200 hours local time). The horizontal axis from right to left, follows the satellite trajectory. The satellite altitude as a function of latitude typically decreases from 240 km at low northern hemisphere latitudes on the nightside to 200 km near the pole down to about 170 km near 30°N on the dayside. It then increases to about 180 km at the equator. Since the orbit is not quite polar, no data are available for the 85-90° bins. Model ratios indicate dayside relative density enhancements near 20°N and 65°N. Nighttime densities are underestimated, particularly near 30°N, by 10-15%. J71 tends to overestimate the geomagnetic activity response at all latitudes and particularly at night. The high K_p bin data are about 8% (dayside) and 15% (nightside) lower than those of the low K_p bin. The MSIS models show good agreement of the low and high K_p bins on the dayside and about a 7% overestimation on the nightside.

Mean values of SETA-2 data (Jul-Nov 82) are compared to J71, MS83B and MSS86B in Figs. 5-7 respectively. Peaks in ratios near 65°N on the dayside and increasing ratios with decreasing latitude on the nightside are again prominent features of all data sets. The geomagnetic activity representation of MSIS is less accurate than for SETA-1 data. Maximum density response overestimations occur for the highest K_p bin at high latitudes on the nightside. J71 provides a better estimation of the nightside density response than it did for SETA-1 data and than MSIS83B for the SETA-2 data.

Figs. 8 and 9 show the standard deviations for J71 and MSIS83 respectively. These Figures show a striking latitude dependence. The major errors occur at auroral and polar latitudes, even during geomagnetically quiet conditions. The maximum error of about 15% occurs for the highest K_p bin in both cases. Similar results were shown by Marcos [13] for the SETA-2 and S3-4 data relative to the J71 model. The MSIS86 data (not shown) give a similar result.

The previous analyses show that lower mean values and standard deviations are obtained with the SETA-1, -2 and -3 and S3-4 satellite data set. However, systematic differences between the data from these satellites and the data from the AE/S3-1 satellites are to be expected [14].

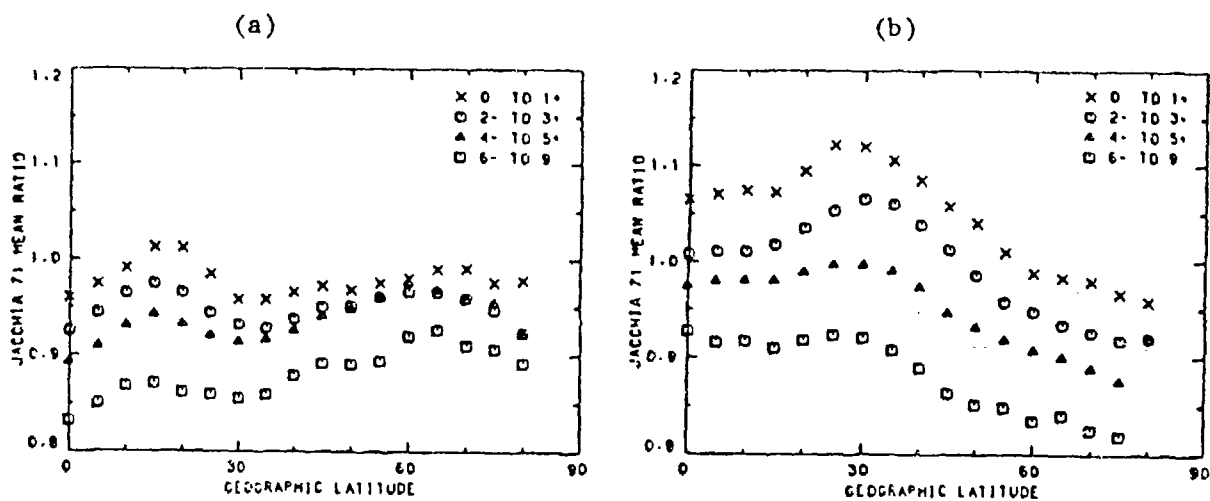


Fig. 2 Mean values of SETA-1 data to J71 model plotted as a function of geographic latitude (four Kp bins).

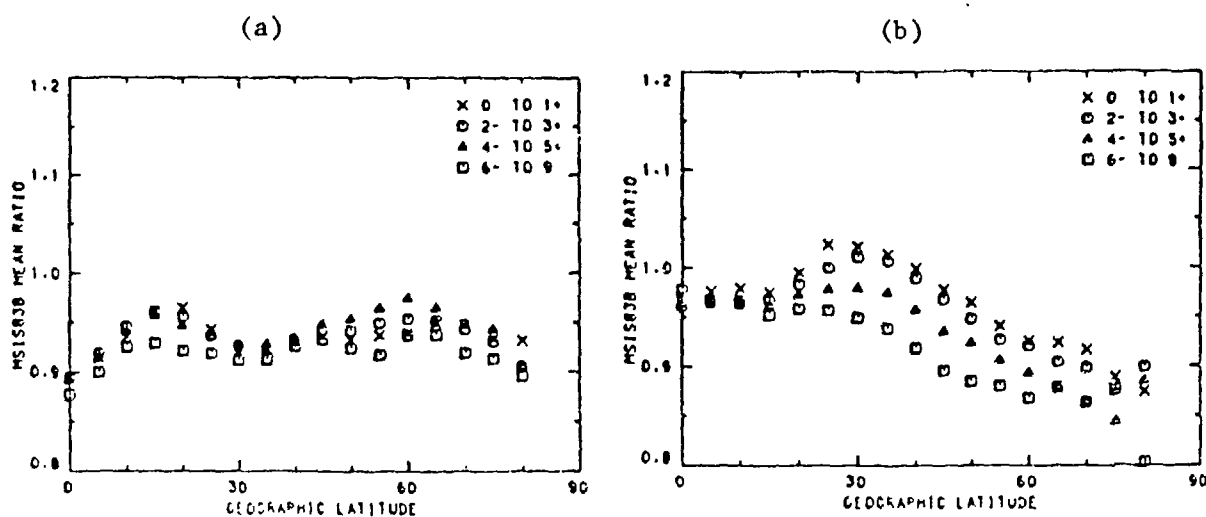


Fig. 3 Mean values of SETA-1 data to MSIS 83 model plotted as a function of geographic latitude (four Kp bins).

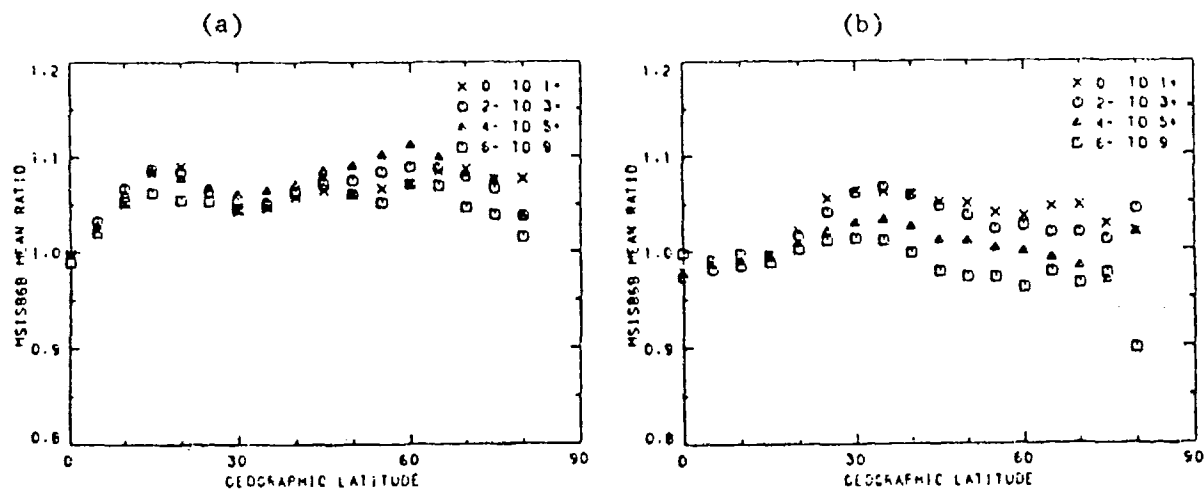


Fig. 4 Mean values of SETA-1 data to MSIS 86 model plotted as a function of geographic latitude (four Kp bins).

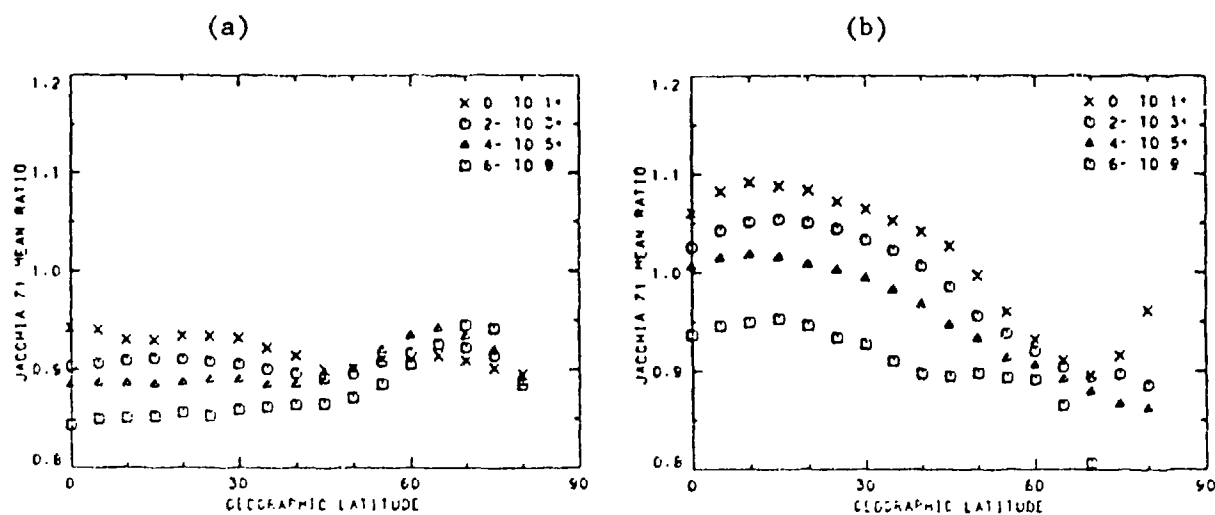


Fig. 5 Mean values of SETA-2 data to J71 model plotted as a function of geographic latitude (four Kp bins).

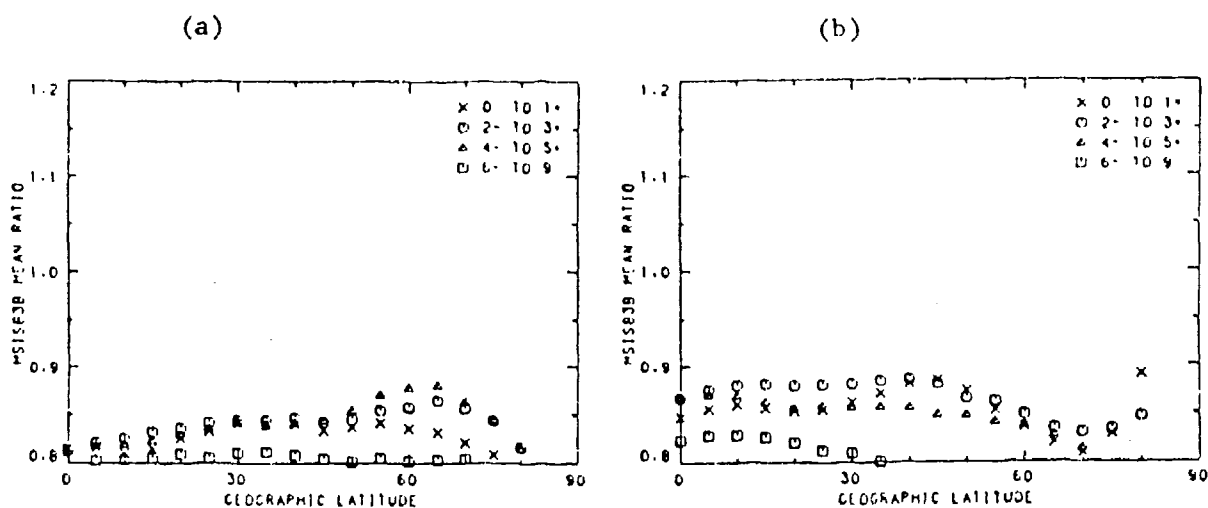


Fig. 6 Mean values of SETA-2 data to MSIS 83 model plotted as a function of geographic latitude (four Kp bins).

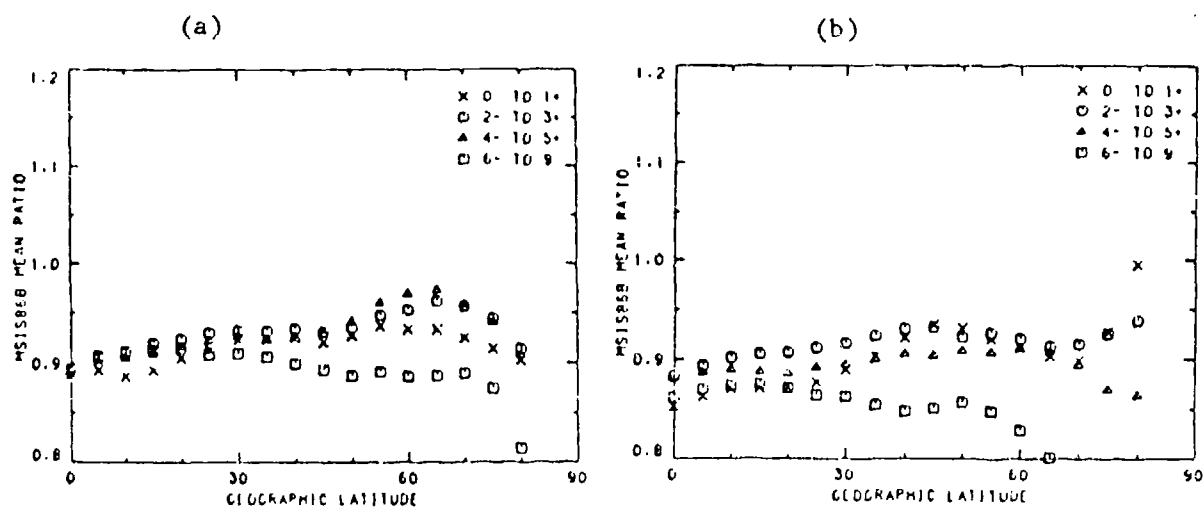


Fig. 7 Mean values of SETA-2 data to MSIS 86 model plotted as a function of geographic latitude (four Kp bins).

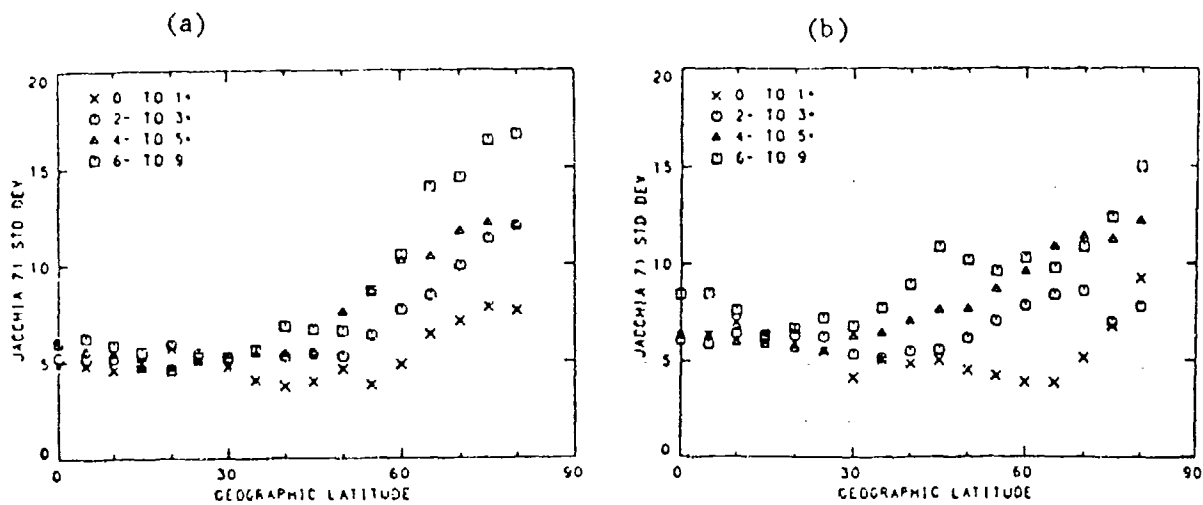


Fig. 8 Standard deviations of ratios of SETA-1 data to J71 model plotted as a function of geographic latitude (four Kp bins).

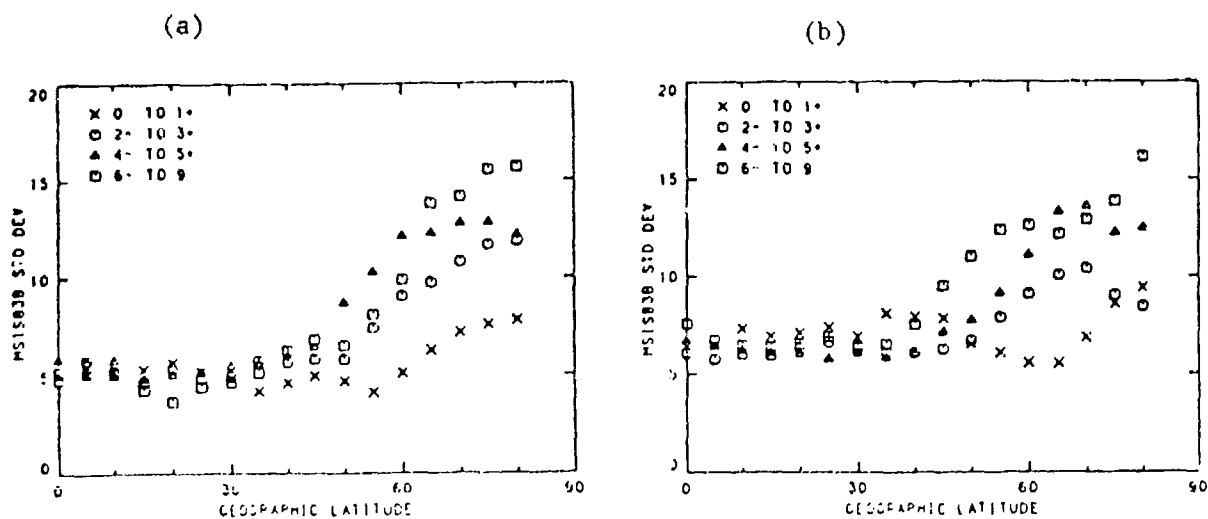


Fig. 9 Standard deviations of ratios of SETA-1 data to MSIS 83 model plotted as a function of geographic latitude (four Kp bins).

The Table 2 AE/S3-1 ratios imply densities generally above model values while the SETA ratios imply densities below model values. This difference between the two satellite data sets is believed due mainly to uncertainties in the ballistic coefficients used to convert orbital drag measurements to atmospheric density values. Drag coefficient (C_D) estimates contribute the major uncertainty to ballistic coefficient errors. Our estimated errors in C_D are $\pm 10\%$. It is possible that the SETA C_D errors exceed $\pm 15\%$ due to the spacecraft shape [21]. Therefore, systematic errors in drag coefficient may completely account for the absolute value differences between AE/S3-1 and SETA total mass densities. We conclude that, on average, recent models reflect density to within the $\pm 10\%$ accuracy of the Atmosphere Explorer accelerometer measurements.

The standard deviation difference has been attributed to be the manner in which altitude, latitude and local time variations were sampled for each data set. The AE/S3-1 data were sampled over a mix of altitudes, latitudes and local times. For SETA data, these parameters were highly correlated; e.g., mid-latitudes were sampled near 170 km and 1030 hrs LT on the dayside. AE-E and S3-1 data have been further analyzed at low latitudes to show quantitatively that reducing the range of variables over which a model must predict density leads to a reduced standard deviation in agreement with the SETA values.

The AE-E satellite acquired data between $\pm 20^\circ$ latitude over a period of about one year. During this time data were sampled over four local time cycles. Data obtained in the spinning mode were analyzed in altitude, latitude, K_p , local time and seasonal bins. Results presented in Table 3, show reductions in σ associated with these bin limitations. The AE-E 170 - 175 km data, grouped by season show values of σ between 5% and 7% in good agreement with SETA low latitude values. A similar analysis was performed with the S3-1 data. Results of binning are given in Table 4 for 170 - 175 km 0-20°N and for 170 - 200 km for 0-80°N. Local time was near 0730 hours for this data set. Note that for 0-10°N, 170 - 200 km, σ is 6.5% in excellent agreement with the Table 4 AE-E data. Therefore the typically 15% standard deviations obtained from the AE/S3-1 data, not the lower values obtained with the S3-4/SETA flights, are representative of model errors over "all" conditions.

DISCUSSION

Accelerometer data have revealed unmodeled features of lower thermospheric structure. Particularly significant are observed variations at high latitudes as a function of latitude, local time and level of geomagnetic activity. The importance of new knowledge at auroral and polar latitudes is borne out by the maximum standard deviations of models in those regions. However, additional density data alone

Table 3. Atmosphere Explorer - E Statistical Results with Local Time, Latitude, Season, Altitude and Kp Bins Spinning Orbit Data

Altitude	Lat	Kp	LT	Mo	N.	J71		MSIS 83	
						\bar{R}	σ	\bar{R}	σ
170-175	±20	All	All	All	1929	0.088	0.136	0.028	0.108
↓	0+10	0-3+	All	All	280	0.104	0.142	0.025	0.100
	±20	0-3+	10-11	DJF	47	0.058	0.078	-0.041	0.071

Table 4. S3-1 Statistical Results vs. Latitude; Kp 0 to 3+

Altitude	Lat	Mean LT	N.	J71		MSIS 83	
				\bar{R}	σ	\bar{R}	σ
170-175	0-10	0736	51	0.214	0.066	0.058	0.068
170-175	10-20	0737	66	0.206	0.059	0.076	0.066
170-200	0-10	0736	136	0.194	0.065	0.016	0.073
↓	10-20	.737	244	0.180	0.061	0.025	0.073
	20-30	0736	188	0.138	0.075	0.026	0.068
	30-40	0733	134	0.132	0.084	0.068	0.086
	40-50	0734	101	0.153	0.104	0.122	0.088
	50-60	0748	226	0.095	0.117	0.106	0.098
	60-70	0805	306	0.038	0.081	0.090	0.076
	70-80	0846	232	0.131	0.124	0.172	0.109

will not be sufficient to improve models. More recent models, utilizing extensive satellite measurements of atmospheric composition have been shown to specify total density with about the same accuracy as older models based on satellite orbital decay measurements.

Problems in accurately describing the spatial/temporal characteristics of density variability are indicated by the diagram of Fig. 10. The complex phenomena contributing to atmospheric heating and dynamics are dominated by two sources of solar energy: electromagnetic radiation and particles. Solar EUV, the most important thermospheric heat source, is deposited mainly at low latitudes and in the summer hemisphere. The circulation and structure of the thermosphere are controlled primarily by this heating. The processes involved are reasonably well understood. At auroral latitudes, the situation is different. The thermosphere is driven by electrodynamic coupling between the solar wind, magnetosphere, ionosphere and neutral atmosphere. Energetic charged-particle precipitation from the magnetosphere and Joule (resistance) heating due to electric current systems within the ionosphere are the major energy sources. Also, ionospheric plasma, driven by the magnetospheric convection electric field, transfers momentum to the neutral particles and can produce winds of about one km sec⁻¹. Both the magnitude and spatial extent of the auroral processes are extremely variable and related to the level of geomagnetic activity. During large storms, the energy dumped into the relatively narrow auroral region can exceed the global EUV input. These localized heat sources can cause large and sudden density variations, perturb circulation patterns and launch gravity waves. High latitude processes can therefore significantly alter thermospheric density, composition and temperature on a global scale as a result of large geomagnetic disturbances. Hence, density observed at a given location can depend on both the past history of density at that location and on events that occurred at varying distances and times.

Dynamic models are now being developed [22 and 23]. These are theoretical three-dimensional and time-dependent models that numerically solve the primitive energy and momentum equations. They attempt to understand the physics, chemistry and dynamics responsible for thermospheric structure. Parameterizations of various input fields are necessary for the specification of the physical processes described in these models. These inputs include solar UV and EUV energy and their heating efficiencies and energy, and momentum sources resulting from the solar wind-magnetosphere interaction. The output is a global simulation of the structure and dynamics of the thermosphere. In their present form, the models would not be feasible for operational use since they require a CRAY computer. However, these numerical models provide the means for guiding development of a new generation of operational models utilizing realistic physical concepts.

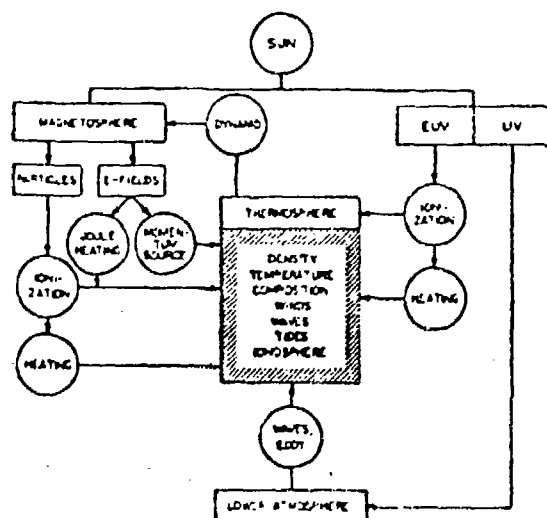


Fig. 10. Schematic block diagram illustrating interactions between the lower atmosphere, thermosphere and magnetosphere.

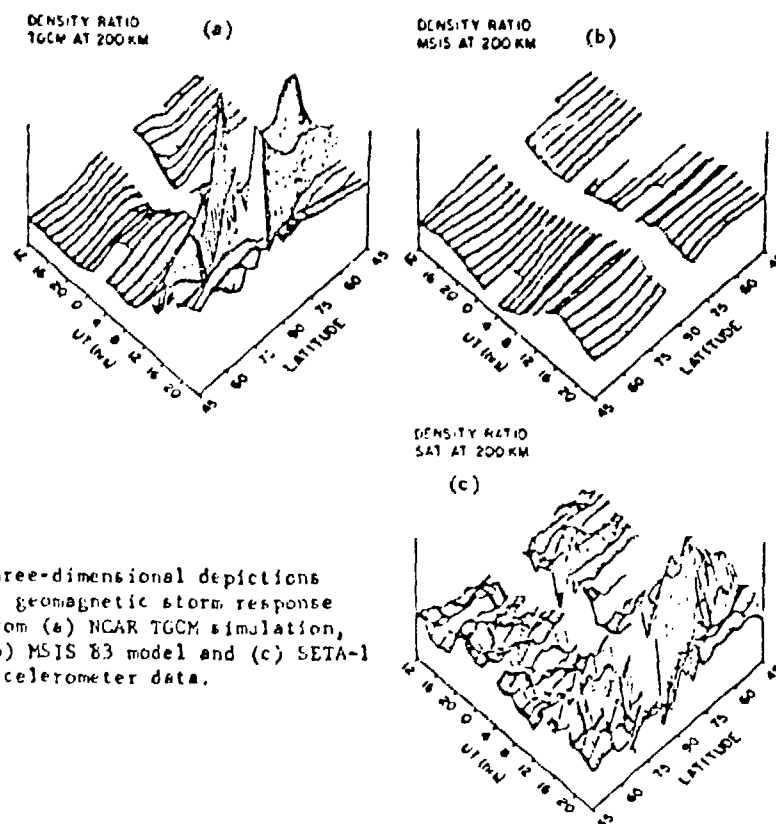


Fig. 11 Three-dimensional depictions of geomagnetic storm response from (a) NCAR TCGM simulation, (b) MSIS 83 model and (c) SETA-1 accelerometer data.

SETA-1 density and winds obtained during the March 22, 1979 geomagnetic storm have provided a unique opportunity to test and evaluate our knowledge and modeling capability of the magnetosphere/ionosphere/thermosphere system. This period was one of intense solar-terrestrial observations and analysis. As a result, the time-dependent variations of auroral and magnetospheric convection model parameterizations incorporated within the National Center for Atmospheric Research thermospheric general circulation model (TGCM) were prescribed in detail as input to the storm simulation [24]. The TGCM predictions of density variability for this storm period are compared [25] with the satellite data and the MSIS83 model in Fig 11. Three-dimensional depictions are given for latitudes above 45° in the northern hemisphere for local times ~ 2200 hrs (left side) and ~ 1100 hrs (right side). In the day sector, the SETA measurements clearly confirm the TGCM predictions of a high-latitude (60° - 85°) localized region of intense heating and density enhancement ($\sim 60\%$) between 1400 and 1500 UT (Universal Time), the period of maximum magnetic disturbance. The night sector is characterized by more wavelike structures and density perturbations of 20-40% in both the SETA and TGCM data. The extension of the TGCM "hot spot" farther into the nighttime sector than is consistent with SETA data is believed due to inaccuracies in the TGCM convection model position, orientation or latitudinal extent. Over the complete range of latitudes, Ref. 25 shows that the TGCM and SETA data are characterized by generally elevated densities (10-20%) after the storm (2200 UT) as compared with pre-storm conditions (0800 hrs GMT). The MSIS model predicts density enhancements of only 10-20% between 1100 UT and 1800 UT, without the pronounced latitudinal and temporal structure indicated by the TGCM and the SETA data. It is evident that the TGCM accounts for time-dependent localized processes with a much higher time resolution than the MSIS83 model.

CONCLUSIONS

Satellite accelerometer measurements have provided the first extensive description of density variability at low satellite altitudes and high latitudes. The data have been obtained over a wide range of solar and geomagnetic conditions. Statistical evaluations of density results from seven satellites demonstrate that model accuracies have not progressed significantly in the past 20 years. Mean values are given within $\pm 10\%$ with standard deviations of $\pm 15\%$. Errors encountered for specific applications have been shown to be sensitive to geographic location, local time and level of geomagnetic activity as well as to the model used. Development of better models will result from improvements in our knowledge of the magnitude, distribution and transport of thermospheric heating. This requires coordinated theoretical/observational programs. Specific recommendations for the lower thermosphere include:

Extensive interpretation and analyses of the accelerometer data base. Emphasis should be placed on case studies of spatial/temporal variations related to geomagnetic activity as a function of solar flux, season, latitude, longitude and local time.

Continued development of dynamic global circulation models. Accelerometer density and winds data as well as Dynamics Explorer satellite data are needed to validate and improve input assumptions.

More realistic indices to describe energy inputs related to auroral processes and their interaction with the magnetosphere/ionosphere system. Auroral electrojet parameters and new high latitude indices derived from ground-based magnetometers can be evaluated with accelerometer density data for the same periods.

An extensive lower thermosphere measurements program that provides a basis for developing accurate relationships between energy inputs and global density variability. An initial payload measuring density, composition, winds, temperature and ionospheric properties is required. A low eccentricity sun-synchronous orbit (1400/0200 LT) would provide data in local time-latitude regions not covered by the present data set. Coordination with ground-based thermosphere dynamics measurements programs (such as the Coupled Energetics and Dynamics of Atmospheric Regions program) will greatly enhance data interpretation.

The above recommendations have focussed on applications of accelerometer data to improve density models. Since these data measure the parameter to be modeled, atmospheric density, they must be an integral part of future programs that attempt to improve density models. Continued progress in numerical modeling and in geomagnetic index development together with interpretations of present data and a critical new measurements program can provide important advances in thermospheric models.

ACKNOWLEDGEMENTS

Critical data support was provided by: E. Robinson, AFGL/LCY; and K. Bhavnani, J. Bass, C. Bryant and N. Bonito of RADEX Corp. Critical typing support was provided by Ms. Nancy Fleming and Mrs. Nadine Mayo of the Ionospheric Physics Division.

REFERENCES

1. L.G. Jacchia, Static Diffusion Models of the Upper Atmosphere with Empirical Temperature Profiles, SAO Special Report No. 170, 1965.
2. L.G. Jacchia, New Static Models of the Thermosphere and Exosphere with Empirical Temperature Profiles, SAO Special Report No. 313, 1970.
3. L.G. Jacchia, Revised Static Models of the Thermosphere and Exosphere with Empirical Temperature Profiles, SAO Special Report No. 332, 1971.
4. L.G. Jacchia, Thermospheric Temperature Density and Composition: New Models, SAO Special Report No. 375, 1977.
5. A.E. Hedin, J.E. Salah, J.V. Evans, C.A. Reber, G.P. Newton, N.W. Spencer, D.C. Kayser, D. Alcayde, P. Bauer, L. Cogger, and J.P. McClure, "A global thermospheric model based on mass spectrometer and incoherent scatter data, MSIS 1, N₂ density and temperature," J. Geophys. Res. Vol. 82, 1977, p. 2139.
6. A.E. Hedin, C.A. Reber, N.W. Spencer, and H.C. Brinton, "Global model of longitude/UT variations in thermospheric composition and temperature based on mass spectrometer data," J. Geophys. Res., Vol. 84, 1979, p. 1.
7. A.E. Hedin, "A revised thermospheric model based on mass spectrometer and incoherent scatter data; MSIS-83," J. Geophys. Res., Vol. 88, 1983, p. 10, 170.
8. A.E. Hedin, MSIS-86, to be published.
9. H.E. Hinteregger, "Development of Solar Cycle 21 Observed in EUV Spectrum and Atmospheric Absorption," J. Geophys. Res., Vol. 84, 1979, p. 1933.
10. J.M. Forbes and F.A. Marcos, "Tidal variations in total mass density as derived from the AE-E MESA experiment," J. Geophys. Res., Vol. 84, 1979, p. 31.
11. A.E. Hedin, N.W. Spencer and H.G. Mayr, "The semidiurnal and ter-diurnal tides in the equatorial thermosphere from AE-E measurements," J. Geophys. Res., Vol. 85, 1980, p. 1781.
12. F.A. Marcos, and K.S.W. Champion, "Gravity waves observed in high latitude neutral density profiles," Space. Res. Vol. 12, 1972, p. 791.

13. J.M. Forbes, and F.A. Marcos, "Thermospheric density variations associated with auroral electrojet activity," J. Geophys. Res. Vol. 78, 1973, p. 3841.
14. F.A. Marcos, Application of Satellite Accelerometer Data to Improve Density Models, AFGL-TR-84-0211, 1984, AD A154904.
15. F.A. Marcos and E.R. Swift Application of the Satellite Triaxial Accelerometer to Atmospheric Density and Wind Studies, AFGL-TR-82-0091, 1982, AD A120852.
16. F.A. Marcos, and J.M. Forbes, (1985) "Thermospheric Winds From The Satellite Electrostatic Triaxial Accelerometer System", J. Geophysical Res., Vol 90, 1985, p. 6543.
17. A.S. Bramson and J.W. Slowey, Some Recent Innovations in Atmospheric Density Programs, AFCRL-TR-74-0370, 1974, AD 786414.
18. J.H. Butler, A Preliminary Upper Atmosphere Density Model Derived from Satellite Drag Density, Lockheed Missiles and Space Co., NASA Contractor Report No. 61298, Aug. 1969.
19. COESA, U.S. Standard Atmosphere, 1962, U.S. Government Printing Office, Washington, D.C., 1962.
20. COESA, U.S. Standard Atmosphere Supplements, 1966, U.S. Government Printing Office, Washington, D.C., 1966.
21. J.M. Forbes, and F.A. Marcos, "Thermospheric Winds, Densities and Temperatures During an Isolated Magnetic Substorm", submitted to J. Geophysical Res., 1985.
21. F.A. Herrero, "The Drag Coefficient of a Cylindrical Spacecraft in Orbit at Altitudes Greater than 150 km," NASA-TM-85043, 1983.
22. R.G. Roble, R.E. Dickinson, and E.C. Ridley, (1982) "Global circulation and temperature structure of thermosphere with high-latitude plasma convection", J. Geophys. Res., Vol 87, 1982, p. 1599.
23. D. Rees, T.J. Fuller-Rowell, and R.W. Smith, "Measurements of high latitude thermospheric winds by rocket and ground-based techniques and their interpretation using a three-dimensional time-dependent dynamical model", Planet Space Sci., Vol 28, 1980, p. 919.
24. R.G. Roble, J.M. Forbes and F.A. Marcos, "Thermosphere Dynamics During the March 22, 1979 Magnetic Storm, 1, Model Simulations," J. Geophys. Res., Vol, 92, 1987, P. 6045.
25. J.M. Forbes, R.G. Roble and F.A. Marcos, "Thermosphere Dynamics During the March 22, 1979 Magnetic Storm, 2, Comparisons of Model Predictions with Observations," J. Geophys. Res., Vol. 92, 1987, P. 6069.

6. THERMOSPHERIC GENERAL CIRCULATION MODELS

6.1 Modeling the Global Structure of the Thermosphere: Circulation, Temperature and Density

R.G. Roble^{*} and T.L. Killeen⁺

The earth's thermosphere is driven primarily by the absorption of solar ultraviolet radiation at wavelengths less than 200 nm. In the upper thermosphere, solar heating drives a diurnal circulation from the dayside to the nightside of the earth. In the lower thermosphere, a semi-diurnal circulation dominates driven primarily by semidiurnal in situ heating components and by upward propagating tides from the lower atmosphere. Thermospheric winds calculated by the National Center for Atmospheric Research (NCAR) thermospheric general circulation model (TGCM) have been used with a global ionospheric dynamo model to calculate the global distribution of electric currents and fields for equinox conditions during solar minimum.

At high latitudes, the solar-driven circulation is modified greatly by magnetospheric convection and auroral particle precipitation. Time-dependent thermospheric responses to auroral energy and momentum sources calculated by the TGCM display a wide variety of dynamic phenomena that depends upon the nature and time history of the forcings. Results from two TGCM simulations, November 21-22, 1981, and March 22, 1979, are described.

INTRODUCTION

Measurements from various U.S. Air Force and the NASA Dynamics Explorer satellites and from ground-based optical and radar observatories have provided considerable information on global thermospheric dynamics and its response to various magnetospheric forcings. There has also been considerable progress in our ability to model many of the observed features of the global circulation, temperature, and compositional structure of the thermosphere. A brief review of this progress is presented.

^{*} Senior scientist at the High Altitude Observatory, National Center for Atmospheric Research, Boulder, CO 80507. The National Center for Atmospheric Research is sponsored by the National Science Foundation.

⁺ Associate Professor of Atmospheric Science at the University of Michigan, Space Physics Research Laboratory, Ann Arbor, MI 48109. Also visiting scientist at the High Altitude Observatory, National Center for Atmospheric Research, Boulder, CO 80507.

PROGRESS IN MODELING THE GLOBAL THERMOSPHERIC STRUCTURE

Solar EUV and UV Driven Circulation

Solar energy in the EUV ($5 \leq \lambda \leq 103$ nm) and UV ($103 \leq \lambda \leq 200$ nm) portions of the solar spectrum is absorbed primarily by the major constituents of the thermosphere. In the optically thin upper thermosphere, above about 200 km, the solar heating distribution is rather uniform over the dayside, whereas below 200 km the optical depth increases and solar heating varies with the solar zenith angle. The solar heating distributions in the upper and lower thermosphere for equinox conditions at solar cycle minimum are shown in Figure 1 (Dickinson *et al.*, 1984). Solar EUV radiation also ionizes the constituents of the thermosphere and produces the ionosphere as shown in Figure 1. Photochemical equilibrium exists in the lower ionosphere and produces an electron density distribution that varies with the solar zenith angle as shown in Figure 2b. In the upper ionosphere, near 300 km, the ion gyrofrequency exceeds the ion-neutral collision frequency and the plasma is controlled by the geomagnetic field line configuration which produces the complex structure illustrated in Figure 2a. The ionospheric plasma, above 150 km, moves under the combined influence of the earth's geomagnetic field and any superimposed electric field. Its motion is largely independent of the neutral gas motion and collisions between the ions and neutrals exert an ion drag on the neutral gas motions. This ion drag provides either a resistance to the neutral flow or it can accelerate it. The ion drag is proportional to the electron number density and the relative velocity difference between the ionospheric plasma and neutral gas (e.g., Roble *et al.*, 1982; Killeen and Roble, 1984). At low- and mid-latitudes, the thermospheric flow above 150 km, to a first approximation, is governed by a balance between the pressure force, generated by solar heating, and the ion drag force. Below 150 km, the coriolis force becomes important. Using the solar heating and electron density distributions shown in Figures 1 and 2 for equinox conditions during solar minimum the NCAR thermospheric general circulation model has been used to calculate the global circulation, temperature, and composition structure for the idealized case where auroral processes are neglected (Dickinson *et al.*, 1981, 1984). The calculated global circulation and perturbation temperature structure, from a global mean value, driven by in situ solar heating only, is shown in Figure 3.

In the upper thermosphere, the distribution of solar heating drives a largely diurnal circulation from the high temperature and high pressure region on the dayside to the low temperature and low pressure region on the nightside (Figure 3a). The magnitude of the wind speed is less on the dayside because of increased electron density, and hence ion drag, than on the nightside. In the lower thermosphere, there are larger semidiurnal in-situ heating components that give rise to a semidiurnal circulation and temperature structure as shown in Figure 3b.

The solar-driven circulation of the thermosphere is also influenced by upward propagating tides that are excited by absorption of solar energy by ozone and water vapor in the middle and lower atmosphere. Fesen *et al.* (1986) have specified the tidal structure at the lower boundary of the NCAR-TGCM and calculated their influence on the global thermospheric structure as shown in Figure 4. By comparing Figures 3 and 4 it can be seen that tides primarily affect the structure of the lower thermosphere and they are gradually dissipated by viscosity, thermal conductivity, and ion drag as they reach

the upper thermosphere. The longer vertical wavelength 2,2 tidal mode does, however, reach the upper thermosphere and produces the midnight temperature bulge that has been observed at equatorial latitudes.

Global Dynamo

Richmond and Roble (1987) have developed a global dynamo model that calculates the ionospheric electric fields and currents, and the associated ground magnetic variations, that are generated by the dynamo actions of winds simulated with the NCAR-TGCM. The calculated electrodynamic structure, using the winds shown in Figure 4, is shown in Figure 5. The dynamo model uses a tilted dipole geomagnetic field and allows for field-aligned current flow between conjugate points, but no magnetospheric dynamo effects are included. Richmond and Roble (1987) have shown that without tidal forcing the TGCM winds produce ground magnetic variations that have the general pattern of S_q variations but that are about only about half as strong. The addition of tidal forcing improves the agreement between calculated and observed magnetic variations and electric fields. The calculated electric potential, field-aligned current distribution, total horizontal, and equivalent current function at 11 UT for equinox conditions during solar cycle minimum are shown in Figure 5. The calculated potential distribution in Figure 5 is in reasonable agreement with empirical model predictions by Richmond *et al.* (1980). Field-aligned currents between southern and northern magnetic hemisphere are substantial even at equinox, with about 290 kA flowing at 11 UT. The field-aligned current distribution is considerably more sensitive to the wind and conductivity patterns than is the horizontal ionospheric current distribution. Other details of the dynamo simulation are discussed in detail by Richmond and Roble (1987).

High-Latitude Thermospheric Dynamics

At high latitudes, the solar-driven circulation is modified greatly by magnetospheric convection and auroral particle precipitation. The ion drag momentum source of magnetospheric plasma convection drives a largely rotational, nondivergent, double vortex wind system at F region altitudes that essentially follows the two cell pattern of magnetospheric convection. Wind velocities vary with the magnitude of the cross-polar cap potential drop and magnitudes greater than 500 ms^{-1} are common at high latitudes during moderate levels of geomagnetic activity. The circulation and perturbation temperature structure over the summer hemisphere (southern for December solstice) polar cap for three different cases is shown in Figure 6 (Roble *et al.*, 1983). The solar only driven circulation, shown in Figure 6a, has a wind speed of about 100 ms^{-1} and it flows from the dayside to the nightside over the polar cap. With magnetospheric convection ion drag forcing, with a cross-polar cap potential drop of 20 kV, the wind speeds in the polar cap increase to 200 ms^{-1} with the two cell pattern of magnetospheric convection being superimposed on the solar-driven flow. At 60 kV cross-polar cap potential drop, the two cell pattern clearly stands out in the neutral wind pattern with speeds approaching 400 ms^{-1} . Joule heating raises the perturbation temperature increasing from 200 K to 300 K to 450 K for the three cases, respectively.

The vortices generated by magnetospheric convection extend downward into the lower thermosphere, as shown in Figure 7, with a cold low pressure cyclonic circulation near the dawn terminator and a warm high pressure anti-cyclonic circulation in the evening sector. The strength of the vortices increases with the cross-polar cap potential

drop as shown in the figure.

The Air Force and Dynamics Explorer satellites have made major contributions to our overall understanding of thermospheric dynamics at high latitudes and its response to various magnetospheric forcings. High-latitude neutral winds have been shown to be driven mainly by and generally follow the basic two cell pattern of magnetospheric convection (Killeen *et al.*, 1982, 1983, 1984, 1985, 1986, 1987; Hays *et al.*, 1984; Rees *et al.*, 1983, 1985a,b; Roble *et al.*, 1983, 1984, 1987; Forbes *et al.*, 1987; Marcos and Forbes, 1985). Neutral wind measurements have shown relationships dependent upon the B_z (Killeen *et al.*, 1985) and the B_y component directions of the interplanetary magnetic field (McCormac *et al.*, 1985). In addition, satellite data have shown considerable variability and small-scale structure in both the ion drift velocity and neutral wind vectors.

A number of the observed large-scale features of high-latitude dynamics have been well modeled by TGCMs. These include the strong anti-sunward flow over the polar caps (Rees *et al.*, 1983, 1985a; Roble *et al.*, 1983, 1984, 1987; Hays *et al.*, 1984; Larsen and Mikkelsen, 1983), a strong sunward-directed flow observed in the evening auroral oval (Fuller-Rowell and Rees, 1984; Rees *et al.*, 1985b; Roble *et al.*, 1986), the thermospheric response to the changing ion drift pattern associated with the B_y component of the interplanetary magnetic field (Rees *et al.*, 1986), and the general temperature and compositional structure over the polar (Roble *et al.*, 1984, 1987; Forbes *et al.*, 1987; Rees *et al.*, 1985a).

Time-Dependent TGCM Simulations

The NCAR-TGCM has been modified recently to accommodate time-dependent auroral forcings and it has been used to calculate the time-dependent thermospheric circulation, temperature, and compositional patterns for specific events or days. An empirical magnetospheric convection pattern (Heelis *et al.*, 1982) is used to specify the ion drift and it has been modified to mimic the observed B_y interplanetary magnetic field-induced shifts. The time-dependent cross-polar cap potential drop is determined using measured solar wind parameters and an empirical relationship developed by Reiff *et al.* (1985).

Aurora oval parameters are based on the empirical model developed by Fuller-Rowell and Evans (1987) using NOAA satellite data of aurora particle precipitation. The oval characteristics are specified by a single parameter, the estimated hemispherical power input from which particle energy flux, characteristic energy, and auroral boundaries are obtained through empirical relationships. A fast parameterization that allows the ionization rate and the ion and electron density to be calculated self-consistently within the NCAR TGCM has been described by Roble and Ridley (1987). The enhanced electron density from auroral processes is appropriately added to the electron density obtained from the Chiu (1975) empirical model and the sum is used to derive the high-latitude ion drag parameters for time-dependent TGCM simulations.

The parameterized auroral forcings were used in the TGCM to investigate thermospheric dynamics during November 21-22, 1981. Geomagnetic activity was relatively steady and a detailed comparison of the TGCM predicted high-latitude winds was made with wind measurements made by the Dynamics Explorer (DE) satellite on an orbit-by-orbit basis during the period (Roble *et al.*, 1987a). DE 2 measurements of electric fields and auroral particle precipitation also enabled a detailed comparison to be made between the TGCM auroral parameterizations and measurements. TGCM predictions and DE 2 measurements for six different passes over the northern and southern hemisphere polar

caps are shown in Figure 8. In general, this study (Roble *et al.*, 1987a) shows that at least for this period of steady forcing during moderate geomagnetic activity there is good general agreement between model predictions and observations of the large-scale structure on the evening side of the auroral oval and polar cap. There is, however, considerable small-scale structure observed by the DE 2 satellite that is not predicted by the TCGM.

Roble *et al.* (1987b) also used the TCGM to study the thermospheric response to the geomagnetic storm of March 22, 1979. The magnetospheric and ionospheric characteristics of this storm have been studied intensively by the CDAW-6 coordinated workshop (McPherron and Manka, 1985). The time-dependent auroral forcings were estimated from the studies done by CDAW-6 and used as inputs for the TCGM. The calculated thermospheric temperature and wind structure on a constant pressure surface near 300 km at various times during the storm are shown in Figure 9. Geomagnetic activity was low for the period preceding the storm and the wind velocities were generally small with a uniform temperature over the polar cap as shown in Figure 9a. At 1230 UT the storm intensified and both the wind velocities and temperature increased as shown in Figure 9b. By 1530 UT, near the peak of the storm when the auroral electrojet index AE was near 1600, the wind velocities approached 1 km s^{-1} with temperatures exceeding 2000 K near the throat of the convection pattern as shown in Figure 9c. By 2030 UT (Figure 9d) both the wind velocities and temperatures decreased but there was still residual heating and dynamics lingering after the intense storm period. In the lower thermosphere, near 120 km, the dawn and dusk vortices were spun up during the storm period as shown in Figure 10. Once the vortices were spun up, they decayed slowly with time with some residual dynamics remaining at 2400 UT, 9 hours after the peak of the event.

Because of the impulsive nature of the storm, large-scale thermospheric disturbances were generated at F region heights that propagated equatorward from both auroral zones. To illustrate the stormtime response two TCGM simulations were made and difference fields were constructed: TCGM storm simulation minus a TCGM simulation where the auroral forcing remained constant at its pre-storm values. The aurora-generated disturbances in magnetic conjugate hemispheres propagated equatorward and both reached the equator in about 2 hours, as shown in Figure 11. The disturbances interacted. Converging waves are associated with sinking motion and subsequent diverging motion is associated with upwelling and adiabatic heating. As a result, the temperature at the equator first increases by about 100 K and then decreases by about 50 K. These interacting waves were shown by Fesen *et al.* (1987) to have an important influence on the equatorial ionosphere especially in the midnight sector where impulses travel effectively toward lower latitudes. Finally, comparisons of temperature difference fields of the storm response calculated by the TCGM and MSIS-83 empirical model are shown in Figure 12. There is general agreement in the large-scale features indicating that the overall magnitude of the storm is well modeled, however, there is considerably more structure associated with local regions of intense heating and wave propagation in the TCGM fields that is not shown in the MSIS-83 predictions. It appears that MSIS-83 gives a good climatology or mean representation of the storm response whereas the TCGM accounts for time-dependent weather processes with a much higher time resolution.

Forbes *et al.* (1987) compared TCGM predictions of winds and neutral density with measurements made from a satellite electrostatic triaxial accelerometer (SETA)

experiment (Marcos and Forbes, 1985) for several orbits during the 22 March 1979 geomagnetic storm. The satellite measurements, TGCM predictions and MSIS-86 empirical model predictions of the neutral density ratio at 200 km along the satellite orbital path are shown in Figure 13. Also plotted are the vertical winds at 200 km obtained from TGCM predictions. In comparing the density ratio figures, it is seen that the TGCM predictions give a better agreement with satellite measurements than MSIS-86. This indicates that the TGCM has a better representation of small scale structure than MSIS-86, however, the satellites show considerably more variability than either TGCM or MSIS-86 predictions.

CONCLUDING REMARKS

Considerable progress has been made in recent years in improving our understanding of the main physical processes operating in the thermosphere and ionosphere. This progress was possible because of the availability of satellite data on the structure and dynamics of the thermosphere and ionosphere as well as in the development of new global dynamic models for use in interpreting measurements and for predictions of global phenomena. It appears that it may be possible, in the near future, to develop a sufficiently realistic TGCM for use in the prediction of thermospheric weather that can be used to improve forecasts of satellite drag.

ACKNOWLEDGEMENTS

This research effort was supported in part by the AFGL in-house laboratory independent research program.

REFERENCES

1. Chiu, Y.T., An improved phenomenological model of ionospheric density, *J. Atmos. Terr. Phys.*, **37**, 1563, 1975.
2. Dickinson, R.E., E.C. Ridley, and R.G. Roble, A three-dimensional, time-dependent general circulation model of the thermosphere, *J. Geophys. Res.*, **86**, 1499, 1981.
3. Dickinson, R.E., E.C. Ridley, and R.G. Roble, Thermospheric general circulation with coupled dynamics and composition, *J. Atmos. Sci.*, **41**, 205, 1984.
4. Fesen, C.G., R.E. Dickinson, and R.G. Roble, Simulation of thermospheric tides at equinox with the NCAK thermospheric general circulation model, *J. Geophys. Res.*, **91**, 1471, 1986.
5. Fesen, C.G., R.G. Roble, and G. Crowley, Ionospheric effects at low latitudes during the March 22, 1979 geomagnetic storm, *J. Geophys. Res.*, in press, 1987.
6. Forbes, J.M., R.G. Roble, and F.A. Marcos, Thermospheric dynamics during the March 22, 1979, magnetic storm: 2, Comparison of model predictions with observations, *J. Geophys. Res.*, **92**, 6069-6081, 1987.
7. Fuller-Rowell, T.J. and D. Rees, Interpretation of an anticipated long-lived vortex in the lower thermosphere following simulation of an isolated substorm, *Planet. Space Sci.*, **32**, 69, 1984.
8. Fuller-Rowell, T.J. and D.S. Evans, Height integrated Pedersen and Hall conductivity patterns inferred from the TIROS-NOAA satellite data, *J. Geophys. Res.*, in press, 1987.

9. Hays, P.B., T.L. Killeen, N.W. Spencer, L.E. Wharton, R.G. Roble, B.E. Emery, T.J. Fuller-Rowell, D. Rees, L.A. Frank, and J.D. Craven, Observations of the dynamics of the polar thermosphere, *J. Geophys. Res.*, **89**, 5597, 1984.
10. Heelis, R.A., J.K. Lowell, and R.W. Spiro, A model of the high-latitude ionospheric convection pattern, *J. Geophys. Res.*, **87**, 6339, 1982.
11. Killeen, T.L. and R.G. Roble, An analysis of the high latitude thermospheric wind pattern calculated by a thermospheric general circulation model, 1, Momentum forcing, *J. Geophys. Res.*, **89**, 7509, 1984.
12. Killeen, T.L., P.B. Hays, N.W. Spencer, and L.E. Wharton, Neutral winds in the polar thermosphere as measured from Dynamics Explorer, *Geophys. Res. Lett.*, **9**, 957, 1982.
13. Killeen, T.L., P.B. Hays, N.W. Spencer, and L.E. Wharton, Neutral winds in the polar thermosphere as measured from Dynamics Explorer, *Adv. Space Res.*, **2**, 10, Pergamon Press, Oxford, 133, 1983.
14. Killeen, T.L., P.B. Hays, G.R. Carignan, R.A. Heelis, W.B. Hanson, N.W. Spencer, and L.H. Brace, Ion-neutral coupling in the high latitude F-region: Evaluation of ion heating terms from Dynamics Explorer 2, *Geophys. Res.*, **89**, 7495, 1984.
15. Killeen, T.L., R.A. Heelis, P.B. Hays, N.W. Spencer, and W.B. Hanson, Neutral motions in the polar thermosphere for northward interplanetary magnetic field, *Geophys. Res. Lett.*, **12**, 159, 1985.
16. Killeen, T.L., R.W. Smith, N.W. Spencer, J.W. Meriwether, D. Rees, G. Hernandez, P.B. Hays, L.L. Cogger, D.P. Sipler, M.A. Biondi, and C.A. Tepley, Mean neutral circulation in the winter polar F-region, *J. Geophys. Res.*, **91**, 1633, 1986.
17. Killeen, T.L., J.D. Craven, L.A. Frank, J.-J. Ponthieu, N.W. Spencer, R.A. Heelis, L.H. Brace, R.G. Roble, P.B. Hays, and G.R. Carignan, On the relationship between the dynamics of the polar thermosphere and the morphology of the aurora: Global-scale observations from Dynamics Explorers 1 and 2, *J. Geophys. Res.*, in press, 1987.
18. Larsen, M.F. and I.S. Mikkelsen, The dynamic response of the high-latitude thermosphere and geostrophic adjustment, *J. Geophys. Res.*, **88**, 3158, 1983.
19. Marcos, F.A. and J.M. Forbes, Thermospheric winds from the satellite electrostatic triaxial accelerometer (SETA) system, *J. Geophys. Res.*, **90**, 6543-6552, 1985.
20. McCormac, F.G., T.L. Killeen, E. Gombosi, P.B. Hays, and N.W. Spencer, Configuration of the high-latitude neutral thermosphere circulation for IMF By negative and positive, *Geophys. Res. Lett.*, **12**, 155, 1985.
21. McPherron, R.L. and R.H. Manka, Dynamics of the 1054 UT March 22, 1979, sub-storm event: CDAW 6, *J. Geophys. Res.*, **90**, 1175, 1985.
22. Rees, D., T.J. Fuller-Rowell, R. Gordon, T.L. Killeen, P.B. Hays, L.E. Wharton, and N.W. Spencer, A comparison of wind observations of the upper thermosphere from the Dynamics Explorer satellite with the predictions of a global time-dependent model, *Planet. Space Sci.*, **31**, 1983, pp. 1299.
23. Rees, D., R. Gordon, T.J. Fuller-Rowell, M. Smith, G.R. Carignan, T.L. Killeen, P.B. Hays, and N.W. Spencer, The composition, structure, temperature and dynamics of the upper thermosphere in the polar regions during October to December, 1981, *Planet. Space Sci.*, **33**, 617, 1985a.

24. Rees, D., T.J. Fuller-Rowell, M.F. Smith, R. Gordon, T.L. Killeen, P.B. Hays, N.W. Spencer, L.E. Wharton, and N.C. Maynard, The westward thermospheric jet-stream of the evening auroral oval, *Planet. Space Sci.*, **33**, 425, 1985b.
25. Rees, D., T.J. Fuller-Rowell, R. Gordon, J.P. Heppner, N.C. Maynard, N.W. Spencer, L.E. Wharton, P.B. Hays, and T.L. Killeen, A theoretical and empirical study of the response of the high-latitude thermosphere to the sense of the "Y" component of the interplanetary magnetic field, *Planet. Space Sci.*, **34**, 1, 1986.
26. Reiff, P.H., R.W. Spiro, R.A. Wolf, Y. Kamide, and J.H. King, Comparison of polar cap potential drops estimated from solar wind and ground magnetometer data, *J. Geophys. Res.*, **90**, 1318, 1985.
27. Richmond, A.D., M. Blanc, B.A. Emery, R.H. Wand, B.G. Fejer, R.F. Woodman, S. Ganguly, P. Amayenc, R.A. Behnke, C. Calderon, and J.V. Evans, An empirical model of quiet-day ionospheric electric fields at middle and low latitudes, *J. Geophys. Res.*, **85**, 4658, 1980.
28. Richmond, A.D. and R.G. Roble, Electrodynamic effects of thermospheric winds from the NCAR thermospheric general circulation model, *J. Geophys. Res.*, in press, 1987.
29. Roble, R.G., R.E. Dickinson, and E.C. Ridley, Global circulation and temperature structure of the thermosphere with high-latitude plasma convection, *J. Geophys. Res.*, **87**, 1599, 1982.
30. Roble, R.G., R.E. Dickinson, E.C. Ridley, B.A. Emery, P.B. Hays, T.L. Killeen, and N.W. Spencer, The high latitude circulation and temperature structure of the thermosphere near solstice, *Planet. Space Sci.*, **31**, 1479, 1983.
31. Roble, R.G., B.A. Emery, R.E. Dickinson, E.C. Ridley, T.L. Killeen, P.B. Hays, G.R. Carignan, and N.W. Spencer, Thermospheric circulation, temperature and compositional structure of the Southern Hemisphere polar cap during October-November, 1981, *J. Geophys. Res.*, **89**, 9057, 1984.
32. Roble, R.G. and E.C. Ridley, An auroral model for the NCAR thermospheric general circulation model, *Annales. Geophysicae*, in press, 1987.
33. Roble, R.G., T.L. Killeen, G.R. Carignan, N.W. Spencer, R.A. Heelis, P.H. Reiff, J.D. Winningham, and D.S. Evans, Thermospheric dynamics during 21/22 November 1981: Dynamics Explorer measurements and TGCM predictions, *J. Geophys. Res.*, in press, 1987a.
34. Roble, R.G., J.M. Forbes, and F.A. Marcos, Thermospheric dynamics during the March 22, 1979 magnetic storm (a) Model simulations, *J. Geophys. Res.*, 6045-6068, 1987b.

FIGURE CAPTIONS

Fig. 1 Contours of calculated neutral gas heating rate ($\text{J kg}^{-1}\text{s}^{-1}$) for equinox conditions during solar cycle minimum along (a) the model $Z = +2$ constant pressure surface level near 300 km and (b) the $Z = -4$ level near 120 km (Dickinson *et al.*, 1984).

Fig. 2 Contours of the electron number density [$\log_{10}(n_e; \text{cm}^{-3})$] obtained from the Chiu (1975) empirical model for equinox conditions during solar minimum (a) along the 300 km constant height surface and (b) along the 120 km constant height surface.

Fig. 3 Perturbation temperatures from a constant global mean value (solid curves) and winds (arrows) at fixed pressure levels for equinox conditions during solar minimum calculated by the TGCM without tides (Fesen *et al.*, 1986). The pressure levels $Z = +2$ and -4 correspond to approximate altitudes of 300 and 135 km. The maximum wind arrows are 136 and 24 ms^{-1} on the $Z = +2$ and -4 pressure levels, respectively.

Fig. 4 Same caption as for Figure 3 except with inclusion of tides in the TGCM (Fesen *et al.*, 1986). The maximum wind arrows are 166 and 71 ms^{-1} on the $Z = +2$ and -4 pressure levels, respectively.

Fig. 5 (a) Electrostatic potential at 300-km altitude computed at 11 UT for the case including semidiurnal tidal forcing. The contour interval is 1 kV. (b) Total horizontal current flowing between 90 and 300 km at 11 UT for the case including tidal forcing. A vector equal in length to 1 hour of magnetic local time represents 0.1 A m^{-1} . (c) Downward component of field-aligned current at 300 km computed for 11 UT for the case including tidal forcing. The contour interval is $2 \times 10^{-9} \text{ A m}^{-2}$. Downward currents have solid contours; upward currents have dashed contours. (d) Equivalent current function for the entire three-dimensional ionospheric-magnetospheric current system at 11 UT for the case including tidal forcing. The contour interval is 20 kA. Equivalent current flows counterclockwise around the dashed contours and clockwise around the solid contours (Richmond and Roble, 1987).

Fig. 6 Polar plots giving the direction and magnitude of the calculated southern hemisphere (summer) high-latitude circulation and contours of perturbations temperature (K) along the $Z = +1$ (~ 300 km) constant pressure surface at December solstice for (a) solar heating only, (b) solar heating plus magnetospheric convection with a cross-polar cap potential drop of 20 kV, and (c) same as (b) except for 60 kV. The wind speed associated with the maximum arrow is 110 ms^{-1} in (a), 200 ms^{-1} in (b), and 380 ms^{-1} in (c), respectively (Roble *et al.*, 1983).

Fig. 7 Same as in Figure 6 except along the $Z = -4$ (~ 130 km) constant pressure surface. The wind speed associated with the maximum arrow is 75 ms^{-1} in (a), 77 ms^{-1} in (b), and 89 ms^{-1} in (c), respectively (Roble *et al.*, 1983).

Fig. 8 Measured meridional neutral wind by the wind and temperature spectrometer instrument along the DE 2 satellite track over northern and southern hemisphere polar caps for six orbits (a) 1639, NH; (b) 1640, NH; (c) 1641, NH; (d) 1641, SH; (e) 1644, NH; and (f) 1646, NH, on November 22, 1981. Also shown are TGCM predicted neutral temperature pattern (K) and neutral wind vectors along the model $Z = +2$ constant pressure surface (~ 400 km) over the polar caps at the times of the DE 2 satellite passes. The outer circle represents a latitude of either ± 37.5 latitude depending upon the hemisphere (Roble *et al.*, 1987a).

Fig. 9 Contours of TGCM calculated neutral temperature (K) and neutral wind vectors (ms^{-1}) on the $Z = +1$ constant pressure surface near 300 km over the northern hemisphere polar cap for four different times on March 22, 1979: (a) 0830 UT, (b) 1230 UT, (c) 1530 UT, and (d) 2030 UT. The length of the maximum arrow is 1400 ms^{-1} and is shown for reference (Roble *et al.*, 1987b).

Fig. 10 Same as in Figure 9 except for the $Z = -4$ constant pressure surface near 120 km. The length of the maximum arrow is 275 ms^{-1} and all arrows are scaled relative to this maximum value (Roble *et al.*, 1987b).

Fig. 11 Contours of the time variation of difference fields (storm simulation minus quiet variation). (a) Meridional wind (ms^{-1}), (b) zonal wind (ms^{-1}), (c) temperature (K), and (d) vertical wind (ms^{-1}) along the $Z = +1$ constant pressure surface near 330 km. Contour intervals are: (a) and (b) 100 ms^{-1} , (c) 100 K , and (d) 5 ms^{-1} (Roble *et al.*, 1987b).

Fig. 12 Contours of the time variation of the zonally averaged temperature difference fields (K) (storm simulation minus quiet variation) calculated by the TGCM and MSIS-83 models, respectively, illustrating the response to the March 22, 1979, substorms: (a) TGCM-calculated temperature difference along the 325-km constant height surface, (b) a perspective illustration of that temperature response, (c) MSIS-83 calculated temperature difference along the 325-km constant height surface, and (d) a perspective illustration of that temperature response. Contour intervals are 50 K . (Roble *et al.*, 1987b).

Fig. 13 Three-dimensional depictions of latitude-UT density ratio variations to an average prestorm density value at 200 km. The upper left panel gives TGCM predictions of the density ratio, the upper right lower right panels give the MSIS-86 predictions and satellite measurements, respectively. TGCM predictions of vertical winds are shown in the lower left panel. The vertical scale ranges are indicated by the numbers in parenthesis for each figure (Forbes *et al.*, 1987).

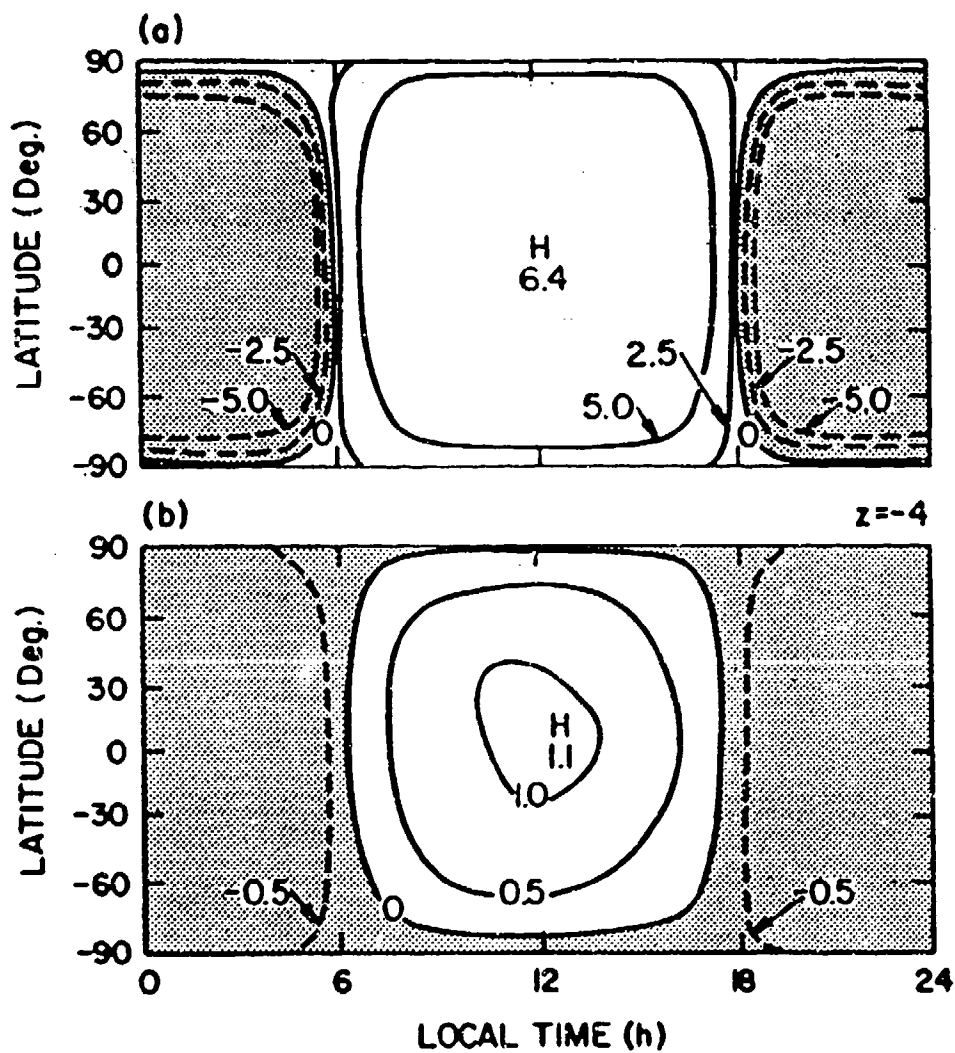


Fig. 1

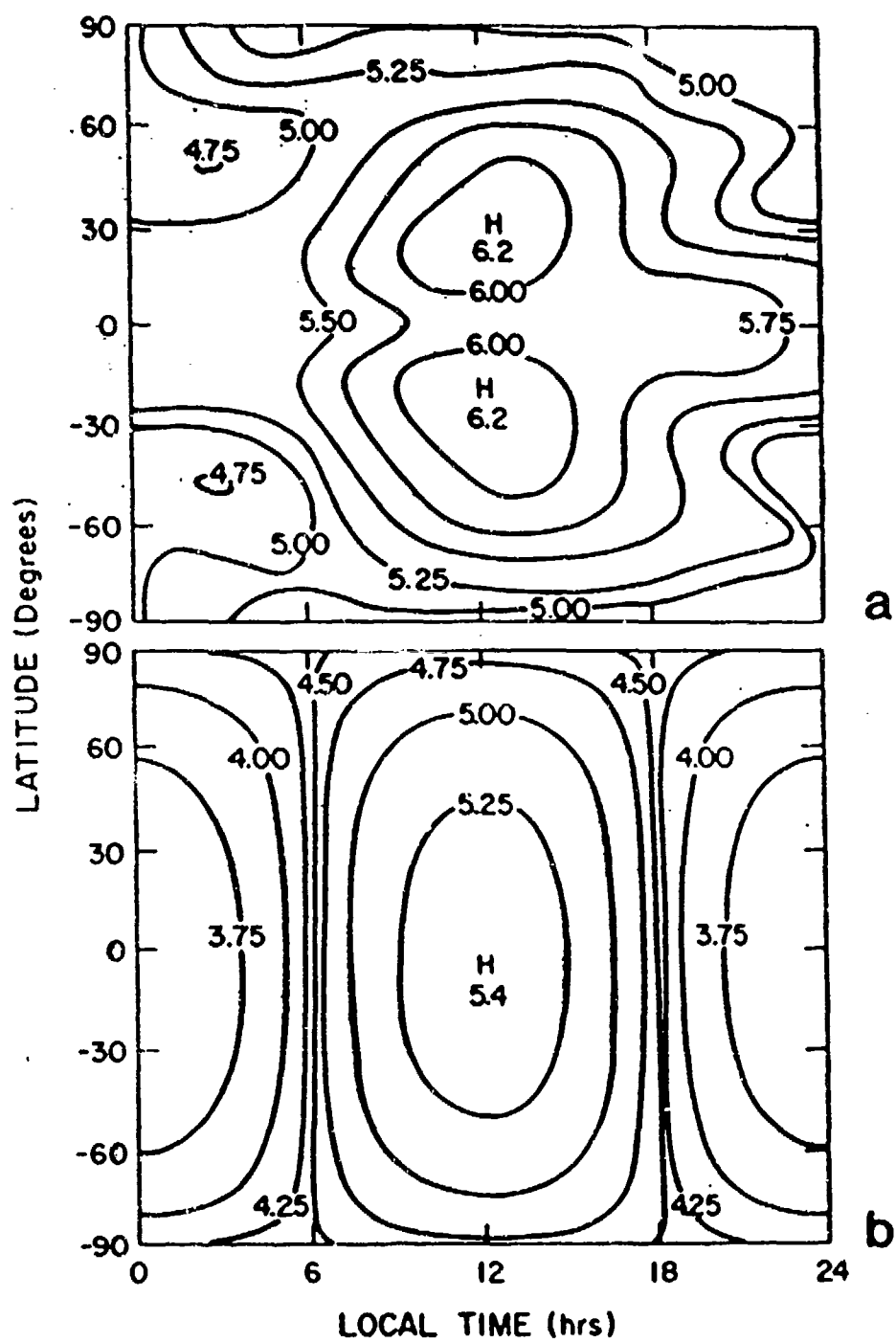


Fig. 2

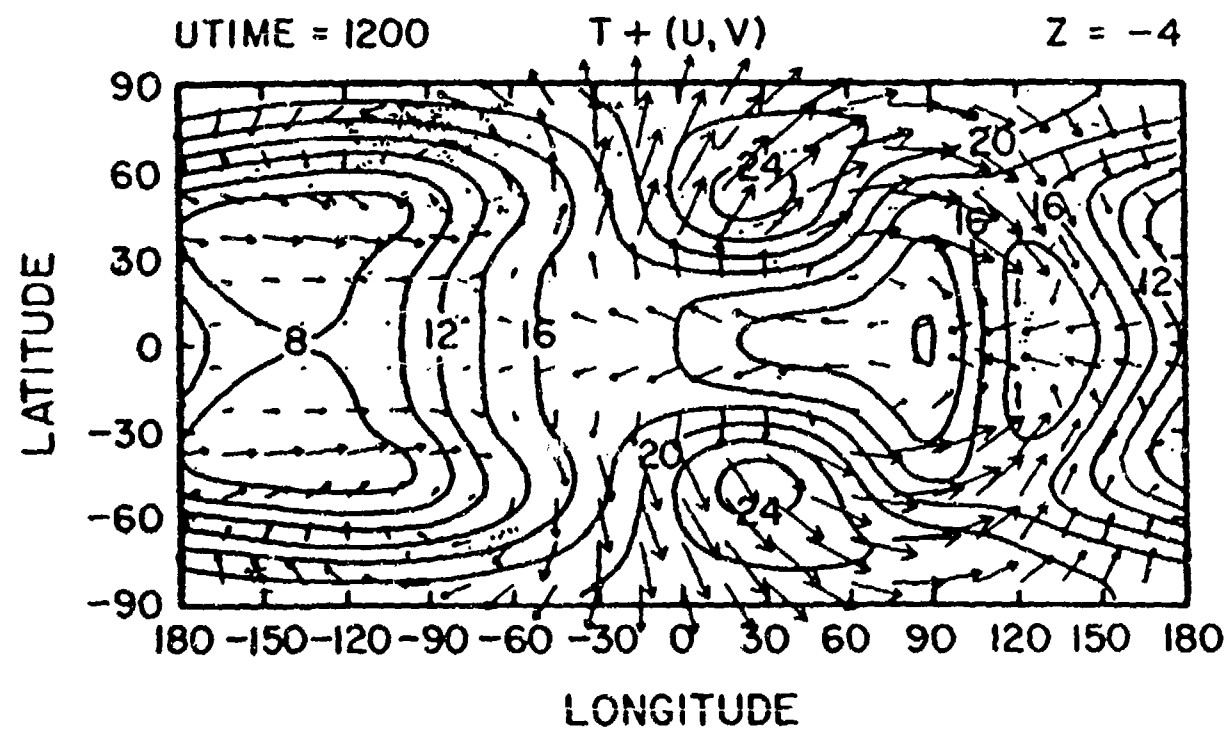
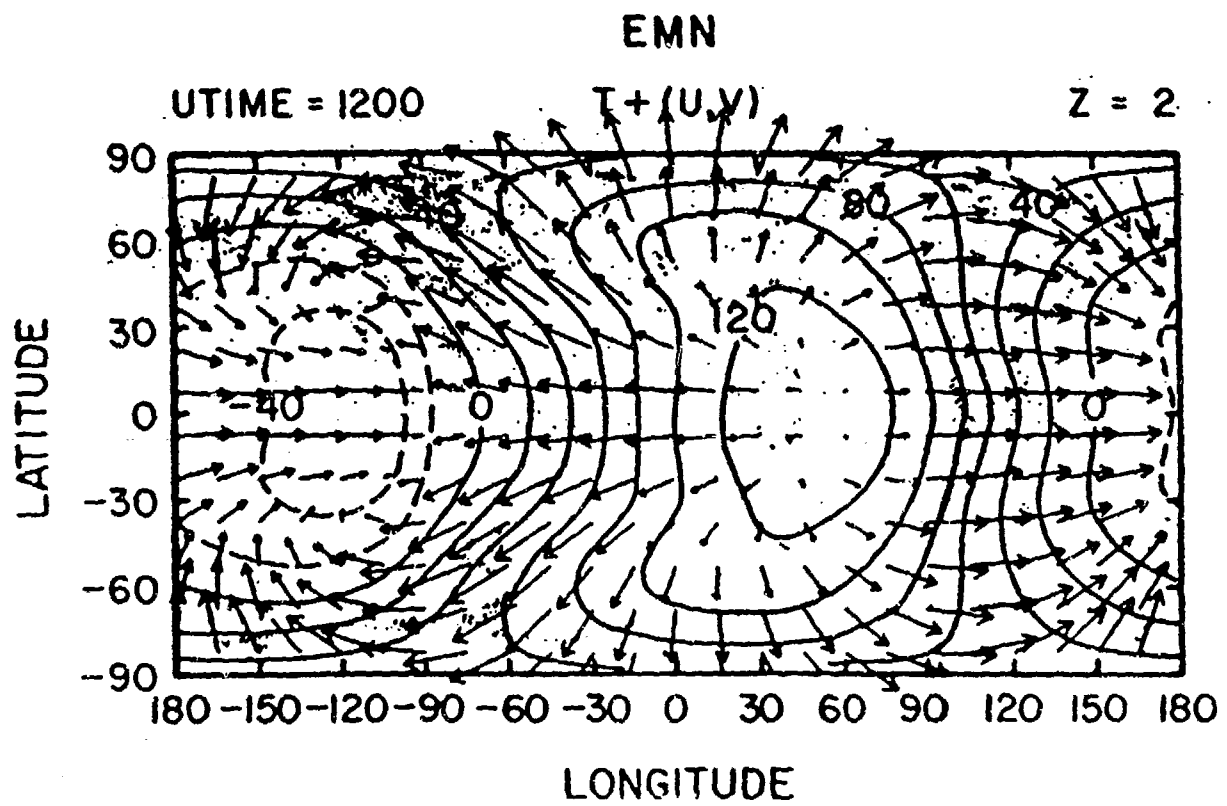


Fig. 3
6 - 15

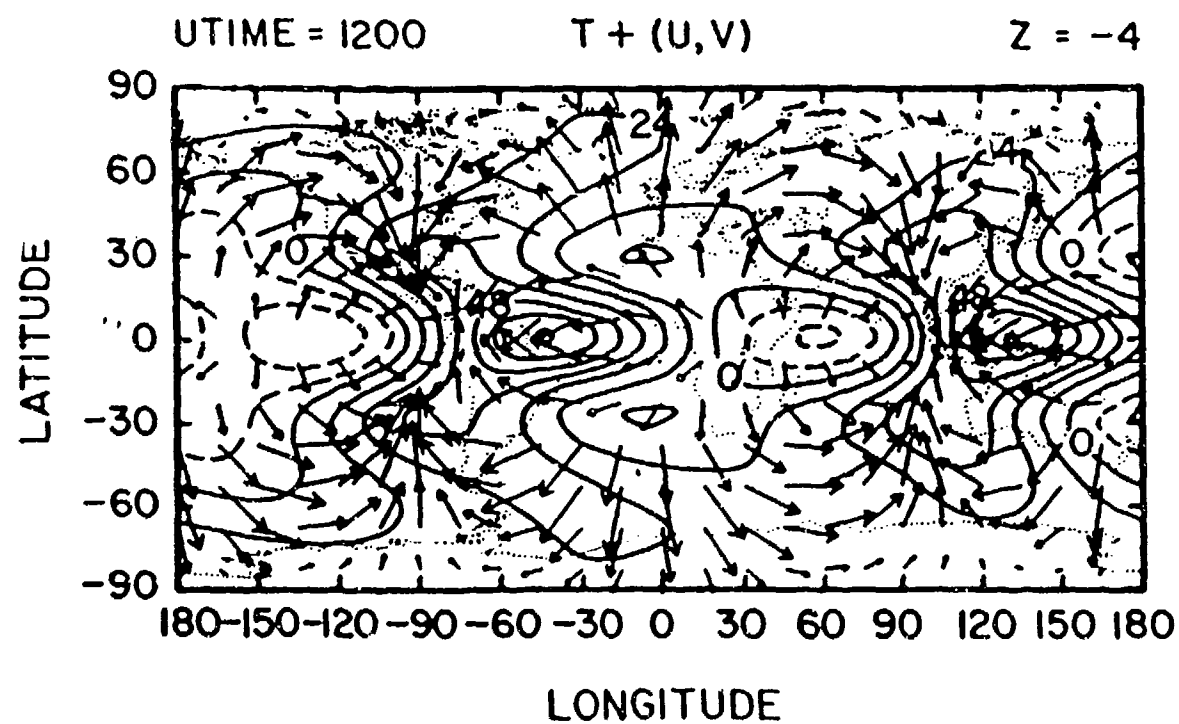
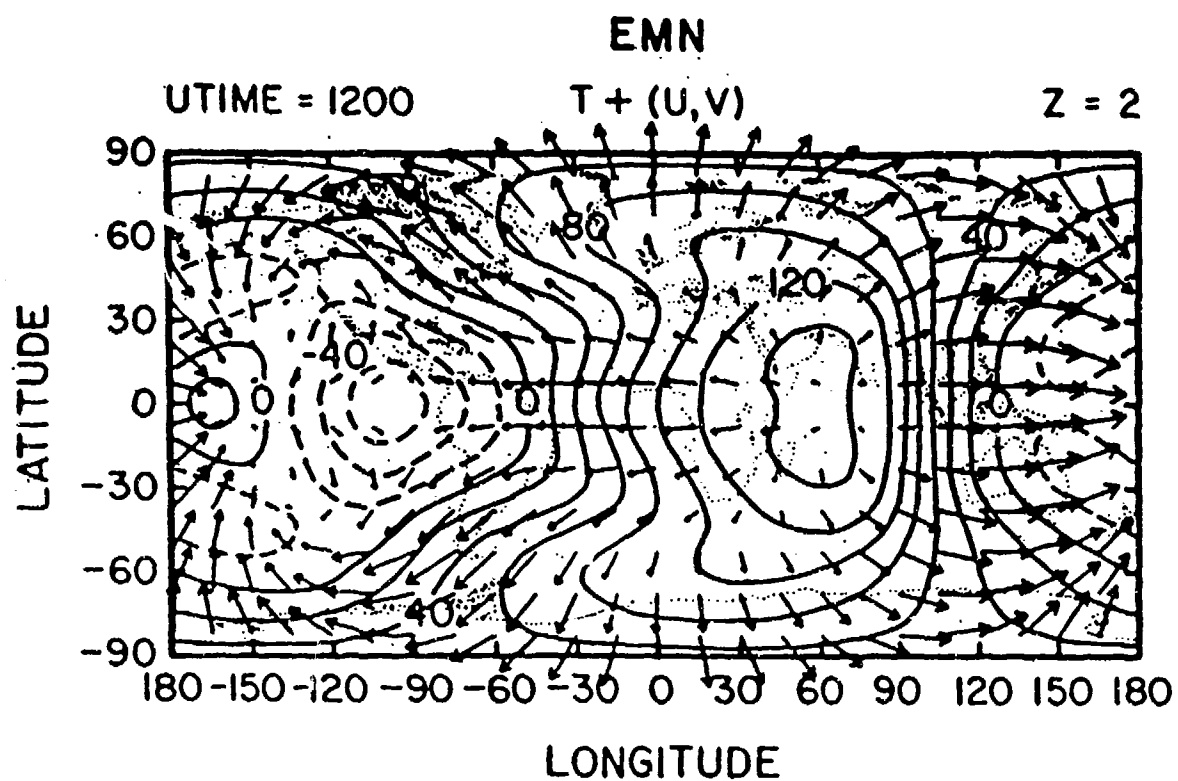


Fig. 4

11 UT

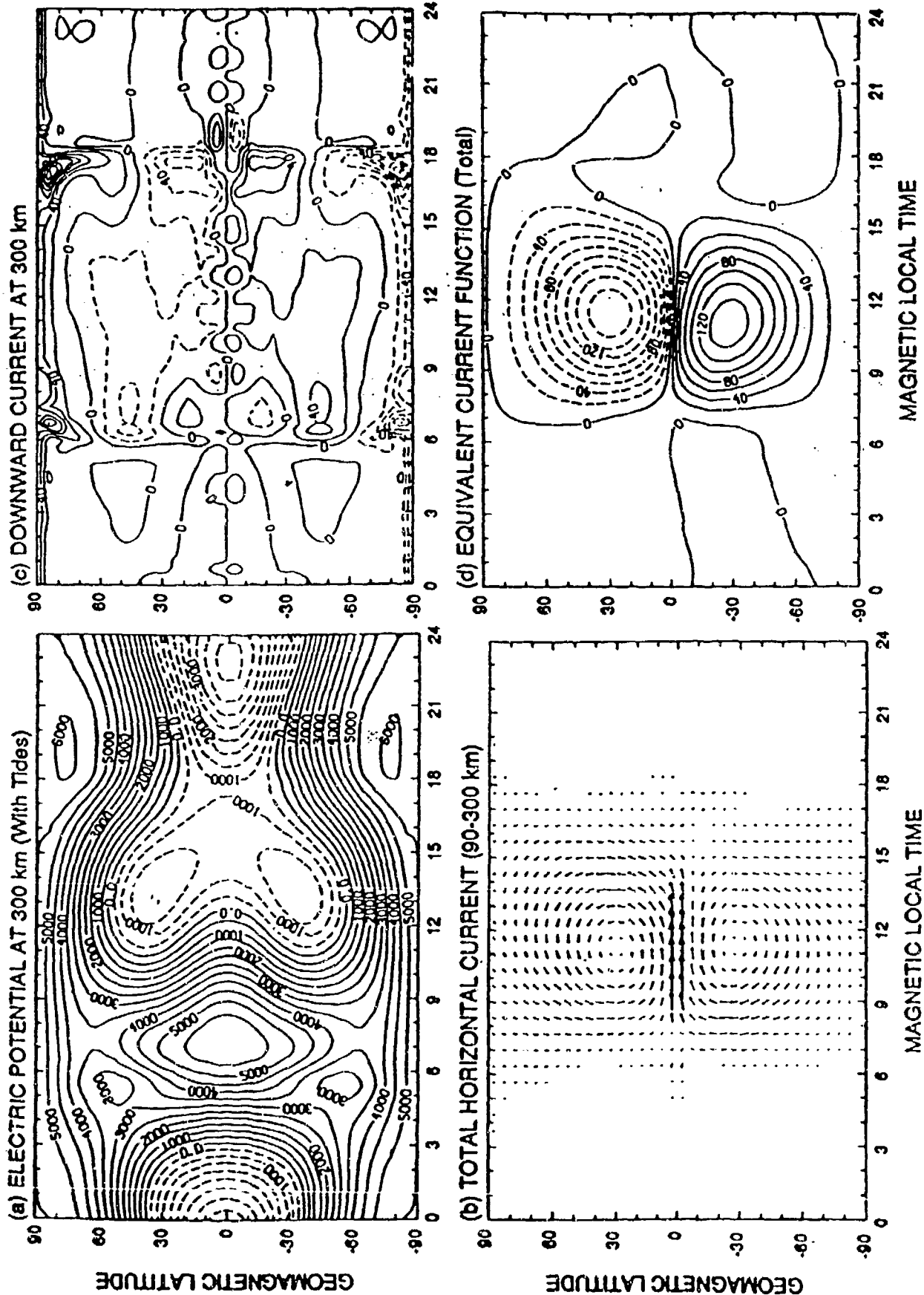


Fig. 5

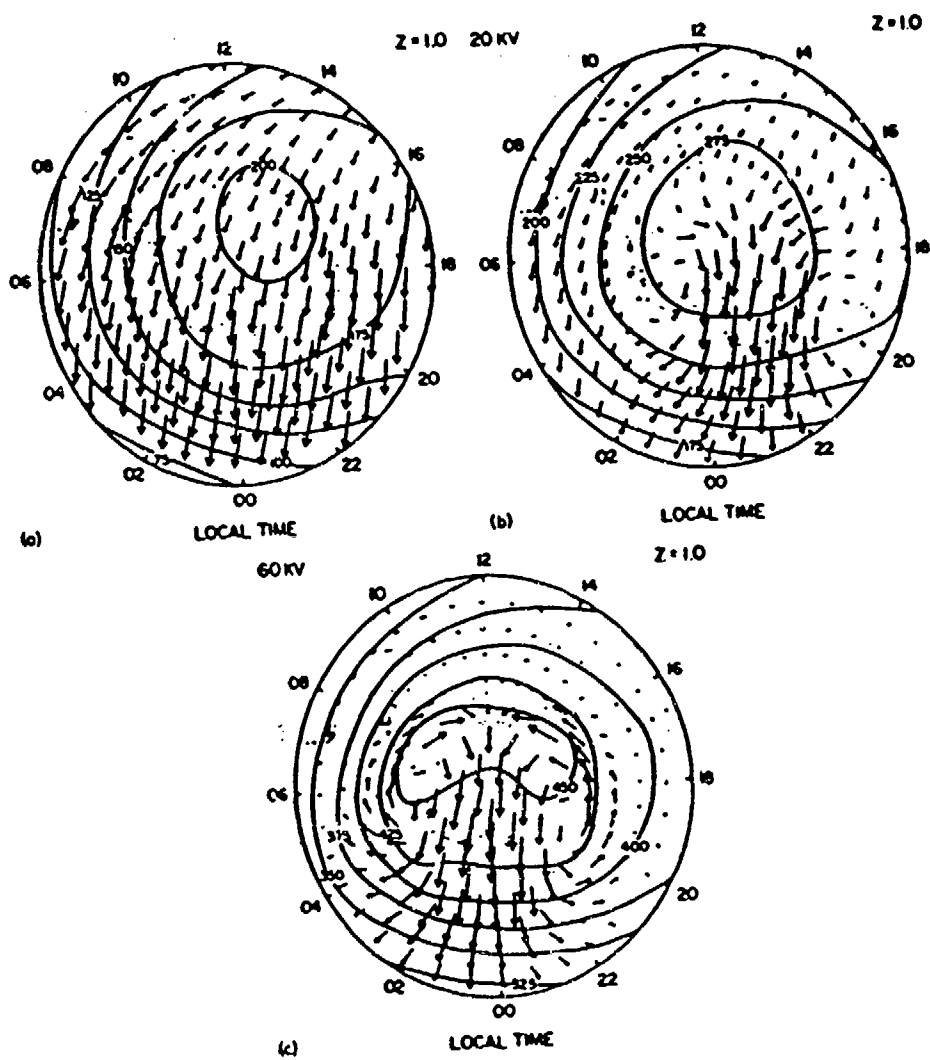


Fig. 6

R. G. RIMLF *et al.*

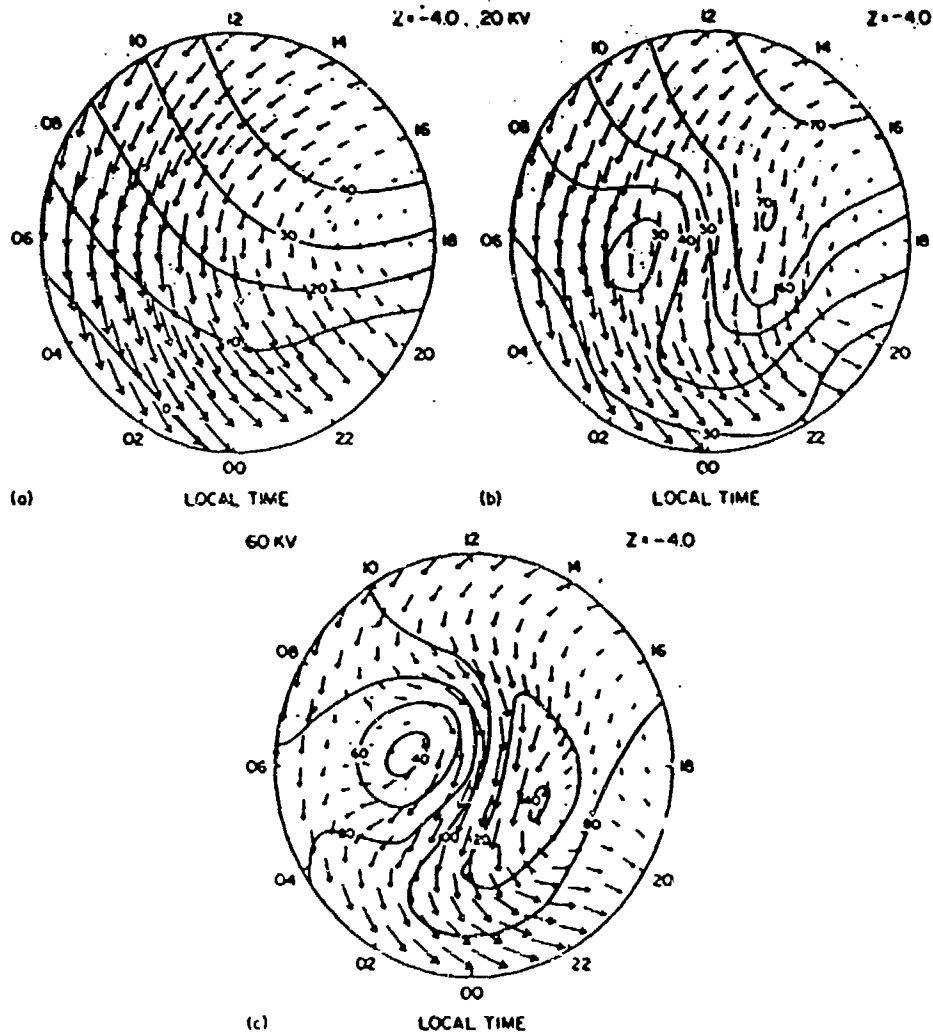


Fig. 7

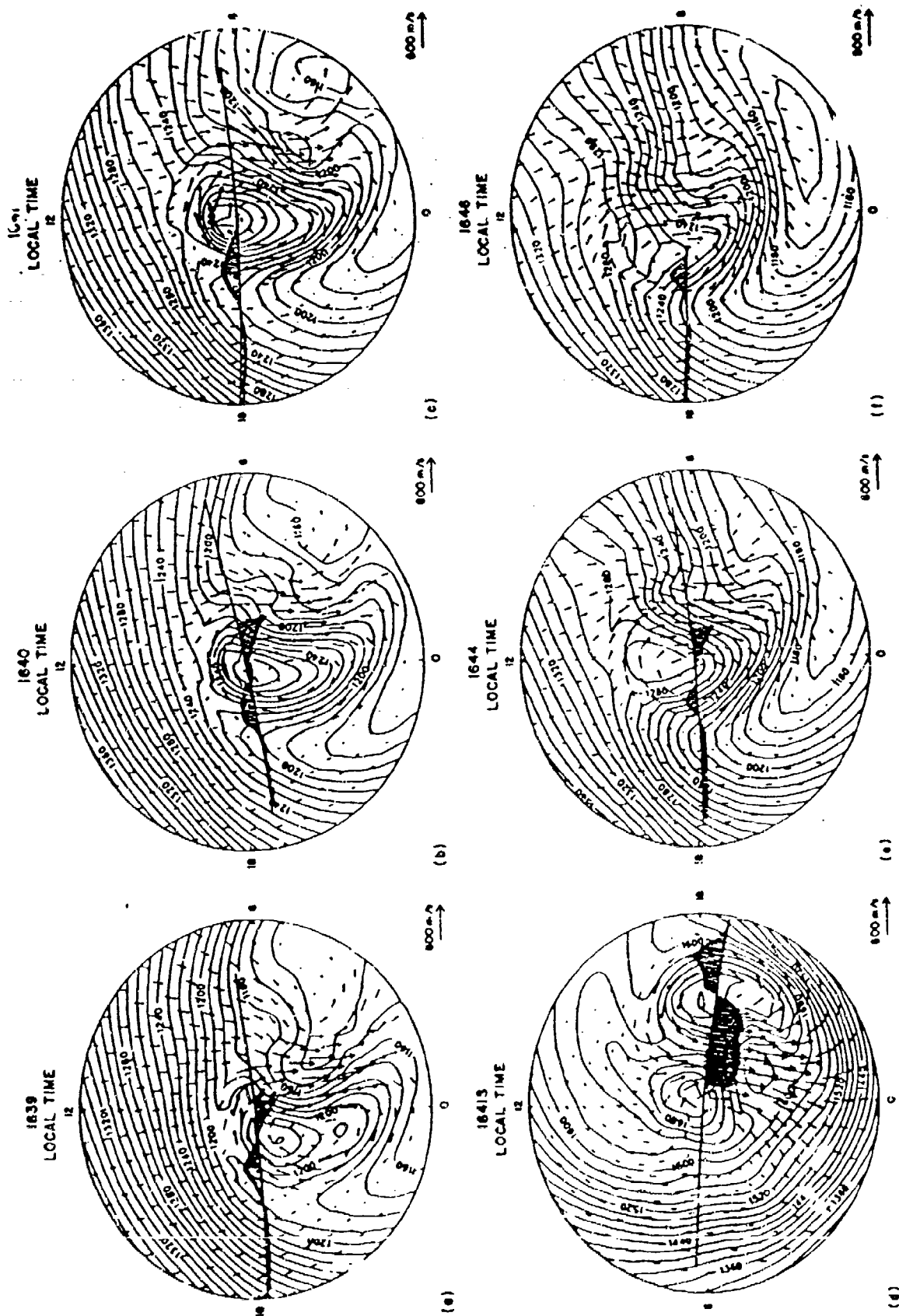
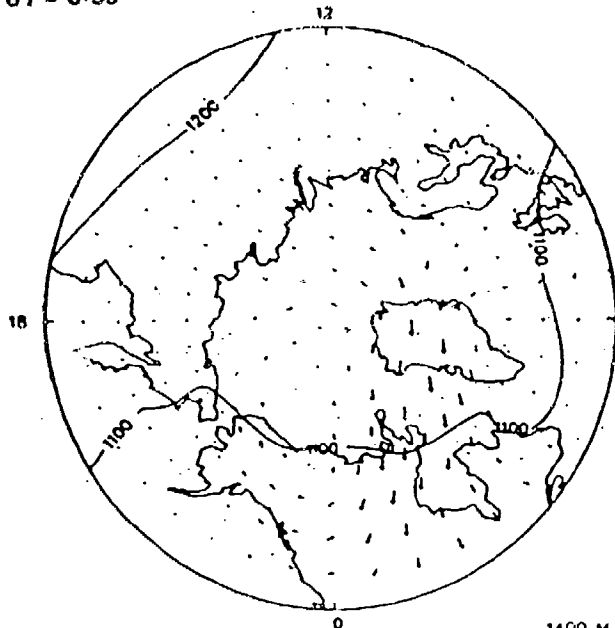


Fig. 8

UT = 8:30

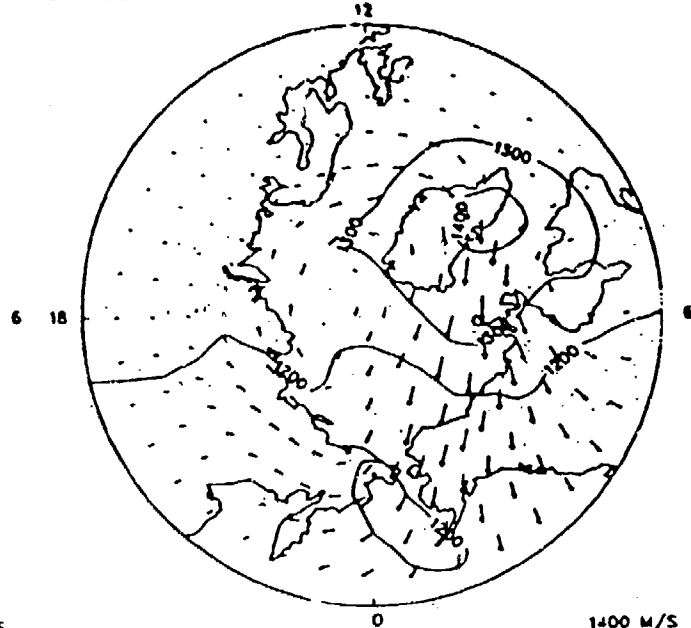
LOCAL TIME



(a)

UT = 12:30

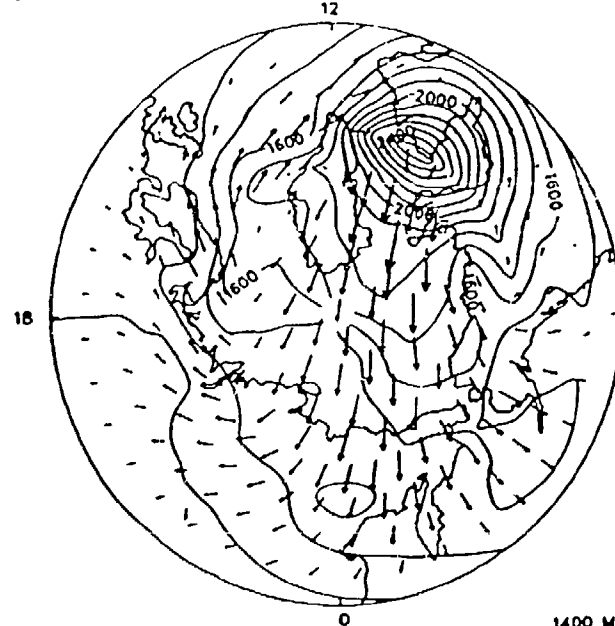
LOCAL TIME



(b)

UT = 15:30

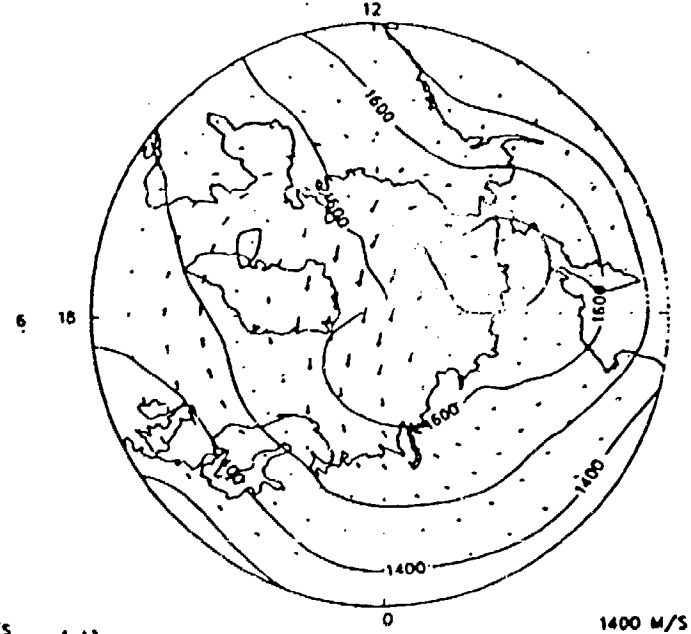
LOCAL TIME



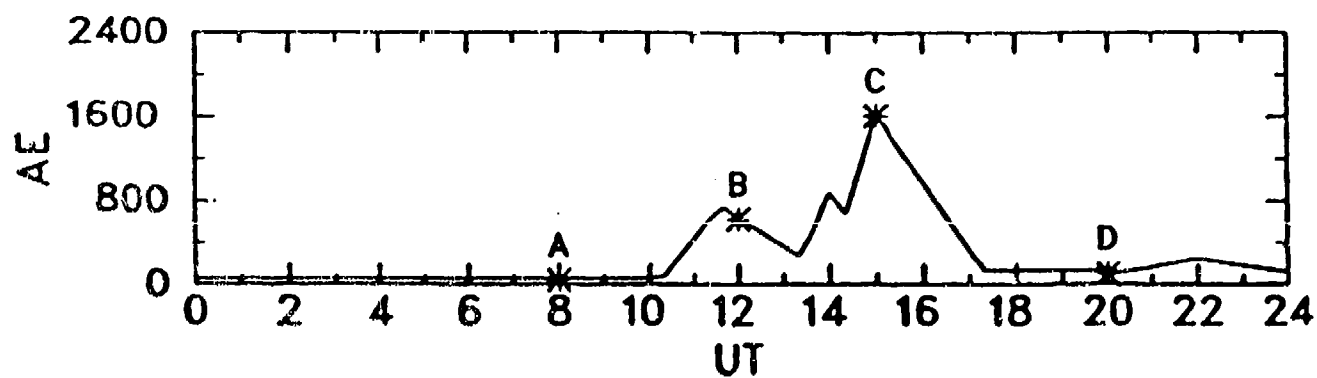
(c)

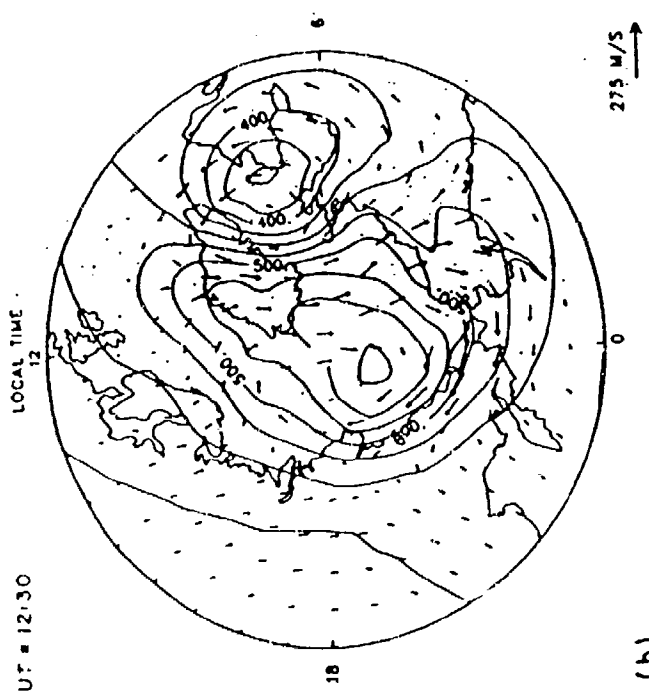
UT = 20:30

LOCAL TIME

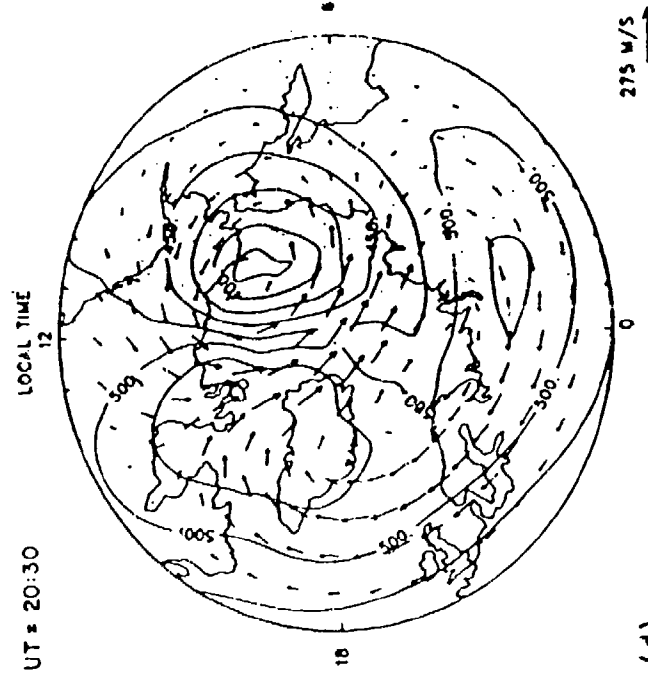


(d)

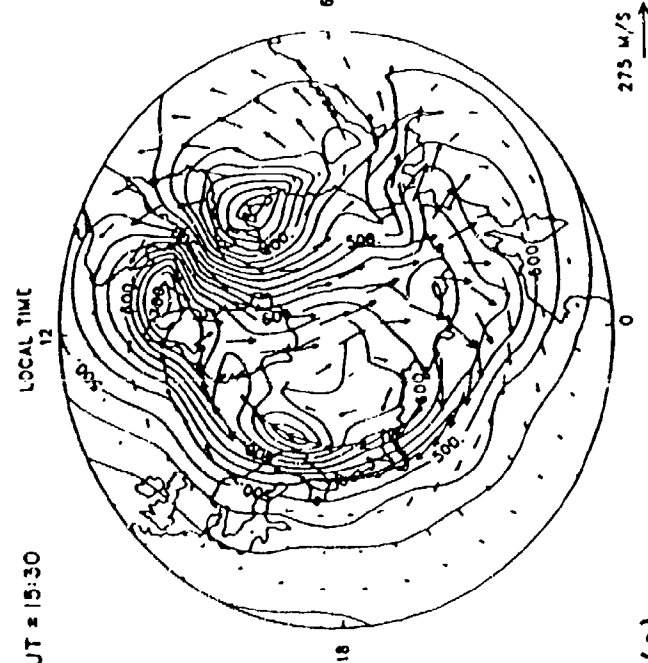




(a)



(b)



(c)

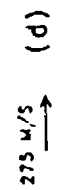


Fig. 10

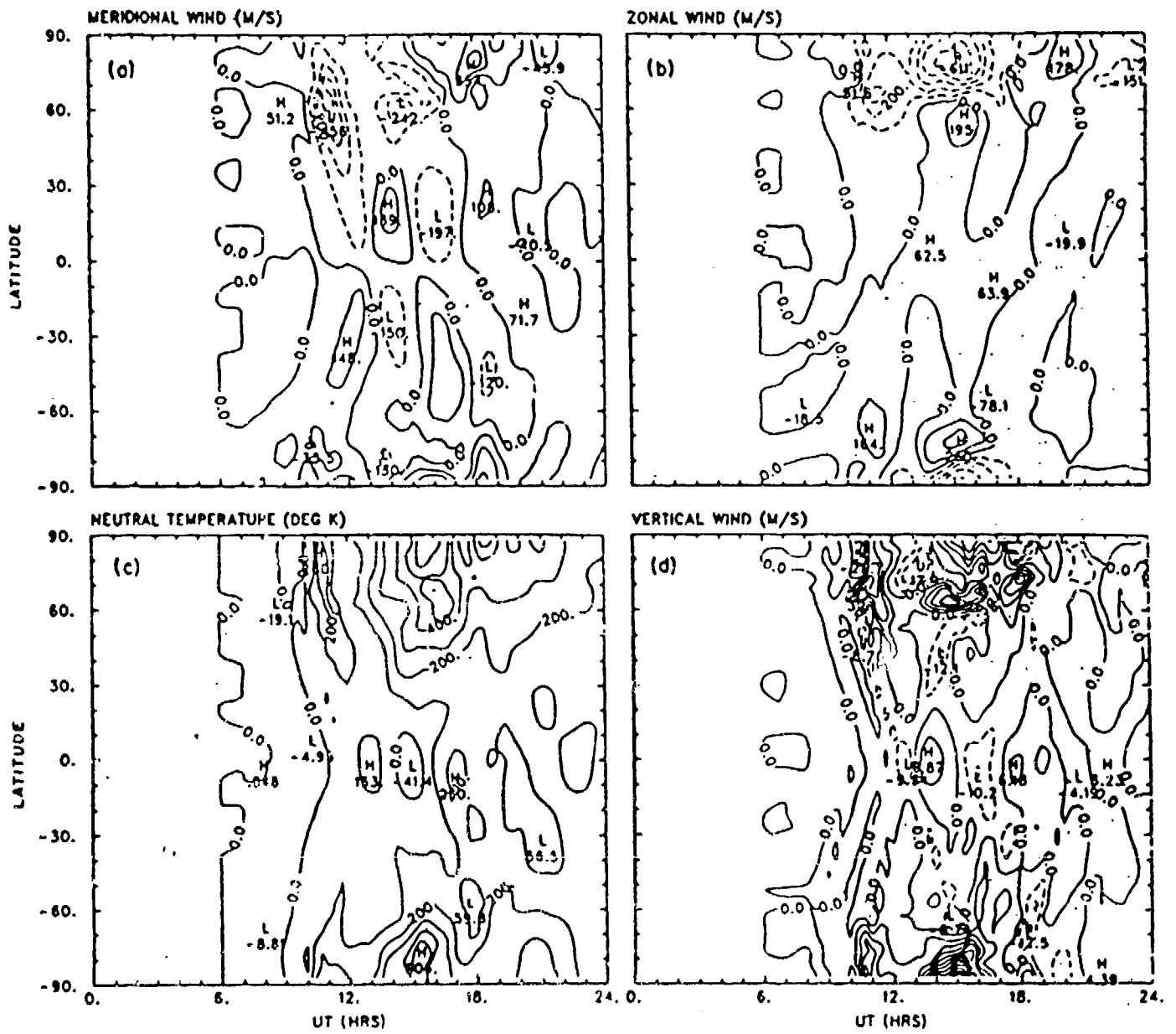


Fig. 11

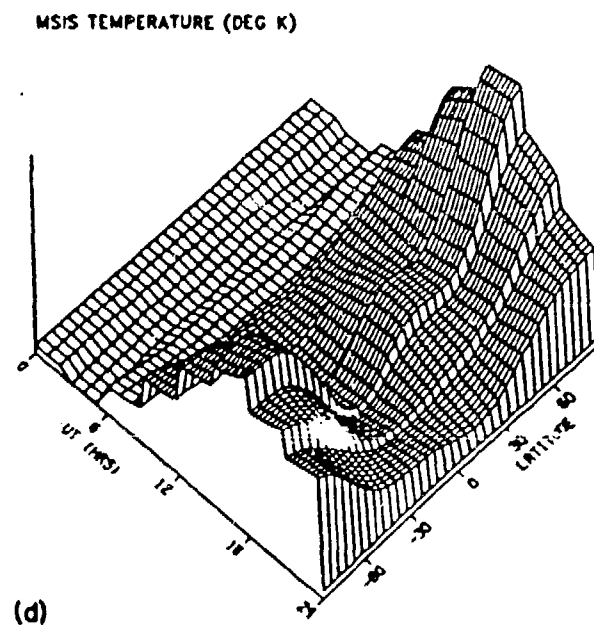
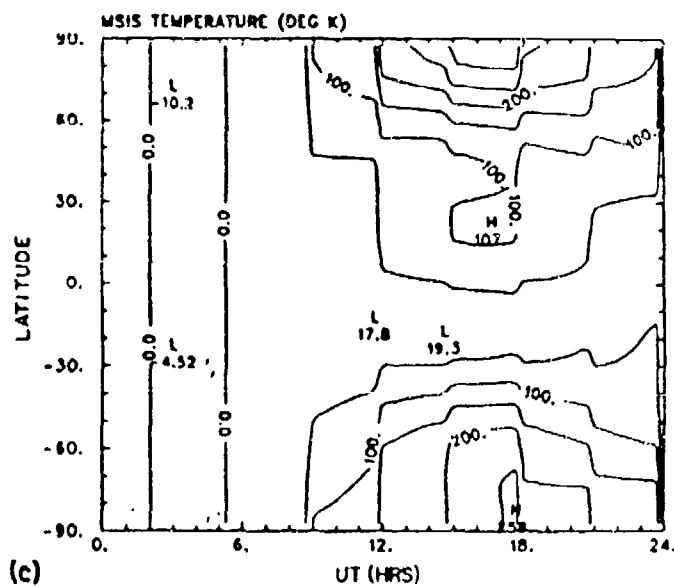
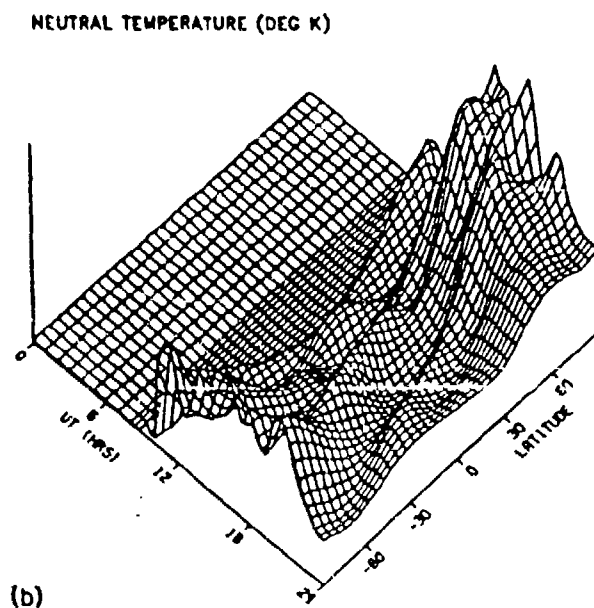
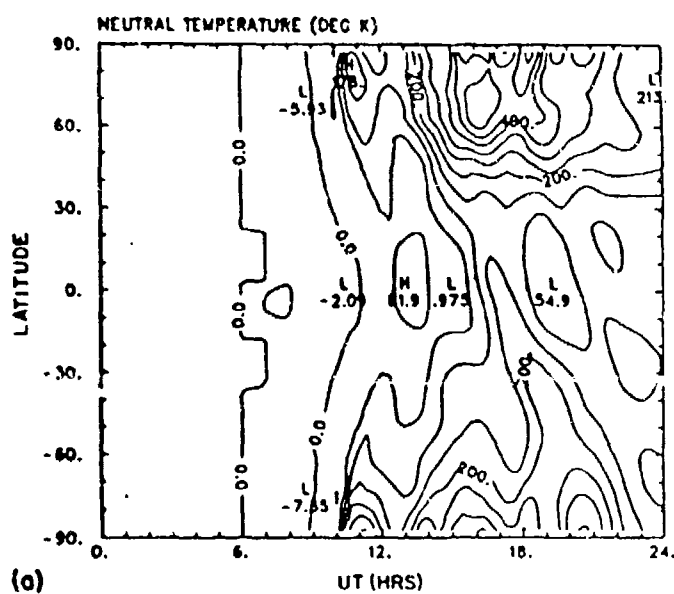
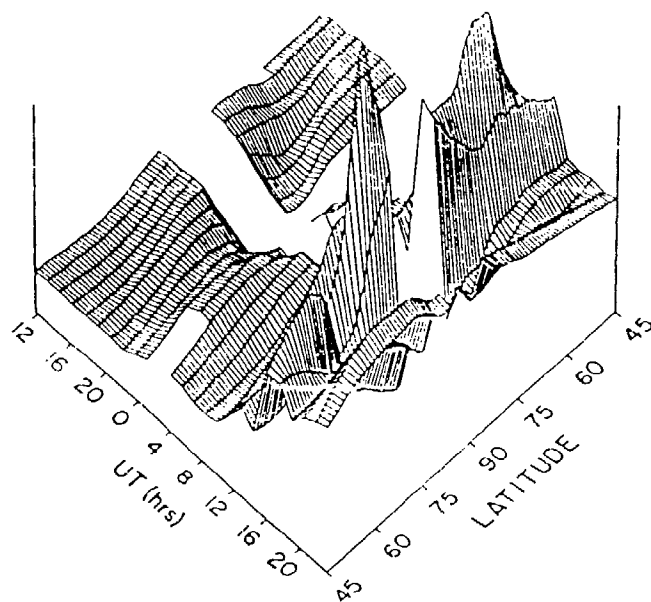
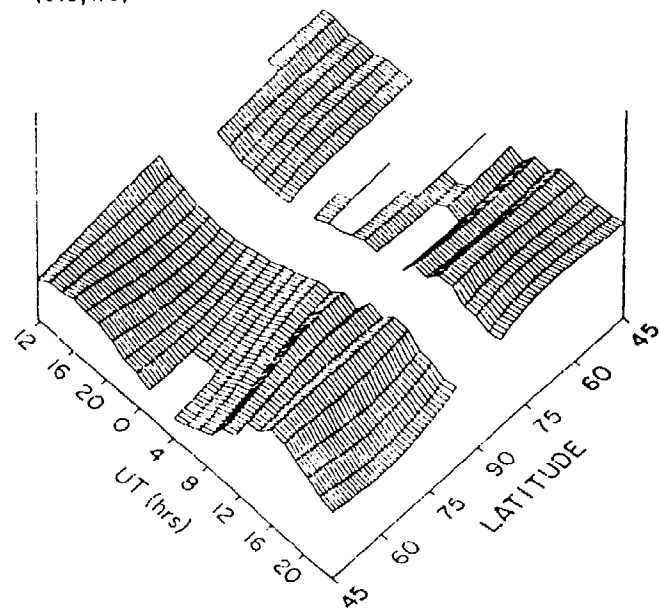


Fig. 12

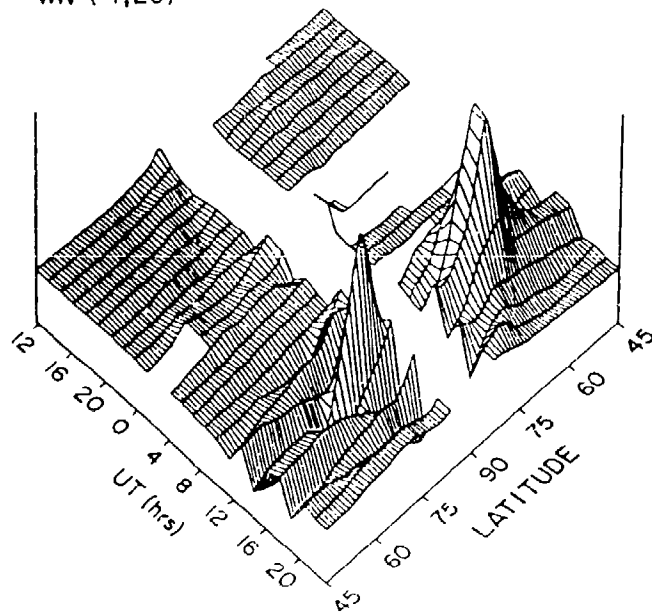
DENSITY RATIO
TGCM AT 200 KM
(0.8,1.6)



DENSITY RATIO
MSIS AT 200 KM
(0.8,1.6)



VERTICAL WIND (M/S)
TGCM AT 200 KM
WN (-7,20)



DENSITY RATIO
SAT AT 200 KM
(0.8,1.6)

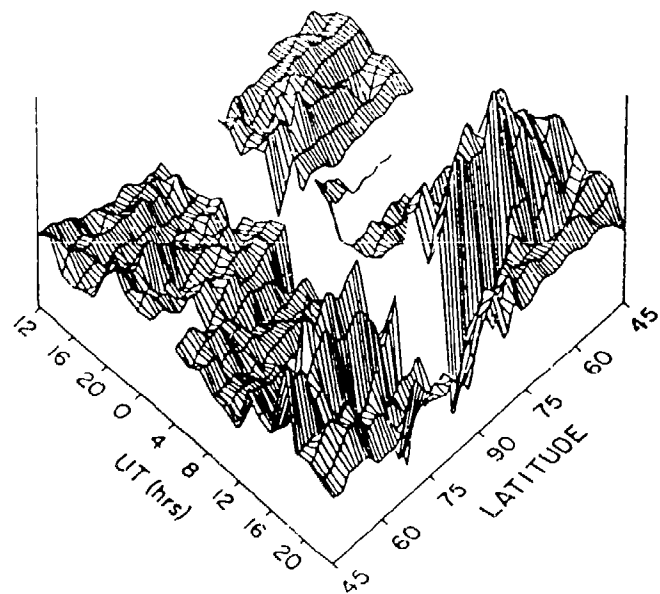


Fig. 13

NUMERICAL COMPUTATION OF THERMOSPHERIC DENSITY, USING COUPLED IONOSPHERIC /
THERMOSPHERIC CODES AND PARAMETERISED SOLAR AND GEOMAGNETIC INPUTS.

David Rees, T. J. Fuller-Rowell.

Department of Physics and Astronomy,
University College London,
Gower Street, London WC1E 6BT, UK.

Abstract:

Numerical codes, describing the structure, chemistry and dynamics of the coupled thermosphere and ionosphere system as computed from first principles, are now available. These fully-coupled numerical models provide a more accurate means of computing the structure of both the thermosphere and the ionosphere than previous generations of ionospheric or thermospheric numerical models, and are also more useful than independent empirical models. Strong ionosphere - thermosphere interactions, particularly those resulting from geomagnetic forcing, cause major changes in the structure of the ionosphere, and in both the structure and dynamics of the thermosphere. Parameterising the solar energy input, and the geomagnetic energy and momentum input remains one of the major areas of uncertainty. The thermospheric response to a geomagnetic storm, as simulated by a coupled ionosphere - thermosphere model, is compared using three distinct means of parameterising the geomagnetic input: the Global Kp Index, the NOAA / TIROS Precipitation Activity Index, and the AE index. Daily Mean global predictions of thermospheric temperature, density and composition are relatively similar, using each of these indices, and compare with the equivalent MSIS empirical model predictions. However, at progressively shorter time intervals, quite large discrepancies are found in predicted energy input, according to which index is chosen. Thus the simulated ionospheric and thermospheric response sometimes depends critically on the chosen index. The data obtained from recent space-borne global auroral imaging shows that local and regional variations are not well described by global geomagnetic parameters. We can conclude that generally, global and diurnal mean values can be predicted to the accuracy with which major indices represent the actual thermospheric inputs. Prediction of small scale and short-period variations require considerably improved empirical data to describe the geomagnetic inputs and their variations.

Presented at the Thermospheric Density Workshop AFGL OCT. 22-24, 1987.

ORGANISER: Dr. Frank Marcos, AFGL.

1. INTRODUCTION.

A knowledge of the density, temperature, composition and dynamics of the thermosphere has a large number of practical applications both for the design and operation of space-borne systems, and in understanding and predicting the behaviour of the ionosphere as a medium for transmission or reflection of radio signals used in communication and in radar operations.

It may be considered that density and temperature of the thermosphere should be the primary objectives of any programme to determine "space-weather". However, in practice, knowledge of the temperature and density at a single location, without a knowledge of the composition (mean molecular mass) will even cause an extrapolation of density to another location within one scale height, vertically above the original location, to err significantly.

Wind velocity knowledge is also important. Within the polar regions, typical thermospheric wind speeds during periods of relatively quiet geomagnetic activity reach 400 - 500 m/sec. Such winds will cause an apparent modulation of perceived drag or lift forces in excess of 10 %, depending on the wind direction relative to the spacecraft velocity. Winds of such magnitudes thus need to be known with reasonable accuracy if true atmospheric density is to be determined from drag, accelerometer or mass spectrometer measurement, with a target accuracy better than about 10 - 15 %. During geomagnetic storms, the wind modulation of lift and drag forces may easily exceed 20 % amplitude, due to winds approaching 1 km/sec.

Since thermospheric wind systems show a large-scale response to strong geomagnetic forcing, sustained mass movements resulting from combined convection and advection cause changes of thermospheric composition which are large in magnitude, and which also affect very large regions. Such changes are fully self-consistent, that is, they can be calculated a-priori, as long as a global picture of density, temperature, composition and wind velocity, and their evolution is known. However, such a broad picture is rarely, if ever, available, and the incomplete nature of the data bases from which empirical models have been derived provides few examples of the complex thermospheric interactions which occur during strongly disturbed periods. Major changes of the thermospheric composition following major geomagnetic disturbances, also have widespread consequences for the density and structure of the ionosphere. Major and large-scale enhancements or depletions of ionospheric plasma density have drastic consequences for radio communications over a wide range of frequencies. For complex and critical space-borne remote sensing systems such as synthetic aperture radar etc, perturbation of raw data, and large errors in the data recovery process, can occur. These result partly from dramatic ionospheric path and wavefront changes when ionospheric plasma densities are strongly perturbed, and partly from unexpected and short-duration perturbations of the spacecraft orbit or attitude due to anomalous drag and lift forces.

Since it is impractical to observe the structure and dynamics of the thermosphere at all places and at all times, a series of numerical models have been developed to fulfill the requirements for knowledge of the properties of the thermosphere. The earliest models were based purely on satellite drag results (Harris and Priester, CIRA 1962. Jacchia 1961, etc), combined with

theoretical extrapolation (mainly for determining altitude variations using the principle of static diffusive equilibrium, based on Nicolet, 1961). Later models incorporated direct measurements of thermospheric composition (from mass spectrometers) and temperature, derived from incoherent scatter radar and satellite optical measurements. A complete synopsis of the development and status of these empirical models can be found in Hedin (1983, 1987), and more generally within the GIRA 1987.

Empirical models do not reflect the physical processes which cause specific departures from a "mean" atmosphere. The variability included within empirical models, in response to important geophysical indices, does contain descriptions of the strong perturbations which are observed. However, there is a very large degree of spatial and temporal variability of individual geophysical disturbances, and recorded thermospheric variations are not keyed to the geophysical processes or phenomena themselves. Therefore, there are several intrinsic reasons why thermospheric parameters which should be strongly correlated or anti-correlated by their underlying common cause, may show weaker common variations within an empirical model. Moreover, when very important parameters are not well measured, as is the case with thermospheric winds, empirical models will neither be able to successfully represent the variations of such parameters, nor can the correlation or anti-correlation with other parameters be properly represented.

It is partly to solve this dilemma that theoretical numerical models of the thermosphere have been developed during the past decade: A theoretical model can never exactly predict the real state of the atmosphere, but may, by relating back to the effects of common physical processes, show the clear relationship between variations of important parameters. Also, the variations of parameters which are unmeasurable or unmeasured, or in regions which are not accessible to measurement can be investigated. Such models have to be dragged back to the real world by comparison with experimental data, and several examples of such intercomparisons will be presented and discussed here.

Numerical simulation of the thermosphere from first principles requires that the most important physical processes which occur within the thermosphere are treated correctly in mathematical and numerical senses (Fuller-Rowell and Rees, 1980, 1983, Dickinson et al 1981, 1984, Roble et al 1982). The energy and momentum sources which drive the thermosphere can be assumed to be predetermined, and to be invariant to an induced response of the thermosphere. This pragmatic assumption is often valid: the thermosphere does not determine the nature of the solar UV and EUV inputs which provide important heat and ionisation sources. However, the thermosphere does react strongly to forcing. The wind, temperature and composition response of the polar thermosphere to ion convection and heating associated with the auroral oval and polar cap are well documented by ground-based and space-borne observation (e.g. Hays et al 1984, Rees et al 1983, 1985, 1986). Certain of these responses of the thermosphere may change the nature or magnitude of the forcing process itself. A back-EMF may develop, due to ion-drag induced E-region winds. Also, plasma density may be modified through the effects of induced winds or by neutral composition changes. Such changes will affect ionospheric conductivity, Joule heating and ion drag.

Magnetospheric convection drives plasma within the polar cap and auroral oval into rapid motion (Heppner 1977, Heppner and Maynard, 1987). These rapid motions force acceleration of the auroral thermosphere via the process commonly known as ion drag.

The resulting ion-neutral frictional drag causes direct heating of both ions and neutrals, commonly known as Joule heating (Cole, 1962, 1972). Induced winds may increase or decrease (but generally decrease) the ion drag, and the resulting frictional heating. The induced winds (or more correctly, changed winds, since there is always a complex wind system in existence prior to a given geomagnetic disturbance) may induce a 'back-EMF', opposing the initial magnetospheric convective electric field. This wind system will also induce ion drifts (or changes in ion drifts) parallel to the local magnetic field. Such 'parallel' ion drifts will also induce a field-aligned electron flow, to maintain quasi-charge neutrality. Thus the entire vertical plasma distribution will respond to wind changes. This change of ion density distribution will modify the consequent ion drag on the neutrals, and thus the wind acceleration terms, and finally the winds themselves.

Large induced changes of upper thermospheric composition are caused by combined advection and convection, induced by strong thermospheric heating in the polar regions. These composition changes (enhanced concentrations of molecular nitrogen) are particularly pronounced at F-region heights during geomagnetic storm periods and within the summer geomagnetic polar region. Enhanced concentrations of molecular nitrogen cause significant depletions of F-region plasma densities by greatly increasing the effective recombination coefficient, while the ionisation rates, due to the combination of solar photo-ionisation and auroral precipitation, are only slightly changed.

The first serious efforts to create an interactive model for the polar ionosphere and thermosphere were published by Quegan et al (1982) and Fuller-Rowell et al (1984). In this model, UT-independent data sets from a global thermosphere model (UCL) and the 'Sheffield' polar ionosphere model were iteratively exchanged until stability was achieved. The effects of the model iterations showed that significant changes in plasma density were caused by the effects of induced winds. The auroral oval plasma densities were greatly enhanced compared with those of the Chiu model. As a result, induced winds and heating were generally greatly increased compared with previous simulations using the global Chiu (1975) model. These higher winds, naturally, increased the feedback effect on the ionosphere.

We can contrast this approach with the global ionospheric modelling work of the Utah State University group (Sojka et al 1979, Sojka and Schunk 1983). They include quite complex ionospheric codes in their models, and use uniformly high spatial resolution. However, they have also ignored the light ions, which can be very important in the regions of the sub-auroral trough (and elsewhere, Quegan et al 1986). They also assume that the neutral atmosphere composition is unchanged from a standard atmosphere model by any consequent thermospheric or ionospheric processes. Also, while they have assimilated a very simplified anti-sunward cross-polar cap neutral wind flow as an initial condition, such wind distributions are clearly over-simplified, and in the real world, both the wind patterns and the neutral thermospheric chemistry change very markedly in response to geomagnetic forcing. Such

changes have important consequences for the transport of ionisation, and for fundamental ionospheric chemistry.

However, even the relatively simple interactive model described by Quegan et al (1982) could not be universally applied to study UT variations, let alone the effects of variable solar, geomagnetic and seasonal conditions. The next stage, developing a fully interactive thermosphere and polar ionosphere model, was complex, and is described in some detail in a series of papers by Fuller Rowell et al (1987 b,c) and by Rees and Fuller-Rowell (1987 a,b). This fully coupled model exchanges ionospheric and thermospheric parameters throughout the region poleward of 55° geomagnetic latitude. At lower latitudes, the numerical model is presently still dependent on empirical ionospheric descriptions. Thus, the major purpose of this paper will be to discuss results, in terms of numerical simulations of local and global thermospheric density response, when the physics of the major ionospheric-thermospheric interactions is included within the coupled model. The 'geomagnetic' energy and momentum sources required to explain the observed thermospheric heating, density changes, and disturbances of the neutral circulation occur naturally through the medium of the coupled and interactive physics, and the new model takes care of the feedback processes in a credible and correct way. A particular geomagnetic disturbance which occurred between March 1 and March 2 1982 will be chosen to discuss the results of the simulations.

2. THE COUPLED GLOBAL THERMOSPHERE / POLAR IONOSPHERE MODEL.

The UCL Three Dimensional Thermospheric Model (or GCM) simulates the time-dependent structure of the vector wind, temperature, density and composition of the neutral atmosphere, by numerically solving the non-linear equations of momentum, energy and continuity (Fuller-Rowell and Rees, 1980), and a time-dependent mean mass equation (Fuller-Rowell and Rees, 1983). The global atmosphere is divided into a series of elements in geographic latitude, longitude and pressure. Each grid point rotates with the earth to define a non-inertial frame of reference in a spherical polar coordinate system. The latitude resolution is 2° , the longitude resolution is 18° , and each longitude slice sweeps through all local times, with a 1 min time step. In the vertical direction the atmosphere is divided into 15 levels in log (pressure), each layer is equivalent to one scale height thickness, from a lower boundary of 1 Pascal at 80km height.

The time-dependent variables of southward and eastward neutral wind, total energy density, and mean molecular mass are evaluated at each grid point by an explicit time stepping numerical technique. After each iteration the vertical wind is derived, together with temperature, heights of pressure surfaces, density, and atomic oxygen and molecular nitrogen concentrations. The data can be interpolated to fixed heights for comparison with experimental data, or with empirical models. The momentum equation is non-linear and the solutions fully describe the horizontal and vertical advection, i.e. the transport of momentum.

The neutral atmosphere numerical model uses an Eulerian approach. However, the ionospheric code (Quegan et al 1982, Fuller-Rowell et al 1987 b,c) has to be evaluated in a Lagrangian system. The complex convection patterns imposed by a magnetospheric electric field on plasma movements within the polar

regions are referenced to a fixed Sun - Earth frame, assuming pure $\mathbf{E} \times \mathbf{B}$ drifts. The electric field is derived by merging a model of magnetospheric convection (for example one of the models presented by Heppner and Maynard, 1987) with the co-rotation potential (induced by the earth's rotation). Parcels of plasma are traced along their convection paths, which are often complex.

In the ionospheric code, atomic (H^+ and O^+) and molecular ion (O_2^+ , N_2^+ , NO^+ etc) concentrations are evaluated over the height range from 100 to 1500 km, and used in the thermospheric code within 35° magnetic latitude of the north and south magnetic poles. The use of the self-consistent ionosphere at high-latitudes and an empirical description at low- and mid-latitudes can result in a discontinuity in the vicinity of the plasmapause. The ionospheric code is presently being extended to include the self-consistent calculation at mid- and low-latitudes, including computation of the equatorial anomaly, but these new results will not be discussed here.

To avoid further repetition of the details of the numerical codes, the reader is referred to the series of papers previously cited for details of the UCL thermospheric model (Fuller-Rowell and Rees 1980, 1983), for information on the Sheffield ionospheric code (Quegan et al 1982, Quegan et al 1986, Watkins, 1978 and Allen et al 1986) and for information on the procedures used to couple the UCL thermospheric and Sheffield polar ionospheric models (Fuller-Rowell et al 1987 b,c).

3. PARAMETERISING THE SOLAR AND GEOMAGNETIC INPUTS.

Parameterisation of the solar activity within the UCL thermospheric model has been described by Fuller-Rowell and Rees (1980, 1983). The extension of this parameterisation to the coupled ionospheric / thermospheric model has been described by Fuller-Rowell et al (1987 a,b). In each case, the heating and photo-ionisation terms are directly linked to the solar EUV and UV fluxes, and the only local linkage is by means of the solar zenith angle, and the use of an appropriate Chapman function to describe the vertical variation of heating or ionisation rate.

Geomagnetic activity variations present a greater degree of difficulty, since it is not practical to record the full three-dimensional and time-dependent variations of all energetic particle inputs, and of the polar convective electric field distribution. Three descriptions of geomagnetic activity have been considered for this study. The first is based on the description presented by Fuller-Rowell and Evans (1987), using the "Power Indices" derived from measurements of auroral electron fluxes from the NOAA / TIROS series of spacecraft. This index is therefore keyed directly to one of the fundamental features of geomagnetic activity (i.e. the auroral intensity).

The second index is derived by using published correlations between the NOAA / TIROS Power Index and the Auroral electrojet (AE) index. The time-dependent AE index is available with better time resolution than is the Power Index itself (which has to be based on the availability of a satellite pass over a specific region of the auroral oval). On the other hand, the AE index should reflect the overall behaviour of the entire auroral oval, rather than that of a specific region which just happens to be under the orbit path of a specific

satellite. The disadvantage is that AE is derived from measurements of the surface magnetic field perturbations generated by the ionospheric current system, in particular the Hall currents, which are non-dissipative, rather than the currents themselves, their source, or the Field-Aligned Currents which provide the geomagnetic power source for the high-latitude ionosphere / thermosphere system.

The final mode of utilising the NOAA / TIROS Power Index is by relating it to the variations of the 3-hour global Kp index. This index has been shown, in studies using empirical thermospheric data, to be well correlated with thermospheric mean density and temperature variations. The major disadvantage of using the Kp index is the poor time resolution implied by its 3-hour sampling.

We would thus expect to see several key variations in the use of the three different methods of keying the NOAA / TIROS Power Index to geomagnetic activity. The AE index should provide the most realistic descriptions of time-variations on a global scale; the Power Index provides a direct measurement of the auroral precipitation source, but not of electric fields. Also specific orbit passes may cross the auroral oval in regions which are not representative of the activity of the auroral oval as a whole, and at times when activity is anomalously high or low, compared with the average activity between successive auroral oval crossings. Kp should describe the overall mean inputs rather well, however, the consequences of its poor time resolution may be apparent, and there may be some large-amplitude artificial waves induced by the often abrupt changes of successive 3 hr. values of Kp. The 3 hr. time variations of Kp also imply that geomagnetic energy inputs will be maintained at high or low levels for unrealistically extended intervals.

4. THERMOSPHERIC SIMULATIONS.

Results from three time-dependent coupled thermospheric / ionospheric simulations will be presented here. These simulations have been generated using three alternative time-dependent indices to describe the geomagnetic activity level during the period from 0.0 UT on February 27 1982 until 0.0 UT on March 3 1982. The geomagnetic index presentation is used to key an auroral particle precipitation source, which also acts as a source of heat, as well as ionisation, and which is matched to the appropriate cross-polar cap electric field, with a related expansion or contraction of the size of the polar cap and auroral oval. The solar activity was also high during this period ($220 < F_{10.7} \text{ cm} < 265$), and the simulation also takes this large heat and solar photo-ionisation input into account in a time-dependent way.

During the UT day, at all seasons, the geomagnetic polar caps are carried into and out of sunlight. There is, therefore, a large modulation of the solar photo-ionisation and UV/EUV heating of the geomagnetic polar regions which causes quite large UT variations in plasma density, conductivity, ion drag and Joule and solar heating of the thermosphere. There are consequent large modulations of the thermospheric and ionospheric response. However, the phenomena which develop during these simulations show that the UT modulation is completely dominated by the effects of the large and time-dependent geomagnetic forcing of the thermosphere and ionosphere.

5. COMPARISONS OF THE EFFECTS OF USING SPECIFIC INDICES.

The results of the three methods of keying the Power Index variations (NOAA / TIROS activity levels) are illustrated respectively in Figures 1, 2 and 3 for the period 0 UT to 24 UT on March 1 1982. Figure 1 shows the directly-measured TIROS electron power input, Figure 2, the Power Input keyed to the AE Index, and Figure 3 the Power Index keyed to the Planetary Kp index. The distinctive characteristics of the three alternative methods of keying to geomagnetic activity and its variations can be seen by comparing both mean values and the nature of the temporal variations during the 24 hour period. Values are taken into the input data stream of the 3-D coupled model at 12 min intervals for each of the data sets shown in Figures 1 to 3, and for the same indices for the days immediately before and after March 1, 1982.

In comparing the three alternative methods of keying geomagnetic activity, it is important to recall that the total geomagnetic energy dumped into the thermosphere is considerably greater than the electron precipitation alone (i.e. as directly measured by NOAA / TIROS). The electron precipitation causes a considerable increase in the ionospheric conductivity within the polar regions. The further increase of the cross-polar cap electric field normally associated with enhanced levels of geomagnetic activity, and the equatorward expansion of the auroral oval and polar cap, cause the integrated Joule heating to exceed the particle heating by a considerable factor (* 3 - 5 - Fuller-Rowell and Rees, 1987). Thus, sustained and elevated levels of the activity index will cause far greater thermospheric heating (and consequent ionospheric effects as well) than might be inferred from considering the electron precipitation rates alone.

The sustained high values of Kp, late on March 1 (10 to 24 UT, Figure 3), will therefore provide inputs (through the appropriate keying of the Power Index) which will energise the thermosphere / ionosphere system considerably more than when the direct Power Index (Figure 1), or the AE-driven Power Index (Figure 2) are used. There are also very important differences in the time variations. The AE-driven values lag the direct NOAA / TIROS Power Index variations, by about 2 hours. It is not obvious what causes this lag, and we have not investigated whether the lag is purely coincidental for this period, or is a systematic effect. The consequence is that major geomagnetic effects in the thermosphere, particularly in temperatures and winds, which are quick to respond to high activity levels, follow quite different temporal variations, depending on the chosen method of keying the Power Index. Some major mid-latitude effects, due to the propagation of gravity waves, for example, and any subsequent ionospheric effects, will thus also show a quite different evolution.

On the second day of the storm, both the AE and Kp indices show a fall in geomagnetic activity at the end of the second 24 hour period (not illustrated here) while the direct NOAA / TIROS Power Index (i.e. the real-time satellite electron measurements) maintains high values. In analysing the simulations, and comparing with the real thermospheric data available from DE-2 (NACS), we should be careful to assess which of these indices may provide the most appropriate description of the way in which the thermosphere really behaved in this period. In this paper, however, we will only attempt a very preliminary assessment of the comparisons.

6. VARIATIONS IN THE TIME-DEPENDENT BEHAVIOUR OF THE THERMOSPHERE.

NOAA / TIROS POWER INDEX DRIVEN BY THE AURORAL ELECTROJET.

The behaviour of the thermosphere (240 Km) in the model simulation which uses the NOAA / TIROS power index driven by the AE geomagnetic index is illustrated in the set of Figures 4 to 9. Figure 4 is at 06 UT, Figure 5 is at 14.4 UT, Figure 6 is at 15.6 UT, Figure 7 is at 16.8 UT, Figure 8 is at 18 UT, Figure 9 is at 21.6 UT, respectively.

Prior to about 06 UT, the geomagnetic activity had been relatively low, although with some brief excursions, corresponding to levels of around $3 < K_p < 4$. At 06 UT, the density values at 240 km (Figure 4), reflecting the generally quiet period beforehand, show a variation between 12.6 and $19.2 \times 10^{-11} \text{ kg m}^{-3}$. The highest density values are near 14 LST, and at low latitudes, with generally the lowest values in the early morning hours at northern (winter) mid to high latitudes. The period before 06 UT had been relatively quiet before the March 1 / 2 storm, the consequences of earlier moderate activity can be seen: there are strong waves in the density structure. These are most obvious in the noon sector, but actually endemic, throughout the entire thermosphere. These are propagating gravity waves, of typical amplitude 10 % in density, which have equivalent counterparts in temperature and wind velocity. These propagating time-dependent 'waves' usually show only small signatures in mean molecular mass: all species co-vary, since there is no time for diffusive separation, or the re-establishment of chemical / diffusive equilibrium.

At 14.4 UT, following the major build-up of geomagnetic activity and the associated increase in energy and momentum inputs, the density distribution has changed quite dramatically. There are regions of high density at high (50°) mid-latitudes, and in the polar regions, as well as at low latitudes. Most of the peaks densities are found near 12 - 14 LST in both hemispheres, with increases of the order of 20 - 30 % compared with values in the same regions (latitude, local time) at 06 UT. The signatures of sharply-intensified winds around the auroral oval also show the dramatic effects of the increased geomagnetic activity immediately before 14 UT.

A general tendency can already be noted: during major disturbances, the highest density values will increase, and the density contrast will also increase. The highest density values can be often found adjacent to the regions of strongest heating, and not necessarily (except for 'peak' effects due to the coincidence of several propagating gravity waves) in the regions which are most strongly heated by geomagnetic forcing.

At 15.6 UT, some very high density values ($> 24 \times 10^{-11} \text{ kg m}^{-3}$) are found in the dusk auroral oval, in both hemispheres. These values represent an increase of nearly a factor of 2 compared with the same regions at 06 UT, before the major activity of the storm. These values are the result of the intense geomagnetic activity (as measured by AE) which occurred between 12 and 14.5 UT. The highest density values at 15.6 UT occur in regions where there is very intense Joule heating and ion drag wind acceleration.

Following the period of high geomagnetic activity between 12 and 14.5 UT, there is a steady increase in the global lowest density values, a trend which continues through 21.6 UT.

At 16.8 UT, the highest density values have decreased slightly ($23 \times 10^{-11} \text{ kg m}^{-3}$), and are at high mid-latitudes (50°) in each hemisphere. The polar wind systems, as at 14.4. and 15.6 UT, are still very energetic. There are maximum sunward winds in excess of 600 m/sec in the dusk auroral oval and anti-sunward winds of similar values over the central part of the polar cap.

The regions of highest density continue to propagate equatorward, and by 18 UT, are found around $30^\circ - 40^\circ$ latitude in each hemisphere. By this time, the highest density values have decreased some 10 % below the maximum values at 15.6 UT. At 18 UT, also, some regions of quite low density have developed within the polar caps ($9 \times 10^{-11} \text{ kg m}^{-3}$), where temperatures are still quite high, following the previous extensive activity. A night-side equatorial region of high density has also developed at 18 UT, where the density is virtually equal to the maximum mid-latitude daytime value ($22 \times 10^{-11} \text{ kg m}^{-3}$), and significantly higher than the sub-solar value ($18 \times 10^{-11} \text{ kg m}^{-3}$). This midnight density maximum is quite a transient feature, caused by the equatorward propagation and merging of waves from both polar regions.

By 21.6 UT, new high-latitude regions of high density have developed, particularly in the southern (summer) hemisphere, however, this time in the early morning hours. The lowest global values ($14 \times 10^{-11} \text{ kg m}^{-3}$) have increased 50 % in the period since 18 UT, with a modest (10 %) increase in the maximum density values. There is still a great deal of structure throughout the entire global thermosphere. It should be noted that in complex disturbances, such as the one simulated here, while it becomes difficult to identify wave-like structures after they have crossed the equator, from their high-latitude origin, they certainly do propagate for quite long periods. In simpler simulations, a single strong geomagnetic pulse results in individual waves which can be identified and observed while they propagate around the globe.

DIRECT NOAA / TIROS POWER INDEX

The storm-time response of the thermosphere (240 Km) in the model simulation which uses the direct NOAA / TIROS power index is illustrated in the set of Figures 10 to 15. Figure 10 is at 06 UT, Figure 11 is at 14.4 UT, Figure 12 is at 15.6 UT, Figure 13 is at 16.8 UT, Figure 14 is at 18 UT, Figure 15 is at 21.6 UT, respectively.

This sequence of Figures shows the evolution of thermospheric density during the first day of the storm, comparable to that shown in Figures 4 through 9 for the AE-driven Power Index. At 06 UT (Figure 10), the structure, mean, peak and lowest values are quite similar to those shown in Figure 4.

By 14.4 UT, however, there are two significant differences. Firstly, the peak density values are 10 % higher than in the AE-driven simulation. At all subsequent times, however, the simulation using the AE-driven Power Index shows the highest density values. Secondly, the density 'wave' structure is considerably changed. The highest density values in the direct Power Index simulation are found at mid-latitudes in both hemispheres, and not near the

equator. In a considerable number of areas, detailed differences of density structure of the order of 20 - 30 % occur.

By 15.6 UT, the regions of high density, which were located near 40° - 50° latitudes at 14.4 UT, have migrated toward the equator, reaching about 30° latitude. This process continues, so that by 16.8 UT, the highest density values have reached the equatorial region. There is also a very pronounced density wave activity (amplitudes 10 - 20 %) at 16.8 UT.

A further series of high amplitude density waves are being generated at high latitudes at this time, due to the high activity. By 18 UT (Figure 18), there are several series of propagating waves en route toward the equator. At 21.6 UT, the geomagnetic activity is again very high, and, for the first time in this sequence, the highest global density occurs at southern polar latitudes (80°). The density distribution is highly structured at 21.6 UT. Compared with the real world, the peak amplitudes of 'density waves' within the simulations are smaller. We would also anticipate that low spatial and temporal frequencies are emphasised in the simulations.

By 21.6 UT, the globally lowest value of air density at 240 km, which was at high (80°) northern latitude at 06 LT, has climbed to $14.5 \times 10^{-11} \text{ kg m}^{-3}$, a factor of 40 % greater than the lowest density value at 06 UT, early in the development of the storm.

NOAA / TIROS INDEX DRIVEN BY Kp.

In this simulation, the changes of geomagnetic input occur abruptly. Abrupt changes of activity from low to high levels, and vice versa, generate major wave-like disturbances, at times of sharp increases and decreases of activity. Figures 16, 17 and 18 show global distributions of density and winds at 240 km at 06, 14.4 and 21.6 UT, respectively, as taken from this simulation. The wind and density patterns, for periods of several hours after abrupt increases or decreases of energy input rates, show wave disturbances of comparable magnitudes to those in the simulations where the direct Power Index is used, or when the Power Index is driven by AE. Although the frequency of changes in the energy input is lower for the Kp-driven simulation, strong waves are still generated.

At 06 UT, the global density patterns and peak, minimum and average values are similar to those obtained with the other two simulations. However, at 14.4 UT and particularly at 21.6 UT, the density values generated within the Kp-driven simulation are considerably higher than those displayed in the direct or the AE-index driven simulations. At 21.6 UT, due to the sustained high Kp values, and thus geomagnetic energy inputs, the peak densities are 50 % higher than in the other simulations, and a factor of 2 above the pre-storm values (for example at 06 UT).

Quite obviously, the geomagnetic energy input levels during the period between 12 and 24 UT in the Kp-driven simulation correspond to a sustained full storm. Anti-sunward neutral winds over the polar cap reach close to 1 km/sec, similar to peak values observed by the Dynamics Explorer FPI (Hays et al 1983, Rees et al 1986). Similarly in the dusk auroral oval, the sunward wind speeds are similar to those observed rather rarely during very disturbed periods, both

from DE-2, and by ground-based Fabry-Perot interferometers (Rees et al 1984, Meriwether et al 1984).

7. COMPARISON OF THEORETICAL MODEL SIMULATIONS, EMPIRICAL MODEL PREDICTIONS AND OBSERVED THERMOSPHERIC DENSITIES.

7.1 COMPARISON WITH MSIS-86 DENSITY AND COMPOSITION PREDICTIONS FOR THE MARCH 1 / 2 1982 DISTURBANCE.

Figures 19, 20 and 21 show presentations of the predictions from the MSIS 1986 empirical model (at 240 Km) for 06 UT, 14.4 UT and 21.6 UT, respectively, on March 1 1982. The MSIS model has been used in its full time-dependent form (Season, UT, ap), and at maximum resolution available with the number of available harmonics available within the MSIS formulation.

Early on in the disturbance, at 06 UT, and also at 14.4 UT, the MSIS model predicts values which are systematically lower than the three simulations, although the average values are only perhaps about 10 % lower than those by generated by the AE-driven simulation, and 20 % less than those of the simulation directly-driven by the Power Index. Later, at 21.6 UT, the MSIS density values also rise, driven by the increase in Ap. The rise in MSIS densities is slightly less than that produced in the simulation directly-driven by the Power Index, about 10 % less than the AE-driven simulation, but as much as 50 % less than the values obtained when the simulation is indexed to Kp. In overall values, the MSIS densities at 21.6 UT are very similar to those of the AE-driven simulation at 15.6 UT (when AE has been at high values for about 2 hours)

7.2 COMPARISON OF THE NUMERICAL MODEL RESULTS WITH OBSERVED DE-2 (NACS) DENSITY AND COMPOSITION VALUES DURING THE MARCH 1 / 2 1982 DISTURBANCE.

In Figures 22, 23 and 24, the observed and simulated density values for three perigee passes of the DE-2 spacecraft are compared (6.4, 12.9 and 23.6 UT respectively, March 1, 1982). The spacecraft altitude variations around perigee are shown, along with the measurements of total gas density, and the separate atomic oxygen and molecular nitrogen densities. The model results were obtained by cutting through and sampling the full 4-dimensional data set from the time-dependent model, exactly corresponding to the altitude, latitude, longitude and time variations of the DE-2 spacecraft for each specific orbit. The full global simulated model data sets are illustrated by the Figures discussed earlier, although it is clearly not practical to display two-dimensional plots at all altitudes for each exact time.

One of the unfortunate facts was that during the very interesting period between 14 UT and 23 UT, on March 1, 1982, there was little NACS data available. It is thus not possible to compare in detail the expected rapid time-dependence of the thermosphere in density and composition during this period, as predicted by the numerical simulations, responding to the changes in geomagnetic activity.

Near perigee, on each of these three passes, the simulated density values exceed the observed values, but only by about 15 - 20 %. Around 400 km, the

observed and simulated densities 'cross-over', with the simulated values being lower than observed values at higher altitudes, and also at the higher latitudes. This presentation (log scale) tends to under-emphasise any wave-like variations of density. In detail, the observed and simulated atomic oxygen values agree remarkably well at lower latitudes and altitudes (within 10 %). At low latitudes and altitudes, simulated molecular nitrogen density values are greater than observed values, and cause the simulated total density values to exceed those actually observed.

It should be noted that the perigee location during this period was at low latitudes, well away from any high-latitude source of geomagnetic energy. The excess molecular nitrogen densities in the simulation are thus not due to the simulation over-estimating the effects of auroral upwelling and outflow (wind-driven diffusion) resulting from high-latitude heating.

At high latitudes, the DE-2 spacecraft was also at high altitudes (above 400 km). There is a trend, which is modest at 06 UT, and which then becomes progressively larger at 13.6 UT and at 23.6 UT, for the observed high latitude molecular nitrogen and total density values to consistently exceed those in the AE-driven simulation. Atomic oxygen, in the simulation, is about 40 % too low at 23.6 UT, and closer in the previous orbits, however, molecular nitrogen is a factor of 5 greater in the real world than in the AE-driven simulation, while observed total density was a factor of 3 higher than in the AE-driven simulation (at the high altitudes (> 500 km) and latitudes), a marked departure from the quite good agreement obtained earlier, around 06 UT and at 12.9 UT.

The high latitude DE-2 NACS N2 density increase appears to be related to geomagnetic heating, and the very high observed values are confined to the geomagnetic polar caps.

7.3 COMPARISON BETWEEN OBSERVED DE-2 (NACS) DENSITY AND COMPOSITION DATA AND MSIS VALUES DURING THE MARCH 1 / 2 1982 DISTURBANCE.

In Figures 25, 26 and 27, the DE-2 NACS observed and MSIS density values for the same three perigee passes of the DE-2 spacecraft are compared (6.4, 12.9 and 23.6 UT respectively, March 1, 1982). The spacecraft altitude variations around perigee are shown, along with the measurements of total gas density, and the separate atomic oxygen and molecular nitrogen densities. The MSIS values were obtained exactly corresponding to the altitude, latitude, longitude and time variations of the DE-2 spacecraft for each specific orbit. The full global MSIS data sets are illustrated by the Figures discussed earlier.

Below 400 km, the total density values observed by DE-2 NACS, and predicted by the MSIS (86) model are in very good agreement (10 - 20 %). At higher altitudes, somewhat larger discrepancies appear (20 - 30 %). In the individual constituents, the agreement is not so good. There is a persistent tendency for MSIS to over-estimate atomic oxygen density and thus total density, while MSIS molecular nitrogen values are close to NACS observed values, below about 400 - 450 km. At higher altitudes, there is no such obvious trend, molecular nitrogen is over-estimated by MSIS compared with NACS observations at 06 UT and at 12.9 UT.

At 23.6 UT, MSIS does a better job of predicting the total and constituent gas densities. This appears to be somewhat anomalous, since the general global MSIS values are lower than those in the AE-driven simulation at this time! It appears that the model has predicted regions of high density, but not where they were actually observed! This is probably an indicator that the time variation used to key the Power Index is imperfect, compared with the real temporal variations of geomagnetic energy input. We have not plotted the data in the Kp-driven simulation for comparison at this stage: the peak densities are a factor of 50 % higher than in the AE-driven simulation, and thus should be closer to the NACS data. However, that does not necessarily mean that the Kp indexed simulation is, overall, the most realistic simulation.

In general, MSIS predicts total density and nitrogen density up to 400 km slightly more accurately than any of the theoretical numerical simulations. However, the theoretical model does better at predicting atomic oxygen density than MSIS at both low altitudes and at high altitudes. The obvious advantage of the theoretical model is that the simulations include self-consistent neutral wind, temperature and high latitude ionospheric data. Similarly, the theoretical model does provide some explanation for specific phenomena and departures of the atmosphere from a mean state. The theoretical model also provides some insight into the magnitude of wave-like disturbances in winds, temperature and composition, related to the time-dependence of geomagnetic activity.

8. A NUMERICAL DATA BASE OF THEORETICAL THERMOSPHERIC PARAMETERS FOR VAX AND PERSONAL COMPUTERS.

Considerable amounts of computer time are required to complete a simulation using the coupled numerical codes described in this paper. In addition, a considerable amount of effort is required to maintain the suite of programmes, which comprise the numerical model, and the many data routines which describe the physical processes occurring within the thermosphere and ionosphere. A convenient method has been developed to enable the model data to be accessed and used more widely. The large numerical data base has been reduced by a factor of about 150 in size by a process called High Energy Fourier Filtering. The coefficients which are produced by this process can be decompressed quite quickly by a VAX or IBM PC-class computer (Batten et al 1987). This process is described in a little more detail in the Appendix, or the reader is referred to Batten et al (1987). A VAX data tape, or suitable floppy disks for use with an IBM PC can be obtained on request from the UCL group.

SUMMARY

Three numerical simulations have been performed to investigate the response of thermospheric density to the March 1/2 1982, geomagnetic storm. These simulations have been driven, respectively, by the geomagnetic energy and momentum sources related to the TIROS/NOAA Precipitation (Power) Index, where the time-dependence has been defined by AE, the direct observed Power Index, or by Kp.

The time variation of each index differs substantially and consequently the thermospheric response has a distinctive character in each case. During the

quiet initial phase of the simulations, the simulated thermospheric responses are similar, and compare favourably in magnitude and structure with the MSIS empirical model predictions. During the major phase of the disturbance, however, large differences exist between the three numerical simulations and in comparison with the empirical MSIS model.

At high latitudes and at 240 km, the numerical model density predictions exceed MSIS derived densities by 50%, at times when the geomagnetic sources are at their most intense. At the end of the UT day of March 1, 1982, a sustained period of high Kp, not matched by the AE index, or by the direct Power Index, causes the 240 km densities in the Kp-driven simulation to exceed those generated in the other two simulations by a factor of 50 %.

Comparison of the numerical model predictions with the DE-2 NACS density data showed agreement to within about 20% for the periods when experimental data was available, with the exception of high altitudes (> 450 Km) and high latitude regions on the DE-2 orbit at 23.6 UT. During that orbit, the observed (NACS) densities at high altitudes and in the polar region, considerably exceeded the simulated values, although the results of the simulations and the NACS data were in quite good agreement at low altitudes and latitudes, even at that time.

Generally, the observed (NACS) and simulated (theoretical model) values of atomic oxygen densities agreed closely (10 - 20 %) at both low altitudes and at high altitudes, with larger departures for molecular nitrogen.

In general, MSIS predicts total density and nitrogen density up to 400 km somewhat more accurately than the theoretical numerical models. However, MSIS, in general, was not so impressive with its predictions of atomic oxygen density, which frequently departed further from the NACS data than the predictions of the theoretical simulations.

The theoretical model has the advantage that the simulations include self-consistent neutral wind, temperature and high latitude ionospheric data. The theoretical model also provides some explanation for specific phenomena and departures of the atmosphere from a mean state.

The theoretical model also provides some insight into the magnitude of wave-like disturbances in winds, temperature and composition, related to the time-dependence of geomagnetic activity.

These conclusions would, however, be of more practical value, were it clearer which geomagnetic activity index provided the most accurate key to the magnitude and temporal variations of geomagnetic forcing of the thermosphere.

At the time of this analysis, the experimental data available from NACS do not quite provide enough time resolution to clearly distinguish between the merits of the three geomagnetic indices which have been used to drive the theoretical model. For each of the three orbits studied in some detail, there are indications that a different one of the three simulations is doing slightly better than the other two. However, there is no clear indication that one particular index does consistently better than the others.

The most serious anomaly in density prediction occurred with data obtained during the orbit at 23.6 UT. NACS densities at high altitudes and high (polar) latitudes exceed those in the theoretical model by a significant factor. While the MSIS density predictions at this time at 240 km fall below those in the theoretical model, the MSIS densities at the high polar latitudes and high altitudes do follow the NACS data better than those generated by the theoretical model. Investigating the detailed reasons why this anomaly occurs is beyond the scope of the present study, but will be the subject of a future analysis.

As a general conclusion, it appears that self-consistent theoretical numerical models which properly account for the major thermospheric-ionospheric interactions resulting from particle heating, Joule heating and ion drag are now capable of predicting thermospheric density over the height range up to 400 - 500 km with a comparable accuracy to empirical models. This accuracy cannot be achieved with simulations which do not contain the physics of the self-consistent thermospheric - ionospheric interactions.

Significant additional work is required on the evaluation of geomagnetic indices, since these provide the critical key for understanding the way in which energy and momentum is transferred through the magnetosphere, into the polar ionosphere, and finally energises the thermosphere. None of the present indices seem ideal, and consideration will have to be given, as the result of a more detailed study, to producing a new index, either by combining and weighting existing indices, or by developing a new approach.

Initiatives to enlarge the range of frequently-measured geophysical parameters such as observations of cross-polar cap electric fields, Field-aligned currents, etc, will be of very great value, since they directly measure the major factors in the energy and momentum inputs. AE and Kp only measure ground-level magnetic effects which are indirectly, rather than directly, related to thermospheric momentum and energy sources.

The present global average accuracy of the theoretical model at 240 km (20 %) for [O] and total density, rather worse for N₂, has been considered during a storm period. The 'quiet time' accuracy is rather better. The accuracy could be improved by a better geomagnetic index, in particular, one which included real-time monitors of the actual geomagnetic inputs.

Wind velocity, in addition to air density, is of importance for computation of drag and lift forces on space structures, since both are proportional to the square of the relative velocity. The theoretical models therefore have major advantage during large disturbances. With winds reaching 1 km/sec, the maximum uncertainty or error in calculating aerodynamic drag or lift, due to ignorance of wind velocity, can be as high as 50 %, a worst case difference between a 1 km head wind or tail wind, at an orbital velocity of 8 km/sec.

For similar reasons, there is a necessity to allow for wind velocity in the derivation of density by drag or mass spectrometer techniques, with the latter being less prone to severe error, since the mass spectrometer density is proportional to relative air impact velocity, rather than its square (for drag and lift).

ACKNOWLEDGEMENTS

We would like to express our thanks to Shaun Quegan, Roy Moffett and Graham Bailey for their invaluable participation in developing the UCL / Sheffield coupled ionospheric / thermospheric model used in some of these simulations. Dr. Nelson Maynard provided much of the stimulation required to formulate this project, and considerable assistance in identifying and evaluating the March 1982 storm period. Dr. Fred Rich provided the Heppner and Maynard polar electric fields in the form of harmonic coefficients. Dr. George Carignan and Dr. Tim Killeen kindly provided the DE-2 NACS Mass Spectrometer data. We would also like to express our particular thanks to John Harmer, Hilary Hughes and Israel Perla for their assistance in preparing, running and processing the computer simulations using the UCL / Sheffield coupled ionospheric / thermospheric model. Computer time was made available by the University of London Computer Center (CRAY 1-S), and the CRAY-XMP-48 at the Rutherford Appleton Laboratory. The research was supported by grants from the UK Science and Engineering Research Council, and from the European Office of Aerospace Research and Development (AFOSR-86-341).

REFERENCES

- ALLEN B.T., G.J. BAILEY and R.J. MOFFETT, (1986), *Ann. Geophysicae*, 4 A, 97-106.
- BATTEN S., FULLER-ROWELL T.J. and D. REES, (1987), (1987), *Planet. Space Sci.*
- CIRA 1961, COSPAR INTERNATIONAL REFERENCE ATMOSPHERE, North Holland Publishing Co. Amsterdam.
- CIRA 1965, COSPAR INTERNATIONAL REFERENCE ATMOSPHERE, North Holland Publishing Co. Amsterdam.
- CIRA 1987, COSPAR INTERNATIONAL REFERENCE ATMOSPHERE, to be published by Pergamon.
- COLE K.D., (1962), *Aust. J. Phys.*, 15, 223-235.
- COLE K.D., (1972), *Planet. Space Sci.* 19, 59-75.
- CHIU Y.T., (1975), *J. Atmos. Terr. Phys.* 37, 1563-1570.
- DICKINSON R.E., E.C. RIDLEY and R.G. ROBLE, (1981), *J. Geophys. Res.* 86, 1499-1512.
- DICKINSON R.E., E.C. RIDLEY and R.G. ROBLE, (1984), *J. Atmos. Terr. Phys.* 41, 205-219.
- FULLER-ROWELL T.J. and D. REES, (1980), *J. Atmos. Sci.* 37, 2545-2567.
- FULLER-ROWELL T.J. and D. REES, (1983), *Planet. Space Sci.* 31, 1209-1222.
- FULLER-ROWELL, T.J., D. REES, S. QUEGAN, G.J. BAILEY and R.J. MOFFETT, (1984), *Planet. Space Sci.* 32, 469-480.
- FULLER-ROWELL T.J. and D. EVANS, (1987), *J. Geophys. Res.* 92, 7606-7618.
- FULLER-ROWELL T.J., D. REES, S. QUEGAN, R.J. MOFFETT and G.J. BAILEY, (1987a), *Symposium on Quantitative Modeling of Magnetosphere-Ionosphere coupling processes*. Convenors: Y. Kamide and R.A. Wolf, March 9-13, 1987 Kyoto Sangyo University. p20.
- FULLER-ROWELL T.J., S. QUEGAN, D. REES, R.J. MOFFETT and G.J. BAILEY, (1987b), *J. Geophys. Res.* 92, 7744-7748.
- FULLER-ROWELL T.J., D. REES, S. QUEGAN, R.J. MOFFETT and G.J. BAILEY, (1987c), Simulations of the seasonal and universal time variations of the thermosphere and ionosphere using a coupled, three-dimensional, global model. PAGEOPHYS, in press.
- HARRIS I. and W. PRIESTER, (1962), *J. Atmos. Sci.* 19, 286.

- HAYS P.B., T.L. KILLEEN, N.W. SPENCER, L.E. WHARTON, R.G. ROBLE, B.A. EMERY, T.J. FULLER-ROWELL, D. REES, L.A. FRANK AND J.D. CRAVEN, (1984), J. Geophys. Res. 89, 5547-5612.
- HEDIN A.E., (1983), J. Geophys. Res. 88, 10170-10188.
- HEDIN A.E., (1987), CIRA 87, Chapter 1, The Empirical Model Atmosphere: Atmospheric Model in the Region 90 to 2000 km, to be pub. Pergamon.
- HEPPNER J.P., (1977), J. Geophys. Res. 82, 1115-1125.
- HEPPNER J.P. and N.C. MAYNARD, (1987), J. Geophys. Res. 92, 4467-4490.
- JACCHIA L. G., (1965), Smithsonian Contrib. Astrophys. 8, 215.
- NICOLET M., (1961), Planet. Space Sci. 5, 1.
- QUEGAN S., G.J. BAILEY, R.J. MOFFETT, R.A. HEELIS, T.J. FULLER-ROWELL, D. REES and R.W. SPIRO, (1982), J. Atmos. Terr. Phys. 44, 619-640.
- QUEGAN S., G.J. BAILEY, R.J. MOFFETT and L.C. WILKINSON, (1986), J. Atmos. Terr. Phys. 48, 25-40.
- REES D., T.J. FULLER-ROWELL, R. GORDON, T.L. KILLEEN, P.B. HAYS, L.E. WHARTON and N.W. SPENCER, (1983), Planet. Space Sci. 31, 1299-1314.
- REES D., R. GORDON, T.J. FULLER-ROWELL, M.F. SMITH, G.R. CARIGNAN, T.L. KILLEEN, P.B. HAYS and N.W. SPENCER, (1985), Planet. Space. Sci. 33, 617-666.
- REES D., T.J. FULLER-ROWELL, R. GORDON, M.F. SMITH, J.P. HEPPNER, N.C. MAYNARD, N.W. SPENCER, L.E. WHARTON, P.B. HAYS and T.L. KILLEEN, (1986), Planet. Space Sci. 34, 1-40.
- REES D. and T.J. FULLER-ROWELL, (1987a), Global Thermospheric Modelling, (in press) Adv. Space Res. pub. Pergamon.
- REES D. and T.J. FULLER-ROWELL, (1987b), CIRA 1987, Chapter 2: Theoretical Thermospheric Model (to be published, Pergamon).
- ROBLE, R.G., R.E. DICKINSON and E.C. RIDLEY, (1982), J. Geophys. Res. 87, 1599-1614.
- SOJKA J.J. W.J. RAITT AND R.W. SCHUNK, (1979), J. Geophys. Res. 84, 5943-5951.
- SOJKA J.J. and R.W. SCHUNK, (1983), J. Geophys. Res. 88, 2112-2122.
- WATKINS B.J., (1978), Planet. Space Sci., 26, 559-569.

FIGURE CAPTIONS.

Figure 1. NOAA / TIROS Power Index or Activity Level, 0 - 24 UT March 1 1982: Direct satellite measurements, as available. Note mean level is about 8, with rapid fluctuations between 6 and 10.

Figure 2. NOAA / TIROS Power Index or Activity Level, 0 - 24 UT March 1 1982: Scaled from the observed variation of the Auroral Electrojet Index (AE). The mean level is also about 8, but the AE driven Power Index falls sharply at the end of the period, after 21 UT.

Figure 3. NOAA / TIROS Power Index or Activity Level, 0 - 24 UT March 1 1982: The index is driven by the global Kp values, which stay very high (10+) until 15 UT, and then fall steadily to 8 at the end of the period.

Figure 4. SIMULATION SA2, USING THE TIME-DEPENDENT MILLSTONE HILL E-FIELD, TIROS POWER INDEX, driven by AE, MAR 1 82. HIGH SOLAR ACTIVITY, COUPLED IONOSPHERE-THERMOSPHERE MODEL, 240 km TOTAL DENSITY. 06 UT.

Figure 5. SIMULATION SA2, USING THE TIME-DEPENDENT MILLSTONE HILL E-FIELD, TIROS POWER INDEX, driven by AE, MAR 1 82. HIGH SOLAR ACTIVITY, COUPLED IONOSPHERE-THERMOSPHERE MODEL, 240 km TOTAL DENSITY. 14.4 UT.

Figure 6. SIMULATION SA2, USING THE TIME-DEPENDENT MILLSTONE HILL E-FIELD, TIROS POWER INDEX, driven by AE, MAR 1 82. HIGH SOLAR ACTIVITY, COUPLED IONOSPHERE-THERMOSPHERE MODEL, 240 km TOTAL DENSITY. 15.6 UT.

Figure 7. SIMULATION SA2, USING THE TIME-DEPENDENT MILLSTONE HILL E-FIELD, TIROS POWER INDEX, driven by AE, MAR 1 82. HIGH SOLAR ACTIVITY, COUPLED IONOSPHERE-THERMOSPHERE MODEL, 240 km TOTAL DENSITY. 16.8 UT.

Figure 8. SIMULATION SA2, USING THE TIME-DEPENDENT MILLSTONE HILL E-FIELD, TIROS POWER INDEX, driven by AE, MAR 1 82. HIGH SOLAR ACTIVITY, COUPLED IONOSPHERE-THERMOSPHERE MODEL, 240 km TOTAL DENSITY. 18 UT.

Figure 9. SIMULATION SA2, USING THE TIME-DEPENDENT MILLSTONE HILL E-FIELD, TIROS POWER INDEX, driven by AE, MAR 1 82. HIGH SOLAR ACTIVITY, COUPLED IONOSPHERE-THERMOSPHERE MODEL, 240 km TOTAL DENSITY. 21.6 UT.

Figure 10. SIMULATION SM1, USING THE TIME-DEPENDENT MILLSTONE HILL E-FIELD, TIROS POWER INDEX, MAR 1 82. HIGH SOLAR ACTIVITY, COUPLED IONOSPHERE-THERMOSPHERE MODEL, 240 km TOTAL DENSITY. 06 UT.

Figure 11. SIMULATION SM1, USING THE TIME-DEPENDENT MILLSTONE HILL E-FIELD, TIROS POWER INDEX, MAR 1 82. HIGH SOLAR ACTIVITY, COUPLED IONOSPHERE-THERMOSPHERE MODEL, 240 km TOTAL DENSITY. 14.4 UT.

Figure 12. SIMULATION SM1, USING THE TIME-DEPENDENT MILLSTONE HILL E-FIELD, TIROS POWER INDEX, MAR 1 82. HIGH SOLAR ACTIVITY, COUPLED IONOSPHERE-THERMOSPHERE MODEL, 240 km TOTAL DENSITY. 15.6 UT.

Figure 13. SIMULATION SM1, USING THE TIME-DEPENDENT MILLSTONE HILL E-FIELD, TIROS POWER INDEX, MAR 1 82. HIGH SOLAR ACTIVITY, COUPLED IONOSPHERE-THERMOSPHERE MODEL, 240 km TOTAL DENSITY. 16.8 UT.

Figure 14. SIMULATION SM1, USING THE TIME-DEPENDENT MILLSTONE HILL E-FIELD, TIROS POWER INDEX, MAR 1 82. HIGH SOLAR ACTIVITY, COUPLED IONOSPHERE-THERMOSPHERE MODEL, 240 km TOTAL DENSITY. 18 UT.

Figure 15. SIMULATION SM1, USING THE TIME-DEPENDENT MILLSTONE HILL E-FIELD, TIROS POWER INDEX, MAR 1 82. HIGH SOLAR ACTIVITY, COUPLED IONOSPHERE-THERMOSPHERE MODEL, 240 km TOTAL DENSITY. 21.6 UT.

Figure 16. SIMULATION SM1, USING THE TIME-DEPENDENT MILLSTONE HILL E-FIELD, TIROS POWER INDEX, DRIVEN BY KP, MAR 1 82. HIGH SOLAR ACTIVITY, COUPLED IONOSPHERE-THERMOSPHERE MODEL, 240 km TOTAL DENSITY. 06 UT.

Figure 17. SIMULATION SM1, USING THE TIME-DEPENDENT MILLSTONE HILL E-FIELD, TIROS POWER INDEX, DRIVEN BY KP, MAR 1 82. HIGH SOLAR ACTIVITY, COUPLED IONOSPHERE-THERMOSPHERE MODEL, 240 km TOTAL DENSITY. 14.4 UT.

Figure 18. SIMULATION SM1, USING THE TIME-DEPENDENT MILLSTONE HILL E-FIELD, TIROS POWER INDEX, DRIVEN BY KP, MAR 1 82. HIGH SOLAR ACTIVITY, COUPLED IONOSPHERE-THERMOSPHERE MODEL, 240 km TOTAL DENSITY. 21.6 UT.

Figure 19. MSIS prediction, MAR 1 82. HIGH SOLAR ACTIVITY, R60, 240 km TOTAL DENSITY. 06 UT.

Figure 20. MSIS prediction, MAR 1 82. HIGH SOLAR ACTIVITY, R60, 240 km TOTAL DENSITY. 14.4 UT.

Figure 21. MSIS prediction, MAR 1 82. HIGH SOLAR ACTIVITY, R60, 240 km TOTAL DENSITY. 21.6 UT.

Figure 22. Comparison between DE-2 NACS data and the numerical simulation for the orbit at 06.4 UT, Mar 1 1982. The data are shown in four segments. These display spacecraft altitude versus latitude, and the latitude profiles of Total Density, Molecular Nitrogen Density and Atomic Oxygen Density variations are shown.

Figure 23. Comparison between DE-2 NACS data and the numerical simulation for the orbit at 12.9 UT, Mar 1 1982. The data are shown in four segments. These display spacecraft altitude versus latitude, and the latitude profiles of Total Density, Molecular Nitrogen Density and Atomic Oxygen Density variations are shown.

Figure 24. Comparison between DE-2 NACS data and the numerical simulation for the orbit at 23.6 UT, Mar 1 1982. The data are shown in four segments. These display spacecraft altitude versus latitude, and the latitude profiles of Total Density, Molecular Nitrogen Density and Atomic Oxygen Density variations are shown.

Figure 25. Comparison between DE-2 NACS data and MSIS for the orbit at 06.4 UT, Mar 1 1982. The data are shown in four segments. These display spacecraft altitude versus latitude, and the latitude profiles of Total Density, Molecular Nitrogen Density and Atomic Oxygen Density variations are shown.

Figure 26. Comparison between DE-2 NACS data and MSIS for the orbit at 12.9 UT, Mar 1 1982. The data are shown in four segments. These display spacecraft altitude versus latitude, and the latitude profiles of Total Density, Molecular Nitrogen Density and Atomic Oxygen Density variations are shown.

Figure 27. Comparison between DE-2 NACS data and MSIS for the orbit at 23.6 UT, Mar 1 1982. The data are shown in four segments. These display spacecraft altitude versus latitude, and the latitude profiles of Total Density, Molecular Nitrogen Density and Atomic Oxygen Density variations are shown.

Figure 28. Numerical simulation: J3, A2 / A2 polar electric fields, DEC 21, CHIU ionosphere, CIRA 1987 simulation, ORIGINAL data, PRESSURE LEVEL 12. 00 UT.

Figure 29. Numerical simulation: J3, A2 / A2 polar electric fields, DEC 21, CHIU ionosphere, CIRA 1987 simulation, reconstructed from the * 150 reduction. PRESSURE LEVEL 12. 00 UT.

Figure 30. Numerical simulation: J3, A2 / A2 polar electric fields, DEC 21, CHIU ionosphere, CIRA 1987 simulation, differences between Figures 29 and 28. PRESSURE LEVEL 12. 00 UT.

APPENDIX.

A DATA BASE FOR NUMERICAL MODELS FOR VAX AND PERSONAL COMPUTERS.

Some 436,000 real numbers, describing 15 pressure levels, 91 steps in latitude, 20 steps in Longitude, 20 steps in UT, and at least 7 geophysical (atmospheric) parameters are required for each 24 hours of the thermospheric simulations.

High energy Fourier filtering (HEFF) has been used (Batten et al 1987) to reduce the data volume for convenient storage and transmission via magnetic tape or floppy disk. A four dimensional array i.e. latitude vs. longitude vs. height vs. time, is set up for each individual parameter.

The first stage of the process is to obtain the Fourier transform (Ft) of the 'initial data array'. Two of the dimensions, time and longitude, are already cyclic over the data range. The other two (latitude and height) can be made so, by treating them as half of a symmetric array, folded about their end points. This reduces the corruption of the FT by discontinuities at the edges without, in fact, increasing the number of coefficients which need to be stored.

A threshold value is set for all Fourier coefficients. If a particular coefficient value falls below this level, it is deemed to be insignificant relative to coefficients with larger values, and is set to zero. This produces what is called the 'filtered transform' array of coefficients.

The inverse Fourier transform of the 'filtered transform' is computed, and compared with the 'initial data array'. If the fit is then satisfactory, the filtered data is stored in a compressed fashion. All non-zero values of the 'filtered array' are recorded, with a label indicating their position in the array, and thus which frequencies they relate to.

The stored coefficients, with their labels, occupy about one part in 150 of the volume of the 'initial data array'. The coefficients can be expanded, by repadding with zero's, to recreate the 'filtered transform'. The inverse transform produces the 'reconstructed data', a smoothed but accurate approximation of the 'initial data'. To reproduce the details of high latitude processes necessarily requires a larger number of coefficients than are used in the MSIS harmonic representation.

The data base, comprising the filtered coefficients from which the data from each of the simulations can be reconstructed, has been prepared for widespread circulation in two computer-readable forms:

The first form is usable with a VAX computer running a VMS operating system. The data base for any specific model includes the routines necessary to read the directory, and to re-calculate / sample / plot the parameters. The user guide is presented as a HELP file, and provides the detailed description of how to use the data base and under which conditions a specific simulation should be used. Data is available either on constant pressure surfaces, which is often convenient for a physical interpretation of the thermosphere, or interpolated to constant altitude surfaces, which is often convenient for comparison or prediction purposes. The data may also be interpolated to the precise orbit parameters of a specific spacecraft.

The data base includes some graphics routines for plotting various parameters as functions of :

Latitude / Longitude (Global Snapshot at given U.T.);
Latitude / Local Time (Diurnal variation at a given station);
Altitude / Latitude (at given Longitude and Local Time);
Altitude / Longitude (for given Lat and Long)

An equivalent data base is also available (written in Fortran) for the IBM PC-AT and closely equivalent computers. The filtered sets take up considerably less storage space than do the full parameter sets, and may thus be conveniently handled on a PC. For example, all the programmes and the full coefficient sets for global reconstruction of all parameters at 15-levels, for several simulations can be conveniently fitted within a single high-density floppy disk (1.2 MB). The trade-off is that some computational time is required to reconstruct the parameters themselves for any particular level, UT, longitude etc. It will be for the individual user to decide how best to store and reconstruct the data base. Graphics routines are again included within the data base to plot the vector and scalar parameters.

Figure 27 shows the original global data set at pressure level 12 (winds and temperatures) at one specific UT for a "quiet" period simulation (J3). The results of the reconstruction from a set of coefficients occupying 1/150 of the original data array (in four dimensions) are shown in Figure 28. There are obviously small differences between the reconstructed data set and the original data. These differences are shown in Figure 29. The differences, as expected, are largest in regions where there are highly structured perturbations of the thermosphere, due to high latitude, magnetospheric, forcing. However, the magnitude of the differences from the original data array very rarely reach 20 m/sec in wind speed, or 10 K in temperature. Such differences are well within uncertainties involved in the simulation process under most conditions (i.e. defining the solar and geomagnetic conditions and appropriate energy and momentum inputs).

The model data sets are described in more detail in several recent UCL papers discussing the coupled model simulations, and form the basis of the theoretical model incorporated in CIRA 1987 (Chapter 2, Rees and Fuller-Rowell, 1987). The model coefficient data sets can be made available via VAX magnetic tape, or on floppy disk, from UCL, upon request.

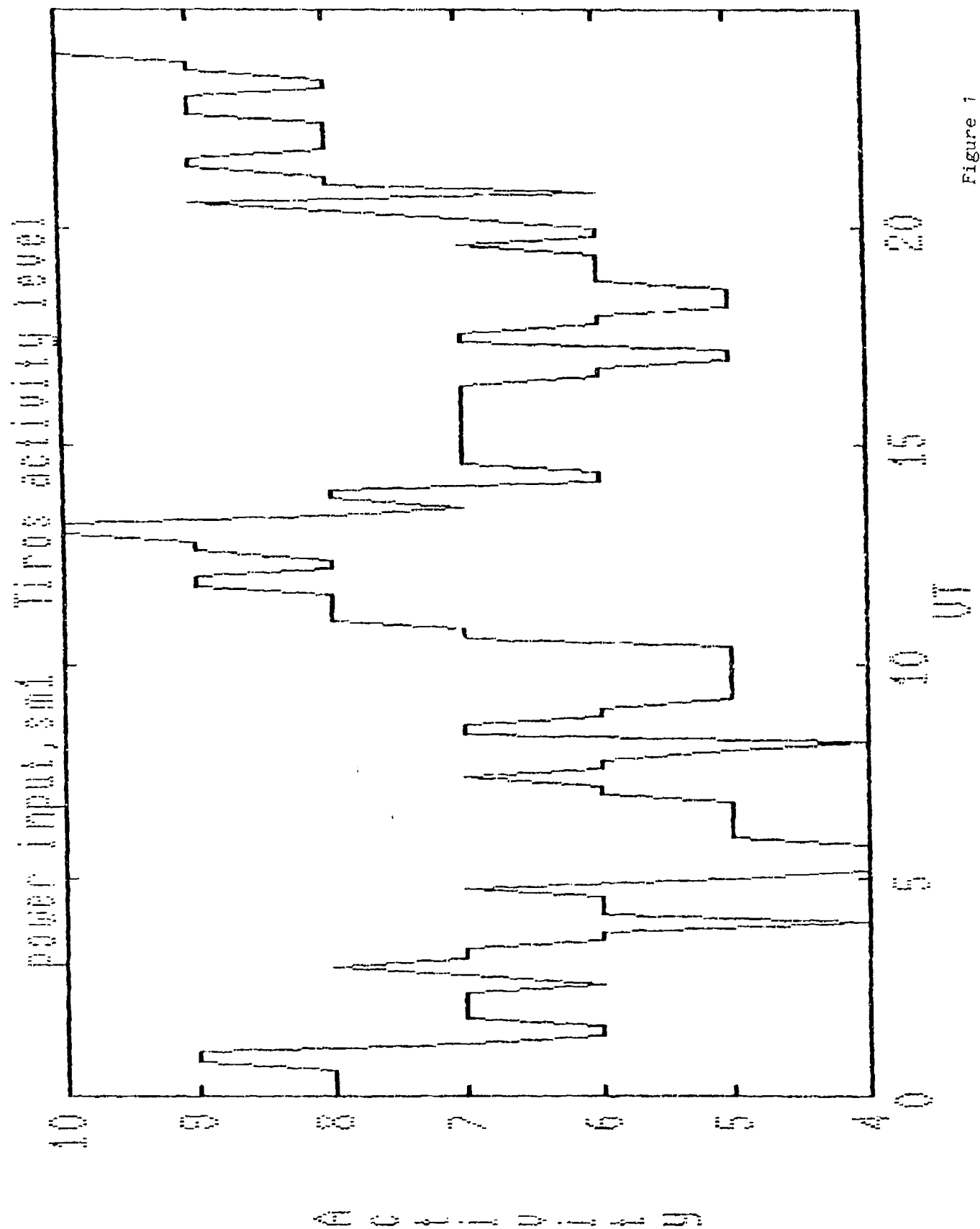


Figure 7

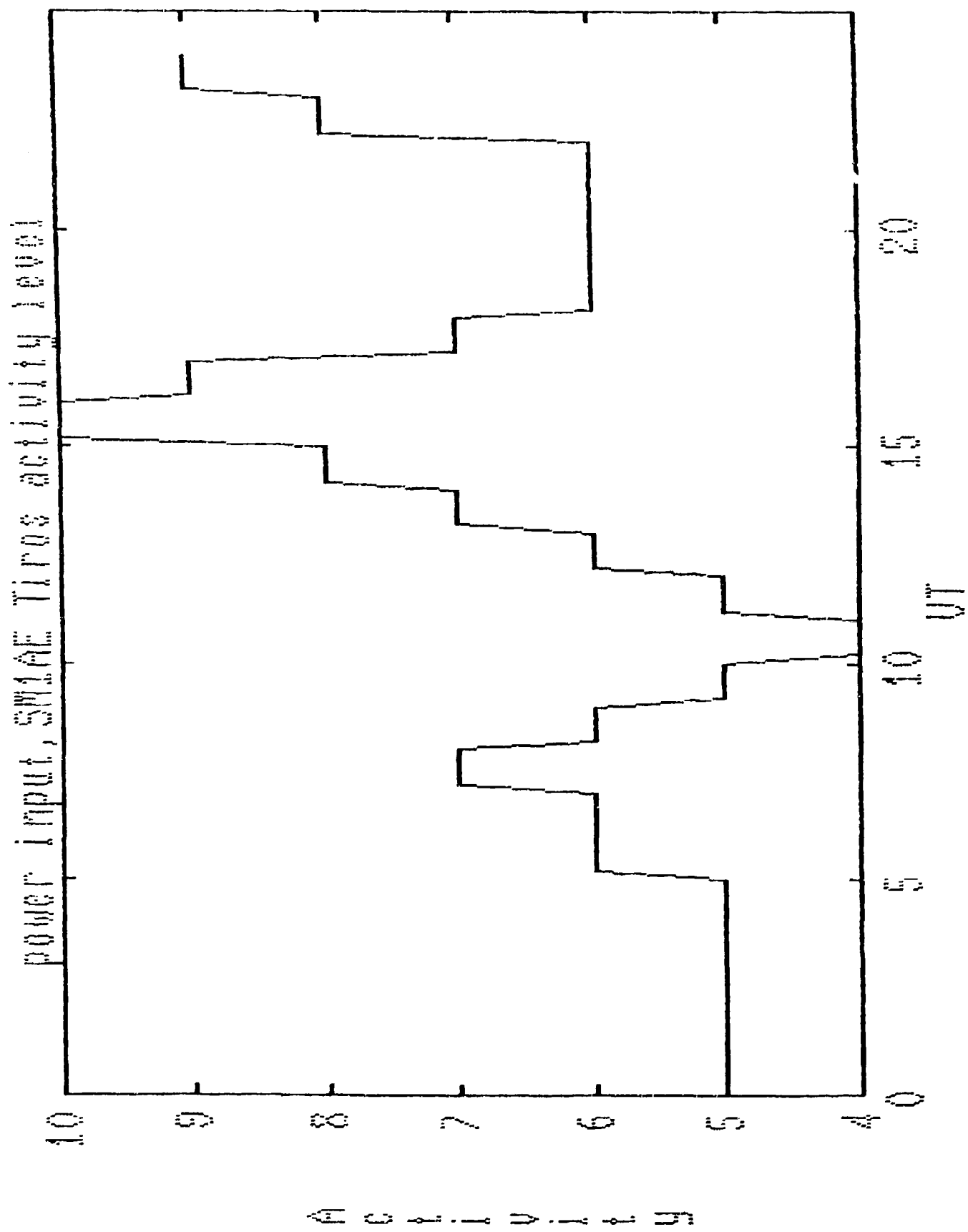


Figure 2

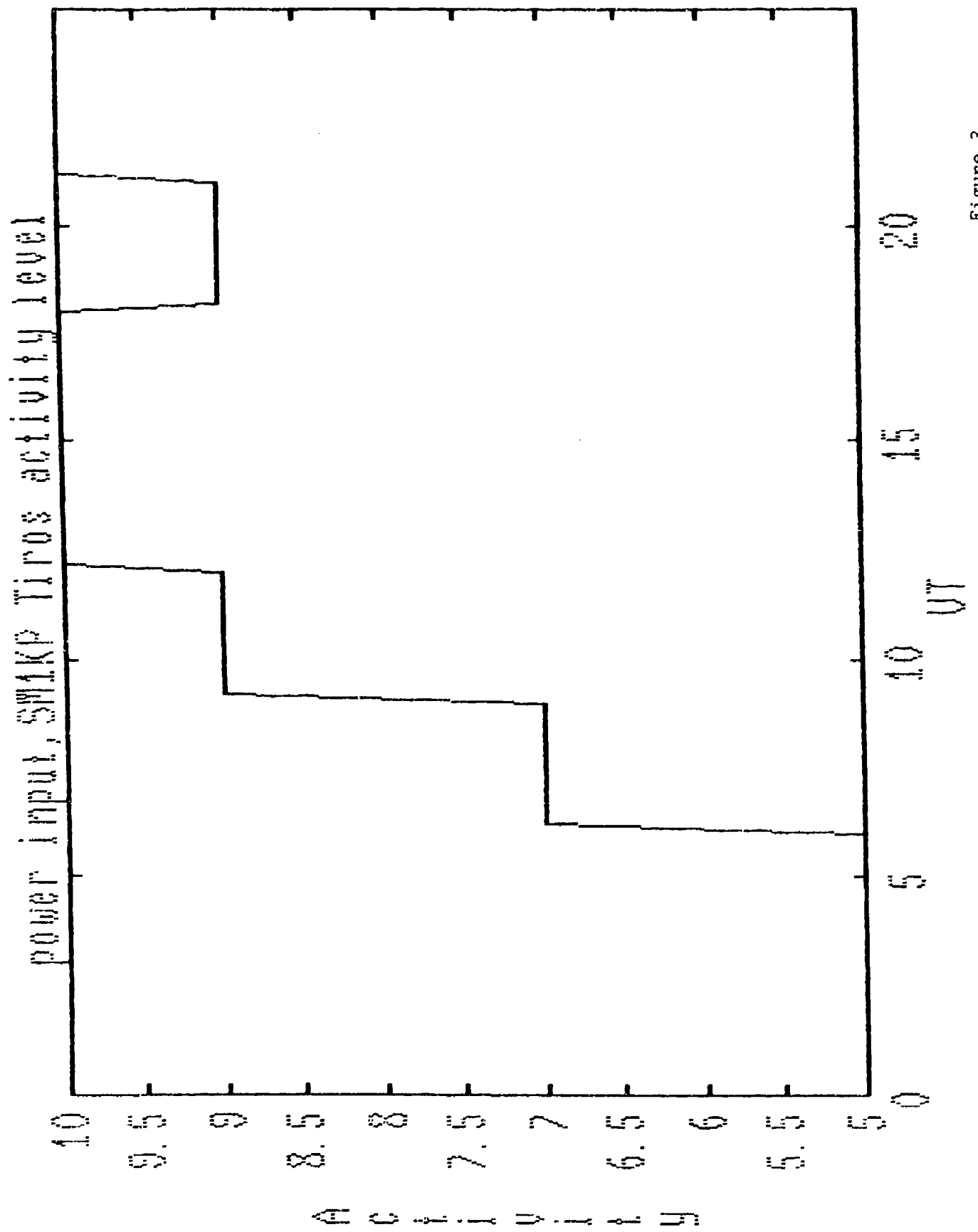
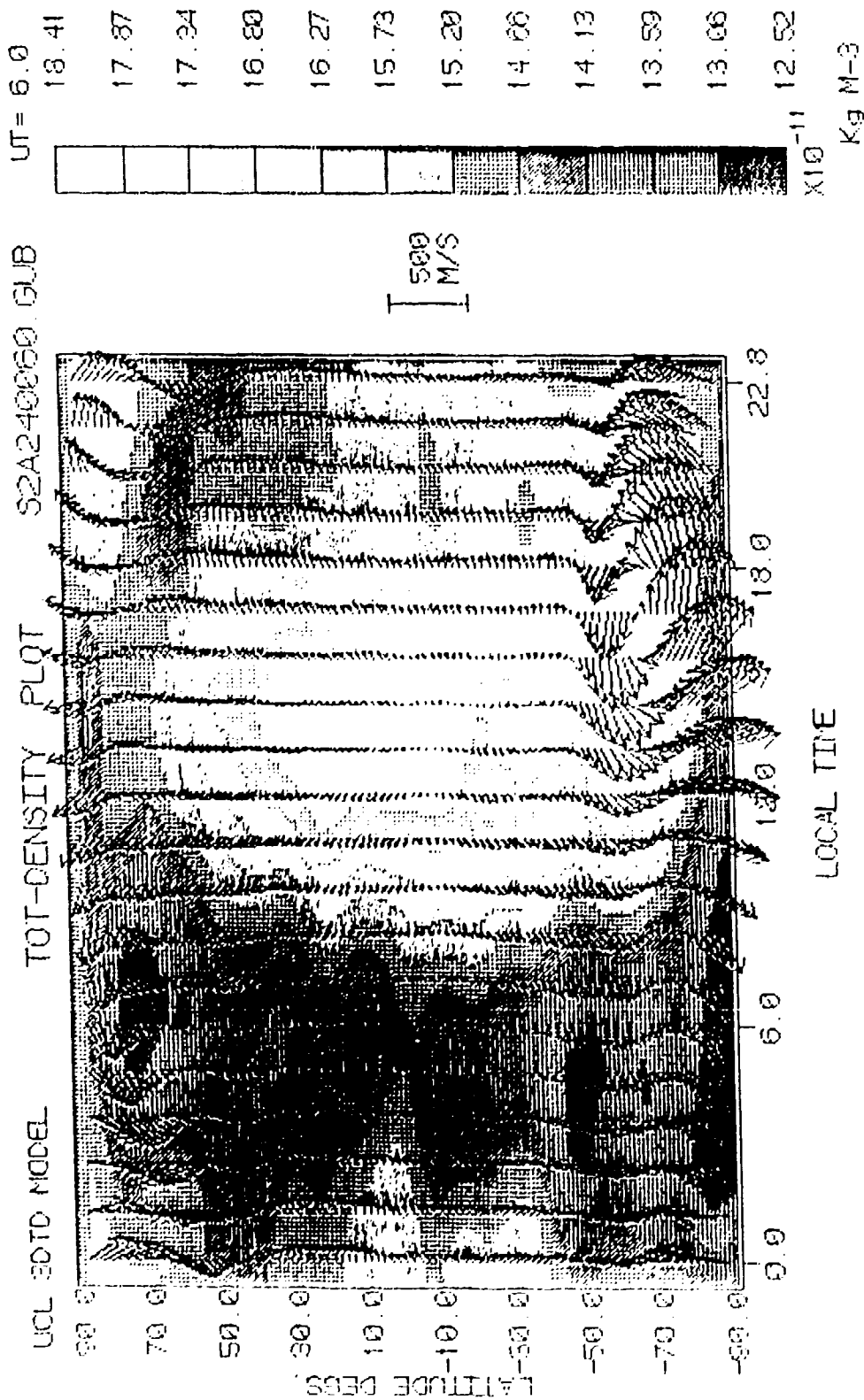
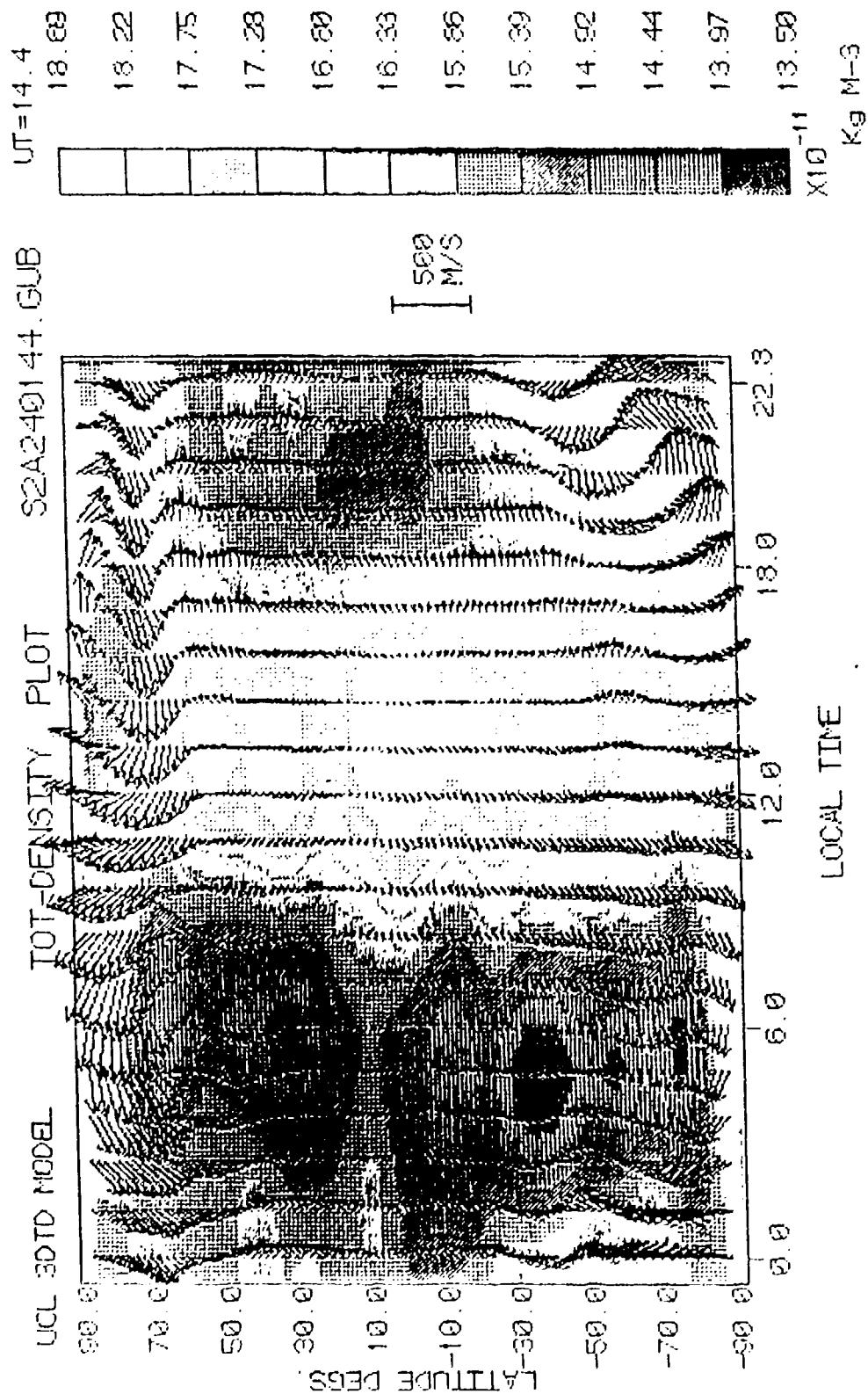


Figure 3



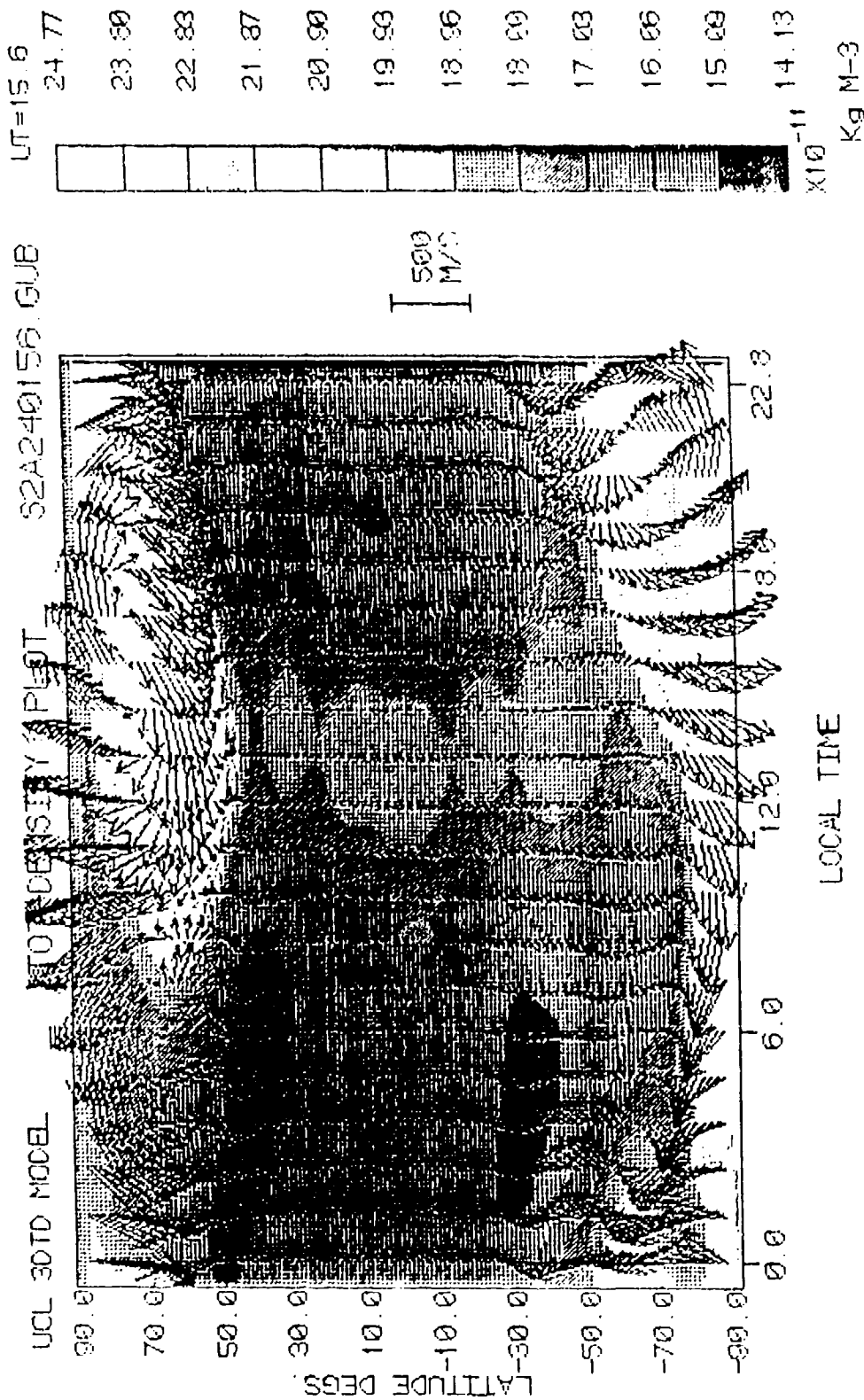
Elec F1d TD-NH
Elec Dens SHEFF/CPLD STORM SIMULATION
Date: MAR 1 F10 7cm 231 TIROS DERIVED FROM AE DATA

Figure 4.



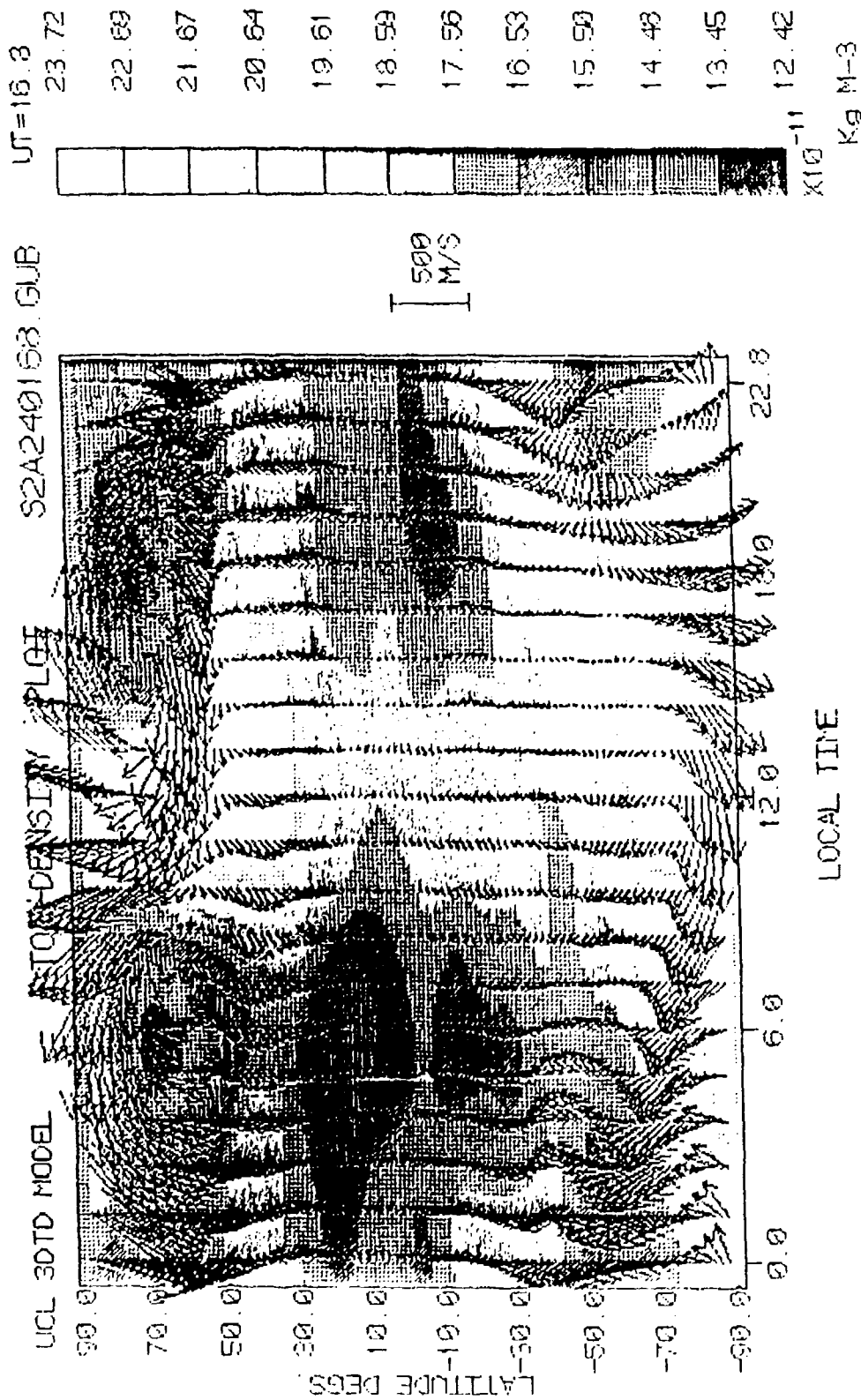
Elec Fld: TD-MH
Elec Dens: SHEFF/CPLD STORM SIMULATION
Date: MAR 1 F10.7cm 231 TIROS DERIVED FROM AE DATA

Figure 5.



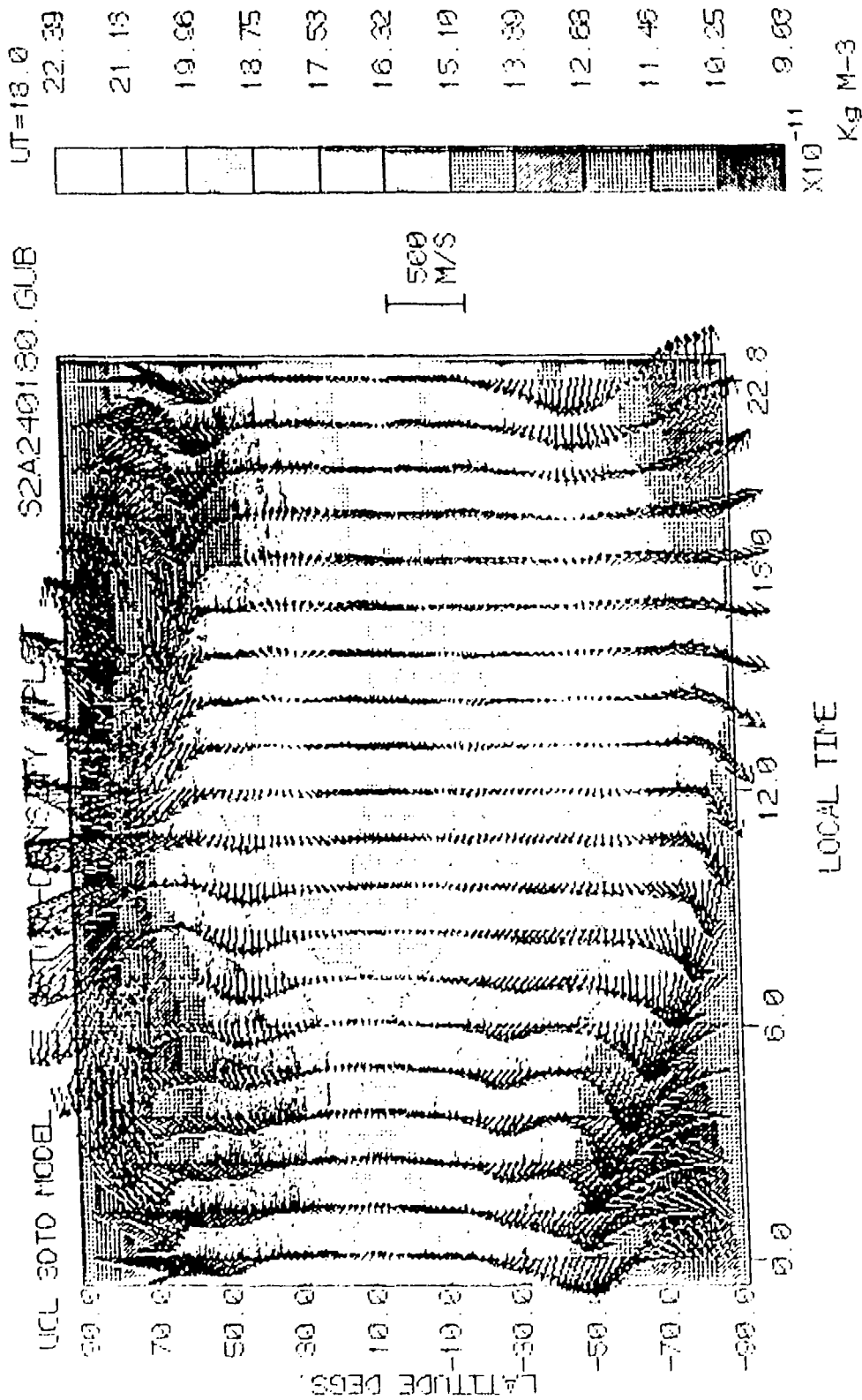
Elec. Fld. TD-MH
 Elec. Dens: SHEFF/CPLD STORM SIMULATION
 Date: MAR 1 F10.7cm 231 TIROS DEPICTED FROM AE DATA

Figure 6.



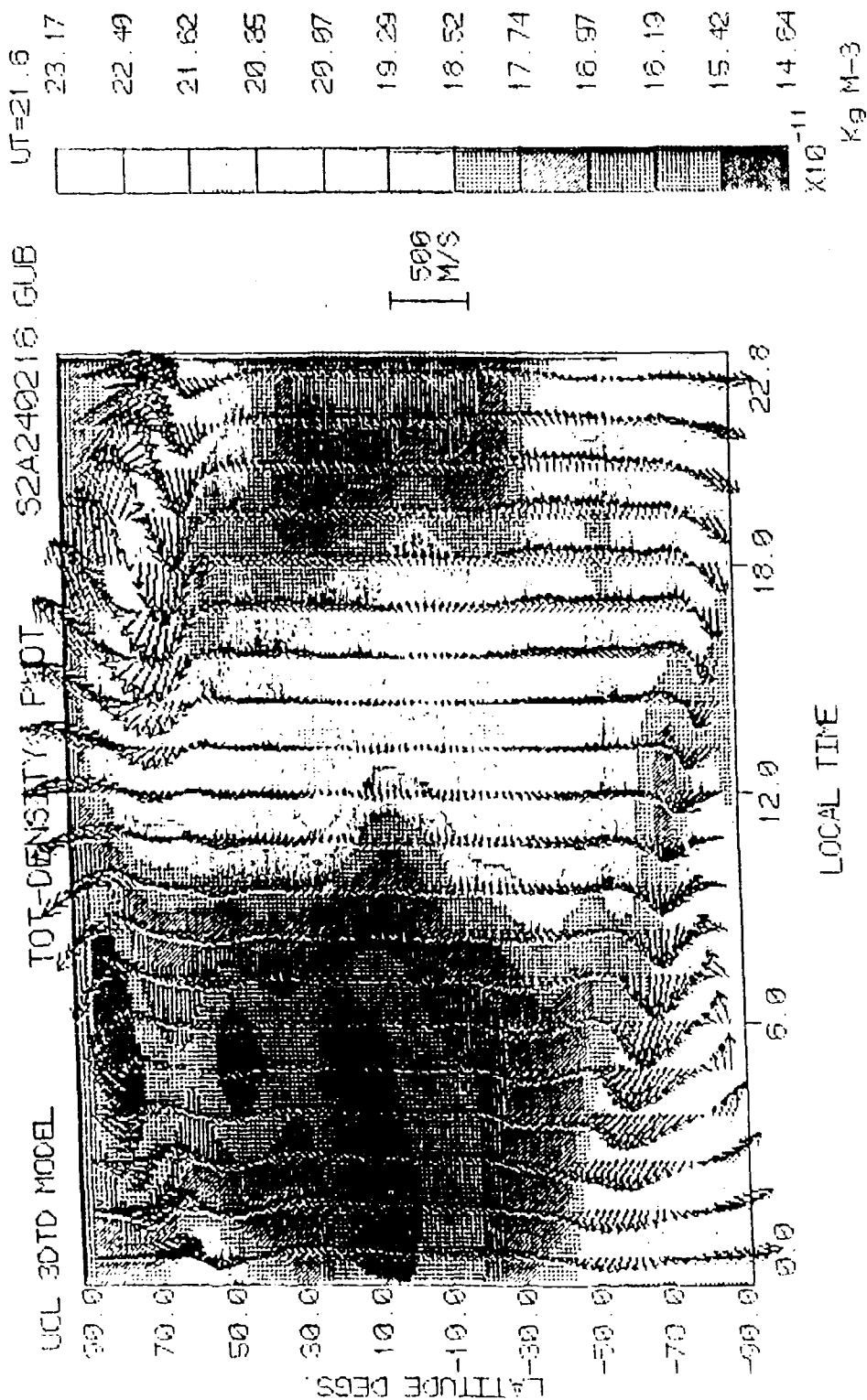
Elect. Fld: TD-MH
 Elec. Dens SHEFF/CPLD STORM SIMULATION
 Date: MWP 1 F10.7cm 231 TIROS DERIVED FROM AE DATA

Figure 7.



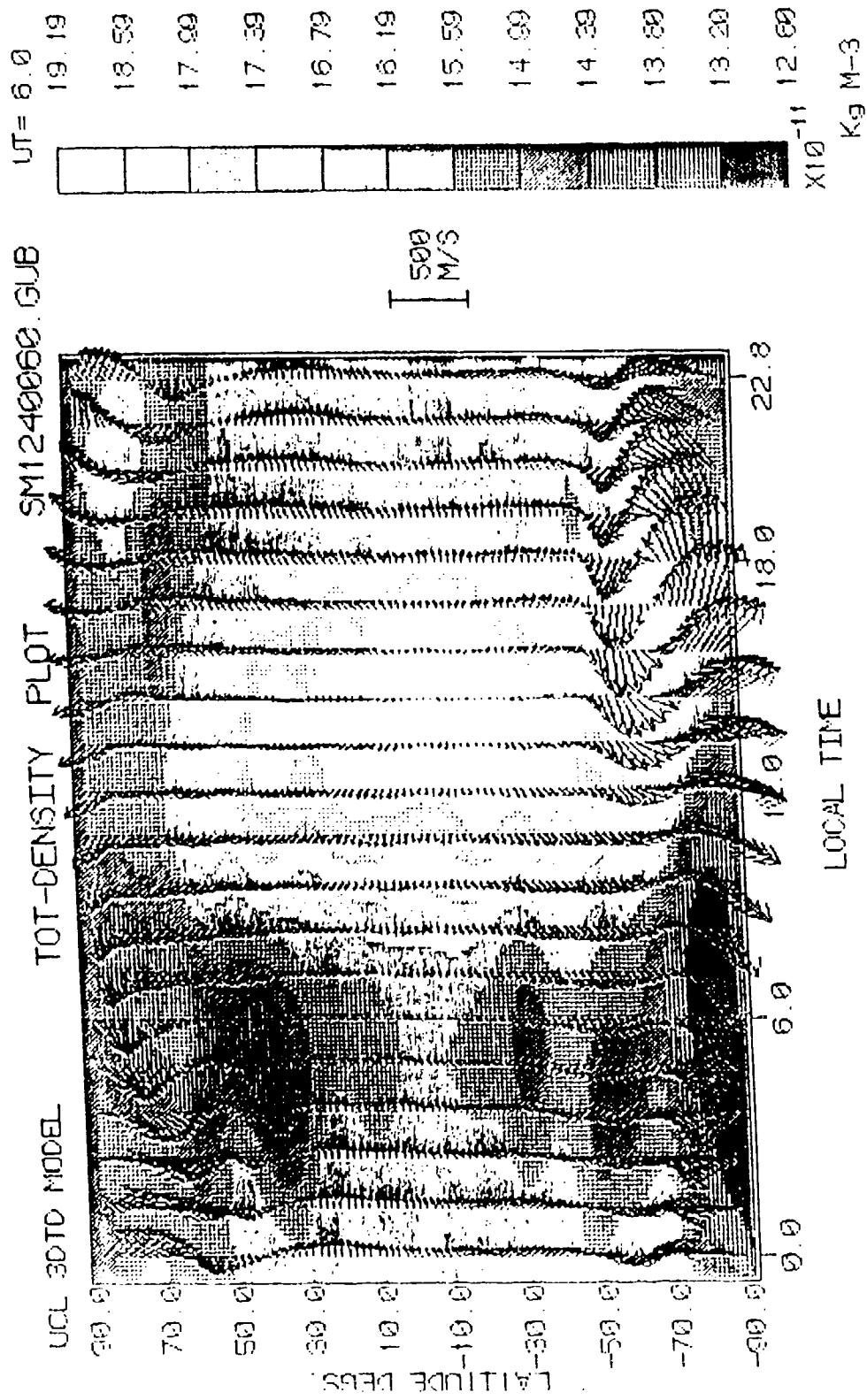
Elec: Fld: TD-MH
Elec: Dens: SHEFF/CPLD STORM SIMULATION
Date: MAR 1 10.7cm 231 TIROS DERIVED FROM AE DATA

Figure 8.



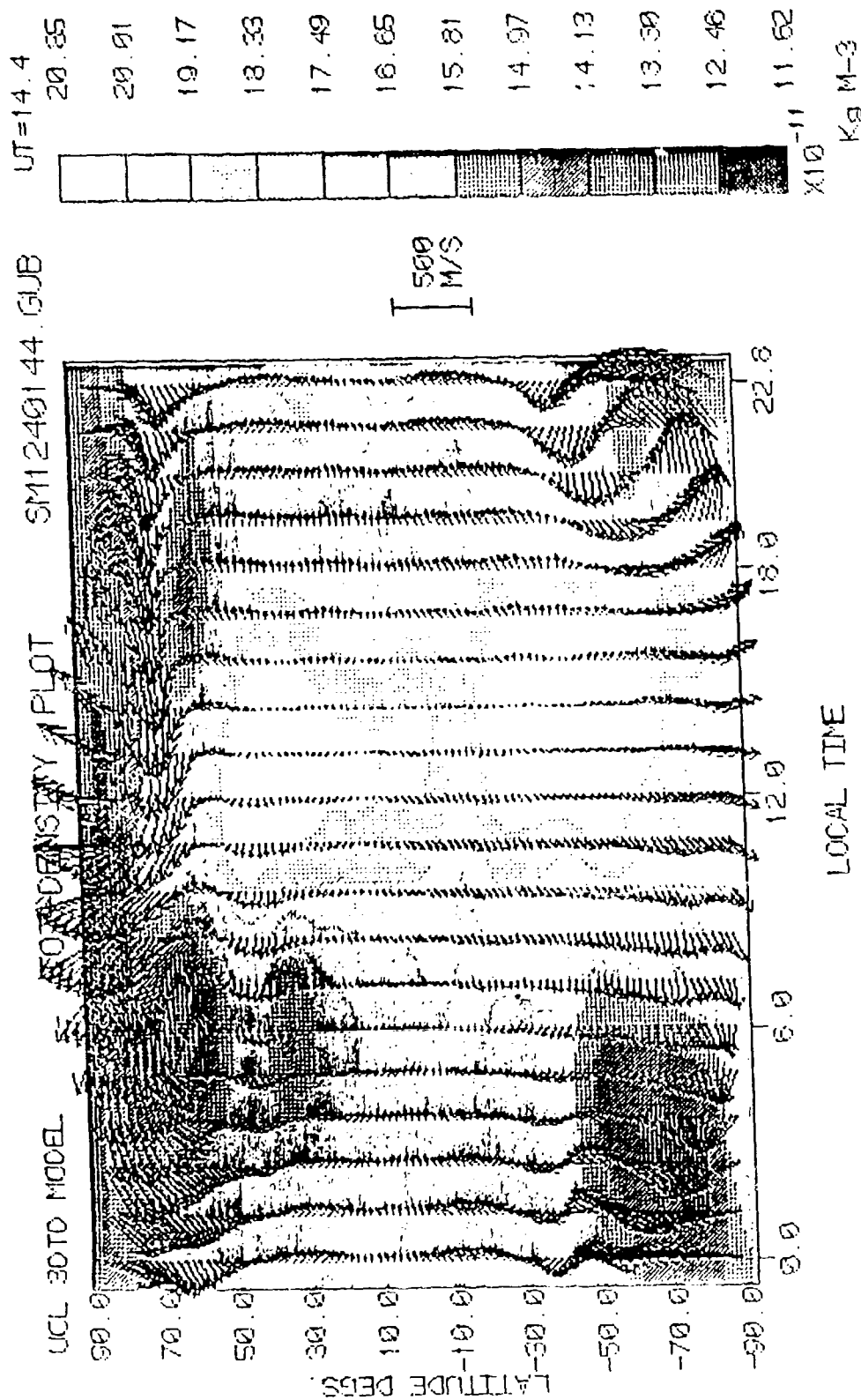
Elec. Fld: TD-MH
 Elec. Dens: SHEFF/CPLD STORM SIMULATION
 Date: MAR 1 F10.7cm 231 TIROS DERIVED FROM AE DATA

Figure 9.



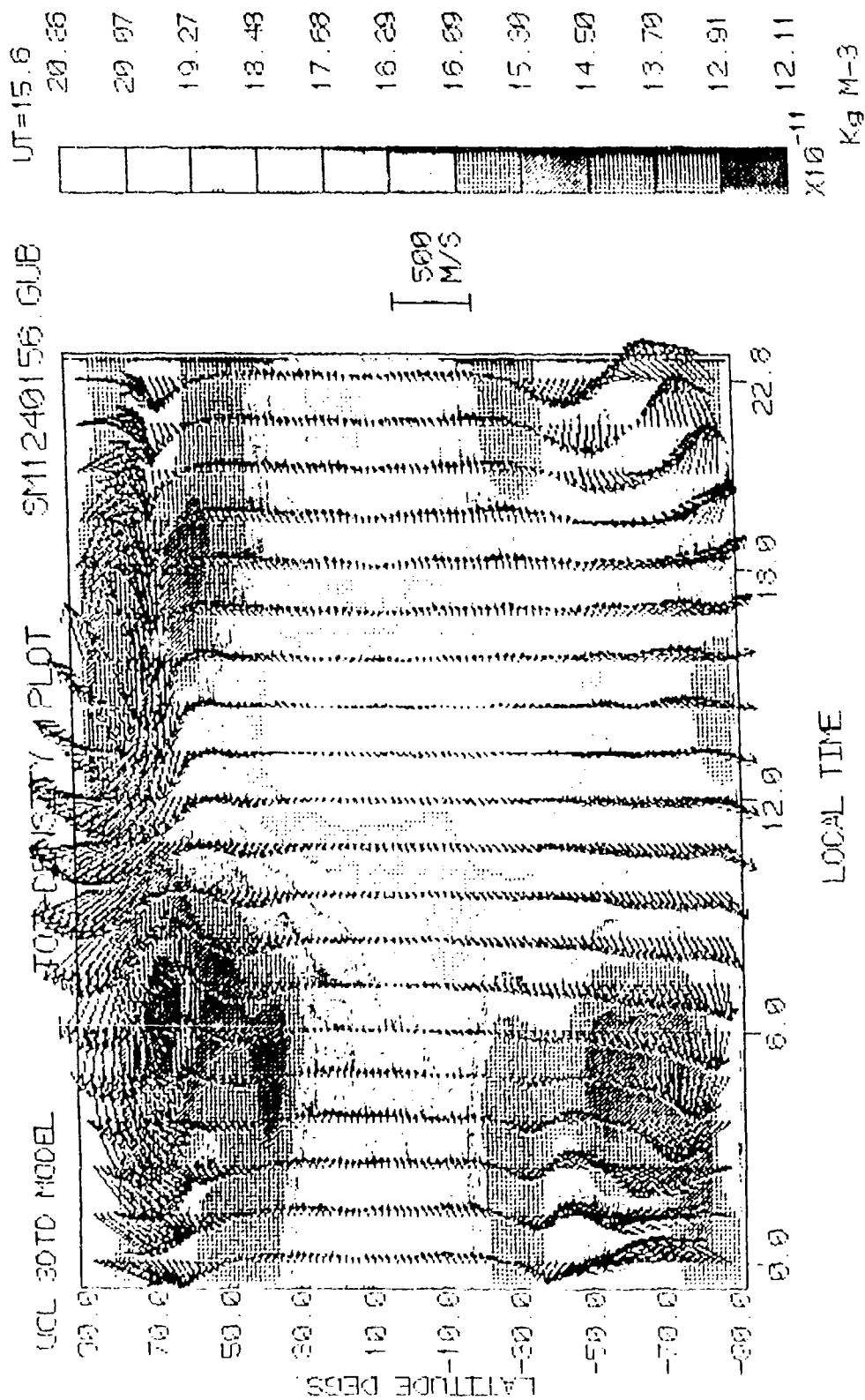
Elec. Fld: TD-MH
 Elec. Cons: SHEFF/CPLD
 Date: MAR 1 F10 7cm 231 gmp=1.5, HIGH NOAA/TIROS

Figure 10.



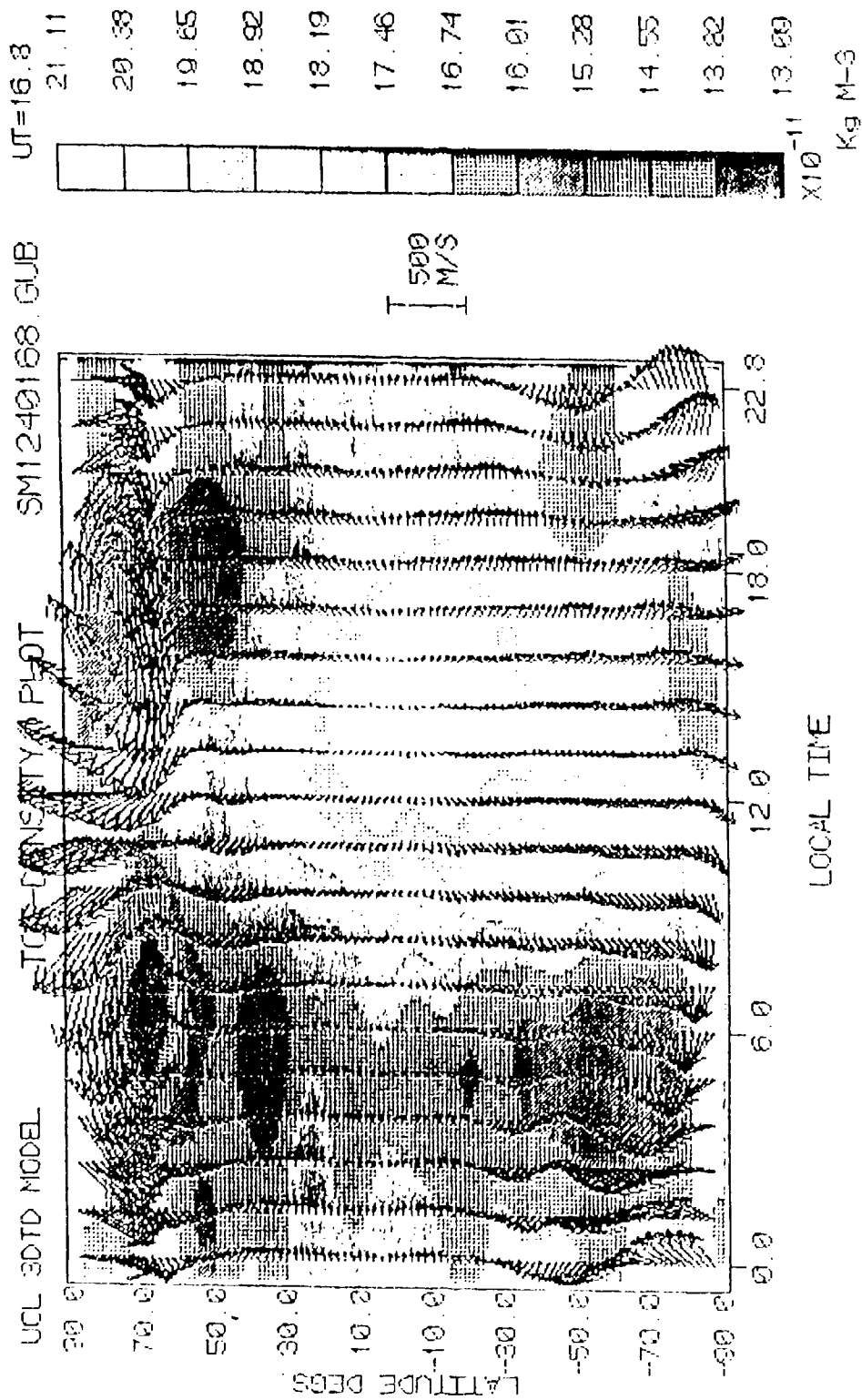
Elec. Fld: TD-MH
 Elec. Dens: SHEFF/CPLD TIME DEPENDENT STORM
 Date: MAR 1 F10.7cm 231 dHP=1.5 HIGH NOAA/TIROS

Figure 11.



Elec. Fld: TU-MH
Elec. Dens: SHEFF/CPLD
Gate: MRP 1 F10.7cm 231 AMP=1.5, HIGH NOAA/TIR06

Figure 12.



Elec. Fld: TD-NH
 Elec. Dens: SHEFF/CPLD TIME DEPENDENT STORM
 Date: MAR 1 F10.7cm 231 ANP=1.5, HIGH NOAA/TIROS

Figure 13.

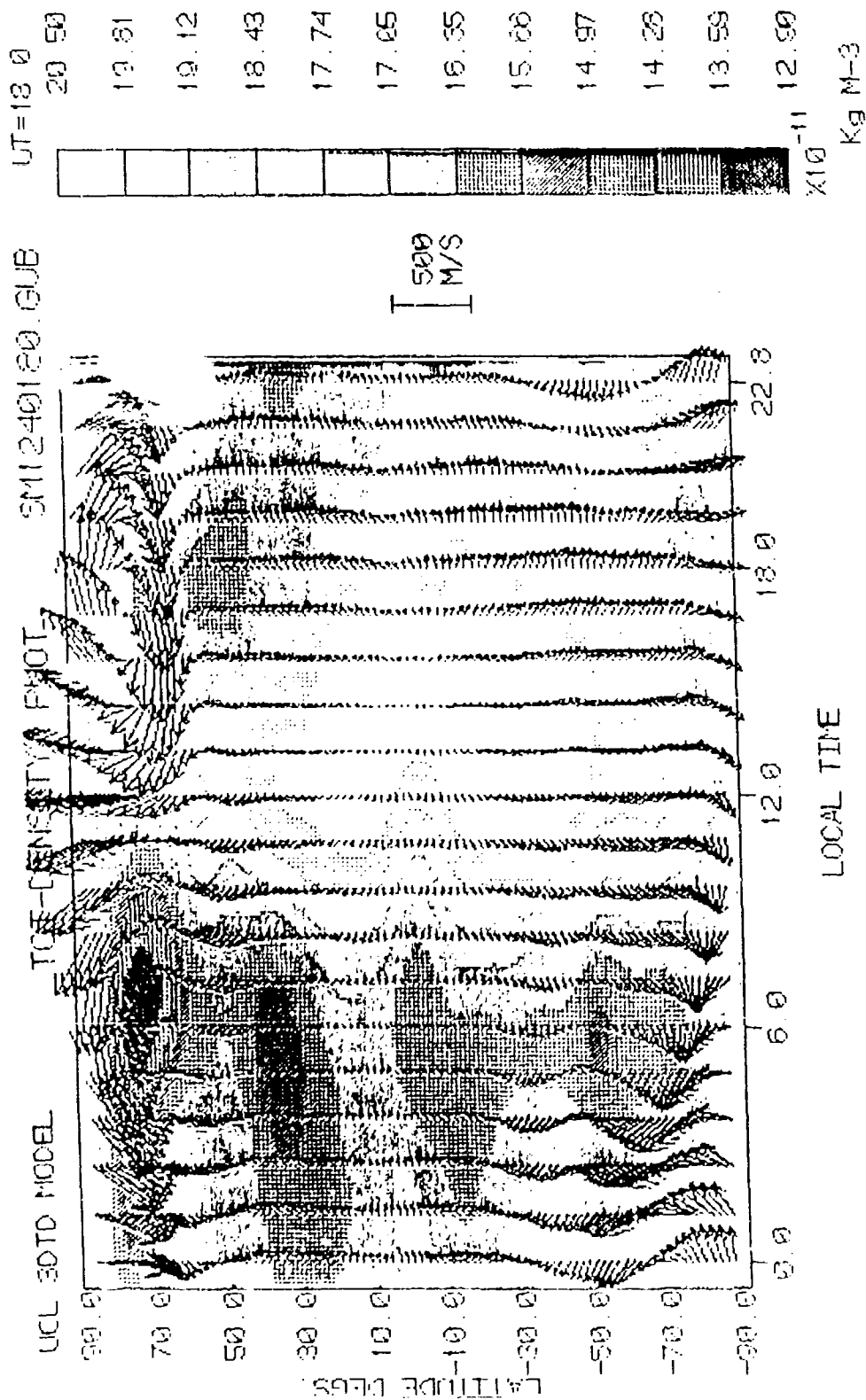
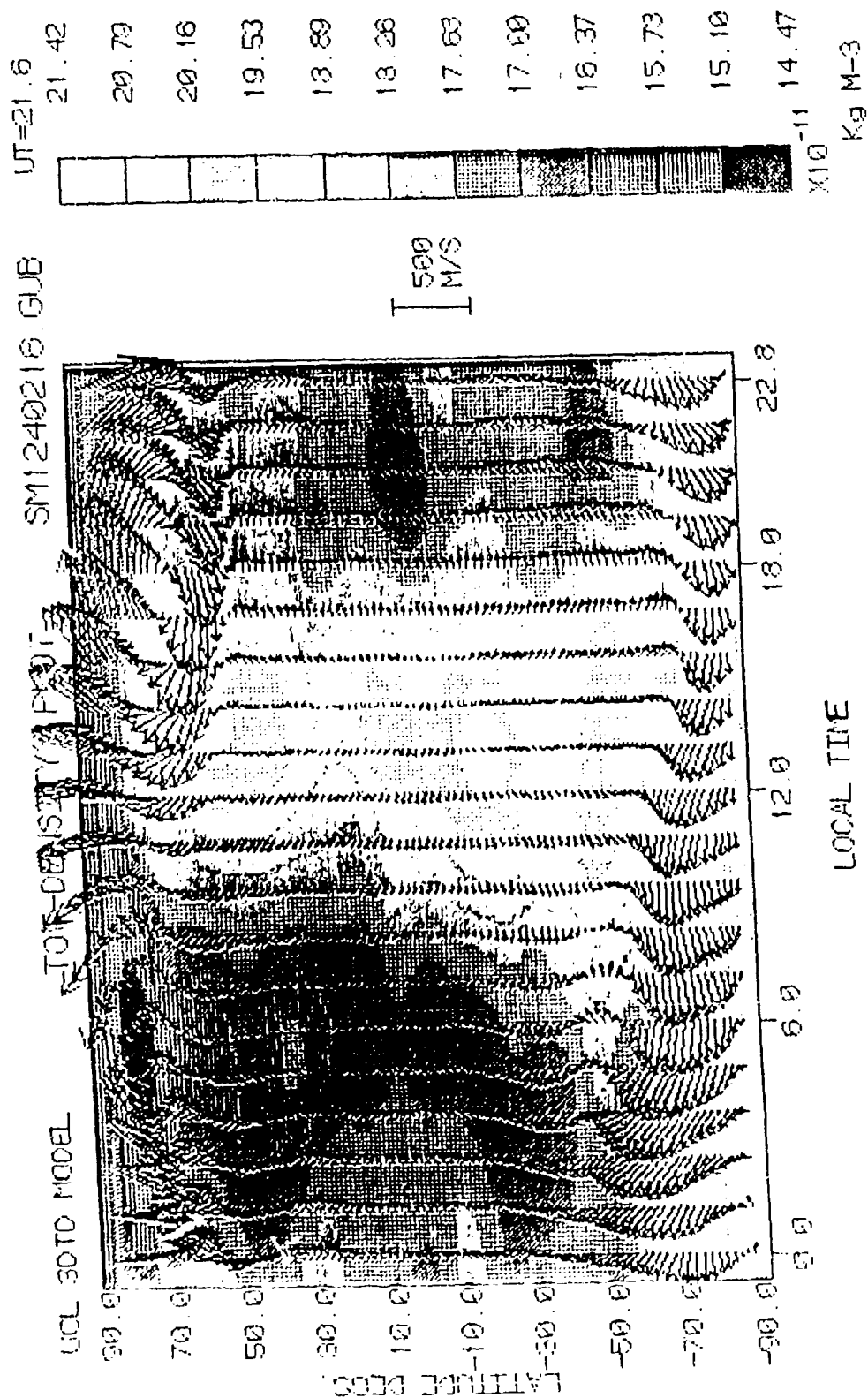


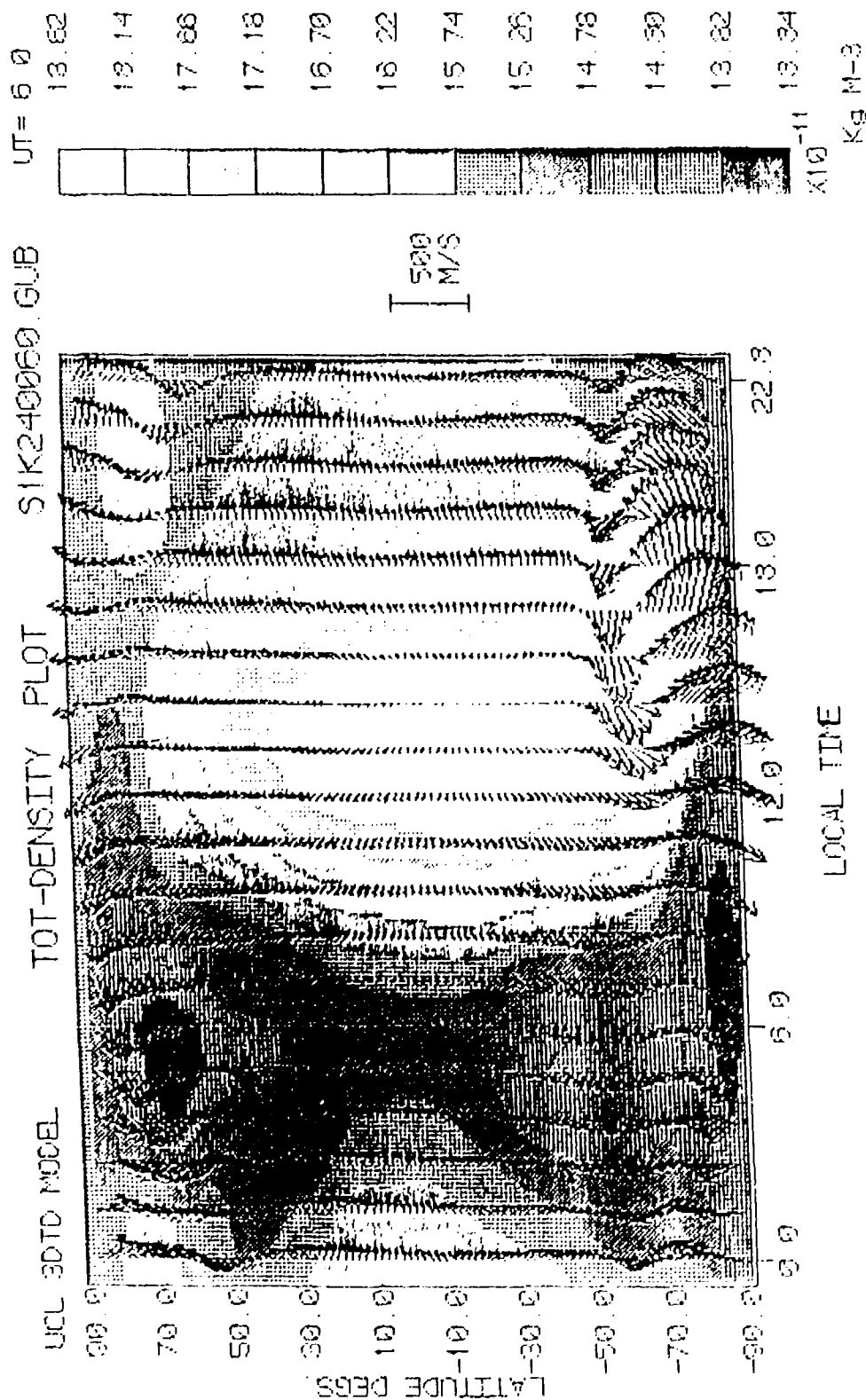
Figure 14.

Elec. Fld. TD-MH
 Elec. Dens. SHEFF/CPLD TIME DEPENDENT STORM
 Date MAP | F10.7cm 231 MP=1.5, HIGH NOAA/TIPUS



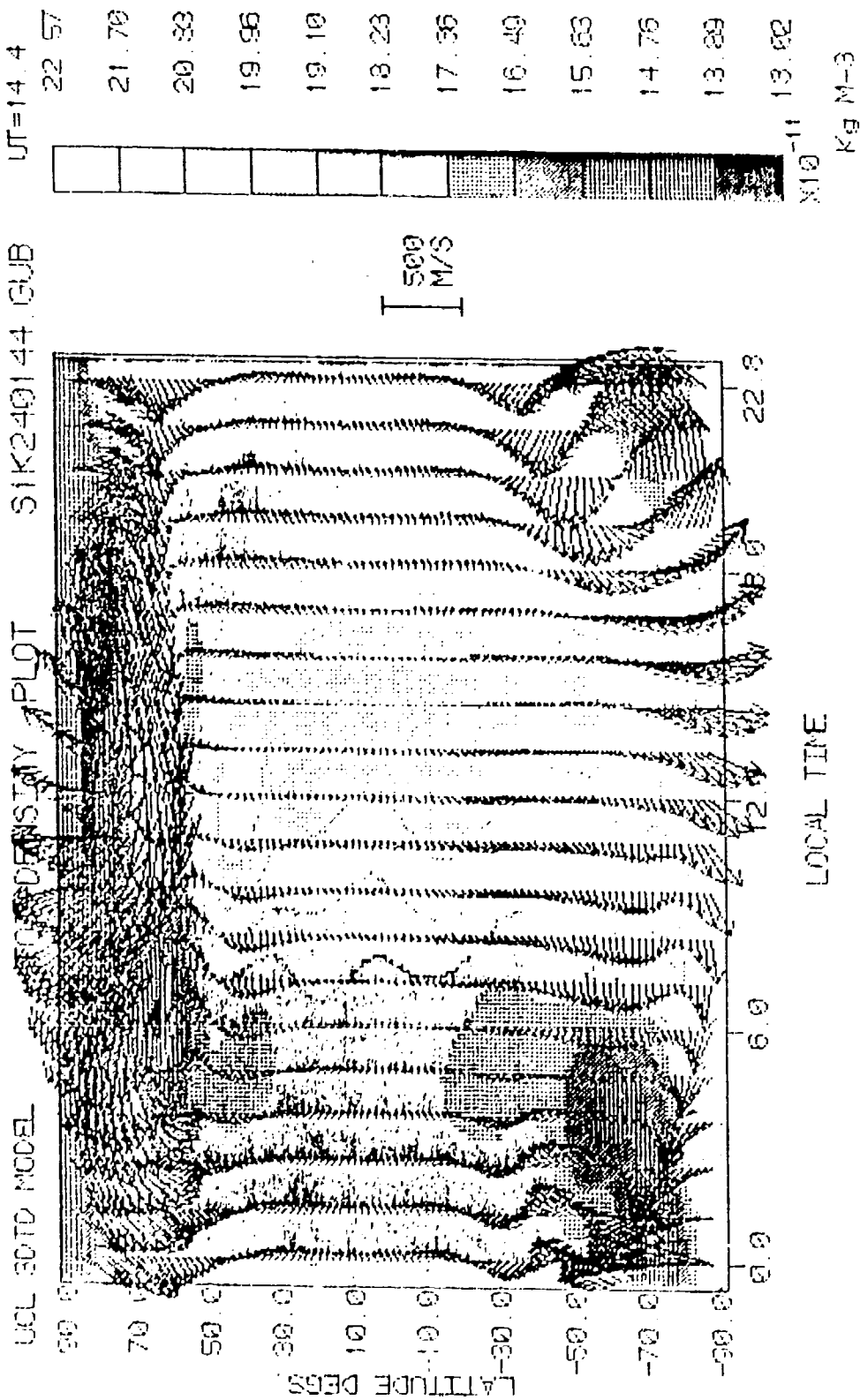
Elec. Fld. TD-MH
 Elec. Dens. SHEFF/CPLD TIME DEPENDENT STORM
 Date: MAR 1 F12.7cm 231 AMP=1.5, HIGH NOAA/TIROS

Figure 15.



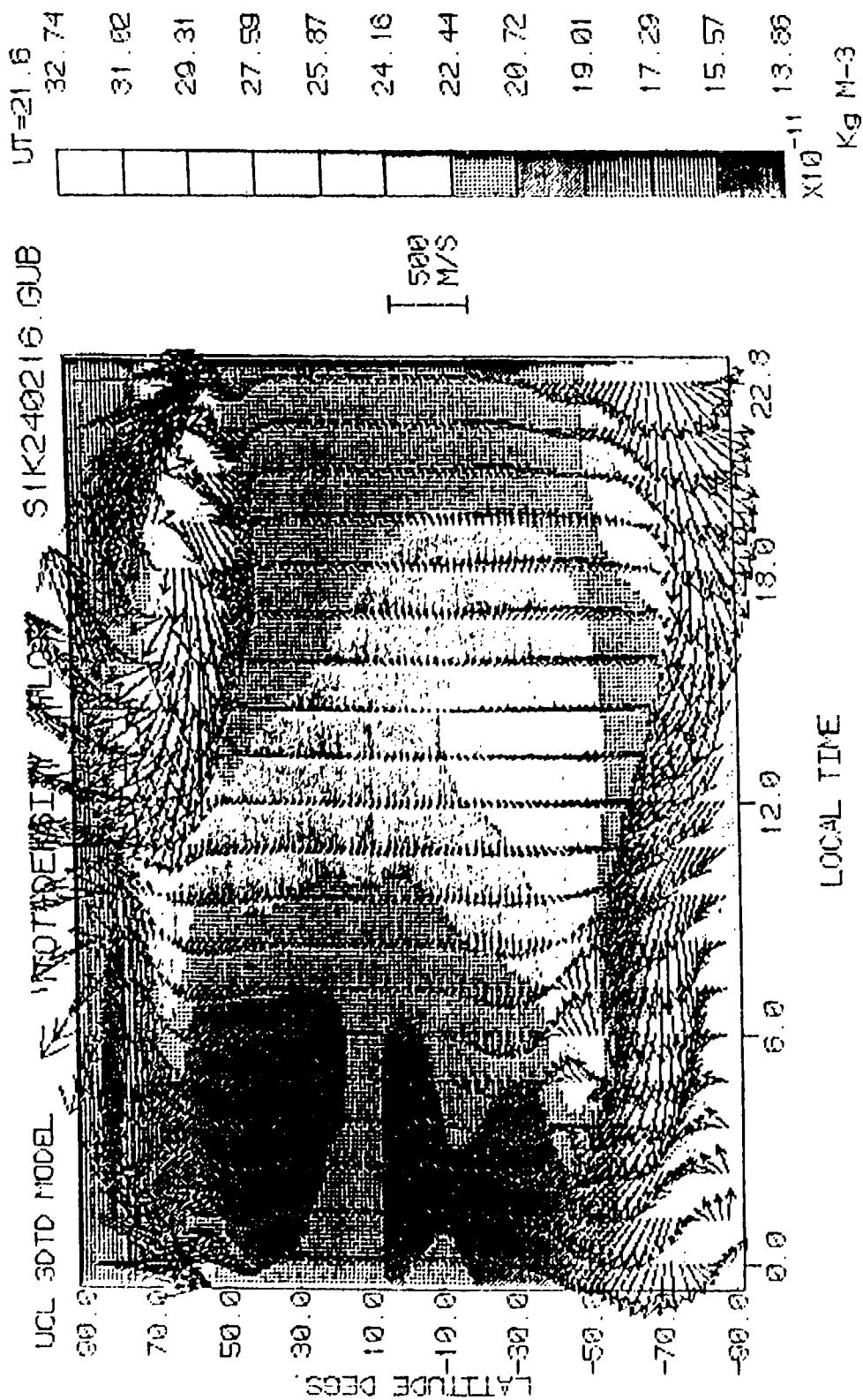
File: TD-MH
Case: SHEFF-CPLD STORM SIMULATION
Date: 1991 F10 7am 231 CEIVED FROM KP DATA

Figure 16.



Elec F1d TD-MH
 Elec Dens SHEFF/CPLO STORM SIMULATION
 Date: 1989 1 F10.7cm 231 CEPTIVED FROM KP DATA

Figure 17.



Elec. Fld: TD-MH
 Elec. Cons: SHEFF/CPLD STORM SIMULATION
 Date: MAR 1 1970 7:23:16 DEPICTED FROM KP DATA

Figure 18.

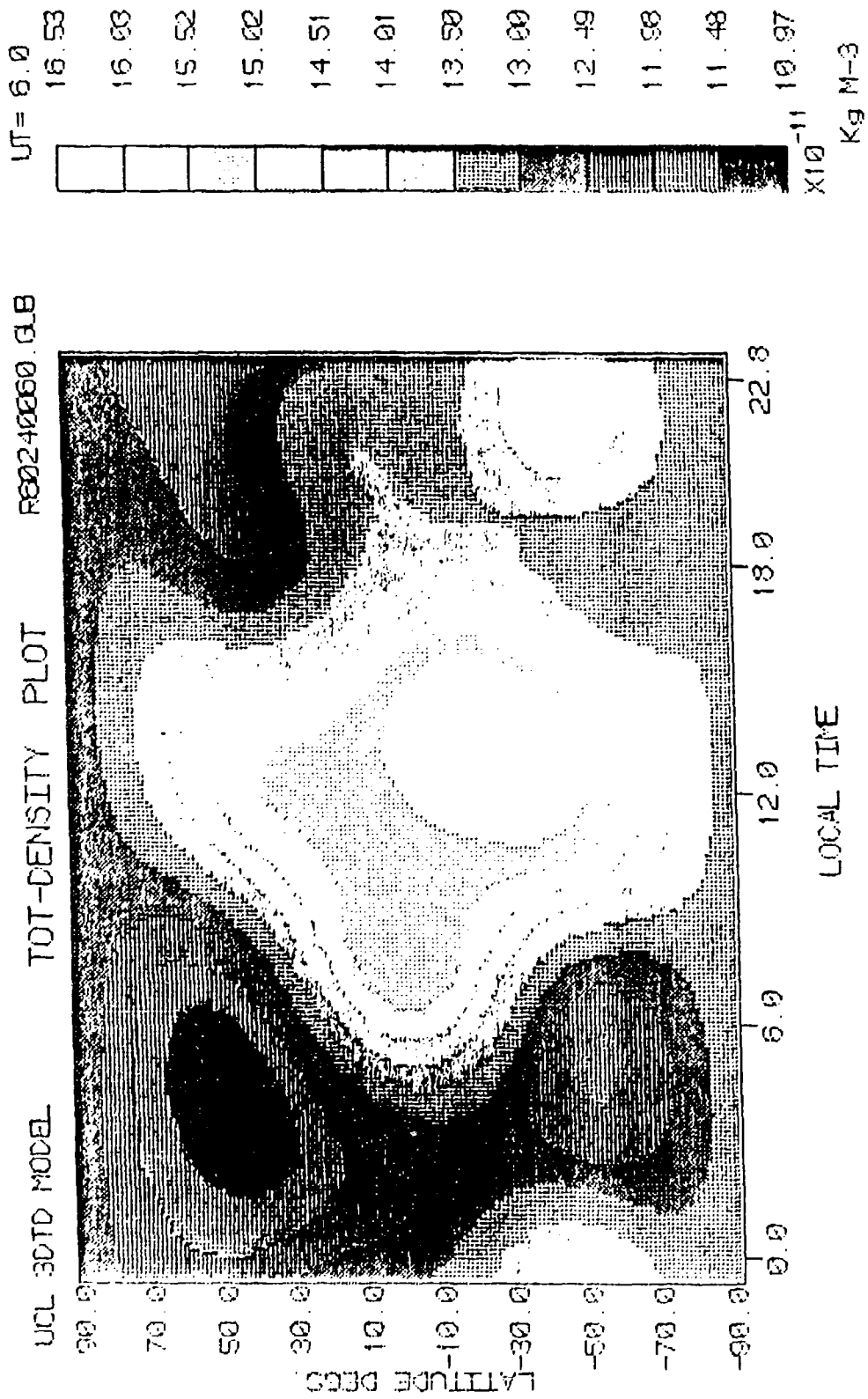


Figure 19.

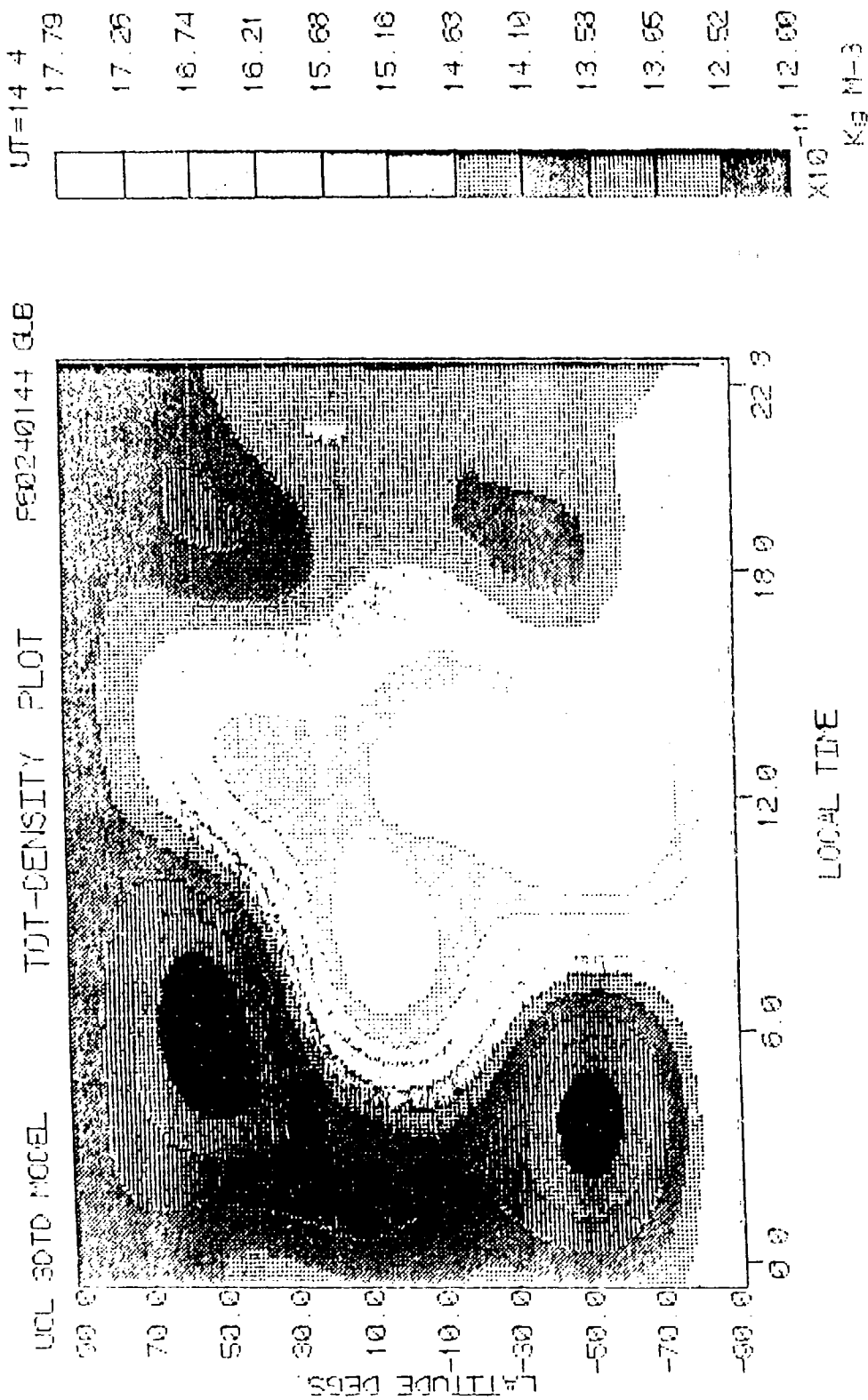


Figure 20.

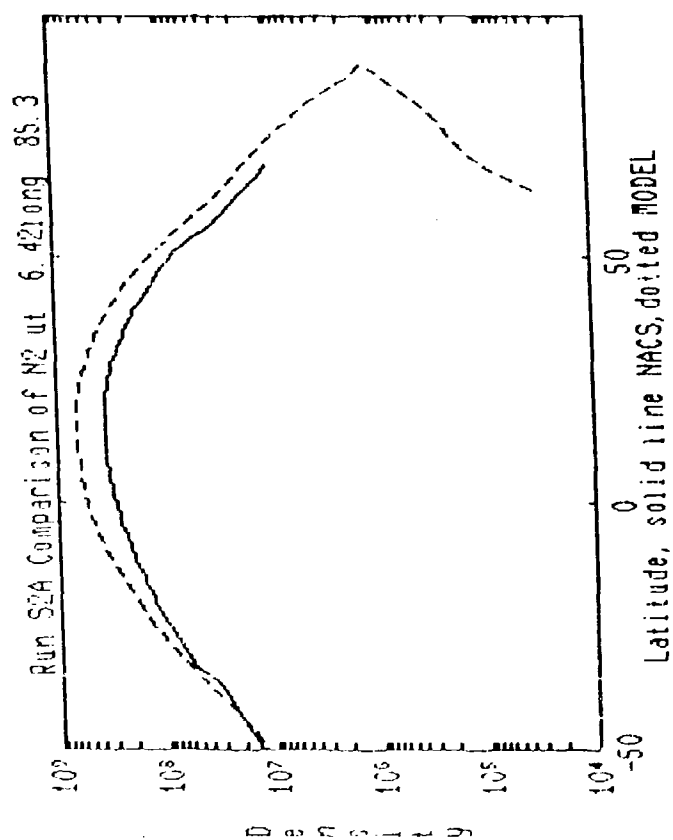
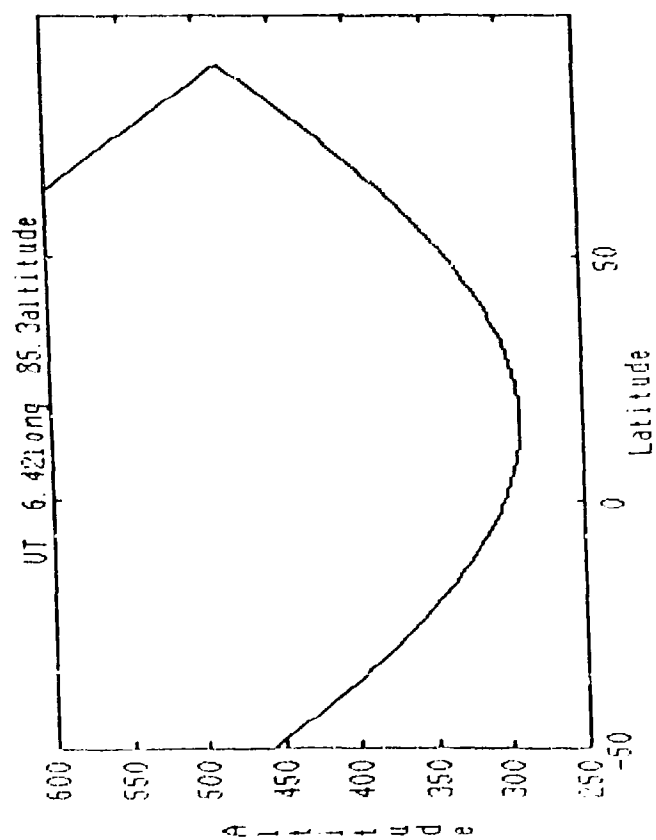
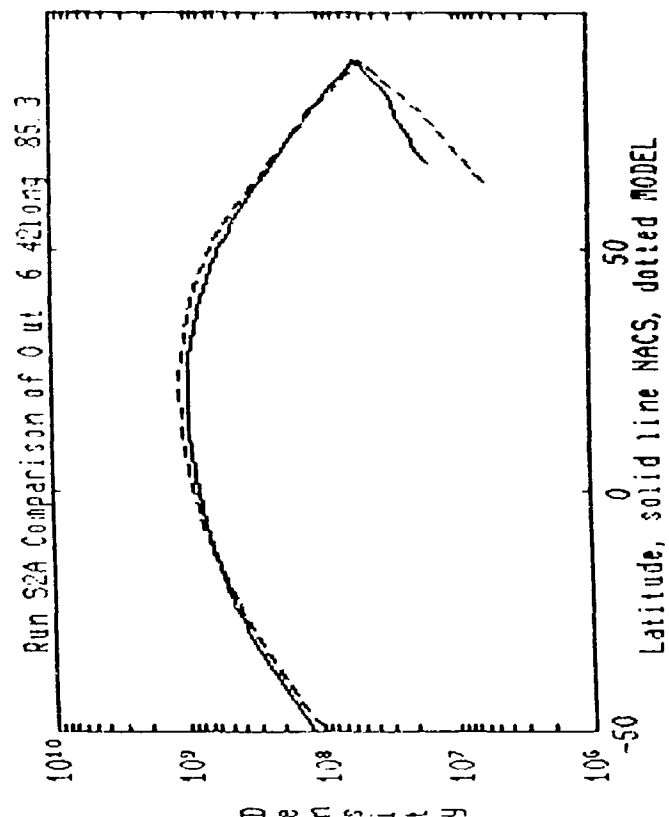
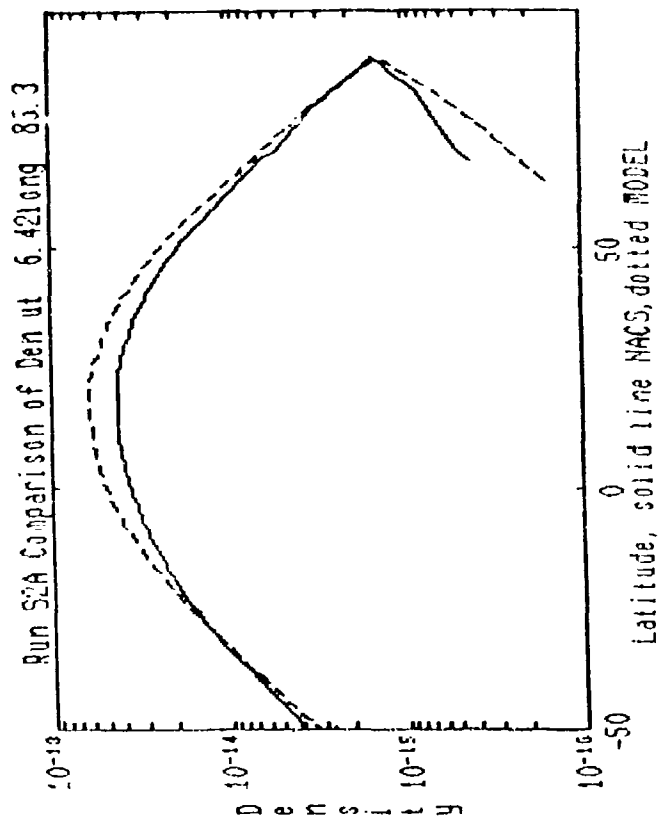


Figure 22

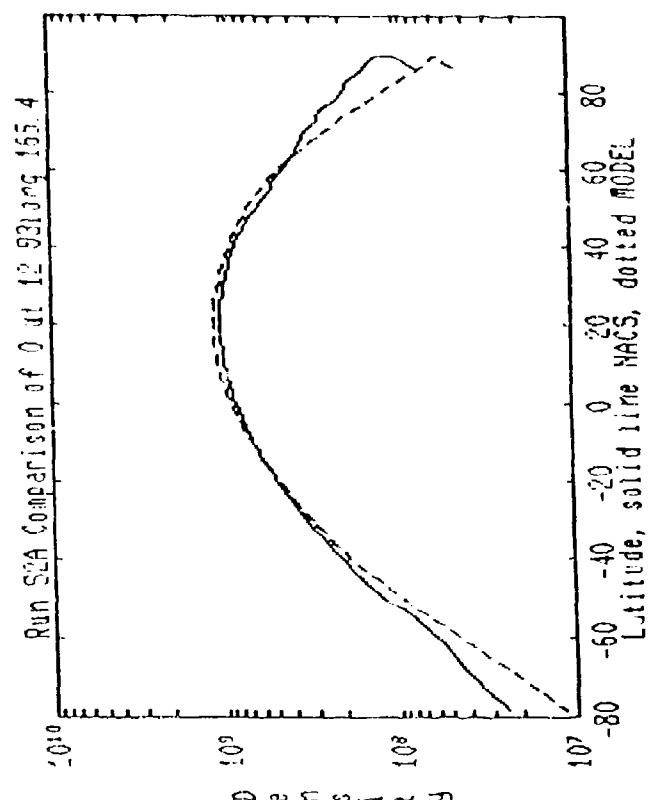
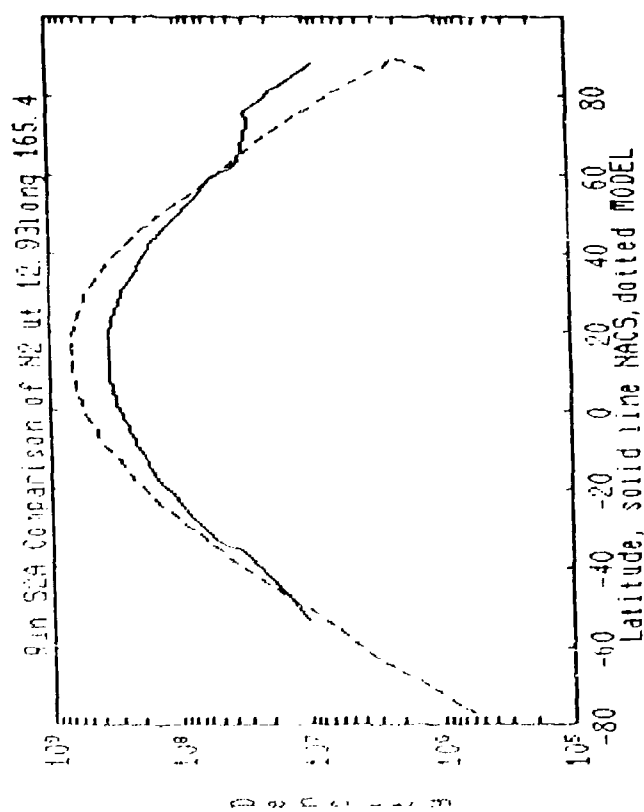
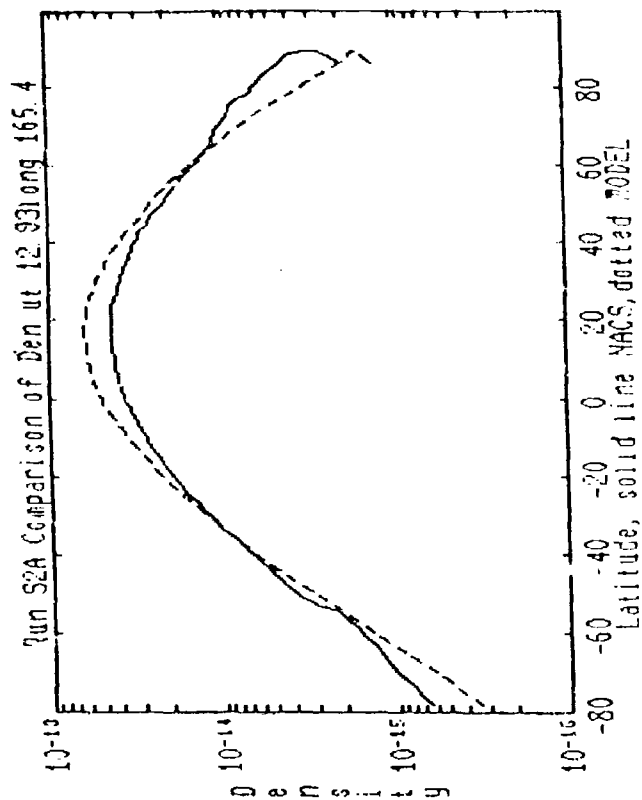
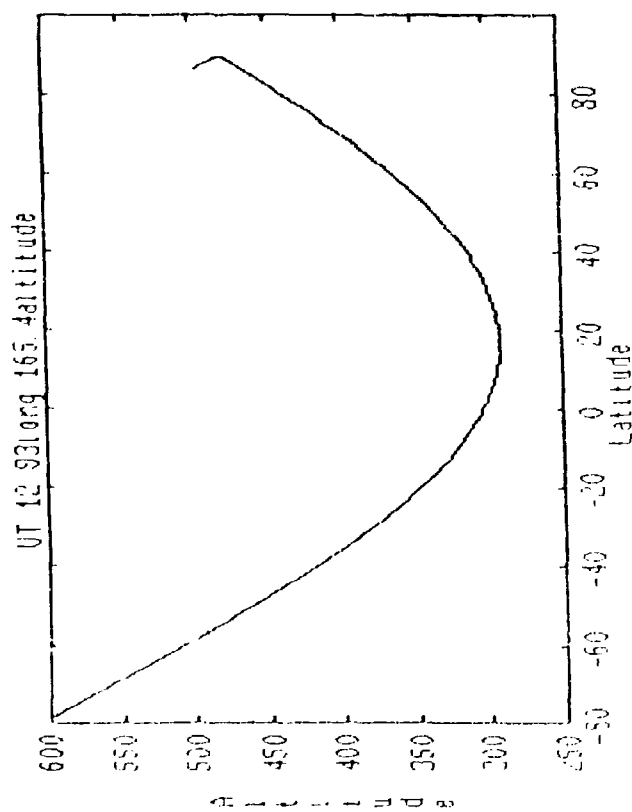


Figure 23

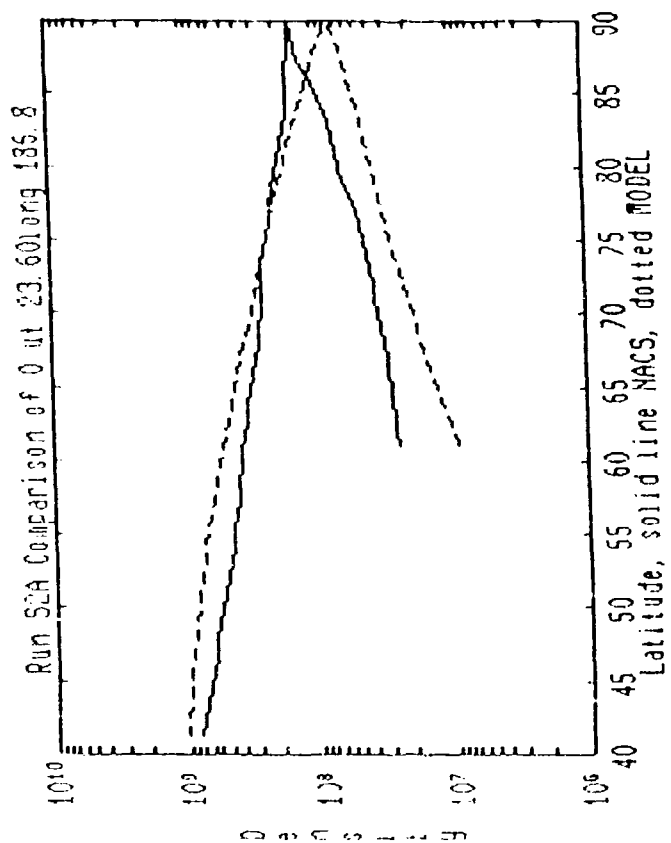
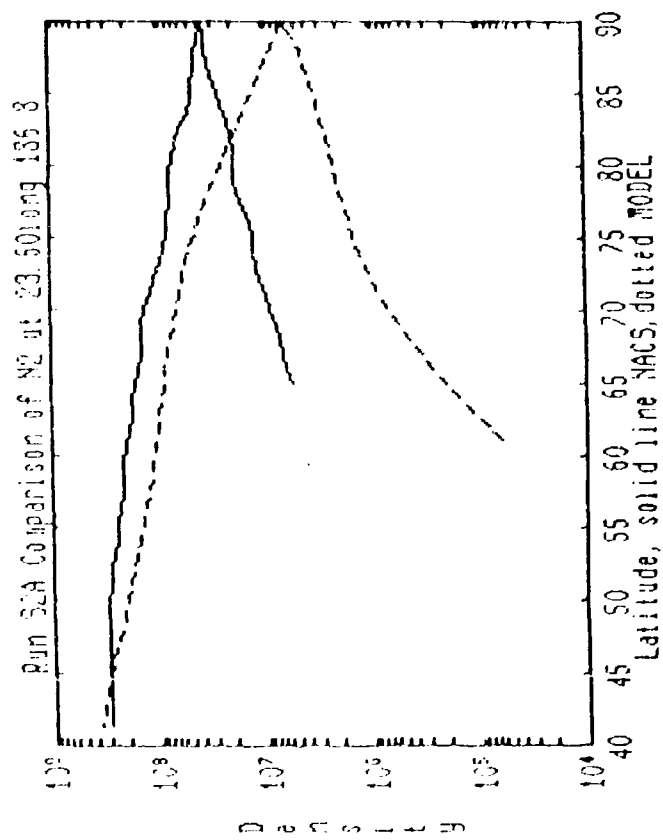
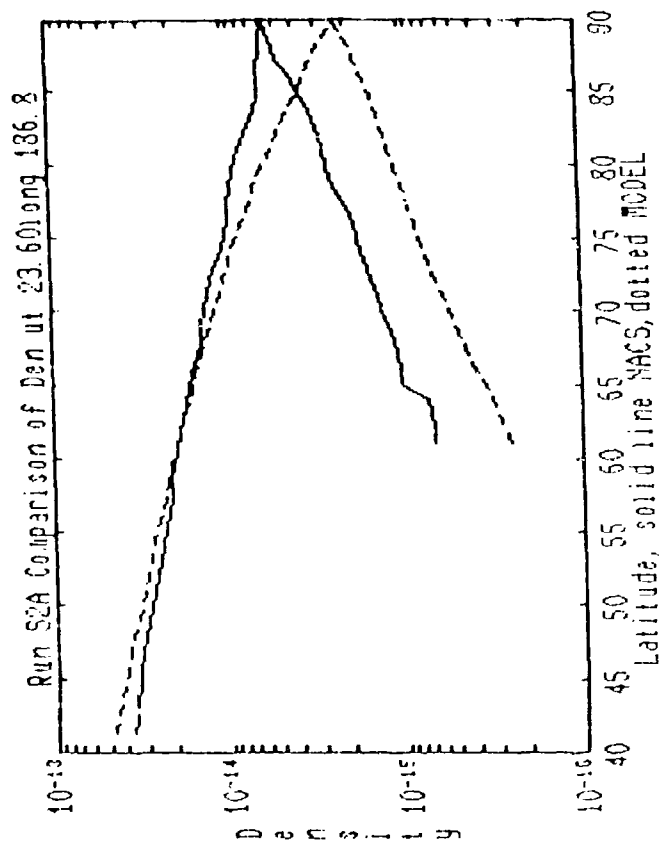
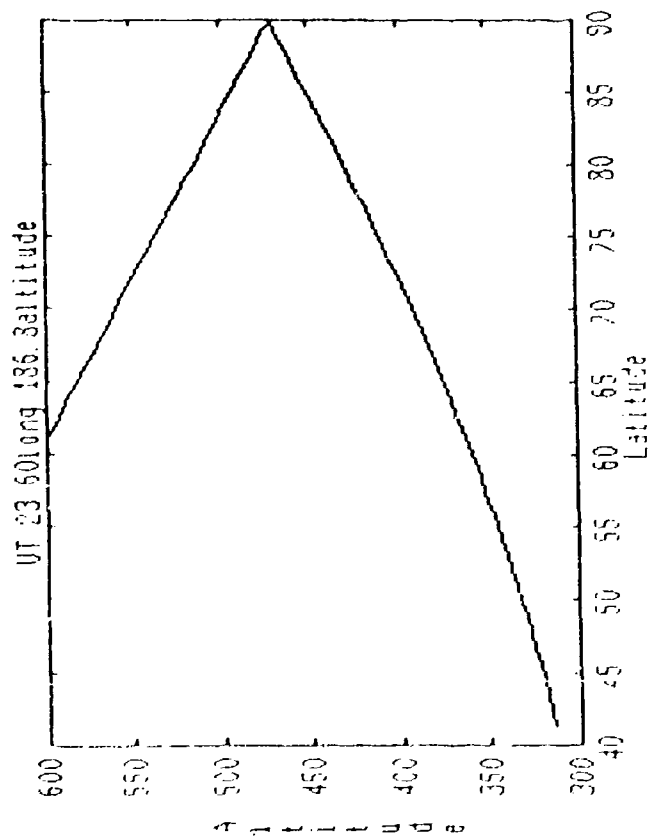


Figure 24

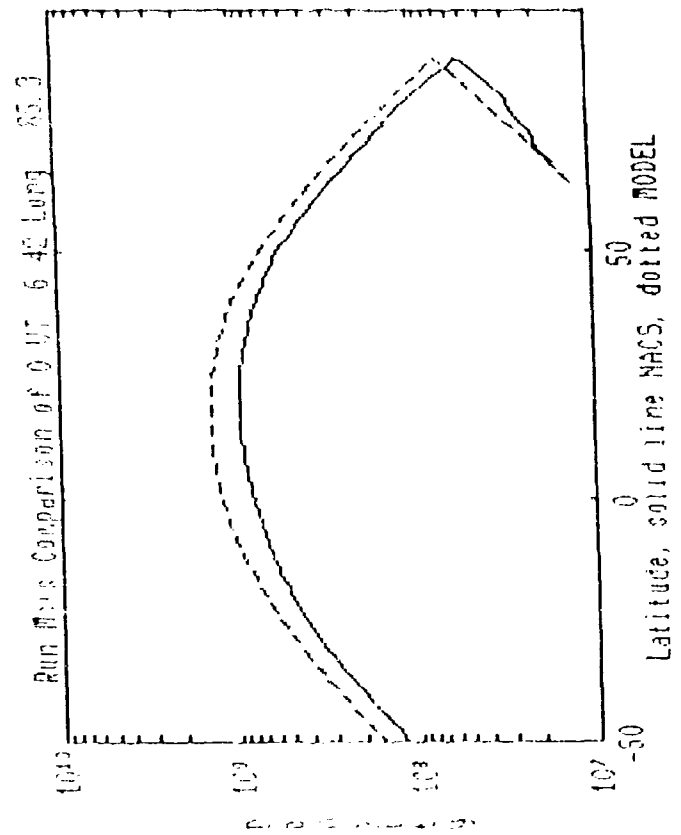
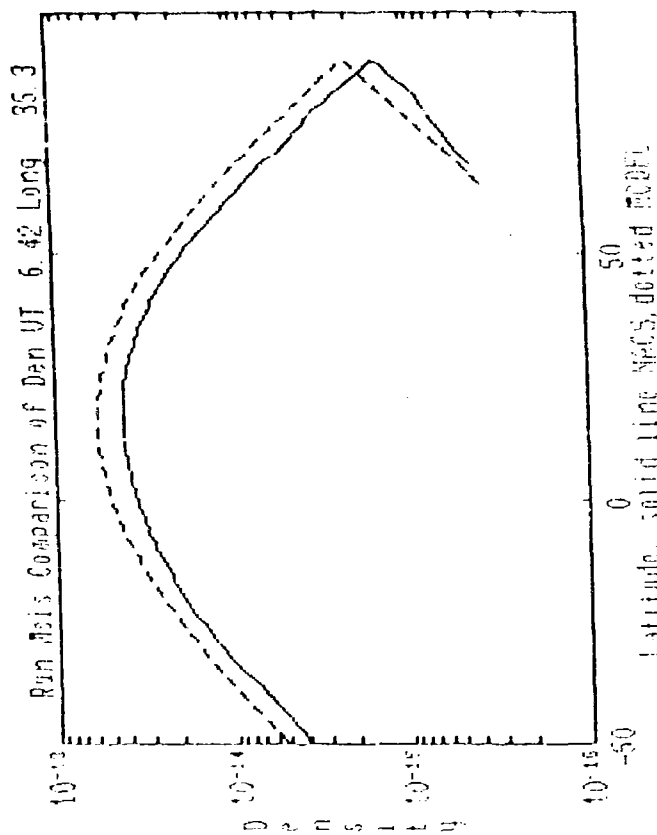
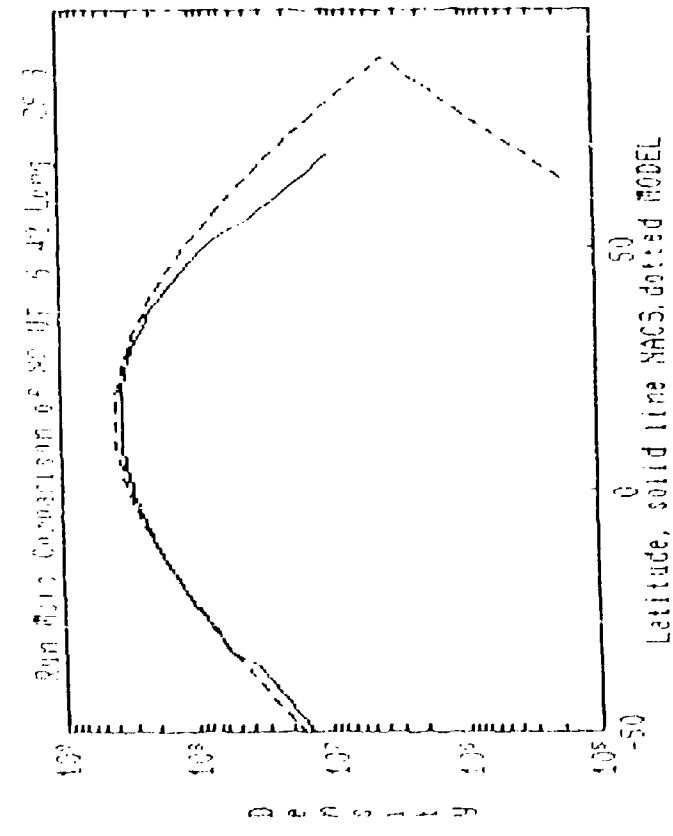
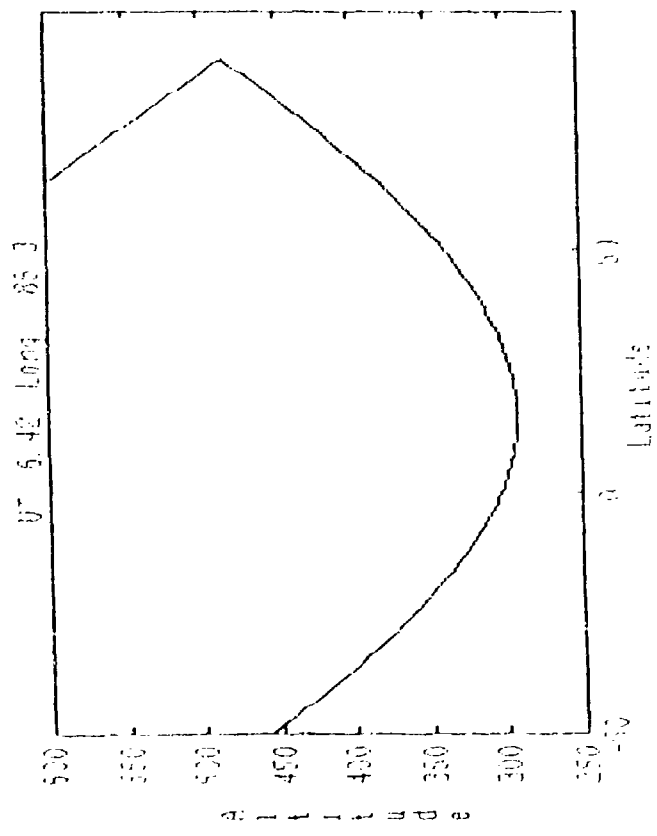


Figure 25



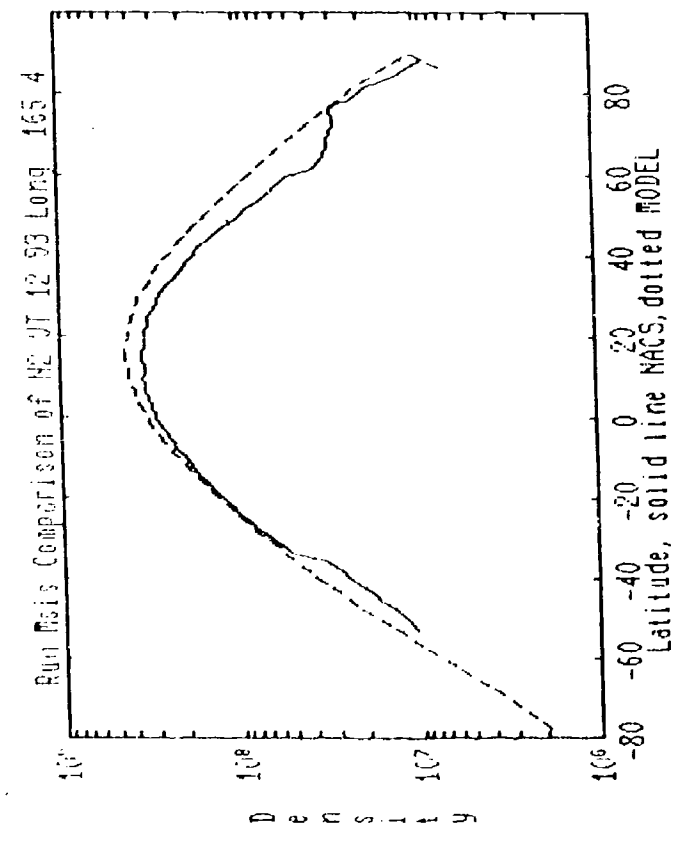
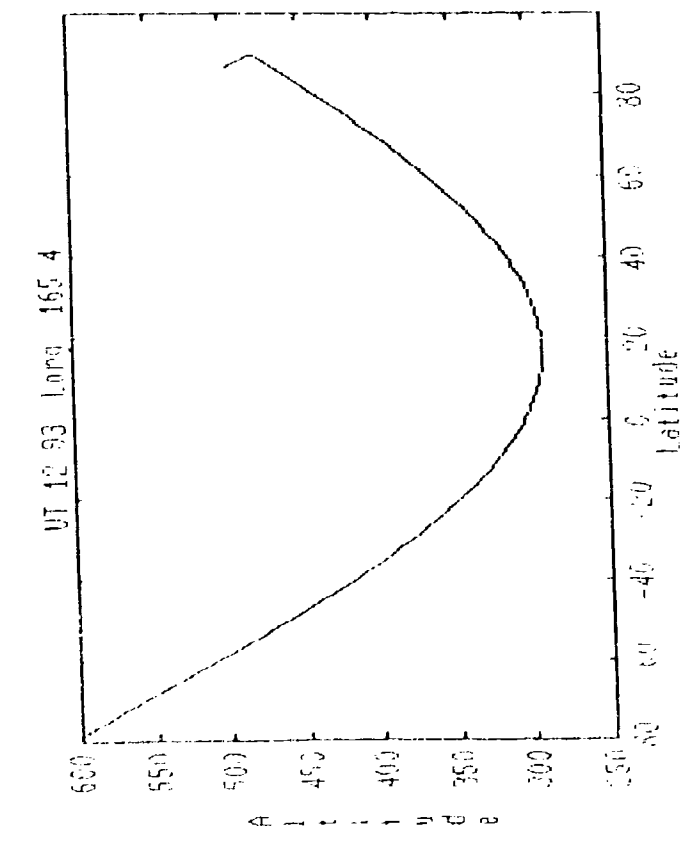
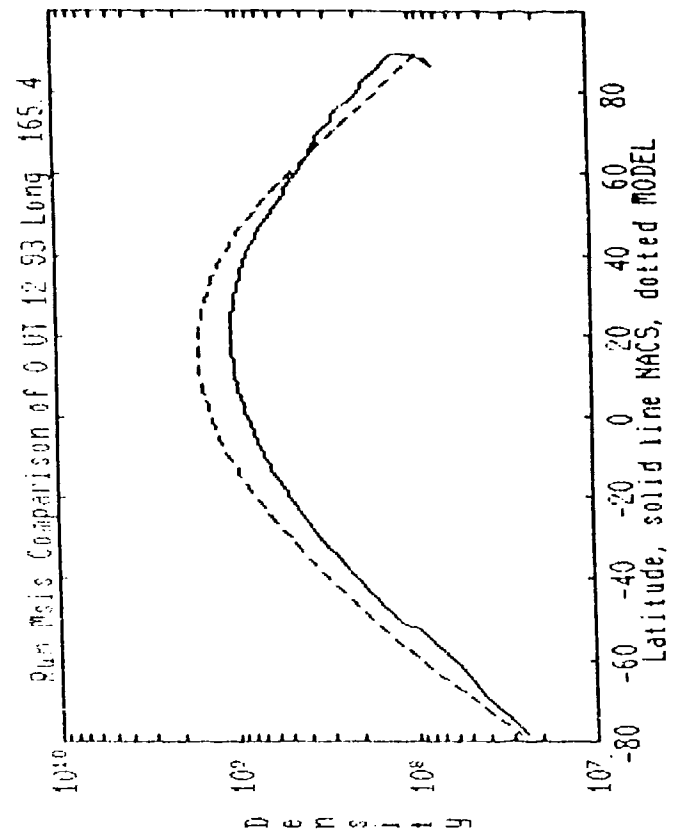
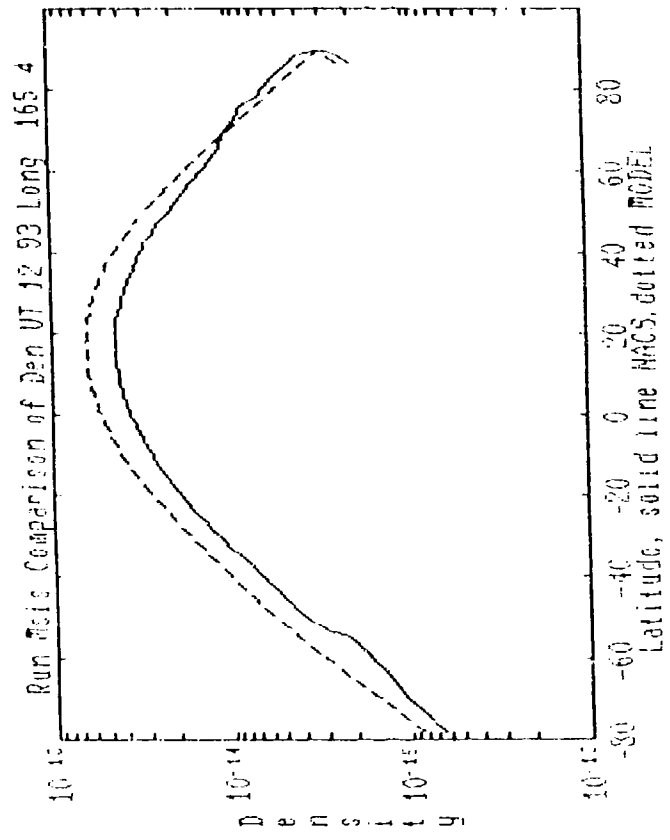


Figure 26

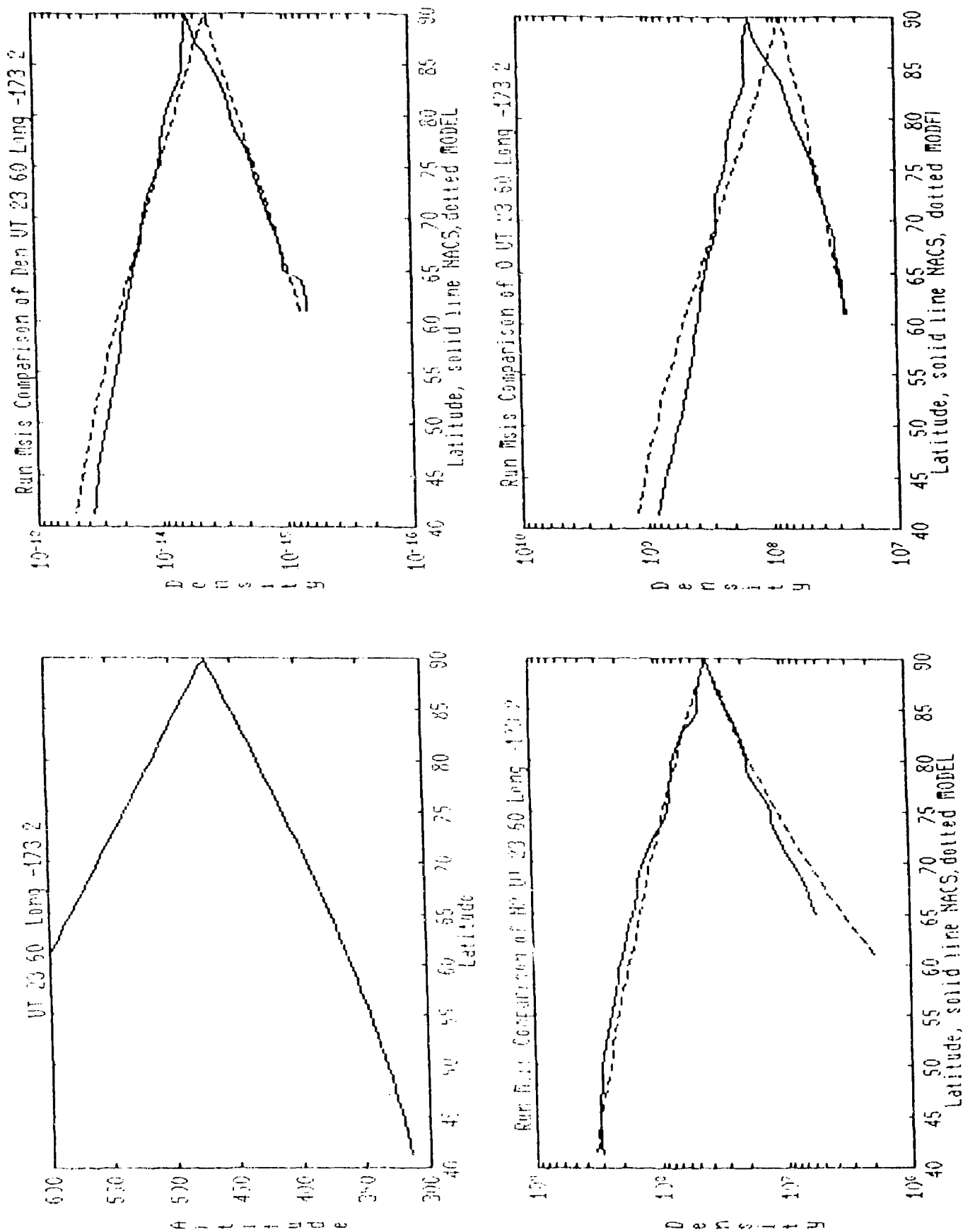
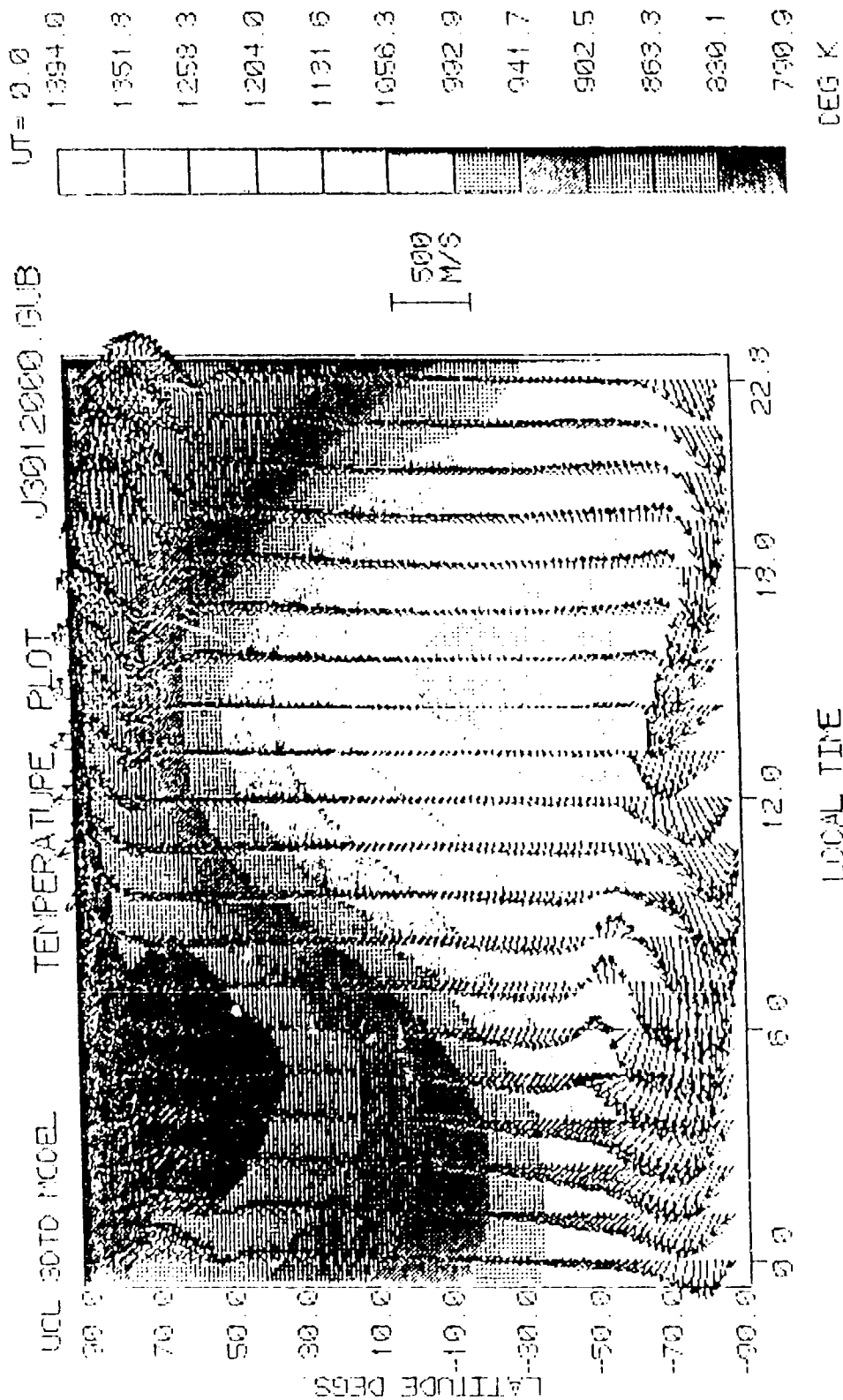
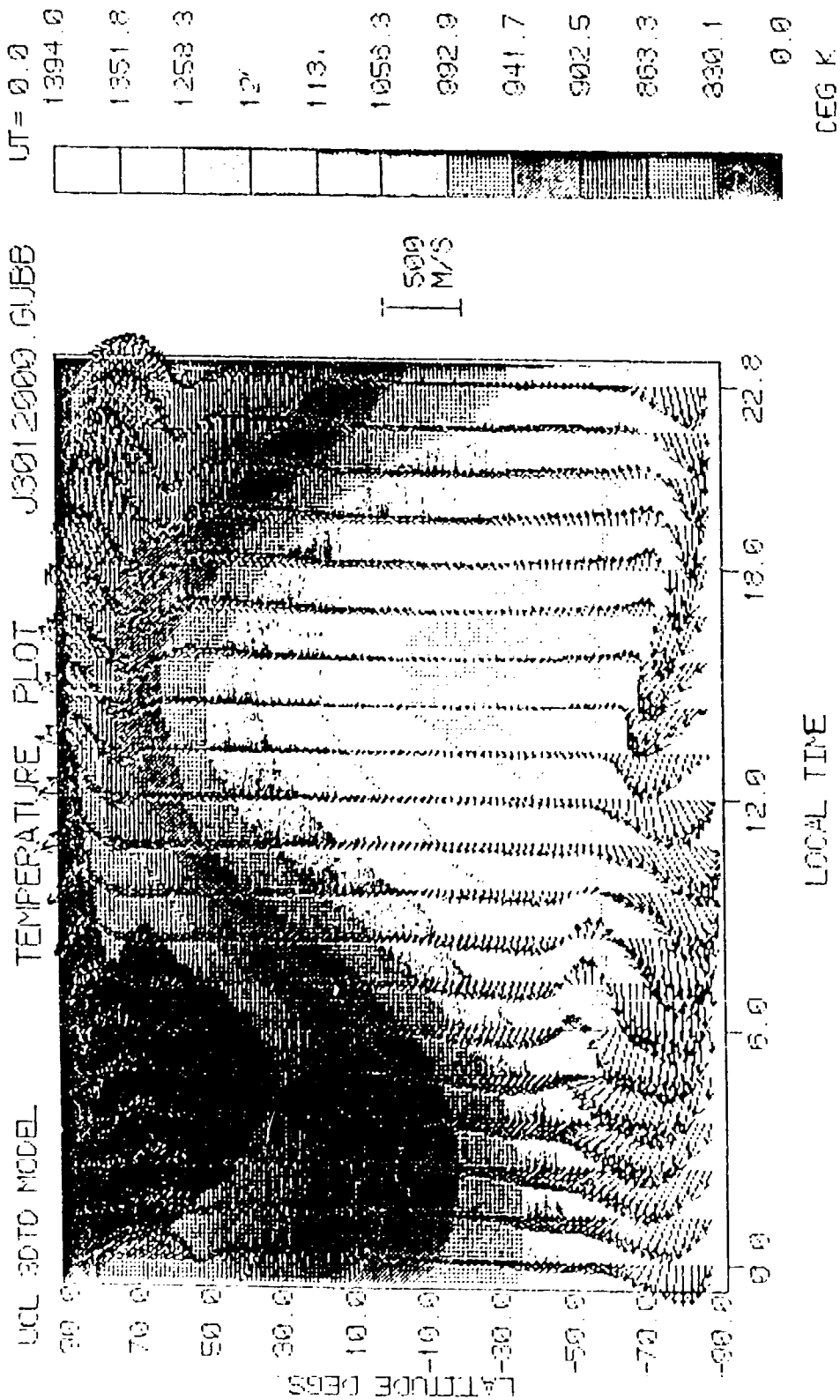


Figure 27



Elec Fld A2-32
 Elec Chans CHIU CIPA
 Date DEC 21 F10 7am 185

Figure 28

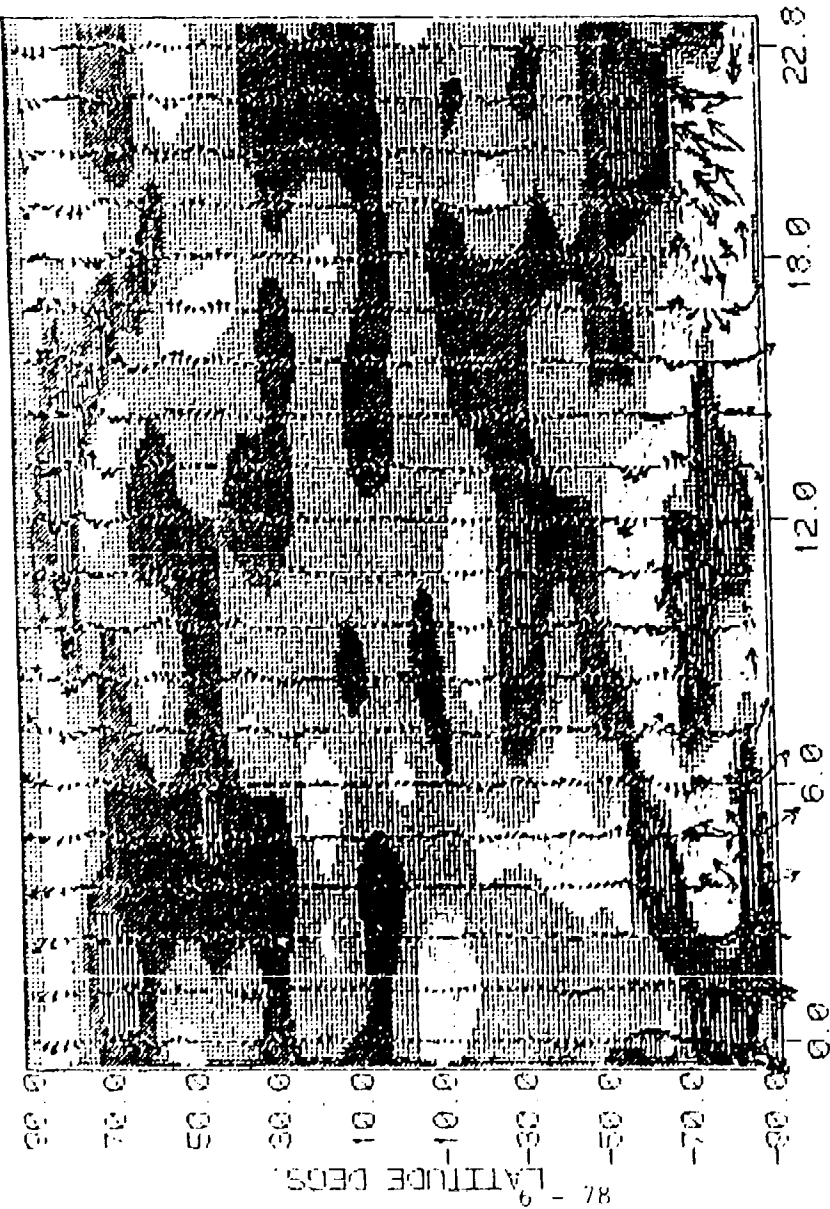


Elec F1d: A2-A2
Elec Cens CHIU CIPA
Date DEC 21 F10.7cm 185 150% REDUCTION

Figure 29

TEMPERATURE PLOT

UCL 30TD MODEL



LOCAL TIME

J3912569.6UB
Elec: F1d: A2-42
Elec: Date: CHDU
Date: DEC 21 F10 7am 185
CIRA

COMPARISON: Diff.

J3912300.6UB8
Elec: F1d: A2-42
Elec: Date: CHDU
Date: DEC 21 F10 7am 185
CIRA

Figure 30

6.3 DEVELOPING AN OPERATIONAL VERSION OF
THERMOSPHERE GENERAL CIRCULATION MODELS

T. L. KILLEEN¹, R.G. ROBLE²,

and

N. W. SPENCER³

¹Space Physics Research Laboratory
The University of Michigan
Ann Arbor, Michigan 48109

²High Altitude Observatory
National Center for Atmospheric Research *
Boulder, CO 80307

³Goddard Space Flight Center, Greenbelt, Maryland 20771

* The National Center for Atmospheric Research is sponsored
by the National Science Foundation.

ABSTRACT

A computer model of the global, time-dependent, thermospheric horizontal vector neutral wind and neutral temperature fields has been constructed based on output from the NCAR thermospheric general circulation model (NCAR-TGCM). The wind field is represented by a vector spherical harmonic (VSH) expansion in the horizontal, a Fourier expansion in Universal Time, and a polynomial expansion in altitude. The global temperature field representation differs in that a scalar spherical harmonic expansion is used in the horizontal and a Bates model temperature profile is used in altitude. A set of suitably-truncated spectral coefficients contains the wind and temperature description for a diurnally-reproducible run of the NCAR-TGCM. The VSH model is coded in a FORTRAN subroutine that returns vector wind and temperature values for a given UT, geographic location, and altitude. The model has applicability for studies of thermospheric and/or ionospheric physics where reasonable time-dependent neutral wind and temperature values are of interest. The routine is novel since portable computer models of thermospheric wind fields have not previously been available to researchers. The current version of the model is valid for solar maximum, December solstice only, although the model can be extended to any season and specific set of geophysical conditions for which TGCM results are available. Results from the VSH computer model are presented to compare with global-scale wind measurements from the Dynamics Explorer (DE-2) satellite. The agreement between the computer model results and data from individual orbits of DE-2 is good, indicating that the model provides reasonable wind values, having the appropriate characteristic latitudinal, diurnal, and Universal-Time-dependent signatures observed from the satellite at upper thermospheric altitudes. The VSH thermospheric temperature values are in general agreement with MSIS-83 temperatures but illustrate smaller-scale horizontal temperature structures than are resolved by MSIS-83, owing to the larger number of spectral harmonics retained.

1. INTRODUCTION

Significant progress has been made over the last several years in the modeling and empirical description of the global thermospheric neutral wind and temperature system. The Dynamics Explorer (DE 2) spacecraft, in particular, was instrumented to measure the thermospheric vector wind and temperature along the track of the polar-orbiting spacecraft (Hays et al., 1981; Spencer et al., 1981; Killeen et al., 1982). Published results from this mission have served to characterize the global-scale thermospheric wind field for the solar maximum conditions pertaining to the 1981-1983 period (Killeen et al., 1982, 1984a, b, 1986; Spencer et al., 1982; Wharton et al., 1984; Hays et al., 1984). In addition to the new information provided by the DE 2 spacecraft and other experimental techniques, the theoretical understanding of thermospheric motions has progressed rapidly. Various theoretical models exist that can simulate the dynamical response of the upper atmosphere for a variety of geophysical conditions. In particular, two numerical general circulation models, the NCAR-TGCM (Dickinson et al., 1981; Roble et al., 1982) and the UCL-TGCM (Fuller-Rowell and Rees, 1980) have had a large measure of success in calculating wind and temperature fields similar to those observed from DE 2 (Roble et al., 1983, 1984; Rees et al., 1983, 1985, 1986; Hays et al., 1984; Killeen et al., 1986). The spectral model of Mayr et al., (1985a, b) has also provided significant additional insight into global-scale thermospheric dynamics.

In spite of these recent theoretical modeling efforts, no simple "user-friendly" computer model of the global thermospheric wind field has been previously constructed to enable neutral winds to be conveniently used in other theoretical studies or in straightforward comparisons with new data sets. The underlying reasons for this situation involve the sophistication and complexity of the TGCMs and the large physical size of the data arrays necessary to contain the numerically-simulated wind fields. Moreover, the fragmentary nature of the global-scale wind measurements collated to date from all experimental sources has postponed the construction of a purely empirical model. For

thermospheric temperatures, the situation is better in that semi-empirical models, such as the MSIS-83 model of Hedin (1983), have, for many years, provided researchers with reliable values for thermospheric temperatures, incorporating explicit dependences on geomagnetic activity, solar activity, and season.

The purpose of this report is to describe a new computer model of the global, horizontal, thermospheric vector wind and neutral temperature structure from 130 to 600km altitude. We call it the VSH model, since it contains a description of the wind field using vector spherical harmonics. The new model is based on a spectral expansion of the gridded output wind and temperature fields provided by specific runs of the NCAR-TGCM. As such, the physical description provided by the VSH model is determined by the physical, chemical and dynamical processes contained within the NCAR-TGCM structure. The VSH model formulation does not, as yet, include an explicit dependence on season, solar cycle or geomagnetic activity level. It does, however, allow for such effects to be catered for through generation of separate sets of VSH model coefficients, each of which describes specified geophysical conditions and shares a common retrieval subroutine.

The VSH model is coded in a FORTRAN subroutine that returns vector wind and temperature values for a given UT, geographic location, and altitude. It, therefore, has applicability for many studies of thermospheric and/or ionospheric physics where reasonable, UT-dependent neutral wind profiles or single-point values are of interest. We note that portable computer models of thermospheric wind fields have not previously been available to researchers. The VSH model temperature values are of interest for two reasons. Firstly, they enable the temperature predictions of the NCAR-TGCM to be made generally available for comparison with measurements and semi-empirical models. Secondly, since the number of spectral coefficients retained in the VSH representation is large compared with MSIS-83 and other semi-empirical models, the VSH temperature fields contain localized temperature structures, such as cusp temperature enhancements, that are commonly filtered out of the semi-empirical models. This last

feature, of course, comes at the expense of computer time (see below).

The current version of the VSH model is valid for solar maximum, December solstice conditions only, although the model can be extended to any season and any set of geophysical conditions for which TGCM results are available. The formulation of the VSH model has been designed to allow for experimental data to be included in the fitting procedure, enabling the future development of a semi-empirical model of thermospheric winds through the suitable merging of experimental measurements with the TGCM gridded predictions.

In section 2, we describe the formulation of the new computer model. In section 3, we present results from the model for a solar maximum, December solstice case corresponding to moderately active geomagnetic conditions, and compare these with 1) global-scale wind measurements from the DE 2 spacecraft and 2) temperature profiles from the MSIS-83 semi-empirical model. In section 4 we summarize our results and discuss the utility of the VSH model and future planned developments.

2. VSH MODEL FORMULATION

The basis for the VSH model is a spectral expansion of output from the NCAR-TGCM. The expansion is performed as part of the TGCM diagnostic package described by Killeen and Roble (1984). We briefly discuss the TGCM and the specific output used in the present work before describing the formulation of the VSH model.

The NCAR-TGCM has been discussed in detail in a series of papers (Dickinson et al., 1981, 1984; Roble et al., 1982, 1983) and here we review only the basic features. The TGCM solves the hydrodynamic, thermodynamic and continuity equations appropriate to the Earth's thermosphere for a given set of geophysical, time-dependent input conditions and stores the calculated wind, temperature and composition (mass mixing ratio) output fields at selected Universal Times (UTs) during the model run. The model has a 5° latitude-by-longitude grid with 24 constant-pressure surfaces in the vertical, extending from approximately 97 to 500 km in altitude. The version of the TGCM used in this work

incorporates the coupling of dynamics and composition (Dickinson et al., 1984), and calculates the solar heating distribution and O_2 photodissociation rates using the procedure described by Dickinson et al. (1981, 1984). The Hinteregger (1981) solar EUV flux values and the Torr et al. (1980) solar UV flux values are used to provide the direct solar input corresponding to the geophysical conditions appropriate to the particular model run. The ion-convection model of Heelis et al. (1982) is used for the specification of high-latitude ion drifts. For the examples discussed here, the Heelis et al. model input parameters were chosen to yield a Volland-type symmetric ion-convection geometry. The Chui (1975) model of ionospheric densities is supplemented by auroral particles according to the prescription of Roble et al. (1986) to provide the ion-drag tensor values necessary for the calculation of both the ion-drag momentum source and the Joule heat source to the thermosphere. The auroral oval used is similar to the statistical patterns described by Spiro et al. (1982) and Whalen (1983). The TGCM run used to construct the present VSH computer model has been employed previously in several theoretical studies and for comparisons with DE-2 data (Hays et al., 1984; Killeen et al., 1986; Killeen and Roble 1984, 1986). It is, therefore, well documented and we refer readers to these papers for more detailed information.

The TGCM diagnostic processor (Killeen and Roble, 1984) is exercised following the basic TGCM model run. It reads in the history file produced by the TGCM as well as other relevant input parameters and then proceeds to calculate diagnostic information at selected model grid points and UTs. The spectral analysis capability of the diagnostic package, to be described in more detail in a forthcoming paper, is used to provide the coefficients for the VSH model (see below). The history file contains records of the global wind, temperature and composition fields calculated by the TGCM at each hour of UT for the 24 hour simulation. Geophysical conditions corresponding to December solstice, solar maximum, and moderately active geomagnetic conditions ($K_p \sim 3$) were used for the specific TGCM run that has provided the coefficients for the first version of the VSH

model, presented here. The TGCM was run until diurnal-reproducibility was attained, i.e., "steady-state", diurnally-modulated forcings were used.

For the purpose of the horizontal wind expansion, the gridded vector wind predictions at each of 24 UTs and at each of three constant-pressure levels ($z=-4$, corresponding to $\sim 130\text{km}$ altitude; $z=-1$, corresponding to $\sim 250\text{km}$; $z=1$, corresponding to $\sim 400\text{km}$) are expanded using vector spherical harmonic functions which are the appropriate eigen-functions for vector fields on the sphere. This expansion has the following form:

$$V = \sum (a_{m,n} \mathbf{P}_{m,n} + b_{m,n} \mathbf{B}_{m,n} + c_{m,n} \mathbf{C}_{m,n}) \quad (1)$$

where V is the vector wind field and $a_{m,n}$, $b_{m,n}$, $c_{m,n}$ are the complex vector spherical harmonic coefficients; m is the zonal harmonic (order) and n is the degree. Here,

$$\begin{aligned} \mathbf{P}_{m,n} &= \begin{bmatrix} P_n^m \\ 0 \\ 0 \end{bmatrix} e^{im\phi}; \\ \mathbf{B}_{m,n} &= \begin{bmatrix} 0 \\ A_n^m \\ iB_n^m \end{bmatrix} \frac{e^{im\phi}}{\sqrt{n(n+1)}}; \\ \mathbf{C}_{m,n} &= \begin{bmatrix} 0 \\ iB_n^m \\ -A_n^m \end{bmatrix} \frac{e^{im\phi}}{\sqrt{n(n+1)}}. \end{aligned} \quad (2)$$

where ϕ is east longitude, and A_n^m and B_n^m are functions of θ (colatitude) only:

$$A_n^m = \frac{dP_n^m}{d\theta}$$

$$B_n^m = \frac{m}{\sin\theta} P_n^m$$

(3)

P_n^m are the associated Legendre functions given by

$$P_n^m(\theta) = \frac{1}{2^n n!} (\sin\theta)^m \frac{d^{(m+n)}}{dx^{m+n}} (x^2 - 1)^n; \quad x = \cos\theta.$$

(4)

The complex coefficients are obtained using a least-squares fit of the TGCM output winds to the above formula. Conversely, once the coefficients are available, the global wind field can be readily reconstituted in whole or in part, using equation 1. Since the resolution of the TGCM grid is 5 degrees, only those coefficients for which $0 < n < 37$ and $0 < m < n$ are of significance. We note that equation 1 is an expression for the full vector wind, including the radial (vertical) component involving $P_{m,n}$. While the two horizontal wind components are coupled via the functions A_n^m and B_n^m , the vertical component is uncoupled and, therefore, can be simply expressed in terms of a (scalar) spherical harmonic expansion involving the associated Legendre functions. Since the vertical winds calculated by the TGCM are small in magnitude and, for some applications, not of particular interest, we (optionally) substitute for the vertical wind a scalar field such as temperature or mass mixing ratio and use the coefficients $a_{m,n}$ to describe the selected scalar field conveniently within our three-dimensional vector spherical harmonic representation. For the present VSH model, we choose to fit for neutral temperature to provide a direct comparison with the MSIS-83 model. The complete array of coefficients for the fit represents a large set of numbers, commensurate in size to the history file record of winds and temperatures itself. Thus, the desired reduction in the size of the set of numbers describing the output TGCM fields can only be attained by truncating the coefficients. Such truncation, of course,

tends to destroy progressively the fidelity with which the wind fields can be reconstituted, and must be carried out carefully to ensure that important morphological features in the thermospheric wind pattern are not lost unwittingly.

Figure 1 presents contours of the log (base 10) amplitude for the VSH coefficients (real and imaginary) calculated for the spectral expansion of horizontal winds on the $z=1$ and $z=-4$ constant pressure surfaces at 1200UT. As mentioned above, the specific TGCM run was chosen since it corresponds to the geophysical conditions for which much of the DE 2 data applies. In the figure, the bottom right triangular section is unfilled since only coefficients with $0 < m < n$ are non-zero. As can be seen, the amplitude and, therefore, the power in the expansion is a maximum at the lower wavenumbers. The amplitudes tend to diminish in magnitude with increasing wavenumber, as would be expected, though the amplitude drops much more rapidly with increasing m than with increasing n . The amplitudes for the $z=-4$ surface are smaller in magnitude than for the $z=1$ surface since the wind speeds are generally much reduced at the lower altitudes (e.g., Robie et al., 1982). The shape of the contours shown in figure 1 provides the key to the design of a suitable truncation scheme to reduce the mass of numbers required for the spectral representation of the thermospheric wind field.

In setting the level of truncation for the VSH model we used the stringent criterion that the high-latitude reversals and vortices in the neutral wind pattern associated with ionospheric convection should be retained. It was found that a rectangular truncation scheme in n - m space gave excellent results in terms of the fidelity of the reconstituted high-latitude wind field for the minimum number of coefficients. Three levels of truncation are indicated in Figure 1a. Level A corresponds to the number of harmonics commonly retained for semi-empirical models (e.g., MSIS-83) employing scalar spherical harmonics. Level C (i.e. truncating the coefficients at $n=30$, $m=9$) was found to provide almost perfect fidelity for the neutral wind reconstitution. For the VSH model, we employ truncation at level B ($n=25$, $m=5$), which represents a good compromise between

minimising the size of the retained coefficient array (and therefore the computational time for wind syntheses) and keeping the required high-latitude wind structure. Note that the empirically-optimised truncation scheme favored higher values of n over m . This is due to the relatively large amplitudes of the fitted coefficients for large n , small m : these particular coefficients contain the information necessary to describe the relatively small-scale high-latitude neutral wind structure.

The VSH expansion, discussed above, is only for a single constant-pressure level and for a given UT. To extend the expansion to include the temporal evolution of the wind field over the 24 hour diurnal TCCM simulation, we repeat the vector spherical harmonic expansion for all 24 hourly history file records and then perform a conventional complex fourier time series fit to the individual VSH coefficients. We have found that the fourier coefficients so obtained may be truncated such that only seven (including odd and even fourier coefficients) need to be stored to describe the diurnal variation of the "steady-state" neutral wind field reasonably well, incorporating the well-known "UT effects" associated with the diurnal revolution of the geomagnetic pole about the geographic pole. Clearly, for a situation where the thermosphere is disturbed, such as during a geomagnetic storm, additional fourier coefficients would be required to describe the more complex time-dependences. The fourier series truncation used here, however, is adequate for the diurnally-reproducible case. The final part of the expansion deals with the altitudinal structure of the winds and temperatures. Since the variation in altitude of the neutral thermospheric horizontal wind predicted by the NCAR-TCCM is relatively smooth (see, for example, figure 12 of Sica et al., 1986), we complete the wind expansion by fitting the fourier time series coefficients to a simple, second order polynomial in altitude. The conversion from constant-pressure levels to altitudes is made using the calculated global averages for the heights of the specific constant-pressure levels carried forward to the VSH model. This conversion introduces small inconsistencies between the TCCM and VSH wind predictions that are not considered to be of importance for the stated purposes of the

present work. In the case of the wind altitudinal variation, an additional constraint is placed on the VSH altitude profile to force the individual wind component values to reach constant (i.e., exospheric) values above $\sim 400\text{km}$. This constraint is justified, on theoretical grounds, by the high kinematic viscosity of the atmosphere at these heights (which tends to reduce vertical wind shears) and, on experimental grounds, by the DE 2 data which show little altitudinal structure above $\sim 400\text{km}$.

For temperatures, we replace the polynomial altitude expansion with a two-parameter fit to a Bates model profile (Bates, 19xx; Walker 197x), having the appropriate monotonic form, with the asymptotic (exospheric) temperature and scale-height parameter given by the fit.

The three expansions, namely, the VSH expansion in the horizontal (including the scalar spherical harmonic expansion for temperature), the fourier series in time, and the polynomial (or Bates profile) expansion in altitude, complete the full description of the TGCM wind and temperature simulations. The full set of numbers containing this description at the maximum accuracy would comprise an array of dimensions $37 \times 18 \times 6 \times 25 \times 24$, corresponding to, respectively, the order (n), the degree (m), the components of the complex coefficients (a , b , and c), the fourier time series, and the altitude polynomial. With the truncation levels discussed above, we reduce the coefficient array size to the dimensions $25 \times 5 \times 6 \times 7 \times 3$. Thus a total of 15750 coefficients are stored for the VSH model. We consider this to be close to the minimum number required to describe the full diurnal, spatial and altitudinal variation of the thermospheric vector neutral wind and temperature fields using spherical harmonics while retaining the important high-latitude wind structures (vortices and reversals) observed from DE 2. It might be possible in the future to further reduce the size of the required coefficient array by choosing a different set of orthonormal functions for the expansion, optimised to provide high spatial frequencies at high latitudes (A. D. Richmond, 1985, private communication).

The VSH model consists of the stored set of coefficients occupying approximately

300 blocks of disk space on a VAX or PDP-type computer), plus a subroutine designed to reconstitute the vector wind and temperature values at any given geographic location, altitude and time. The subroutine performs the inverse set of transformations to those that provided the coefficients, recovering, successively, the temporal, spatial, and altitudinal information to return geophysical winds and temperatures. The computer time necessary for this "synthesis" of model predictions is significantly longer than for similar calculations using MSIS-83, due to the much larger number of calculations necessary. We have found that full global 5 degree x 5 degree wind and temperature fields can be calculated using the VSH model within a few minutes CPU time on a VAX 750 machine. Much shorter computer times, however, are required to calculate, for example, the diurnal variation of the neutral winds over a given ground-based observatory. For most applications, computer time can be reduced considerably by using the most efficient nesting of DO loop calls to the subroutine.

In the next section we present various results from the VSH model to illustrate its current capabilities. The VAX FORTRAN subroutine and documentation necessary for its use can be obtained from one of the authors (TLK).

3. EXAMPLES OF RESULTS FROM THE VSH MODEL.

As mentioned earlier, the present version of the VSH model was designed to correspond with much of the DE 2 data base. In figures 2a (b), we show north (south) polar projections illustrating VSH model vector winds (in cyan) calculated for an altitude of 400km at the appropriate Universal Time corresponding to orbit 1819 (7438) of DE 2. The VSH winds are overlaid with the measured vector wind measurements from DE 2 (in yellow) made at altitudes of ~400km by the Fabry-Perot interferometer, FPI, (Hays et al., 1981) and the Wind and Temperature Spectrometer, WATS, (Spencer et al., 1981). The DE 2 vector winds are generated from the measurements of these two instruments using the data-merging technique of Killeen et al., (1982). The DE 2 data shown were selected on the basis of the moderate-to-active levels of geomagnetic activity existing at the time of the orbital passes (see Kp values indicated). In both northern and southern cases, excellent qualitative agreement between the VSH model winds and the DE 2 measurements is evident, with the UT-dependent locations of the various high-latitude morphological wind features well described by the model. While exact agreement between individual DE 2 measurements and VSH model values is not obtained, nor expected, the VSH winds clearly provide reasonable results that are directly comparable with the observations, both in magnitude and direction. They are also useful in providing a hemispheric context for the interpretation of the DE 2 measurements.

The results shown in Figure 2 indicate that the various high-latitude features built into the NCAR-TGCM, such as the differing offsets between geographic and geomagnetic poles in the two hemispheres and the dominating influence on the neutral wind pattern of ion drag associated with the twin vortex ionospheric convection, are reflected in the VSH computer model. It is, of course, these high-latitude features that determine the VSH coefficient truncation criteria discussed above.

To provide a more fully global perspective of the VSH model winds, we show in Figure 3 a cartesian plot of global vector winds calculated using the VSH subroutine at the

400km altitude level. Also shown for comparison are the DE 2 vector wind measurements made between altitudes of $\sim 350 - 500$ km during orbit number 7431. The measured vector winds again illustrate reasonable qualitative agreement with the VSH model calculations in all regions, including the mid-latitude, high-latitude and equatorial regions. In general, for this orbit, the measured high-latitude winds were larger in magnitude than the VSH model values, although the reversal boundaries and the locations of the main morphological structures are in good agreement. Once again, our conclusion is that the VSH winds provide reasonable values (at least at upper thermospheric altitudes) that compare well with DE 2 global-scale measurements made during moderately-active geomagnetic conditions.

A third example of VSH wind comparisons with DE 2 data is shown in Figure 4. Here, we plot averaged zonal wind measurements made using the WATS instrument during 1981 and 1982 for measurements taken within 5° latitude of the geographic equator. These results are taken from the paper of Wharton et al. (1984) and depict the average of many orbits of data. The VSH wind results are shown by the solid line together with a low-order fourier fit to the data made by Herrero et al. (1986). It can be seen that the VSH zonal winds provide a good first-order fit to the averaged WATS data at all local times, with a small phase lead.

As a further example of the utility of the VSH model, we show in Figures 5 and 6 the VSH model calculations for (a) zonal wind, (b) meridional wind and (c) temperature, calculated as a function of UT and altitude over locations at the geographic equator (Figure 5) and at Svalbard, Norway, (78.2°N , 15.6°W) (Figure 6). Also shown for comparison in these figures are (d) the MSIS-83 temperatures for the same solar maximum, December solstice conditions. These figures serve to illustrate the altitude structure given by the computer model for a low-latitude location and a high-latitude location. It can be seen that the altitude variations of the VSH wind and temperature results have the required asymptotic form. There are, unfortunately, no global-scale measurements of lower

thermosphere winds available with which to compare the results at altitudes less than ~ 250 km and the validity of the VSH model here is, therefore, linked solely to the confidence placed in the the parent NCAR-TGCM calculations. Since the NCAR-TGCM solves the full set of "primitive equations" for thermospheric dynamics and since it has proved remarkably successful in the experimental tests at upper thermospheric altitudes, we believe that the VSH model provides valuable estimates for the entire altitude profile of thermospheric winds.

The comparisons between MSIS-83 and VSH model temperatures, shown in Figures 5c and d and 6c and d, are of interest since they point out the major difference between the two model profiles. For the equatorial location shown in Figure 5, the MSIS-83 and VSH temperature profiles are in excellent agreement, as would be expected since MSIS-83 provides the background model input atmosphere for the initial "spin-up" of the NCAR-TGCM. There are, however, appreciable differences evident between the VSH temperature contours and the corresponding MSIS-83 profiles at the high-latitude Svalbard location, shown in Figure 6c and d. The reason for the apparent discrepancy here is related to two factors, (1) the different number of spectral harmonics used in the MSIS-83 and VSH representations, and (2) the high-latitude heat source due to soft particle precipitation in the dayside cusp region employed in the NCAR-TGCM. MSIS-83 uses relatively few spherical harmonics and is, therefore, limited in the extent to which it can model local structures in the temperature field. The VSH model, on the other hand, uses ~ 3 times as many harmonics for the synthesis of its temperature field and is thereby able to model relatively smaller-scale features. The basic difference between the shapes of the MSIS-83 and VSH temperature contours in Figure 6 is due to the passage of the Svalbard location through the dayside cusp region near 0500-0900 hours UT. The NCAR-TGCM employs a high-altitude soft particle heat source in this region as discussed by Reble et al., (1984), leading to a significant local high-altitude temperature enhancement. The VSH model reflects this modeled dayside cusp high altitude heating, while the MSIS-83 model does not

show the feature.

We conclude that the VSH model, by virtue of the relatively large number of harmonics retained in order to model the high-latitude wind structure, is capable of modeling local temperature features that are filtered out from models that use fewer harmonics. It remains an open experimental question whether features such as the cusp temperature enhancement illustrated in Figure 6 (see also Figure xx of Roble et al., 198xx), are indeed present in spacecraft data sets.

3. DISCUSSION AND SUMMARY.

A computer model of the thermospheric wind and temperature fields, based on output from the NCAR-TGCM, has been constructed using a vector spherical harmonic expansion technique. The model is coded in a portable FORTRAN subroutine that reads in a set of coefficients containing the diurnal, altitudinal and spatial information necessary to synthesize the global wind and temperature fields. The current version of the model is valid for solar maximum, December solstice conditions. It has applicability for users who require reasonable values of neutral winds and temperatures in theoretical or comparative experimental studies. Comparisons with DE 2 observations have been used to illustrate the validity of the wind results at upper thermospheric altitudes.

The model framework can be extended to incorporate seasonal, solar cyclical and geomagnetic activity dependencies simply by running the NCAR-TGCM for specified geophysical conditions and calculating a set of spectral coefficient arrays. We plan to create a family of coefficient arrays in this manner that will provide reasonable wind and temperature results for a systematic ranges of conditions (solstice, equinox, solar minimum, active, moderate, quiet, disturbed, etc.) The retrieval subroutine will be common to these coefficient arrays. We also plan to use the VSH model framework to develop a semi-empirical model of thermospheric winds by appropriately merging observational data from DE 2 with the TGCM gridded calculations prior to performing the vector spherical harmonic expansion described in this paper. This work is underway.

ACKNOWLEDGEMENTS

We acknowledge support from NSF grant number ATM-8412828 and NASA grant number NAG5-465 to the University of Michigan. This work was partially performed when one of the authors (TLK) was a visiting scientist at the High Altitude Observatory of the National Center for Atmospheric Research. Support from the Observatory is gratefully acknowledged. The authors are particularly grateful to Dr. P. Swartztrauber of NCAR for invaluable assistance with the vector spherical harmonic expansion and to Drs. H. G. Mayr, A. E. Hedin, R. E. Dickinson and A. D. Richmond for generously-given advice and

consultations.

FIGURE CAPTIONS

- Fig. 1. Contours of the logarithmic amplitude (base 10) for the vector spherical harmonic coefficients calculated by fitting the global thermospheric wind field calculated by the NCAR-TGCM are plotted as a function of degree and order for the geophysical conditions discussed in the text and for 1200UT. Figure 1a is for the $z=1$ constant-pressure surface and figure 1b for the $z=-4$ constant-pressure surface. Shown in Figure 1a are three regions illustrating various levels of truncation: level B is used for the VSH model.
- Fig. 2. Polar projections (solar local time and geographic latitude from pole to 40 degrees) illustrating the VSH model wind field (cyan arrows) for a) the Northern high-latitude region and b) the southern high-latitude region. The VSH wind vectors were calculated, in each case, at 400km and for the UT appropriate to the DE 2 observations shown in yellow. The solar terminator is given by the curved blue line. Dotted yellow arrows indicate sections of the DE 2 pass for which there were no FPI (meridional) wind measurements available. The wind scale is shown at lower right.
- Fig. 3. Cartesian plot (geographic latitude and local solar time), illustrating the VSH global vector wind field at 400km (cyan arrows). Also shown for comparison are the observed vector winds (in yellow) from orbit 7431 of DE 2. The wind scale is to lower right and the curved red line represents the solar terminator.
- Fig. 4. Averaged equatorial zonal wind measurements from the WATS instrument on DE 2 taken from the paper by Wharton et al., (1984). The results are plotted as a function of local solar time and correspond to data taken within $\pm 5^\circ$ degrees latitude of the equator.
- Fig. 5. Contour plots illustrating the altitudinal and UT-dependent variation of (a) the zonal wind, (b) the meridional wind, and (c) the temperature from the VSH model for calculations made at a location on the equator (latitude 0.0, longitude 0.0). Also shown (d) are results from the MSIS-83 model for solar maximum December solstice conditions.
- Fig. 6. Same as for Figure 5 except for the location at Svalbard, Norway (78.2 latitude, 15.6 longitude).

REFERENCES

Bates

- Chiu, Y. T., An improved phenomenological model of ionospheric density, J. Atmos. Terr. Phys., 37, 1563-1570, 1975.
- Dickinson, R. E., E. C. Ridley, and R. G. Roble, A three-dimensional general circulation model of the thermosphere, J. Geophys. Res., 86, 1499-1512, 1981.
- Dickinson, R. E., E. C. Ridley and R. G. Roble, Thermospheric general circulation with coupled dynamics and composition, J. Atmos. Sci., 41, 205-219, 1984.
- Fuller-Rowell, T. J., and D. Rees, A three dimensional time dependent global model of the thermosphere, J. Atmos. Sci., 37, 2545-2567, 1980.
- Hays, P. B., T. L. Killeen, and B. C. Kennedy, The Fabry-Perot interferometer on Dynamics Explorer, Space Sci. Instrum., 5, 395-416, 1981.
- Hays, P. B., T. L. Killeen, N. W. Spencer, L. E. Wharton, R. G. Roble, B. E. Emery, T. J. Fuller-Rowell, D. Rees, L. A. Frank, and J. D. Craven, Observations of the dynamics of the polar thermosphere, J. Geophys. Res., 89, 5597, 1984.
- Heelis, R. A., J. K. Lowell, and W. T. Kasprzak, A model of the high-latitude ionospheric convection pattern, J. Geophys. Res., 87, 6339-6345, 1982.
- Hedin, A. E., A revised thermospheric model based on mass spectrometer and incoherent scatter data: MSIS-83, J. Geophys. Res., 88, 73-83, 10170-10188, 1983.
- Herrero et al., Geophys. Res. Lett., 1986.
- Hinteregger, H. E., Representations of solar EUV fluxes for aeronomical purposes, Adv. Space Res., 86, 801-813, 1981.
- Killeen, T. L., and R. G. Roble, An analysis of the high latitude thermospheric wind pattern calculated by a thermospheric general circulation model, 1. Momentum forcing, J. Geophys. Res., 89, 7509-7522, 1984.
- Killeen, T. L., P. B. Hays, N. W. Spencer, and L. E. Wharton, Neutral winds in the polar thermosphere as measured from Dynamics Explorer, Geophys. Res. Lett., 9, 957-960, 1982.
- Killeen, T. L., P. B. Hays, G. R. Carignan, R. A. Heelis, W. B. Hanson, N. W. Spencer, and L. H. Brace, Ion-neutral coupling in the high-latitude F-region: Evaluation of ion heating terms from Dynamics Explorer 2, J. Geophys. Res., 89, 7495-7508, 1984a.
- Killeen, T. L., R. W. Smith, P. B. Hays, N. W. Spencer, L. E. Wharton, and F. G. McCormac, Neutral winds in the high latitude winter F-region: Coordinated observations from ground and space, Geophys. Res. Lett., 11, 311-314, 1984b.

- Killeen, T. L., R. G. Roble, R. W. Smith, N. W. Spencer, J. W. Meriwether, D. Rees, G. Hernandez, P. B. Hays, L. L. Cogger, D. P. Sipler, M. A. Biondi, and C. A. Tepley, Mean neutral circulation in the winter polar F-region, J. Geophys. Res., 91, 1633-1649, 1986.
- Rees, D., T. J. Fuller-Rowell, R. Gordon, T. L. Killeen, P. B. Hays, L. E. Wharton, and N. W. Spencer, A comparison of wind observations of the upper thermosphere from the Dynamics Explorer satellite with the predictions of a global time-dependent model, Planet. Space Sci., 31, 1299-1314, 1983.
- Rees, D., R. Gordon, T. J. Fuller-Rowell, M. Smith, G. R. Carignan, T. L. Killeen, P. B. Hays, and N. W. Spencer, The composition, structure, temperature and dynamics of the upper thermosphere in the polar regions during October to December, 1981, Planet. Space Sci., 33, 617-666, 1985.
- Rees, D., T. J. Fuller-Rowell, R. Gordon, J. P. Heppner, N. C. Maynard, N. W. Spencer, L. E. Wharton, P. B. Hays, and T. L. Killeen, A theoretical and empirical study of the response of the high-latitude thermosphere to the sense of the "Y" component of the interplanetary magnetic field, Planet. Space Sci., in press, 1986.
- Roble, R. G., R. E. Dickinson, and E. C. Ridley, Global circulation and temperature structure of the thermosphere with high-latitude plasma convection, J. Geophys. Res., 87, 1599-1614, 1982.
- Roble, R. G., R. E. Dickinson, E. C. Ridley, B. A. Emery, P. B. Hays, T. L. Killeen, and N. W. Spencer, The high latitude circulation and temperature structure of the thermosphere near solstice, Planet. Space Sci., 31, 1299-1314, 1983.
- Roble, R. G., B. A. Emery, R. E. Dickinson, E. C. Ridley, T. L. Killeen, P. B. Hays, G. R. Carignan, and N. W. Spencer, Thermospheric circulation, temperature and compositional structure of the southern hemisphere polar cap during October-November, 1981, J. Geophys. Res., 89, 9057-9068, 1984.
- Roble, R. G., E. C. Ridley, and R. E. Dickinson, An auroral model for the NCAR Thermospheric General Circulation Model, J. Geophys. Res., submitted, 1986.
- Sica, R. J., M. H. Rees, G. J. Romick, G. Hernandez, and R. G. Roble, Auroral zone thermospheric dynamics: 1 Averages, J. Geophys. Res., 91, 3231-3244, 1986.
- Spencer, N. W., L. E. Wharton, H. B. Niemann, A. E. Hedin, G. R. Carignan, and J. C. Maurer, The Dynamics Explorer wind and temperature spectrometer, Space Sci. Instrum., 5, 417-428, 1981.
- Spencer, N. W., L. E. Wharton, G. R. Carignan, and J. C. Maurer, Thermosphere zonal winds, vertical motions and temperature as measured from Dynamics Explorer, Geophys. Res. Lett., 9, 953-956, 1982.
- Spiro, R. W., P. H. Reiff, and L. J. Maher, Precipitating electron energy flux and auroral zone conductances - an empirical model, J. Geophys. Res., 87, 8215-8227, 1982.
- Torr, M. R., D. G. Torr, and H. E. Hinteregger, Solar flux variability in the Schumann-Runge continuum as a function of solar cycle 21, J. Geophys. Res., 85, 6063-6068, 1980.

Walker, J. C. G.,

Whalen, J. A., A quantitative description of the spatial distribution and dynamics of the energy flux in the continuous aurora, J. Geophys. Res., 88, 7155-7169, 1983.

Wharton, L. E., N. W. Spencer, and H. G. Mayr. The Earth's thermospheric superrotation from Dynamics Explorer 2, Geophys. Res. Lett., 11, 531-533, 1984.

LOG₁₀ AMPLITUDE VSH COEFFICIENTS

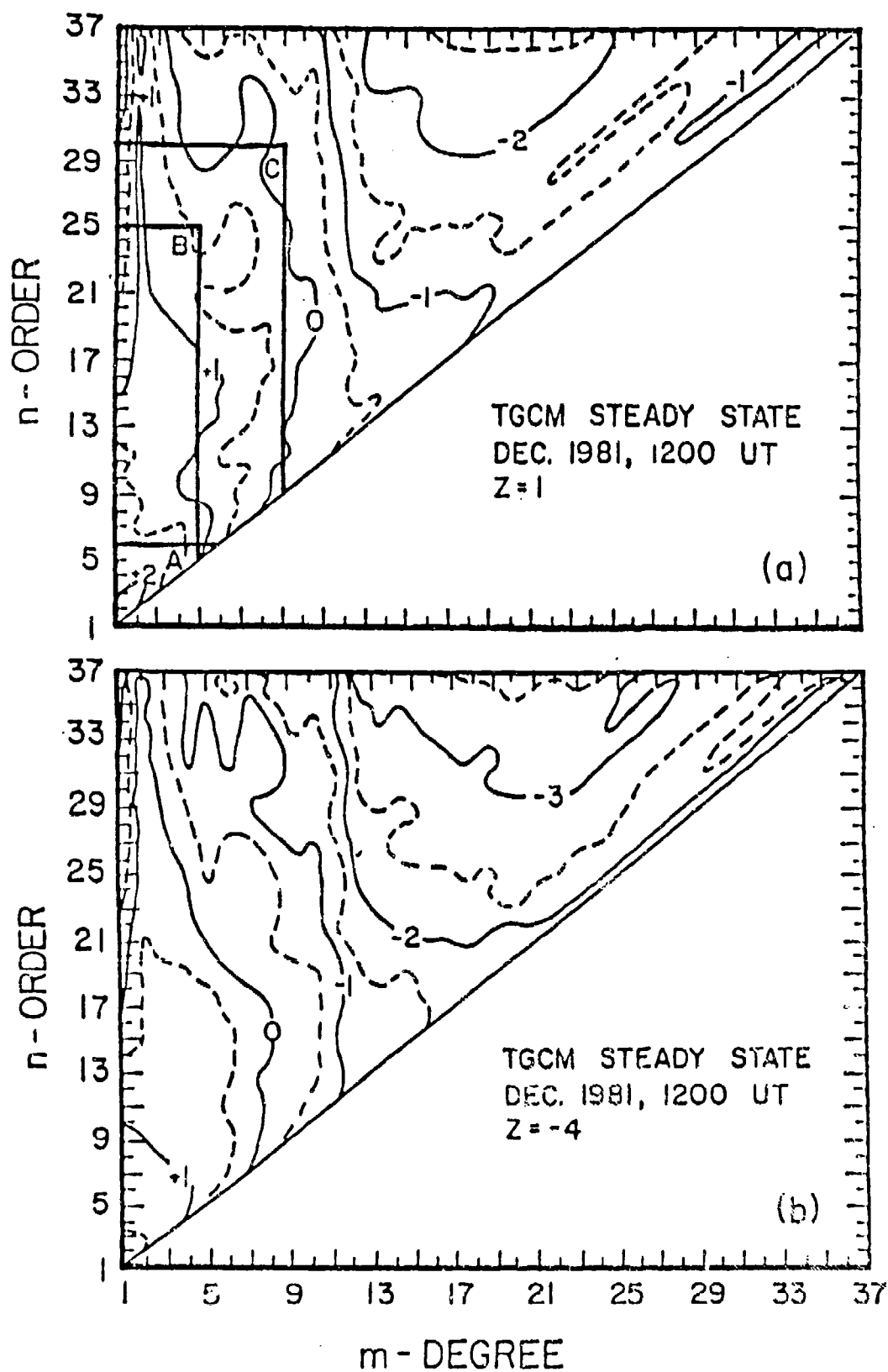


FIGURE 1

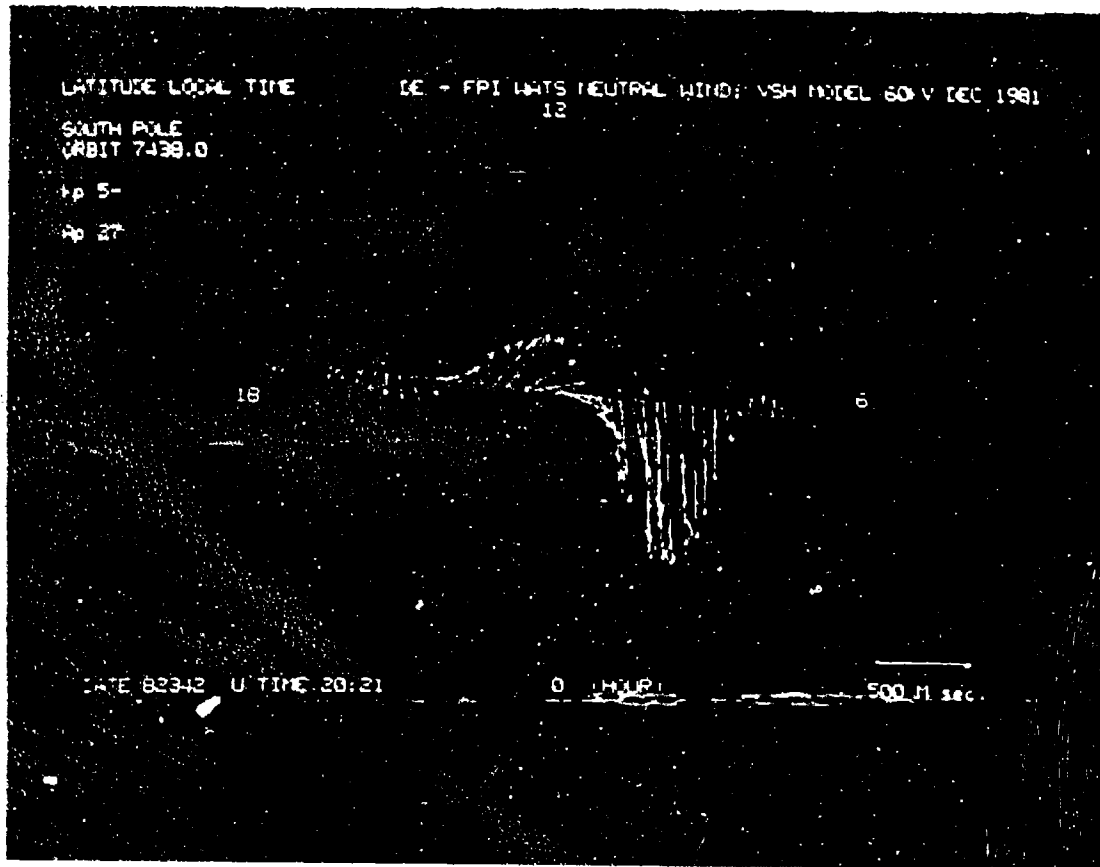


Fig. 2a

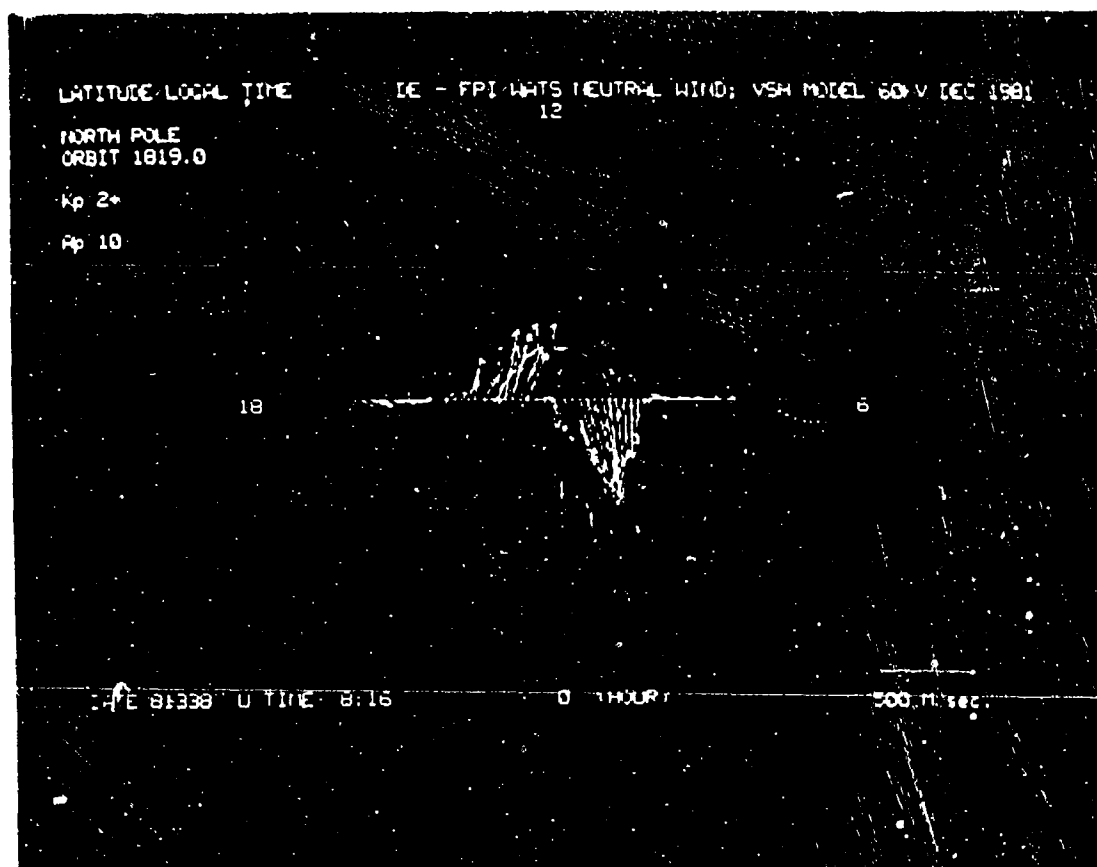


Fig. 2b

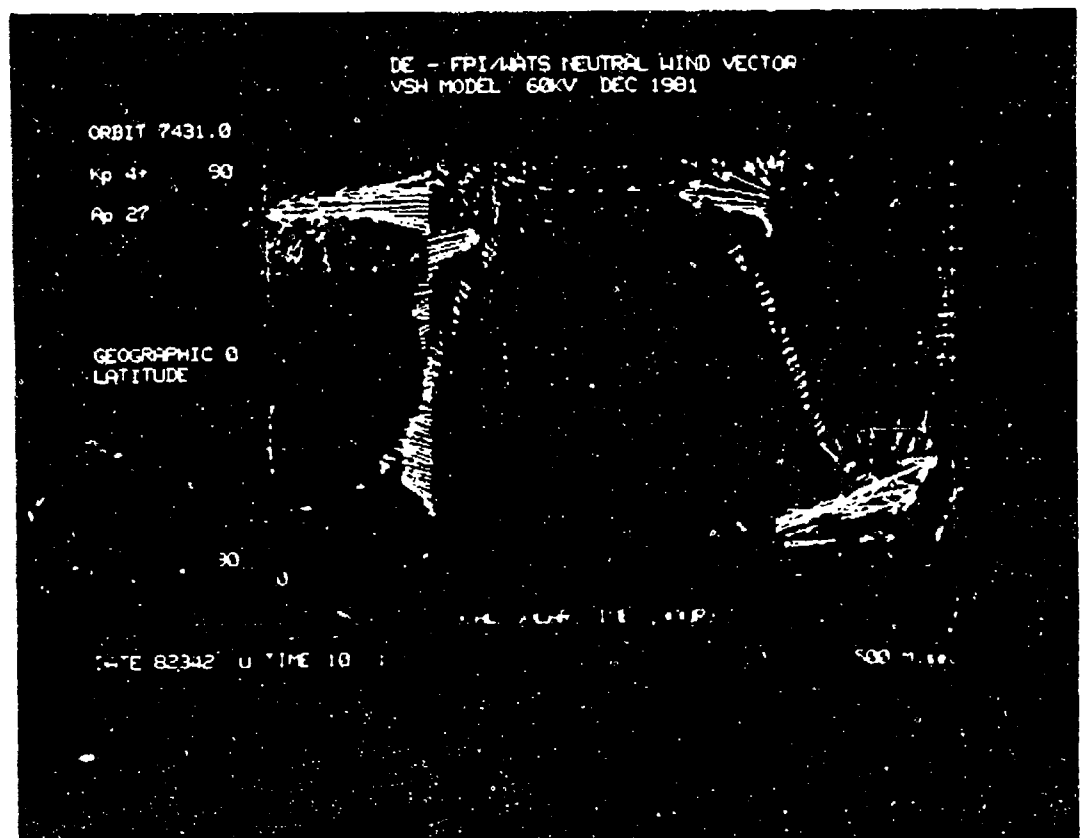


Fig. 3

EQUATORIAL ZONAL NEUTRAL WIND
DE/2 WATS (1981)

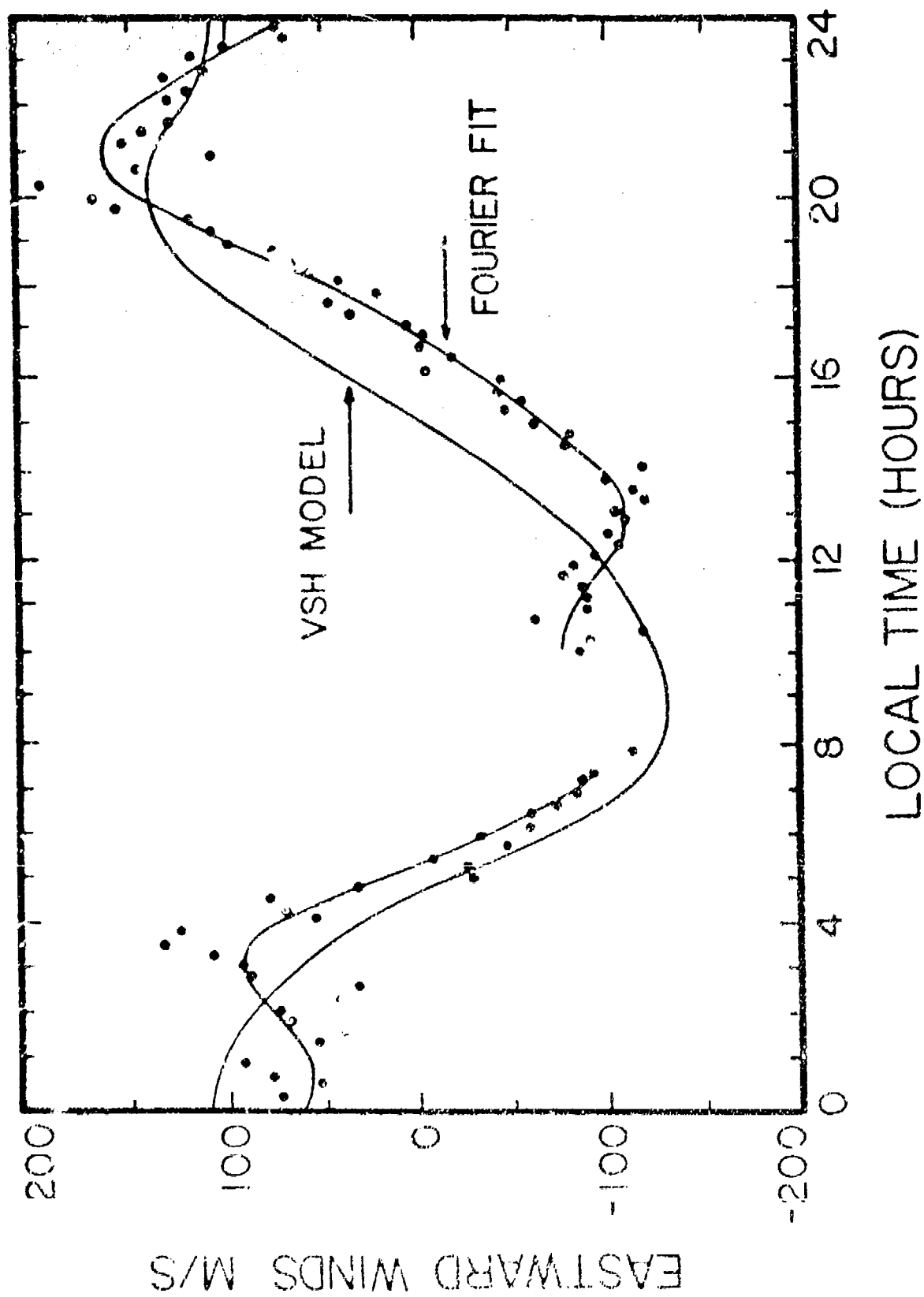


FIGURE 4

VSH MODEL DEC 1980
EQUATOR (0.0, 0.0)

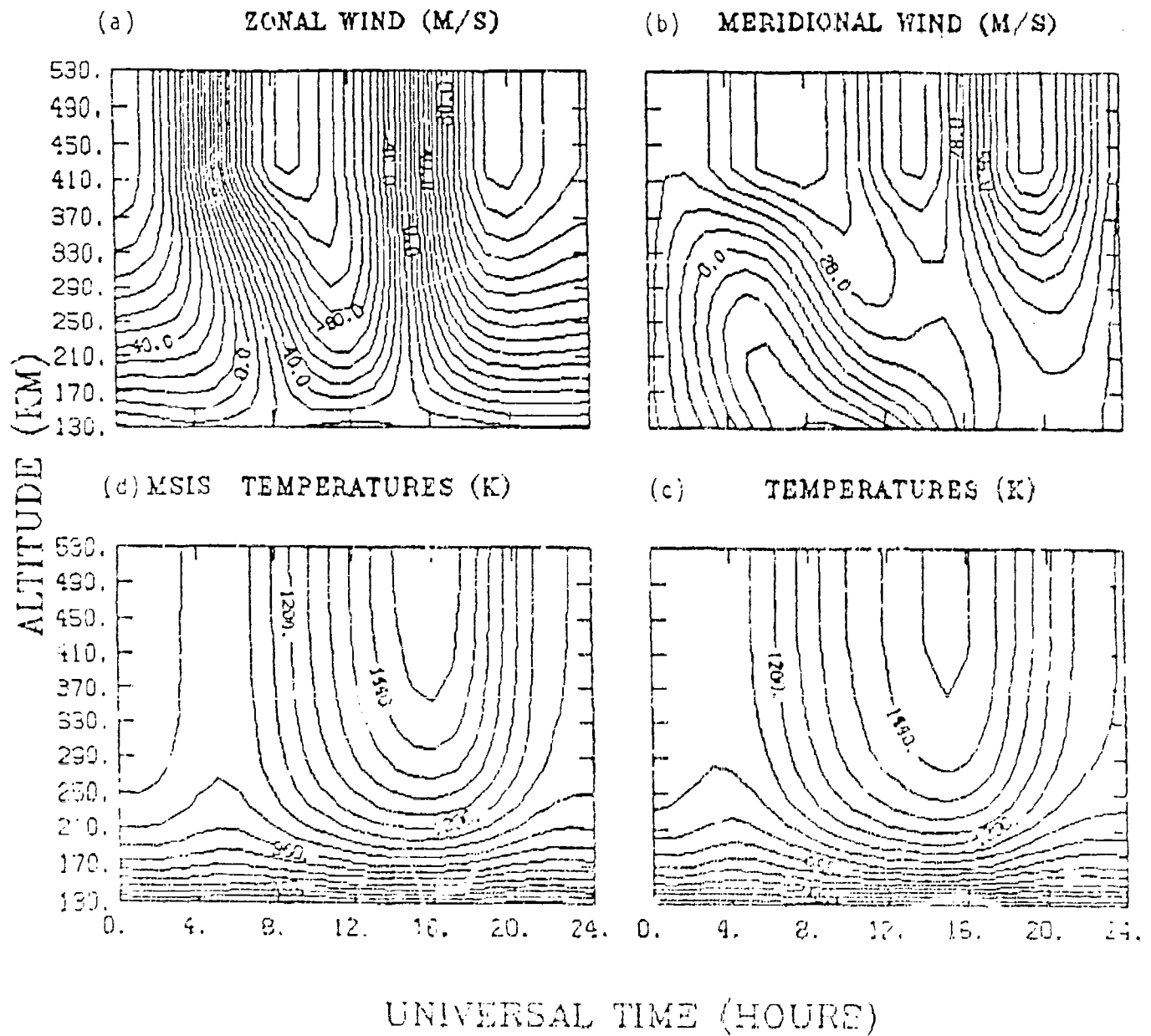
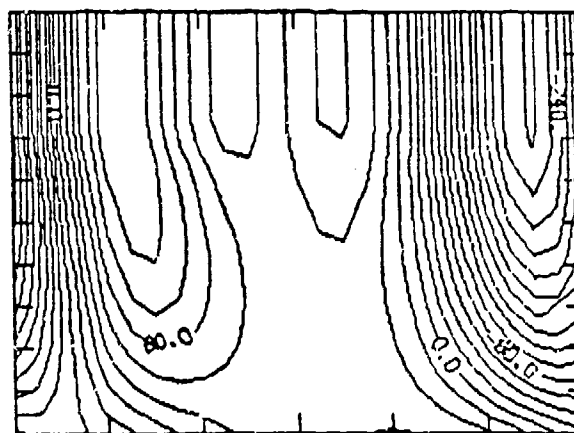
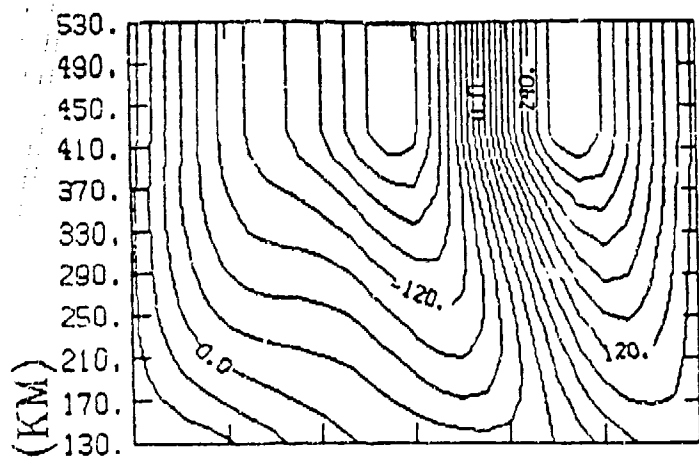


FIGURE 5

VSH MODEL DEC 1980
SVALBARD (78.2, 15.6)

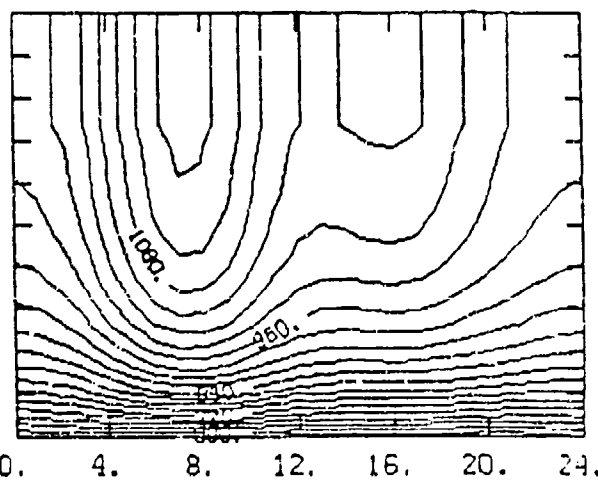
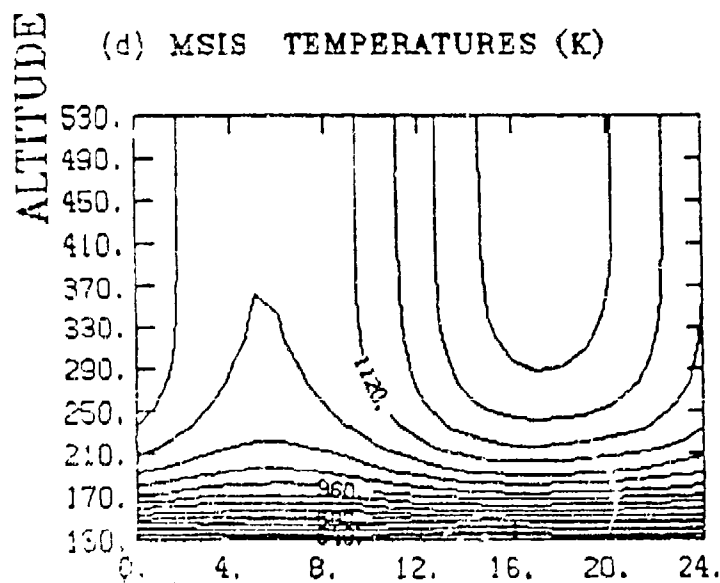
ZONAL WIND (M/S)

(b) MERIDIONAL WIND (M/S)



(d) MSIS TEMPERATURES (K)

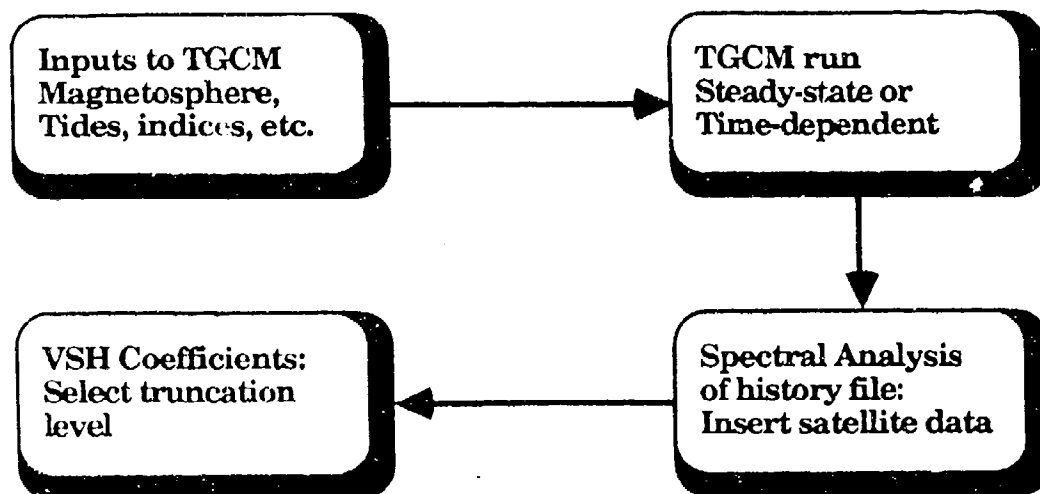
(c) TEMPERATURES (K)



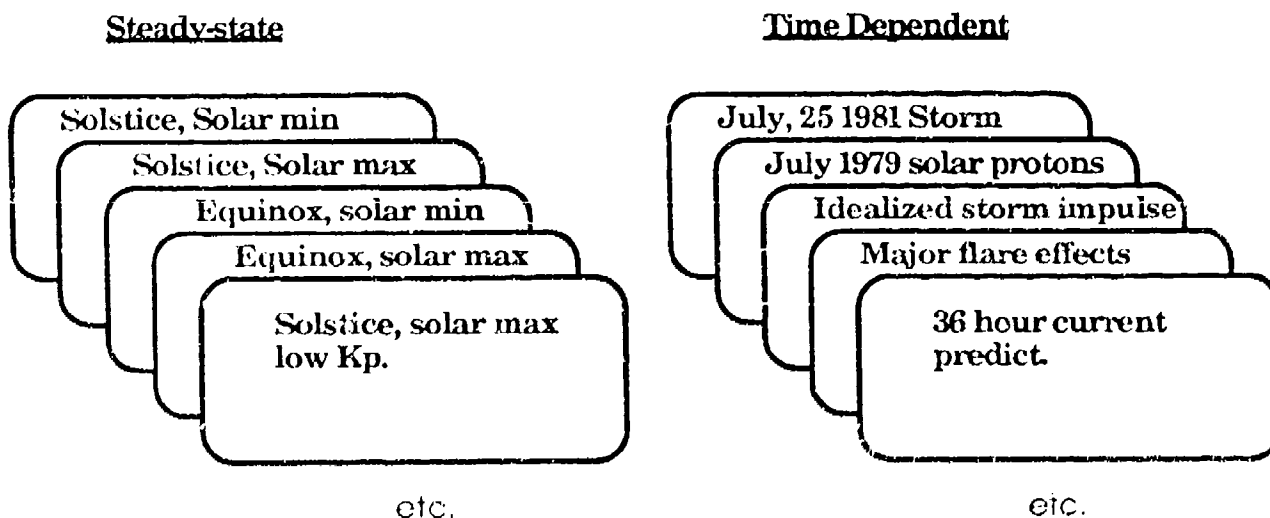
UNIVERSAL TIME (HOURS)

FIGURE 6

VSH MODEL DEVELOPMENT AND USE



COEFFICIENT SETS:



VSH Subroutine:
densities, winds, temperatures,
thermospheric composition
ionospheric composition

6.4 Future Thermospheric General Circulation Model (TGCM) Needs

R. W. SCHUNK

Center for Atmospheric and Space Sciences

Utah State University

Logan, Utah 84322-4405

Workshop on
Atmospheric Density and Aerodynamic Drag Models
for Air Force Operations

October, 1987

1. INTRODUCTION

Significant progress has been made during the last decade with regard to our understanding of the interactions between the ionosphere and thermosphere, especially in the polar regions. However, most of the studies have been qualitative in nature, since they were based on empirical model inputs for the important magnetospheric parameters (convection electric field, particle precipitation pattern, etc.). Typically, these empirical models are constructed from data collected over many months or years from many ground-based sites or satellite orbits. The data are synthesized and then fitted with simple analytical expressions, and consequently, the empirical models of plasma convection and particle precipitation represent 'average' magnetospheric conditions not 'instantaneous' patterns. Also, most of the TGCM simulations were concerned with diurnally reproducible patterns, i.e., the empirical convection and precipitation inputs were held fixed for five days so that the maximum thermospheric response could be achieved. In addition, for most of the TGCM simulations, the ionosphere was not included in a self-consistent manner, but instead, empirical models of a featureless ionosphere were used to drive the thermosphere. Only during the last year have fully coupled ionosphere-thermosphere models been developed. In the near future, these coupled models will be used with improved spatial and temporal resolutions so that the 'weather' of the ionosphere-thermosphere system can be modelled. The future needs of this new breed of TGCM's are discussed in the following sections.

2. MAGNETOSPHERIC REQUIREMENTS

The important magnetospheric parameters for TGCM simulations are the plasma convection and particle precipitation patterns, and possibly, the downward heat flow from the inner magnetosphere. The current state of these inputs and future TGCM needs are described below.

2.1. *Plasma Convection*

At the present time, there are numerous empirical models that describe the plasma convection pattern imposed on the ionosphere via magnetospheric electric fields [cf. *Schunk, 1987*]. The empirical models take account of the IMF (B_x , B_y , B_z) and K_p variations of the convection pattern, and simple two-cell, distorted two-cell, and multi-cell patterns have been modelled. Figure 1 shows the plasma convection trajectories that are obtained from a Volland-type empirical model with corotation added. The left panel shows the pattern for quiet geomagnetic activity ($K_p \sim 0.07$) and the right panel shows a possible pattern for strong geomagnetic activity ($K_p \sim 5$). Patterns of this nature have been used successfully to model a wide range of ionospheric and thermospheric conditions. However, the patterns represent average magnetospheric conditions and not instantaneous pictures of convection, and in most TGCM simulations such patterns were held fixed for an extended period of time. In a few cases, storm and substorm simulations were attempted [*Sojka and Schunk, 1983*; *Rishbeth et al., 1985*], but the storm conditions were simulated simply by varying the convection pattern from a quiet pattern (left panel) to an active pattern (right panel) in a linear manner. This procedure was adopted primarily because of the lack measurements related to storm dynamics. Furthermore, note that both the quiet and disturbed convection patterns shown in Figure 1 lack structure. The real convection pattern, however, can at times exhibit a considerable amount of spatial structure, as shown in Figure 2.

In the future, 'instantaneous' global pictures of plasma convection must be obtained with high spatial resolution. Also, the temporal variation of the convection pattern must be measured during storms and substorms on a global scale. Such information is needed for weather modelling.

2.2. Particle Precipitation

The problems with the existing empirical particle precipitation models are similar to those associated with the convection models. Basically, these models represent average precipitation conditions and not instantaneous patterns. Figure 3 shows typical precipitation patterns obtained from empirical models for both low and high K_p values. In modelling applications, patterns are either held fixed or varied from one pattern to another simply

by varying the K_p index with time. The validity of such a procedure is currently unknown. Also, the empirical precipitation patterns tend to blend the different precipitation regions into one continuous zone. The real auroral oval, however, contains several precipitation regions, as shown schematically in Figure 4. In addition to diffuse auroral precipitation, there are discrete auroral arcs in the nocturnal oval, polar rain and sun-aligned arcs in the polar cap, soft precipitation in the dayside cusp, and diffuse auroral patches in the morning oval.

In the future, the different precipitation regions in the auroral oval must be better represented in the modelling. Also, the 'instantaneous' auroral oval must be obtained via satellite images in order to improve the spatial resolution, and these images need to be acquired at regular intervals throughout the day.

2.3. Heat Flow

The downward flow of heat from the inner magnetosphere could have a significant effect on the ionospheric densities and temperatures, which are important for ionosphere-thermosphere momentum and energy coupling. At the present time, however, this magnetospheric parameter is virtually unknown. In the future, the downward heat flux must be measured on a global scale so that its contribution can be assessed.

3. IONOSPHERIC REQUIREMENTS

It has recently become clear that the structure of the ionosphere plays an important role in determining the thermospheric response to a given magnetospheric forcing function. This result was shown by *Fuller-Rowell et al.* [1984] using the UCL time-dependent global model of the thermosphere. For a given geophysical situation, the thermospheric circulation was calculated using different ionospheric models; the *Chiu* [1975] empirical model and the *Quegan et al.* [1982] numerical model. The geophysical conditions adopted were for low solar activity, equinox and a two-cell convection pattern. The convection pattern was asymmetric with slightly enhanced ion drifts in the dawn cell. The ion drifts were strongest near the edge of the polar cap and weak in the central polar cap.

Figure 5 shows electron density contours at 300 km in the polar region for the *Chiu* [1975] empirical model (top panel) and for the *Quegan et al.* [1982] numerical model (bottom panel). For the Chiu model, the electron density variation is smooth, with a gradual decay of N_e over the polar region from high values near noon to low values in the midnight–0300 LT sector. For the Quegan et al. model, on the other hand, the N_e variation over the polar region is much more dramatic. A distinct enhancement in the electron density occurs in the auroral region, with N_e a factor of 5 greater in the dusk oval and a factor of 2.5 greater in the dawn oval relative to the Chiu densities. Outside the auroral region the Chiu and Quegan et al. electron densities do not differ significantly.

The effect of the different ionospheric models on the thermospheric circulation is shown in Figure 6. For the Chiu ionospheric model, the imprint of two-cell plasma convection is evident. There is antisunward neutral flow over the polar cap at a speed greater than that expected from solar heating alone, and there is a return flow at lower latitudes in the dusk sector. For the Quegan et al. ionospheric model, the effect of plasma convection on the thermospheric circulation is much more pronounced, particularly in the auroral region where the Quegan et al. model predicts higher electron densities. In the dusk sector outside of the polar cap, a strong sunward neutral flow develops in response to the enhanced momentum forcing associated with the higher electron densities, and a detectable sunward flow also develops on the dawn side. These results clearly illustrate the importance of the electron density in determining the strength of the momentum forcing for a prescribed plasma convection pattern.

Even in the few cases where a self-consistent ionosphere was used in the TGCM simulations, only gross ionospheric features were modelled (see Figure 5). The real ionosphere, on the other hand, exhibits a significant amount of structure. Density irregularities, ranging from 10's to 100's of kilometers, are frequently observed in the high latitude ionosphere [cf. *Schunk*, 1988]. These density irregularities, more commonly referred to as blobs, patches, and enhancements, have been observed in the dayside cusp, nocturnal auroral zone, and polar cap. They have been observed in the *B*-region, *F*-region, and topside ionosphere. The density enhancements associated with the irregularities vary from 10% to a factor of 10

relative to background densities. Figure 7 shows examples of the irregularity structure in the nocturnal auroral ionosphere on three different evenings; these data were acquired by the Chatanika radar using elevation scans [Robinson *et al.*, 1985]. The irregularities are not restricted to high latitudes, but are found all over the globe, particularly in the *E*-region where sporadic-*E* is prevalent. Figure 8 shows examples of the sporadic-*E* phenomenon at middle, equatorial, and auroral latitudes. In some locations, sporadic-*E* represents the normal ionospheric state, not a temporary disturbed state.

The effect of ionospheric structure on the thermospheric circulation is shown in Figure 9. In this example, a simple plasma convection channel 150 km wide and aligned in the *x*-direction was created. The electron density profile in the channel was characterized by an $N_m F_2$ of 10^5 cm^{-3} , while the profile outside the channel had an $N_m F_2$ of 10^4 cm^{-3} . In the channel at *F*-region altitudes the plasma was $\mathbf{E} \times \mathbf{B}$ drifting in the *x*-direction at a speed of about 2 km/s, while outside the channel the plasma was not drifting. The thermospheric response to this momentum forcing is seen to be a strong function of altitude. In the *E*-region, the thermospheric response is restricted to the convection channel, but the neutral flow is rotated owing to Coriolis forces. In the *F*-region, on the other hand, the effects of the convecting plasma on the thermospheric motion are felt well beyond the channel owing to horizontal viscous dissipation.

The above example indicates that small-scale ionospheric structures in the *E*-region will produce small-scale thermospheric structures in this region. In the *F*-region, small-scale ionospheric structures will affect the thermospheric flow over a much greater distance and the accumulated effect of many small-scale ionospheric structures could have a significant effect on the global mean circulation and temperature. In the future the small-scale structures must be included in TGCM simulations.

4. SUMMARY

In future TGCM simulations, the following items will be needed in order to provide the basis for modelling ionosphere-thermosphere weather patterns:

- (1) Instantaneous global pictures of plasma convection are needed with a high spatial

resolution. Also, the temporal variation of the convection pattern must be measured during storms and substorms on a global scale.

- (2) The different precipitation regions in the auroral oval must be better represented in the modelling.
- (3) Instantaneous particle precipitation patterns are needed at regular intervals during the day.
- (4) The unknown flow of heat from the magnetosphere to the ionosphere-thermosphere system needs to be measured.
- (5) The small-scale ionospheric structure (blobs, patches, enhancements, irregularities) needs to be included in future TGCM simulations.
- (6) Storm and substorm variations need to be rigorously modelled.
- (7) Gravity and tidal waves propagating up from the lower atmosphere need to be parameterized and included in future TGCM simulations.

Acknowledgement. This research was supported by the University Research Initiative grant AFOSR F49620-86-C-0109 to Utah State University.

REFERENCES

- Chiu, Y. T., *J. Atmos. Terr. Phys.*, **37**, 1563, 1975.
- Frank, L. A., et al., *J. Geophys. Res.*, **91**, 3177, 1986.
- Fuller-Rowell, T. J., D. Rees, S. Quegan, G. J. Bailey, and R. J. Moffett, *Planet. Space Sci.*, **32**, 469, 1984.
- Quegan, S., G. J. Bailey, R. J. Moffett, R. A. Heelis, T. J. Fuller-Rowell, D. Rees, and R. W. Spiro, *J. Atmos. Terr. Phys.*, **44**, 619, 1982.
- Robinson, R. M., R. T. Tsunoda, and J. F. Vickery, *J. Geophys. Res.*, **90**, 7533, 1985.
- Schunk, R. W., *AFGL Report*, this issue, 1987.
- Schunk, R. W., *Physica Scripta*, in press, 1988.
- Schunk, R. W., and E. Szuszczewicz, *Ann. Geophys.*, in press, 1987.
- Sojka, J. J., and R. W. Schunk, *J. Geophys. Res.*, **88**, 2112, 1983.
- St.-Maurice, J.-P., and R. W. Schunk, *J. Geophys. Res.*, **86**, 11,299, 1981.

ILLUSTRATIONS

Fig. 1. Plasma drift trajectories in the polar region for both quiet (left panel) and active (right panel) geomagnetic conditions. The trajectories are shown in a magnetic latitude-MLT reference frame including the effects of corotation. The quiet case is for a symmetric two-cell convection pattern with a cross-tail potential of 20 kV ($K_p \sim 0.07$), while the active case is for an asymmetric two-cell convection pattern with enhanced flow in the dusk sector and a total cross-tail potential of 90 kV ($K_p \sim 5$). From *Sojka and Schunk* [1983].

Fig. 2. Plasma convection velocities in the high latitude *F*-region in a magnetic latitude-MLT reference frame. The data were obtained with the ion drift meter on the Dynamics Explorer-2 satellite. From *Frank et al.* [1986].

Fig. 3. Contours of the auroral electron energy flux for both quiet (left panel) and active (right panel) geomagnetic conditions. The precipitation patterns are shown in a magnetic latitude-MLT frame and the contours are labelled in $\text{erg cm}^{-2} \text{s}^{-1}$. The quiet case corresponds to a $K_p \sim 0.07$ and the active case to $K_p \sim 5$. From *Sojka and Schunk* [1983].

Fig. 4. Schematic diagram showing the different particle precipitation regions in the auroral oval.

Fig. 5. Electron density contours at 300 km in the polar region. The top panel shows electron densities calculated with the *Chiu* [1975] empirical model, while the bottom panel shows those calculated with the numerical model developed by *Quegan et al.* [1982]. The densities are shown from 50° latitude to the pole in units of 10^{10} m^{-3} . In both panels, noon is at the bottom and midnight at the top. From *Fuller-Rowell et al.* [1984].

Fig. 6. Neutral circulation at 300 km in the polar region. The top panel shows the results for the *Chiu* electron densities, while the bottom panel shows the results for the *Quegan et al.* electron densities. The calculation is shown from 50° latitude to the pole. The wind scale is $5^\circ \text{ latitude} = 400 \text{ m s}^{-1}$. Noon is at the bottom and midnight

at the top. From *Fuller-Rowell et al.* [1984].

Fig. 7. Electron density as a function of altitude and invariant latitude measured in the nocturnal auroral zone by the Chatanika radar on three different evenings. From *Robinson et al.* [1985].

Fig. 8. Altitude profiles of electron density measured by in-situ probes on rockets at middle, equatorial, and auroral latitudes. From *Schunk and Szuszczewicz* [1987].

Fig. 9. Thermospheric velocities in and near a convection channel. The channel is 150 km wide and is extended in the x direction. The peak electron density in the channel is $N_m F_2 = 10^5 \text{ cm}^{-3}$, while outside the channel it is 10^4 cm^{-3} . The electric field in the channel is 100 mV m^{-1} and is directed in the $-y$ direction so that the F -region plasma $\mathbf{E} \times \mathbf{B}$ drifts in the x direction at about 2 km s^{-1} . There is no electric field outside the channel. From *St.-Maurice and Schunk* [1981].

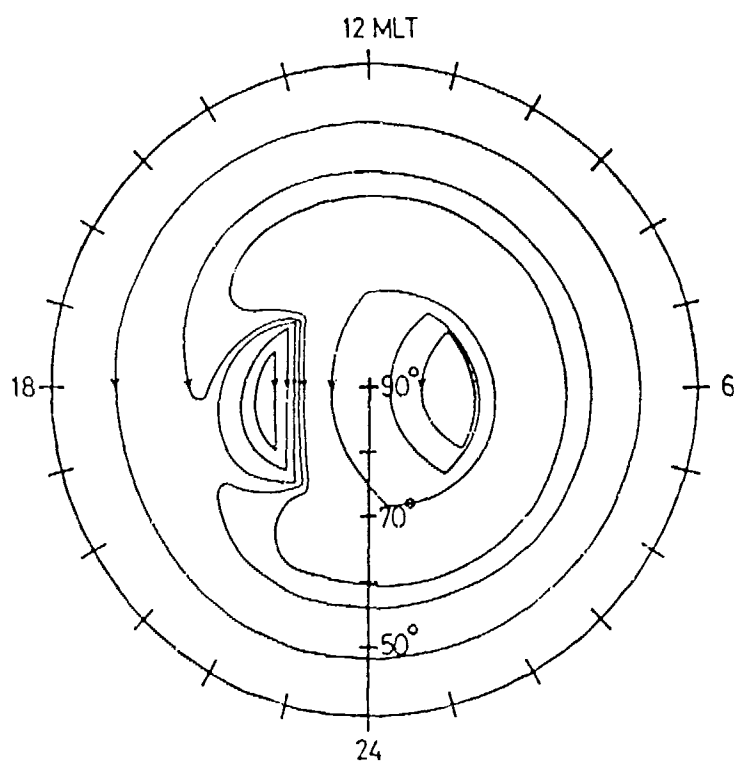
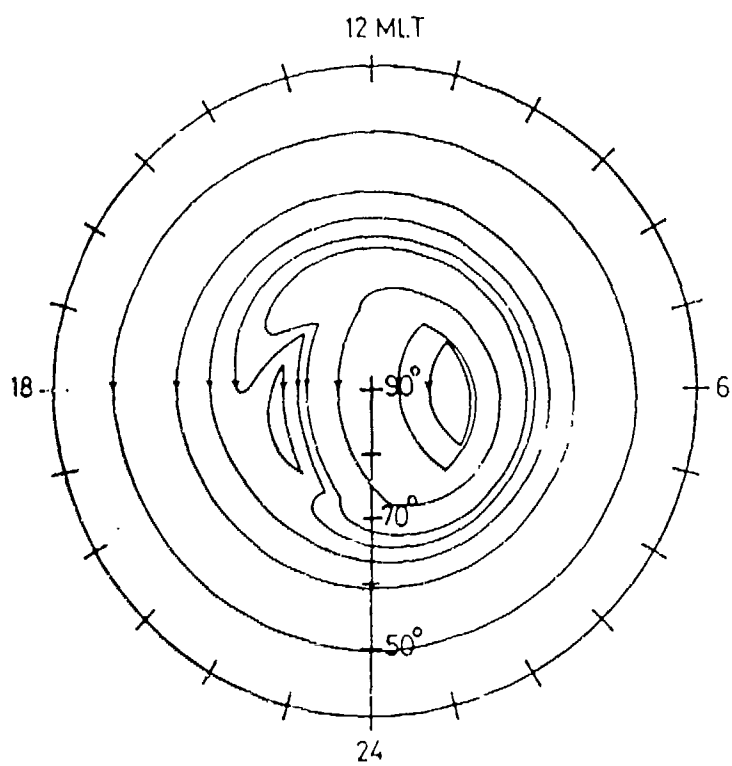


Figure 1

ION DRIFT METER, DE-2
UNIVERSITY OF TEXAS AT DALLAS
OCTOBER 17, 1981
1634-1646 UT

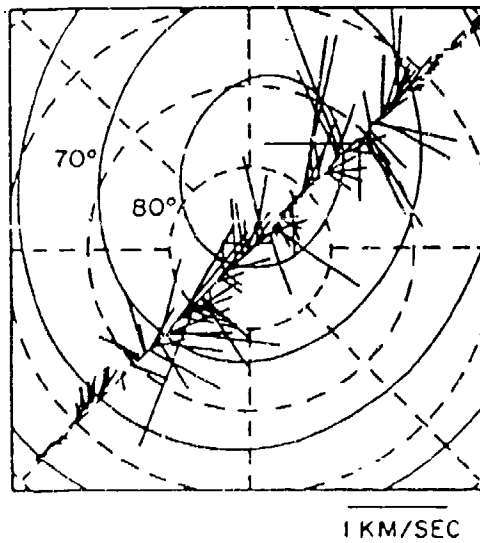


Figure 2

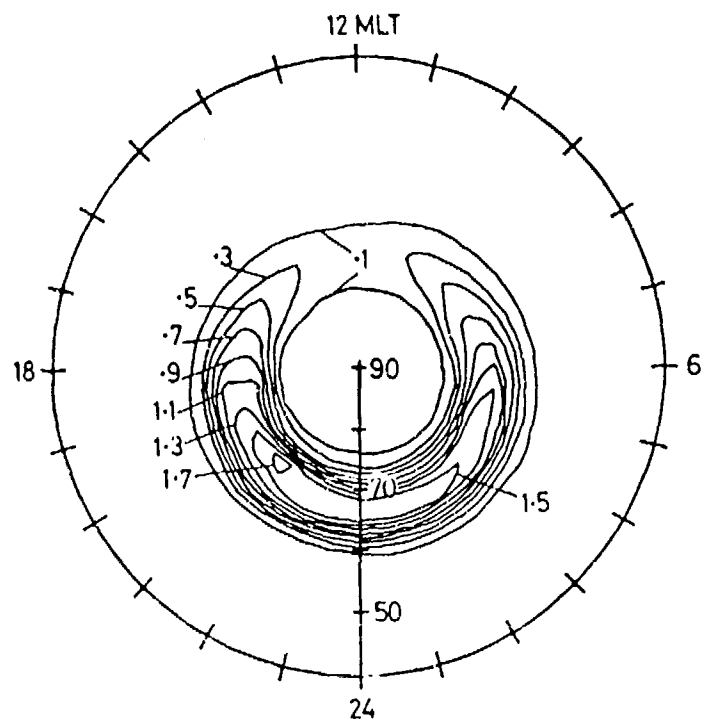
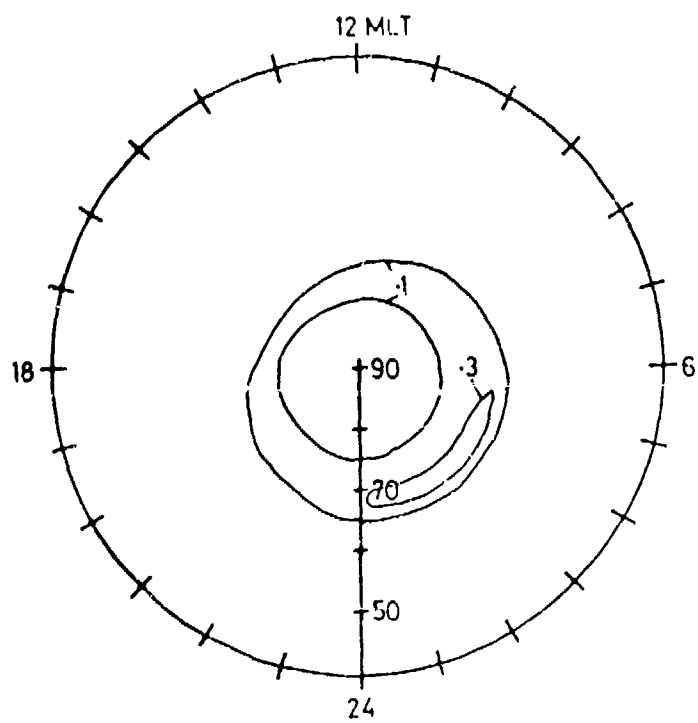


Figure 3

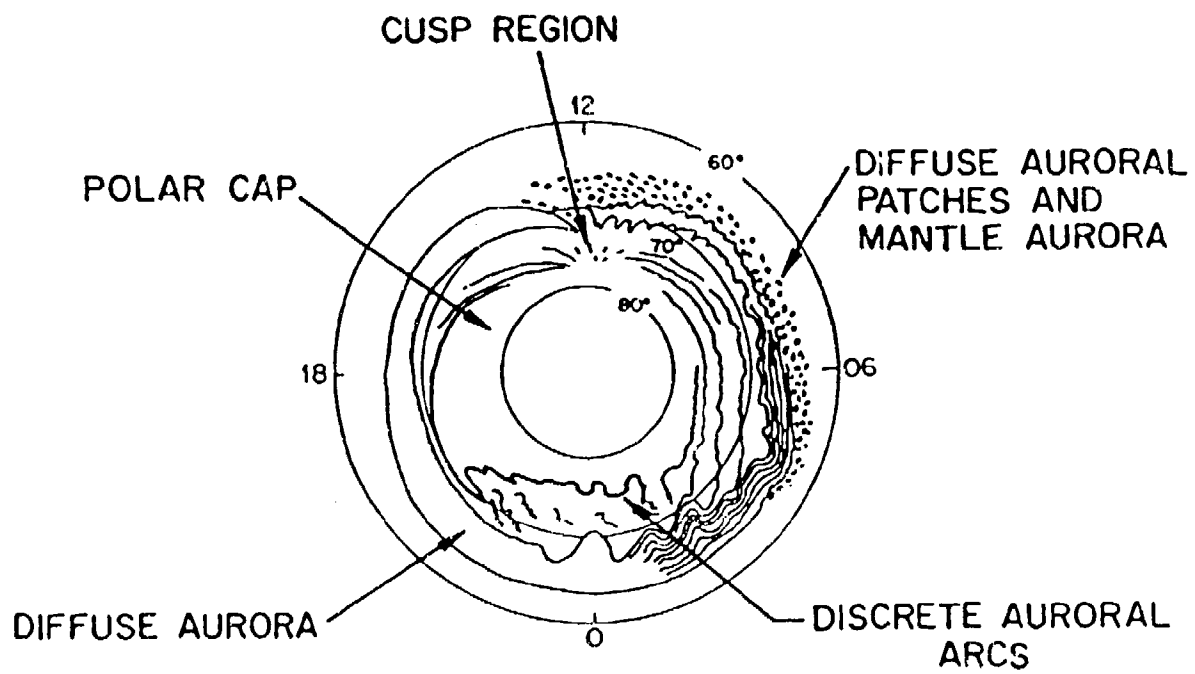


Figure 4

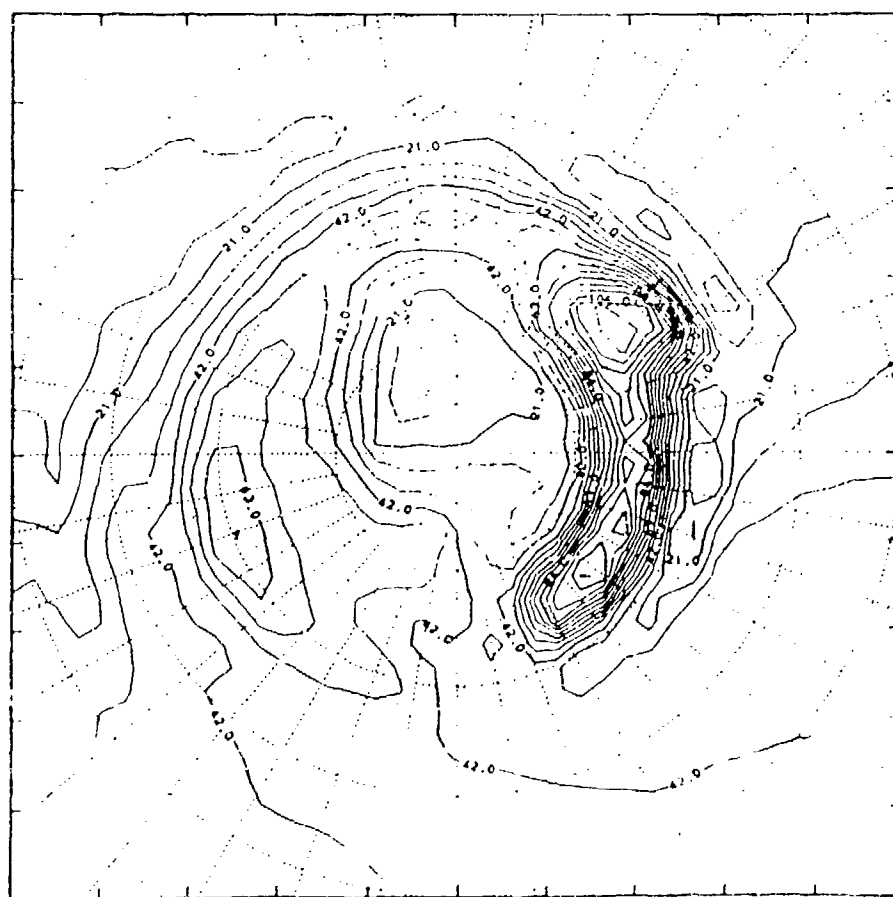
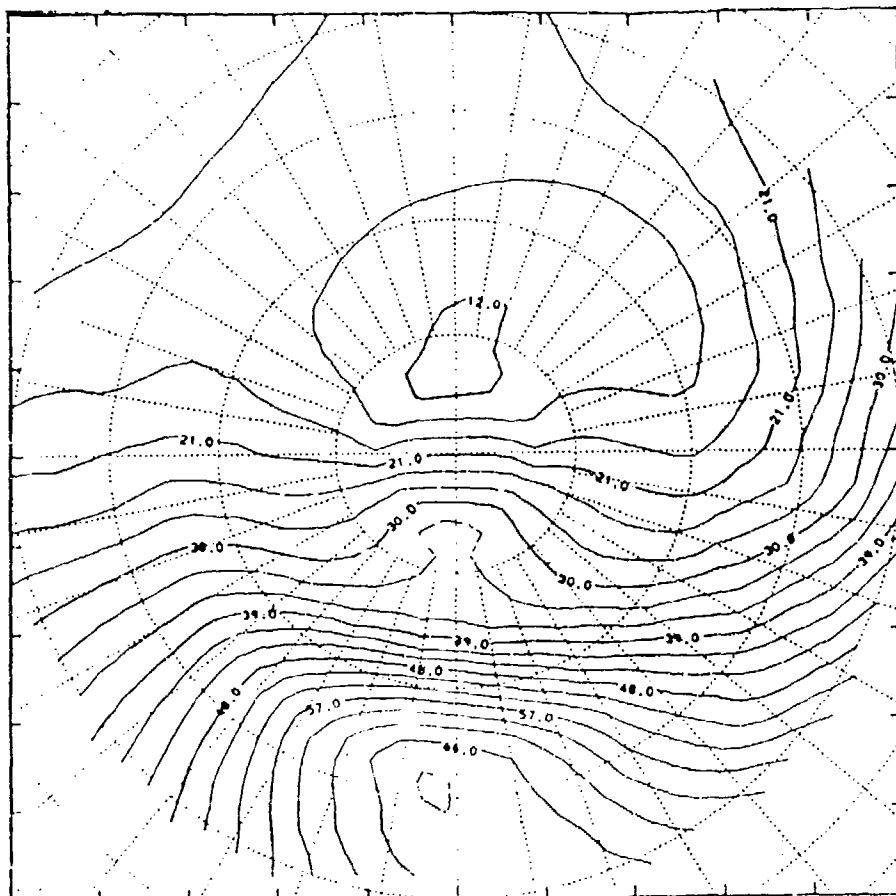


Figure 5

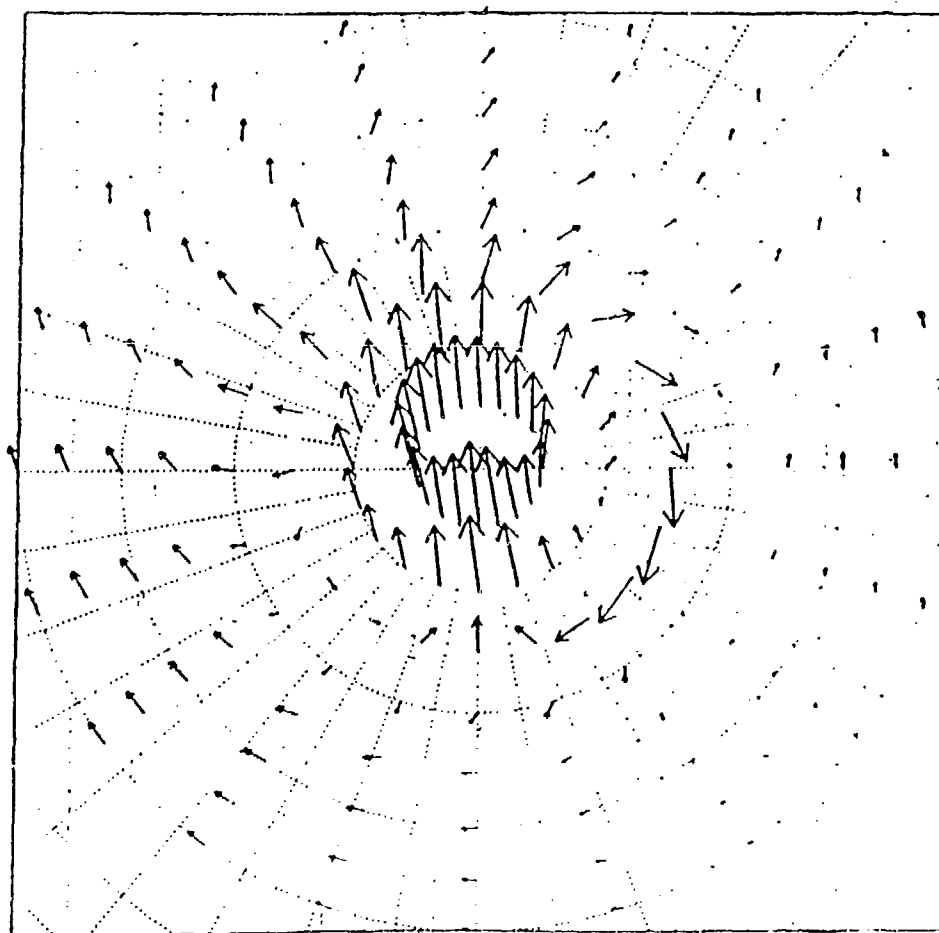
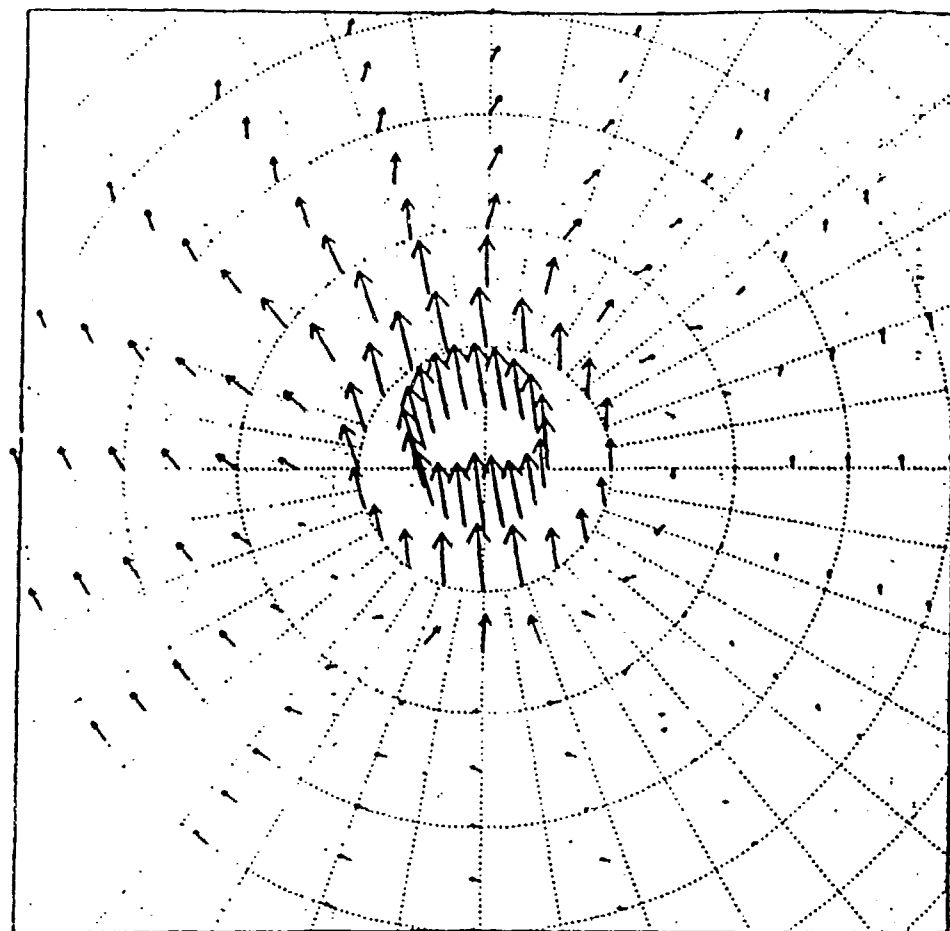


Figure 6

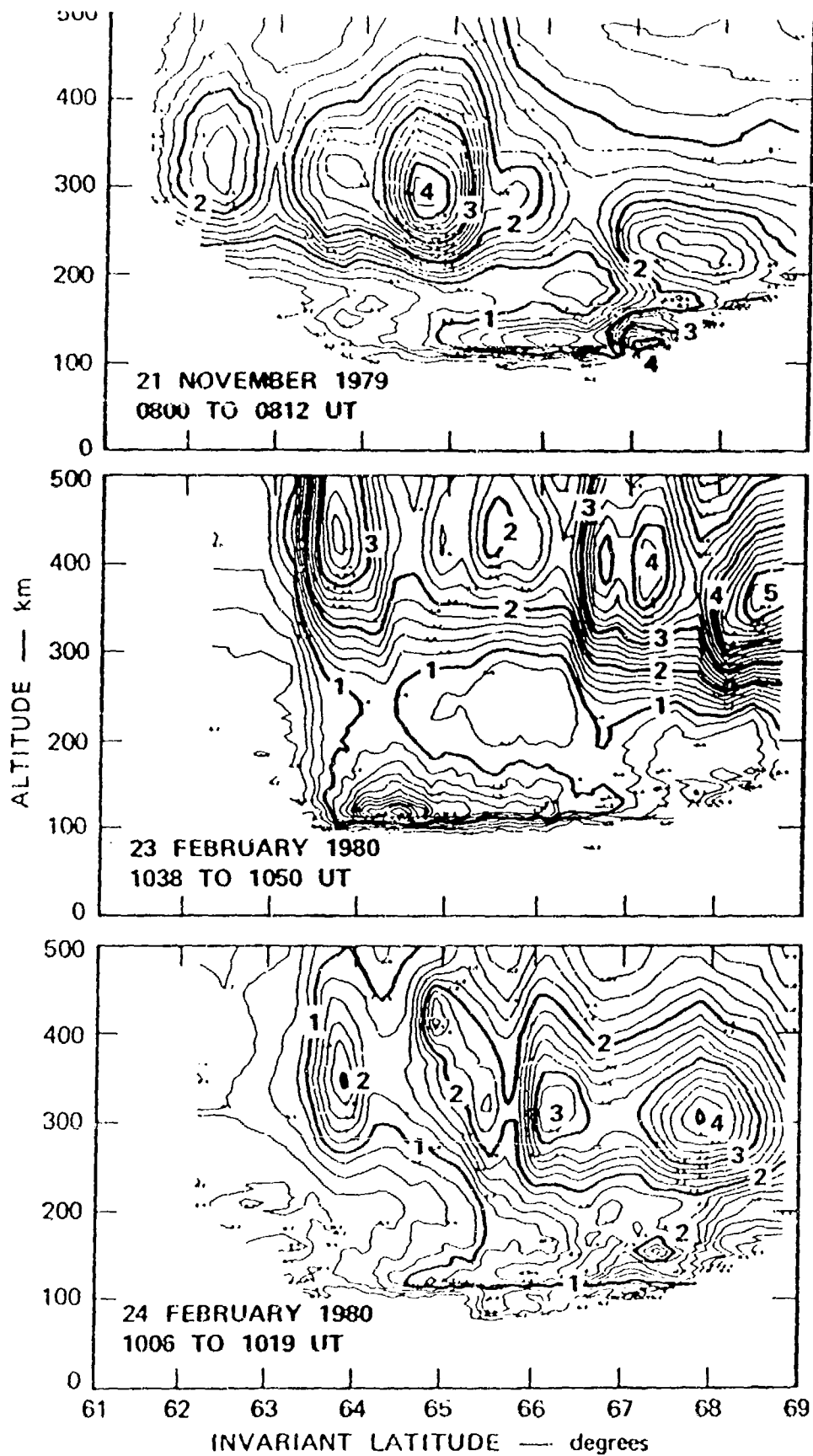


Figure 7

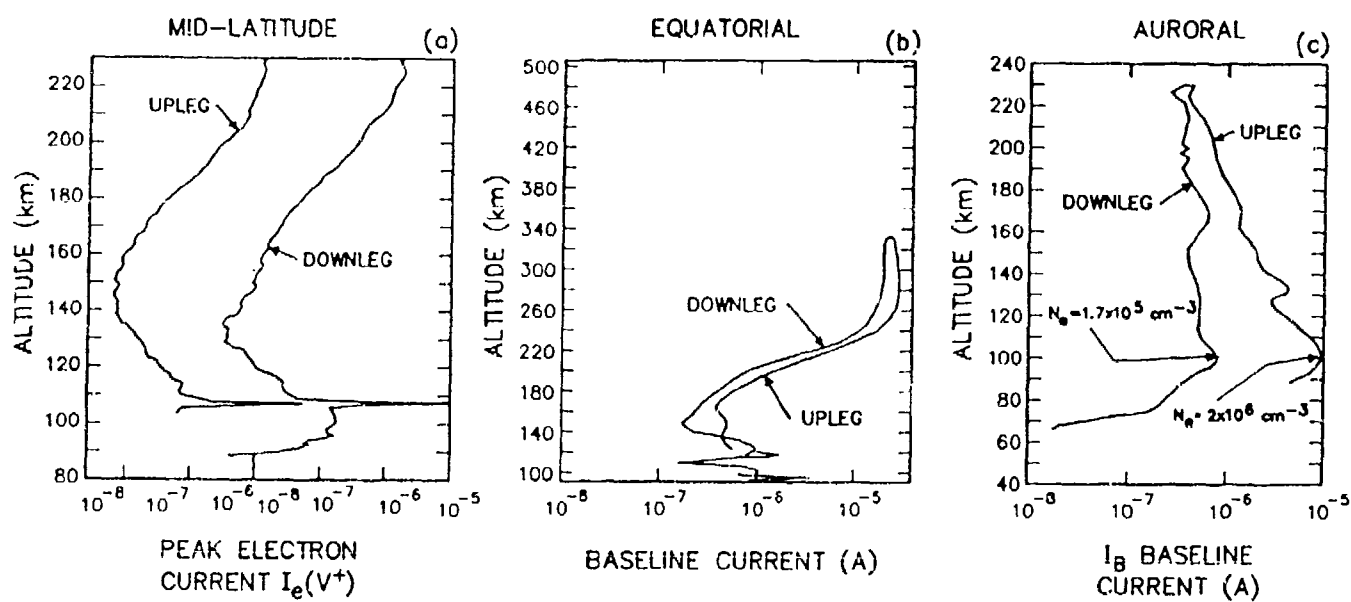


Figure 8

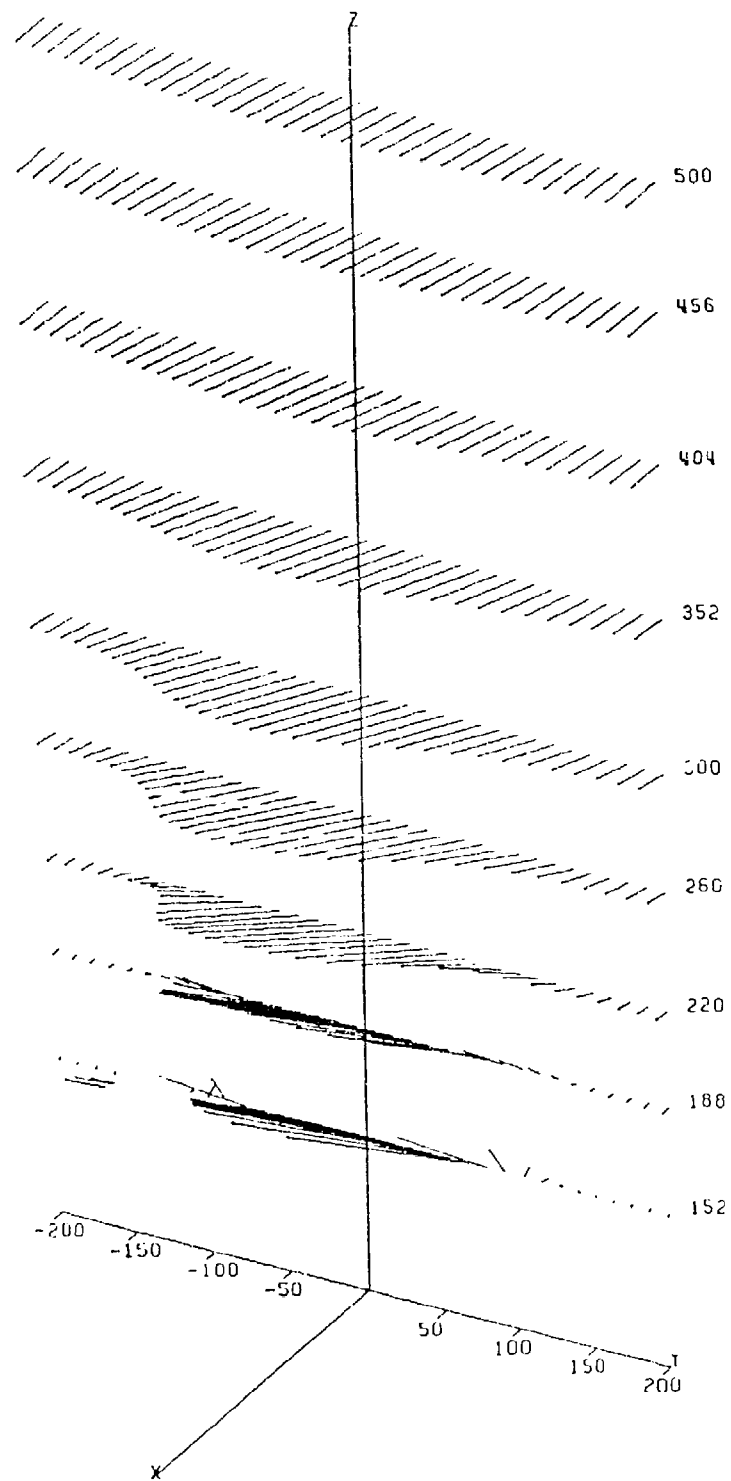


Figure 9

6.5 Thermosphere-Ionosphere-Magnetosphere Coupling

R. W. SCHUNK

Center for Atmospheric and Space Sciences

Utah State University

Logan, Utah 84322-4405

Workshop on
Atmospheric Density and Aerodynamic Drag Models
for Air Force Operations

October, 1987

1. INTRODUCTION

The magnetosphere-ionosphere-atmosphere system is strongly coupled via electric fields, particle precipitation, field-aligned currents and heat flows, as shown schematically in Figure 1. For example, convection electric fields induce a large-scale motion of the high-latitude ionosphere, which affects the electron density morphology. As the plasma drifts through the neutrals, the ion temperature is raised owing to ion-neutral frictional heating. The elevated ion temperature then alters the ion chemical reaction rates, which affect the ion composition. The changes in the ionosphere, in turn, affect the thermospheric structure, circulation, and temperature. At *F*-region altitudes, the neutral atmosphere tends to follow, but lags behind, the convecting ionospheric plasma. The resulting ion-neutral frictional heating induces vertical winds and O/N₂ composition changes. These changes then affect the ionospheric density and temperature structure. Also, the ionosphere-thermosphere system has a significant effect on the magnetosphere. Precipitating auroral electrons produce conductivity enhancements which can modify the convection electric field and large-scale current systems. In addition, once the thermosphere is set in motion due to convection electric fields, the large inertia of the neutral atmosphere will act to produce dynamo electric fields whenever the magnetosphere tries to change its electrodynamic state.

2. MAGNETOSPHERIC PARAMETERS

2.1. *Convection Electric Field*

The most important parameter that controls the ionosphere-thermosphere system at high latitudes is the magnetospheric convection electric field. It is now well-known that the electric field pattern varies markedly with K_p and the interplanetary magnetic field (IMF), and several empirical models of plasma convection are currently available [Heppner, 1977; Volland, 1978; Heelis *et al.*, 1982; Foster, 1983; Oliver *et al.*, 1983; Heelis, 1984; Sojka *et al.*, 1986]. When the IMF is southward ($B_z < 0$), two-cell plasma convection patterns exist with the strength of the dawn and dusk cells depending on B_y . When the IMF is

northward ($B_z > 0$), on the other hand, multiple-cell or distorted two-cell patterns can occur. Figure 2 shows a representative plasma convection pattern of the Volland-type for southward IMF and a total cross-tail potential of 90 kV. Note that the corotational electric field has been added to the two-cell convection pattern and that the pattern is asymmetric with enhanced flow in the dusk sector. In the polar cap, the plasma flow is antisunward at a speed of about 1 km/s, and this flow should induce a large thermospheric response. In the strong dusk convection cell, the convection speed approaches 2 km/s and intense ion and neutral heating can be anticipated. As lower latitudes in the dusk sector, the opposing effects of corotation and sunward plasma convection act to produce a stagnation region, and if this region is in darkness a deep plasma trough can be anticipated.

2.2. Particle Precipitation

Another important magnetospheric parameter is auroral precipitation. This parameter is known to be strong function of K_p , and several empirical models have been developed to describe this variation with K_p [Spiro *et al.*, 1982; Wallis and Budzinski, 1971; Whalen, 1983]. Figure 3 shows representative auroral electron energy fluxes for the northern hemisphere and for active geomagnetic conditions ($K_p \sim 5$). These energy fluxes were obtained from the Spiro *et al.* [1982] empirical model, which is based on Atmospheric Explorer satellite data. For the case shown, the energy flux approaches $2 \text{ erg cm}^{-2} \text{ s}^{-1} \text{ sr}^{-1}$ in the night sector. The precipitating auroral electrons act as an ionization source and a heat source for both the ionosphere and thermosphere.

2.3. Birkeland Currents

The Birkeland (field-aligned) currents are a means by which the magnetosphere and ionosphere communicate changes of state to each other. Figure 4 shows this current system in the northern hemisphere for active geomagnetic conditions. The Birkeland currents are concentrated in two principal areas which encircle the geomagnetic pole. In three dimensions the currents appear as large field-aligned sheets of flowing electrons. The dotted region shows the current away from the ionosphere (downward precipitating electrons), while the shaded region shows the current into the ionosphere (upward ionospheric elec-

trons; return current). The Birkeland currents connect to the horizontal currents that flow in the *E*-region, which affect the circulation of the thermosphere. They also affect the ambient electron temperature, and hence, ion-electron recombination rate. This, in turn, affects the momentum and energy coupling between the ionosphere and thermosphere.

2.4. *Heat Flow*

Another magnetospheric process that could affect the ionosphere-thermosphere system is a downward heat flow from the inner regions of the magnetosphere. Unfortunately, there is very little experimental information on this parameter, and consequently, its effect has not been included in the bulk of the large-scale ionospheric and thermospheric modelling efforts.

3. IONOSPHERE-THERMOSPHERE SYSTEM

The various magnetospheric processes act in concert to produce a number of interesting effects and morphological features and some of these will be discussed in this section.

3.1. *Effect of Convection and Precipitation*

The effect of sustained strong geomagnetic activity on the ionosphere is shown in Figure 5, where 'snapshots' of N_e , T_e , and T_i are shown for solar maximum and winter solstice conditions. The snapshots show the ionospheric parameters in the northern polar region at altitudes of 180 and 300 km and at 1700 UT. As this UT, more of the polar region is sunlit than at any other time of the day; the terminator extends from 1800 to 0700 MLT. In the calculation of these ionospheric parameters, the convection and precipitation patterns shown in Figures 2 and 3 were adopted.

At 180 km, horizontal plasma transport is not as important as local production and loss processes for N_e because the neutral atmosphere is fairly dense at this altitude. Consequently, the N_e variation directly reflects the production sources, and elevated electron densities occur on the dayside due to solar EUV production and in the auroral oval due to impact ionization from precipitating magnetospheric electrons. At 300 km, on the other

hand, horizontal plasma convection is important and this affects the electron density morphology in several ways. First, the enhanced densities in the auroral oval and the sharp dropoff in N_e near the terminator are smeared out. Also, the high electron densities on the dayside are transported into the polar cap via antisunward convection, which produces a 'tongue of ionization'. On the nightside, the slow convection speeds near the stagnation region (see Figure 2) allow the plasma to decay in darkness and an electron density trough forms just equatorward of the auroral oval. Note that in the evening sector the trough extends across the terminator (1800 MLT) and into sunlight. Such a situation only occurs at this UT and, as will be shown later, produces an interesting T_e effect.

At both 180 and 300 km, T_i exhibits very little solar control, and the ion energy balance is mainly determined by ion-neutral interactions. Because the adopted convection pattern contains large plasma convection speeds in the dusk sector poleward of the stagnation region, the ion-neutral frictional heating is strong and an ion temperature 'hot spot' develops in this region. This heating mechanism produces ion temperatures that are more than double the neutral temperature in the center of the hot spot.

Unlike the T_i behavior, T_e at 180 km is strongly controlled by local heating and cooling processes. The electron temperature is elevated both on the dayside due to photoelectron heating and in the auroral region due to heating by precipitating magnetospheric electrons. At 300 km, T_e has the same auroral oval and dayside features as at 180 km, but two additional electron temperature 'hot spots' appear at 300 km (and above) in the dusk sector. The T_e hot spot at 70° latitude and 1800 MLT coincides with the location of the T_i hot spot, and it arises simply because the hot ions heat the electrons via collisions ($T_i > T_e$). The second T_e hot spot at 65° latitude and 1600 MLT is a region where $T_e > T_i$. This hot spot coincides with the extension of the N_e trough across the terminator and into sunlight. As the low density plasma convects into sunlight, T_e increases rapidly owing to the short time constant for photoelectron heating and the low heat capacity of this low-density plasma.

3.2. *Effect of Heat Flow*

From modelling studies, it has been determined that the dominant parameter controlling the T_e behavior above 200 km is the magnetospheric heat flux into the ionosphere, which is essentially unknown. In the calculations shown in Figure 5, the upper boundary electron heat flux was taken to be zero owing to a lack of measurements of this parameter. However, a downward magnetospheric heat flux can have a significant effect on T_e , as shown in Figure 6 where contours of T_e are plotted at 1700 UT for downward electron heat fluxes of 0 (left panel) and 1×10^{10} (right panel) $\text{eV cm}^{-2} \text{s}^{-1}$ at 800 km. It is apparent from Figure 6 that a magnetospheric heat flux does not penetrate to altitudes as low as 180 km, since the T_e variation over the polar region is the same with and without the magnetospheric heat flux. At 300 km, on the other hand, the magnetospheric heat flux has a dominating effect on T_e . Not only are the electron temperatures significantly enhanced with the magnetospheric heat flux, but major T_e features are masked. In particular, the T_e hot spots in the dusk sector, which are related to enhancements associated with a sunlit trough and a T_i hot spot due to frictional heating, are masked by the elevated electron temperatures resulting from the magnetospheric heat flux.

3.3. *Effect of Ionospheric Return Currents*

An electron heat flow can occur in a partially-ionized plasma in response to either an electron temperature gradient (thermal conduction) or an electron current (thermoelectric heat flow). Figure 7 shows the effect on the T_e profile of different values of the ionospheric return current for a range of seasonal and solar cycle conditions. The profiles were calculated with the total heat flux through the upper boundary set at $-1 \times 10^{10} \text{ eV cm}^{-2} \text{s}^{-1}$. For all the cases shown in Figure 7, thermoelectric heat transport corresponds to an upward flow of energy at all altitudes, and for most of the cases it acts as a heat sink. Thermoelectric cooling can decrease auroral electron temperatures by more than 1000°K for large ionospheric return currents.

3.4. *Thermospheric Response*

The convecting ionosphere at high latitudes can be a significant source of momentum

and energy for the thermosphere via ion-neutral collisions. The resulting interactions act to modify the thermospheric circulation, temperature, and composition, and this, in turn, affects the ionosphere. The strong effect of plasma convection on the thermosphere is clearly shown in Figure 8, where measured neutral winds and ion drifts are shown along the track of the DE-2 satellite for one crossing of the northern hemisphere. At the time of the crossing, the IMF was strongly northward and a multi-cell signature is evident in the ion velocities, with sunward flow in the polar cap. The neutral circulation pattern tends to mimic the ion convection pattern. The neutral flow is sunward in the central polar cap, but the wind speed is much smaller than the ion convection speed. Also, the neutral reversal regions are colocated with the ion reversal regions. These results provide evidence for the strong coupling of the ionosphere and thermosphere in the polar regions.

3.5. *Currents, Conductivities, and Convection*

There is a direct relationship between Birkeland currents, ionospheric conductivities, and plasma convection. For example, if the Birkeland currents are known via measurements and the ionospheric conductivities can be calculated, then the convection electric field pattern can be obtained from Ohm's law and the requirement of current continuity. When the IMF is southward, the Region 1 and 2 Birkeland currents dominate (see Figure 4) and the plasma convection pattern has a two-cell signature (see Figure 2). However, when the IMF is northward, an additional current system exists in the polar cap (NBZ currents) and the plasma convection pattern can have multiple cells or become a severely distorted two-cell pattern. Unfortunately, the Birkeland current system has not been measured with a sufficient spatial coverage to resolve this problem. Consequently, the results one obtains are dependent upon how the measured Birkeland current pattern is extended into regions where there are now measurements [*Rasmussen and Schunk, 1987*].

Figure 9 illustrates the above problem for the case when the IMF is strongly northward ($B_z > B_y > 0$). Shown in the upper-left dial of this figure are the unmodified Birkeland currents measured by *Iijima and Shibaji [1987]*. The upper-right dial, on the other hand, shows a possible extension of these currents into the dayside where measurements are

lacking. The extension was accomplished by interpolating along lines of constant latitude so that the dusk region 1 system connects to the dawnside NBZ system. The electric potential patterns calculated from the two Birkeland current patterns are shown in the middle panel. In comparing the two potential patterns, it is apparent that the extension of the current on the dayside is important for northward IMF. For the unmodified currents on the left-hand side, the flow in the morning sector is broken into multiple cells. Although there is evidence for three-cell convection, the NBZ currents are so strong in comparison to the net region 1/region 2 currents, that the strongest flow occurs within the polar cap and the rotation of the equatorward cell in the dawn sector is reversed from its normal sense. For the dayside extension of the currents in the upper-right dial, the flow also has a three-cell nature, although because of the connection of flow on the dayside, convection appears more as a distorted two-cell pattern similar to that shown by *Heppner and Maynard* [1987]. From this viewpoint, convection in the morning sector is seen as a continuation of the evening cell and the resulting large cell raps around the original morning cell, which has been shifted into the polar cap.

4. SUMMARY

Significant progress has been made during the last decade with regard to our understanding of magnetosphere-ionosphere-thermosphere coupling phenomena. However, the bulk of the studies have been qualitative in nature, being based on empirical model inputs for the important magnetospheric parameters (convection electric field, particle precipitation, field-aligned currents, etc.). Therefore, the bulk of the studies pertain to the climatology of the ionosphere-thermosphere system. Nevertheless, the knowledge gained about the system has increased to the point where an understanding of ionosphere-thermosphere weather patterns is on the horizon.

Acknowledgement. This research was supported by the University Research Initiative grant AFOSR F49620-86-C-0109 to Utah State University.

REFERENCES

- Foster, J. C., *J. Geophys. Res.*, **88**, 981, 1983.
- Heelis, R. A., *J. Geophys. Res.*, **89**, 2873, 1984.
- Heelis, R. A., J. K. Lowell, and R. W. Spiro, *J. Geophys. Res.*, **87**, 6339, 1982.
- Heppner, J. P., *J. Geophys. Res.*, **82**, 1115, 1977.
- Heppner, J. P., and N. C. Maynard, *J. Geophys. Res.*, **92**, 4467, 1987.
- Iijima, T., and T. A. Potemra, *J. Geophys. Res.*, **83**, 599, 1978.
- Iijima, T., and Shibaji, *J. Geophys. Res.*, **92**, 2408, 1987.
- Killeen, T. L., R. A. Heelis, P. B. Hays, N. Spencer, and W. B. Hanson, *Geophys. Res. Lett.*, **12**, 159, 1985.
- Oliver, W. L., J. M. Holt, R. H. Wand, and J. V. Evans, *J. Geophys. Res.*, **88**, 5505, 1983.
- Rasmussen, C. E., and R. W. Schunk, *J. Geophys. Res.*, in press, 1987.
- Schunk, R. W., J. J. Sojka, and M. D. Bowline, *J. Geophys. Res.*, **91**, 12,041, 1986.
- Schunk, R. W., J. J. Sojka, and M. D. Bowline, *J. Geophys. Res.*, **92**, 6013, 1987.
- Sojka, J. J., and R. W. Schunk, *J. Geophys. Res.*, **88**, 2112, 1983.
- Sojka, J. J., C. E. Rasmussen, and R. W. Schunk, *J. Geophys. Res.*, **91**, 11,281, 1986.
- Spiro, R. W., P. H. Reiff, and L. J. Maher, *J. Geophys. Res.*, **87**, 8215, 1982.
- Volland, H. J. *J. Geophys. Res.*, **83**, 2695, 1978.
- Wallis, D. D., and E. E. Budzinski, *J. Geophys. Res.*, **86**, 125, 1971.
- Whalen, J. A., *J. Geophys. Res.*, **88**, 7155, 1983.

ILLUSTRATIONS

- Fig. 1. Block diagram showing the four main magnetospheric processes that affect the ionosphere-thermosphere system.
- Fig. 2. Plasma drift trajectories in the polar region for active geomagnetic conditions. Both magnetospheric and corotational electric fields are included. The magnetospheric convection pattern is an asymmetric two-cell pattern of the Volland-type with enhanced flow in the dusk sector and a total cross-tail potential of 90 kV. A magnetic latitude-MLT reference frame is used. From *Sojka and Schunk* [1983].
- Fig. 3. Contours of the auroral electron energy flux for active geomagnetic conditions ($K_p \sim 5$). The contours are labelled in $\text{erg cm}^{-2} \text{s}^{-1}$ and a magnetic latitude-MLT reference frame is used. From the *Spiro et al.* [1982] empirical model.
- Fig. 4. The distribution of Birkeland currents in the northern high-latitude region for active geomagnetic conditions. From *Iijima and Potemra* [1978].
- Fig. 5. Contours of $\log_{10} N_e$ in cm^{-3} (left panel), ion temperature in $^{\circ}\text{K}$ (middle panel), and electron temperature in $^{\circ}\text{K}$ (right panel) in the northern polar region at 1700 UT. The contours are shown in a magnetic latitude-local time reference frame at altitude of 180 and 300 kilometers. From *Schunk et al.* [1986].
- Fig. 6. Contours of electron temperature at 1700 UT for upper boundary electron heat fluxes of 0 (left panel) and -1×10^{10} (right panel) $\text{eV cm}^{-2} \text{s}^{-1}$. An MLT-magnetic latitude coordinate system is used. From *Schunk et al.* [1986].
- Fig. 7. Electron temperature profiles in the nocturnal return current region for three values of the field-aligned return current and for different seasonal and solar cycle conditions. The field-aligned current values are 0 (solid curves), -1×10^{-5} (dotted curves), and -5×10^{-5} (dashed curves) amp m^{-2} . The total heat flux through the upper boundary is $q_T = -1 \times 10^{10} \text{ eV cm}^{-2} \text{s}^{-1}$. From *Schunk et al.* [1987].
- Fig. 8. Neutral winds (bottom panel) and ion drifts (top panel) along a DE-2 track in the northern hemisphere for a northward IMF. The curved lines represent the solar

terminator. Note the scale difference of a factor of 2 for the ion and neutral velocities. From *Killeen et al.* [1985].

Fig. 9. Birkeland currents (upper panel), ionospheric electric potential (middle panel) and ionospheric currents (lower panel) for $B_z > B_y > 0$. The upper-left dial represents the unmodified Birkeland currents of *Iijima and Shibaji* [1987], while the currents in the upper-right dial have been extended into the dayside and nightside. In the upper panel, current flowing into the ionosphere is plotted as solid curves, while current flowing away from the ionosphere is plotted as dashed curves (the difference between contour levels is $0.3\mu\text{A}/\text{m}^2$). In the middle panel the solid curves represent a positive potential, while the dashed curves represent a negative potential (the difference between contour levels is 3kV). For the lower panel the vector scale is 400 A/km. From *Rasmussen and Schunk* [1987].

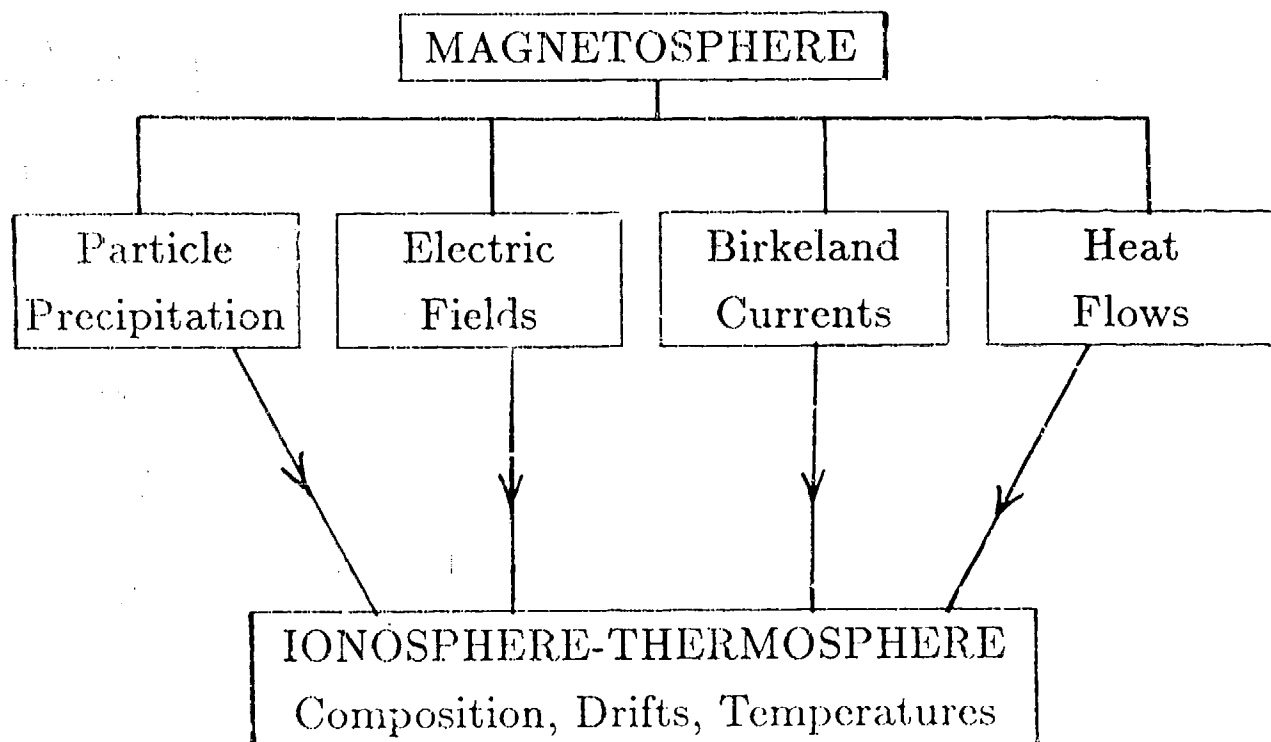


Figure 1

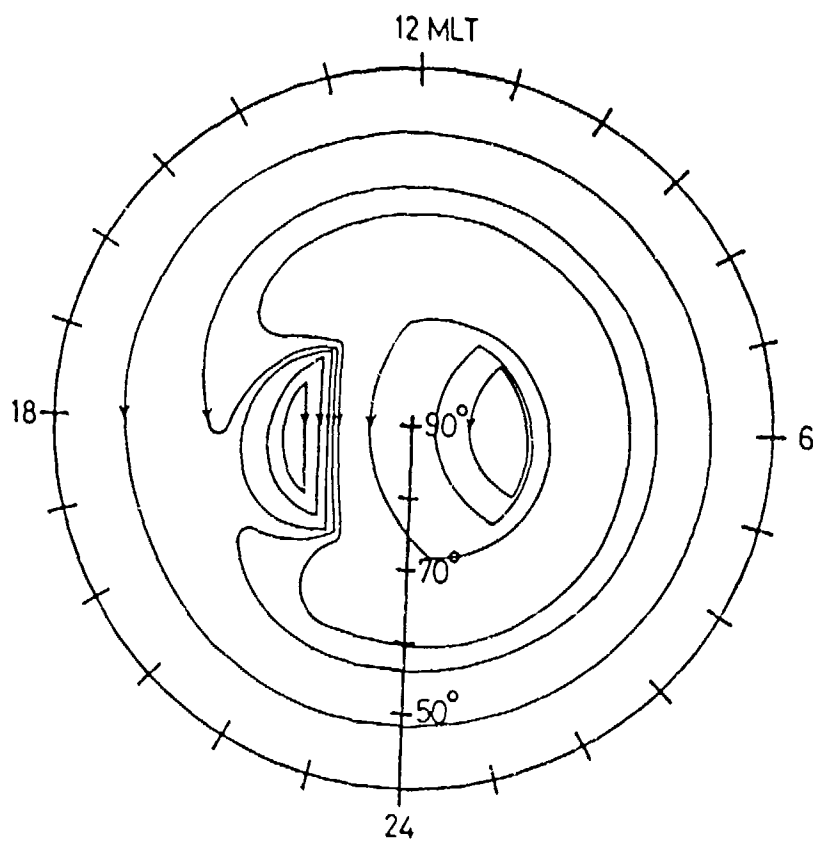
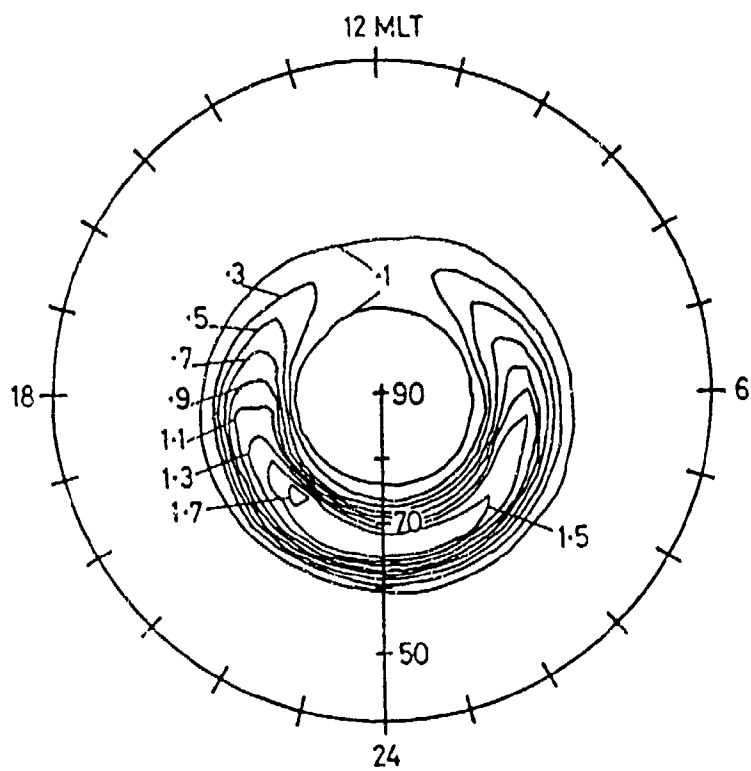


Figure 2



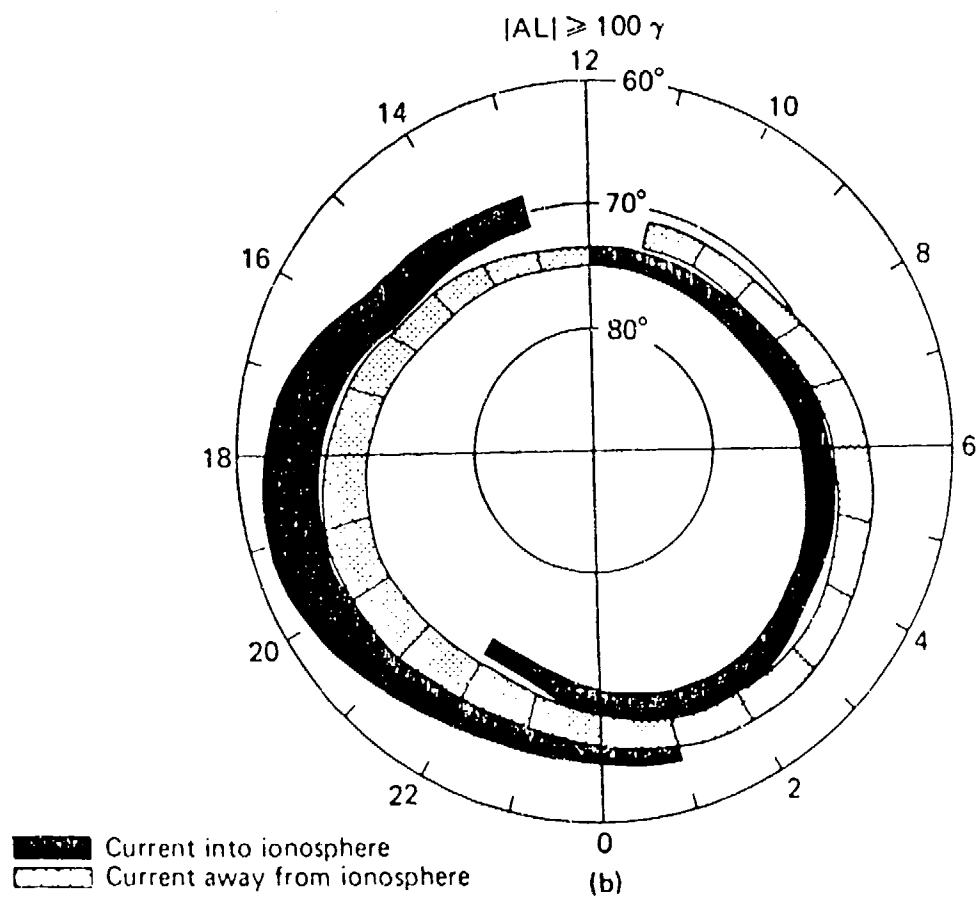
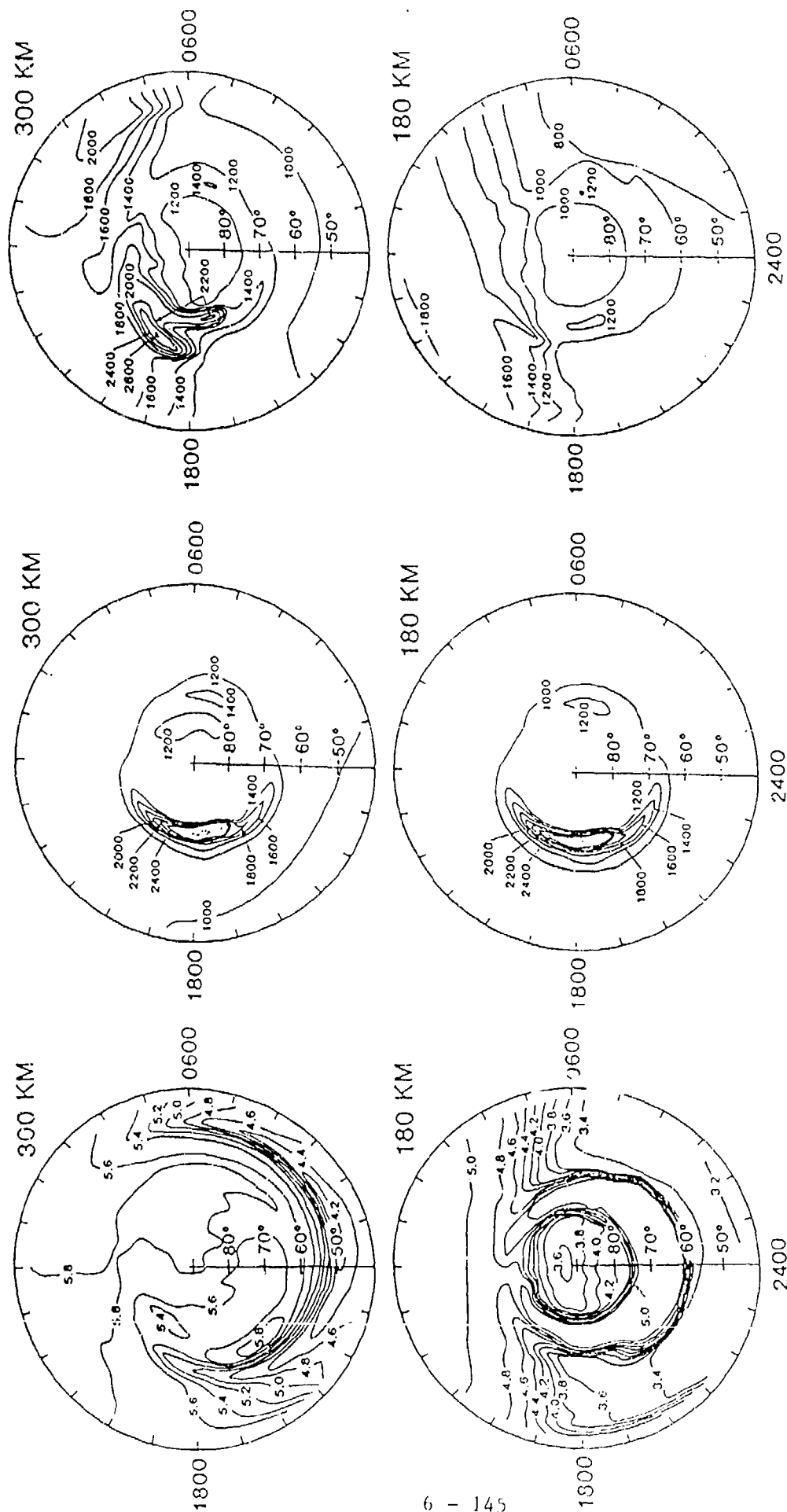


Figure 4



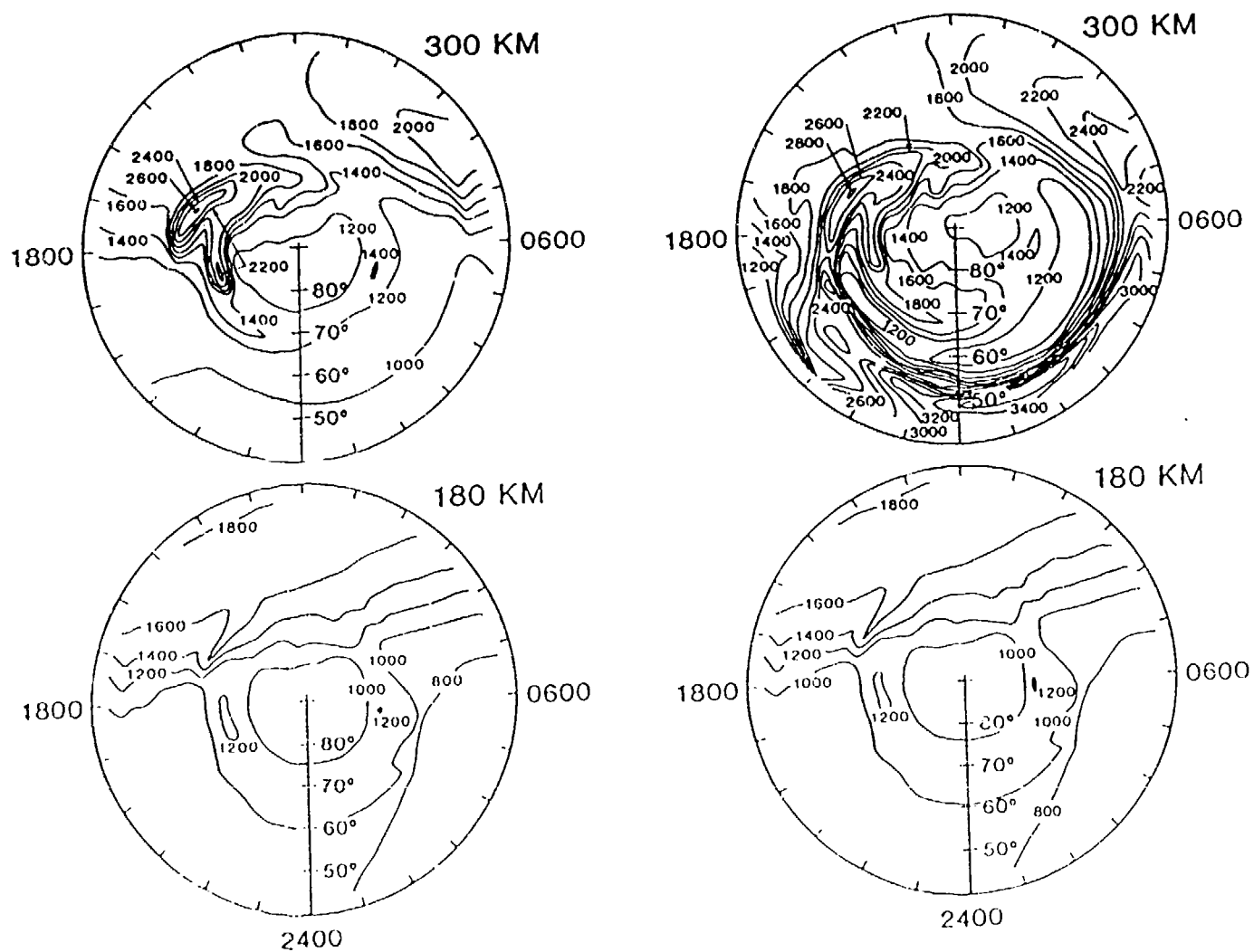


Figure 6

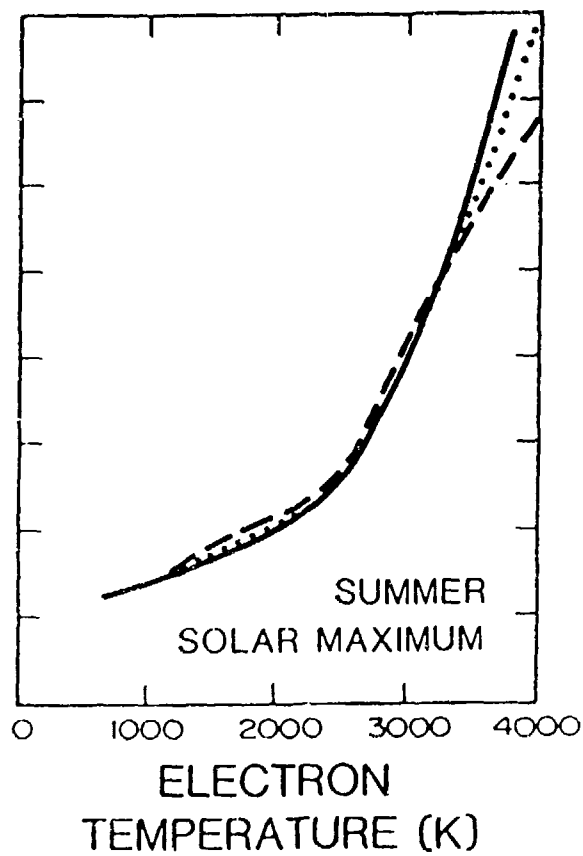
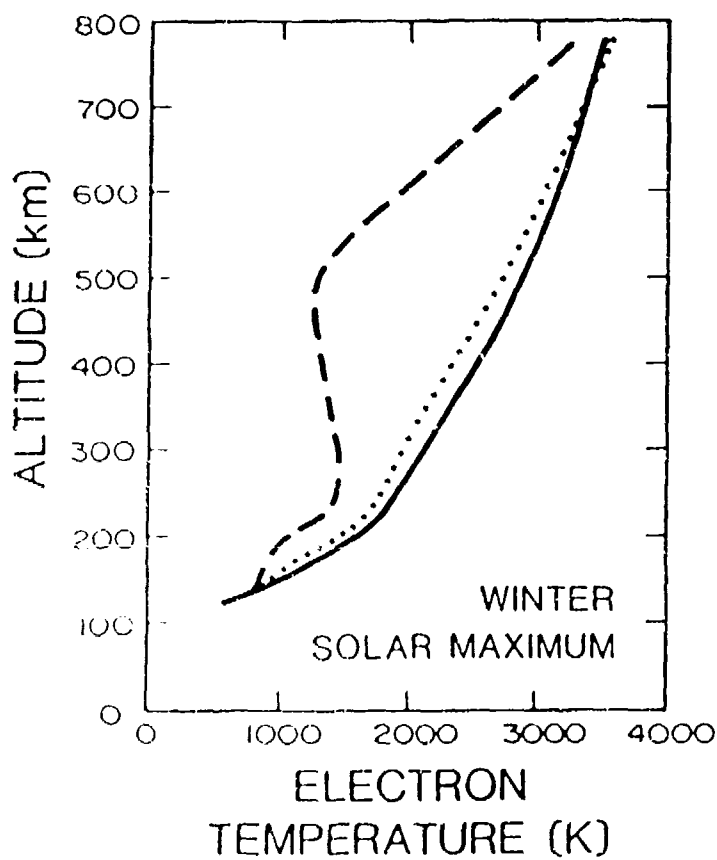
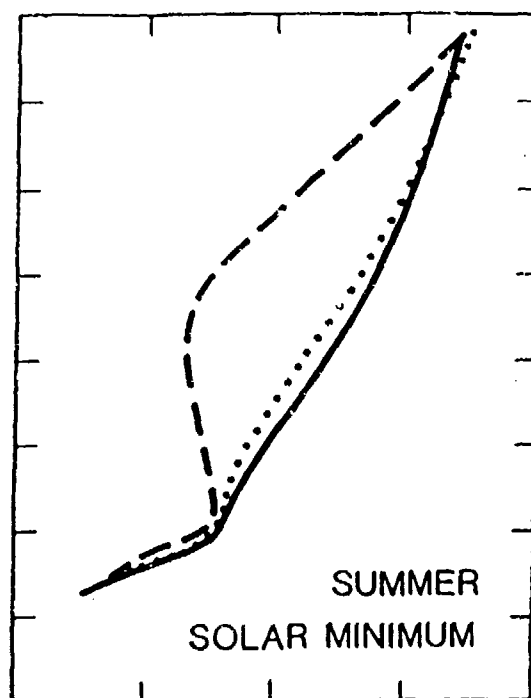
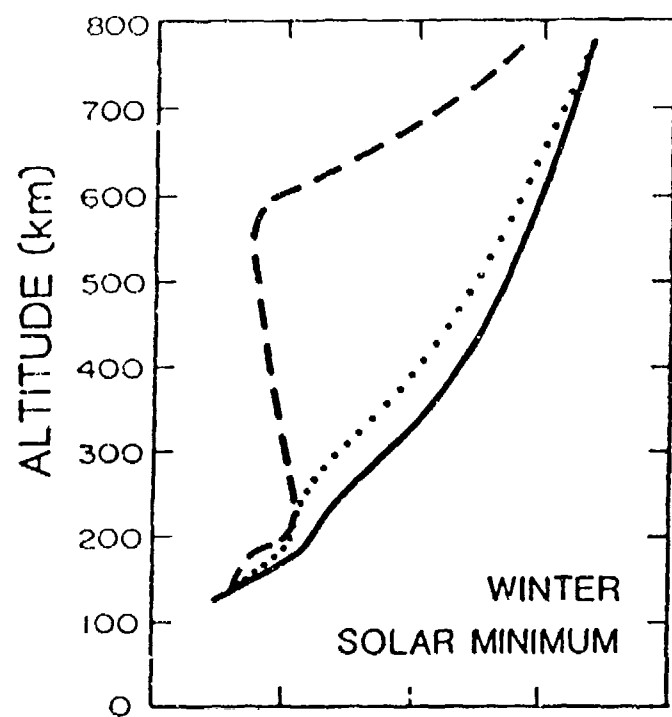


Figure 7

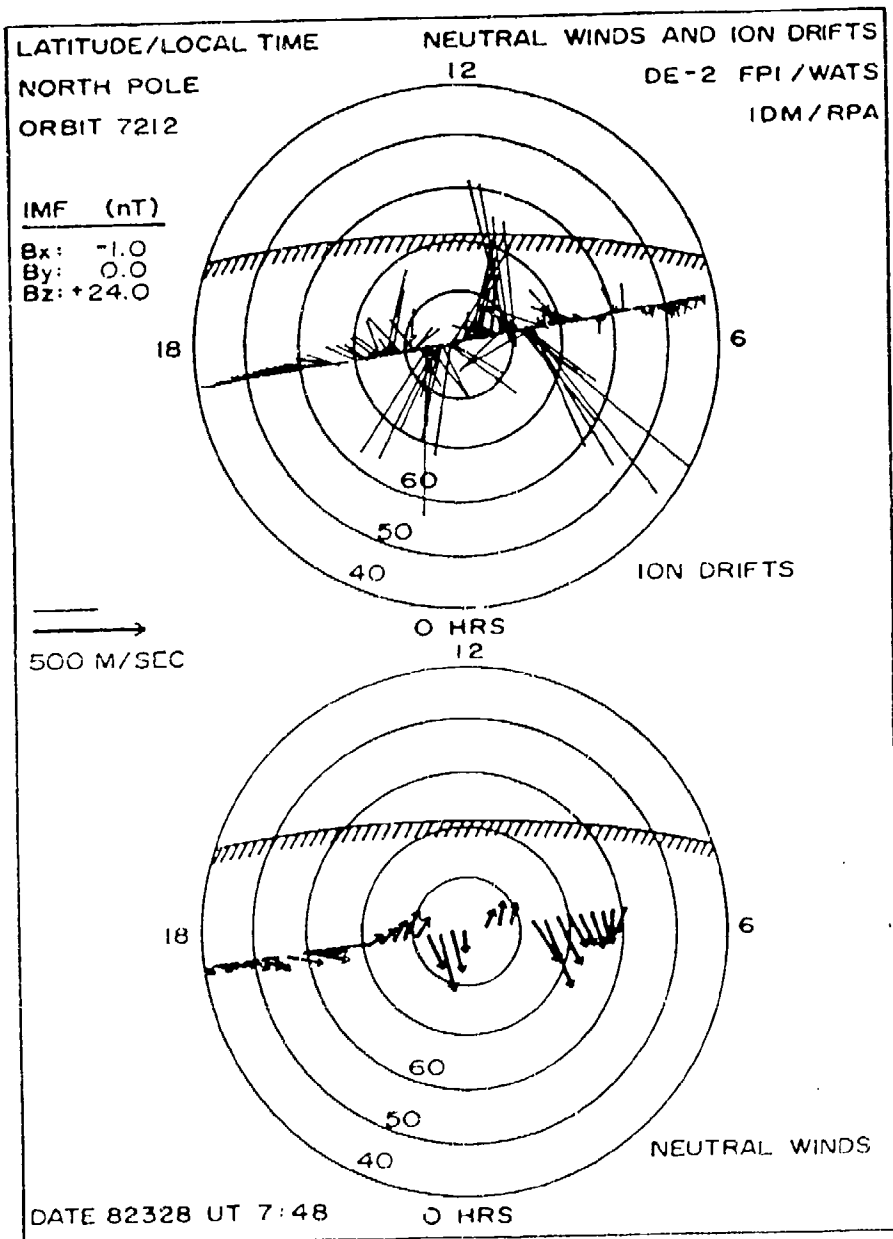


Figure 8

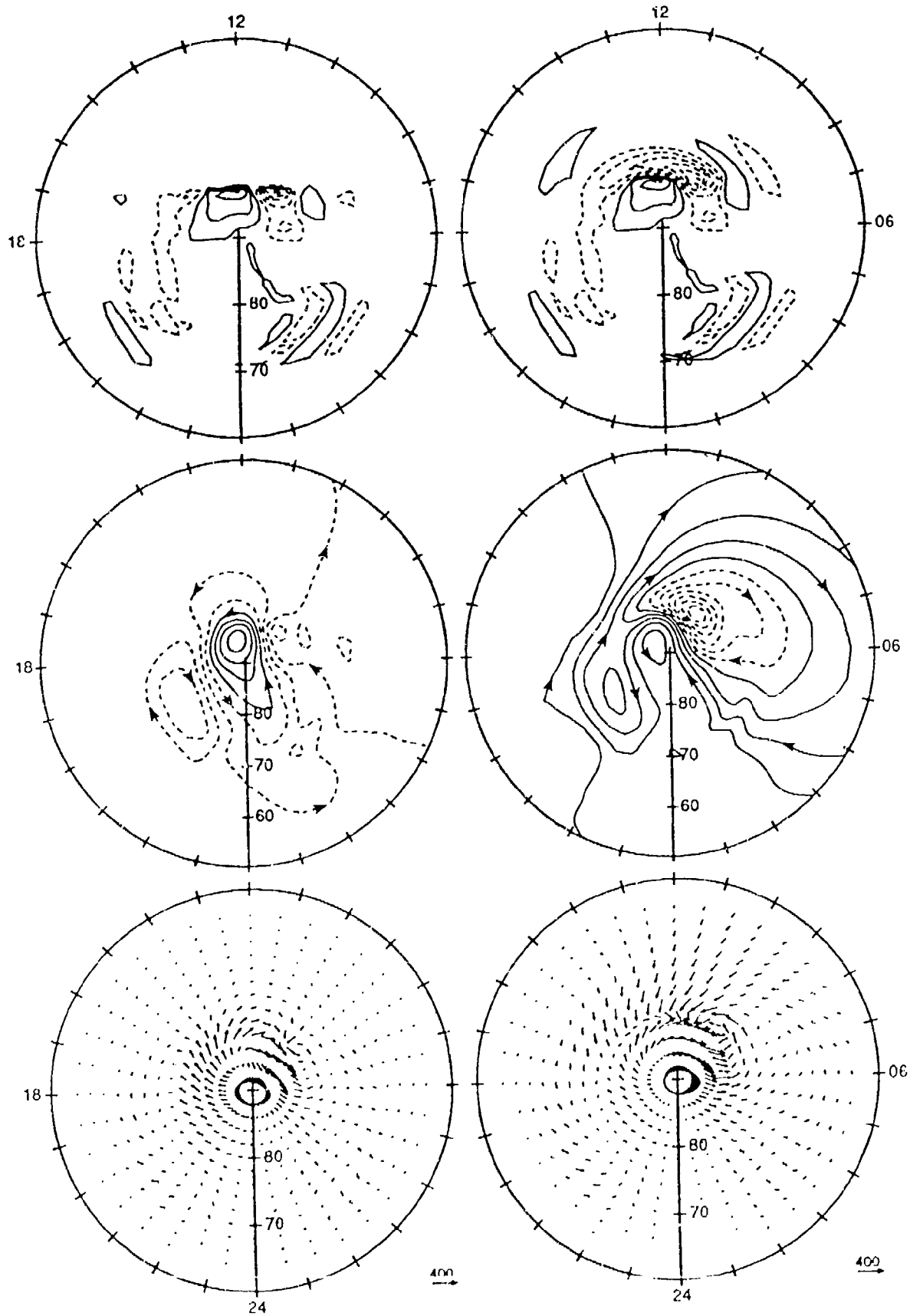


Figure 9

6.6

IONOSPHERE/THERMOSPHERE
COUPLING

by

D. N. Anderson
Geophysics Laboratory

IONOSPHERIC COUPLING

WITH TGCM'S

O NCAR MODEL

EULERIAN APPROACH FOR BOTH IONOSPHERE AND NEUTRAL ATMOSPHERE - GLOBAL

O UCL MODEL

EULERIAN - NEUTRAL ATMOSPHERE

LAGRANGIAN - IONOSPHERE

COUPLED AT HIGH LATITUDES

EMPIRICAL CHIU MODEL AT MID AND LOW LATITUDES

O USU MODEL

EULERIAN - NEUTRAL ATMOSPHERE

LAGRANGIAN - IONOSPHERE

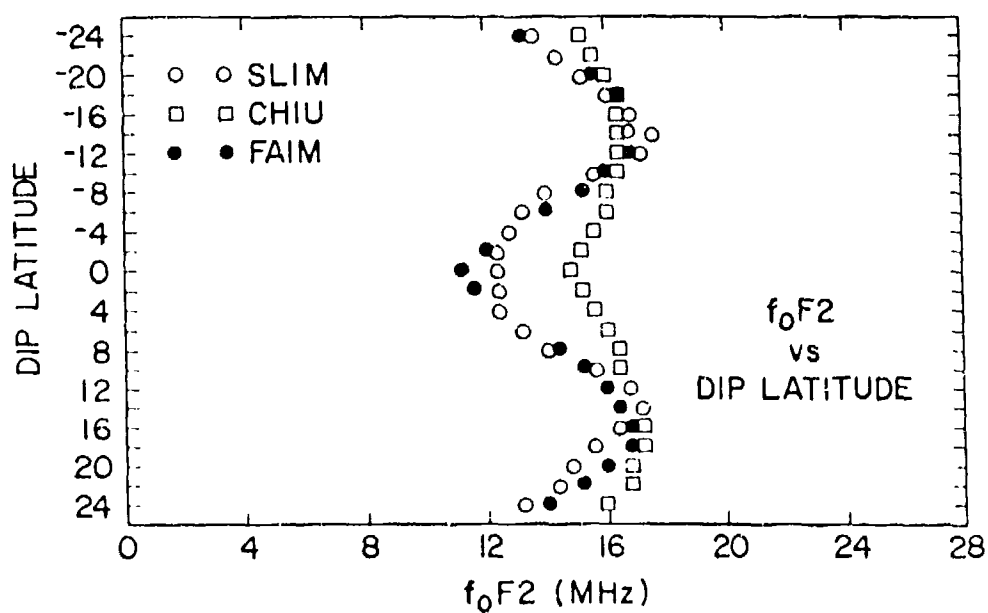
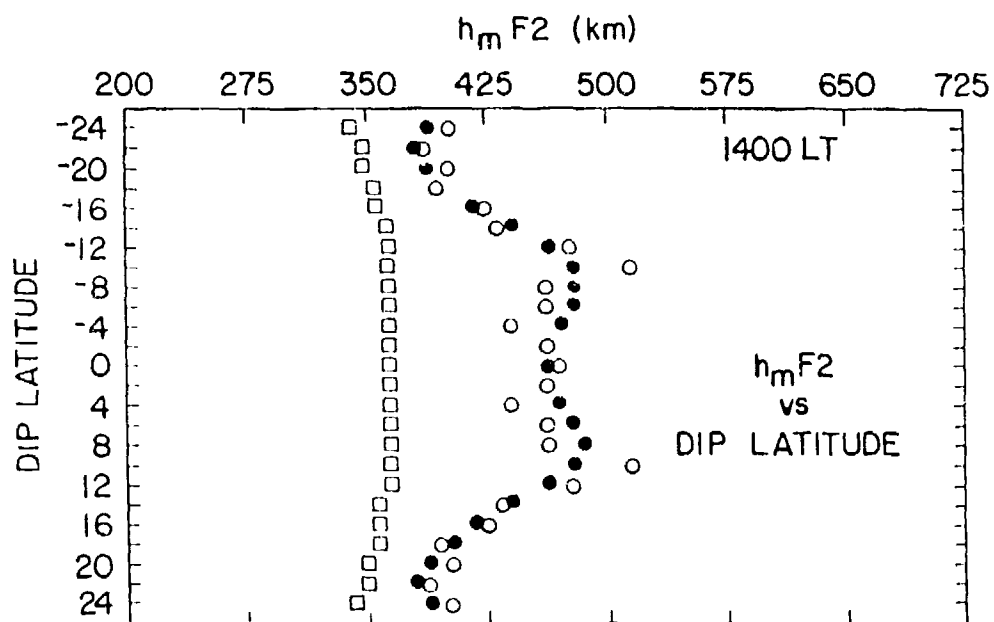
CAPABILITY EXISTS TO USE EULERIAN FOR BOTH - GLOBAL

COMPUTATIONALLY - FAST
IONOSPHERIC MODELS

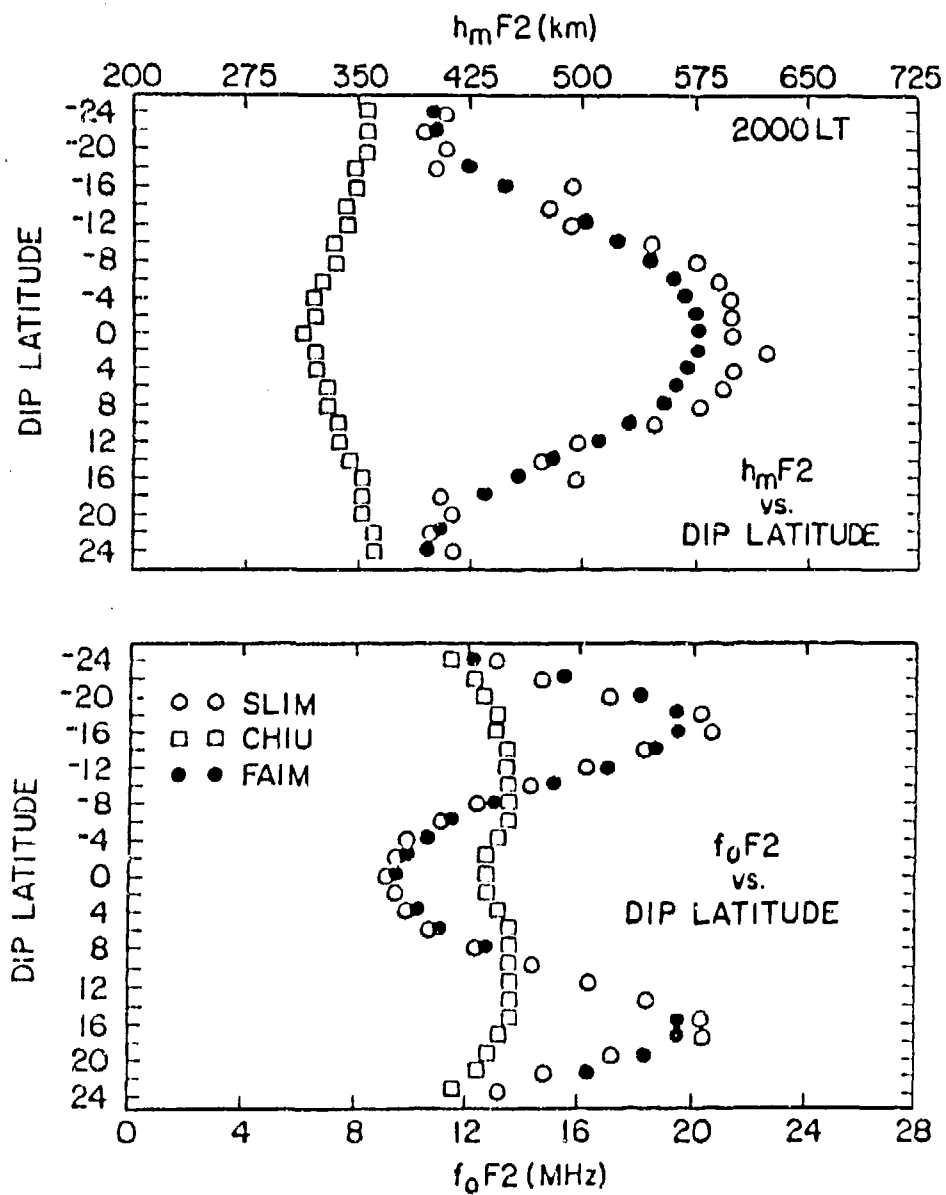
U CHIU	-	EMPIRICAL
O IRI	-	EMPIRICAL
O ICED	-	AWS OPERATIONAL MODEL
O SLIM	-	SEMI-EMPIRICAL, LOW-LATITUDE IONOSPHERIC MODEL

A Fully Analytic, Low and Middle Latitude Ionospheric Model

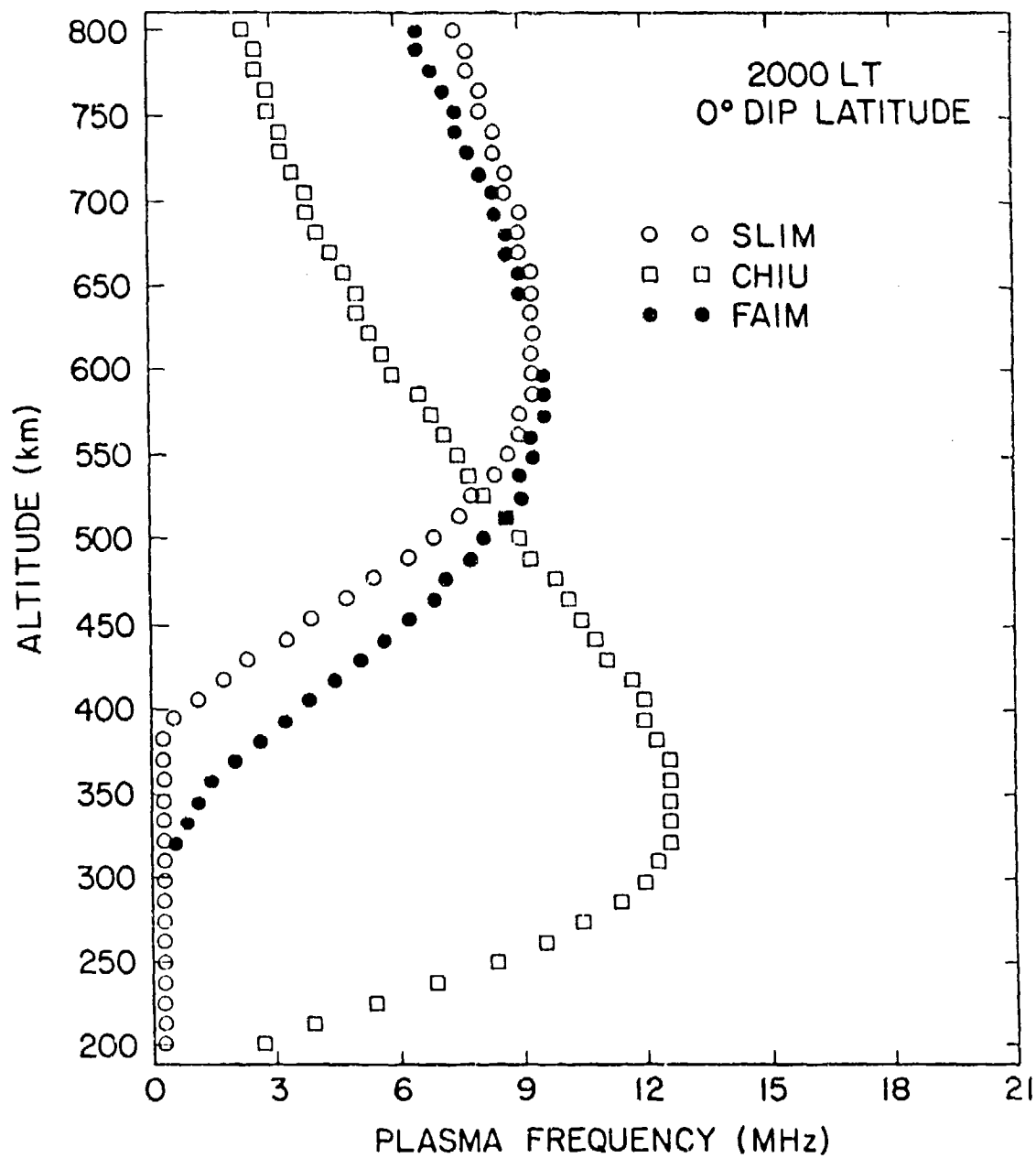
The well-known Chiu ionospheric model is a global empirical model which calculates electron density profiles as a function of latitude, local time, season and solar cycle. It is extensively used by thermospheric dynamicists because its analytic formulation can quickly provide global electron density values. The model, however has serious shortcomings. Recently, a fully analytic ionospheric model (FAIM) based on the Chiu formulation has been developed which provides much more realistic, low and mid-latitude electron density distributions. This is accomplished by redefining the latitude and local time dependence of parameters such as hmF2, nmF2 and the topside and bottomside scale heights. The modifications are based on recently-developed Semi-empirical, Low-latitude Ionospheric Model (SLIM) and involves decomposing hmF2, nmF2 and plasma density scale heights into harmonic terms to describe the local time variations and then applying Hermite polynomials to obtain latitude variations. The analytic model generates electron density profiles under solar cycle minimum, moderate and maximum conditions for winter, summer and equinox periods.



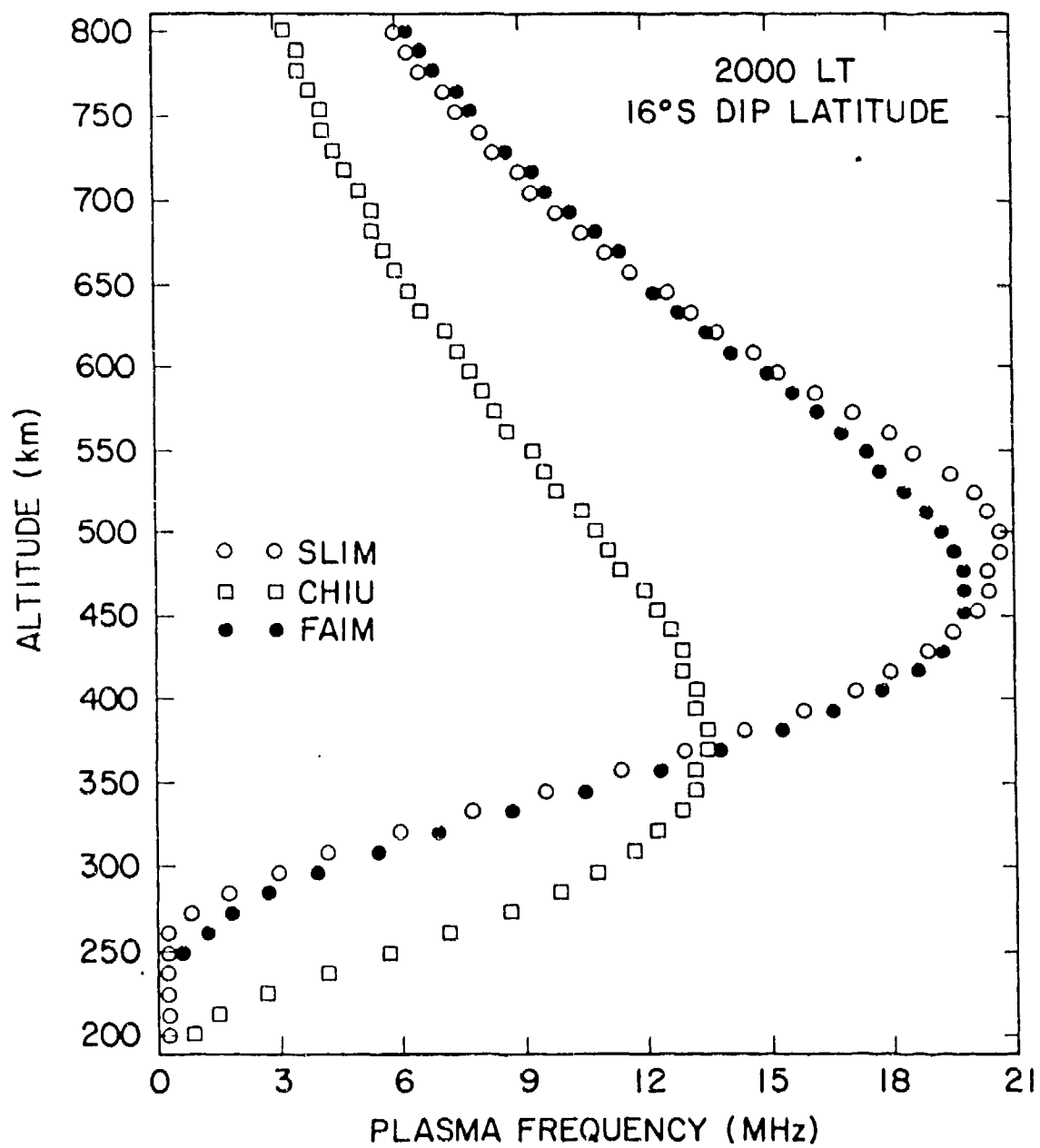
Comparison of $h_m F2$ and $f_o F2$ values as a function of dip latitude at 1400 LT given by SLIM, CHIU and FAIM for solar cycle maximum, equinoctial conditions.



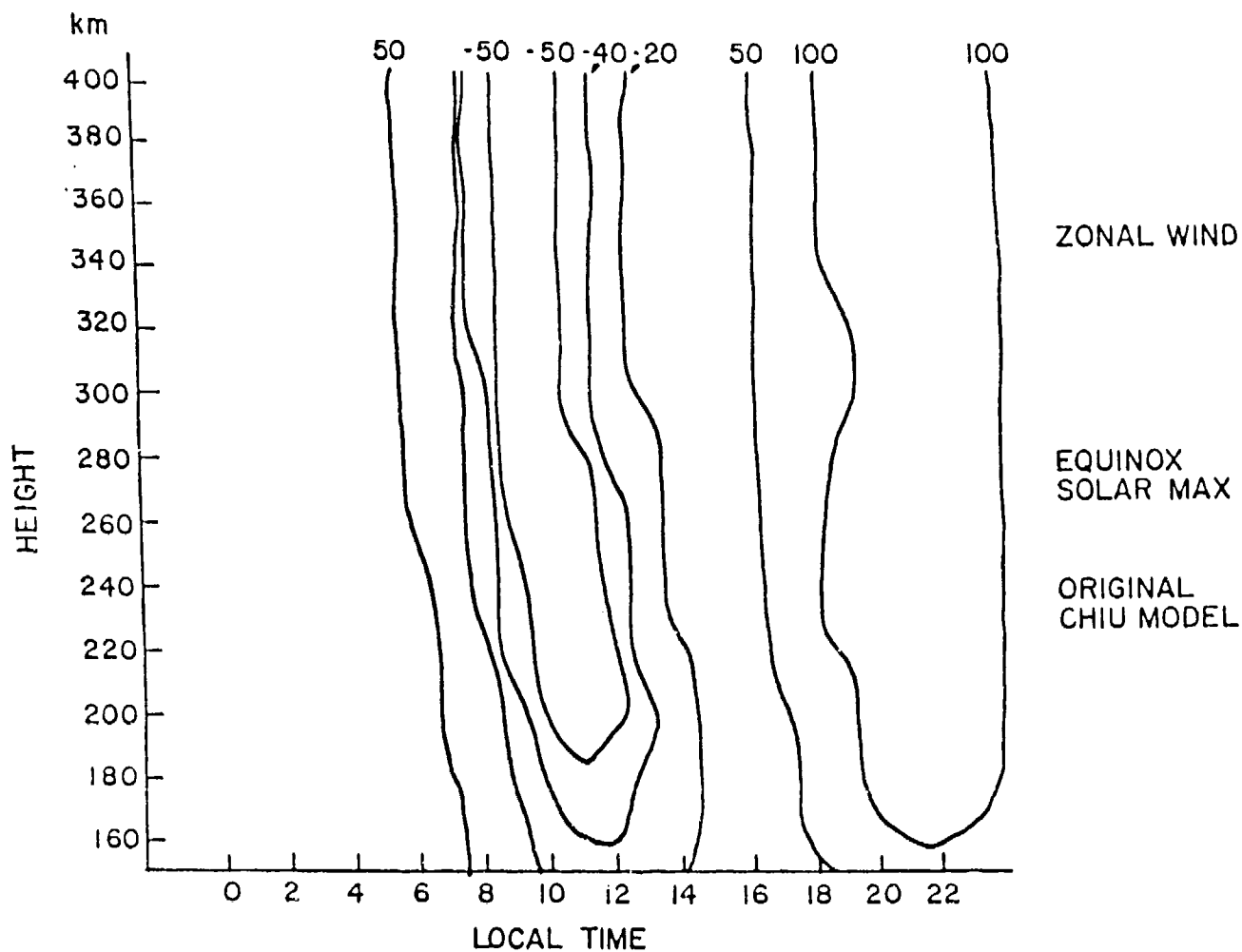
Comparison of h_mF2 and f_oF2 values as a function of dip latitude at 2000 LT given by SLIM, CHIU and FAIM for solar cycle maximum, equinoctial conditions.



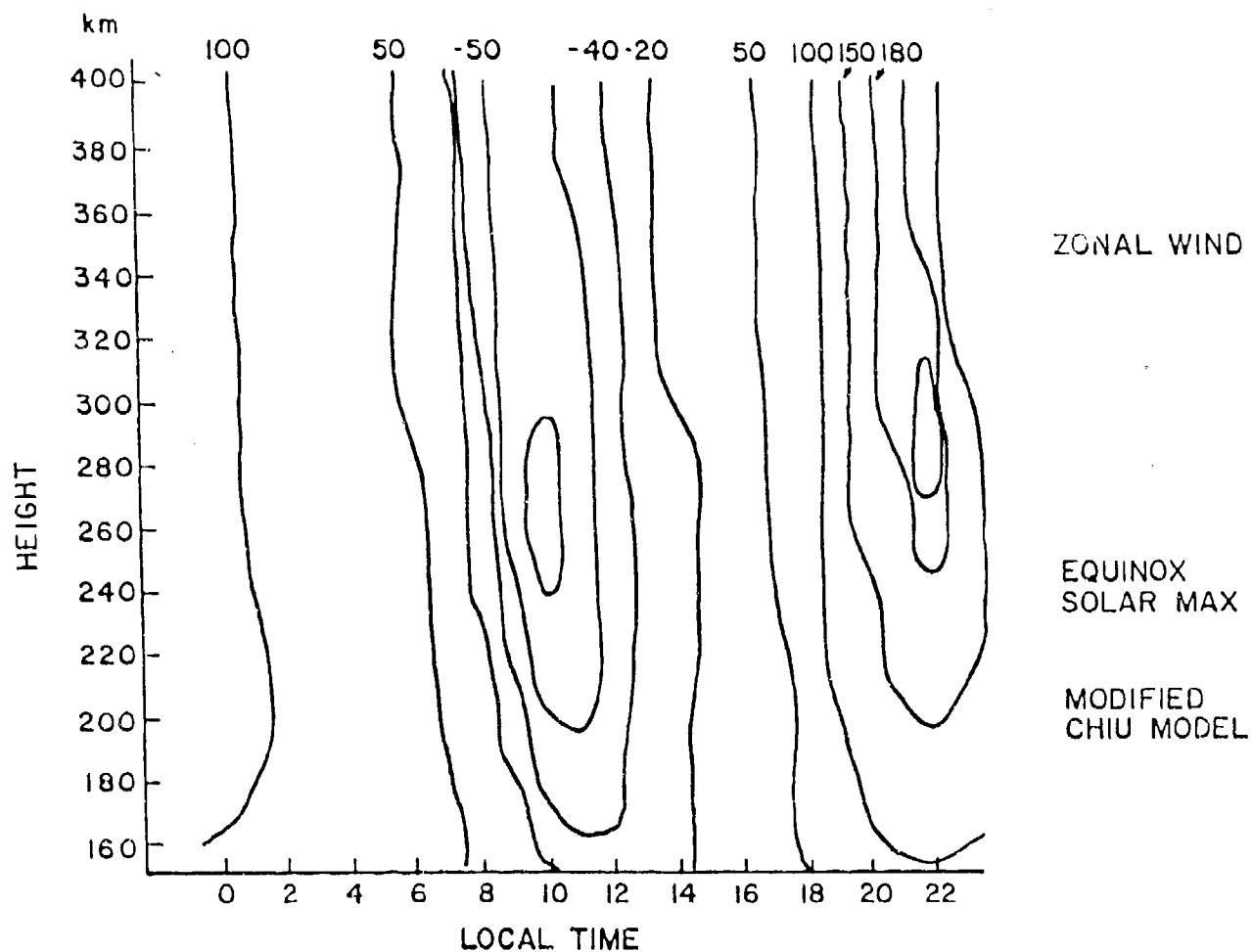
Comparison between SLIM, CHIU and FAIM electron density profiles at the magnetic equator at 2000 LT.



Comparison between SLIM, CHIU and FAIM electron density profiles
at 16° S. dip latitude at 2000 LT.



Contours of calculated wind velocity (m/sec) at the magnetic equator as a function of altitude and local time. The original Chiu ionospheric model was incorporated under equinoctial, solar maximum conditions. Positive values represent an eastward neutral wind.



Contours of calculated zonal neutral wind velocity (m/sec) at the magnetic equator as a function of altitude and local time. The modified Chiu of FALM model was incorporated under equinoctial, solar maximum conditions. Positive values represent an eastward neutral wind.

FUTURE DIRECTIONS

- | | | |
|--|---|-----------------|
| O THERMOSPHERE/IONOSPHERE
COUPLING - FIRST PRINCIPLES | - | EXISTS |
| O TGCM/ANALYTIC IONOSPHERE
COUPLING | - | BEING DEVELOPED |
| O ANALYTIC THERMOSPHERE/
IONOSPHERE COUPLING | - | POSSIBLE? |
| O HOW TO INCORPORATE REAL TIME DATA | | |

6.7 GLOBAL

THERMOSPHERIC SPECIFICATIONS AND FORECASTING

Capt. Chris Tschan
HQ AWS/DNXP

(This paper is an excerpt from "Upper-Thermospheric Observations and Neutral-Gas Dynamics at High Latitudes During Solar Maximum", University of Michigan Technical Report submitted in partial fulfillment of Ph. D. requirement, 1987)

ABSTRACT

The primary objective of this work was to understand the neutral-gas dynamics in the high-latitude regions of the Earth's upper thermosphere. To achieve this, an understanding of the morphology of the neutral winds and the forces which drive or modify them was required. To this end, a unique 70-orbit December-solstice dataset was established, which included satellite neutral winds and other supporting data from Dynamics Explorer 2 (DE-2), with coverage of both polar caps during the same orbit. Analysis of this data led to the characterization of four basic high-latitude neutral-wind signature categories for each hemisphere under various interplanetary-magnetic-field (IMF) configurations. Furthermore, sunward neutral winds on the duskside of the polar cap, resulting from the mapping of the twin-cell ion convection onto the neutral gas through ion-neutral collisions, were well established in all cases. However, the dawnside sunward neutral winds were not as well established. The existence of a small region of dawnside neutral winds was noted in the winter northern hemisphere, but was usually absent in the summer southern hemisphere. Analysis of the individual neutral-gas forces for solar-maximum December-solstice from the NCAR thermospheric general circulation model (TGCM), led to the realization that the polar-cap pressure-gradient force in the winter northern hemisphere had a different orientation than in the summer southern hemisphere, resulting in the observed dawnside neutral-wind signatures. The variations in the orientation of the polar-cap pressure-gradient forces in opposite hemispheres were ascribed to temperature gradients, resulting from a superposition of solar-EUV, Joule and cusp heating, as well as density variations.

The unique DE-2 dataset was then applied to two different time-dependent tests of the NCAR-TGCM, with the intention of evaluating the eventual use of the TGCM for thermospheric forecasting. The first test was a quantitative evaluation of the accuracy of TGCM-simulated neutral winds, which were compared against DE-2 measured neutral

winds. The results of this test were that the NCAR-TGCM provides good first-order simulated neutral winds. However, the TGCM time-dependent neutral winds were, on average, in error by 10 - 40% of the measured neutral-wind velocity. This was primarily attributed to the inability to accurately model the ion-drag neutral-gas momentum source. The second test was intended to assess our ability to use DE-2 measured ion-drift data to provide a more realistic time-dependent prescription of model ion-convection parameters in both hemispheres for the TGCM. Results show that use of ion-drift data, under selected geophysical conditions, can improve the ability of the TGCM to simulate thermospheric neutral winds.

Finally, a possible technique for providing a time-dependent prescription of the high-latitude ion-convection parameters in both hemispheres, for use in a short-range numerical thermospheric forecast of 12 to 24 hours, was noted. This technique involves associating a past series of observed ion-convection parameters corresponding to particular change in the orientation of the IMF, with a similar epoch currently being observed. This technique shows promise, but more data, of the type provided by DE-2, is needed before a full-scale evaluation can take place.

PROSPECTS FOR NUMERICAL THERMOSPHERIC FORECASTS

1 Possible Methods of Forecasting the High-Latitude Ion-Convection Parameters

Based on the results of the time-dependent thermospheric modeling, it has been shown that knowledge of the interplanetary-magnetic-field (IMF) is required to simulate the high-latitude thermospheric dynamics. The most important influence on the high-latitude thermospheric circulation at high latitudes of both hemispheres is the distribution of the polar-cap electric field. Furthermore, the time-dependent morphology of the polar-cap electric field is controlled mainly by the orientation of the north-south component of the IMF. Therefore, in order to numerically forecast thermospheric circulation, one must have a series of model-ion-convection parameters which will precisely describe how the ion convection will vary with time. This requires a reasonable prediction of the IMF orientation or more simply, the future polar-cap electric-field distribution. However, there are many problems in understanding the seemingly random behavior of the IMF. Furthermore, without a prediction of the IMF orientation, accurate predictions of the polar-cap electric field are not likely.

In the search for a practical method with which to provide the model-ion-convection parameters for numerical thermospheric forecasts, a couple of different approaches were tried. These included attempts to forecast the IMF B_z component for the next 24 hours, based on its trend over the previous two hours. The approach which offered the most encouragement for use in establishing an early thermospheric-forecast capability was a mixture of statistical techniques borrowed from tropospheric

meteorology. The mix of techniques involves forecasting persistence in the IMF and polar-cap electric-field conditions during slowly-changing conditions. However, when a large and persistent change in the north-south component of the IMF was recorded over a two-hour period, then a new time-dependent series of ion-convection parameters would be used, corresponding to a historical variation of ion-convection parameters for IMF conditions most closely matching the currently-observed trends. These ion-convection parameters would be based on IMF parameters observed in real time and would be used as input to a numerical thermospheric global-circulation model (TGCM). The output of the model would be the thermospheric neutral-wind forecast.

One may also ask why a thermospheric-forecast capability be of interest? A thermospheric-forecast capability would be an excellent research tool, allowing us to test our current knowledge against the natural variability which exists in every aspect of atmospheric science. In addition, there are practical interests related to the horizontal transport of ionic and neutral species.

2 Attempts to Forecast the IMF

It has been known for many years that fluctuations in the IMF, ΔB , are on the same order of magnitude as the magnetic-field itself (Barnes et al., 1984). The random behavior of the IMF is similar to that measured by a surface-wind-direction recorder. With this in mind, the approach usually taken to categorize the IMF is statistical and is similar to that used in turbulent fluid mechanics.

Using statistical autocorrelation theory, Jokipii (1972) used Mariner-4 IMF data to observe the power spectra of IMF fluctuations. In figure 1, it is seen that most of the power is in the low-frequency oscillations. The high-frequency oscillations had very little power and were almost totally uncorrelated. The correlation time, after which the IMF has no memory of its past, is estimated to be on the order of several hours. This

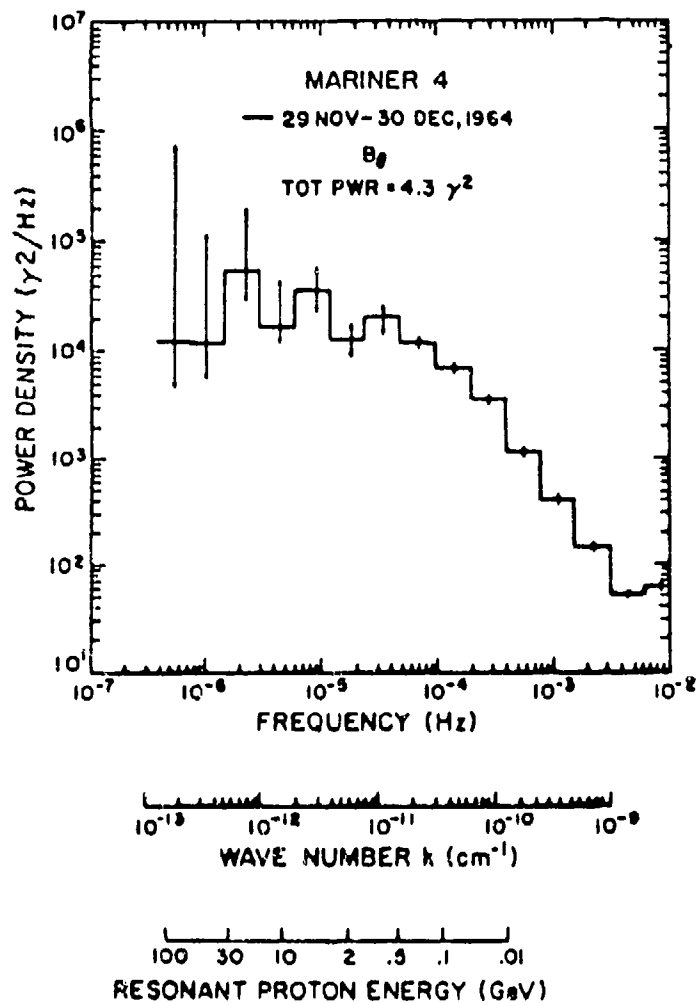


Figure 1 - The power spectrum of the component of the IMF normal to the solar-equatorial plane, observed by Mariner-4 (Jokipii, 1972).

makes it virtually impossible to forecast the IMF for periods longer than one correlation time.

After taking the above factors into consideration, it was still considered interesting to see if the IMF B_z component, which controls the magnitude of the cross-polar-cap convection-electric field could be forecast under certain conditions. If IMF forecasting proved to be impossible for useful time periods, at least quantification of these attempts could be useful. Hourly-averaged IMF data, covering the 507 days of the DE-2 mission from August 1981 to February 1983, was used as the database from which IMF "hindcasting" was attempted. Although use of hourly-averaged IMF data eliminated most of the higher-frequency fluctuations, this data still represents a reasonably accurate mean for each hour and its use in IMF forecasting for the 12 - 24 hour period was the goal.

In order to use the hourly-averaged IMF data over the DE-2 mission, to provide insight on how the IMF B_z component responded over the next 24 hours, given an observed trend, the data must be properly binned. It was determined that the selection criteria for binning the IMF data, over a 24-hour period, would be a change in IMF B_z component over the past two hours. A one-hour trend in B_z was sometimes shown to be a false indicator of an ongoing IMF trend because the time scale of the trend and the time resolution of the averaged IMF data were the same. Thirty bins of $\partial(B_z)/\partial t$ were created, from +15 to -15 nanoTesla (nT), separated by a one nT absolute value change in B_z over two hours.

The mean values of the actual IMF B_z component at the end of the two hours were used to designate the proper bin row, then the corresponding IMF B_z values for the next 24 hours were placed in this bin row. Selected results are shown in figure 2. Basically, if the IMF goes up by several nT during a two-hour period, then the starting value of B_z is large and the wave train appears to move back to background levels over the next 24 hours. The same is true for a significant IMF downward trend over two hours. In that case, the B_z component returns to approximately zero after a few hours. When the $\partial(B_z)/\partial t$ value was unchanged over two hours, the follow-on hours also showed little change.

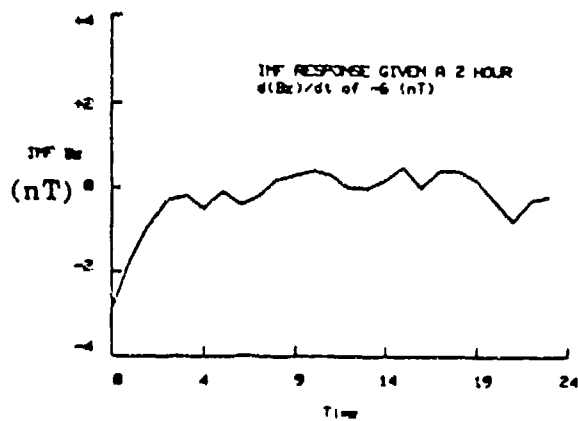
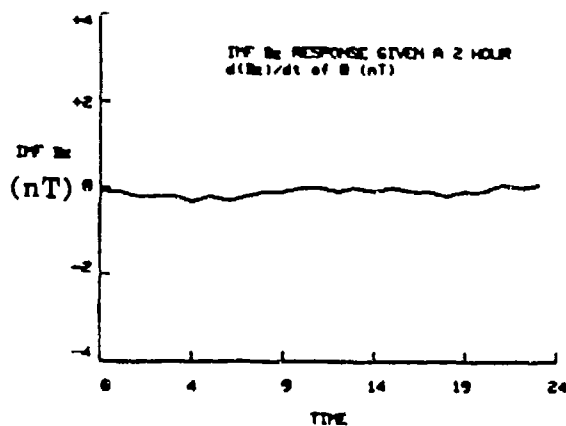
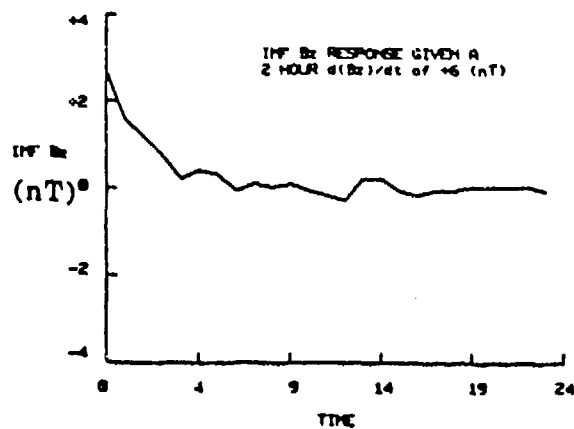


Figure 2 - A three-panel plot of the time response of the average value of the IMF B_z-component (in nT) to various changes in the IMF B_z-component over a two-hour period, using hourly-averaged ISEE-3 data for the 507 days of the DE-2 mission.

Though the above results were intuitively expected and seemed hopeful, it was not known if the reason that the mean B_z component after several hours was close to zero was because the magnitude of B_z was decreasing, as hoped or, at the other extreme, that random, large-scale fluctuations in B_z were cancelling each other out. To discover the answer to this question, the same procedure as above was repeated, except the mean absolute value of B_z over a 24-hour period was found. The results are also shown in figure 3. They show that even though most of the high-frequency oscillations are eliminated, the hourly-averaged data has little memory of past events and the absolute magnitude of the IMF varies little over the 24 hour "forecast" period. This left little hope for forecasting the IMF B_z component.

3 Forecasting Model-Ion-Convection Parameters

Only long-lived major changes in the IMF B_z component, not small ripples, were expected to exert a significant influence on the thermosphere by causing major changes in the ion convection. It was arbitrarily assumed that the change necessary to see a significant effect in thermospheric circulation due to a change in ion convection, is on the order of $\Delta B \sim 5$ nT or greater. Furthermore, it was assumed that this change must remain in effect for more than one hour to have a significant effect on the thermospheric neutral winds, based on the actual ion-neutral time constants. Therefore, it was desirable to make the connection between significant changes in the IMF B_z component, which would effect IMF/magnetospheric/ionospheric coupling, and ion-convection parameters. The intent here was to track past changes in the IMF and relate them to a set of time-dependent ion-convection parameters in both hemispheres. Then, after observing many such events, it might be possible to associate past changes in the IMF with a respective set of time-dependent ion-convection parameters, then apply this historical time sequence of ion-convection parameters as the prescription for future changes. This is based on the assumption that time-dependent model-ion-convection

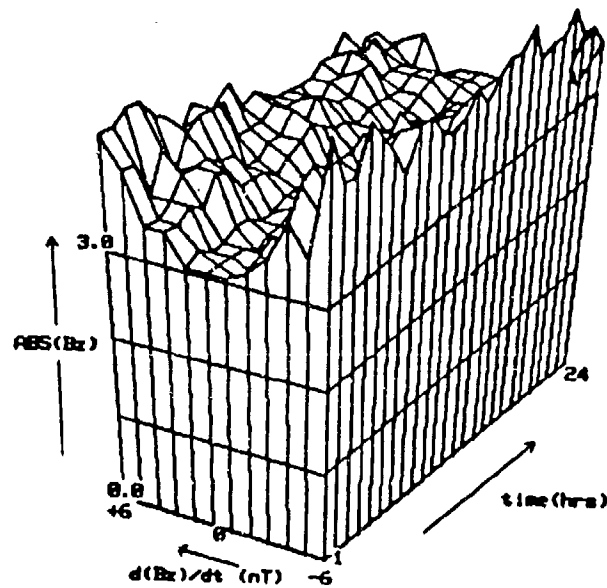


Figure 3 - A three-dimensional plot of the time response of the absolute value of the IMF B_z -component to various changes in the IMF B_z -component over a two-hour period, using the same ISEE-3 data as in figure 2.

parameters respond similarly under similar time-dependent variations in IMF conditions.

To illustrate this, assume the IMF turns sharply southward. Under these conditions, the electric field, transmitted via the magnetosphere to the polar-cap ionosphere as a result of increased magnetic merging. As a result, the ion drifts quickly increase and the polar-cap region expands, just like the storm case analyzed in Sec. 1.

The thermospheric circulation is "spun-up" due to this "kick" and over the next several hours, slowly spins down. Based on observations of the DE-2 neutral winds for the time-dependent case used previously, subsequent southward turnings of the IMF or "kicks", especially if they are smaller than the original, have a little effect on the thermosphere because the difference between the ion and neutral velocities is reduced resulting in a smaller ion-drag force. Recall from figure 1 that there were several transitions from $B_z > 0$ to $B_z < 0$ following the onset of the large geomagnetic storm. However, the highest-velocity polar-cap neutral winds were established early in the storm and decreased with time. The polar-cap neutral winds did not appear to reach new maximum velocity levels each subsequent time the IMF turned sharply southward. This upper-thermospheric observation may be related to the thermospheric-modeling efforts of Roble et al. (1987a) where it was found that the lower-thermospheric-circulation features, once established, tended to persist several hours after the substorm forcings have subsided. The same effect is seen here for upper-thermospheric neutral-wind-circulation systems. This means that the most important ion-convection parameters to model are those associated with the initial southward-turning of the IMF (i.e., the "kick").

At the other extreme, for periods when the averaged-IMF turns sharply positive, the coupling between the IMF and the magnetosphere is reduced. Ion-convection parameters corresponding to a similar northward-turning IMF case could then be used as input to the TGCM. In the case where the measured IMF B_z component is quasi-

steady, no changes would be required. A forecast of persistence would be applied and there is no need to change the set of ion-convection parameters currently being used.

The advantage of this method is simplicity. To illustrate this see the flowchart for a tentative thermospheric-forecasting capability (figure 4). Only certain, directly-measured IMF quantities are required to be monitored and the need for much of the uncertain aspects of solar and magnetospheric physics is eliminated. Further, only when significant long-lived changes in the IMF occur, would an update of the present forecast required. In addition, the thermospheric circulation has been shown previously to display a daily periodicity and only a finite number of IMF B_z trend bins and the associated averaged time-dependent ion-convection parameters, for both storm and steady states are anticipated. The number of sets of ion-convection parameters is estimated to be on the order of 20, for the solar-maximum conditions considered here. This means all cases could be run in advance and the results stored for later use. Under these conditions, the vector-spherical-harmonics (VSH) model of Killeen and Roble (1986) could be extremely useful. The output of each run of the TGCM could be reduced to a set of truncated coefficients which can be stored on a microcomputer. When the need for a new forecast arises, the set of coefficients corresponding most closely to the IMF B_z changes measured can be used with the VSH model to regenerate the neutral winds at selected altitudes and universal times. The reconstituted neutral-wind circulation has been shown to be an almost perfect match to the original neutral-wind results. Furthermore, use of the VSH model no longer requires a significant period of time for the TGCM to be run in realtime on a supercomputer.

This tentative thermospheric-forecasting capability is quite unusual in the world of atmospheric science. The ability to quickly forecast the dynamics of the atmosphere using a finite set of pre-run coefficients is quite different from forecasting tropospheric weather. All that's required to provide the foundation for this forecasting capability is to continue the "hindcasting" process begun previously.

Flowchart of thermospheric forecasting methodology

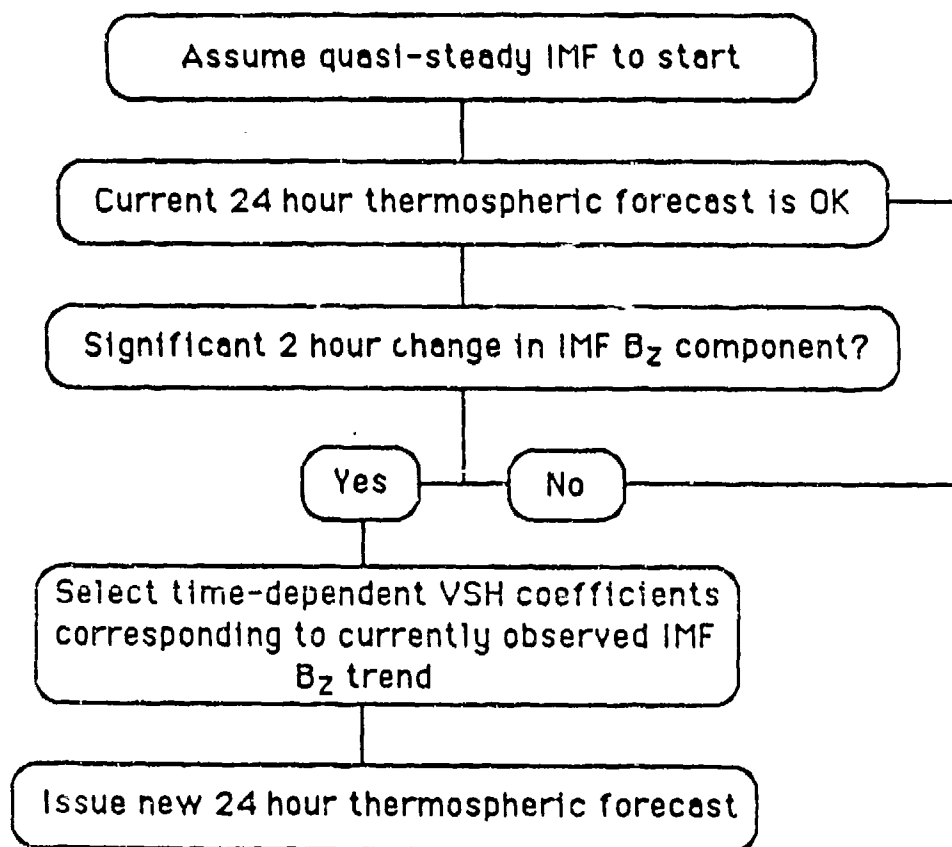


Figure 4 - Flowchart of the tentative methodology for a basic thermospheric-forecast capability.

4 Areas Requiring Additional Effort Before An Effective Thermospheric-Forecast Capability Can Be Established

It is obvious that for the methodology described above to work, additional spacecraft ion-drift and neutral-wind data is needed. Without the ion drift data, time-dependent histories of ion convection in both hemispheres cannot be determined. Furthermore, neutral-wind data is required to conduct ion-neutral coupling studies, both at solar maximum and solar minimum. The desired improvements in neutral-wind-simulation capability cannot be verified without globally-measured neutral-wind data.

There are also some ionospheric features which need to be represented in TGCMs, if the models are going to more realistically reproduce naturally-occurring thermospheric phenomena. Some of these areas include the following: (a) more realistic ion-density fields in the TGCM; (b) incorporation of the day-to-night conductivity-gradient effect, which will shift the antisunward ion-drift region more to the dawnside of the polar-cap, regardless of IMF configuration; (c) realistic ion-convection models for IMF $B_z > 0$ conditions. To the author's knowledge, efforts to incorporate items (a) and (c) into the NCAR-TGCM are underway. However, the incorporation of the day-to-night conductivity-gradient effect should be addressed by ionospheric modelers.

RESULTS AND CONCLUSIONS

1 Summary of Research

The primary objective of this work has been to develop a better understanding of the neutral-gas dynamics of the high-latitude regions of the Earth's upper thermosphere. To achieve this, an understanding of the morphology of the neutral winds and the forces which drive or modify them was required. To this end, a unique dataset was established which utilized satellite neutral winds and other supporting data from Dynamics Explorer 2 (DE-2), with coverage of both polar caps during the same orbit.

Analysis of these data led to the characterization of four basic neutral wind signature categories for the various interplanetary-magnetic-field (IMF) configurations, as well as observations of similarities and asymmetries in the neutral circulation between hemispheres for solar-maximum December-solstice conditions. Averaging of the neutral-wind data in various IMF categories has provided preliminary indications of the influence of IMF-controlled ion-convection on the polar-cap antisunward and duskside sunward neutral winds. Analysis of the individual neutral-gas forces from the diurnally-reproducible version of the NCAR thermospheric general-circulation model (TGCM) provided insight into the causes of "seasonal" and diurnal variations in the high-latitude neutral-wind-circulation system. This resulted in the "seasonal" differences of the polar-cap pressure-gradient force between hemispheres explaining the virtual absence of dawnside-sunward neutral winds in the summer southern hemisphere which are usually observed in the winter northern hemisphere.

The knowledge acquired above was applied to two tests of the time-dependent capabilities of the NCAR-TGCM, with the intention of evaluating the use of TGCMs for thermospheric forecasting. The first TGCM simulation was accomplished in an effort to quantitatively evaluate the ability of the TGCM to yield accurate time-dependent neutral winds. The results of this test were that the NCAR-TGCM provided good first-order time-dependent neutral winds with errors from the DE-2 measured neutral winds of 10 - 40%. A second TGCM simulation was intended to assess our ability to use DE-2 measured ion-drift data to provide a more realistic time-dependent prescription of model-ion-convection parameters in both hemispheres. Results here, show that use of DE-2 measured ion-drift data, under selected geophysical conditions, can improve the ability of the TGCM to simulate thermospheric neutral winds.

2 Synopsis of Major Results

2.1 Major Morphological Results

Four basic characteristic neutral-wind signatures have been identified that may be categorized according to the orientation and magnitude of the IMF, viz: 1) $B_z < 0$, $B_y > 0$; 2) $B_z < 0$, $B_y < 0$; 3) $B_z > 0$; and 4) $B_z \gg 0$. For all $B_z < 0$ conditions, there was a two-cell structure to the neutral circulation in both hemispheres with a well-established dusk cell and a small weak dawn cell. Under $B_z < 0$, $B_y > 0$ IMF conditions, the maximum antisunward neutral winds were clearly located on the dawnside of the polar-cap flow in the northern hemisphere and on the duskside of the polar-cap flow in the southern hemisphere. For $B_z < 0$, $B_y < 0$ IMF conditions, the maximum antisunward neutral winds were located on the duskside of the polar-cap flow in the northern hemisphere and on the dawnside of the polar-cap flow in the southern hemisphere, although this case was not as clearly pronounced as the $B_z < 0$, $B_y > 0$ case.

When B_z was slightly northward, a transitory neutral-wind state existed, where the neutral-wind signatures varied greatly between hemispheres. In the winter northern

hemisphere, the antisunward-neutral-wind speeds were diminished in the center of the polar cap, as though in preparation for a change to sunward flow in the center of the polar cap. In the summer southern hemisphere, the neutral circulation retained the two-cell circulation structure with the maximum-antisunward neutral winds located in the center of the polar cap. Under $B_z \gg 0$ conditions, the neutral winds in both hemispheres had a multicell structure, although the region of sunward-neutral-wind speed in the center of the polar cap was small and associated with relatively small neutral-wind speeds.

In the analysis of the interhemispheric neutral-wind signatures, two universal-time periods were given special attention, namely 09 - 11 and 21 - 23 UT. During these periods, the local-time plane of the invariant-geomagnetic-pole longitude in both hemispheres, was such that the DE-2 spacecraft-sampled essentially-conjugate regions. Data obtained during these universal times enabled characteristic differences in the neutral-wind signatures of both hemispheres to be examined, without the ambiguity caused by the hemispheric differences in the displacements of the invariant-geomagnetic and geographic poles. At "conjugate-sampling" universal times, with the spacecraft in the dawn-to-dusk local-time plane, the (latitudinal) width of the antisunward polar-cap neutral winds was found to be two to six degrees larger in the northern hemisphere than in the southern hemisphere, under quasi-steady IMF conditions. This asymmetry was due to the different geomagnetic topology in the northern hemisphere, with the non-dipolar terms being of significantly greater importance in the northern hemisphere, than the southern hemisphere. For the conjugate-sampling periods, the major axis of the ellipse describing the contours of constant invariant latitude was approximately aligned with the 0600/1800 local-time plane, and therefore the spacecraft observed the maximum asymmetry at these universal times. This asymmetry between northern and southern hemispheres was not predicted by the current theoretical models. These models need to be reformulated using a more

realistic magnetic-field topology in order to be able to simulate these asymmetric-neutral-wind fields.

At the conjugate-sampling time ranges of 09 - 11 and 21 - 23 UT, individual orbits in the DE-2 dataset showed that the winter-northern-hemisphere polar cap had larger maximum antisunward neutral-wind speeds than the summer-southern-hemisphere polar cap when the IMF was in a $B_z < 0$, $B_y > 0$ configuration. The results were reversed for the $B_z < 0$, $B_y < 0$ IMF orientation. This finding was unexpected since the summer hemisphere generally has higher average levels of ionization and ion drag. Therefore, the summer southern hemisphere was intuitively expected to have higher convection-driven neutral-wind speeds. Averaged DE-2 neutral winds in the dawn/dusk plane, at the conjugate-sampling UTs, provided preliminary indications that higher-velocity antisunward neutral winds were seen in the hemisphere which has the largest-duskside ion-convection cell, which is controlled by the sign of the IMF B_y component. The maximum-average-antisunward neutral winds were 160 m/s higher in the northern hemisphere than the southern hemisphere at 09 - 11 UT and 220 m/s higher in the northern hemisphere for 21 - 23 UT, when IMF $B_y > 0$ conditions prevailed. This was contrasted by summer-southern-hemisphere maximum-average-antisunward neutral-wind speeds which exceeded those of the winter northern hemisphere by 170 m/s at 09 - 11 UT and by 15 m/s for 21 - 23 UT under IMF $B_y < 0$ conditions. However, the number of DE-2 neutral-wind orbits available for this very selective study was not considered sufficient to provide conclusive results. It is for this reason, that the results are considered "preliminary."

Both the DE data and TGCM neutral-wind calculations, in the dawn/dusk local-time plane, show that the dusk cell was usually the dominant of the two neutral-circulation cells, in both size and magnitude of sunward-return flow. Under conditions identical to those mentioned above for the antisunward neutral flow, the magnitude of the maximum-duskside sunward-return flow averaged 260 m/s and the sunward winds extended over a 25-degree-wide region in either hemisphere when the dusk ion-

convection cell was dominant (i.e., $B_y > 0$ ($B_y < 0$) in the northern (southern) hemisphere). However, when the dawn ion-convection cell was dominant in either hemisphere, the maximum-average duskside-sunward-return flow was about the same at 230 m/s, but the neutral-wind reversal extended over only a 17-degree wide region. As with the antisunward neutral flow, the IMF B_y configuration was seen to control the ion convection, which in turn influenced the sunward-duskside neutral flow to a large extent, with only minor variations between hemispheres.

The dawn-cell neutral circulation, as seen by the latitudinal extent and magnitude of the sunward neutral flow, was found to be stronger and more organized in the winter northern hemisphere than in the summer southern hemisphere in both individual orbits which covered both hemispheres and averaged data. The maximum-sunward-dawnside return flow averaged 120 m/s in the northern hemisphere and was virtually non-existent in the summer southern hemisphere. Further, the summer-hemisphere-dawnside circulation was shown to be more divergent than the winter-hemisphere-dawnside circulation, even though the summer hemisphere is more tightly-coupled to the non-divergent twin-cell ion convection. From modeling studies, these relationships were ascribed to the orientation of the polar-cap pressure-gradient forces, which were dawn-to-dusk-directed in the summer hemisphere and sunward-directed in the winter hemisphere. The dawnside portion of the thermospheric neutral circulation was seen to be largely controlled by "seasonal" differences in both the measured data and model calculations.

Based on diurnally-reproducible IMF $B_y = 0$ TGCM model results, the calculated summer-southern-hemisphere antisunward neutral winds were oriented at an angle of 5 to 15 degrees counterclockwise from that of the antisunward-convecting ions. The angle from which the polar-cap antisunward neutral winds deviated from the noon-midnight local-time plane was larger in the winter northern hemisphere than in the summer southern hemisphere by an additional 5 - 10 degrees due to the increased importance of

forces other than ion drag. The diurnal variation of the angle the TGCM antisunward-drifting ions made with the noon-midnight local-time plane was followed by the TGCM neutral winds. Unfortunately, insufficient DE-2 ion-drift data was available to provide an indication of the averaged-diurnal variation of the angle the actual antisunward-drifting ions made with respect to the noon-midnight local-time plane. Using averaged DE-2 neutral-wind data, an IMF B_y -dependent difference is seen in the variation of the angle the antisunward neutral winds make with respect to the noon-midnight local-time plane. Under IMF $B_y > 0$ ($B_y < 0$) conditions, the counterclockwise twist is greater in the northern (southern) hemisphere.

2.2 Neutral-Gas Momentum-Forcing Mechanisms

Mean ion-neutral momentum-coupling time constants, which are an estimate of the time required for the neutral winds to approach the ion-drift velocity following an instantaneous-ion-drift-velocity change, were computed using DE-2 data for the four-characteristic neutral-wind-signature categories and for the regions poleward of 40 degrees in both hemispheres. The winter-hemisphere time constants were at least twice as large as the summer-hemisphere values, in all cases. The mean time constants for the first three cases were approximately one hour in the summer hemisphere and two to three hours in the winter northern hemisphere. However, for the $B_z \gg 0$ case, the summer-hemisphere time constant exceeded two hours while the winter-hemisphere time constant increased to over four hours.

The momentum forcing over both invariant poles was analyzed from the diurnally-reproducible TGCM run. It was found that the zonal and meridional components of the individual forces in opposite hemispheres, for a solar-maximum December solstice, were remarkably similar. However, the differences between the vector magnitude of the individual forces, in opposite hemispheres, were significant. In general, the pressure-gradient force was the most important force in both hemispheres.

The peaks and valleys in the diurnal variation of the pressure-gradient force occurred at approximately the same local time in both hemispheres. However, the relative magnitude of the peaks varied for different seasons. During the post-midnight hours, the pressure-gradient force was often twice as strong as ion drag. During the day, the peaks and valleys of both the ion-drag and pressure-gradient forces had similar magnitudes. In addition, viscous drag was generally twice as large in the winter northern hemisphere as in the summer southern hemisphere, indicating greater vertical-neutral-wind shears in the winter northern hemisphere.

The antisunward neutral winds from the diurnally-reproducible TGCM simulation were observed to exceed the antisunward ion drifts inside the polar cap. This occurred because the ion-drag force inside the polar cap was secondary in importance to the pressure-gradient force. Theoretical studies of the neutral-gas parcel-trajectory-forcing history over both invariant poles show this to be true in both hemispheres at solstice.

The radius of the diurnally-reproducible neutral-wind-circulation system was typically 30 degrees, while the radius of the high-latitude ion convection was typically 25 degrees. Through all 24 hours of universal time and in both hemispheres, the duskside boundary of the high-latitude ion-convection and neutral-wind-circulation systems were seen to coincide. The dawnside of the neutral-wind-circulation system was seen to extend out, past the boundary of the ion convection. This larger spatial extent of the neutral circulation over the driving non-divergent ion convection, in the inertial-reference frame, was caused primarily by the dusk-to-dawn component of the polar-cap pressure-gradient force. This polar-cap pressure-gradient force was shown to be due to both the spatial variations in neutral temperature and density. The polar-cap temperature distribution was, in turn, shown to result from the superposition of the solar-EUV, cusp, and Joule heating.

2.3 NCAR-TGCM Neutral-Wind-Verification Test

The first database of neutral winds, with coverage over both polar regions on individual orbital passes (~ 70 orbits), enabled the global accuracy of neutral-wind simulations from a TGCM to be critically-evaluated. Two time-dependent runs of the NCAR-TGCM, each simulating the same period in November 1982, but using different techniques to prescribe the high-latitude ion convection were compared against measured DE-2 neutral winds. The objective was twofold. First, validate the time-dependent TGCM neutral-wind-simulation capability and second, determine the weak and strong points of each of the high-latitude ion-convection-parameterization techniques. One technique analytically determined all the ion-convection parameters from a series of relationships which required knowledge of the IMF. The other technique found the ion-convection parameters by fitting the ion-convection model to experimental DE-2 ion-drift data.

The TGCM model inputs which need to be most realistically characterized at high latitudes are: the average ion convection and spatial variations in the ion densities. In this work, the search for a method to more realistically characterize the average ion convection was undertaken. Neither the analytical or experimental high-latitude parameterization techniques proved to specify the ion convection as accurately as hoped. Looking only at the number of times that one of the high-latitude parameterization techniques was more accurate than the other, the analytical technique was more accurate in simulating DE-2 satellite neutral winds in both hemispheres. However, there were several orbits when the center of the ion-convection model was moved significantly from the standard location associated with the invariant pole and the accuracy of the neutral-wind simulation was increased. In these cases, the high-altitude ion-convection-parameterization technique, which used DE-2 ion-drift data, was significantly more accurate. In general, the best way to improve TGCM neutral-wind-simulation accuracy

may be to combine the analytical and experimental ion-convection-parameterization techniques, whenever possible.

2.4 High-Latitude Ion-Convection Modeling

Ion-drift data from DE-2 were used to specify the time-dependent model-ion-convection parameters for an experimental run of the NCAR-TGCM. If the DE-2 ion-drift data, in the dawn/dusk plane, showed the center of the antisunward ion convection to be located some distance from the invariant-pole location, then both the ion-convection and auroral-oval models were picked up and placed in a position where the model-ion-convection reversals closely matched those of the DE-2 data, in both radius and position. In addition, the model cross-cap electric potentials were specified using the integrated potential gradients from the DE-2 satellite data in the dawn-dusk plane.

Results of the test between the analytical and experimental high-latitude ion-convection-parameterization techniques, mentioned above, are as follows: the analytic technique should be used in the winter hemisphere, where frequent irregularities in the measured ion convection make it difficult to derive ion-convection parameters which represent the average ion-convection system. The experimental technique is more applicable to the summer hemisphere, where the measured ion drifts are more representative of the time-averaged ion convection. Furthermore, the experimental technique was superior at providing average ion-convection parameters in both hemisphere during the onset of a large geomagnetic storm.

2.5 Numerical Thermospheric Forecasting

To forecast the dynamics of the thermosphere, it was found that a forecast of model-ion-convection parameters was required. The methodology for an initial thermospheric-forecast capability was established, based on the hypothesis that a historical series of derived model-ion-convection parameters could be associated with a

currently-observed trend in the IMF. This historical time-dependent series of model-ion-convection parameters would subsequently become input for the TGCM ion-convection-prescription forecast. If a number of cases corresponding to different sets of historical model-ion-convection parameters were run in advance (i.e., a number of diurnally-reproducible as well as time-dependent cases corresponding to increasing and decreasing IMF B_z) these cases could be reduced to sets of VSH coefficients, which could be used to quickly regenerate the thermospheric-neutral-wind fields which would serve as a thermospheric forecast. In this way, re-issuing a 12 - 24 hour thermospheric forecast based on a change in observed IMF could become trivial, as the only task becomes selecting the proper set of VSH coefficients.

2.6 Future Work

The diurnally-reproducible NCAR-TGCM results have provided the insight necessary to understand the universal-time and "seasonal" variations in neutral-gas momentum forcing at solar-maximum December solstice, in both hemispheres. However, this was only done for simple IMF $B_z < 0$, $B_y = 0$ conditions. To use TGCM model data to fully interpret DE-2 data in the four-basic neutral-wind-signature categories, additional diurnally-reproducible runs need to be attempted. The $B_y > 0$ and $B_y < 0$ simulations can be run in the near future. The $B_z > 0$ and $B_z \gg 0$ run require additional capabilities in ion-convection models.

To conclusively determine which variations in the high-latitude neutral-wind signatures are truly hemispheric and which are seasonal, a solar-maximum June solstice also needs to be examined. Unfortunately, neutral-wind vectors for June are not available from DE-2 because the satellite was inverted during this period, so no FPI data is available. This means that conclusive determination of "seasonal" differences in the neutral winds at solstice will have to wait at least until the next solar-cycle maximum, or later. For the same reasons, the qualifier "preliminary" cannot be removed from the

observations which resulted from the averaged DE-2 neutral winds. All available orbits of DE-2 neutral winds at the conjugate-sampling universal times and in the 0600/1800 local-time plane were used and the statistics are still low to be conclusive.

It is obvious that continuation of work on high-latitude thermospheric-neutral-gas dynamics could be fruitful, for both research and practical interests. However, the DE-2 mission supplied a tantalizing but insufficient quantity of neutral wind measurements from which to draw long-term conclusions. It is indeed unfortunate that there are no known spacecraft missions currently planned which can be expected to globally measure the neutral winds of the terrestrial upper thermosphere, either for solar maximum or solar minimum.

REFERENCES

Barnes, A., M. Goldstein, J. Hollweg, J. Mariska, W. Matthaeus, C. Smith, E. Smith, R. Stein, G. Withroe, and R. Woo. MHD waves and turbulence in the sun and interplanetary medium. *Solar Terrestrial Physics: Present and Future*. Edited by D. M. Butler and K. Papadopoulos, Chapter 4. NASA Reference Publication 1120, 1984.

Jokipii, J. R. Propagation of cosmic rays in the solar wind. *Rev. Geophys. Space Phys.*, 9, 27 - 87, 1972.

Killeen, T. L. and R. G. Roble. An analysis of the high-latitude thermospheric wind pattern calculated by a thermospheric general circulation model 2. Neutral parcel transport. *J. Geophys. Res.*, 91, 11291 - 11307, 1986.

Roble, R. G., J. M. Forbes, and F. A. Marcos. Thermospheric dynamics during the March 22, 1979 magnetic storm (CDAW-6): (1.) model simulation. Submitted to *J. Geophys. Res.*, 1987a.

7. DRAG COEFFICIENTS

SESSION VII DRAG COEFFICIENTS

AGENDA

AGENDA REVIEW

BLANCHARD

HIGH ALTITUDE DRAG COEFFICIENTS

BIRD

DIRECT SIMULATION MONTE CARLO DRAG PREDICTIONS

MOSS

IN-ORBIT MEASUREMENTS ON ATOM SCATTERING
FOR DRAG COEFFICIENTS

KARR

SATELLITE DRAG COEFFICIENT VARIABILITY

TOBISKA

SUMMARY REMARKS

BLANCHARD

7.1

HIGH ALTITUDE DRAG COEFFICIENTS

G.A. Bird

**Department of Aeronautical Engineering
University of Sydney**

NON-DIMENSIONAL COEFFICIENTS

Drag Coefficient	Knudsen Number
$C_D = \frac{D}{\frac{1}{2} \rho V^2 S}$	$K_n = \lambda / d$

Accommodation Coefficients

$$= \frac{\text{STREAM or -- REFLECTED}}{\text{INCIDENT}} \\ \text{STREAM -- SURFACE}$$

Speed Ratio

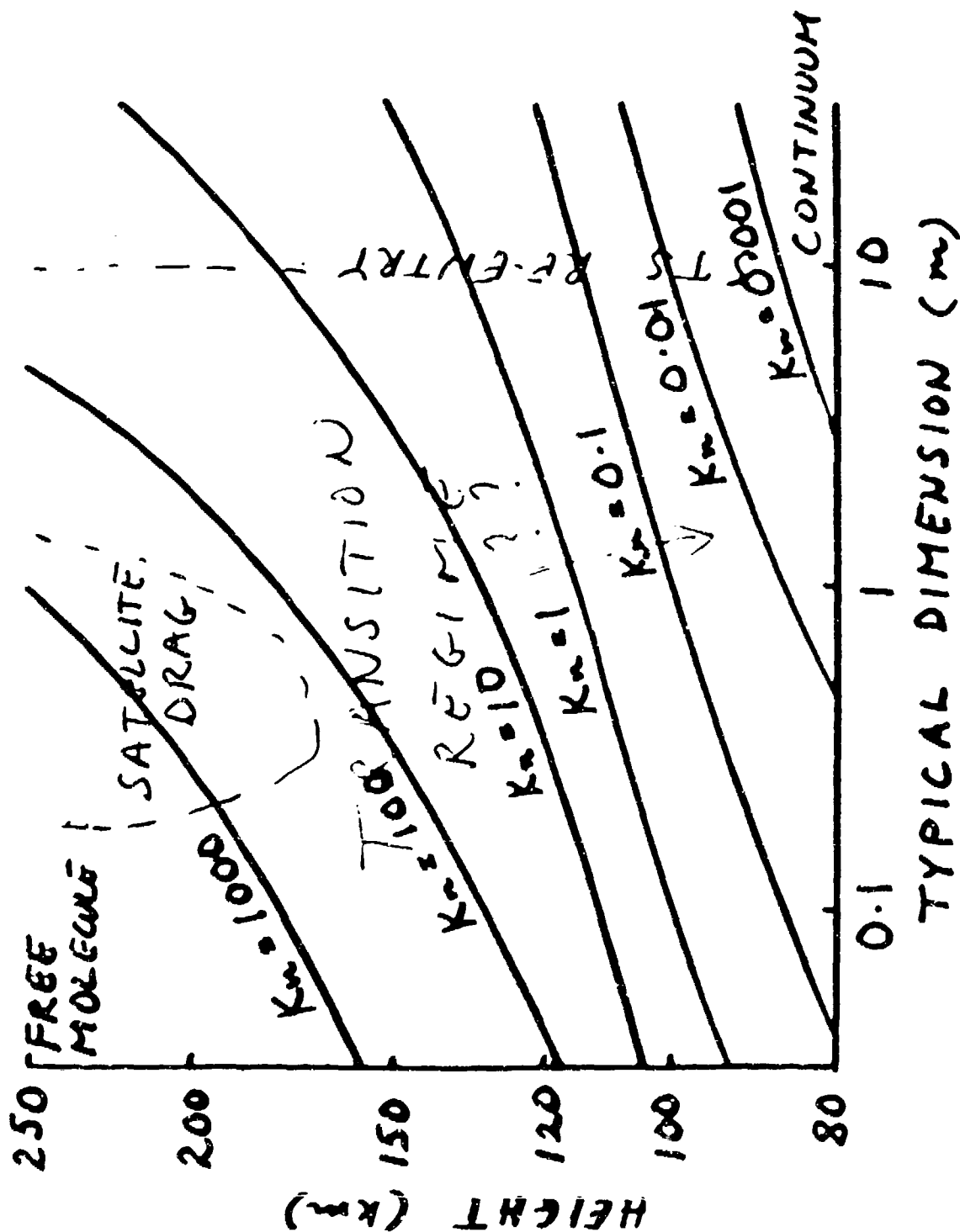
$$S = \frac{V}{(2kT/m)^{1/2}}$$

Temperature Ratio

$$T_w / T_\infty$$

etc.

KAUDSEN NUMBERS



UNDERSTANDING OF HIGH ALTITUDE DRAG COEFFICIENTS

1957

Reliable theory for convex bodies in free-molecule regime.

Poor theory and little data for transition regime.

Slight concern about gas-surface interaction, diffuse assumed.

1987

Practical CFD methods available for all flow regimes.

Existing gas-surface interaction models clearly inadequate.

Insufficient data to permit formulation of adequate models.

UNDERSTANDING OF GAS-SURFACE INTERACTIONS.

1967

Theory based on classical models.

Extensive experimental data on "engineering" surfaces indicated diffuse reflection with near full accommodation.

Confusion about detailed balancing and 2nd Law of Thermo.

Low thermal accommodation on very clean surface (Roberts, 1930)

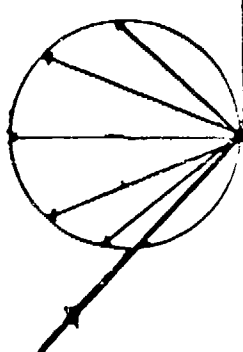
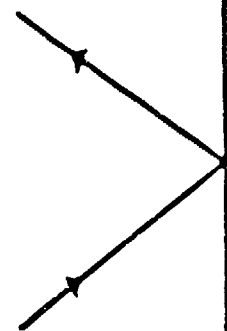
1987

Diffuse reflection from "dirty" surfaces, but when "clean", measured thermal acc. coeffs. are as low as 0.01 to 0.02 and measured tangential acc. coeffs. are as low as 0.1.

"Reciprocity" constraint is generally accepted.

Much additional data, but insufficient for engineering studies.

SURFACE REFLECTION MODEL **Maxwell (1879)**

DIFFUSE	SPECULAR
	
Thermal Accommodation Coefficient usually 1.	Thermal Accommodation Coefficient 0.
Parallel Momentum Accommodation Coefficient 1.	Parallel Momentum Accommodation Coefficient 0.

RECIPROCITY CONDITION

Cercignani (1969), Wenaas (1971), Kuscer(1971)

$$C_i \cdot e \cdot P(-C_r, -C_i) \exp(-E_r/kT) =$$

$$-C_i \cdot e \cdot P(C_i, C_r) \exp(-E_i/kT)$$

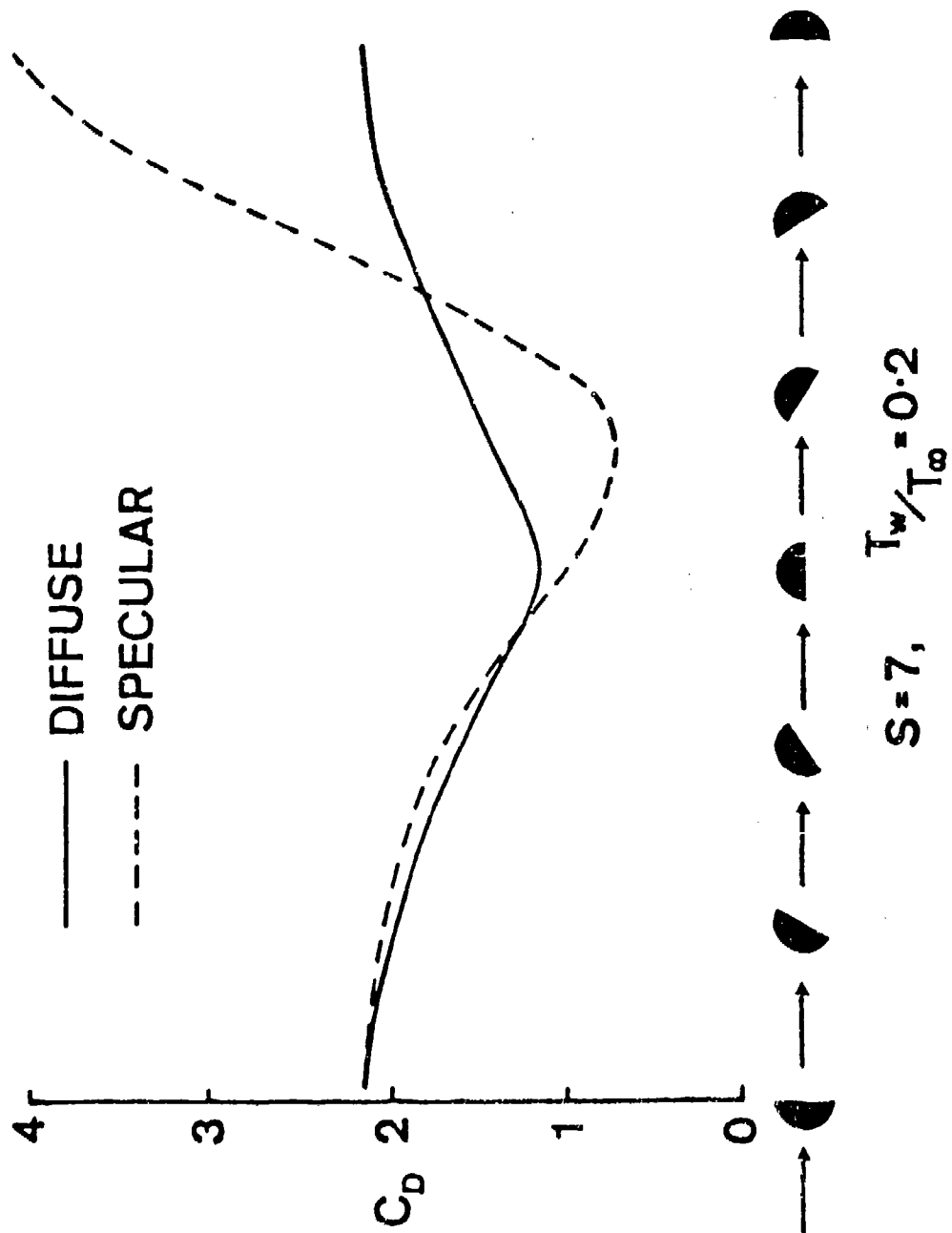
C_i and C_r incident and reflected velocities

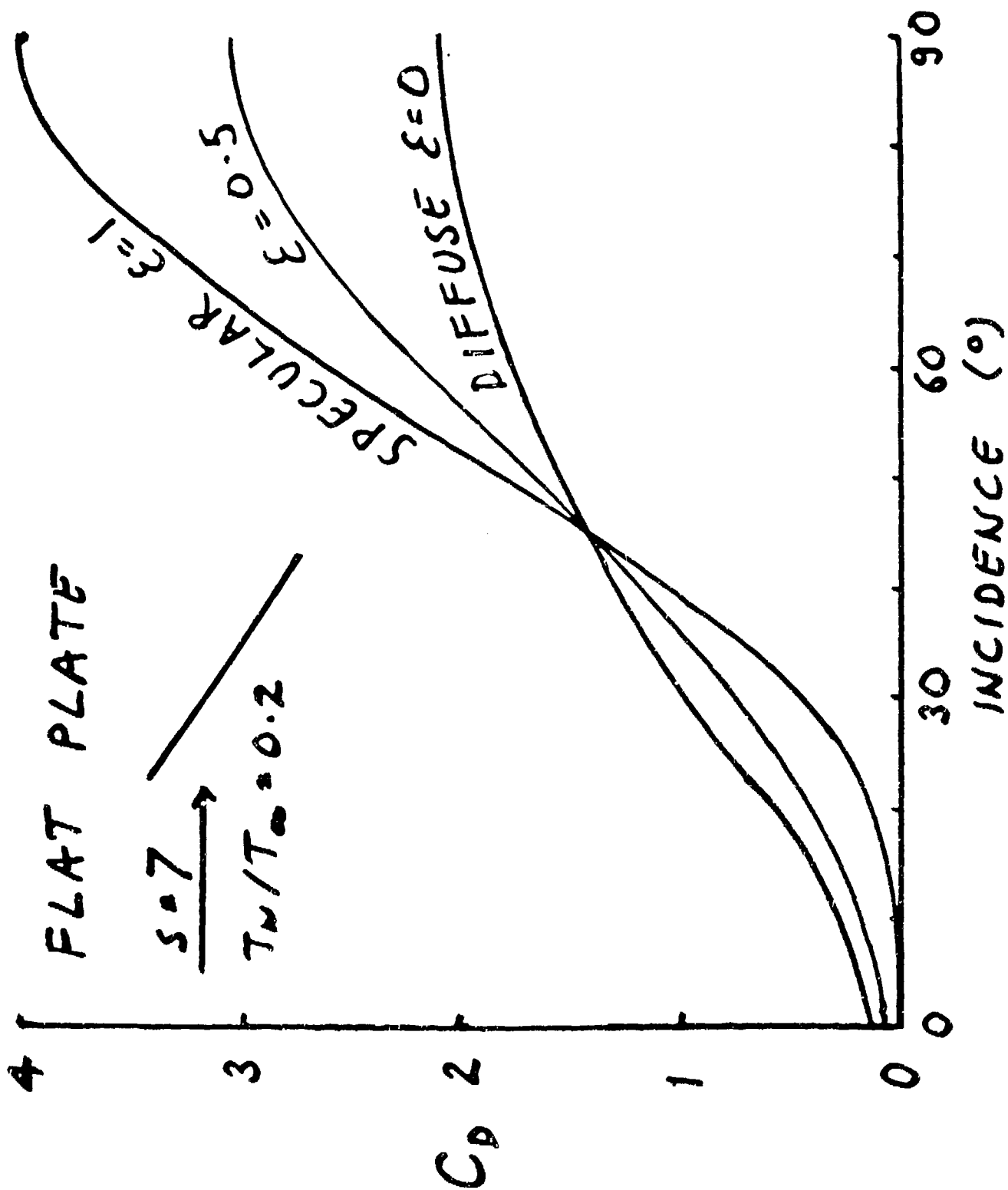
e unit normal vector

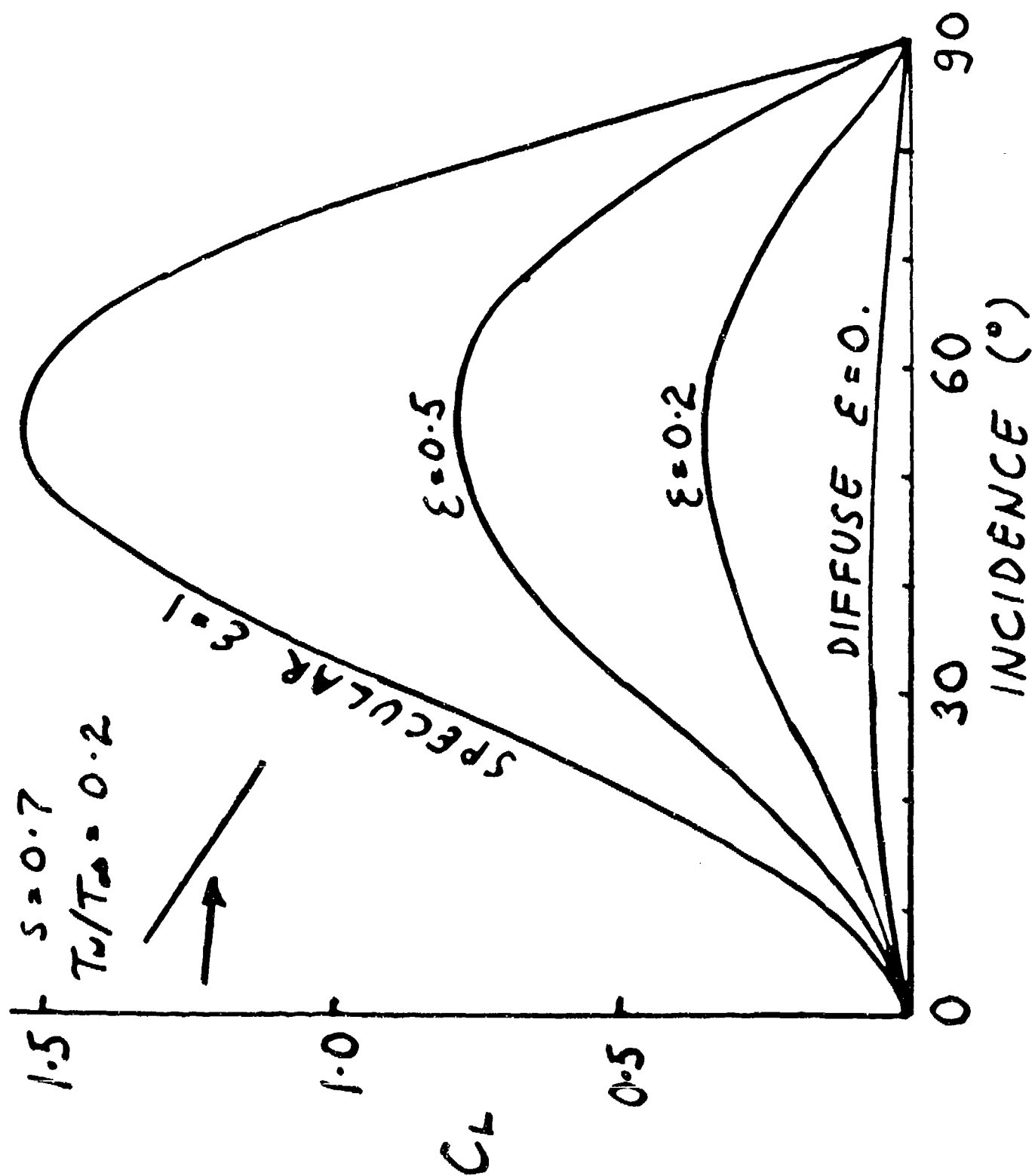
P Probability

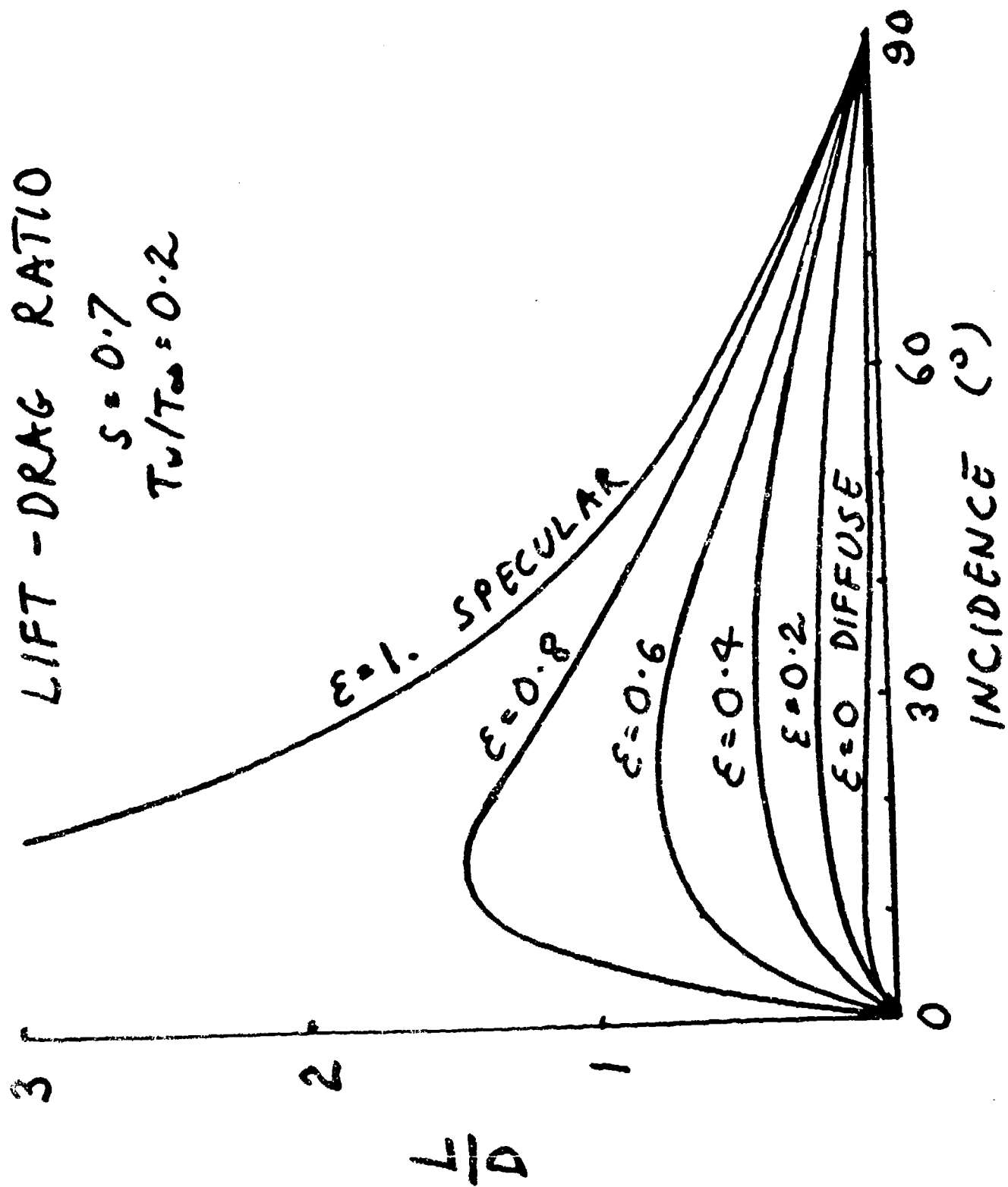
E_i and E_r Incident and reflected energies

kT Boltzmann constant \cdot Temperature









MOLECULAR BEAM STUDIES

Prog. in Aero & Astro Vol 51 (1977)

568 FUJIMOTO, FURUYA, HAYASHI, AND TAKIGAWA

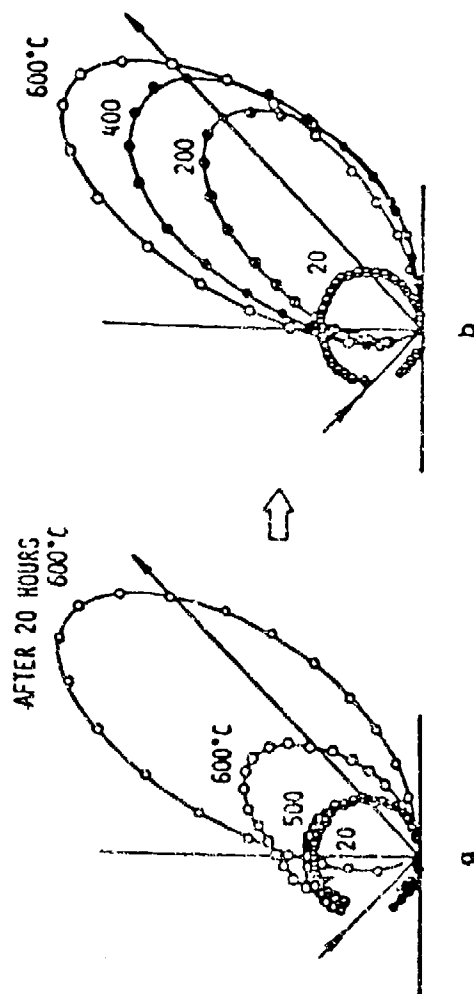
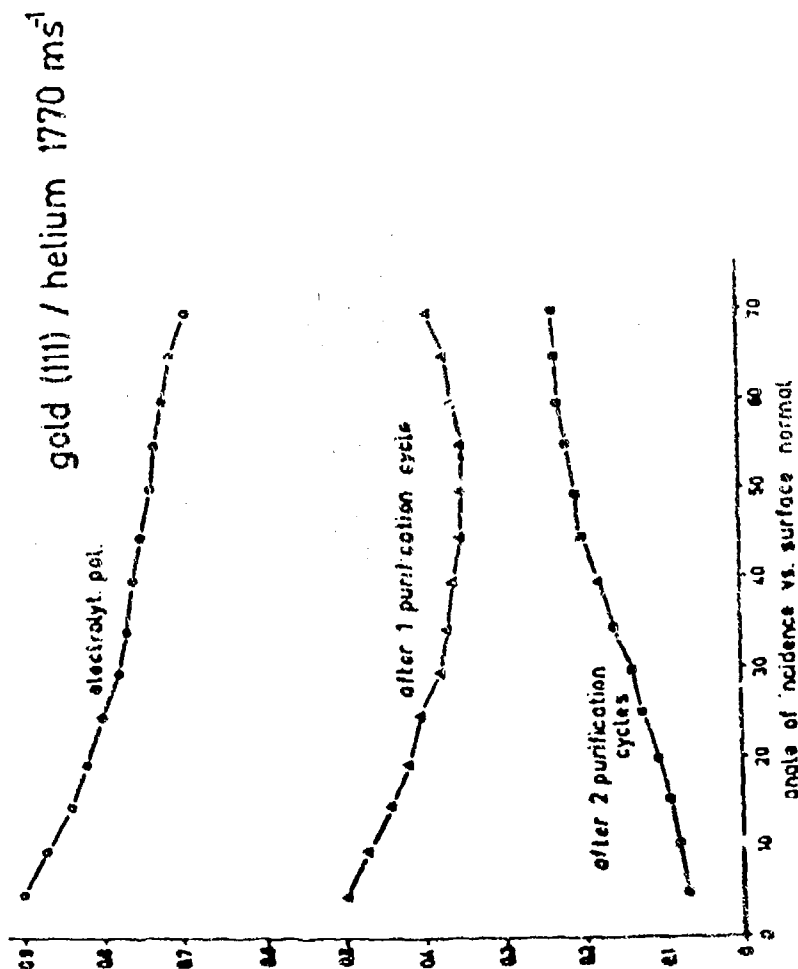


Fig. 2 Flux distributions of argon beam reflected from polycrystalline nickel surface. a) Target has been exposed previously to the atmosphere. b) After target is heated beyond 600°C.

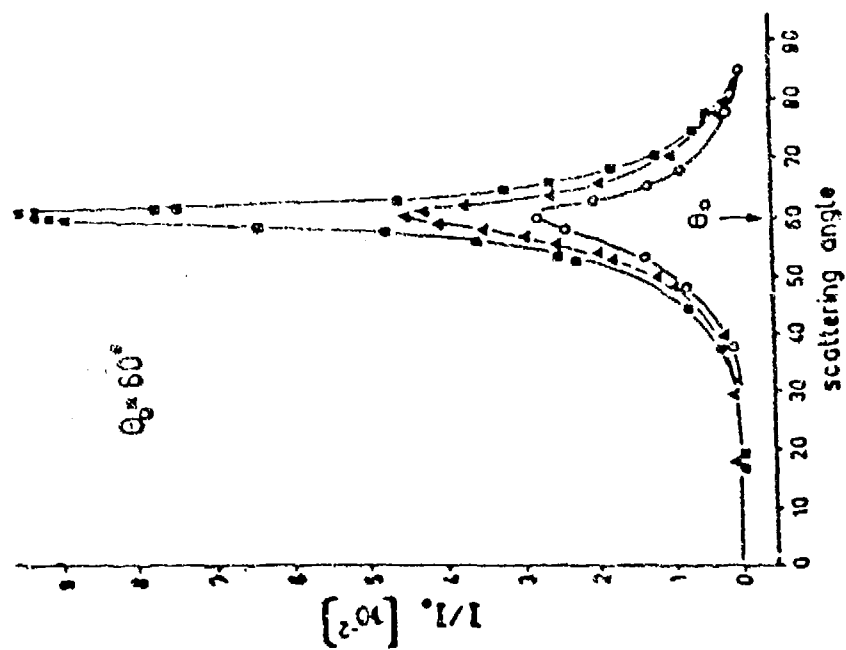
Steinheil et al.
 Aug. in *Adv. & Astro* Vol 51 (1977)
 p. 589

Parallel Momentum Accommodation Coeff



MOLECULAR BEAM

Steinhil et al (1977)



MOLECULAR BEAM

Steinhil et al (1977)

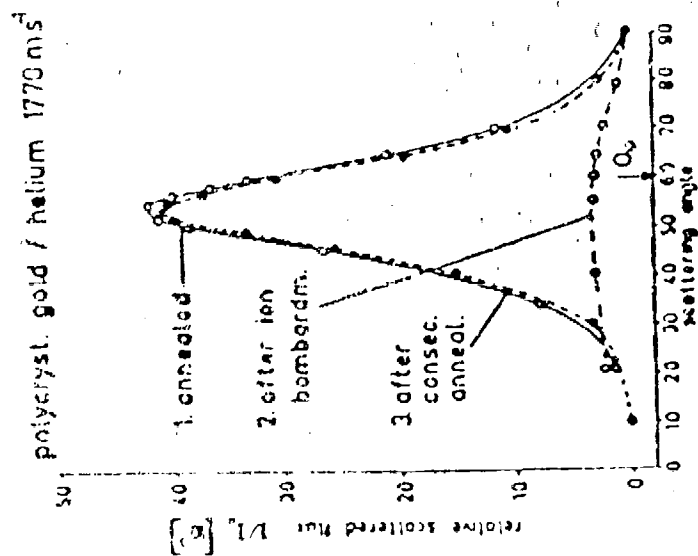


Fig. 5 Effect of microroughness (lattice defects): gold, medium grain size pol. cryst. film/helium.

MOLECULAR BEAM

[illegible]

7 - 21

Gregory & Peters 15th RGD 1986

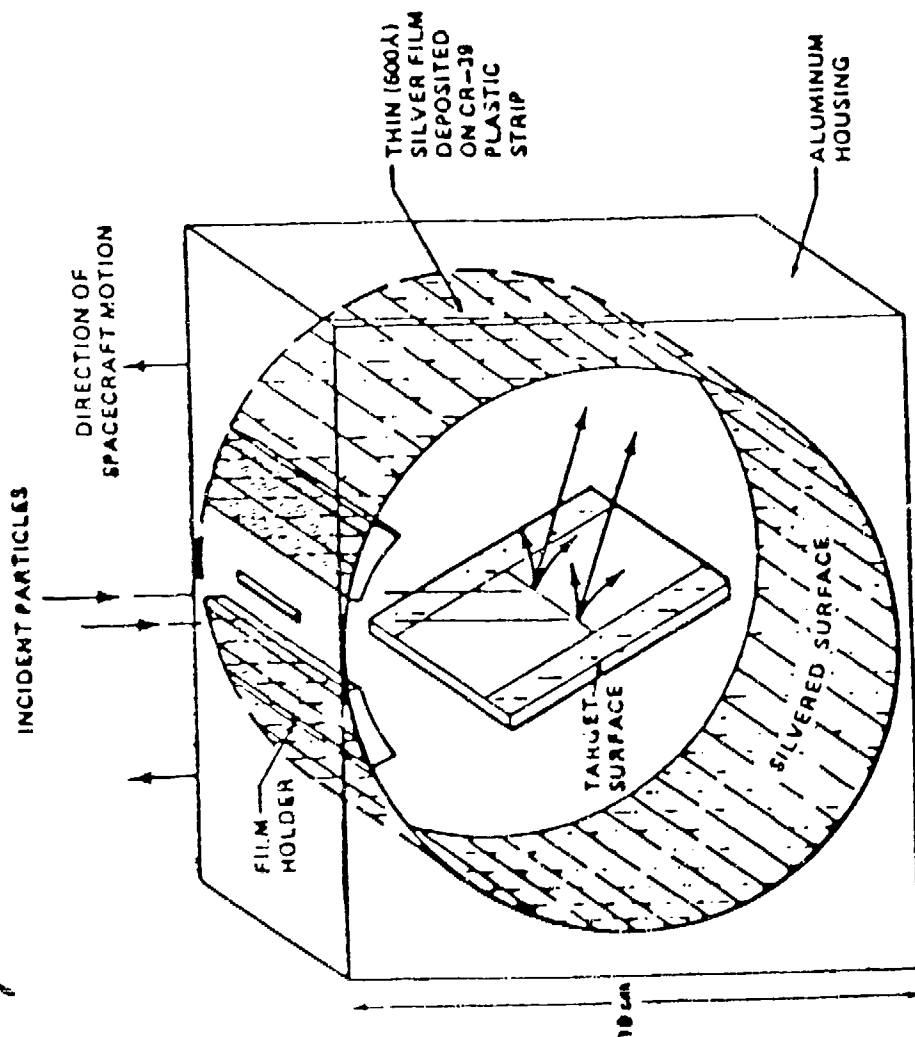


FIGURE 1. THE OXYGEN ATOM REFLECTOMETER FLOWN ON SHUTTLE STS-8 AND THE LONG DURATION EXPOSURE FACILITY

STS EXPERIMENT

STS FLIGHT DATA
 Gregory and Peters ISIL RGD 1986

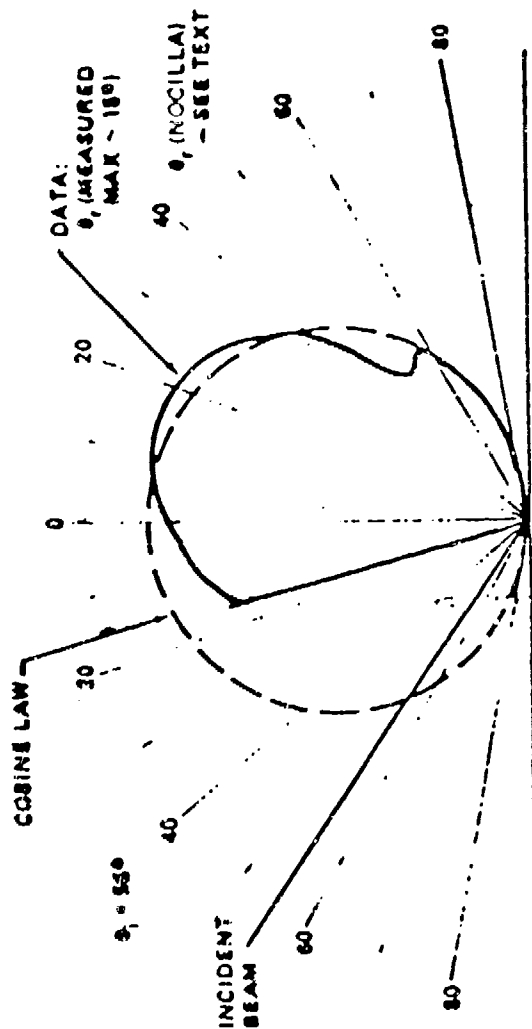


FIGURE 2. POLAR DIAGRAM OF ANGULAR DISTRIBUTION OF 54V OXYGEN ATOMS SCATTERED FROM POLISHED VITREOUS CARBON (ORBITAL FLIGHT DATA). A PURE COSINE LAW RE-EMISSION IS SHOWN FOR COMPARISON. THE CUT-OFF IN THE BACKWARD HEMISPHERE WAS CAUSED BY THE DETECTOR FILM HOLDER.

Diffuse
 $S = 9.03$
 $T_w / T_\infty = .25$

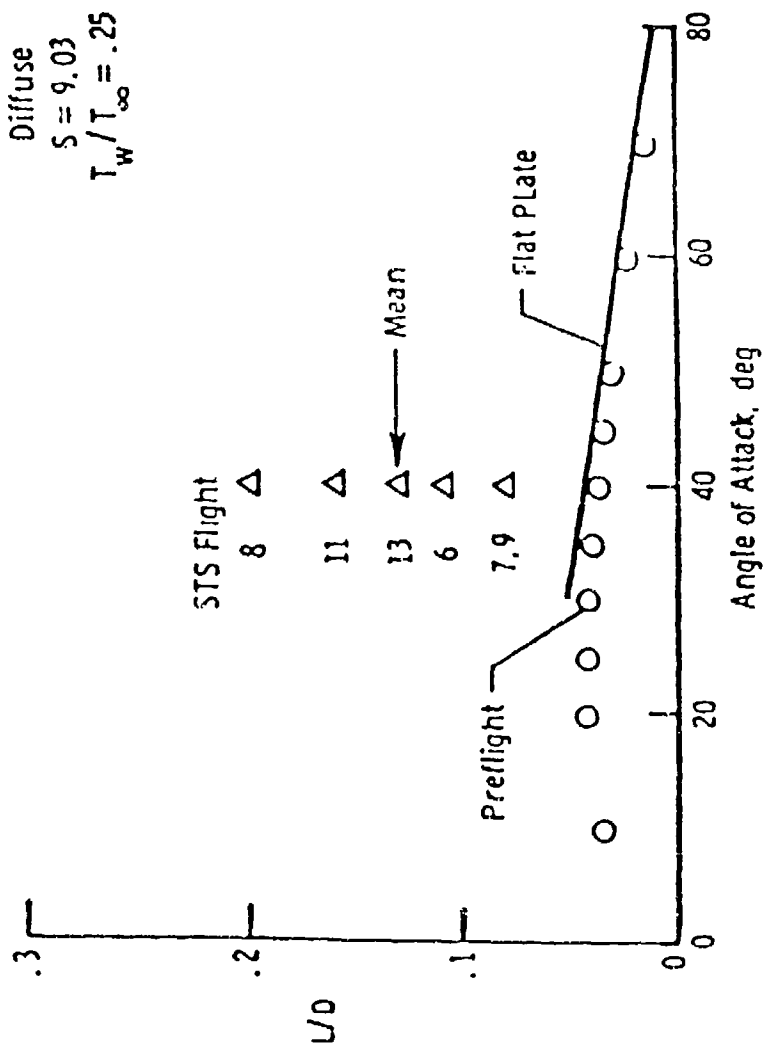


Fig. 10 Comparison of measured free molecule flow L/D with preflight predictions.

STS RE-ENTRY

CONCLUSIONS

- (i) Drag (and lift) above 85 km is strongly affected by the gas-surface interaction process.
- (ii) Reliable engineering studies are not possible in the absence of extensive in-orbit measurements.

7.2

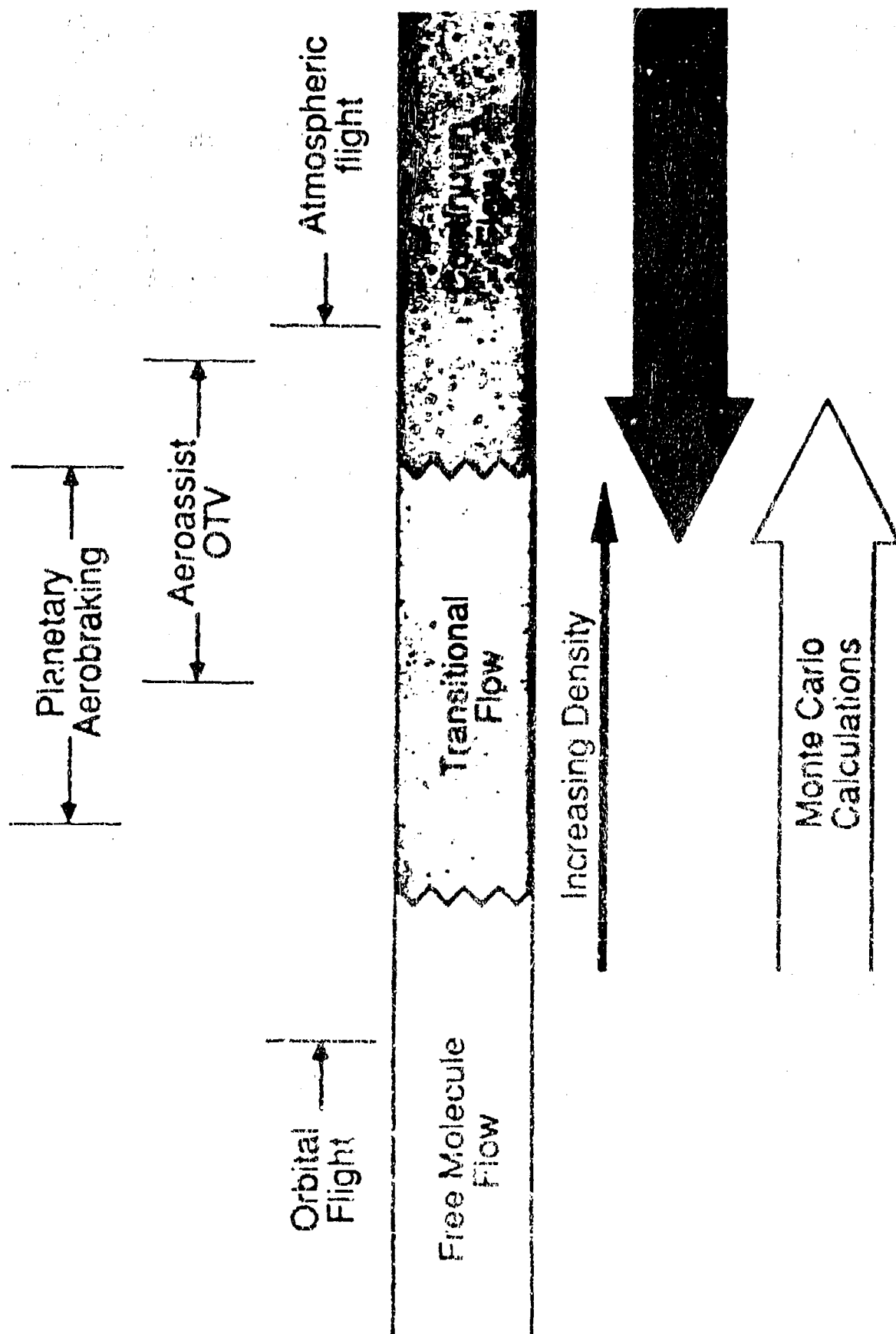
DIRECT SIMULATION MONTE CARLO (DSMC)
DRAG PREDICTIONS

James M. Moss
Mail Stop 366
NASA Langley Research Center
Hampton, VA 23665

Workshop on Atmospheric Density and Aerodynamic Drag
Models for Air Force Operations

AFGL, Hanscom AFB
October 20-22, 1987

ANALYZING THE TRANSITIONAL FLOW REGIME



DIRECT SIMULATION MONTE CARLO METHOD

- THE REAL GAS FLOW IS MODELED BY SOME THOUSANDS OF SIMULATED MOLECULES
- THE POSITION COORDINATES AND VELOCITY COMPONENTS ARE STORED IN THE COMPUTER
- THE MOLECULES ARE SIMULTANEOUSLY FOLLOWED THROUGH REPRESENTATIVE INTERMOLECULAR COLLISIONS AND BOUNDARY INTERACTIONS IN SIMULATED PHYSICAL SPACE

- ELASTIC COLLISIONS
 - VARIABLE DIAMETER HARD SPHERE
- ROTATION AND VIBRATION
 - LARSEN-BORGNAKKE MODEL
- CHEMICAL REACTIONS
 - COLLISION THEORY WITH REACTIVE CROSS SECTIONS
FROM CONTINUUM RATE CONSTANTS
- PLASMA EFFECTS
 - ELECTRICAL NEUTRALITY
 - AMBIPOLAR DIFFUSION IN SHOCK
- THERMAL RADIATION (BOUND-BOUND)
 - ELECTRONIC STATE DISTRIBUTION FROM ANALOG OF
LARSEN-BORGNAKKE METHOD
 - MEAN RADIATIVE LIFETIME FROM DATA
 - FINITE ABSORPTION CROSS-SECTION

FEATURES OF THE DIRECT SIMULATION MONTE CARLO METHOD

- COMPUTATION IS IN PHYSICAL SPACE
- STEADY OR UNSTEADY FLOWS
- ARBITRARY BOUNDARY CONDITIONS
EASILY IMPLEMENTED
- MULTICOMPONENT FLOW
- THERMODYNAMIC AND CHEMICAL NONEQUILIBRIUM

STS-2 ENTRY

Altitude = 92.35 km

Mach No. = 27.9

Incidence = 40.4 deg

Wall Temp. = 1590 K

MOLECULAR SPECIES

N₂

(Position and Velocity)

— = 10 km/s

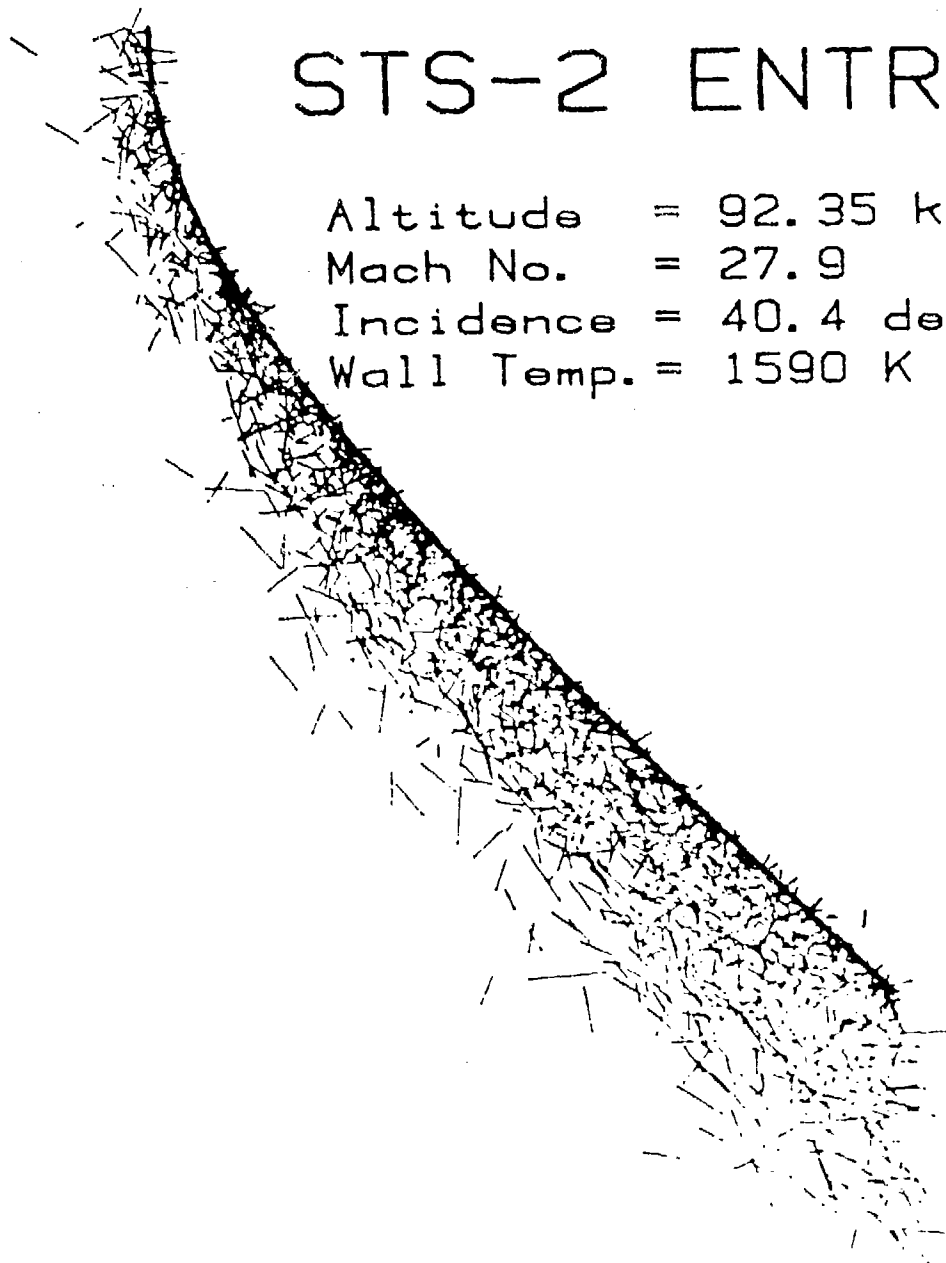
STS-2 ENTRY

Altitude = 92.35 km

Mach No. = 27.9

Incidence = 40.4 deg

Wall Temp. = 1590 K



MOLECULAR SPECIES

N

(Position and Velocity)

— = 10 km/s

STS-2 ENTRY

Altitude = 92.35 km

Mach No. = 27.9

Incidence = 40.4 deg

Wall Temp. = 1590 K

MOLECULAR SPECIES

O₂

(Position and Velocity)

— = 10 km/s

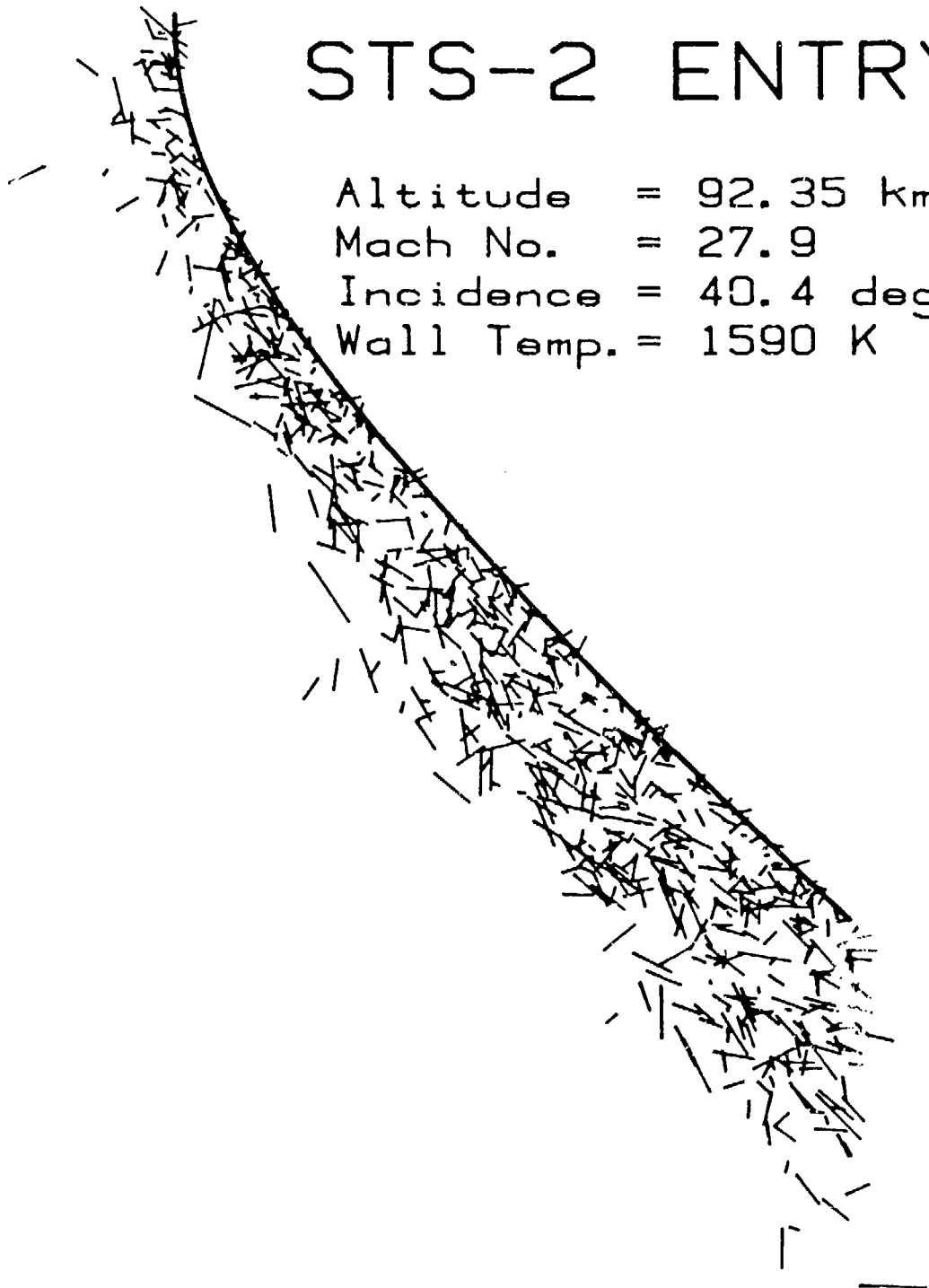
STS-2 ENTRY

Altitude = 92.35 km

Mach No. = 27.9

Incidence = 40.4 deg

Wall Temp. = 1590 K



MOLECULAR SPECIES

0

(Position and Velocity)

— = 10 km/s

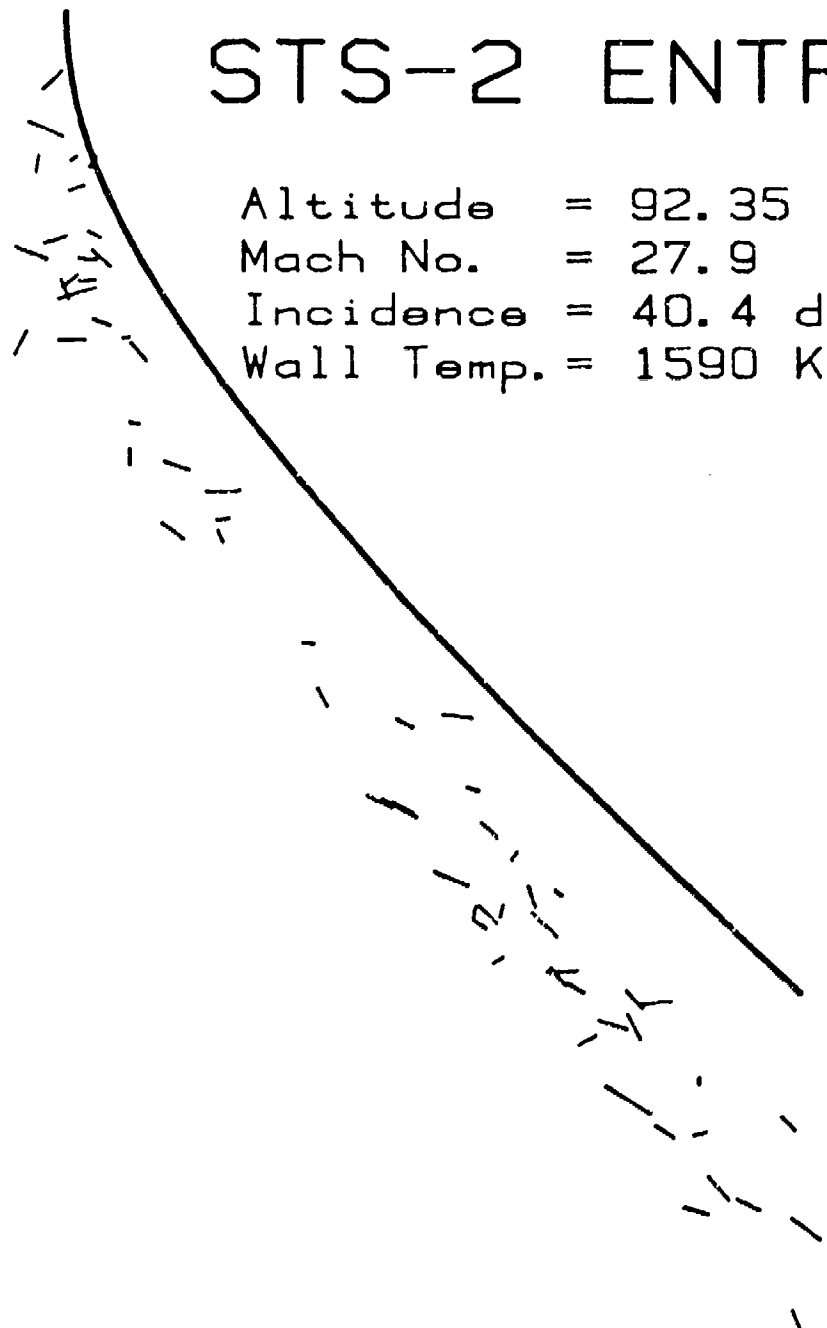
STS-2 ENTRY

Altitude = 92.35 km

Mach No. = 27.9

Incidence = 40.4 deg

Wall Temp. = 1590 K



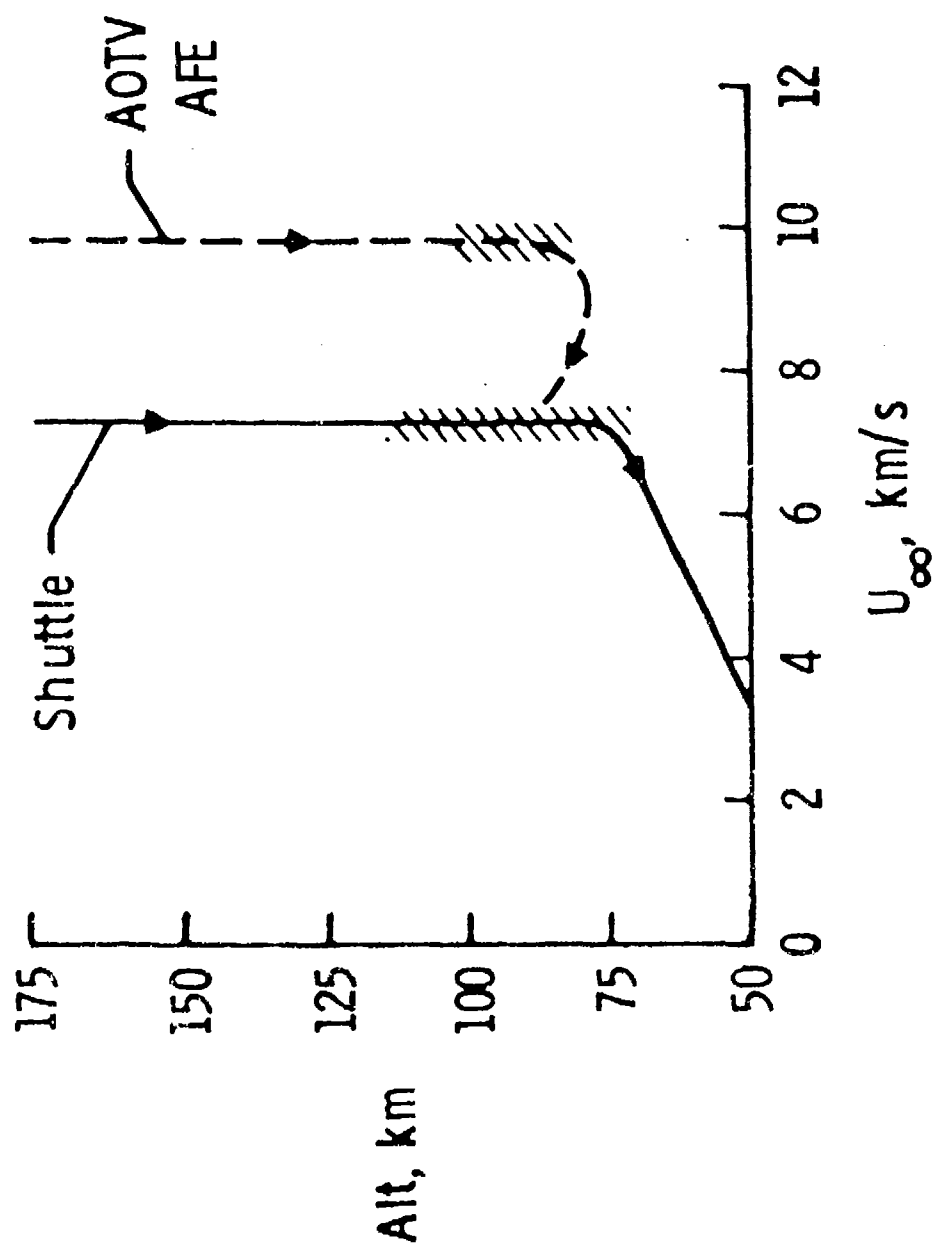
MOLECULAR SPECIES

NO

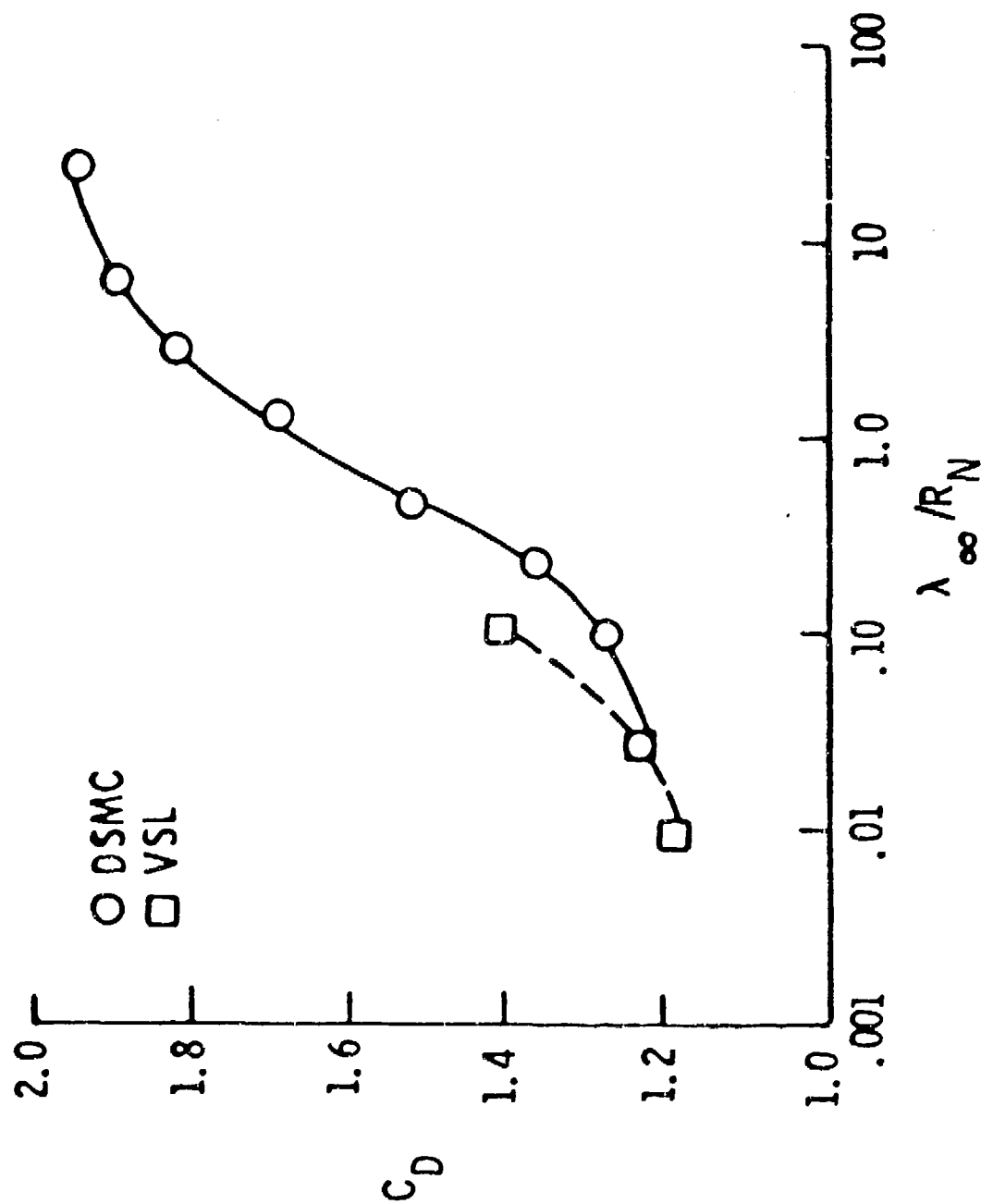
(Position and Velocity)

— = 10 km/s

DSMC CALCULATIONS FOR HYPERSONIC TRANSITIONAL FLOWS

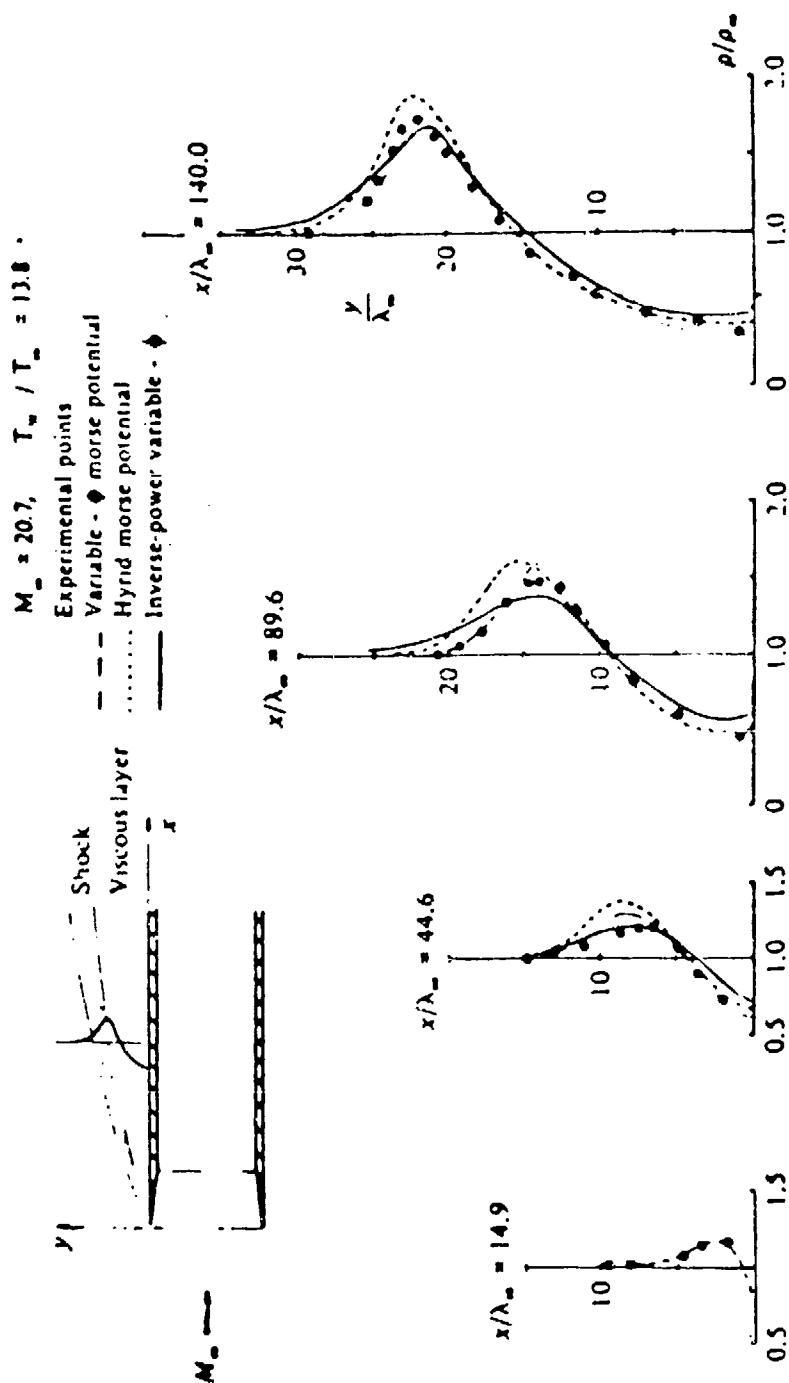


COMPARISON OF PREDICTED DRAG *



* Shuttle entry conditions.
 Progress in Astronautics & Aeronautics, Vol. 96

COMPARISON OF DSMC CALCULATIONS AND MEASUREMENTS FOR SHARP LEADING EDGE PROBLEM*



Hollow cylinder density profiles.

* J.K. HARVEY (JFM, 1983)

DSMC CALCULATIONS FOR FLAT PLATE AT
ZERO ANGLE OF INCIDENCE

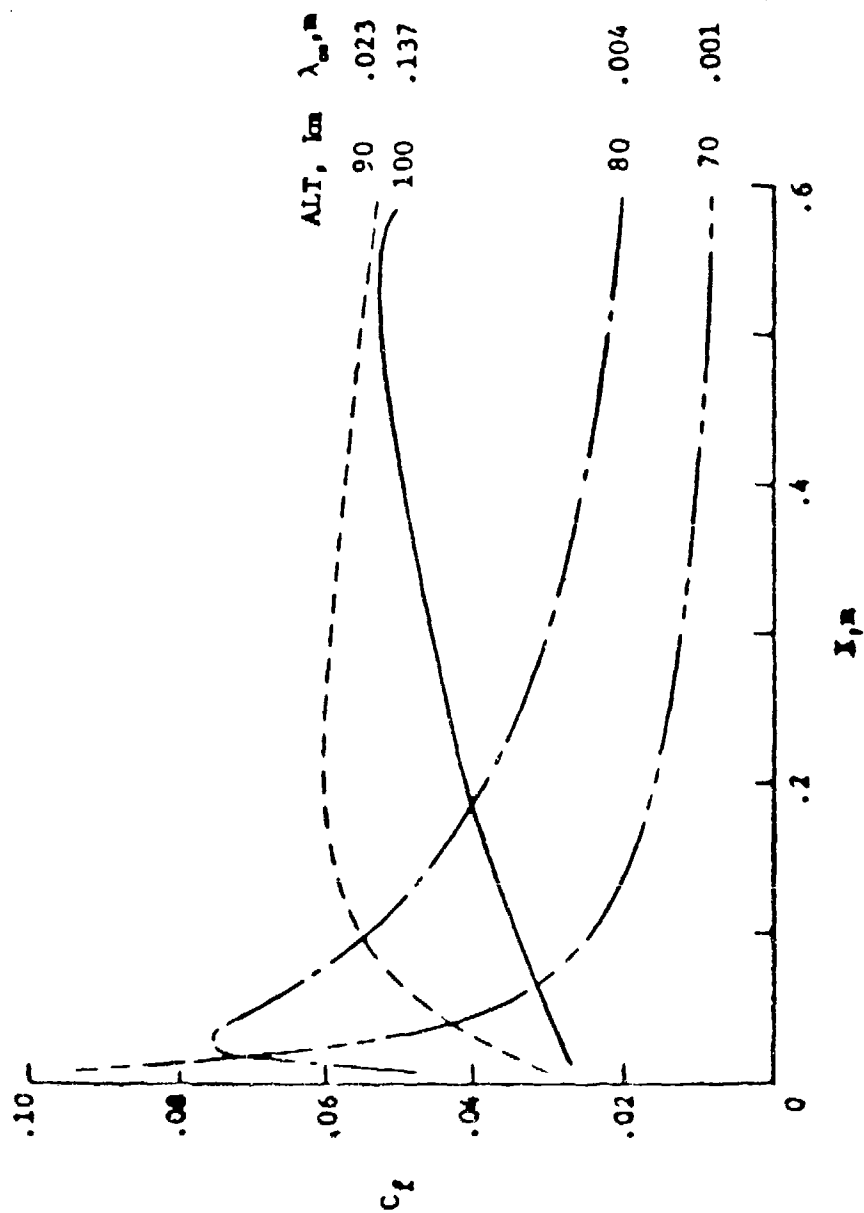
GAS: REACTING AIR--5 SPECIES

ALTITUDE: 70 TO 100 KM

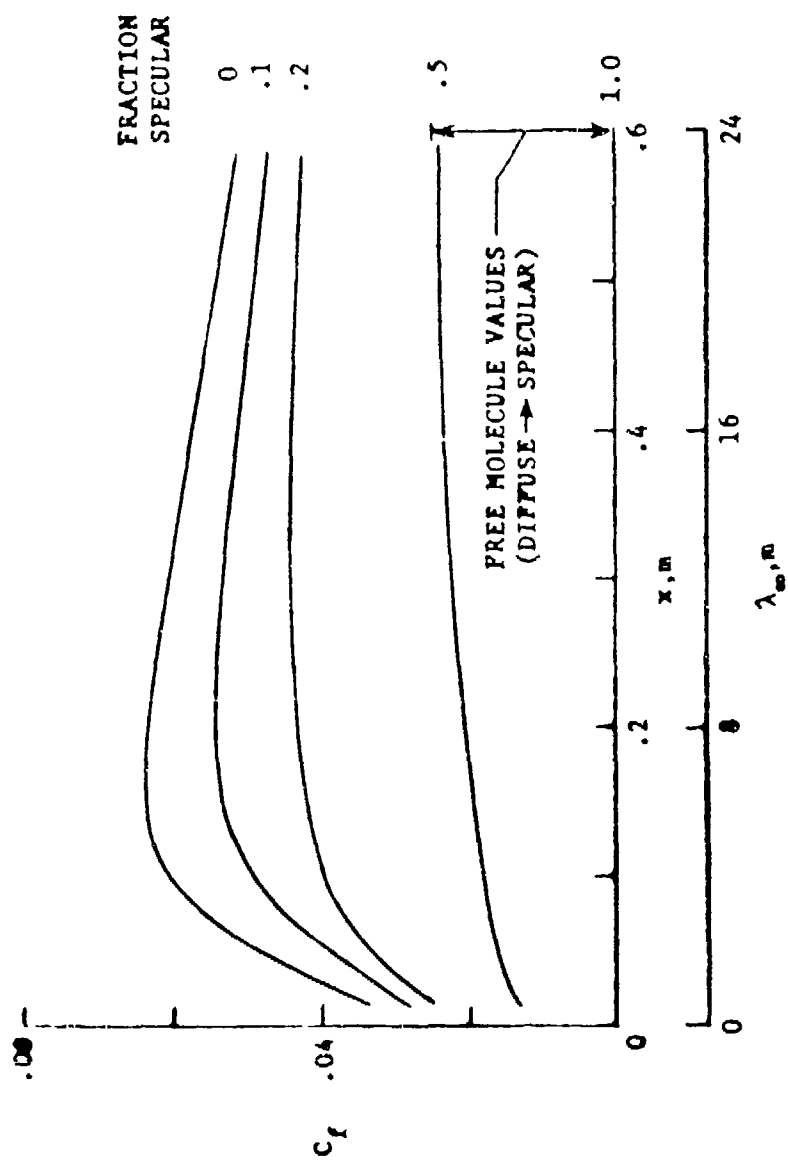
MACH NUMBER: 27.2

WALL TEMPERATURE: 1000K

EFFECT OF ALTITUDE ON SKIN FRICTION COEFFICIENT
 ($T_w = 1000K$, DIFFUSE, $n_w = 27.2$, ZERO THICKNESS)



EFFECT OF REFLECTION MODEL ON SKIN FRICTION COEFFICIENT
(FLAT PLATE, $T_w = 1000K$, $U_\infty = 7.5 \text{ km/s}$, $ALT = 90 \text{ km}$)



DSMC CALCULATIONS FOR FLAT PLATE AT
15° ANGLE OF INCIDENCE

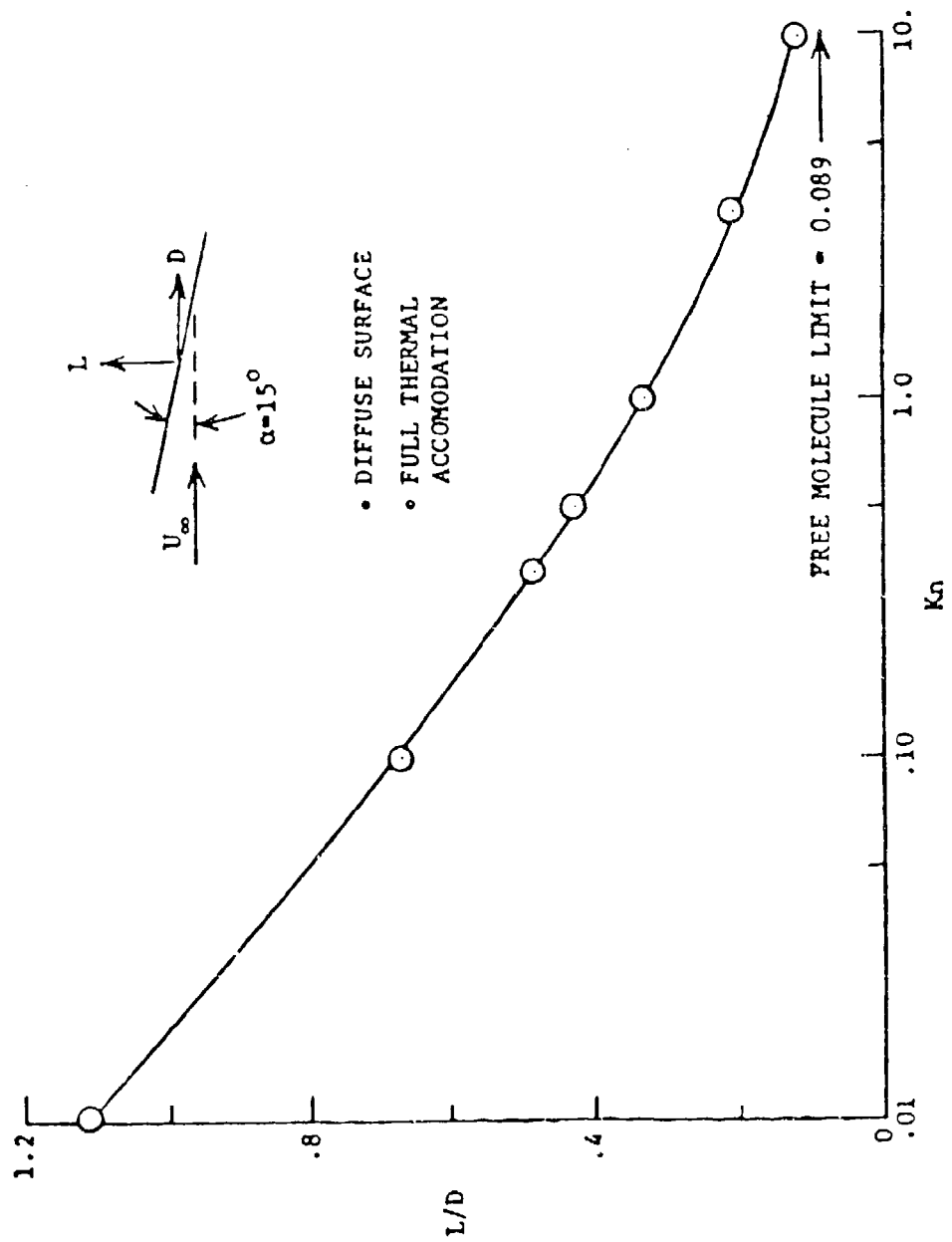
GAS: ARGON

KNUDSEN NUMBER: 0.01 TO 10

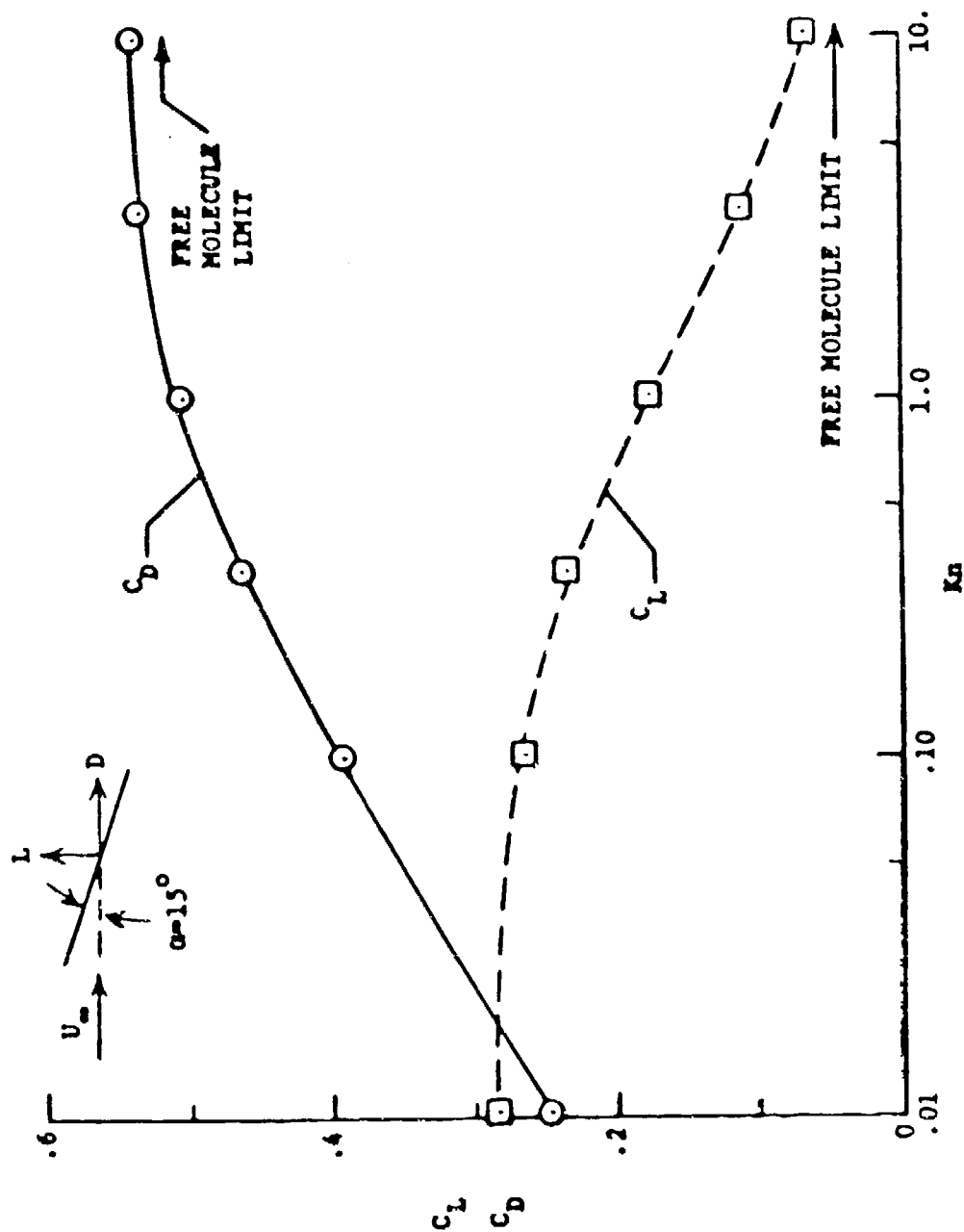
SPEED RATIO: 7

WALL TEMPERATURE: 300K

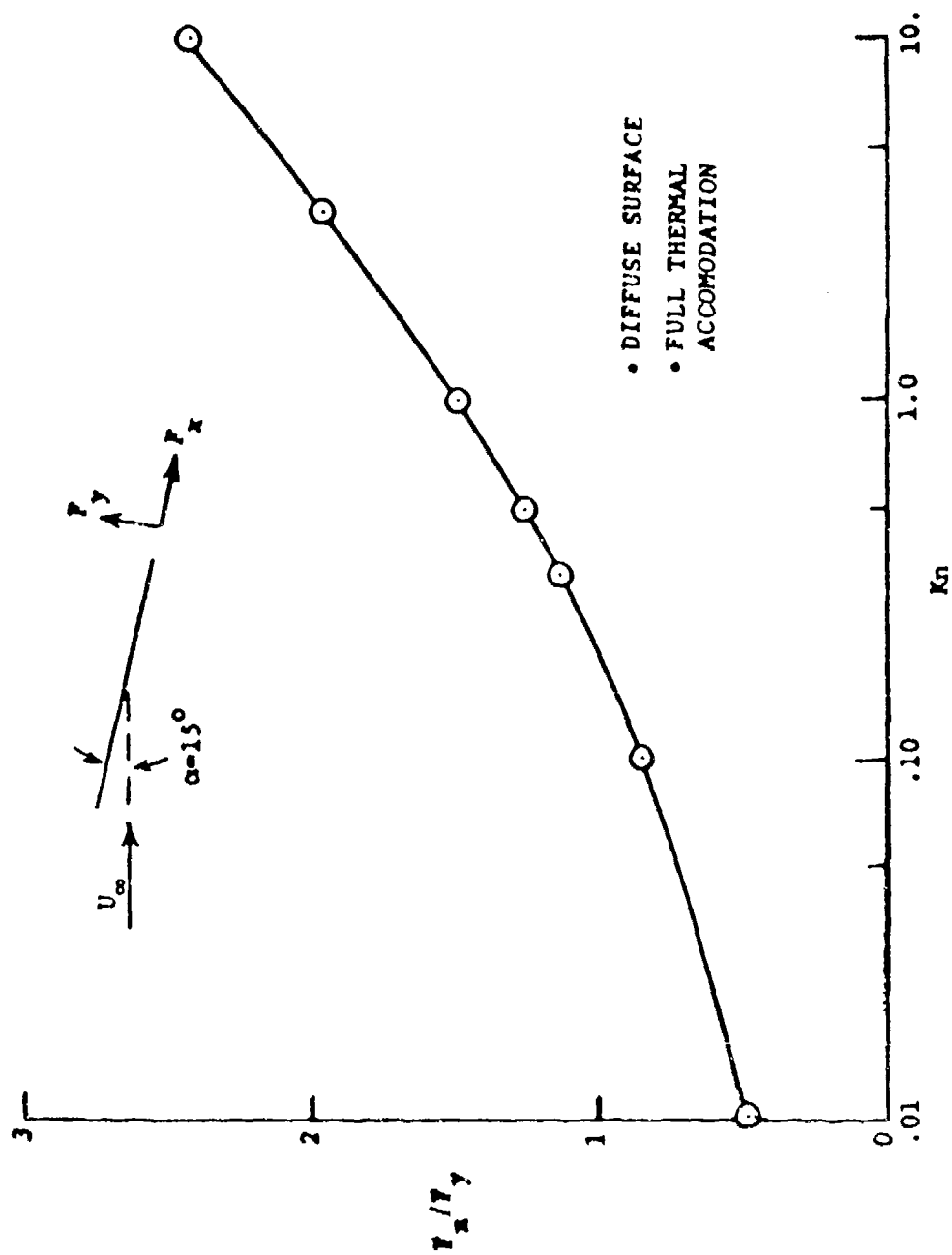
LIFT-DRAG RATIO AS A FUNCTION OF PLATE KNUDSEN NUMBER
 (S = 7, $T_w = 300K$, $T_\infty = 1500K$, $U_\infty = 5.532$ KM/S, ARGON)



LIFT AND DRAG COEFFICIENTS AS A FUNCTION OF PLATE KNUDSEN NUMBER
 (S = 7, $T_w = 300K$, $T_\infty = 1500K$, $U_\infty = 5.53 \text{ km/s}$, ARGON)



RATIO OF FRICTION TO PRESSURE FORCES ON A PLATE IN TRANSITIONAL FLOW
 (S = 7, $T_w = 300K$, $T_\infty = 1500K$, $U_\infty = 5.53 \text{ km/s}$, ARGON)



NUMERICAL SIMULATION SITUATION

- A METHOD (DSMC) EXISTS FOR CALCULATING REAL GAS FLOWS ABOUT SIMPLE OR COMPLEX CONFIGURATIONS IN THE TRANSITIONAL AND FREE-MOLECULE REGIMES.
- CURRENT GAS-SURFACE INTERACTION MODEL IMPLEMENTED IN THE DSMC METHOD (DIFFUSE, SPECULAR, OR A COMBINATION OF THE TWO) IS NOT ADEQUATE. HAS IMPORTANT IMPLICATIONS CONCERNING LIFT AND DRAG PREDICTIONS.
- NEEDS
 - IMPROVED GAS-SURFACE MODEL THAT IS COMPATIBLE WITH DSMC METHOD. A MODEL THAT IS GENERAL, RIGOROUS, AND SATISFIES KNOWN EXACT SOLUTIONS AND EXPERIMENTAL OBSERVATIONS.
 - FLIGHT AND GROUND BASED EXPERIMENTAL DATA ON GAS-SURFACE INTERACTIONS - REALISTIC SURFACES AND FLOW CONDITIONS. PROVIDE A BROAD EMPIRICAL BASE FOR MODELING AND COMPUTATIONAL PREDICTION.

Presentation for AFGL - Workshop on Atmospheric Density and Aerodynamic Drag Models for Air Force Operations, 20-22 October 87

1. "Satellite Drag and Lift Deduced From Measured Gas-Surface Interaction at 5 ev".

G.R. Karr and J.C. Gregory, University of Alabama in Huntsville, Huntsville, AL.

The space shuttle flight STS-8 carried a gas-surface interaction experiment prepared by Drs. Peters and Gregory of NASA/MSFC and the University of Alabama in Huntsville (UAH) respectively. The experiment recorded the angular distribution of atomic oxygen atoms reflecting from a surface. We have used the Nocilla reflection model to determine the speed ratio and direction of drifting velocity of these scattered atoms. From these results we have derived a model of the atomic oxygen reflection with which the lift and drag coefficient of various aerodynamic shapes can be calculated. In this section of the presentation, the lift and drag coefficient of spheres, cylinders, cones, and flat plates will be presented. The dependence of these aerodynamic coefficients on the gas-surface interaction will be discussed.

Gerald R. Karr, Mechanical Engineering Department, The University of Alabama in Huntsville, Huntsville, Alabama, 35899, USA

John C. Gregory, Chemistry Department, The University of Alabama in Huntsville, Huntsville, Alabama, 35899, USA

Palmer N. Peters, ES63, George C. Marshall Space Flight Center, Marshall Space Flight Center, Alabama, 35812, USA

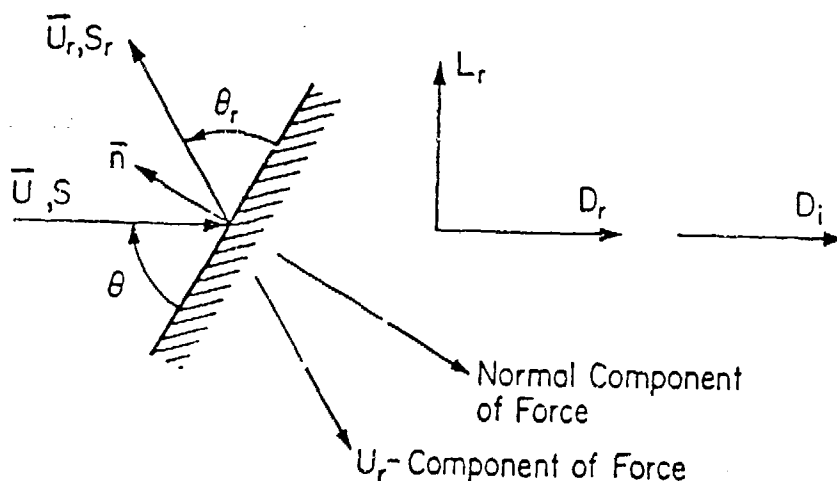


Fig. 1.1 Notation used in the Nocilla model.

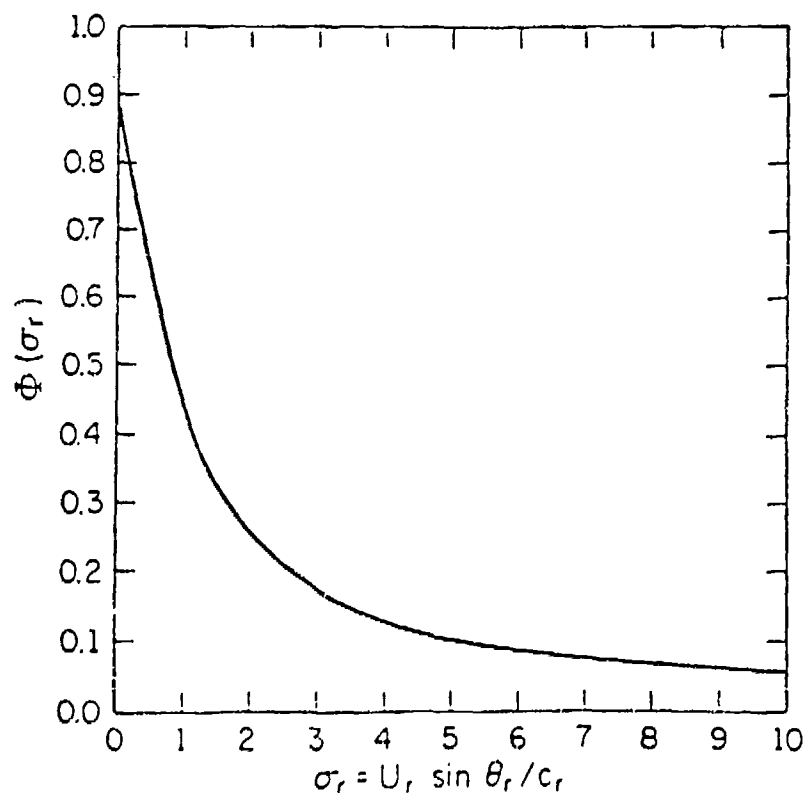


Fig. 1.2 Plot of the coefficient of the normal component of force for the Nocilla model as a function of σ_r .

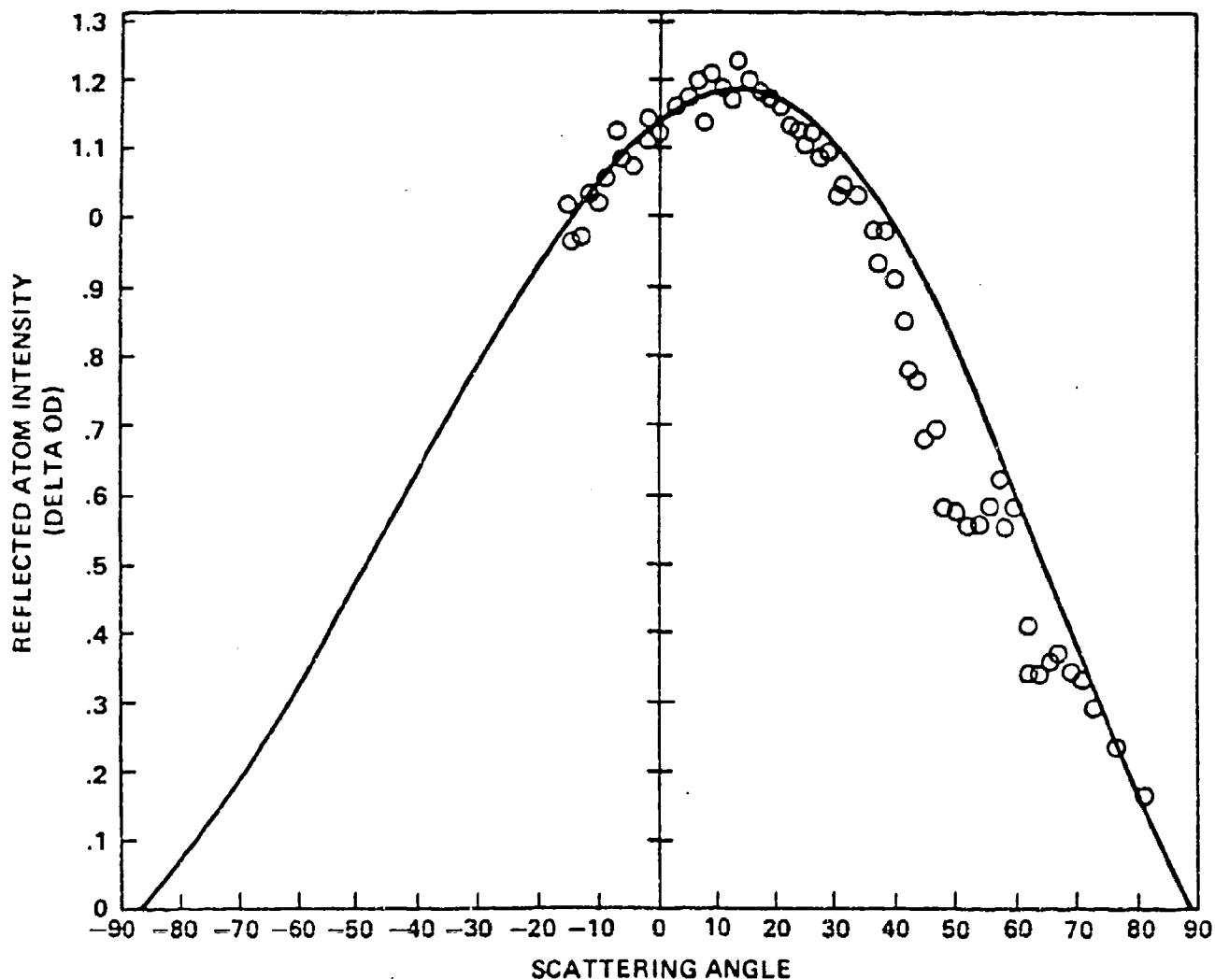


FIG. 1.3 FIT USING NOCILLA MODEL TO THE OUTSIDE ENVELOPE OF THE FLIGHT DATA. DISCREPANCIES ASSUMED DUE TO ABSORPTION ARTEFACTS IN THE SILVER FILM θ_r (NOCILLA) = 40° ; S_r = 0.2

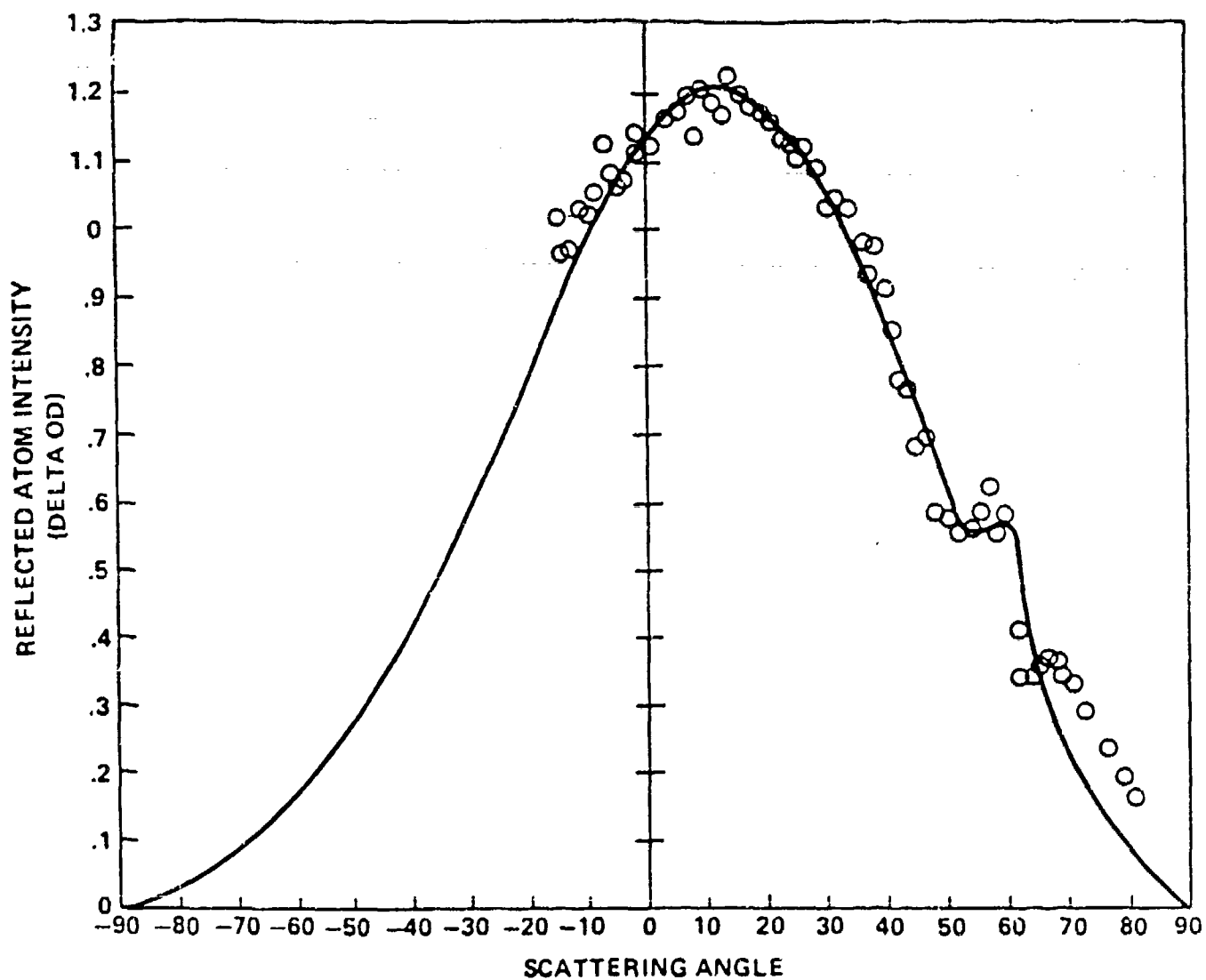


FIG. 1.4 FIT USING NOCILLA MODEL TO THE FLIGHT DATA ASSUMING A BI MODAL DISTRIBUTION. PARAMETERS WERE θ , (NOCILLA): MAIN LOBE 19° , SUPRASPECULAR LOBE 62° ; S , (MAIN LOBE) = 0.6, SUPRASPECULAR LOBE, 8.8. ONLY ABOUT 2% OF THE REFLECTED ATOMS WERE IN THE SUPRASPECULAR LOBE.

$$(1) \quad \hat{F}_{\text{reflection}} = \vec{U} \cdot \vec{n} \left[\vec{U}_r + \frac{1}{2} \phi(\sigma_r) c_r \vec{n} \right]$$

where

$$(2) \quad \phi(\sigma_r) = \frac{\pi^{\frac{1}{2}}}{2} \frac{1 + \text{erf } \sigma_r}{\chi(\sigma_r)}$$

$$(3) \quad c_r = (2RT_r)^{\frac{1}{2}}$$

$$(4) \quad \chi(\sigma_r) = e^{-\sigma_r^2} + \pi^{\frac{1}{2}} \sigma_r (1 + \text{erf } \sigma_r)$$

$$(5) \quad \sigma_r = S_r \sin \theta_r$$

Parameters

$$(6) \quad U_r = a U$$

$$(7) \quad c_r = b U$$

$$(8) \quad \theta_r = \frac{\pi}{2} P_r + (1-P_r) \theta$$

$$(9) \quad s_r = U_r / c_r = a/b$$

$$(10) \quad d\vec{F} = \vec{U} \cdot \vec{n} \, dA \, (-\vec{U} + \vec{U}_r + \frac{1}{2}(\sigma_r) c_r \vec{n})$$

$$(11) \quad C_D = 2.0 - s_r b \cos[\frac{\pi}{2}P_r + (2-P_r)\theta] + \frac{1}{2}(\sigma_r) b \sin\theta$$

$$(12) \quad C_L = s_r b \sin[\frac{\pi}{2}P_r + (2-P_r)\theta] + \frac{1}{2}(\sigma_r) b \cos\theta$$

Drag of Sphere

$$(13) \quad C_D = 2 + \left[s_r \frac{1 - \cos \frac{\pi}{2} P_r}{P_r (4 - P_r)} + \frac{.85}{3} \right] b$$

Results

(14) Case 1: $s_r = 0.2$; $P_r = 0.27$; $0.067 < b < 0.69$

(15) Case 2: $s_r = 0.6$; $P_r = 0.66$; $0.067 < b < 0.62$

(16) Case 1: $2.03 < C_D \text{ (plate @ 35 degrees)} < 2.315$

(17) Case 2: $2.03 < C_D \text{ (plate @ 35 degrees)} < 2.312$

(18) Case 1: $0.06 < C_L \text{ (plate @ 35 degrees)} < 0.62$

(19) Case 2: $0.09 < C_L \text{ (plate @ 35 degrees)} < 0.79$

(20) Case 1: $2.02 < C_D \text{ (sphere)} < 2.21$

(21) Case 2: $2.03 < C_D \text{ (sphere)} < 2.26$

2. "A Low-Cost Instrument for Direct Measurement of Atomic Oxygen-Scattering Profiles in the Molecular Flow Regime".

J.C. Gregory and G.R. Karr, University of Alabama in Huntsville, Huntsville, AL.

An instrument is described that was flown on STS-8 to measure the angular distribution of 5 ev atomic oxygen. The instrument was of novel design, was completely passive, and used thin silver films as the recording device. The devices are low cost and may be rapidly deployed in space to provide early return of the needed data. The method of data analysis will be discussed and the results of the STS-8 flight will be presented.

A proposed flight test will be discussed in which a number of the flight proven instruments are used to obtain improved information on molecular scattering at orbital energies. We propose to utilize a set of solid substrates at various angles of incidence and surface temperatures. The objective is to obtain a detailed understanding of scattering for a representative set of angles of incidence on materials of engineering interest. The preliminary plans for the flight program will be presented.

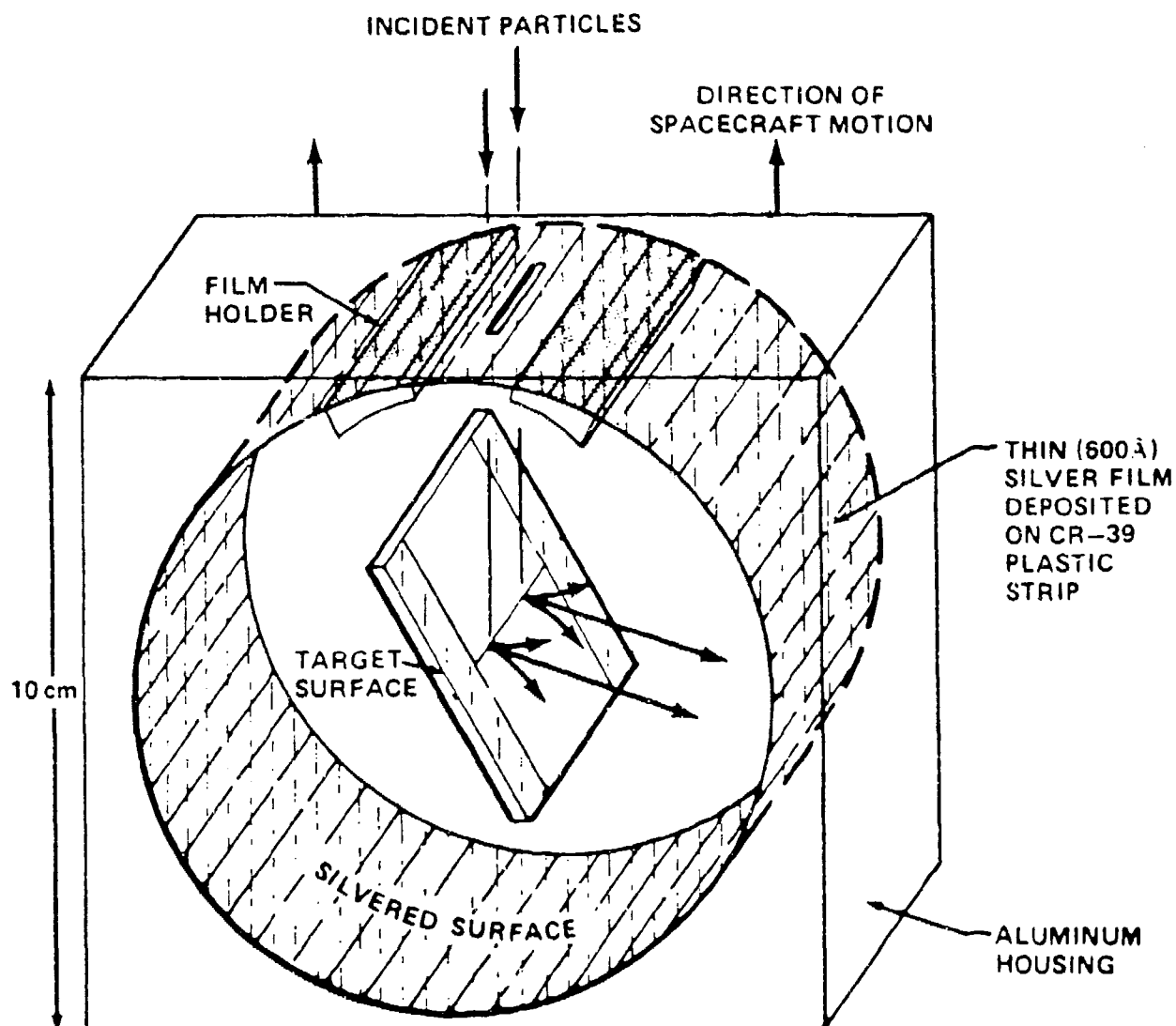


FIG. 2.1 THE OXYGEN ATOM REFLECTOMETER FLOWN ON SHUTTLE STS-8 AND THE LONG DURATION EXPOSURE FACILITY

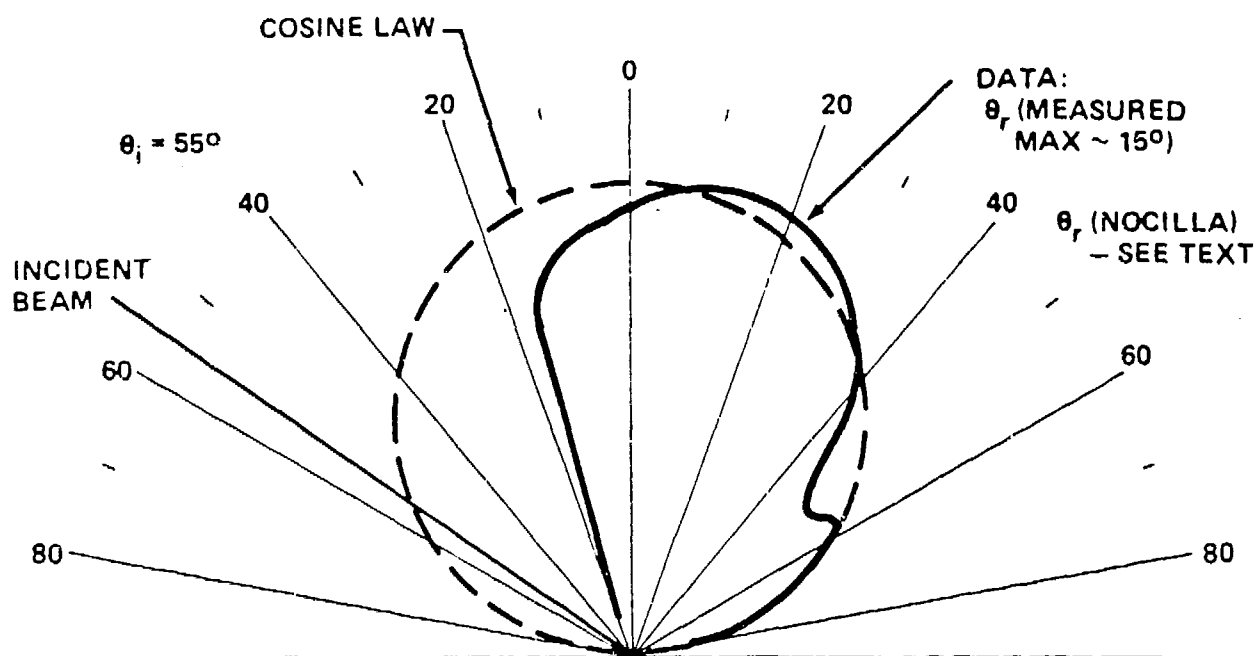


FIG. 2.2 POLAR DIAGRAM OF ANGULAR DISTRIBUTION OF 5eV OXYGEN ATOMS SCATTERED FROM POLISHED VITREOUS CARBON (ORBITAL FLIGHT DATA). A PURE COSINE LAW RE-EMISSION IS SHOWN FOR COMPARISON. THE CUT-OFF IN THE BACKWARD HEMISPHERE WAS CAUSED BY THE DETECTOR FILM HOLDER.

7.4

Variability in the Satellite Drag Coefficient C_d

W. Kent Tobiska
Aerospace Engineering Sciences Department
and
Laboratory for Atmospheric and Space Physics
Campus Box 392
University of Colorado, Boulder CO 80309

October 15, 1987

Variability in the Satellite Drag Coefficient C_d *

W. Kent Tobiska **

University of Colorado, Boulder Colorado

In most contemporary satellite orbit determination work, the spacecraft drag coefficient, C_d , is treated as a constant near the value of 2. This is not necessarily the most accurate value since variations are caused by surface angle of attack, temperature of atmospheric gas particles, and vehicle surface temperatures. When precisely determining drag, C_d varies considerably. In this paper, the classic theory detailing C_d in free molecular flow is first outlined where spacecraft surfaces are modeled as flat plates in rarefied gas flows. A comparison is made between the full C_d solution and contemporary simplifications. Then, first and second order evaluations of the full C_d formulation are made to estimate the range of C_d variation from two parameters: angle of attack and thermospheric temperature changes. The angle of attack determines the overall value of C_d while thermospheric temperatures contribute small variations. As a final result, a multiparameter C_d is formulated as $C_d(t, \alpha, T)$ and a method of experimentally deriving $C_d(t, \alpha, T)$ is proposed.

Nomenclature

A	spacecraft surface area
C_d	drag coefficient
C_d	expected drag coefficient
ΔC_d	incremental change in drag coefficient
E	kinetic energy of atmospheric particles
EUV	extreme ultraviolet solar wavelengths (xrays to 1031 Å)
erf	error function
F_d	atmospheric drag force on a satellite
g	gravity
H	density scale height
ΔH	incremental change in density scale height
k	Boltzman's constant
m	mass of a particle or spacecraft
$[N_2]$	molecular nitrogen concentration
O	atomic oxygen
$[O]$	atomic oxygen concentration
$[O_2]$	molecular oxygen concentration

* Submitted to *Journal of Spacecraft and Rockets* August 28, 1987.

** Research Assistant, Laboratory for Atmospheric and Space Physics; Ph.D. candidate, Aerospace Engineering Sciences, University of Colorado

\dot{P}	satellite orbit period rate change
r	ratio of reemitted to incident particle velocities
\bar{r}	circular orbit semimajor axis
S	molecular speed ratio
T	temperature (Kelvin)
ΔT	incremental change in temperature (Kelvin)
t	time
v	velocity of a particle or spacecraft
x, y, z	Cartesian coordinate system axis designations; z is also altitude
Δz	incremental change in altitude
α	angle of attack
α_{th}	thermal accommodation coefficient
ρ	atmospheric mass density
$\Delta\rho$	incremental change in atmospheric mass density

Subscripts

d	drag
$diff$	diffuse reflection
i	incident
r	reemitted
rms	root mean square
sc	spacecraft
$spec$	specular reflection
th	thermal
w	wall or surface
0	reference value
∞	exospheric when related to temperature

Introduction

During the era of space flight over the past 3 decades, the aerospace engineering community has tackled a wide variety of orbit determination problems. Among them has been the modeling of orbit decay induced by atmospheric drag. This has a significant effect on the lifetimes of low Earth orbiting satellites. Space station, co-orbiting platform, aerospaceplane, and acrocapture vehicle environmental designs need the most accurate atmospheric densities and drag coefficients possible.

The commonly used equation describing the drag force

$$F_d = \frac{1}{2} C_d A \rho v^2 \quad (1)$$

is derived from the kinetic energy of a space vehicle and relates the atmospheric drag force, F_d , to the satellite effective area, A , atmospheric mass density, ρ , and spacecraft velocity, v^2 . Historically, the greatest uncertainty in numerically solving this equation has been estimating ρ , determining A , and calculating C_d , in that order. As a result, much effort has been expended toward developing time dependent,

empirical model atmospheres [1,2] since the late 1950's. While satellite areas are estimated with more or less accuracy, C_d is often set to a first order approximation. Flat plate, spherical, or cylindrical satellite shapes are assumed and an "effective" or projected area perpendicular to the spacecraft direction of motion is used. This method of approximating or simplifying C_d has allowed for use of a maximum angle of attack ($\alpha = 90$ degrees) for the reduced area [3] and has yielded generally acceptable results, enabling modeled and satellite derived atmospheric densities to be matched. However, it is not appropriate for studying variations in C_d .

The classical treatment of C_d is rigorously developed on the basis of geometry, conservation of energy, and conservation of momentum in gas dynamics. This differs from the use of the contemporary "ballistic coefficient," $\frac{C_d A}{m}$ (in units of $\text{m}^2 \text{kg}^{-1}$) where C_d and A are described above and m is the spacecraft mass. This coefficient is an empirical term which folds the uncertainties in all three variables within one term, allowing a match between the theoretical atmospheric drag force on a satellite and the observed force obtained from the orbit decay rate.

A number of sources have discussed the evaluation of C_d in free molecular flow, which is a rarefied gas flow [4,5,6,7,8,9,10]. Free molecular flow differs from Newtonian flow in that the latter assumes the particles are at rest with respect to one another. Zahn [11] noted that a free molecular flow becomes a Newtonian particle flow in the limit where an extremely large ratio of the mass velocity (or spacecraft velocity), v_{sc} , to the gas thermal velocity, v_{th} , exists. This ratio is defined as the molecular speed ratio, S , where

$$S = \frac{v_{sc}}{v_{th}} \quad (2)$$

and $S \rightarrow \infty$ in the limiting case. In equation (2), if $S > 1$, then particles are assumed to strike only the forward face of a body. If $S \gg 1$, the thermal velocities of the particles can be neglected and there is an approximated Newtonian flow. However, as will be shown below, when $S < 10$, gas particle thermal velocities may be accounted for in evaluating C_d . The impinging gas particle velocities vary in magnitude as well as direction and assume a Maxwellian distribution, as do the reemitted particles adsorbed onto the surface, which come off with no "memory" of their initial velocity magnitudes or directions.

From the principle of equipartition, the Maxwellian distribution of velocities in a gas can be summarized as

$$v_{rms} = \sqrt{v_x^2 + v_y^2 + v_z^2} = \sqrt{\frac{3kT}{m}} \quad (3)$$

Using SI units, k is Boltzman's constant, T is the temperature in degrees Kelvin, and m is the mass of the particle. This analysis uses $v_{th} = v_{rms}$.

A gradual development of the atmospheric drag coefficient at satellite altitudes followed from the efforts of Millikan [12], who analyzed spheres moving through a gas with a large mean free path and with specular reflection. Epstein [13] showed

that diffuse reflection of gas particles plays an important role in momentum exchange between a body and a gas and that this interaction has a gas temperature dependence. Sanger [4] pioneered work with extremely rarified gases, analyzing the air pressure on bodies of various shapes and outlining drag and lift coefficients. The three regimes of gas kinetics, including rarified gases, and their differences as related to aerodynamics was explained by Tsien [5], followed by the analytic and experimental work of Stalder, et al. [6,7,8]. Stalder calculated surface temperatures in a rarified gas flow, experimentally determined drag coefficients and temperatures on bodies of varying shapes, and noted that the drag coefficient C_d was dependent upon the molecular speed ratio, S , and the body surface temperature, T_w . The total C_d due to diffusive and specular reflections was summarized by Schaaf and Chambre [9] while Hoerner [10] simplified the expression for C_d in his work.

Theoretical Drag Coefficient

The fundamental physics describing gas particle interactions at and with spacecraft surfaces encompasses the concepts of body geometry, the conservation of energy in heat transfer and the conservation of momentum. In this paper, the heat transfer between particle and surface "wall", which includes defining a thermal accommodation coefficient, is referenced only in comparison to other work. It is analyzed in depth by Stalder and by Schaaf and Chambre. The conservation of momentum combined with geometry are discussed in detail below.

The drag coefficient for diffuse reflection analytically described by Stalder, et al. [8] and summarized by Schaaf and Chambre [9], is

$$C_{d_{diff}} = \frac{2}{\sqrt{\pi}S} \left[e^{-(S \sin \alpha)^2} + \sqrt{\pi} S \sin \alpha \left(1 + \frac{1}{2S^2} \right) \operatorname{erf}(S \sin \alpha) + \frac{\pi S}{S_w} \sin^2 \alpha \right]. \quad (4)$$

Similarly, the specular reflection C_d described by the same authors is

$$C_{d_{spec}} = \frac{4 \sin \alpha}{\sqrt{\pi}S^2} \left\{ (S \sin \alpha) e^{-(S \sin \alpha)^2} + \sqrt{\pi} \left[\frac{1}{2} + (S \sin \alpha)^2 \right] \operatorname{erf}(S \sin \alpha) \right\}. \quad (5)$$

These are expressions for a flat plate at an angle of attack, α , and are shown in figures 1 and 2. The flat plate approximation may be used in free molecular flow for a number of spacecraft surfaces since the vehicle dimensions "seen" by a particle, compared to its own size, are extremely large. S_w in equation (4) is the molecular speed ratio referenced to the temperature of the surface, where

$$S_w = \frac{v_{Ac}}{\sqrt{\frac{3kT_w}{m}}}. \quad (6)$$

These equations do not use the ratio of specific heats, γ , and hence are valid for either monatomic or diatomic gases.

Equations (4) and (5) represent two component formulations of C_d which include impinging momentum terms related to the angle at which incident particles strike the surface and terms describing the diffuse or specular reflection of particles.

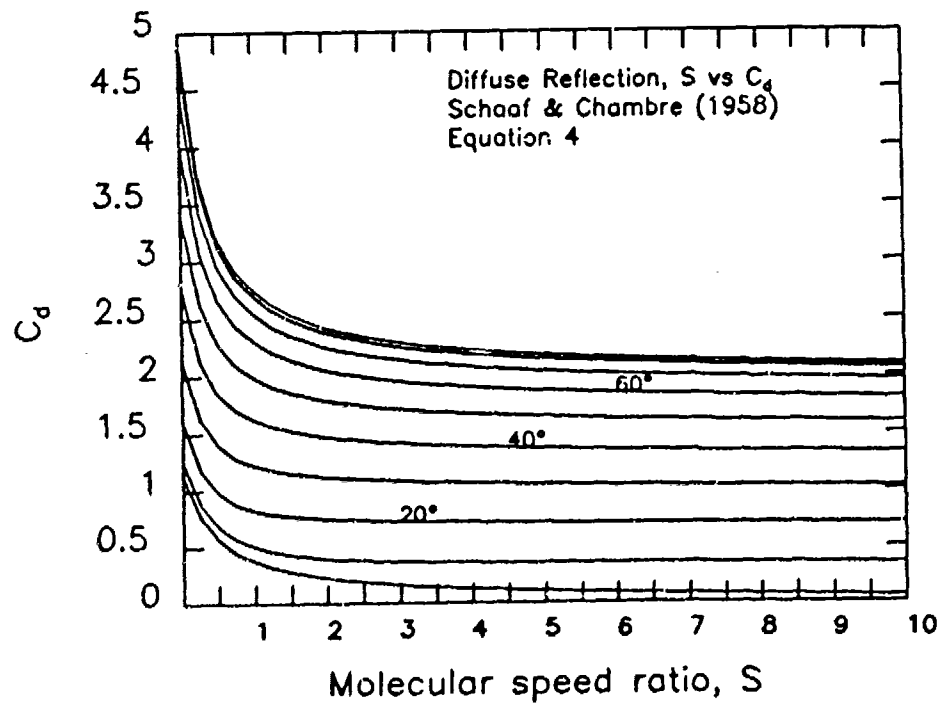


Fig. 1. Diffuse reflection and reemission drag coefficient (equation (4)) for angles of attack between 0 and 90 degrees. From Schaaf and Chambre [9].

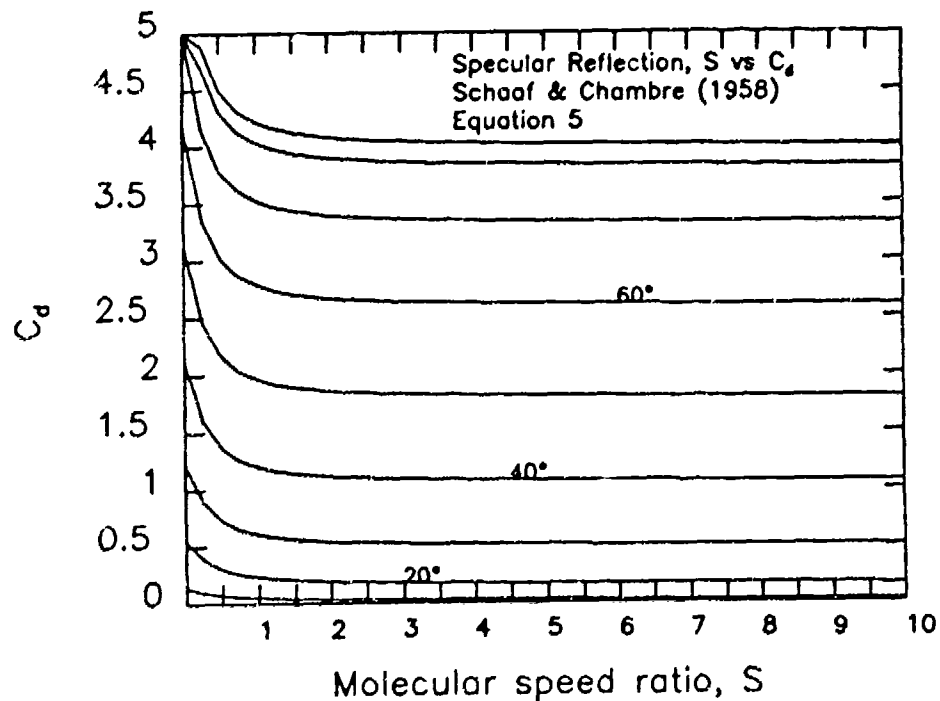


Fig. 2. Specular reflection drag coefficient (equation (5)) for angles of attack between 0 and 90 degrees. From Schaaf and Chambre [9].

These equations are derived from the conservation of momentum and geometry of the system as detailed by Sanger [4] and Stalder, et al. [8]. The 90 degree contour in figure 1 may be compared to the flat plate drag coefficient given by Cook [3]. His formulation for a diffuse reemission drag coefficient, plotted in figure 3, is

$$C_{diff} = 2(1 + \frac{2}{3}r) \quad (7a)$$

where r is related to the thermal accommodation coefficient, α_{th} , and is written as

$$r = \frac{v_r}{v_i} = \{1 + \alpha_{th}[\frac{T_w}{T_i} - 1]\}^{\frac{1}{2}}. \quad (7b)$$

Cook defines v_r as the speed of the reemitted particle, v_i as the speed of the incident particle, T_w as the surface temperature, T_i as the kinetic temperature of the incident particle, and

$$\alpha_{th} = \frac{E_i - E_r}{E_i - E_w} \quad (7c)$$

where the subscripts i, r, w refer to the incident, reemitted, and surface ("wall") average kinetic energies. Equation (7a) may be a helpful simplification of equation (4) under certain conditions, although differences arise from the weighting of $\frac{T_w}{T_i}$ in each equation.

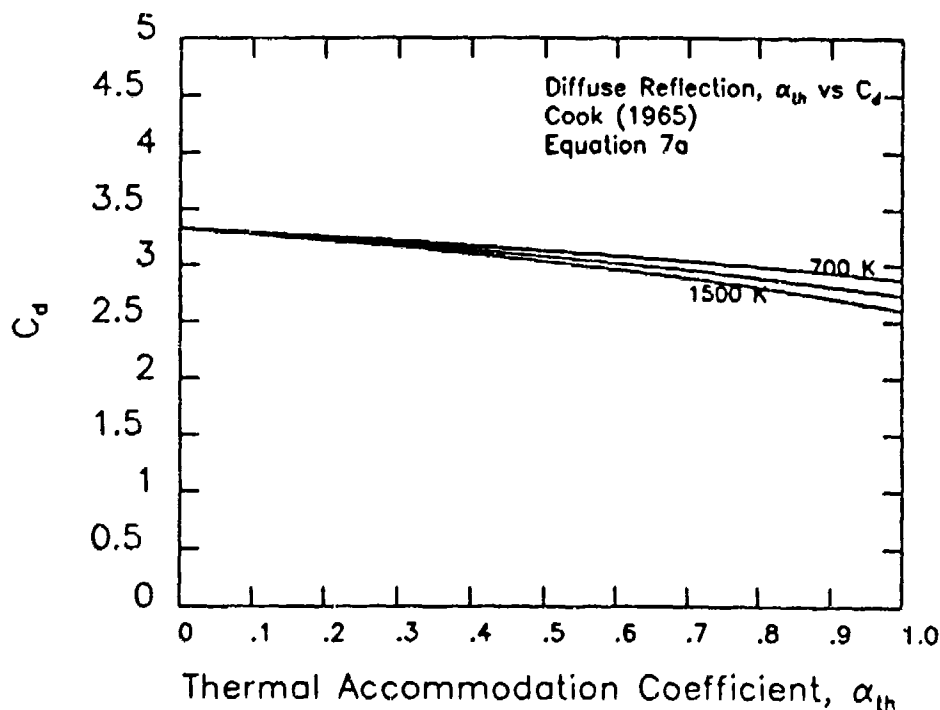


Fig. 3. Diffuse reflection and reemission drag coefficients from Cook [3] assuming an angle of attack of 90 degrees for a projected spacecraft area, a thermal accommodation coefficient between 0 and 1, T_i at 700, 1000, 1500 K, and T_w at 300 K.

Equation (7a) is based on a projected area perpendicular to the direction of motion. This "effective" area is coupled with the drag coefficient where the angle of attack is set to 90 degrees. The equation can properly be used for an approximated C_d based on a projected area and accounting for skin temperature effects. The full expression, equation (4), is properly used with the full surface area at an angle of attack, accounting for gas thermal velocities as well as skin temperature effects.

Using equation (7a), or figure 3, one notes that $C_d = 2$ for the impingement component. It can be shown that for low Earth orbiting spacecraft, the contribution of the reemission term is between $\frac{1}{3}$ and $\frac{1}{2}$ for r equal to $\frac{1}{2}$ to $\frac{3}{4}$. Summing the impingement and reemission components, a value between 2 and 2.5 has been commonly used. However, one may see below that it is not necessarily an accurate value for use in the drag equation (1). An example of a more reasonable impingement plus diffuse reemission value ranges from 0.7 to 1.0 for a flat plate angle of attack between 20 and 30 degrees and a moderate speed ratio, S , between 5 and 7.25.

Although a C_d value of 0.7 to 1.0 may appear low, it should be understood that a spacecraft surface likely combines both diffuse and specular reflection as well as flat plate and spherical or cylindrical surface geometry. Non flat plate geometry tends to give higher-valued drag coefficients. When performing an in-depth analysis of a particular spacecraft, the diffuse and specular components and surface geometries should be summed in a weighted analysis to give the total C_d . The result may raise the value of C_d from 0.7 to 1.0 to a larger value.

First and Second Order Approximations of C_d Variation

Figures 1 and 2 show a wide range of C_d variation due to different angles of attack. This is clearly the dominant effect. From these figures, one can see that C_d may range from near 0 to 4 for a flat plate. The area exposed to particle impingement strongly defines the first order approximation of a drag coefficient.

The range of variation in C_d due to thermospheric temperature changes can be estimated by referring to the cases of maximum, moderate, and minimum solar activity. Table 1 outlines this. T_∞ is the temperature of the exosphere and closely approximates the temperature in an orbit near the top of the thermosphere. The actual range of S for a low Earth orbiter is 5 to 7.25 for high to low solar activity. This also corresponds to high and low exospheric temperatures during 1982 through 1986. From equation (4), if $S = 5$, $C_d = 0.707$; if $S = 6$, $C_d = 0.703$; and if $S = 7.25$, $C_d = 0.699$. For a $\pm 20\%$ change in S , C_d changes by $\pm \frac{1}{2}\%$ as a result of the change in the v_{rms} of the gas particles. For 1500 K, $v_{rms} = 1.52 \text{ km sec}^{-1}$; for 1000 K, $v_{rms} = 1.24 \text{ km sec}^{-1}$; and for 700 K, $v_{rms} = 1.04 \text{ km sec}^{-1}$ for atomic oxygen, O, which has three degrees of freedom. There is a $\pm 20\%$ variation around the $v_{rms} = 1.24 \text{ km sec}^{-1}$ value which is the basis for the change in S . This translates into a 1% change in C_d due to thermospheric temperature changes over the course of a solar cycle.

Table 1 C_d Variation with Solar Activity

Solar Activity ^a	T_{∞} (K)	v_{rms} (km sec ⁻¹)	S	$C_{d,eff}$ ^b
high	1500	1.52	5	0.707
moderate	1000	1.24	6	0.703
low	700	1.04	7.25	0.699

^asolar cycle 21 ^b C_d evaluated for $\alpha = 20$ degrees, including small S_w term from equation (4) for $T_w = 300$ K.

The diffuse reflection assumption for C_d may be applicable to flight conditions for two reasons. As first noted by Sanger, surfaces are often completely rough based on experimental observations. This, combined with the assumption that the impinging particles at altitudes near 500 km are predominantly reactive O, leads to the heuristic conclusion that diffuse, and not specular reflection, is the major process occurring in an upper thermosphere flight regime.

An initial order of magnitude method of approximating the change in C_d from an expected value, due to thermospheric temperature variations, follows. From equation (1), the change in C_d is written as

$$\Delta C_d = \frac{-2F_d}{Av^2\rho^2} \Delta\rho \quad (8a)$$

or

$$\Delta C_d = \bar{C}_d \frac{\Delta\rho}{\rho}. \quad (8b)$$

ΔC_d can be \pm and is the same sign as $\Delta\rho$ and \bar{C}_d is the expected value. However, in equation (1), C_d and F_d have opposite signs in a rigorous interpretation, with F_d taken as a force directed opposite the motion of the satellite. Therefore, the negative sign of equation (8a) is dropped in equation (8b). $\frac{\Delta\rho}{\rho}$ can be estimated at ± 0.005 . This value is obtained by using a typical O mass density at 500 km for moderately high solar activity of $\rho \approx \rho[O] = 10^{-12}$ kg m⁻³. Figure 4 from the MSIS thermospheric density model [2] shows this for day 300 of 1982, a typical profile during high activity in solar cycle 21. To obtain $\Delta\rho$, one uses the barometric law

$$\rho = \rho_0 e^{\frac{-(z-z_0)}{H(z)}} \quad (9)$$

and the scale height of a constituent (here, atomic oxygen)

$$H(z) = \frac{kT(z)}{mg(z)}, \quad (10)$$

to find the incremental change from the density at a specified altitude and at high solar activity due to temperature changes,

$$\Delta\rho = \rho_0 \frac{\Delta z}{H^2} e^{-\frac{\Delta z}{H}} \Delta H \quad (11)$$

with $\Delta z = z - z_0$. The expression for ΔH is linearly related to ΔT and is

$$\Delta H = \frac{k}{mg} \Delta T. \quad (12)$$

By substituting $\Delta T = 1000 - 700 = 300$ K, $H = 61.25$ km, $\Delta H = 18.37$ km, and $\Delta z = 1$ km, then $\Delta\rho = \pm 5 \times 10^{-15}$ kg m⁻³. Hence, $\frac{\Delta\rho}{\rho_0} = \pm 0.005$ and $\Delta C_d = \pm 0.0035$. From high to low solar activity, C_d therefore has a range of 0.706 to 0.699. This range assumes a constant angle of attack and skin temperature of the spacecraft. The method accounts for both the vehicle kinetic energy and the particle thermal energy, assumes a Maxwellian velocity distribution of the particles, and allows us to look at general range of values of C_d due to solar EUV heating of the thermosphere.

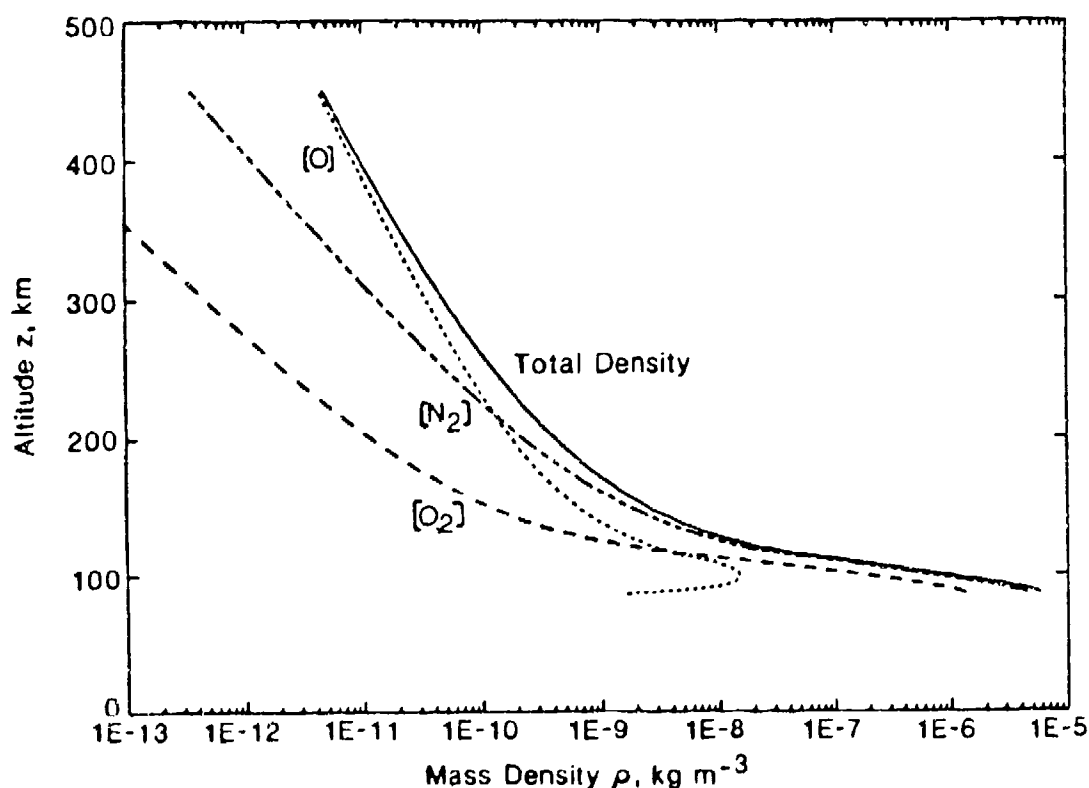


Fig. 4. MSIS model thermospheric densities at high activity during solar cycle 21, day 300 of 1982.

Method for Experimentally Deriving C_d Variation

A more accurate method for determining the second order effect of $C_d(t, \alpha, T)$ changes from thermospheric temperatures is calculated from the relationship

$$C_d(t, \alpha, T) = \bar{C}_d(\alpha, T) + \Delta C_d(t, \alpha, T). \quad (13)$$

This is different from the order of magnitude approximation in equation (8b). $\bar{C}_d(\alpha, T)$ is the expected value obtained from figure 1 for a certain solar activity or S value. The other term

$$\Delta C_d(t, \alpha, T) = \frac{-3\pi \frac{A}{m} \bar{r}(t) \bar{C}_d^2(\alpha, T)}{\dot{P}(t, \alpha, T)} \Delta \rho(t, T) \quad (14)$$

results from an analytic formulation by King-Hele [14], modified by Tobiska [15]. It combines orbit averages of the angle of attack, surface temperature effects, and solar cycle variation through the satellite orbit period data. It uses a modeled density change to obtain $\Delta C_d(t, \alpha, T)$.

$\frac{A}{m}$ is the area to mass ratio of the satellite, $\bar{r}(t)$ is a circular orbit semimajor axis, $\bar{C}_d(\alpha, T)$ is the expected drag coefficient, $\dot{P}(t, \alpha, T)$ is the orbit period rate change data, and $\Delta \rho(t, T)$ is a modeled change in thermospheric density due to EUV heating. The largest uncertainty in this formulation will usually enter from A , $\bar{C}_d(\alpha, T)$, and $\Delta \rho(t, T)$ for a given satellite during a given period of time.

Conclusions

The drag coefficient, C_d , may vary due to changes in the spacecraft surface angle of attack and the gas temperature in rarified gas flows. It is not a constant and may vary significantly from 2, particularly as a result of high to low angles of attack. Assuming that the spacecraft area, angle of attack, and a modeled atmospheric density are relatively well known, the C_d variation due to gas temperature changes can theoretically be derived. This variation is explained by changes in the kinetic energy of the gas particles over a solar cycle resulting from a variation in solar EUV energy input into the atmosphere at satellite altitudes.

It is possible to quantitatively describe the relative drag coefficient variability due to solar cycle activity from long term satellite orbit period rate change observations. In doing this, the spacecraft angle of attack, the expected drag coefficient, the change in atmospheric density, the true surface area of the satellite, its mass, and its semimajor axis each orbit over a period of time must be known or closely estimated. Uncertainties in these variables affect the absolute magnitude of ΔC_d but not the relative variation due to the change in gas thermal energies.

Angle of attack variations should cause extremely large variations in C_d , i.e. up to 100%. Thermospheric temperature changes over the course of a solar cycle should cause variations on the order of 1% in C_d .

Acknowledgements

This work was part of research conducted at the Laboratory for Atmospheric and Space Physics (LASP), University of Colorado. LASP graciously provided the computing facilities which made this work possible. In addition, the author appreciates the timely, in depth comments by D. Siskind and S.A. Stern in the formative stage of this work.

References

- ¹ Jacchia, L.G., "Revised Static Models of the Thermosphere and Exosphere with Empirical Temperature Profiles," SAO Special Report 332, May 1971.
- ² Hedin, A.E. "A Revised Thermospheric Model Based on Mass Spectrometer and Incoherent Scatter Data: MSIS 83," *J. Geophys. Res.*, Vol. 88, Dec. 1983, pp. 10170-10188.
- ³ Cook, G.E., "Satellite Drag Coefficients," *Planet. Space Sci.*, Vol. 13, 1965, pp. 929-946.
- ⁴ Sänger, E., "The Gas Kinetics of Very High Flight Speeds," Translation of ZWB Forschungsbericht Nr. 972, May 1938, NACA Tech. Mem. 1270, May 1950.
- ⁵ Tsien, H., "Superaerodynamics, Mechanics of Rarefied Gases," *J. Aero. Sci.*, Vol. 13, Dec. 1946, pp. 653-664.
- ⁶ Stalder, J.R. and Jukoff, D., "Heat Transfer to Bodies Traveling at High Speed in the Upper Atmosphere," NACA Tech. Rep. 944, August 1948.
- ⁷ Stalder, J.R., Goodwin, G., and Creager, M.O., "A Comparison of Theory and Experiment for High-Speed Free-Molecule Flow," NACA Tech. Note 2244, Dec. 1950.
- ⁸ Stalder, J.R. and Zurick, V.J., "Theoretical Aerodynamic Characteristics of Bodies in a Free-Molecule-Flow Field," NACA Tech. Note 2423, July 1951.
- ⁹ Schaaf, S.A. and Chambré, P.L., "Flow of Rarefied Gases," *Fundamentals of Gas Dynamics*, Vol. III, sec. H, ed. H.W. Emmons, Princeton University Press, 1958.
- ¹⁰ Hoerner, S.F., *Fluid-Dynamic Drag*, sec. 18-17, published by the author, 1958.
- ¹¹ Zahm, A.F., "Superaerodynamics," *J. Franklin Inst.*, Vol. 217, 1934, pp. 153-166.
- ¹² Millikan, R.A., "The General Law of Fall of a Small Spherical Body through a Gas, and its Bearing upon the Nature of Molecular Reflection from Surfaces," *Phys. Rev.*, Vol. 22, July 1923, pp. 1-23.
- ¹³ Epstein, P.S., "On the Resistance Experienced by Spheres in their Motion through Gases," *Phys. Rev.*, Vol. 23, 1924, pp. 710-733.
- ¹⁴ King-Hele, D., *Theory of Satellite Orbits in an Atmosphere*, Butterworths, London, 1964.
- ¹⁵ Tobiska, W.K., "Predictive Model of the Orbit Decay of the Solar Mesosphere Explorer", Thesis, University of Colorado, Boulder, 1985.

Satellite Drag Coefficient Variability
AFGL Density Workshop, Session VII
October 22, 1987
W. Kent Tobiska

In satellite orbit determination work, the spacecraft drag coefficient, C_d , is often considered a constant near 2. This presentation details the variations in C_d caused by the parameters describing the physical changes due to surface angle of attack, temperature of atmospheric gas particles, and vehicle surface temperatures.

The classic theory of C_d in free molecular flow is outlined with mathematical formulations for diffuse and specular reflections from spacecraft surfaces. These surfaces are modeled as flat plates in rarefied gas flows. A comparison is made between the full C_d solution and contemporary simplifications. Evaluations of C_d variations are made to estimate the range of variation due to two parameters: angle of attack and thermospheric temperature changes. The angle of attack determines the predominant magnitude of C_d , which may vary by 100%, while thermospheric temperatures contribute small variations on the order of 1%.

Finally, a multiparameter C_d is formulated as $C_d(t, \alpha, T)$ and a method of experimentally deriving $C_d(t, \alpha, T)$ is proposed. Preliminary results are shown in which this method is used with orbit data from the Solar Mesosphere Explorer (SME) satellite and with a modeled thermospheric density over 5 years at SME altitudes. The derived results compare favorably with the expected range of C_d variations.

Satellite Drag Coefficient Variability

AFGL Density Workshop, Session VII

October 22, 1987

W. Kent Tobiska

I. BASIS FOR C_d VARIATION

1. Concept: A variable C_d accounts for continually changing physical processes affecting a satellite orbit.
2. Terminology: $F = \frac{1}{2} C_d A \rho v^2$, $\beta = \frac{C_d A}{m}$
3. History: Newton, Millikan, Epstein, Sanger, Stalder, Schaff & Chambre, Cook

4. Mathematical formulation of C_d

II. DETAILS OF C_d VARIATION

1. Ranges for α , S
2. Modeling C_d
3. Examples

III. SUMMARY OF RESULTS

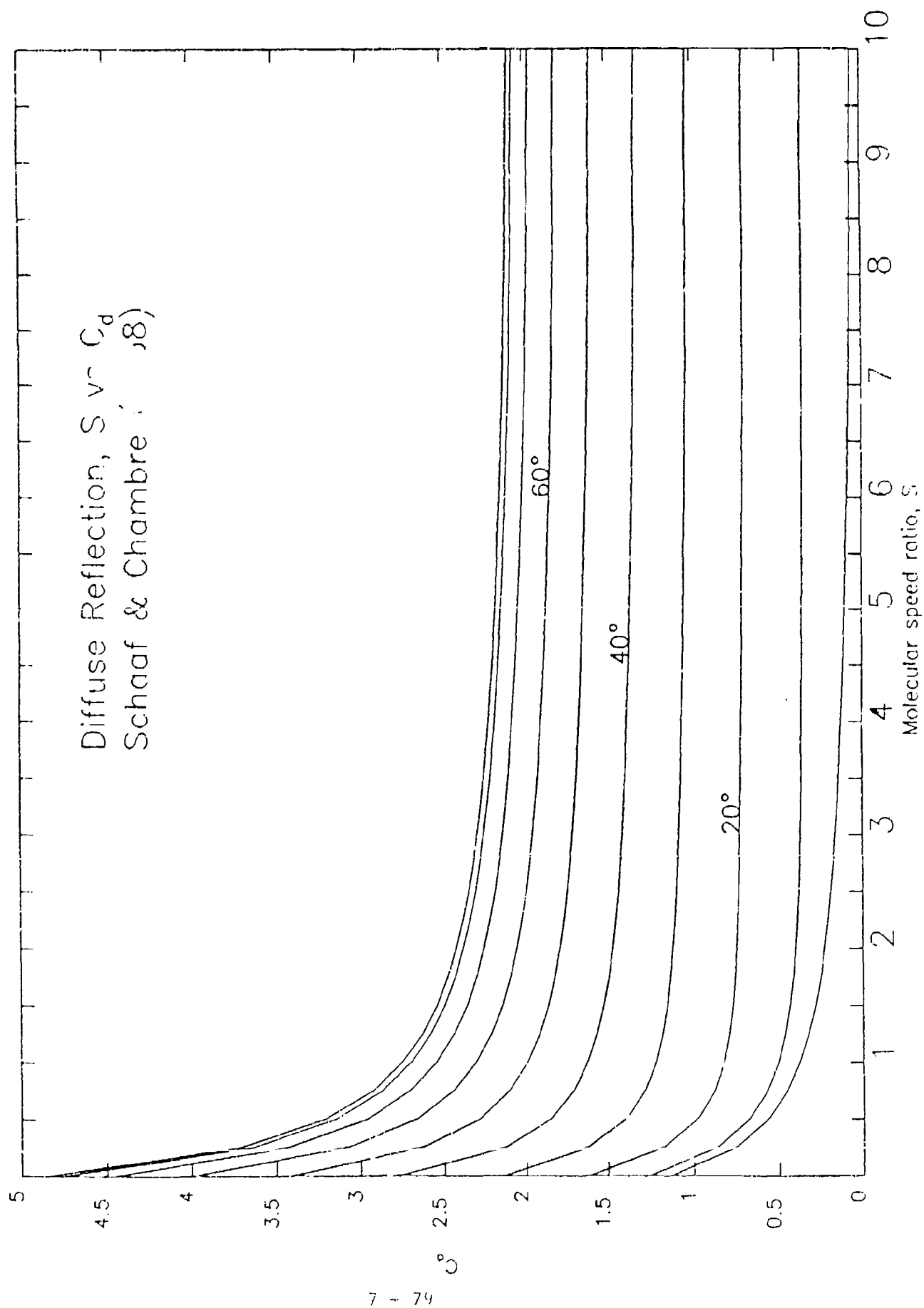
Mathematical formulation of C_d (Full Solution) (Stalker, Schaff & Chambré)

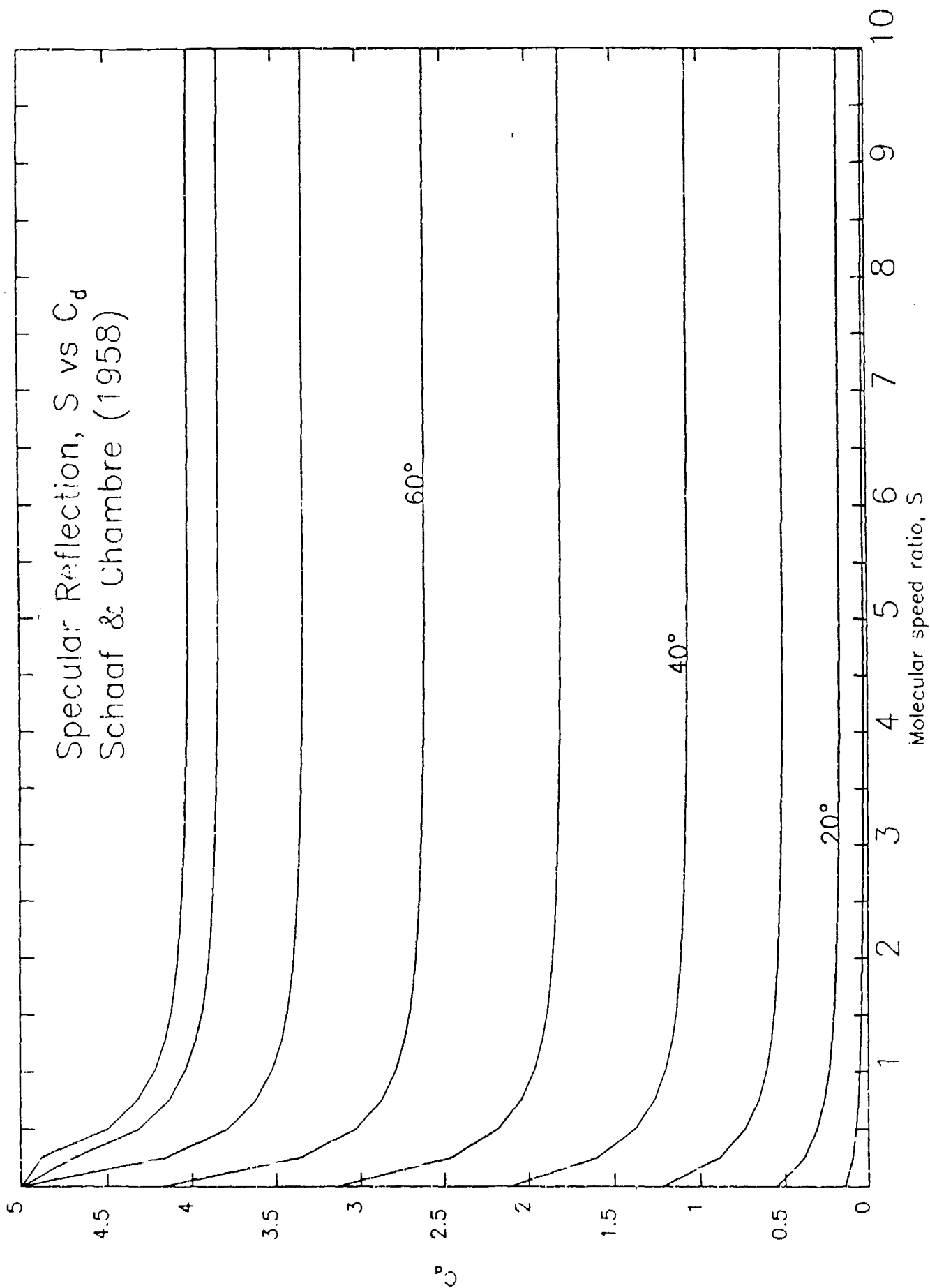
$$C_{d_{aff}} = \frac{2}{\sqrt{\pi}S} [e^{-(S \sin \alpha)^2} + \sqrt{\pi} S \sin \alpha (1 + \frac{1}{2S^2}) \operatorname{erf}(S \sin \alpha) + \frac{\pi S}{S_w} \sin^2 \alpha]$$

$$C_{d_{spec}} = \frac{4 \sin \alpha}{\sqrt{\pi} S^2} \{ (S \sin \alpha) e^{-(S \sin \alpha)^2} + \sqrt{\pi} [\frac{1}{2} + (S \sin \alpha)^2] \operatorname{erf}(S \sin \alpha) \}$$

Variation in 3 parameters, α (surface angle of attack), S (molecular speed ratio), and S_w (molecular speed ratio referenced to spacecraft surface temperatures).

- $G' = \frac{v_{sc}}{v_{th}}$ molecular speed ratio
- $v_{th} = v_{rms} = \sqrt{v_x^2 + v_y^2 + v_z^2} = \sqrt{\frac{3kT}{m}}$ Maxwellian velocity distribution
- $G_w = \frac{v_{sc}}{\sqrt{\frac{3kT_w}{m}}}$





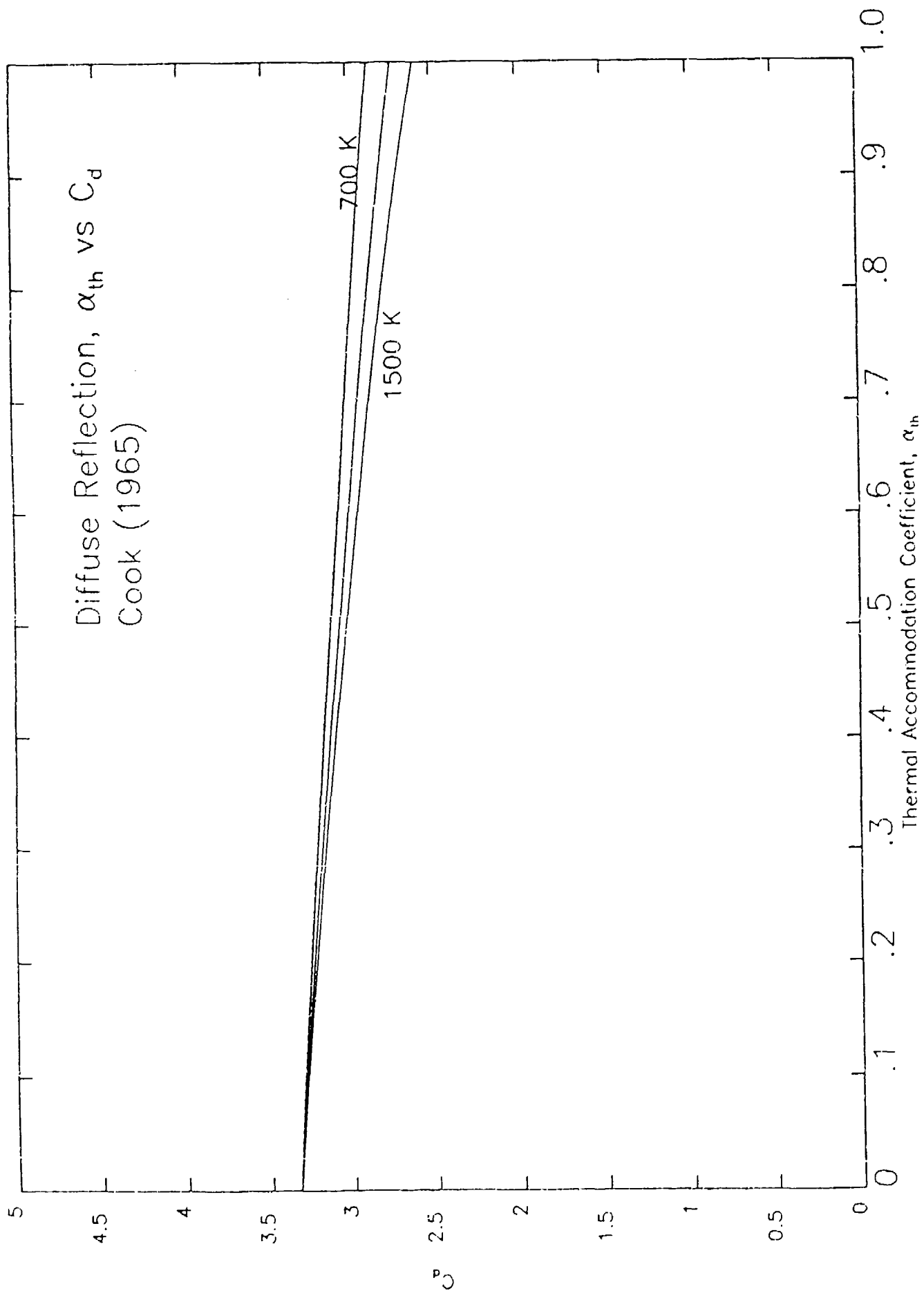
Mathematical formulation of C_d (Cook)

- Application - when using reduced (“effective”) spacecraft area and first order approximation to C_d
- DOES NOT ACCOUNT for collision probabilities at low angles of attack

$$C_{diff} = 2\left(1 + \frac{2}{3}r\right)$$

$$r = \frac{v_r}{v_i} = \left\{1 + \alpha_{th} \left[\frac{T_w}{T_i} - 1\right]\right\}^{\frac{1}{2}}$$

$$\alpha_{th} = \frac{E_i - E_r}{E_i - E_w}$$



II. DETAILS OF C_d VARIATION

- Range of C_d is $\pm 100\%$ for α .

C_d Variation with Angle of Attack, α				
Angle of Attack, α^a	S = 5		S = 6	
	$C_{d_{diff}}$		$C_{d_{diff}}$	
90	2.183		2.153	
60	1.870		1.848	
40	1.363		1.350	
20	0.707		0.703	
0	0.103		0.087	

^a C_d includes small S_w term for $T_w = 300$ K.

II. DETAILS OF C_d VARIATION

- Range of C_d is $\pm 1\%$ for S .

C_d Variation with Solar Activity

Solar Activity ^a	T_∞ (K)	v_{rms} (km sec ⁻¹)	S	$C_{d;H}$ ^b
high	1500	1.52	5	0.707
moderate	1000	1.24	6	0.703
low	700	1.04	7.25	0.699

^asolar cycle 21

^b C_d evaluated for $\alpha = 20$ degrees, including small S_w term for $T_w = 300$ K.

- Drag effects comparable to those of solar radiation pressure.

II. DETAILS OF C_d VARIATION: Modeling C_d

$$F_d = \frac{1}{2} C_d A \rho v^2$$

$$\dot{W} = \frac{1}{2} C_d A \rho v^3$$

$$\dot{E} = \frac{\mu m \dot{r}}{2r^2}$$

$$\dot{W} = \dot{E}$$

$$\dot{r} = \frac{C_d A \rho v^3 2r^2}{2\mu m}$$

$$\rho = \frac{1}{3\pi r \frac{A}{m} C_d} \dot{P}$$

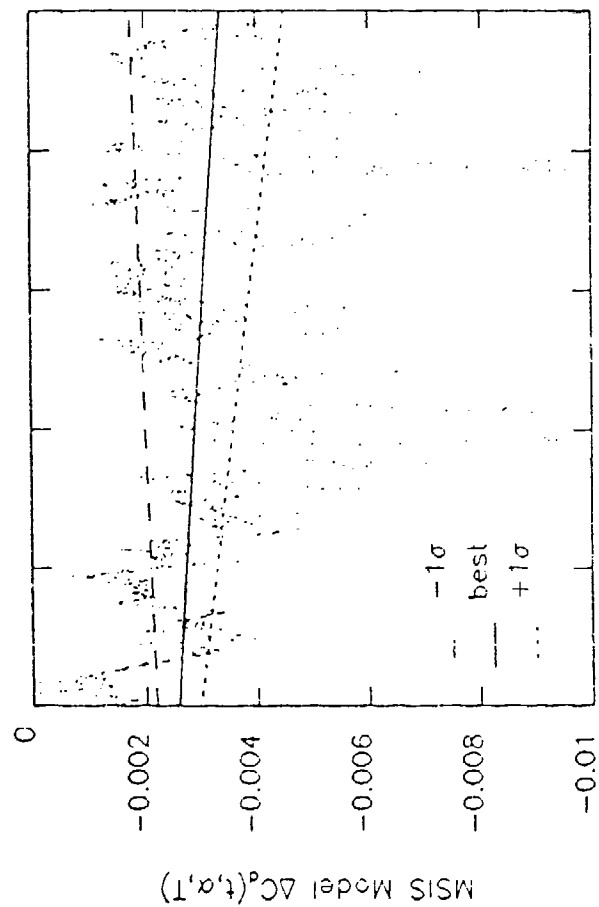
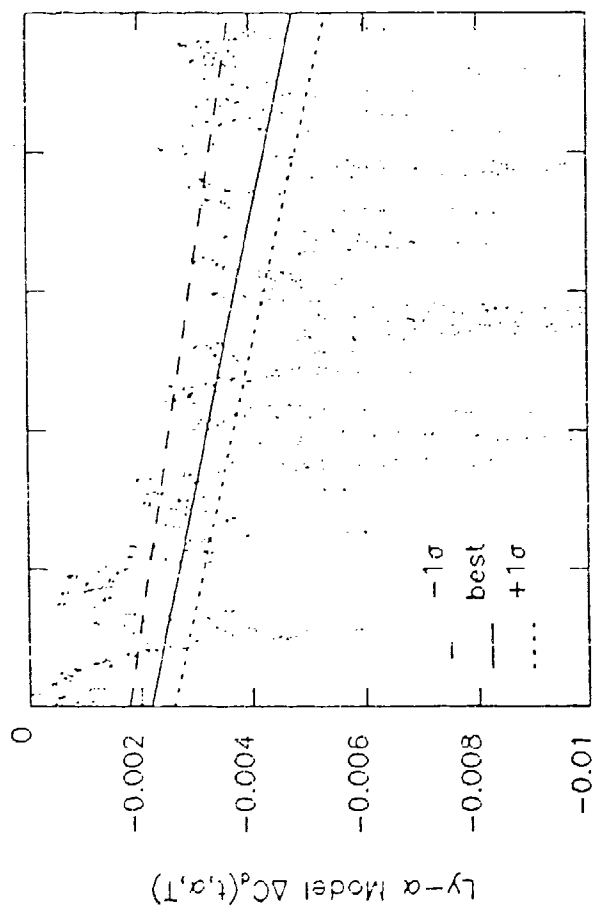
$$\Delta C_d(t, \alpha, T) = \frac{-3\pi \frac{A}{m} \bar{r}(t) \bar{C}_d^2(\alpha, T)}{\dot{P}(t, \alpha, T)} \Delta \rho(t, T)$$

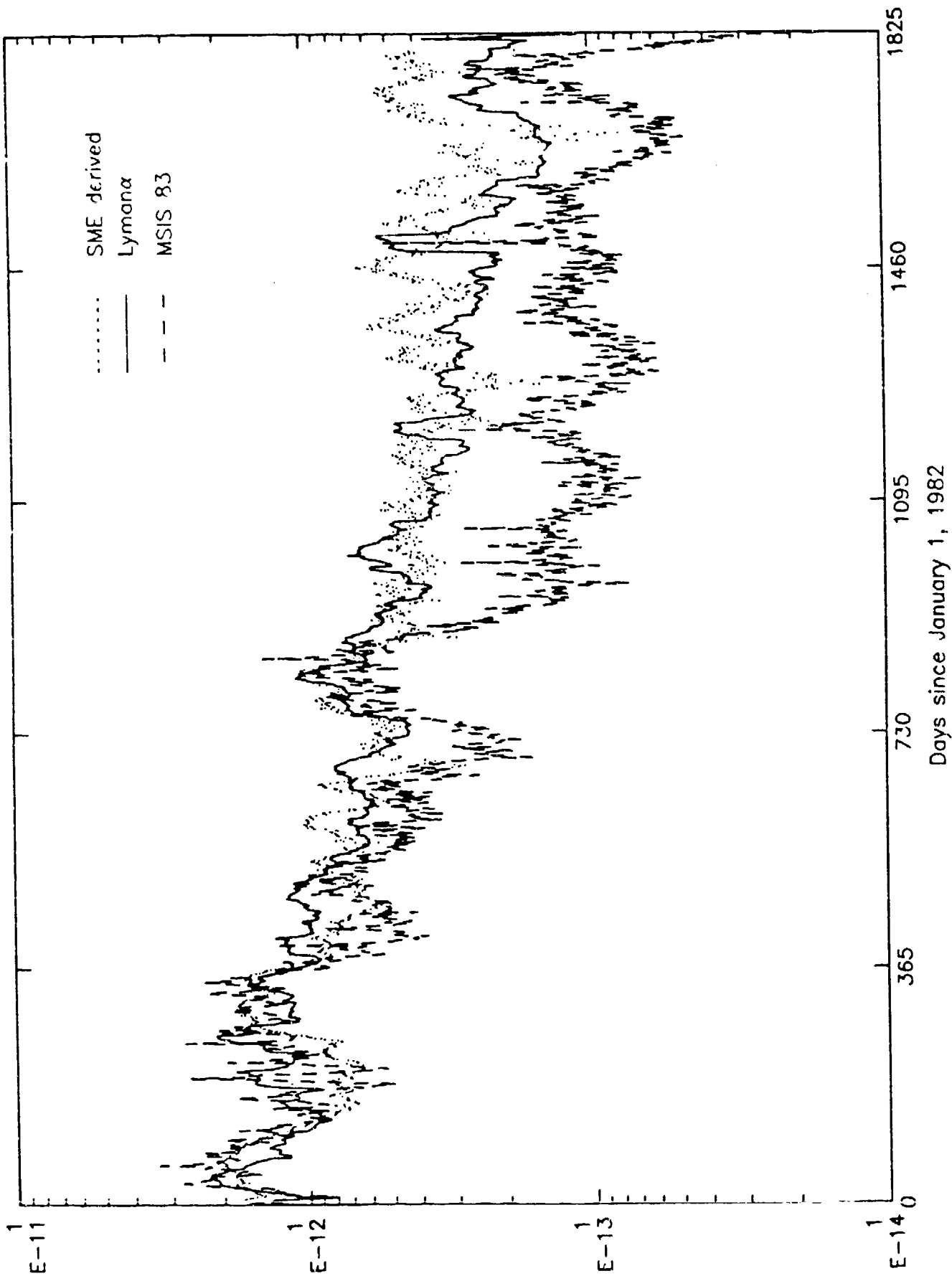
$$C_d(t, \alpha, T) = \bar{C}_d(\alpha, T) + \Delta C_d(t, \alpha, T)$$

II. DETAILS OF C_d VARIATION: Examples

$$C_d(t, \alpha, T) = \bar{C}_d(\alpha, T) + \Delta C_d(t, \alpha, T)$$

- This is derived from circular orbit assumptions.
- Data - $\dot{P}(t, \alpha, T)$, $\bar{r}(t)$ (derived); model atmosphere is $\Delta\rho(t, T)$.
- UNCERTAINTY in $\Delta C_d \sim \frac{\Delta}{m}$, $\bar{C}_d(\alpha, T)$, and $\Delta\rho(t, T)$; magnitude changes, not relative variation.
- SME with polar, circular, 500 km orbit; spacecraft modeled as flat plate with diffuse reflection and average α , ρ , S , S_w over one orbit.
- 2 models - Lyman- α based and MSIS ($F_{10.7}$) based.





σ (kg m⁻² s⁻¹)
 7 - 88

III. SUMMARY OF RESULTS

- C_d is variable, based on variations in α , S , S_w .
- C_d not constant, can vary $\pm 100\%$ by α , $\pm 1\%$ by S , and $< 1\%$ by S_w .
- Satellite data can be used to model variation in all 3 parameters.
- Actual C_d may be a summation of weighted diffuse and specular terms for several surfaces.

7.6

SESSION VII DRAG COEFFICIENTS

REMARKS

GAS-SURFACE INTERACTION PROCESS IS A SIGNIFICANT PROBLEM
FOR PREDICTING RAREFIED FLOW AERODYNAMIC COEFFICIENTS

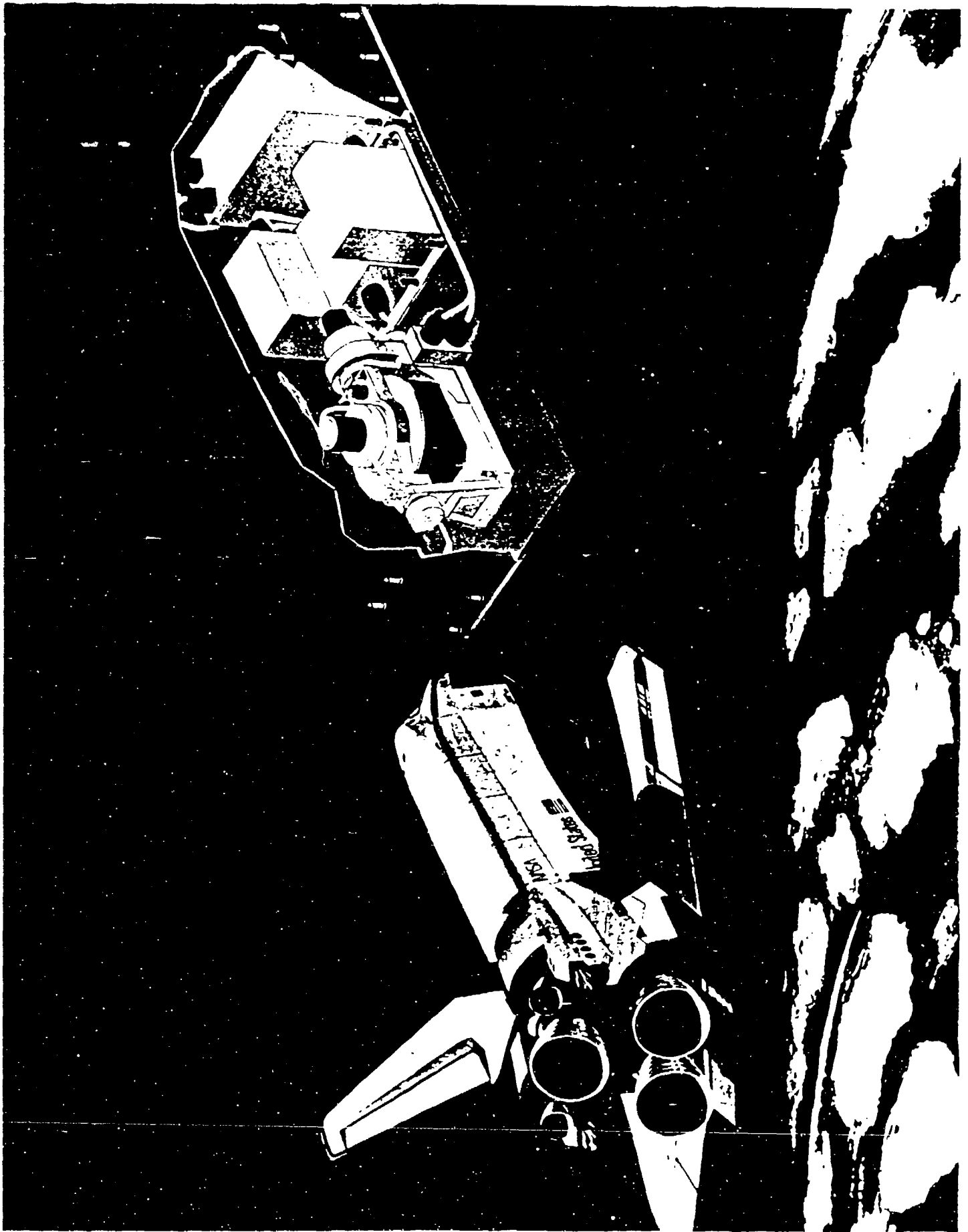
GROUND MEASUREMENTS ARE NEEDED

THEORIES/MODEL DEVELOPED

FLIGHT MEASUREMENTS ARE NEEDED

PROVIDE UNIQUE ENVIRONMENT DATA (SUPPLEMENT
GROUND TESTING)

VERIFY GROUND-TO-FLIGHT EXTRAPOLATIONS



8. SOLAR AND MAGNETOSPHERIC INPUTS

SOLAR X-RAY, EUV AND UV FLUX

Richard F. Donnelly
NOAA ERL ARL
Boulder, Colorado 80303

The main topics discussed below are the following: (1) the "Solar EUV Hole", which is the label used here to describe the lack of solar flux measurements in the 8 - 1200 Å range; (2) the physical reasons why the **combination** of the daily 10.7 cm solar radio flux F10 and its 81-day running average <F10> has been useful for estimating the temporal variations of the solar EUV flux for models of the ionosphere and thermosphere; (3) differences in the temporal variations of F10 and solar EUV fluxes; and (4) SERFS/WITS, i. e. the Solar Electromagnetic Flux Study for the World Ionosphere-Thermosphere Study. The opinions expressed below are the personal comments of R. F. Donnelly and are not official statements of NOAA.

1. The Solar EUV Hole

Figure 1 illustrates the temporal and wavelength coverage of recent satellite monitoring measurements of the solar X-ray, EUV and UV radiation. The AE-E measurements of Hinteregger et al. (1973), which ended shortly after 1980, were the best measurements of the solar EUV flux made to date. Unfortunately, no measurements of the solar EUV flux have been made since then. Schmidtke's future measurements from the San Marco satellite may help fill the void. Currently, there are no approved plans for long-term monitoring of the solar spectral irradiance in the 8 - 1200 Å range. This lack of measurements and plans for the solar EUV flux is called "the Solar EUV Hole". This label is analogous to the term "black hole", where gravitation is so strong that photons do not escape. In the "solar EUV hole", no one is looking to see if those photons are really getting out of the sun.

Figure 1 also shows that monitoring measurements of the solar X-ray flux and UV spectral irradiance are being made with a series of satellite measurements. Techniques used at UV wavelengths to achieve better accuracy and to reduce the errors from unknown drifts in instrumentation could now be used to improve the accuracy of EUV flux measurements. These successful techniques include the following: (1) stowing optical components to protect them from the degrading effects of the harsh space environment except when the solar flux measurements are made, (2) flying radiation standards with the instrument for inflight calibrations, (3) using several components (detectors, diffusers, etc.), where some are used every day while others are used for reference purposes on rare occasions, (4) flying rocket and shuttle borne re-calibration instruments with preflight and postflight calibrations, and (5) flying duplicate instruments, where one views both the sun and at other times the calibration source, while the other one views only the calibration source, to check whether the source drifts when viewed with a similar instrument but one that is not exposed to the sun's photons or the energetic particle radiation in space. So the EUV range is a hole in that monitoring measurements are made at both shorter and longer wavelengths.

The causes of the Solar EUV Hole include the following: (1) The main leaders in the field of measuring the solar EUV spectral irradiance have retired, including Hans Hinteregger and Leon Heroux of AFGL, or moved into other fields of research, like G. Schmidtke of the Fraunhofer Inst, W. Neupert

SOLAR UV SPECTRAL IRRADIANCE MONITORING

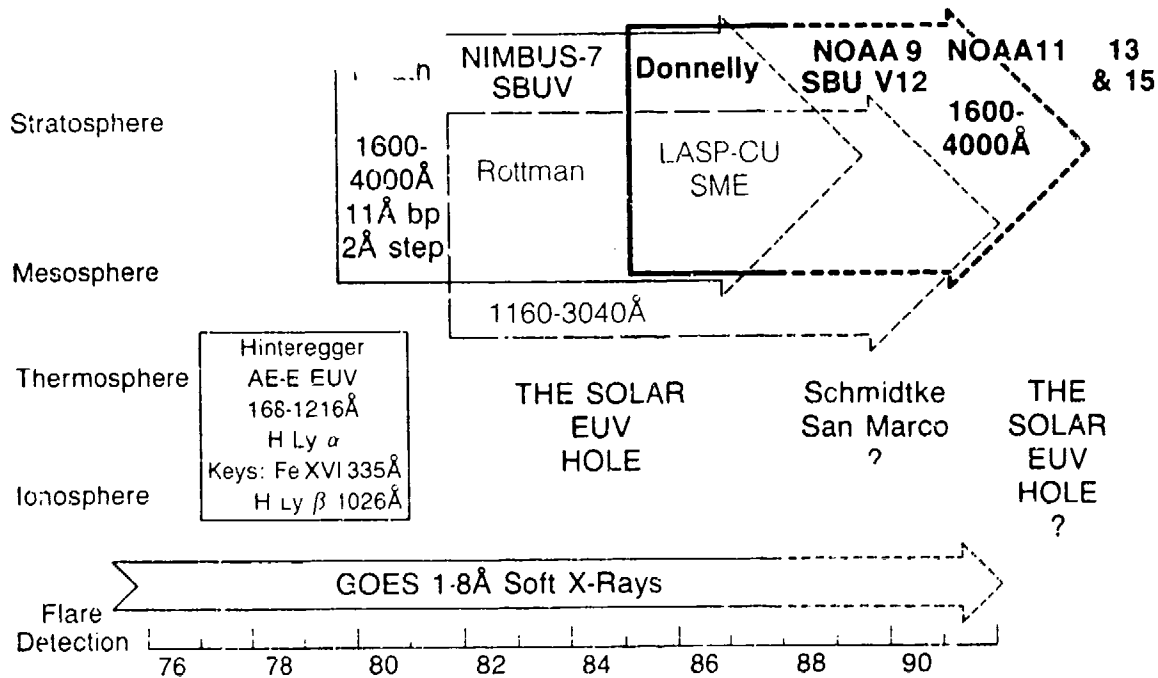


Figure 1 Satellite measurements of the solar spectral irradiance.

of NASA/GSFC and G. Timothy of Stanford U., without young apprentices left to carry on that line of research. (2) Solar physics has moved away from full-disk flux measurements with full wavelength coverage toward higher spatial resolution at selected wavelengths of selected spatial portions of the sun, where these spatially resolved measurements have had little to no impact on improving estimates of solar EUV fluxes for ionospheric and thermospheric modeling. (3) Solar-terrestrial physics (STP) is dominated by concerns for the energetic particle and solar wind connection between the sun and magnetosphere, which involves coronal holes, coronal streamers, flares and transient events, the interplanetary medium and the magnetosphere, none of which are of concern in research of long-term variations of the solar EUV flux; i. e. there is a natural disjointedness between the small group of researchers of the photon connection in STP and the main groups in STP. (4) Research of the photon connection between the sun and atmosphere lies to the terrestrial side of solar physics, to the solar side of atmospheric science, and in a small part of STP that is disjoint from the main body of STP. Monitoring the solar EUV flux appears to have fallen through the cracks between diverging fields, and currently lacks a center of excellence and a national advocate. (5) Emphasis increased on solar UV flux measurements for stratospheric and mesospheric research over the past decade, which has permanently moved several scientists from EUV research to solar UV spectral irradiance measurements, who might otherwise have proposed solar EUV flux measurements. (5) F10 has been fairly successful as a proxy estimator of the temporal variations of the solar EUV flux; however, there are known differences between the changes in F10 and solar EUV fluxes that must limit how well current models of the ionosphere and thermosphere fit reality.

Some may disagree with particular causes suggested above; however, the existence of the solar EUV hole is irrefutable. The hole is deep enough that it will not be easy to fill; simply saying that the solar EUV flux should be monitored on a regular basis will not produce a stampede of excellent proposals. Modeling efforts combined with improved measurements, including the future AF/NOAA X-ray and EUV imager, should be helpful; but they are not a replacement for direct measurements of the solar EUV spectral irradiance in the 8 - 1200 Å range with high quality absolute accuracy. The latter are needed even to test the former.

2. F10 and <F10>

Ionospheric and thermospheric modelers have found using both the daily value of the Ottawa 10.7 solar radio flux F10 and 81-day running averages of F10, labeled <F10>, to be beneficial. The time assigned for <F10> is the date at the midpoint, day 41 of the 81. The physical reason for the benefit of using these two terms is the following. The solar EUV flux involves emission lines and continua, where some are emitted from the hot corona of young major active regions, others are from the cooler portions of the hot corona, or partially from the tenuous transition region between the chromosphere and corona, or from the chromosphere. F10 consists of some emission from all three regions, where the large values at low activity (60 - 67 solar radio flux units) come from the chromosphere and most of the time varying part comes from the corona. The changes in F10 are similar in temporal shape to those of strong coronal EUV lines, like Fe XV and XVI at 284 and 335 Å, respectively, because they originate mostly from similar source regions that are strongly dominated by active region sources. Although chromospheric fluxes dominate the net 10 - 1030 Å flux, the percentage variation of coronal EUV flux is much larger than for chromospheric fluxes so that both chromospheric and coronal fluxes are important when considering temporal changes in the solar EUV flux. Although chromospheric fluxes include variations from the same active regions that emit F10, the chromospheric portions evolve more slowly and persist much longer than the hot coronal portions, and the numerous small remnants of active regions cause a stronger slower-varying component in the chromospheric fluxes than in F10. Consequently, the ratio of long-term variations to short-term solar-rotationally modulated variations changes with EUV wavelength according to whether the emission is from the hot corona, cooler corona, transition region or chromosphere (Donnelly et al., 1986a,b). An 81-day average of F10 removes the solar-rotational modulation and provides a slowly varying function somewhat similar to the slow variations of chromospheric fluxes. Using both F10 and <F10> allows F10 to approximate the short-term solar-rotational variations and <F10> to fit the slower variations of the chromospheric emissions. Using <F10> with 40 days after time t probably fits better than <F10> averaged over 81 days before and including time t because the slowly varying chromospheric emissions are more persistent, or are delayed in time relative to the average of the faster evolving solar-rotational modulation in F10. For example, <F10> based on 81 days in the past would have a smoothed solar cycle curve that precedes that of the chromospheric fluxes. Now that the physical processes involved are clearer, better choices than <F10> should be possible.

3. Differences in $F(t)$ & $EUV(t)$

Three examples of how the temporal variations of F10 differ from those of solar EUV fluxes are listed below. The references to figures, pages or sec-

tions are to those given in Donnelly et al. (1986a,b):

1. The ratio of long-term (years) to short-term (weeks) variations of the solar flux varies according to where in the solar atmosphere is the source of the emission. This ratio is highest for the cooler portions of the corona at temperatures T of $0.5 - 2 \times 10^6$ °K, like that seen in the Fe XIII line near 202 Å. I sometimes refer to this part of the corona as the old corona, because many of its features are long lasting. The ratio has medium values for chromospheric fluxes, like that for the H Lyman beta line at 1026 Å. The ratio is a little lower for the strong coronal lines of Fe XV and XVI at 284 and 335 Å, respectively, from the hot corona ($T \geq 3 \times 10^6$ °K) and lower yet for F10 (Fig. 8, a; Chapter 8, b).

2. Periodicity in the 13- to 14-day range caused by two peaks roughly half a rotation apart in the distribution of active regions as a function of solar longitude is as follows: (a) negligible for F10 and strong coronal EUV lines like Fe XV and XVI at 284 and 335 Å, respectively; (b) moderately strong and peaking at limb passage for soft X-rays and weak coronal EUV lines, like Fe XIII at 202 Å; (c) moderately strong and peaking with central meridian passage for chromospheric EUV and UV fluxes and (d) strongest and peaking with central disk passage for the more photospheric UV fluxes (Fig. 4, a; Chapt. 5 & 6, b).

3. During episodes of major groups of active regions, the solar flux rises, peaks and decays (and sometimes rejuvenates for another round of activity), while being 27-day modulated by solar rotation. This rise and decay tends to be slightly shorter for F10 than for the strong coronal lines of Fe XV and XVI at 284 and 335 Å. The evolution is slower yet for the chromospheric EUV fluxes and the old cool coronal emissions, like Fe XIII (Fig. 3, a; sect. 3.1, 3.4, 3.5, 4.1, 4.3, 4.4, b; and Donnelly, 1987).

4. SERFS/WITS

The Solar Electromagnetic Flux Study (SERFS) for the World Ionosphere-Thermosphere Study (WITS) will attempt to improve estimates of the solar EUV flux compared to the current practice of using F10 by including additional information from the soft X-ray and UV monitoring measurements described in Figure 1, ground-based measures of chromospheric variability, and spatially resolved measurements. WITS is sponsored by SCOSTEP. To participate in SERFS, write to the author for more information.

REFERENCES

- Donnelly, R. F., H. E. Hinteregger and D. F. Heath, Temporal variations of solar EUV, UV and 10830-Å Radiations, J. Geophys. Res., 91, 5567-5578, 1986a.
- Donnelly, R. F., L. C. Puga, and W. S. Busby, Temporal characteristics of solar EUV, UV and 10830-Å full-disk fluxes, NOAA Tech. Memo. ERL ARL-146, NOAA ERL, Boulder, Colo., 127 pp, 1986b.
- Donnelly, R. F., Temporal trends of solar EUV and UV full-disk fluxes, Solar Phys., 109, 37-58, 1987.
- Hinteregger, H. E., D. E. Bedo and J. E. Hanson, The EUV spectrophotometer on Atmosphere Explorer, Radio Sci., 8, 349-359, 1973.

SOLAR FLARES AND THE SOLAR EUV FLUX

Stephen L. Keil and Donald F. Neidig
Air Force Geophysics Laboratory
Sacramento Peak Observatory
Sunspot, NM 88349

INTRODUCTION

This talk on solar flares and the following talk on the corona are intended to give a brief overview of our solar activity prediction programs and how they fit into the problem of specifying atmospheric density. The major concern of AFGL's Solar Research Branch (PHS) is to understand the physics of solar activity and variability and to turn this physical understanding into a predictive capability that can be used to forecast changes in solar emissions. We will very briefly describe some of our ongoing work and future plans that have a direct bearing on solar emissions that serve as inputs to models of atmospheric density and aerodynamic drag. We have concentrated our efforts on solar flares, coronal structure and evolution, and the interaction between solar magnetism and dynamical processes, which must serve as the fundamental energy storage mechanism and trigger for solar flares. To a lesser degree, we have looked at chromospheric variability and solar cycles in general. We currently have programs to measure the daily variation in the integrated Ca II K-line spectra and in several coronal emission lines. PHS has done very little work on specifying solar outputs (much of this work has been done here at AFGL and at NOAA), our prime focus has been on understanding the causes of flares and other forms of solar activity.

As the sun progresses from the quiet to the active phase of the 11 year solar activity cycle, the number of complex magnetic regions which give rise to plages, spots, flares, and mass ejections increases. This causes a general increase in the solar EUV and UV emissions, and during flares, enhances the emissions by a few orders of magnitude, as well as giving rise to enhanced particle emissions and plasma outflow in the solar wind. The increased EUV emissions produces heating in the earth's atmosphere which in turn causes it to expand outward. This can raise densities at satellite altitudes. The increased plasma outflow disturbs the earth's magnetosphere causing oscillations and particle dumping that can also heat the atmosphere and increase densities at satellite altitudes. These increased densities change the drag on satellites and hence their orbital parameters. Attempts to model this density and thus the aerodynamic drag require the solar flux as input. Predictions of the density changes will require predictions of the solar flux. PHS is developing new techniques that will provide the increased solar prediction capabilities that will be needed as our reliance on aerospace systems increases.

STATISTICAL FLARE PREDICTION

Several attempts have been made and are being made to develop numerical procedures for flare prediction. These include regression techniques, multivariate discriminate analysis, and more recently artificial intelligence and expert systems. Regression techniques have been developed by Podsiadlo (and references therein, 1973) and Vecchia *et. al.* (1980). Vecchia *et. al.* use both discriminant analysis and logistic regression. Neidig and his collaborators have developed Multivariate Discriminant Analysis (MVDA) techniques and MVDA techniques combined with a Cooley and Lohnes algorithm (MVDA/CL) which I will talk about here.

The MVDA techniques were developed and extensively tested by AFGL and are currently a technical transition candidate to AWS. The technique uses a set of 10-30 input parameters, collected

daily for each active region on the sun, plus the resulting flare activity for each active region on the following day. Parameters include such things as magnetic classification, sunspot type, flare history of the region, etc. The above data are used to "train" the program, i.e. to derive formulas that will maximize the discrimination between the possible flare outcomes. The output of the program is the probability that the largest flare in the next 24 hours will be of class none, C, M, or X. "Training" of the program consists of classification of each flare in terms of the input parameters, comparing predicted outcomes with actual outcomes and developing a set of classification equations. Ideally, the relationship between a given parameter and the likelihood of a flare would be linear, but often a functional relationship is required. Redundant parameters are eliminated and a final program is constructed. Once the program has been trained, input parameters alone are fed to the program in order to produce a "forecast". As the program is used, the results of the predictions can be verified and a list of significant parameters can be developed. Further refinements of the program can then be implemented.

How well the program will function depends on the quality and completeness of the input data. As the program currently stands, it does as well as subjective forecasts. The table shows a comparison of MVDA forecasts with conventional techniques.

Flare Forecasts Comparison of MVDA with Conventional

MVDA

		Observations			Correctly Accuracy	Events Overall Forecast	Score
		Quiet	Flare	Forecast Total			
Forecast	Quiet	1707	77	1784	96%	86%	85%
	Flare	268	180	448	40%	70%	
	Event Total	1975	257	2232			

MVDA/CL

		Quiet	Flare	Total			
Forecast	Quiet	1829	111	1940	94%	93%	89%
	Flare	146	146	292	50%	57%	
	Event Total	1975	257	2232			

Conventional

		Quiet	Flare	Total			
Forecast	Quiet	1754	98	1852	95%	89%	86%
	Flare	221	159	380	42%	62%	
	Event Total	1975	257	2232			

The best score in each category is shown in bold characters. The study clearly shows that the MVDA techniques can produce forecasts that are generally better than subjective forecasts. The major problem encountered in implementing the program for actual forecasting has been the incompleteness of the data base, caused by weather, down time, loss of observing facilities, etc. The program has been implemented both on main-frame and PC computers. The advantages of using the MVDA program for predicting flares are that it is fast, objective, and the accuracy improves as the quality of the data base improves. The MVDA also allows beginning forecasters to achieve skill levels that only experienced forecasters could previously reach. Indeed, programs such as the MVDA and expert systems provide a means of keeping corporate memory in organizations like AWS which have rapid turnover in personnel.

PHYSICAL MODELS

Empirical models for the conditions leading to solar flares and for the energy content of flares are based on observations of magnetic fields in active regions. Two such models undergoing substantial observational testing include emerging flux models and models which measure the shear in magnetic fields. In the former models, the emergence of new magnetic flux into regions already containing considerable flux can trigger the annihilation of flux tubes and release of magnetic energy. In these models flares are caused by field reconnection, field relaxation and simplification. Observations supporting this type of model include magnetograms showing emerging flux, or migrations of flux loops leading to interaction. The line PHS has been investigating is the build up of shear in magnetic regions.

There is a substantial body of evidence both observational and theoretical that supports the relationship between energy build-up and storage in sheared magnetic fields and flare production. MHD calculations that start with a potential field and then introduce motion of the footpoints of that field indicate that shear will build up to a certain point and then reconnection will occur, releasing energy and accelerating the local plasma. Models for the amount of stored energy have been developed. Flares have been observationally associated with sunspot motions, fibril geometries that indicate shear in the magnetic field, and with measurements of shear in vector magnetograms. We are currently working to develop a set of shear index parameters that can be observed using the current Solar Optical Observing Network (SOON) system and incorporated into the MVDA program. In the future we plan to develop a vector magnetograph for incorporation into the SOON system and to provide advance MHD models that will provide insights on critical shearing velocities and conditions of instability that can be used to refine the observational parameters. This work should lead to an accurate short-term (about 3 hour) forecast of solar activity.

FUTURE EFFORTS

As mentioned above, we will be developing better parameters for use with statistical flare predictions. These include vector magnetograms, flare shear indices, and uses for soft x-ray images that will be provided by the Soft X-ray Imager (SXI) on GOES. We are also attempting to collect better data for the develop of physical models of active regions. Projects in this area include a joint effort with the NSO and HAO to develop stokes polarimetry and the SPO Tower Telescope, development of high resolution vector magnetographs through contracts with NASA and APL, and the development of a payload for high resolution solar imaging in visible and XUV wavelengths (SAMEX). Finally, we plan to devote some of our contract and in-house efforts to the development of better theoretical MHD models.

REFERENCES

Podsiadlo, R. T.: (1973), in *Space Research XIII*, Proceedings of Open Meetings of Working Groups on Physical Sciences on the Fifteenth Plenary Meeting of COSPAR, edited by M.J. Rycroft and S.K. Runcorn, pg 820

Vecchia, D. F., Caldwell, G. A., Tryon, P. V., Jones, R. H.:
(1980), Logistic regression for solar flare probability forecasting, Solar-Terrestrial Predictions Proceedings, 3, U.S. Department of Commerce, National Oceanic and Atmospheric Administration, Boulder Colorado.

Ground-Based Solar Coronal Observations As a Possible Input to Atmospheric Models

Richard C. Altrock
Air Force Geophysics Laboratory
National Solar Observatory/Sacramento Peak
Sunspot, NM 88349

The solar corona is the source of transient and slowly varying phenomena that can affect the upper atmosphere of the earth. Among these phenomena are flares, mass ejections, high-speed solar wind streams from coronal holes, and high-energy ionizing radiation from both the background corona and coronal active regions and streamers.

At the Air Force Geophysics Laboratory's Operating Location AC (Sacramento Peak Observatory, NM), the Solar Research Branch of the Space Physics Division (PHS) operates a program to patrol for the above sources and to perform research designed to improve our understanding of the interaction between the solar processes and the terrestrial consequences. Instrumentation includes the largest coronagraph (which produces an artificial eclipse that allows the corona to be imaged) in the United States, a smaller coronagraph, filters (including one which removes effect of scattered light from the atmosphere) to isolate various coronal spectrum emission lines, spectrographs, and photographic and photoelectric detectors. The scattered-light compensating filter and sensor can detect emissions as faint as $1.E-7$ of the brightness of the solar disk in lines of Fe XIV, Fe X, and Ca XV, which are formed at temperatures of 1-3 million degrees.

Data from the above systems can be used to calculate an estimated flux from the corona. Preliminary comparisons of this flux with measurements of the 10.7 cm solar flux indicate that the visible coronal flux may be a suitable predictor for 10.7 cm flux (which is well-known to have an [indirect] effect on atmospheric density). Although based on the assumption of a static, non-varying corona over a two week period, the visible flux has the advantage of spatial resolution, which allows the effect of coronal enhancements appearing at the East limb to be projected for the ensuing two weeks of disk passage. The flux values are provided to AFGWC, and efforts to produce an algorithm for prediction of F10.7 are continuing.

Coronal Holes (regions of low coronal density) are well-known to be long-lived sources of high-speed solar-wind streams. PHS observations of the Fe XIV corona include information about the location of these sources. Daily full-disk maps of the Fe XIV corona showing the location of coronal holes are produced and telefaxed to U.S. space forecasting centers. Future plans for these data include an algorithm to forecast solar-wind increases at the earth due to coronal holes, which affects upper-atmospheric density.

Observations of 3 MK Ca XV radiation are also taken each day. Previous studies of this radiation have shown that it appears only over active regions that have a high probability of energetic flares. Spatial and temporal information about the presence of Ca XV is provided daily to space forecasting centers. Forecasters there utilize this information in determining the probability of flaring from the underlying regions, which is the source of electromagnetic and particle radiation that can heat the upper atmosphere. Future work will include attempts to quantify objectively the indirect effect of the presence of Ca XV radiation on flare probabilities (and hence on atmospheric heating).

Previous work on satellite drag has established a correlation of uncertain origin between Fe XIV visible estimated coronal flux and anomalous drag B (inferred residual drag after modeled effects are removed). The arrangement of coronal enhancements and

holes on the sun at the time of the study of Skylab reentry, along with the lag between central-meridian passage of solar phenomena and maxima of B, appears to implicate a coronal streamer (high-density, low-velocity stream) as the cause of variations of B. Further work will be required to establish the reliability of this explanation. If correct, streamers may be a major source of variations of B.

Ground-based coronal observations will continue to provide useful input to monitoring of solar processes important to studies of satellite drag for several years. Only if projected space-based systems such as the Solar Mass Ejection Imager (SMEI) and the Solar Activity Measurements Experiment (SAMEX) become a reality will the usefulness of the ground-based data become questionable.

TAKING THE FIRST STEPS IN REAL-TIME EUV MONITORING FOR DRAG: THE SERIES OF USAF-NOAA SOLAR X-RAY IMAGERS (SXIs) ON GOES

William J. Wagner

NOAA/Space Environment Laboratory, Boulder, CO 80303

Abstract. Real-time 255 - 300 Å whole-Sun flux data at high cadence rates will be available for input to neutral density models after launch of the USAF-NOAA Solar X-Ray Imager. It is expected that SXI will contribute significantly to reducing the losses due to drag and orbital decay of both NASA and DOD space systems.

1. INTRODUCTION

We will no longer lack extreme ultraviolet (EUV) data for use in our models in forecasting satellite drag. The National Oceanic and Atmospheric Administration and the U.S. Air Force have agreed to install and operate a series of Solar X-Ray Imagers (SXIs) on the NOAA GOES satellite at geostationary orbit (Wagner and Mulligan 1987). These sensors will provide whole-disk images of the Sun (Figure 1) in two soft X-ray (8 - 20 Å, 20 - 60 Å) and one EUV (255 - 300 Å) bands. The data will be delivered continuously in real time to the NOAA Space Environment Services Center and the USAF Space Forecast Center at rates up to one image per minute. These images, with moderate spatial resolution of 5 arc-seconds per pixel, will be archived at NOAA's National Geophysical Data Center. Launch schedules of the GOES are determined by the need for NOAA to maintain a two-satellite operational system; thus, the first SXI will be in orbit sometime after late 1992.

2. PLANS AND INSTRUMENTATION

The operation of SXIs installed on NOAA's GOES satellites (Figure 2) will upgrade space environment services in a number of areas (Mulligan et al. 1987). These include the predictions of 1) solar energetic particle events at the earth (USAF Scientific Advisory Board 1987; Hirman 1987), 2) sporadic and quasi-recurrent geomagnetic storms (Wagner and Heckman 1985), and 3) anomalous satellite drag due to EUV thermospheric heating. The latter capability, of particular concern to this Workshop, will be accomplished by creation of a full-disk flux index derived from the SXI EUV images.

In addition to monitoring EUV radiant flux for input to drag models, the SXI will also aid in the determination of the heating of the atmosphere which is caused by geomagnetic storms. The location of X-ray coronal holes and the details of their evolution and shape will reveal high speed streams in the solar wind structure. Long-duration X-ray events, believed to mark the launch of coronal mass ejections toward the magnetosphere, will also be detected. Images and EUV flux measurements made through the 255 - 300 Å filter will be compared to the well-established

proxies, Ca II, He I, and 10 cm radio.

Previous grazing-incidence Wolter type 1 X-ray telescopes flown on NASA's Skylab/ATM serve as the technical model for the SXI, whose top-level design is shown in Figure 3. A thermal pre-filter shields the optical surfaces and detector from particulate contamination and undesired light of wavelengths longward of about 350 Å. A commandable rotating wheel will carry a selection of filters (and their backups). Presently, published reports indicate that the band 255 - 300 Å best correlates with observed satellite drag. Nominal plans call for SXI to monitor in this range. The strong He II 304 Å line will be avoided (Hedin 1984); however, the USAF and NOAA are eager to receive advice on the final definition of this EUV channel.



Figure 1. The Sun in soft X-rays.

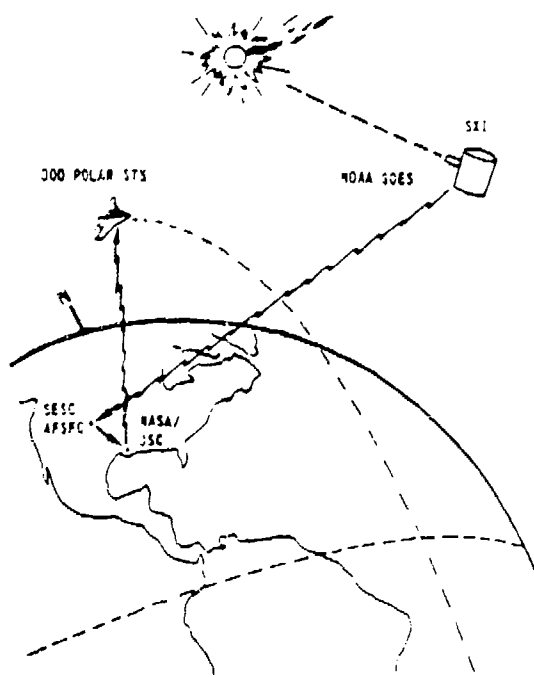


Figure 2. SXI data will be sent in real time to the USAF Space Forecast Center and the NOAA Space Environment Service Center from the GOES in geosynchronous orbit.

Although SXIs will provide a whole-Sun flux measure integrated over a passband rather than detailed spectral information, the band selected (255 - 300 Å) appears to be the best choice for drag effects (Roble 1987). No end-to-end absolute radiometric calibration will be available in orbit, but any sensitivity changes are expected to be gradual and uniform with time and thus amenable to periodic checks by other space instruments. The CCD detector itself will be regularly calibrated onboard in a visible wavelength band.

3. CONCLUSION

Accurate satellite drag forecasts can save the nation real money. In the civil sector, the Challenger accident is behind us and the space program is assumed to be moving again. Yet we stand in danger of losing to re-entry a succession of resources such as the Long Duration Exposure Facility (about 1989) and the multiple mission bus carrying the

Solar Maximum Mission (about 1990). Worries about enhanced drag in the coming solar cycle maximum may keep the high-profile Hubble Space Telescope in storage (at \$7 M per month). The situation today is reminiscent of 1979; at that time we were surprised by the rapid orbit decay of our first space station, Skylab. Today, however, the SXI represents a positive action taken to help avoid these sorts of crises in the future.

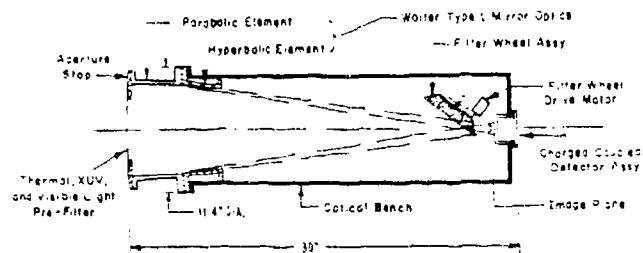


Figure 3. Schematic drawing of SXI

For the U.S. Air Force, with certain of its vehicles passing through still lower altitudes, the financial and national defense costs may even exceed those of NASA. Clearly, the importance of monitoring the inputs and forecasting drag by improved models deserves our best attention. The USAF-NOAA SXIs will be the first steps toward drag forecast capability with on-going real time EUV input data.

Acknowledgements

Dr. J. A. Joselyn very kindly presented this paper for me when I was forced to leave the Workshop unexpectedly.

References

- Hedin, A. E.:1984, J. Geophys. Res., **89**, 9828.
- Hirman, J. W.:1988, in P. D. McCormack, C. E. Swenberg, and H. Bucker (ed.), Terrestrial Space Radiation and Its Biological Effects, NATO Adv. Studies Inst. Series, in press.
- Mulligan, P. J. and Wagner, W. J.:1987, Bull. Am. Astron. Soc., **19**, 944.
- Roble, R. G.:1987, in F. A. Marcos (ed.), Atmospheric Density and Aerodynamic Drag Models for Air Force Operations, summary paper at a workshop held at Air Force Geophysics Laboratory, 20-22 October, Hanscom AFB, MA.
- U.S.A.F. Scientific Advisory Board on Solar Flare Hazards to Man in Space.:1987, February, Department of Air Force.
- Wagner, W. J. and Heckman, G. R.:1985, NOAA Technical Memorandum, ERL SEL-69, U.S. Department of Commerce, Boulder, Colorado 80303.
- Wagner, W. J., Grubb, R. N., Heckman, G. R., and Mulligan, P. J.:1987, Bull. Am. Astron. Soc., **19**, 923.

**SOLAR ACTIVITY MEASUREMENTS EXPERIMENTS (SAMEX)
on the
HIGH RESOLUTION SOLAR OBSERVATORY (HRSO)**

HRSO/SAMEX

Stephen L. Keil and Donald F. Neidig
Air Force Geophysics Laboratory
Sacramento Peak Observatory
Sunspot, NM 88349

INTRODUCTION

The Sun is the source of Geophysical disturbances and it controls conditions in the aerospace environment. Space is rapidly becoming a new theater for DoD operations. The DoD is planning a very large investment, perhaps \$1,000B in systems that may be degraded or destroyed by solar radiation and particle emissions. Planned polar missions will pass through areas of the geomagnetic atmosphere that are especially influenced by solar emissions. Presently, the Air Force does not have the data base nor techniques needed to provide adequate predictions and warnings of solar activity. Much of these data can only be obtained from space-based systems. Yet there are no new planned missions to tackle the problem of solar flare and activity prediction. HRSO/SAMEX is proposed as a joint NASA/Air Force mission that will fill a critical role in providing data required to specify the space weather ("lay of the land") in which DoD will be operating.

HRSO/SAMEX OBJECTIVES:

To build and fly a satellite payload that will provide the solar data required to develop accurate solar activity forecasting techniques and to provide proof-of-concept for high spatial and temporal resolution solar monitoring from space. Currently the reliability of solar forecasting is about 50% for large flares and relies heavily on statistical models. To increase the accuracy and timing of these predictions, better physical models of active regions are required. HRSO/SAMEX will provide high resolution measurements of solar magnetic fields as they develop and interact with convective motions on the sun leading to solar activity. These data will then be used to develop physical models that can reliably predict the time, location and intensity of systems-degrading, solar emissions.

RELEVANCE AND PAYOFFS FOR DOD OPERATIONS:

The sun is the principal modulator of conditions in the aerospace environment. Some examples of the effects of this modulation include:

- a) Communication outages. Example: On 25 April 1984 a white-light solar flare disrupted communications with Air Force 1. Such outages can lead to loss of control of strategic bombers, tankers, and other DoD assets.
- b) Microelectronic failures. Example: The GOES satellite failed on 26 Nov 1982 following a solar flare; numerous other satellite anomalies occur as a result of solar activity resulting in loss of critical remote sensing and space weather data.
- c) Radar Interference. NORAD reports 2 to 3 events per month which can lead to false alerts and miss identification of radar signatures.

- d) Satellite Drag. Early de-orbiting of Skylab and other satellites. Solar activity leads to a marked increases in the number of errors in satellite orbital information and decay of orbits.
- e) Spacecraft charging. Bit flips and power outages. Example: TDRSS pointing errors result in loss of data.
- f) Astronaut Hazards. Violent solar activity can be fatal to military astronauts in polar orbits due to high energy particle flux.

If one can predict when and where solar activity will occur on the sun, and to what extent a particular solar event will lead to geophysical and near-space disturbances, then DoD commanders and planners can both mitigate and exploit space weather. Accurate solar forecasting will make a major contribution to the survivability of space assets, C³I systems and space operations. A successful joint HRSO/SAMEX mission will lead to this vastly improved forecasting at a great savings in cost and resources for both NASA and the DoD. The mission will establish the feasibility of space-based solar predictions and monitoring and will provide data to meet Air Force and NASA science missions.

Air Force Space Command, MAC, NORAD, and other Air Force and DoD commands have strong stated requirements for the ability to predict solar activity and variability. These requirements are clearly specified in AF SON 83-1 and are needed to support AF systems such as C3I, SAC S-77 High Frequency Communication, NORAD, DMSP, NAVSTAR, SAC C2, TAC (OTH-B), USREDCOM, DSCS, and FLTSATCOM/AFSATCOM. The Air Force Space Plan and the MSSTP specify the requirements for the characterization and prediction of solar particle events. These documents also state the requirement for the utilization of military astronauts in space who will be subjected to severe and potentially lethal radiation hazards produced by the sun. Project Forecast II identifies at least three systems that will need accurate solar forecasts for operations planning: PS 46 - Space Object Identification System; PS 24 - Advanced Heavy Lift Space Vehicle; and PS 32 - Space-based surveillance. Solar radiation presents hazards to advanced electronic systems (SDI, etc.) that are operating in the near-earth space environment. Accurate predictions of activity will permit operators of these systems to mitigate its impact. The rapidly expanding role of space in the conduct of the DoD mission makes crucial the accurate prediction of severe solar disturbances.

WHY SPACE-BASED OBSERVATIONS ARE NEEDED:

Solar activity originates in the interaction of solar magnetism with convective motions in the solar atmosphere. All heights in the solar atmosphere play a role in storing energy and in triggering the release of that energy in solar activity. Much of the interaction between the magnetic fields and solar motions takes place on very small spatial scales both over long time periods (during the build-up phase prior to solar activity) and at very rapid rates (during the triggering and release phase). Solar research has led to the recognition that the solution to the solar activity prediction problem lies in high spatial resolution observations of magnetic and velocity fields over a wide range of heights in the solar atmosphere over many different time scales.

Much of the solar activity that affects Air Force systems can be observed only in solar ultraviolet and X-ray emissions which do not penetrate through the earth's atmosphere and must therefore be measured from satellites. Ground-based observing networks are further limited by weather, night-time interruptions, poor observing locations due to international political considerations, and image quality. Image quality is severely limited by the earth's atmosphere which causes both image motion and blurring. The Solar Electro-Optical Network (SEON) provides low to medium image quality and observes the sun about 80% of the time. SEON is an operational, not developmental system. Therefore, while SEON data are of sufficient quality to monitor the occurrence of solar events, they aid very little in developing accurate forecasting algorithms. The accuracy of forecasts has changed little over the eight years SEON has been operational, and remains at about 50% for large flares (with a 24 hour forecast window).

BACKGROUND OF HRSO/SAMEX CONCEPT:

The Solar Activity Measurements Experiments (SAMEX) is a payload defined by the Solar Research Branch of the Air Force Geophysics Laboratory that has been submitted to the Space Test Program. SAMEX is designed to fulfill the needs and requirements of the AF/DoD for accurate and timely solar activity forecasting and Space Weather specification. SAMEX consists of a high-resolution (0.5 arcsecond) vector magnetograph for following the development of magnetic fields and the build-up of energy in active regions in the solar photosphere, a 0.5 arcsecond H-alpha imager for measuring associated structures and fields in the chromosphere, and a high-resolution (0.5-1.0 arcsecond) soft X-ray/extreme ultraviolet (XUV) imager for measuring coronal structures and loops overlying active regions. SAMEX differs from all previous and proposed missions through (1) its combination of instruments that can simultaneously see all heights in the solar atmosphere and (2) its objective of high-spatial resolution, not only for photospheric magnetic fields and motions, but also in a number of selected XUV lines that will reveal the fine-structure of magnetic loops in the corona and chromosphere that control the energetic release of energy in flares and mass ejections. Thus, SAMEX will provide information on the build-up and release of energy through solar activity processes at all heights in the solar atmosphere and will provide the data required for development of solar prediction techniques. SAMEX is proposed as an extended mission capable of following the development of active regions over long periods.

The High Resolution Solar Observatory (HRSO) is a NASA project with a major goal of obtaining very high-spatial resolution measurements of solar velocity and magnetic fields in the solar photosphere and chromosphere. The proposed instrumentation for HRSO includes a one-meter class telescope feeding a tunable filter system capable of measuring polarized light in very narrow spectral bands using a CCD camera system, a filter wheel for making broadband images in H-alpha and several other spectral lines, and a spectrograph. All of these instruments operate at visible wavelengths. HRSO will have a spatial resolution on the sun better than a tenth of an arcsecond and thus fulfills the SAMEX resolution requirements. It is planned to launch HRSO as a free-flyer from an expendable booster on a Delta or Titan vehicle. It will have a lifetime of at least three years and probably longer. NASA is planning to submit the HRSO mission as a new start in 1990.

CONCLUSIONS:

HRSO/SAMEX will provide the data required for doing the science needed to develop accurate solar activity algorithms and to develop an operational capability for solar activity monitoring for the DoD. It will lead to an enhanced solar science program for both DoD and NASA while conserving scarce resources for both agencies.

M. A. SHEA
AFGL (PHP)

TEL: (617) 377-3977

8.6

SIMPL

22 OCT 1987

SIMPL

SYNOPTIC INTERPLANETARY MONITORING PLATFORM AT L1

A CONCEPT FOR REAL TIME MONITORING OF INTERPLANETARY PLASMA
AND MAGNETIC FIELD PARAMETERS

THESE PARAMETERS ARE FUNDAMENTAL FOR ENERGY TRANSFER
INTO THE MAGNETOSPHERE

JED/APL

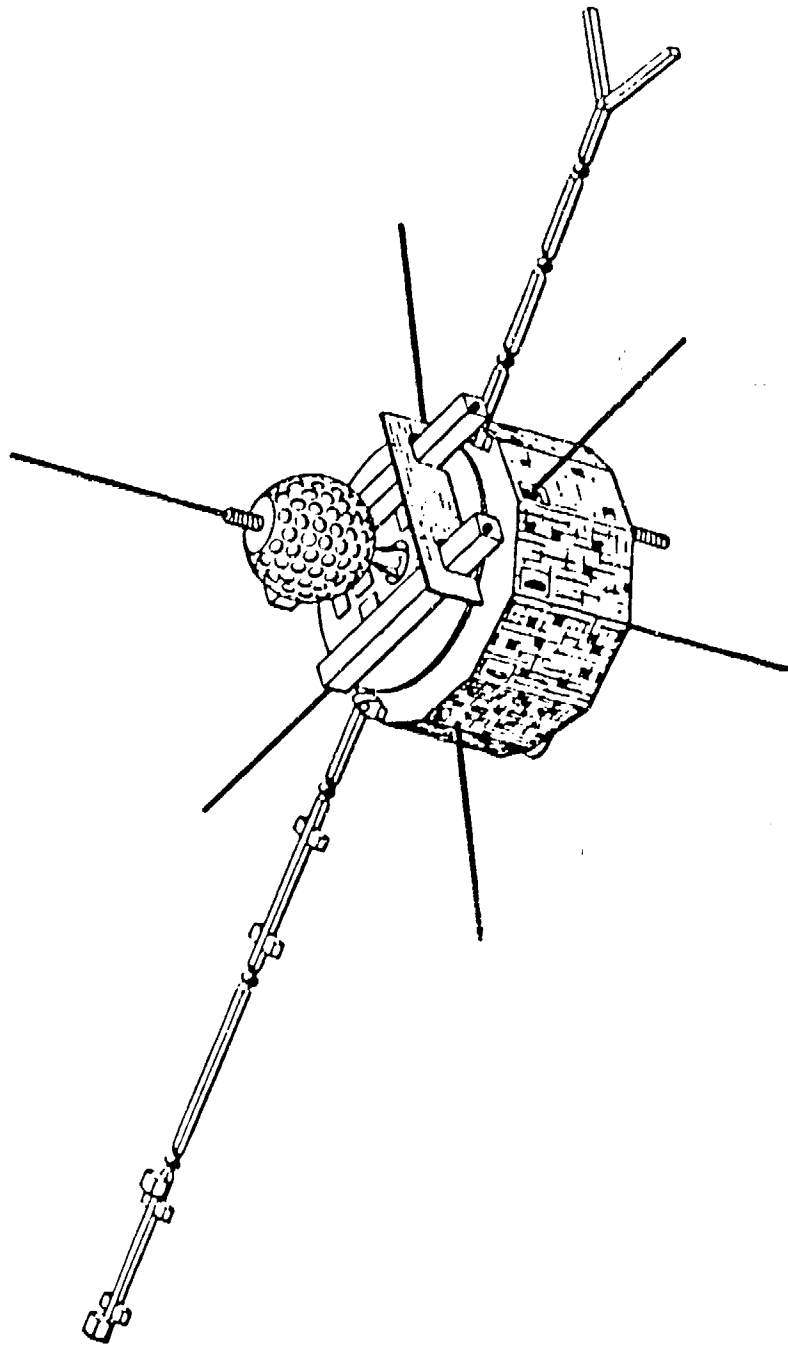


SIMPL CONCEPTS

1. SATELLITE AT L1 POSITION
2. AUTO-TRACK SUN AT
PRESCRIBED DAILY OFFSET
3. SMALL (5 METER) TELEMETRY
ANTENNA AT AWS SOON SITES
4. REAL TIME DATA STREAM
100 BITS/SEC

WIND/SIMPL

1. DISCUSSIONS WITH NASA TO ADD REAL TIME CAPABILITY TO WIND SPACECRAFT
 - A. MAJOR IMPACT TO WIND SPACECRAFT
 - B. REQUIRES SPECIAL ELECTRONIC STEERABLE ANTENNA CONFIGURATION
 - C. REQUIRES 9 METER ANTENNA AT AWS SOON SITES TO SUPPORT 100 BITS/SEC
 - D. ORBITAL CONFIGURATION PROBLEM
 - NASA WANTS DOUBLE LUNAR SWINGBY
 - USAF WANTS L1
 - NASA WANTS LARGE HALO IF AT L1
 - USAF WANTS SMALL HALO IF AT L1
 - E. DATA ENCRYPTION IS A MAJOR PROBLEM
2. CURRENT AFGL FUNDED STUDY UNDERWAY TO MINIMIZE INTERFACE REQUIREMENTS.



Artist's concept of WIND/SIMPL spacecraft.

SAW/SR CONCEPT

(SIMPL AND WIND/SINGLE ROCKET)

1. SEPARATE SPACECRAFT ACCOMMODATES EACH AGENCY'S MISSION
2. MORE SCIENCE CAN BE ACCOMPLISHED
3. REDUCE TOTAL COST FROM SINGLE LAUNCH

ABSOLUTE EXTREME-ULTRAVIOLET SOLAR SPECTRAL IRRADIANCE MONITOR

(A E S S I M)

W. H. PARKINSON AND PETER L. SMITH

Harvard-Smithsonian Center for Astrophysics, Cambridge, MA 02138

ABSTRACT

The solar extreme ultraviolet (EUV) flux, nominally 10 to 120 nm, is the principal source of energy for heating the thermosphere. Upper atmospheric neutral density models, which are needed for assessing the effects of atmospheric drag on spacecraft design and operations, require the best available input parameters if accurate, timely, and spatially-detailed nowcasts and forecasts of atmospheric density are to be made. The Absolute EUV Solar Spectral Irradiance Monitor (*AESSIM*) would consist of one or more EUV standard sources and a spectrometer that would compare, in orbit, the solar output to that of the standards. By this means, uncertainties about degradation of the spectrometer detection efficiency could be eliminated and the solar EUV output would be determined accurately over the long term.

1. TECHNICAL OBJECTIVES

The goals of the Absolute, Extreme-Ultraviolet, Solar Spectral Irradiance Monitor (*AESSIM*) program are development and flight of instrumentation for regular, long-term monitoring of the solar spectral irradiance at extreme-ultraviolet (EUV) wavelengths (nominally 10 to 130 nm). An *AESSIM* flight package would include several secondary standards of spectral irradiance for the EUV and a spectrometer that would compare the spectral irradiance of the sun to that from the standard sources. Use of the proposed in-orbit standards would avoid the uncertainties caused by spectrometer degradation, and the concomitant requirements for recalibration, that have plagued all previous measurements of the solar spectral EUV flux.

2. JUSTIFICATION FOR THE RESEARCH

EUV radiation is the dominant source of energy for heating the thermosphere, whose chemical composition and density vary with the solar EUV output. Satellites in low-earth orbit experience variations in atmospheric drag as the atmosphere expands and contracts in response to the changing solar EUV output. The positions of navigation satellites, the pointing of space-based weapons and of astronomical telescopes, and reentry trajectories, of, for example, the Space Shuttle, are influenced by this drag [see other papers in these proceedings and Davis *et al.* (1987)]. There is no existing or planned and approved instrumentation for long-term monitoring of the solar EUV spectral irradiance (Donnelly 1987). As a consequence, models of thermospheric properties and processes depend upon proxy representations of the solar EUV flux, such as the solar flux at 10.7 cm. Speakers at this Workshop, as well as those in Davis *et al.* (1987), have pointed out that such proxy representations are no longer adequate. For the long term, a facility for regular, accurate monitoring of the spectrally-resolved solar EUV irradiance is required.

The measurement requirements imposed by a desire for a comprehensive understanding of the processes and properties of the thermosphere have been stated by Lean (1987): EUV irradiances must be determined with an uncertainty of, "a few percent, a spectral resolution commensurate with the structure in the absorption spectra of the atmospheric gases, and a temporal resolution of the order of the shortest time scales of EUV irradiance variations (hours and days)."

3. TECHNICAL APPROACH

3.1 Measurement Strategy

Past measurements of the solar EUV spectral irradiance (reviewed by Lean, 1987, and Schmidtke, 1984) and future broadband solar EUV measurements that may be made by the *GOES Solar X-Ray Imager* (Wagner, 1987) or the *San Marco D/L Airglow-Solar Spectrometer Instrument* (Schmidtke *et al.* 1985) have been, or will be, limited in accuracy because of indeterminable changes in the detection sensitivity of the apparatus when in orbit: measured changes in signal cannot be directly correlated with changes in the EUV output of the sun. *AESSIM* will differ from all previous such instruments for measuring the solar EUV flux by incorporating newly-developed, stable, secondary standards of spectral irradiance for the EUV. By this approach, which has become standard for solar irradiance measurements at vacuum ultraviolet wavelengths (Brueckner 1983), concerns about changes in instrument detection sensitivity can be greatly reduced.

3.2 A Standard of Irradiance for the EUV

Synchrotron radiation, usually from electrons in a storage ring, is the primary spectral irradiance standard for the EUV. The radiometric calibration facility of the PTB at the storage ring BESSY in Berlin, is the only laboratory equipped for the calibration of other radiometric sources, in particular, of secondary standards such as those in *AESSIM* (Fischer, Kühne & Wende 1984). Two continuous sources have been investigated as transportable radiometric standards for the EUV: the hollow cathode Danzmann, Fischer & Kühne (1985) and the electron impact source (Risley 1987; Ajello 1987). The latter is poorly matched, in the shape of its emitting region and in its intensity to solar EUV irradiance monitoring.

Some tests by Danzmann *et al.* (1985) and Smith *et al.* (1988) have shown that the PTB hollow-cathode EUV source has a number of properties that make it suitable for calibrations in space:

- The laboratory version is very rugged;
- About 25 lines, roughly evenly-spaced in the wavelength range 10 to 130 nm, appear to be suitable for calibration;
- Most lines are the expected strong lines of neutral or singly- and doubly-ionized, rare-gas atoms;
- The lines are comparable to solar EUV line intensities when the source is operated with input power of 10 to 100 Watts.
- Output from the lamp, which has been quantitatively studied from 13 to 59 nm, was found to be: (i), stable to better than a few percent over time scales of hours; (ii), reproducible after a period of 16 months of irregular use, and, (iii), unchanged after a period of 40 hours of intensive use. [The precision of these measurements was 5 to 10 percent].
- Gas consumption rate is about 1 litre (at one atmosphere pressure) per hour.

Estimates of the resources required for calibration can be made by noting that the sensitivity of the Harvard spectroheliometer on *Skylab* degraded by a factor of about three in the course of a 8-month mission (Reeves *et al.* 1977). If the *AESSIM* spectrometer (see § 3.3) were calibrated every 7 days in a operation that would require about two hours, then the average power required would be less than 20 Watts. 100 litres of gas (at one atmosphere pressure) would be required for a one year mission.

3.3 An *AESSIM* Spectrometer

The *AESSIM* concept is shown schematically in Figure 1. A moderate-resolution spectrometer, with both grazing- and normal-incidence gratings, pivots about its entrance slit so that one of the gratings is illuminated by one of a number of redundant standard EUV irradiance sources or by the Sun.

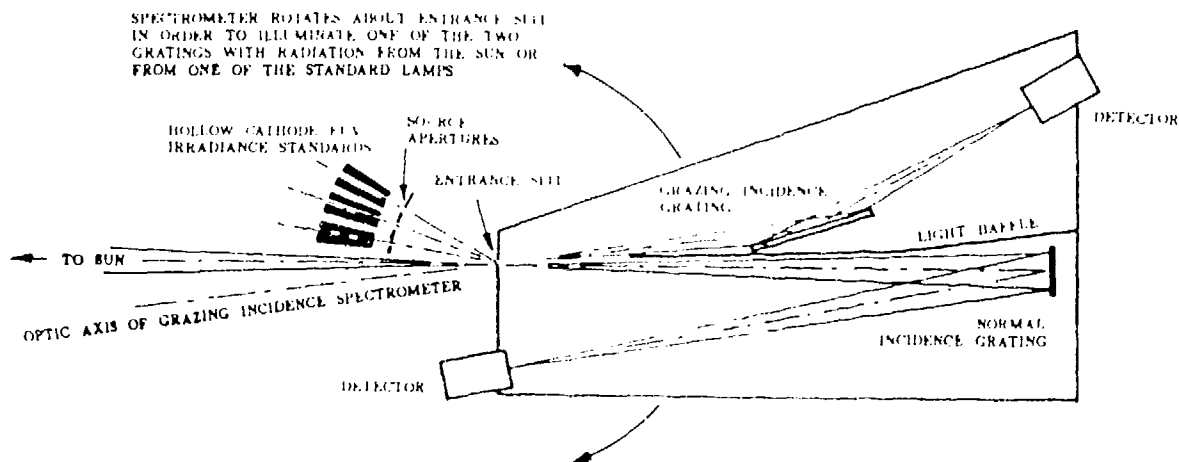


Figure 1. Schematic diagram of the *AESSIM* spectrometer. The f -number shown is about $f/15$; $f/50$ would be more than adequate for *AESSIM*.

AESSIM would not have a telescope; the spectrometer slit would form a 'pinhole camera' image of the solar disk, convolved with the slit dimensions, on the grating. Because the Sun subtends only 32 arc min (1/108 rad.), a high f -number (e.g., $f/50$) spectrometer with its concomitant, small aberrations, will be adequate. Pointing accuracy of ± 1 arc min would be sufficient. An aperture of 1.2 mm diameter in front of a standard source at a distance of 129 mm from the spectrometer entrance slit could be used to calibrate the same portion of the spectrometer as that used to view the sun. The sensitivity of the *AESSIM* spectrometer has been estimated from that of the Harvard spectroheliometer on *SKYLAB* (Reeves *et al.* 1977). 500 counts sec^{-1} would be detected for a flux of 10^9 photons $\text{cm}^{-2} \text{sec}^{-1}$ onto a 250 μm -diameter spectrometer aperture. Actual count rates are expected to vary from this value by about three orders of magnitude, depending upon the solar flux.

Neither the *AESSIM* spectrometer nor the hollow cathode EUV standard sources require state-of-the-art technology. Weight and power requirements are compatible with many orbiting platforms being discussed. Thus, *AESSIM* represents a low-cost, near-term means of obtaining accurate, spectrally-resolved EUV flux data for thermospheric studies.

4. ACKNOWLEDGEMENTS

The authors gratefully acknowledge the assistance of Michael Kühne and Peter Müller [Physikalisch-Technische Bundesanstalt, Berlin, F.R.G.], of Martin C. E. Huber [Space Science Department of ESA at ESTEC, Noordwijk, The Netherlands], Manfred Kock [Institut für Plasmaphysik, Universität Hannover, Hannover, F.R.G.], and George V. Nystrom of the Harvard-Smithsonian Center for Astrophysics. This work was supported in part by NASA Grant NSG-7176 to Harvard University and by a NATO Grant for International Collaboration in Research

5. REFERENCES

- Ajello J M 1987, *A Simple UV calibration source with Reflectance Spectra and Application to the Galileo Orbiter UV Spectrometer*, in Ebbets (1987).
- Brueckner G E 1983, *Solar Radiometry: Spectral Irradiance Measurements* in ADVANCES IN SPACE RESEARCH, COSPAR PROC. 2 (Oxford: Pergamon), 177 - 183.
- Danzmann K, Fischer J & Kühne M 1985, *High-Current Hollow-Cathode as a Source of Intense Line Radiation in the VUV*, J. Phys. D. 18, 1299-1306; see also Danzmann K, Günther M, Fischer J, Kock M & Kühne M, *The High Current Hollow Cathode as a Radiometric Transfer Standard Source for the Extreme Vacuum Ultraviolet*, in preparation.
- Davis M H, Smith R E & Johnson D L 1987 *Upper and Middle Atmospheric Density Modeling Requirements for Spacecraft Design and Operations*, NASA Conference Publication 2460.
- Donnelly R F 1987, "Solar X-Ray, EUV, and UV Flux", these proceedings.
- Ebbets D C, editor, *Proceedings of the Eighth Workshop on the Vacuum Ultraviolet Radiometric Calibration of Space Experiments* (Boulder: Ball Corporation).
- Fischer J, Kühne M & Wende B 1984, *Spectral Radiant Power Measurements of VUV and Soft X-Ray Sources Using the Electron Storage Ring BESSY as a Radiometric Standard Source*, Appl. Opt. 23, 4252-4260.
- Lean J L 1987, *Solar EUV Irradiances and Indices*, to be published in Ad. Space. Res., COSPAR INTERNATIONAL REFERENCE ATMOSPHERE 1986, (Oxford: Pergamon); and *Solar Ultraviolet Irradiance Variations: A Review*, J. Geophys. Res. (Atmospheres), 92, 839-868.
- Reeves E M, Huber M C E, Timothy J G & Withbroe G L 1977, *Photometric Calibration of the EUV Spectroheliometer on ATM*, Appl. Opt. 16, (4), 849-857.
- Risley, J S 1987, *The Electron-Atom Source as a Primary Radiometric Standard for the VUV*, in Ebbets (1987).
- Schmidtke G 1984, *Modelling of the Solar Extreme Ultraviolet Irradiance for Aeronomic Applications*, MODELS OF THE ATMOSPHERE AND IONOSPHERE, Handbuch der Physik 49/7 Geophysics III, ed. Rawer K, (Berlin: Springer Verlag), 1-48.
- Schmidtke G, Seidl P & Wita C 1985, *The Airglow-Solar Spectrometer Instrument (20 - 700 nm) aboard the San Marco D/L Satellite*, Appl. Opt. 24 3206.
- Smith P L, Kühne M, and Müller P 1988, unpublished.
- Smith P L, Parkinson W H, Kühne M, Huber M C E, and Kock M, *Absolute, Extreme Ultra-Violet Solar Spectral Irradiance Monitor*, in Ebbets (1987).
- Wagner W 1987 *The GOES Solar X-Ray Imager*, these proceedings.

Summary of Oct 23, 1987 presentation to AFGL Ionospheric Physics Division Workshop on Atmospheric Density and Aerodynamic Drag Models for Air Force Operations.

The Geomagnetic Activity Outlook for 1987-1997 (Cycle 22)

Jo Ann Joselyn
NOAA Space Environment Laboratory
Space Environment Services Division
Boulder, Colorado

Abstract. As a consequence of various analysis methods that have been applied to the circumstances of the recent solar minimum (September, 1986), most estimates of the amplitude of sunspot cycle 22 have been raised. If these new estimates prove correct, geomagnetic activity is likely to equal or exceed that experienced for cycle 21. In particular, two maxima are expected: one associated with impulsive activity near the actual sunspot number maximum (in approximately 1990), and one associated with coronal holes during the declining phase (in approximately 1994).

Before discussing the outlook for geomagnetic activity, it is necessary to review the sunspot predictions for cycle 22. At the 1985 NASA Workshop on Upper and Middle Atmospheric Density Modeling Requirements for Spacecraft Design and Operations (Huntsville, AL, November 19-21, 1985), it was generally agreed that sunspot cycle 22 would be near average or below. However, less than 2 years later, many predictions now call for an above average cycle (see appendix 1, the most recent SESD advisory on sunspot cycle 22, and the references therein). The implications of the difference between a below average to an above average cycle are significant, especially for satellite mission lifetime calculations. What happened between November 1985 and early 1987 that changed the outlook so dramatically?

There are at least 4 reasons why it seems prudent to expect that cycle 22 may be above average. Most of them are related to the fact that the minimum of the 13-month running average of monthly sunspot numbers is now reliably known to be September, 1986. (There is no doubt that cycle 22 is in progress: the background level of the ten-cm solar flux has been trending upward over the past year and on Monday October 19, 1987, the Boulder sunspot number was 96 with 7 new-cycle polarity spotted regions visible.) These reasons are as follows:

1. Cycle 21 was a short cycle (June 1976-September 1986) and cycle 22 is developing quickly. The level of activity near solar minimum and the rapid rate of rise of the new cycle are both the highest on record (McIntosh, private communication, 1987). Both the McNish-Lincoln and NASA MSFC methods of cycle

prediction (see the appendix) use the rate-of-rise in their calculations: the more rapid the rise, the larger the peak.

2. The general level of geomagnetic activity has remained high in comparison with historical values. For example, the Sargent-Ohl prediction method uses the annual average of the aa-index for the 3 years preceeding sunspot minimum as one of the components in that calculation. Higher aa-indicies increase the maximum anticipated sunspot number. Figure 1 is a plot of the annual average sunspot numbers and the annual average aa-index taken from Feynman and Gu (1986). The data has been extended by hand to include recent years and an estimate for 1987. The recent aa-index values have maintained a relatively high value, especially in comparison with the data for years preceeding about 1930. The estimated annual average for 1987 is 17 whereas the 1965 minimum, the one that preceeded cycle 20, was 14.4.

3. Schatten and Sofia (1987) have recently published their forecast of cycle 22 based on application of a solar dynamo theory that employs solar differential rotation to transform the Sun's poloidal field into a toroidal field. They used the observed magnitude of the solar polar fields during the recent sunspot minimum and predict a smoothed maximum sunspot number of 170 ± 25 , which exceeds the maximum observed for cycle 21.

4. A periodicity of approximately 88 years is present in analyses of sunspot numbers and in geomagnetic data as implied by historical records of aurora [e.g. Feynman and Fougere, 1984]. Looking again at figure 1, this 'Gleissberg cycle' appears to begin around 1900, and seems to maximize with cycle 19 in 1957-58. Cycle 20 was indeed low, and by inspecting the successive minima of the aa index plot between 1900 and 1965 one gathers that geomagnetic activity is also obeying an approximate 88 year periodicity law. However, the large cycle 21 sunspot maximum and recent geomagnetic activity data are inconsistent with an 88 year pattern. Therefore, attempts to use this periodicity in making forecasts have been discarded.

How do predictions of the sunspot cycle impact geomagnetic cycle prediction? Figure 2, reproduced from a report by R.J. Thompson [1987] illustrates the correspondence between the sunspot cycle and the number of geomagnetically disturbed days over the same time period. The geomagnetic cycle is characterized by a double peak and the minimum tends to lag the sunspot cycle minimum. For the cycles shown here (except for cycle 19) the late peak dominates. This peak is associated with coronal holes and recurrent geomagnetic activity. During odd numbered cycles the early peak, associated with significant solar flares, is generally better developed than it is in the even numbered cycles. The relative amplitude of the magnetic disturbances in each phase can be seen in figure 1 and in figure 3, which is from an historical study by Chernosky [1966] using 80 years of the Ci index. Figure 3 shows that the mean amplitude of the early peak in odd cycles is comparable with the mean amplitude of the late peak in even cycles.

So, given that most recent forecasts of sunspot cycle 22 are for a moderate-to-large cycle very similar to cycle 21, what can be expected for geomagnetic activity? The most straightforward expectation is that the magnetic activity in cycle 22 will be very similar to that experienced for cycle 21. Table 1 lists the number of days in cycle 21 that exceeded the Ap index thresholds for minor, major and severe storm levels. Approximately 10% of all days were at storm levels (Kp of at least 5). We can suppose that this will be true for cycle 22. Because 22 is an even numbered cycle, the maximum number of disturbed days is expected two or three years following sunspot maximum, or approximately 1993-4. However, the largest storms will likely follow flare or filament eruption events and could occur at any time during the cycle.

Table 1: the number of geomagnetic storm days in solar cycle 21 (June 1976 - September 1986)

Ap \geq 30 (minor storm)	417
Ap \geq 50 (major storm)	128
Ap \geq 100 (severe storm)	18

(Ap is a daily global measure of geomagnetic activity as determined by the Institut f. Geophysik, Göttingen, F.R. Germany from 13 widely-spaced observatories located at approximately 50 degrees geomagnetic latitude. The total range of Ap is 0-400 in units of 2 nT.)

What factors would change this forecast? An extremely active cycle (an excessive number of X-class flares and especially proton flares) would likely result in a large peak in geomagnetic activity roughly coinciding with the sunspot cycle peak. This 'early' peak could even exceed the later peak, but it would not necessarily diminish it. Under these conditions there could be a sustained, rather high level of geomagnetic activity from 1990 through 1994 with the possibility of a local minimum of activity, separating the 'early' and 'late' peaks, in 1992. On the other hand, if the sunspot cycle is not particularly active, and for some reason stabilizes soon near its present level, we would expect a smaller total number of days at storm level than for cycle 21, although the peak of the recurrent phase might be large and possibly reminiscent of the 'Skylab years', viz., 1973-75.

To summarize, because it is an even-numbered cycle, cycle 22 magnetic activity is expected to maximize late in the cycle (ca. 1994) and be dominated by recurrent activity from large coronal holes. However, based on predictions of a moderate-to-large sunspot cycle, there may be a significant early peak (ca. 1990) and a comparable number of severe magnetic storms to that experienced in cycle 21.

References

- Chernosky, Edwin J., Double sunspot-cycle variation in terrestrial magnetic activity, 1884-1963, J. Geophys. Res. 71, 965, 1966.
- Feynman, J., and P.F. Fougere, Eighty-eight year periodicity in solar-terrestrial phenomena confirmed, J. Geophys. Res. 89, 3023, 1984.
- Feynman, J., and X.Y. Gu, Prediction of geomagnetic activity on time scales of one to 10 years, Rev. Geophys. 24, 650, 1986.
- Schatten, Kenneth H. and Sabatino Sofia, Forecast of an exceptionally large even-numbered solar cycle, Geophys. Res. Lett. 14, 632, 1987.
- Thompson, R.J., The amplitude of solar cycle number 22, IPS Radio and Space Services Tech. Rep. TR-87-03, October, 1987.

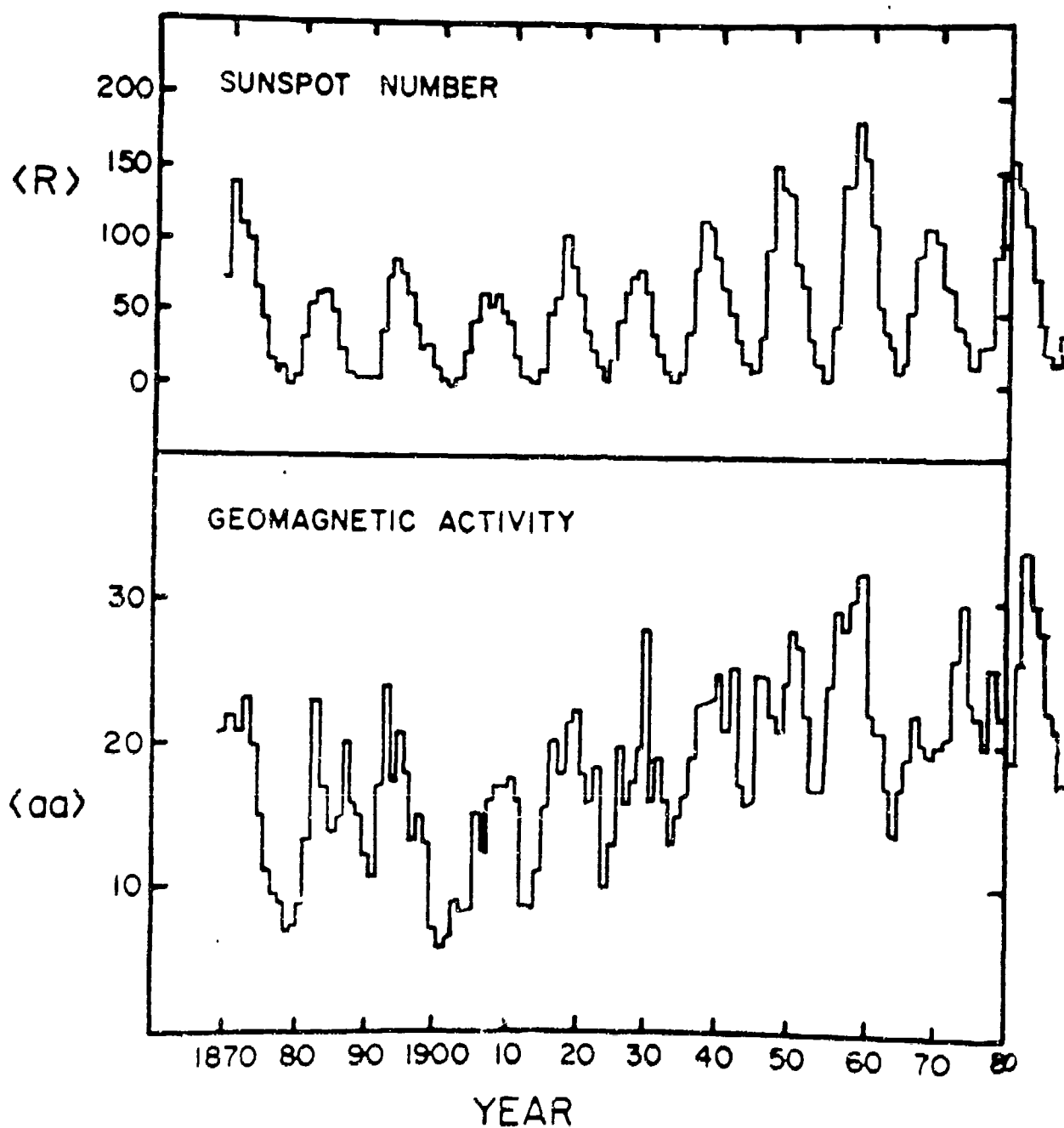


Figure 1. From Feynman and Gu [1986], plots of the annual average values of the monthly average sunspot numbers and geomagnetic aa index. Data for 1979-1986 and the numbers estimated for 1987 have been added by hand.

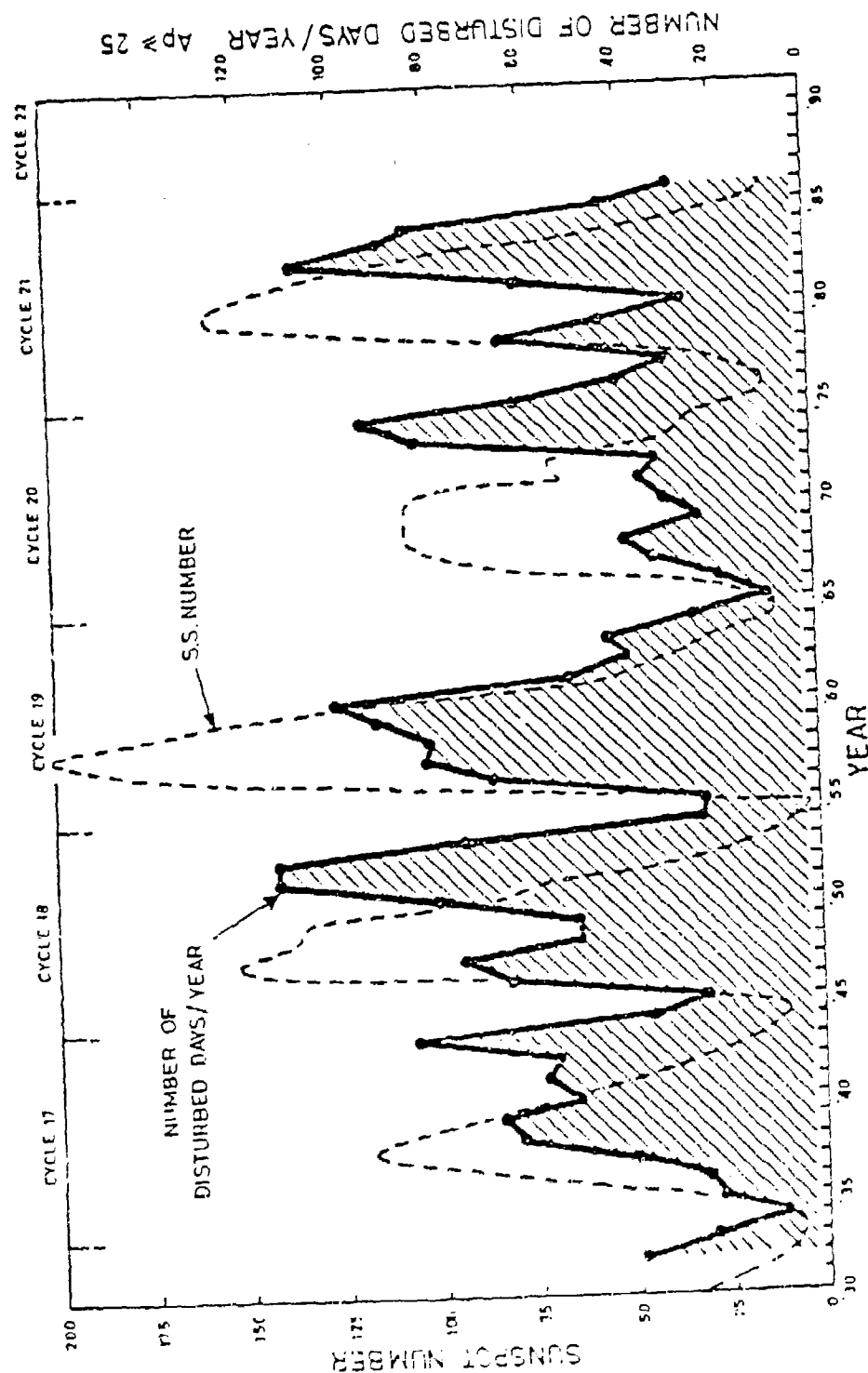


Figure 2. From Thompson (1987), the variation of the yearly-averaged sunspot number since 1930 (dashed line) and the variation in the number of geomagnetically disturbed days since 1932 (solid line). The double peak in geomagnetic activity relative to the sunspot number is evident except for cycle 19; R.J. Thompson notes that the following cycle (20) was very low.

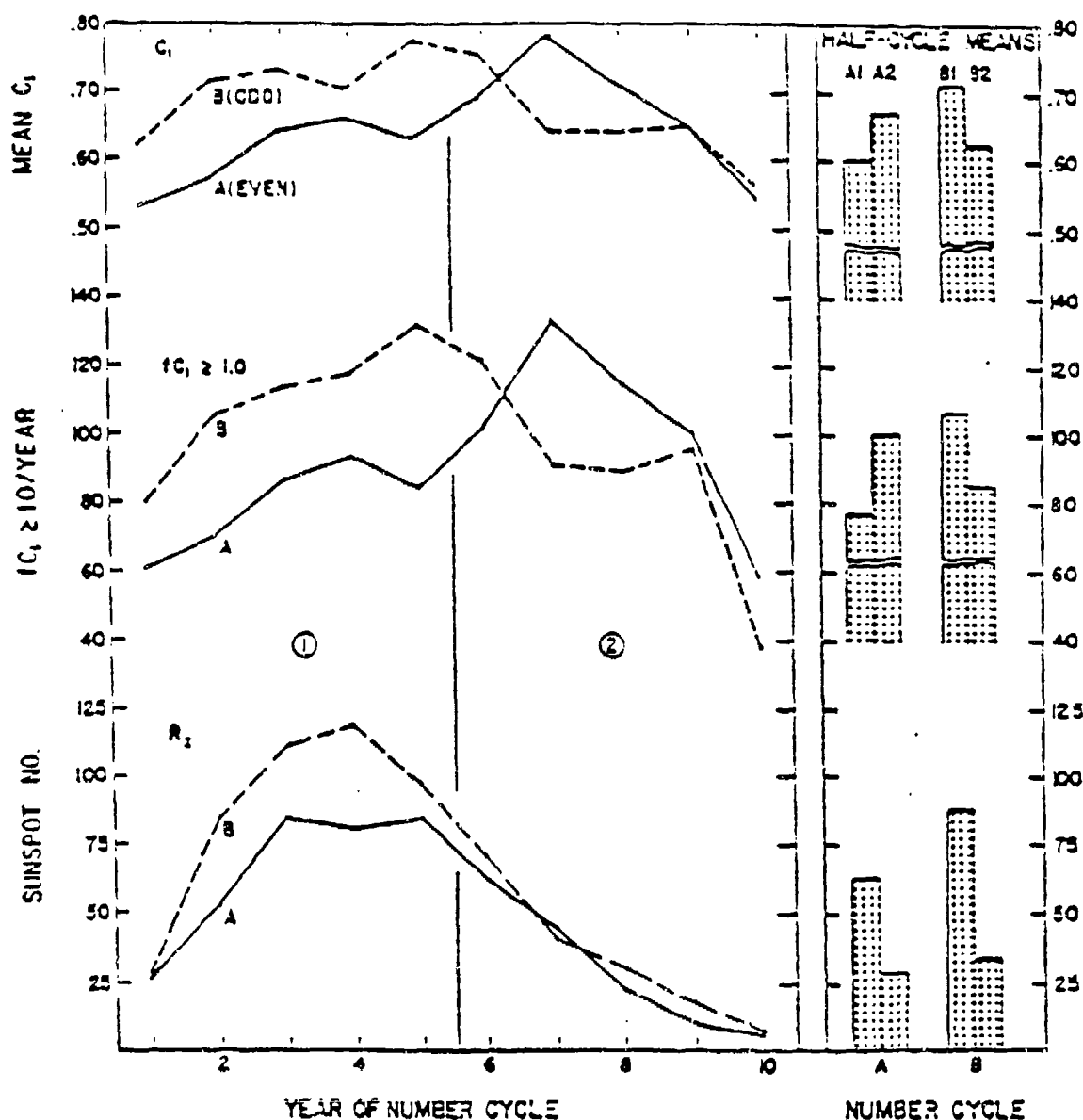


Figure 3. From Chernosky [1966], the change in geomagnetic activity, disturbed-day occurrence, and sunspot numbers for successive full and half 11-year cycles of the composite grouped data, 1884-1963. The daily C_i geomagnetic index ranges in value from 0 to 2, with $C_i=0$ signifying a quiet day, $C_i=2$ signifying disturbed conditions, and $C_i=1$ representing the intermediate case. The solid line (labeled A) plots even-numbered cycles, and the dashed line (labeled B) plots odd-numbered cycles.

Appendix: Solar Cycle Update

Reproduced from the 1 September, 1987 issue (SESC PRF 626) of the Preliminary Report and Forecast of Solar Geophysical Data, published weekly by the Joint NOAA-USAF Space Environment Services Center, 325 Broadway, R/E/SE2, Boulder, Colorado 80303.

SOLAR CYCLE UPDATE

The smoothed sunspot number reached a minimum of 12.3 in September 1986. Recent numbers have been sufficiently large that it is unlikely that a lower number will be observed in the coming months. Assuming that September stands as the minimum, we focus on the question of interest: the size and shape of the new cycle -- designated cycle 22.

A conservative prediction at this early point for cycle 22 is for a mean cycle, having a peak smoothed number of 106, shown as the mean of cycles 8-21 in figure 1 (Coffey, private communication). Most analyses use data starting with Cycle 8 (beginning in 1833) because of indications that the older data either are of a different statistical population (McNish and Lincoln, 1949) or of a lesser quality (Eddy, 1974).

For users who need a more specific prediction, we include several recently published forecasts. Reviews of long-term prediction methods are given in McIntosh (1979) and Brown (1984a). We have selected three of the general methods described in the reviews and provide representative predictions given by each. From these, we can arrive at some indication of the range of possibilities for cycle 22.

Method one is the use of direct or indirect observations of the solar magnetic field, made late in one solar cycle to predict the sunspot number in the ensuing cycle. Brown (1974) and Ohi (1976) suggested methods that correlate some measure of geomagnetic field activity near solar minimum with the peak sunspot number of the following cycle. The assumption is implied that the terrestrial field variation is dominated by solar field variations. Sargent (1978) used a variation of the Ohi method to predict a maximum smoothed number of 156 for cycle 21. The observed value was 164.5. For cycle 22, the Sargent-Ohi method predicts 118.6. Using the observation that sorting the cycles by odd and even numbers provides two sets of typical profiles, Sargent obtained the curve in figure 2 by averaging even cycles in the modern era and adjusting the result to the predicted maximum of 118.6. Other predictions using this general method are listed in Table 1.

Table 1. Predictions of Cycle 22 using observations of solar magnetic field parameters of the preceding cycle.

Author(s)	Predicted Smoothed Sunspot Number	Date of Maximum
Brown	120	----
Kane	185	1990
Sargent	118	1991
Schatten & Sofia	170	1990
Thompson	159	----

Another well-known method of prediction is comparison of the early phase of the new cycle to the average behavior of past cycles to establish a trend for the new one. A venerable technique is that of McNish and Lincoln (op. cit.) whose prediction for cycle 22 is shown in figure 1, with smoothed monthly maxima of 136 in December of 1989 and February of 1990. An updated McNish-Lincoln prediction is published monthly in Solar Geophysical Data, Prompt Reports, along with 90 percent confidence limits. The McNish-Lincoln method is most accurate when limited to predictions 12 months ahead, but for comparison we note that the method at this relative time in the last solar cycle predicted a maximum of 141 for that cycle. A maximum of 164.5 was subsequently observed. The NASA Marshall Space Flight Center Systems Analysis and Integration Laboratory at Huntsville, Alabama uses a comparison of the current solar cycle to past cycles to predict a smoothed maximum 10 cm radio flux. When their number is converted to an equivalent smoothed sunspot number, it gives a smoothed maximum number of 172. Table 2 tabulates published predictions made with the cycle comparison technique.

Table 2. Solar cycle predictions made by comparing the new cycle to past cycles.

Author(s)	Predicted Smoothed Sunspot Number	Date of Maximum
McNish & Lincoln	136	1990
Marshall Group	172	1990

As we move further into the new cycle, additional observations will allow refinement of the predictions made by the cycle comparison technique. The McNish-Lincoln technique essentially depends on the ordering of the cycles according to their rate of rise. Because of this ordering, the error bars begin to narrow through the period of rapid rise of the cycle. We expect these conditions to be met in the next one to two years.

We include a third set of predictions that use what are termed "secular techniques." These methods project future solar cycles on the basis of long-term periodicities that may exist in past cycles such as the observation of an 80 year cycle by Gleissberg (1942). Wilson (1984) provides an extensive discussion of the characteristic rise and decay times and maximum sunspot numbers of past cycles including the identification of longer period variations superimposed on the eleven-year cycle.

Table 3 Cycle 22 predictions made using secular behavior of past cycles.

Author(s)	Predicted Smoothed Sunspot Number	Date of Maximum
Wilson	107	1991

Most operational applications using solar cycle predictions require lower and upper confidence limits. For the present time, we suggest that reasonable limits are the lowest and highest cycles observed in the modern era. The two limiting cases, Cycles 14 and 19, are also shown in figure 1. Users are left to calculate their own confidence limits with the information that these are the extrema in 14 good cycles of observation.

At the time of Brown (1984a), there were already 31 reported predictions for solar cycle 22. As noted in his review, after all the predictions for a cycle are accumulated, predicted maximum numbers typically range from extremely low to very high. We have endeavored to use recently published predictions where the record of the method can be evaluated for past predictions. We apologize for omitting undoubtedly worthy techniques.

From these predictions, we conclude:

1. It is too early to make a consensus forecast with small error bars.
2. The most probable cycle maximum will be average or higher.
3. Users who need worst-case predictions may make use of the maximum value of cycle 19 and the minimum of cycle 14. They need to calculate the probability that the new cycle may still exceed one of these limits.
4. Users who need predictions with legitimate small error bars need to wait for more observations. As the new cycle progresses, the additional data points allow the prediction to be refined by comparison.

We warn that the prediction of solar cycles is inexact and that wide error bars should be assumed. NOAA assumes no responsibility for consequences of the use of these predictions. Regular updates will be provided in this publication.

References:

- Brown, G.M., 1974, Nature , 253, 482.
- Brown, G.M., 1984a, Solar-Terr. Predictions Proc. (Meudon) , 1.
- Brown, G.M., 1984b, Solar-Terr. Predictions Proc. (Meudon) , 41.
- Eddy, J.A., 1976, Science , 192, 1189.
- Gleissberg, W., 1942, Astrophys. J. , 96, 234.
- McIntosh, P.S., 1979, Solar-Terr. Predictions Proc. (Boulder) , 2, 246.
- McNish, A.G. and Lincoln, J.V., 1949, Trans. Am. Geophys. Un., 30, 673.
- Ohl, A.I., 1976, Soln. Dann. , 9, 73.
- Kane, K.P. 1987, Sol. Phys. , 108, 415
- Sargent, H.H., 1978, Proc. 28th. IEEE Vehicular Tech. Conf. (Denver) , 490
- Schatten, and Sofia, 1987, Geophys. Res. Letters , 14, 632.
- Thompson, R.J., 1985, IPS-TR-85-06 (Sydney) .
- Wilson, R.M., 1984, NASA TM-86458 (MSFC) .

From the staff of the NOAA Space Environment Laboratory including the Space Environment Services Center and from the NOAA National Geophysical Data Center Solar Terrestrial Division.

Figure 1. Observed and Predicted Sunspot Numbers from the McNish-Lincoln Analysis

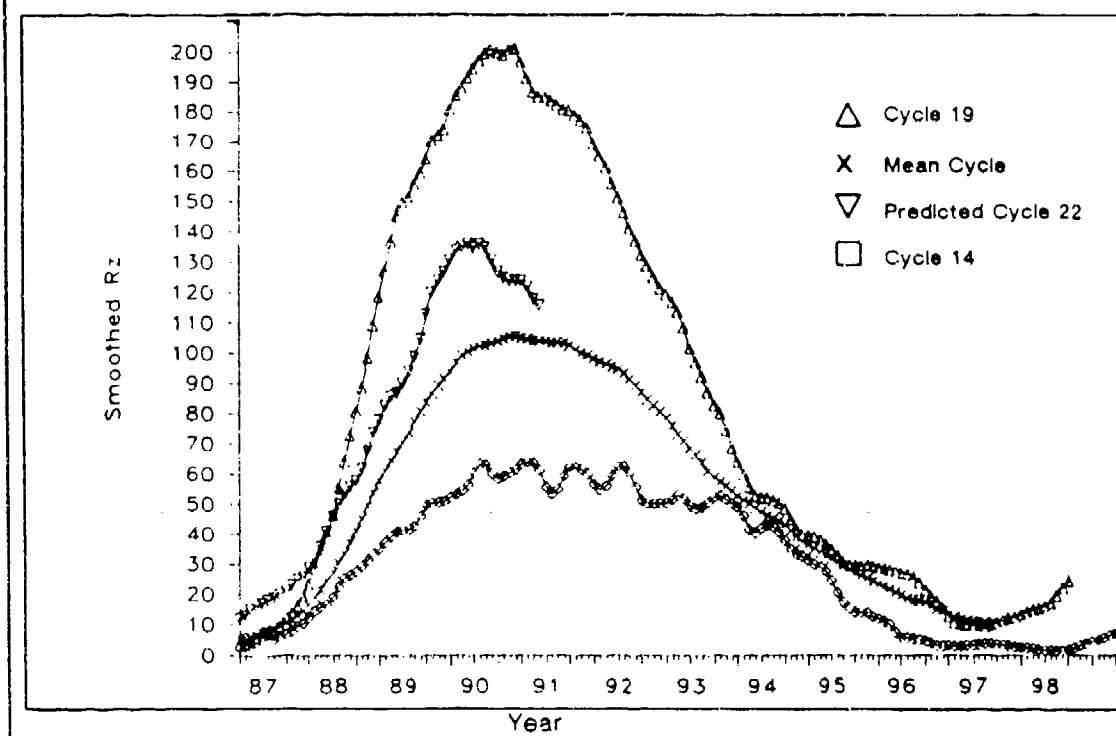
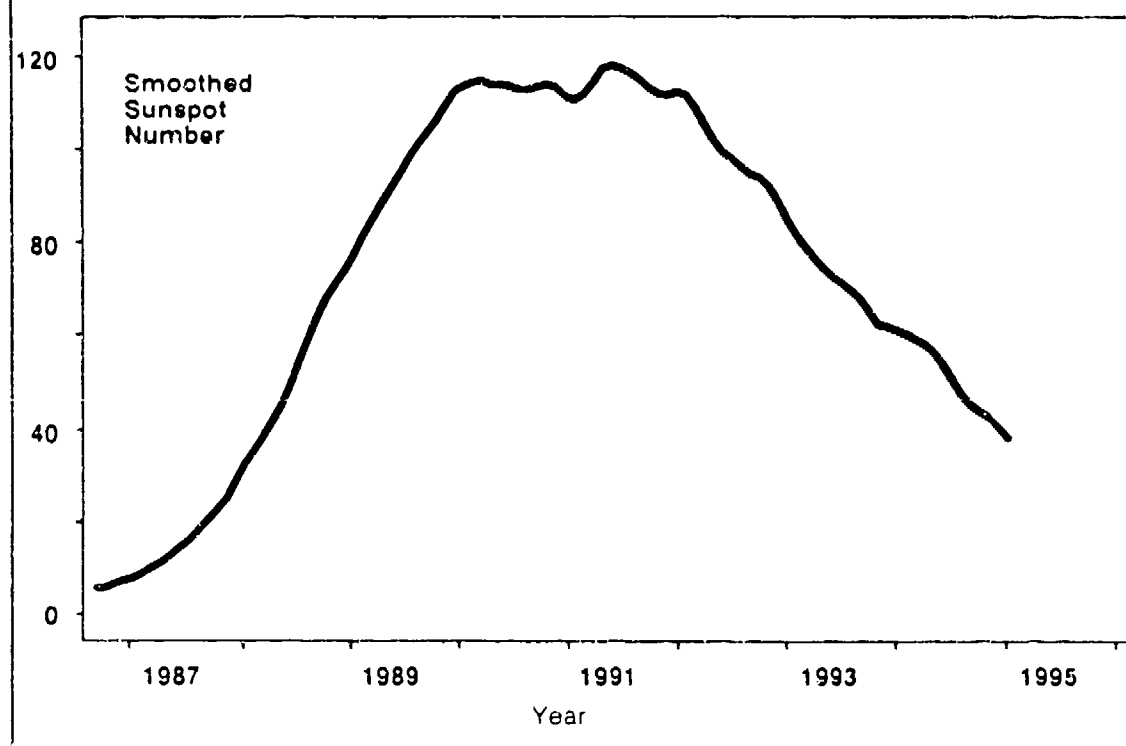


Figure 2. Predicted Sunspot Numbers from the Sargent-Ohl Method



MAGNETOSPHERIC CONVECTION AND IMSP

Nelson C. Maynard
Frederick J. Rich

Space Physics Division
Air Force Geophysics Laboratory
Hanscom AFB, MA 01731

The space environment sensor complement on the IMSP satellites is capable of continuously monitoring the total energy input into the high latitude regions from both particle precipitation and from Joule heating. Two sun-synchronous satellites in dawn-dusk and near noon-midnight orbits provide four different local time cuts through the auroral region in each hemisphere every 100 minutes coupled with the associated polar cap crossings. The energetic particle detector (SSJ/4) determines both the electron and ion precipitating fluxes in the 30 eV to 30 keV spectral range from which the total energy input can be determined as well as the conductivity in the ionosphere resulting from these sources. The magnetometer (SSM) measures the changes in the magnetic field from which field-aligned currents can be calculated. The thermal plasma instrument (SSIIES) monitors the electron density and temperature, and the ion density, temperature, variability and drift. The SSIIES instrument through its ion drift measurement will provide the first continuous monitoring of magnetospheric electric fields that are imposed on the high latitude region. The first SSIIES instrument was launched on the F8 satellite in June 1987 and will be included on all future IMSP satellites. The SSM instrument will become operational in the early nineties starting with S12. The Joule energy input can be determined from a combination of the conductivity calculated from SSJ/4 and either the field aligned currents from SSM or the electric fields determined from SSIIES. The instrument complement provides critical input drivers for the Magnetospheric Specification Model, under development for operational use by Air Weather Service, and will provide real time monitoring of the high latitude energy inputs and convection driving forces critical to dynamic density models.

High latitude convection patterns depict the motion of ions resulting from magnetospherically generated electric fields. Empirical models are now available which describe the changes in the patterns imposed by changes in the interplanetary magnetic field. Heppner and Maynard (1987) show that in addition to the change in the position of the maximum convection in the polar cap from the dusk side to the dawn side as the interplanetary magnetic field y component changes from negative to positive, the direction of the flow across the polar cap changes significantly. Since ion drag is the principal driving force for F region neutral winds, the winds will vary considerably with changes in the interplanetary magnetic field. Distorted two cell patterns, as opposed to three and four cell patterns previously proposed for the high latitude region, have been derived for when the z interplanetary component changes from negative or weakly positive to strongly positive. For both polarities of the interplanetary magnetic y component, the evening cell rotated into or around the dawn cell causing

the distortion. The choice of convection patterns in thermospheric density models is critical in that not only are they a principal driving force in the F region, but they also affect the Joule heat dissipated in the ionosphere.

The Heppner and Maynard patterns have been put in analytical form by a spherical harmonic fit using Legendre polynomials. A twelfth order fit was found to be adequate to describe the basic patterns. The resulting analytical expressions can be used directly in models. For instance, by combining the electric field model with a similar spherical harmonic fit to conductivity data based on average particle precipitation and including conductivity resulting from direct solar input, the horizontal currents can be calculated. Field aligned currents can then be determined by requiring that the divergence of the current be zero. The resulting field aligned current patterns are a good match to the patterns of Iijima and Potemra derived from magnetometer data from the TRIAD and MAGSAT satellites. The region 1 and region 2 patterns are clearly discernable with the observed overlap in the midnight and noontime regions. Height integrated Joule heat can also be determined. The results indicate that the Joule heating peaks in the pre-dusk hours. A secondary maximum exists in the midnight region when B_y is positive.

Methods of using IMSP SSIES ion drift data to determine and scale convection pattern size and shape are in progress. Methods of combining physical models with empirical models utilizing the strong points of each will soon be integrated into magnetospheric models. Better self-consistent electric field models will be important for future model improvements.

PARTICLES AND JOULE ENERGY INPUT

F. J. Rich
M. S. Gussenhoven

Space Physics Division
Air Force Geophysics Laboratory
Hanscom AFB, Massachusetts 01731

The input of energy to the high latitude ionosphere from the magnetosphere is important to the dynamics and structure of the upper atmosphere. Energy deposited in the ionospheric E-layer is transferred to the thermosphere. After solar UV radiation, particle precipitation and Joule heat represent the major energy input to the high latitude ionosphere and, in turn, to the neutral atmosphere.

The energy input to the high latitude ionosphere from particle precipitation has been extensively surveyed by AFGL using data from the DMSP satellites, by NOAA using data from the NOAA/TIROS satellites and by others. In particular, *Hardy et al.* (1985) and *Gussenhoven et al.* (1985) have given detailed maps of the energy flux of precipitating electrons. The AFGL surveys include all precipitating electron from 30 eV to 30 keV. It is generally assumed that precipitating electrons with energies less than approximately 500 eV deposit all their energy above the E-region, and only energy deposited in the E-region is transferred to the neutral atmosphere. Based upon this assumption, *Hardy et al.* (1987) have calculated average height-integrated conductivities due to precipitating electrons. It has generally been assumed that precipitating ions are not important to the energy transfer because the number flux and energy flux of ions are one to three orders of magnitudes less than the electron fluxes. While this is true much of the time in most locations in the high latitude region, the precipitating ion energy flux can be approximately equal to or even exceed the electron energy flux. This is especially true along the equatorward edge of the auroral zone during periods of high activity.

The energy input from Joule heating has not been as well studied because it can not be measured as easily or as directly. However, Joule heat represents 60% to 90% of the energy input from the magnetosphere. At AFGL, recent efforts have been made to measure Joule heat and to prepare a survey of the average quantity of Joule heat input as a function of location, geomagnetic activity and season. This is done by calculating the height-integrated conductivities and ionospheric currents from DMSP data. The conductivities are obtained from the measured precipitating electrons and from a model of the conductivity created by EUV radiation. The ionospheric currents are obtained from the measured field-aligned currents and an assumption that the majority of field-aligned currents are locally connected by Pedersen currents.

While all recent DMSP satellites have instruments to measure precipitating electrons, only the DMSP F7 satellite, which operated from Dec 83 to April 88, has a magnetometer to measure the field-aligned current. Joule heat values from individual passes of the DMSP F7 satellite have been obtained and compared with average values obtained by others. The comparisons are good and efforts are now underway to compile a Joule heat data base from which a statistical survey will be obtained.

References:

- Gussenhoven, M. S., D. A. Hardy and R. L. Carovillano, 1985. Average electron precipitation in the polar cusps, cleft and cap, *The Polar Cusp*, J. A. Holtet and A. Egeland, eds., D. Reidel Pub. Co.
- Hardy, D. A., M. S. Gussenhoven and E. Holeman, 1985. A statistical model of auroral electron precipitation, *J. Geophys. Res.*, 90, A5, 4229-4248.
- Hardy, D. A., M. S. Gussenhoven, R. Raistrick and W. J. McNeil, 1987. Statistical and functional representations of the pattern of auroral energy flux, number flux and conductivity, submitted to *J. Geophys. Res.*.

SOLAR AND MAGNETOSPHERIC INPUTS SECTIONSECTION SUMMARY

Nelson C. Maynard

Input data for use in density models for prediction purposes is available from diverse sources and locations. However, specification of what data is needed depends on the length of the prediction interval. Table 1 specifies the primary location of sources of data that must be considered for particular distances into the future for predictions. A history of data from closer to the source, i.e. the sun, is always useful no matter how far we must look forward.

Several measurement capabilities already in place or planned provide the basis for specification and short term prediction. The thermal plasma and energetic particle measurements now operational on DMSP along with the magnetometer to be operational on future DMSP spacecraft provide the data necessary for continuous monitoring of the magnetospheric energy input into the high latitude thermosphere as well as the magnetospheric convection driving force for neutral winds. The solar X-ray instrument planned for the GOES spacecraft extends into the far UV region to provide limited solar UV input data to determine the conductivity in the ionosphere caused by direct solar illumination. An extension of the range in the UV would be desirable as different wave lengths ionize different molecules and thus affect various altitudes differently. Monitoring the solar wind at the point where the Earth's gravitational pull is balanced by the Sun's in front of the Earth (libration point) is in the planning stage but not funded. These measurements of interplanetary magnetic field and solar wind parameters, which affect the size and shape of the magnetosphere as well as energy flow within the magnetosphere-ionosphere system, are critical for accurate short term forecasting.

The degree of uncertainty in predictions is always going to increase with the length of the prediction until our knowledge of the physical processes improves. For short time scales this is mitigated by the fact that the neutral atmosphere serves as an integrator of the forcing functions. Thus, inputs from near Earth measurements over the previous several hours can now be used for real time specification and limited short term prediction. Libration point monitoring of the solar wind velocity and interplanetary magnetic field will extend the prediction capability significantly. A better understanding of the physics in the whole chain from the Sun to the near Earth atmosphere as well as physical processes on the Sun will be necessary in addition to solar measurements for accurate long term prediction.

Table 1: Sources of Input Data for Density Prediction

Prediction Interval	Data Sources or Theory Needs
12-72 Hrs	<ul style="list-style-type: none"> - Better Understanding of Solar Processes - Solar Monitoring
4-12 Hrs	<ul style="list-style-type: none"> - Libration Point Monitor Solar Wind IMF
1-4 Hrs	<ul style="list-style-type: none"> - Direct Input Monitors Such as DMSP

9. SUMMARY AND CONCLUSIONS

9. SUMMARY AND CONCLUSIONS

After extensive discussions of many of the issues pertaining to the Workshop, the session chairmen developed several overall conclusions regarding the status of density and drag models and possible future progress in this area.

The density specification accuracy of semi-empirical models has reached a plateau of about 15%. Further significant progress using this approach is likely to be at a slow rate. The requirements for further improvements using this approach were summarized as follows:

a) There is an important need for additional well-calibrated data sets to provide standard references for further comparisons. Instruments need to be carefully optimized to allow for drifts, cross-calibrations, ground-truth measurements, etc. There is a need for redundancy in measurement techniques.

b) Existing data sets used within semi-empirical models need to be critically tested to verify consistency. Poorly calibrated and inaccurate data should be removed from the models.

c) Data sets should be continually examined to determine whether unmodeled systematic variations occur in the atmosphere that can be incorporated explicitly into the semi-empirical models.

d) The effects of neutral wind motions should be taken into account when incorporating data into semi-empirical models.

e) Hybrid approaches involving the simultaneous use of semi-empirical techniques as well as numerical modeling calculations should be pursued.

The workshop participants felt that further work was required to determine the absolute limit on accuracy imposed by the stochastic nature of the thermospheric medium. They also felt that in the short term the tools existed to make significant inroads towards the provision of a more accurate density specification model. These tools include the Thermosphere General Circulation Models (TGCM), and hybrid schemes such as the Vector Spherical Harmonic approach described by Killeen at this meeting. It was recognized that the AF does not presently have the capability to run a full TGCM operationally. However, there are clear areas where TGCM's can provide reliable inputs now. An intermediate quasi-analytic/empirical approach along the lines of the VSH formalism was suggested as an initial step. This would provide a base for building in additional sophistication as our capabilities improve.

A long-term program must be laid out showing how new developments in TGCM modeling can be incorporated into the operational system. It must be a planned step-by-step process involving operational people and scientists. For the longer term, since the scientific problem was felt to be a multifaceted one, an attack on a broad front would be needed to improve the basic understanding of the region. This approach would involve both theoretical and experimental elements. It was therefore suggested

that a coordinated program in density specification be initiated, involving scientists from several institutions. The elements of the program would be the following:

a) A density specification spacecraft mission, comprising redundant, well-calibrated instruments, together with supporting observations from DMSP and NOAA/TIROS, as well as ground-based measurements, such as LIDAR and incoherent scatter radar observations.

b) An investigation of gravity waves and tides to establish theoretically and experimentally the ground-floor variability.

c) An effort to compare TGCM calculations with experimental observations, to validate the TGCM in various regions of the atmosphere, leading to an improved theoretical understanding.

d) An effort to improve semi-empirical models (e.g. the Vector Spherical Harmonic approach) through continued critical evaluation of the existing data resource and the incorporation of additional well-calibrated data from the ADS density specification mission.

e) An effort to improve the quantitative specification of magnetospheric and solar thermospheric forcings through observations and theory.

f) A science team approach to the interpretative problem, with focussed workshops.

ATMOSPHERIC DENSITY AND SATELLITE DRAG
MODELS FOR AIR FORCE OPERATIONS

ATTENDANCE LIST

<u>NAME</u>	<u>ADDRESS</u>	<u>PHONE NUMBER</u>
Richard Altrock	AFGL/PHS, Sunspot, NM	505-434-1390 AV-867-7542
Dave Anderson	Hanscom AFB/AFGL/LIS	617-377-3482
G. Anderson	Hanscom AFB/AFGL/OPI	617-377-2335
John Ballenthin	Hanscom AFB/AFGL/LID	617-377-3755
Jim Bass	Radex, Inc., Lexington, MA	617-862-1717
C. L. Belt	HQ AWS/DOSP Scott AFB, IL	618-256-5847
Kris Bhavnani	Radex, Inc., Lexington, MA	617-862-1717
G. A. Bird	Univ. Sydney, Australia	61-2-682-2342
R. C. Blanchard	NASA-LRC, Hampton, VA	804-865-3031
Herbert Carlson	Hanscom AFB/AFGL/LIS	617-377-2458
K. W. Champion	Hanscom AFB/AFGL/LY	617-377-3033
Matt Colello	DET 3 HQAWS	408-752-3902
M. G. Coleman	AFGWC/WSE, Offut AFB, NE 68113	402-592-5463
R. Cormier	Hanscom AFB/AFGL/XOP	617-377-3606
A. Coster	MIT Lincoln Lab.	617-865-5500 X 5658
O. Cote	EOARD, BOX 14 FPONY 09510	AV-235-4437
P. Dao	Hanscom AFB/AFGL/LID	617-377-2081
George R. Davenport	4th Weather Wing/DN Peterson AFB	AV-692-7750
W. Denig	Hanscom AFB/AFGL/PHK	617-377-2933
Richard Donnelly	NOAA Boulder, Colorado	303-497-5100
David Evans	NOAA/SEL Boulder, Colorado	303-497-3269

<u>NAME</u>	<u>ADDRESS</u>	<u>PHONE NUMBER</u>
Cassandra Fesen	LASP/U. of Colorado	303-492-6423
George Fichtl	NASA Marshall Space Flight Cntr.	205-544-1626
Jeff Forbes	Boston University	617-353-9846
J. C. Fox	KMS Fusion, Ann Arbor, MI	313-769-8500
K. Fukui	Hanscom AFB/AFGL/LIU	617-377-4281
Charles Gallagher	Hanscom AFB/AFGL/LID	617-377-8758
Garth Gerber	KMS Fusion, Ann Arbor, MI 48108	313-769-8500
D. Gillette	Hanscom AFB/AFGL/LIS	617-377-3039
D. Grantham	Hanscom AFB/AFGL/LYA	617-377-2982
Maura Hagan	MIT Haystack Observatory, Westford, MA	617-692-4761 X 5628
P. B. Hays	Univ. Of Michigan	313-764-7220
A. E. Hedin	NASA/GSFC Greenbelt, MD	301-286-8393
M.P. Hickey	USRA/NASA MSFC, ED 44, Huntsville, AL	205-544-5692
B. J. Holmes	NASA Langley Res. Ctr., Hampton, VA	804-865-3247
H. L. Hooper	CSC, Silver Spring, MD	301-589-1545
Thomas Jacobs	AFWAL/FIGD WRIGHT PATTERSON AFB	513-255-4618
John Jasperse	Hanscom AFB/AFGL/LIS	617-377-5090
Dale Johnson	NASA/MSFC/ED44	205-544-1665
Roberta Johnson	SRI International, Menlo Park, CA	415-859-2165
Steve Johnson	DET 1, 2WS, Wright Patterson AFB	AV-785-2208 513-255-2208
JoAnn Joselyn	NOAA/SEL/SESC, Boulder, CO	303-497-5147
C. G. Justus	Geophysics Science GATEC4, Atlanta, GA	404-894-3890
Gerald Karr	Univ. of Alabama Huntsville	205-895-6330
David Kayser	Aerospace Corp. Los Angeles, CA	213-336-7016
S. L. Keil	Hanscom AFB/AFGL/PHS	505-434-1390

<u>NAME</u>	<u>ADDRESS</u>	<u>PHONE NUMBER</u>
Tim Killeen	Univ. of Michigan, Ann Arbor, MI	313-747-3430
Wayne Klemetti	Hanscom AFB, AFGL/LID	617-377-8767
Francis Kneizys	Hanscom AFB/AFGL/OPI	617-377-3654
Steve Knowles	NAVSPASUR	703-663-8191
James Koermer	AFOSR/NC	202-767-4960
Michael Kraus	Hanscom AFB/AFGL/LYA	617-377-2475
Tom Kyle	Hanscom AFB/ESD/WE	617-377-2015
Ruth P. Liebowitz	Hanscom AFB/AFGL/SULI	617-377-3643
Joseph Liu	AFSPACECOM/DOA, Peterson AFB, CO	303-554-5467
Frank A. Marcos	Hanscom AFB/AFGL/LIS	617-377-3037
Nelson Maynard	Hanscom AFB/AFGL/PHG	617-377-2431
Bob McCoy	NRL	202-767-6109
Ross T. McNutt	Hanscom AFB/AFGL/LID	617-377-8756
Larry Mendenhall	AWS/OL-F	AV-833-7719
John G. Miller	USAFETAC/DNE Scott AFB, IL 62225	618-256-5211
John N. Moss	NASA-LRC, Hampton, VA	804-865-3770
Steve Musto	AFWAL/WE	AV-785-5496
J. Nicholson	NASA Langley Research Cntr., Hampton, VA	804-865-3031
Daniel O'Connor	MIT Lincoln Laboratory	
Bill Oliver	MIT Haystack Observatory, Westford, MA	617-692-7750
W. H. Parkinson	Harvard-Smithsonian	617-495-4865
Russ Philbrick	Hanscom AFB/AFGL/LID	617-377-4944
R. H. Picard	Hanscom AFB/AFGL/LSI	617-377-2222
D. Rault	SAIC, Mclean, VA	703-821-4596
David Rees	University College London England	01-387-8341
Frederick Rich	Hanscom AFB/AFGL/PHG	617-377-2431

<u>NAME</u>	<u>ADDRESS</u>	<u>PHONE NUMBER</u>
E. Robinson	Hanscom AFB/AFGL/LCY	617-377-3840
R. G. Roble	HOA/NCAR, Box 3000, Boulder, CO	303-497-1562
Chris Roth	Radex, Inc. Lexington, MA	617-862-1717
Paul Rothwell	Hanscom AFB/AFGL/PHG	617-377-2432
Allen Rubin	Hanscom AFB, AFGL/PHK	617-377-2933
H. R. Rugge	Aerospace Corp., Los Angeles, CA	213-336-7086
Joe Rutherford	KMS Fusion, Inc.	713-481-1671
Rita Sagalyn	Hanscom AFB/AFGL/PH	617-377-3227
J. E. Salah	MIT Haystack Observatory, Westford MA	617-692-4764
Mark Sands	SAIC Mclean, VA	703-749-8645
Crystal Schaaf	Hanscom AFB/AFGL/LYA	617-377-2963
Tom Schott	AWS/DNXP, Scott AFB, IL	618-256-4781 AV-576-4781
R.W. Schunk	Utah State University, Logan, UT	801-750-2974
Ramesh Sharma	Hanscom AFB/AFGL/LSI	617-377-4198
W. E. Sharp	Univ. of Michigan, Ann Arbor, MI	313-763-6200
M.A. Shea	Hanscom AFB/AFGL/PHP	617-377-3977
Dwight Sipler	Hanscom AFB/AFGL/LID	617-377-3045
Jack Slowey	SAO Cambridge, MA	617-495-7214
R. E. Smith	125 Westbury Drive, Huntsville, AL	205-881-5190
J. M. Straus	The Aerospace Corp., Los Angeles, CA	213-336-8182
William Swider	Hanscom AFB/AFGL/LID	617-377-3891
Tom Tascione	HQ MAC/XPPT	618-256-2351
C. R. Tschan	AWS/DNXP Scott AFB, IL	618-256-4781
D. J. Thomas	KMS Fusion Inc., Ann Arbor, MI	313-769-8500 X 511
Kent Tobiska	LASP, Boulder, CO	303-492-6527

<u>NAME</u>	<u>ADDRESS</u>	<u>PHONE NUMBER</u>
J. W. Usry	NASA Langley Research Center	804-865-3274
Bob Vincent	Hanscom AFB/AFGL/LIS	617-377-3476
William J. Wagner	NOAA/Space Environment Lab. Boulder, CO	303-497-3274
R. L. Walterschild	Aerospace Corp., Los Angeles, CA	213-336-7352
J. Winick	Hanscom AFB/AFGL/LSI	617-377-3619
S. Zimmerman	Hanscom AFB/AFGL/LIS	617-377-3976